

nature

CELLULAR FLUIDICS

Bio-inspired 3D networks for transport of liquids and gases

Nonillion species
Getting to grips with the vast variety of viruses

Turning the tide
Five ways to ensure flood research will benefit the vulnerable

Hitching a ride
How birds might help plants to relocate in a warming world

Vol. 595 No. 7880

Nature.2021.07.03

[Sat, 03 Jul 2021]

- [This Week](#)
- [News in Focus](#)
- [Opinion](#)
- [Work](#)
- [Research](#)
- [Amendments & Corrections](#)

| [Next section](#) | [Main menu](#) |

Donation

| [Next section](#) | [Main menu](#) |

This Week

- **[Lithium-ion batteries need to be greener and more ethical](#)** [29 June 2021]
Editorial • Batteries are key to humanity's future — but they come with environmental and human costs, which must be mitigated.
- **[COVID's lesson for climate research: go local](#)** [29 June 2021]
World View • To help planners adapt to a warming world, find ways to make predictions practical.
- **[Meddling with RNA slicing cuts a tumour down to size](#)** [24 June 2021]
Research Highlight • Experiments in mice show promise for drugs that modify the integral process called RNA splicing.
- **[Lead used in petrol decades ago dirties London's air today](#)** [24 June 2021]
Research Highlight • Use of the toxic pollutant in fuel was curbed in the 1980s, but it lingers in airborne particles.
- **[Climate warming leaves the US Southwest high and dry](#)** [21 June 2021]
Research Highlight • Humidity on summer days has declined since 1950, threatening water supplies and increasing the risk of wildfires.
- **[Prehistoric dwarf elephants lost weight in no time](#)** [22 June 2021]
Research Highlight • Natural selection tends to shrink large animals living in places with limited food.
- **[Red light, green light: both signal 'go' to deadly algae](#)** [24 June 2021]
Research Highlight • Artificial lighting thought to be more wildlife-friendly than white light could encourage algal blooms.
- **[When digging up the dead was decorous](#)** [23 June 2021]
Research Highlight • Death cults in early medieval Europe included inspections of mortal remains.
- **[Household water crisis affects millions in the United States](#)** [22 June 2021]

Research Highlight • People living in poor neighbourhoods often lack access to running water and plumbing.

| [Next section](#) | [Main menu](#) | [Previous section](#) |

- EDITORIAL
- 29 June 2021

Lithium-ion batteries need to be greener and more ethical

Batteries are key to humanity's future — but they come with environmental and human costs, which must be mitigated.





•

[Download PDF](#)



Around 70% of cobalt is mined in the Democratic Republic of Congo, where workers include children and families and conditions are unsafe. Credit: Sebastian Meyer/Corbis News/Getty

A low-carbon future rests on an essential, yet also problematic, technology. Lithium-ion rechargeable batteries — already widely used in laptops and smartphones — will be the beating heart of electric vehicles and much else. They are also needed to help power the world's electric grids, because renewable sources, such as solar and wind energy, still cannot provide energy 24 hours a day. The market for lithium-ion batteries is projected by the industry to grow from US\$30 billion in 2017 to \$100 billion in 2025.

But this increase is not itself cost-free, as *Nature Reviews Materials* explored in [a recent series of articles](#). Lithium-ion technology has downsides — for people and the planet. Extracting the raw materials, mainly lithium and cobalt, requires large quantities of energy and water. Moreover, the work takes place in mines where workers — including children as young as seven — often face unsafe conditions.

Policymakers, industry leaders and researchers need to mitigate these problems, and quickly, to reduce the unintended consequences of an important technology. One crucial intervention, which needs further study, is the acceleration of battery reuse instead of, or in addition to, recycling them or disposing of them in landfills.



The rise and rise of lithium

Around one-third of the world's lithium — the major component of the batteries — comes from salt flats in Argentina and Chile, where the material is mined using huge quantities of water in an otherwise arid area. Battery-grade lithium can also be produced by exposing the material to very high temperatures — a process used in China and Australia — which consumes large quantities of energy. There are ways to extract lithium more sustainably: in Germany and the United Kingdom, for example, pilot projects are [filtering lithium from hot brines beneath granite rock](#).

Cobalt is an important part of a battery's electrode, but around 70% of this element is found in just one country: the Democratic Republic of the Congo (DRC). Around 90% of the DRC's cobalt comes from its industrial mines (90,000 tonnes annually). But in a country where people earn, on average, less than \$1,200 annually, the world's demand for cobalt has attracted thousands of individuals and small businesses, called artisanal miners — and child labour and unsafe working practices are rife.

Chemists are researching ways to replace cobalt with more abundant metals such as iron or manganese ([J. V. Laveda et al. Chem. Commun. 52, 9028–9031 \(2016\)](#); [R. Sharpe et al. J. Am. Chem. Soc. 142, 21799–21809; 2020](#)). But human-rights groups such as Amnesty International say this should not detract from cleaning up the DRC's existing industry by providing jobs in safe conditions.

Many countries are aware that mining needs to be done responsibly and more sustainably. Yet some are advocating policies — especially in battery recycling — that risk having a detrimental impact on the environment.



A world without electronic waste

The European Union, for example, requires companies to collect batteries at the end of their life and either repurpose them or dismantle them for recycling. The current requirement is for 45% of the EU's used batteries to be collected — but few of these are lithium-ion batteries. This is partly because such batteries are often built into the devices they power and are hard to dismantle, or the devices themselves are valuable, which means they are likely to be exported for resale and disappear from the EU unreported. Meanwhile, the EU is considering a 70% target for batteries to be collected by 2030. In addition, it wants 4% of the lithium in new batteries made in the EU to be from recycled material by 2030, increasing to 10% by 2035.

Such requirements could have unintended consequences. As batteries improve, they will last longer. But if the EU mandates a higher collection rate, companies might feel compelled to take them out of service prematurely — to meet the numerical collection target — even though they could still have useful life left.

Similarly, there could be adverse consequences to mandating the inclusion of more recycled material in lithium-ion batteries. There's already a shortage of recycled material. So, to satisfy the new recycling rules, Europe's manufacturers could, perversely, need to import recycled material, in particular from China — which, along with South Korea, has become an important global centre for battery recycling. This would have a considerable carbon footprint. There is also a risk that battery production will stall because there isn't enough recycled material available.

Battery reuse is one potential solution that more countries should be considering — a target for reuse is not yet part of the EU proposal. Although batteries do eventually run out completely, many are taken out of use when they have merely become inefficient for a particular use, such as powering a car, but still have plenty of life in them for less-intensive applications, such as renewable-energy storage, as Anke Weidenkaff at the Fraunhofer Research Institution for Materials in Germany and her colleagues write ([A. Weidenkaff et al. *Nature Rev. Mater.* 6, 462–463; 2021](#)).

Without incentives in place for battery reuse and repurposing, incinerating batteries or sending them overseas for recycling will remain more economical. A shift in thinking is needed: scientists should consider how materials can be recycled, reused and repurposed as they design them.

Batteries are crucial for Earth's low-carbon future. It's in everyone's interests to make sure they are clean, safe and sustainable.

Nature 595, 7 (2021)

doi: <https://doi.org/10.1038/d41586-021-01735-z>

Editors' note: This Editorial is the first in an occasional series on materials and the circular economy that will run during 2021.

Related Articles

-  [The rise and rise of lithium](#)
-  [A world without electronic waste](#)
-  [Raw materials for a truly green future](#)
-  [Nature Index 2021 Materials science](#)
-  [COVID-19 disruptions to tech-metals supply are a wake-up call](#)
- [Mining our green future](#)

Subjects

- [Climate change](#)
- [Materials science](#)
- [Policy](#)
- [Technology](#)

[Jobs from Nature Careers](#)

- - - [All jobs](#)
 - - **[PhD Student \(m/f/div\) in Bioinformatics](#)**

[Max Planck Institute for Molecular Genetics \(MPI-MG\)](#)

[14195 Berlin, Germany](#)

[JOB POST](#)

■ [PhD Student \(m/f/div\) in Bioinformatics](#)

[Max Planck Institute for Molecular Genetics \(MPI-MG\)](#)

[14195 Berlin, Germany](#)

[JOB POST](#)

■ [PhD candidate - the neurodevelopmental disorder PURA Syndrome \(f/m/x\)](#)

[Helmholtz Zentrum München - German Research Center for Environmental Health \(HMGU\)](#)

[Neuherberg \(bei München\), Germany](#)

[JOB POST](#)

■ [PhD in Molecular Obesity Research within the Collaborative Research Center 1052 "Obesity Mechanisms" \(f/m/x\)](#)

[Helmholtz Zentrum München - German Research Center for Environmental Health \(HMGU\)](#)

[Leipzig, Germany](#)

[JOB POST](#)

[Download PDF](#)

Related Articles

-  [The rise and rise of lithium](#)
-  [A world without electronic waste](#)
-  [Raw materials for a truly green future](#)
-  [Nature Index 2021 Materials science](#)
-  [COVID-19 disruptions to tech-metals supply are a wake-up call](#)
- [Mining our green future](#)

Subjects

- [Climate change](#)

- [Materials science](#)
 - [Policy](#)
 - [Technology](#)
-

This article was downloaded by **calibre** from <https://www.nature.com/articles/d41586-021-01735-z>

| [Section menu](#) | [Main menu](#) |

- WORLD VIEW
- 29 June 2021

COVID's lesson for climate research: go local



To help planners adapt to a warming world, find ways to make predictions practical.

- [Alice C. Hill](#) 0

1. [Alice C. Hill](#)

1. Alice C. Hill is the David M. Rubenstein Senior Fellow for Energy and the Environment at the Council on Foreign Relations and the author of *The Fight for Climate After COVID-19*.

[View author publications](#)

You can also search for this author in [PubMed](#) [Google Scholar](#)





•

[Download PDF](#)

For decades, scientists have built and refined global climate models to predict the changes wrought by greenhouse-gas emissions. The models capture broad trends; they don't make localized predictions. But such predictions are what municipal planners and those running facilities such as power stations and wastewater-treatment plants need to anticipate potential disasters, be they floods in Indonesia, heatwaves in Portugal, or a cold snap that leaves Texans in the dark.

This point was driven home to me by Patsy Parker, mayor of Perdido Beach, Alabama, a small town on the Gulf of Mexico surrounded on three sides by water. In 2004, flooding caused by Hurricane Ivan carried off chunks of the beachfront. I met Parker in 2013, when she served on the State, Local, and Tribal Leaders Task Force on Climate Preparedness and Resilience set up by then-US-president Barack Obama, and I was a climate adviser on the National Security Council. “I’m just a part-time mayor in a small town,” she said. “I don’t have a big planning staff or any resources. So how can I even know the size of the threats we are facing, and what can I do to protect the people of my town?”

Almost a decade later, information is still lacking about extremes at a particular location, and climate adaptation has lagged. In June 2021, the chair of the Adaptation Committee of the UK Climate Change Committee described the topic as “under-resourced, underfunded and often ignored”.



[‘Does anyone have any of these?’ : Lab-supply shortages strike amid global pandemic](#)

During the pandemic, scientists around the globe switched gears to find the answers the world needed. They rapidly solved protein structures, tracked viral genomics, repurposed drugs and developed vaccines, apps and behaviour-change strategies. Our warming world will cause even more disruption, but the research response is too little, too removed and too

theoretical. There needs to be a broader, open shift to apply science to local climate adaptation.

According to the US National Oceanic and Atmospheric Administration, in 2020, the United States suffered a record-smashing 22 weather and climate disasters that caused at least US\$1 billion in damages, including wildfires and hailstorms. Globally, the tally for disasters exacerbated by climate change soared to an estimated \$210 billion. Investing in risk reduction before disaster strikes can save about \$6 for every \$1 spent. In lower-income countries, every \$1 invested in more-resilient infrastructure yields \$4 in benefit.

In my book *The Fight for Climate After COVID-19*, I focus on how communities continue to build homes in areas destined to burn or flood as climate change worsens. Without information about where and how damaging events are likely to unfold, choosing the right adaptations to invest in is little more than guesswork. The smallest resolution of climate models is generally at a scale of 100–150 square kilometres. That sort of area can span several towns and extreme differences. Data about average precipitation isn't much help to a planner deciding where to allow a new housing development or a city council weighing up an update to building codes.

And it's not just discrete communities that need access to localized climate predictions. As supply chains stretch, their vulnerability to disruption grows. One break can cause a cascade of shocks. China has 90% of the world's capacity to make a key component of penicillin. In 2020, coronavirus-related restrictions and severe flooding there disrupted pharmaceutical supply chains, leaving other nations vulnerable during the pandemic. Even when global capacity is less concentrated, disruptions can be huge. In 2011, severe flooding in Thailand shut down factories producing 40% of the world's hard disk drives, doubling prices and squeezing computer manufacturers.



Protect global supply chains for low-carbon technologies

Some businesses have invested in advanced technologies to improve supply-chain management, including in response to the breaks induced by the pandemic. But much more needs to be done.

Basic, localized climate-risk information should be invested in as a public good, like education, law enforcement and vaccination. Wealthier communities and businesses are already hiring consultants to provide tailored climate-risk information. But these services are expensive. A client wanting information about its exposure to hazards such as floods, fires and extreme heat could pay upwards of \$1 million for a year-long subscription; a large corporation would pay a much steeper price. Such for-profit systems leave poor communities without access to information they need to prepare for climate risks.

Governments must work with academia, non-governmental organizations and the private sector to develop publicly available models and tools to give decision-makers basic information at the scale they need. This approach has proved useful for another catastrophic risk: earthquakes. A team of scientists, local and national governments, and partner organizations created InaSAFE, a free platform that produces natural-hazard scenarios to help inform planning and preparedness efforts. After a 6.5-magnitude earthquake

hit Aceh in Indonesia in 2016, disaster managers used it to rapidly determine which communities faced the greatest likelihood of damage.

High-income nations can jump-start the science of practical climate predictions — as they did with vaccine development for COVID-19 — although the need is especially great in low-income countries. It's time to apply science to develop local solutions to the global climate crisis.

Nature **595**, 9 (2021)

doi: <https://doi.org/10.1038/d41586-021-01747-9>

Related Articles



- [Protect global supply chains for low-carbon technologies](#)



- ['Does anyone have any of these?': Lab-supply shortages strike amid global pandemic](#)



- [Farmers transformed how we investigate climate](#)

Subjects

- [Research management](#)
- [Climate change](#)

Jobs from Nature Careers

- - - [All jobs](#)
 - - [PhD Student \(m/f/div\) in Bioinformatics](#)

[Max Planck Institute for Molecular Genetics \(MPI-MG\)](#)

[14195 Berlin, Germany](#)

[JOB POST](#)
 - [PhD Student \(m/f/div\) in Bioinformatics](#)

[Max Planck Institute for Molecular Genetics \(MPI-MG\)](#)

[14195 Berlin, Germany](#)

[JOB POST](#)
 - [PhD candidate - the neurodevelopmental disorder PURA Syndrome \(f/m/x\)](#)

[Helmholtz Zentrum München - German Research Center for Environmental Health \(HMGU\)](#)

[Neuherberg \(bei München\), Germany](#)

[JOB POST](#)
 - [PhD in Molecular Obesity Research within the Collaborative Research Center 1052 "Obesity Mechanisms" \(f/m/x\)](#)

Helmholtz Zentrum München - German Research Center for Environmental Health (HMGU)

Leipzig, Germany

JOB POST

Download PDF

Related Articles



- Protect global supply chains for low-carbon technologies



- ‘Does anyone have any of these?’: Lab-supply shortages strike amid global pandemic

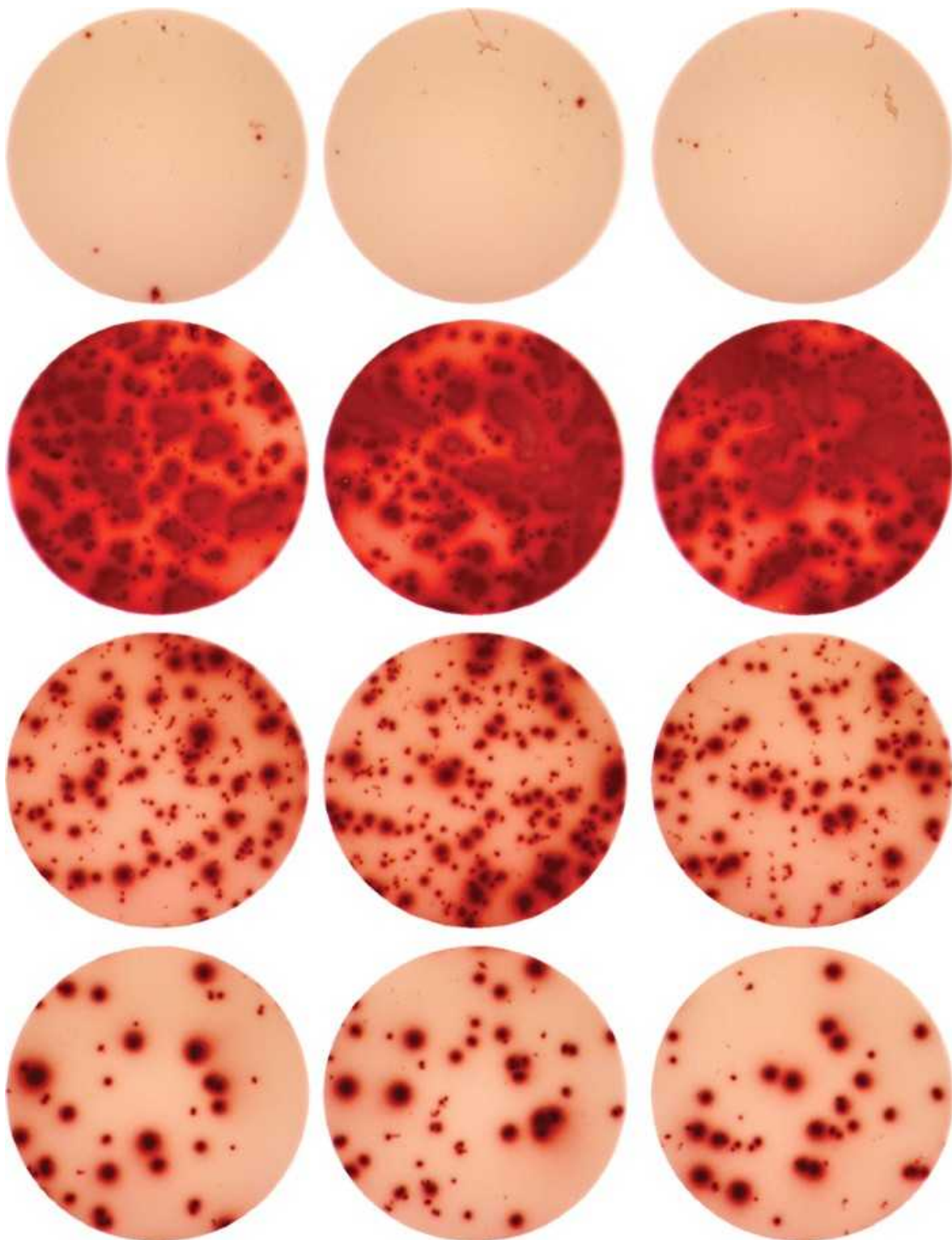


- Farmers transformed how we investigate climate

Subjects

- Research management
- Climate change

| [Section menu](#) | [Main menu](#) |



Mouse T cells have a strong immune reaction (dark spots, bottom two rows) to unusual protein fragments generated by drugs that affect RNA splicing; T

cells that are unexposed (top) or treated with a known antigen (second row) show a different pattern. Credit: Sydney X. Lu, Omar Abdel-Wahab and Robert K. Bradley

Cancer

24 June 2021

Meddling with RNA slicing cuts a tumour down to size

Experiments in mice show promise for drugs that modify the integral process called RNA splicing.





•

Drugs that alter how tumours' RNA molecules are chopped up and stitched back together can enhance the effect of some cancer treatments, according to a study in mice.

Unusual proteins produced by cancer cells can sometimes trigger immune responses against tumours. To amplify such reactions, Omar Abdel-Wahab at the Memorial Sloan Kettering Cancer Center in New York City, Robert Bradley at the Fred Hutchinson Cancer Research Center in Seattle, Washington, and their colleagues, tinkered with the cellular process called RNA splicing, in which RNA molecules are cut and some of the fragments are rejoined. This produces a final RNA that codes for a protein. As a result,

changes to the splicing process can boost the production of atypical protein sequences.

The team treated mice with compounds that alter RNA splicing, and found that this yielded a host of protein fragments capable of rousing immune cells called T cells. The treatment also slowed tumour growth and enhanced the effect of cancer drugs that boost immune responses against tumours.

[Cell \(2021\)](#)

- [Cancer](#)

This article was downloaded by **calibre** from <https://www.nature.com/articles/d41586-021-01717-1>

| [Section menu](#) | [Main menu](#) |



The widespread use of lead as a fuel additive in the twentieth century has had a lingering effect on London's air quality. Credit: David Gee/Alamy

Environmental sciences

24 June 2021

Lead used in petrol decades ago dirties London's air today

Use of the toxic pollutant in fuel was curbed in the 1980s, but it lingers in airborne particles.





•

More than 20 years after UK officials banned leaded car fuel, lead from historical petrol use still lingers in the London air.

Atmospheric concentrations of the toxic pollutant fell markedly in Europe and North America after lead's use as a petrol additive was reduced in the late 1980s. Eléonore Resongles and Dominik Weiss at Imperial College London, and their colleagues, found that old lead in airborne particles continues to affect air quality in the British capital to this day.

The researchers analysed the chemical composition of lead in airborne particles collected between 2014 and 2018 at two central London locations, one at street level and the other at rooftop level. Comparison with historical

measurements showed that the particles' chemical profile remained unchanged over the past decade, suggesting that the sources of air pollution did not change either.

The chemical profiles do not vary seasonally, an indication that persistent lead pollution comes from road dust that is thrown into the air rather than from current coal burning, the researchers say.

[Proc. Natl Acad. Sci. USA \(2021\)](#)

- [Environmental sciences](#)

This article was downloaded by **calibre** from <https://www.nature.com/articles/d41586-021-01723-3>

| [Section menu](#) | [Main menu](#) |



In places like Arizona, heat-relief stations are set up to help keep people hydrated during periods of extreme heat. Credit: Caitlin O'Hara/Getty

Climate sciences

21 June 2021

Climate warming leaves the US Southwest high and dry

Humidity on summer days has declined since 1950, threatening water supplies and increasing the risk of wildfires.





•

It isn't just getting hotter in the US Southwest — the region's climate is also getting drier.

As global temperatures rise, the atmosphere should, theoretically, get damper because warmer air can hold more water. But that prediction might not hold true in all locations, particularly arid regions.

Karen McKinnon at the University of California, Los Angeles, and her colleagues studied temperature and humidity measurements gathered in summer in the Southwest between 1950 and 2019. During this period, atmospheric humidity declined, with the biggest drops seen on hot days.

The drier conditions are due to a drop in the amount of moisture in the soil — which can evaporate into the air — and the chances of days being both dry and hot increasing over time. That raises the risk of wildfires and of much-needed water evaporating from reservoirs.

Regional officials should prepare for these impacts of lower humidity, the scientists say.

Nature Clim. Change (2021)

- [Climate sciences](#)

This article was downloaded by **calibre** from <https://www.nature.com/articles/d41586-021-01660-1>

| [Section menu](#) | [Main menu](#) |



The skeleton of a dwarf elephant found on the island of Sicily, where the creatures underwent a remarkably rapid reduction in size. Credit: Museo Geologico Gemmellaro/SiMuA/Univ. Palermo

Palaeontology

22 June 2021

Prehistoric dwarf elephants lost weight in no time

Natural selection tends to shrink large animals living in places with limited food.





•

Ancient elephants that colonized the island of Sicily no earlier than 200,000 years ago shrank drastically in size generation by generation, probably owing to food scarcity.

The Mediterranean island, now part of Italy, has hosted multiple lineages of miniature elephants over the millennia. Sina Baleka at the University of Potsdam in Germany and her colleagues wanted to know just how fast these lineages shrank.

DNA analysis of a fossil from Puntali Cave suggests that it came from a member of the extinct genus *Palaeoloxodon*. The researchers estimate that this individual would have been just 2 metres tall at the shoulder and would

have weighed 1.7 tonnes. Radiocarbon dating and analysis of protein degradation in the tooth enamel suggest that the elephant died between 175,500 and 50,000 years ago. This petite proboscidean was a direct descendant of the straight-tusked elephant, *Palaeoloxodon antiquus* — estimated to have been 3.7 metres tall with a mass of 10 tonnes — and belonged to a species that seems to have diverged from *P. antiquus* around 400,000 years ago.

Over time, this lineage shrunk to less than 20% of its original mass, at a rate that could have been as high as 200 kilograms per generation, the scientists conclude.

[Curr. Biol. \(2021\)](#)

- [Palaeontology](#)

This article was downloaded by **calibre** from <https://www.nature.com/articles/d41586-021-01659-8>

| [Section menu](#) | [Main menu](#) |



Green and red lighting might be good for migratory birds and sea turtles, but could have undesirable effects if marine algae are present. Credit: Getty

Ecology

24 June 2021

Red light, green light: both signal ‘go’ to deadly algae

Artificial lighting thought to be more wildlife-friendly than white light could encourage algal blooms.





•

Green or red lights in seaside areas have been proposed as alternatives to white light to protect wildlife. But new experiments show that exposure to red or green light at night boosts the growth of some ocean algae — including species known to rob waters of oxygen.

Little is known about the impact of artificial light on marine life, even though many brightly lit cities are coastal. To address that knowledge gap, Sofie Spatharis at the University of Glasgow, UK, and her colleagues exposed a mix of microscopic marine algae collected from Scottish waters to standard white light. They also exposed the mixture to red and green lights,

which have been proposed to minimize impacts on sea turtles and migratory seabirds, respectively.

The team found that all light colours enhanced growth of the microalgae mix. Red light had the most pronounced effect, doubling the number of cells produced. The proportions of species in the mixture also shifted: both red and green light especially favoured growth of harmful species in the *Skeletonema* genus, which form dense blooms that are deadly to fish.

[Proc. R. Soc. B \(2021\)](#)

- [Ecology](#)

This article was downloaded by **calibre** from <https://www.nature.com/articles/d41586-021-01722-4>

| [Section menu](#) | [Main menu](#) |



Some medieval corpses were revisited and rearranged within the container in which they had been interred. Credit: Éveha—*Études et valorisations archéologiques*

Archaeology

23 June 2021

When digging up the dead was decorous

Death cults in early medieval Europe included inspections of mortal remains.





•

People living in Europe some 1,500 years ago regularly reopened graves — but not to pilfer precious artefacts.

Thousands of European graves were reopened between the fifth and eighth centuries AD, a practice that archaeologists have often regarded as tomb raiding. Alison Klevnäs at Stockholm University and her colleagues reanalysed data on dozens of ancient burial places across Europe, from Transylvania in Romania to southeast England. They found that the reopening custom spread during the sixth century and peaked in the seventh century.

Some graves appear to have been opened before the buried bodies were fully decomposed, and in some cases corpses were moved around within intact coffins, which suggests that grave reopening happened soon after burial. In one case, a dog was added to a grave.

Grave openers often removed items from graves, but tended to leave valuable objects, including those made of silver and gold, instead taking artefacts such as brooches and swords. Many of these items were in poor condition and would have had little practical use or economic value. The findings suggest that graves were reopened not for robbing, but as part of widespread mortuary rituals, the authors say.

[Antiquity \(2021\)](#)

- [Archaeology](#)

This article was downloaded by **calibre** from <https://www.nature.com/articles/d41586-021-01695-4>

| [Section menu](#) | [Main menu](#) |



Almost 500,000 US households lack proper plumbing, which includes having a faucet in the sink. Credit: Bonnie Jo Mount/*The Washington Post*/Getty

Public health

22 June 2021

Household water crisis affects millions in the United States

People living in poor neighbourhoods often lack access to running water and plumbing.





•

A legacy of environmental injustice has left millions in the United States without access to clean water and hundreds of thousands without proper plumbing.

For the past two decades, water and sanitation problems have disproportionately affected low-income and non-white households in the country. To map the full scope of the crisis, Tom Mueller at Utah State University in Logan and Stephen Gasteyer at Michigan State University in East Lansing gathered the most recently available data from the US Census Bureau and the Environmental Protection Agency.

The researchers examined how many people lacked complete plumbing — meaning access to hot and cold water, a sink with a faucet, and a bath or shower — and how many lacked clean water, indicated by violations of or noncompliance with water regulations. Between 2014 and 2018, almost 500,000 households did not have complete plumbing. In 2020, 1,165 community water systems were not of adequate quality, and more than 21,000 facilities that discharged directly into US waters posed a severe level of environmental threat.

These water hardships seem to cluster in certain regions, such as Puerto Rico, Appalachia and the Intermountain West. The crisis is disproportionately associated with older, poorer, less-educated people, and populations with higher numbers of people with Indigenous or other non-white backgrounds, the authors say.

Nature Commun. (2021)

- [Public health](#)

This article was downloaded by **calibre** from <https://www.nature.com/articles/d41586-021-01704-6>

News in Focus

- **[Alien view of Earth and deleted coronavirus sequences](#)** [30 June 2021]
News Round-Up • The latest science news, in brief.
- **[Astronomers victimized colleagues — and put historic Swedish department in turmoil](#)** [22 June 2021]
News • Investigations at Lund University found the high-ranking pair guilty of bullying, but staff members say stronger action is needed to repair the damage.
- **[Delta coronavirus variant: scientists brace for impact](#)** [22 June 2021]
News • The rapid rise of the highly transmissible strain in the United Kingdom has put countries in Europe, North America and Africa on watch.
- **[Mathematicians welcome computer-assisted proof in ‘grand unification’ theory](#)** [18 June 2021]
News • Proof-assistant software handles an abstract concept at the cutting edge of research, revealing a bigger role for software in mathematics.
- **[Mysterious skull fossils expand human family tree — but questions remain](#)** [25 June 2021]
News • Fossilized bones found in Israel and China, including a specimen named ‘Dragon Man’, could belong to new types of ancient human. But the findings have sparked debate.
- **[Why Uruguay lost control of COVID](#)** [25 June 2021]
News • Complacency and a coronavirus variant help to explain why the country, once a pandemic success story, couldn’t withstand the surge now rocking South America.
- **[Beyond coronavirus: the virus discoveries transforming biology](#)** [30 June 2021]
News Feature • SARS-CoV-2 is just one of nonillions of viruses on our planet, and scientists are rapidly identifying legions of new species.

- NEWS ROUND-UP
- 30 June 2021

Alien view of Earth and deleted coronavirus sequences

The latest science news, in brief.





•

[Download PDF](#)



An illustration of Earth from space illuminated by the Sun. Stars with a past or future view of Earth as a transiting exoplanet appear brightened. Credit: OpenSpace/American Museum of Natural History

Aliens would glimpse Earth from these 2,000 stars

Astronomers have pinpointed 2,034 stars from which, in the not-too-distant past or future, [Earth could be detected transiting the face of the Sun](#). If there are aliens on planets around those stars with at least a similar level of technological advancement to ours, then they would theoretically be able to spot us ([L. Kaltenegger and J. K. Faherty *Nature* 594, 505–507; 2021](#)).

The work offers a new way of thinking about the search for extraterrestrial life, says Lisa Kaltenegger, an astronomer at Cornell University in Ithaca, New York, who led the analysis. “For whom would we be the aliens?” she asks.

Those aliens would be the natural choice for Earthlings to look for, say the scientists — because they could have already had a chance to spot us, and thus might be primed to receive communications from Earth.

Although previous studies have considered this question, this is the first to incorporate the movement of stars as they slide in or out of the narrow slice of the sky that lines up with both Earth and the Sun. With this information, the scientists were able to predict from where Earth was visible over the past 5,000 years or so of human civilization — and from where it will be visible up to 5,000 years into the future.

In doing so, the study expands astronomers' thinking about which stars have “a better-than-average shot of discovering and characterizing the Earth”, says Sofia Sheikh, an astrobiologist at the Berkeley SETI Research Center in California.

ALL EYES ON EARTH

There are about 2,000 stars, some known to host planets, that in the recent past or future are in a location that allows them to see Earth passing across the Sun. Some are close enough that our radio waves have reached them.

Stars already swept by
human-made radio waves **75**

Stars in the right position to have spotted
Earth in the past 5,000 years **1,715**

Additional stars that will have a view
of Earth in the next 5,000 years **319**

©nature

The discovery was made possible by the European Space Agency's Gaia space observatory, which has compiled the best 3D map of stars so far. Of more than 330,000 stars in the Gaia catalogue that are within 100 parsecs of Earth, just 2,034 happen to have the required viewing geometry. Of those, 1,715 are in the right locations to have spotted Earth so far, and another 319 will have vantage points in the future (see ‘All eyes on Earth’). Seven of the 2,034 are already known to host planets — but many more are likely to have worlds orbiting them.

The method assumed for spying Earth from elsewhere in the Galaxy is the same as that used by astronomers to discover thousands of exoplanets: detecting the light of a star dimming slightly as a planet passes across its face.



SARS-CoV-2 testing in Wuhan, China, where the first cases of COVID-19 were reported. Credit: Zhao Jun/VCG/Getty

Deleted coronavirus sequences trigger scientific intrigue

A biologist in the United States has ‘excavated’ partial SARS-CoV-2 genome sequences from the beginnings of the pandemic’s probable epicentre in Wuhan, China, that were deposited — but later removed — from a US government database.

The sequences [address an evolutionary conundrum](#) about the early genetic diversity of the coronavirus SARS-CoV-2.

Jesse Bloom, a viral evolutionary geneticist at the Fred Hutchinson Cancer Research Center in Seattle, Washington, discovered the sequences after searching for genomic data from the pandemic's early stages. A research paper from May 2020 contained a table of publicly available sequence data, which included entries Bloom had not come across. He worked out that the data had been removed from the Sequence Read Archive (SRA), a US repository for raw sequencing data.

Bloom was able to find archived versions of the sequences on cloud servers, recovering data from 50 samples, 13 of which contained enough raw data to generate partial genome sequences ([J. D. Bloom Preprint at bioRxiv](#), <https://doi.org/gksfmv1>; 2021).

The recovered data help to solve an evolutionary mystery about the early stages of the pandemic. The earliest viral sequences from Wuhan are from people linked to the city's Huanan Seafood Market in December 2019, which was initially thought to be where the coronavirus first jumped from animals to people. But the seafood-market sequences are more distantly related to SARS-CoV-2's closest relatives in bats — the most likely ultimate origin of the virus — than are later sequences.

That is surprising, says Bloom, because you would expect that viruses from the early stages of Wuhan's epidemic would be most closely related to SARS-CoV-2's relatives that infect bats. The recovered sequences, which were probably collected in January and February 2020, show this to be the case — they are more closely related to the bat viruses than are the sequences from people linked to the seafood market.

This adds to a growing body of evidence that the first human cases of COVID-19 were not associated with the Huanan Seafood Market.

It remains unclear why the sequences were removed from the SRA.

Nature **595**, 13 (2021)

doi: <https://doi.org/10.1038/d41586-021-01748-8>

Subjects

- [Astronomy and astrophysics](#)
- [SARS-CoV-2](#)

Jobs from Nature Careers

- - - [All jobs](#)
 -
 - [**PhD Student \(m/f/div\) in Bioinformatics**](#)

[Max Planck Institute for Molecular Genetics \(MPI-MG\)](#).

[14195 Berlin, Germany](#)

[JOB POST](#)

- [**PhD Student \(m/f/div\) in Bioinformatics**](#)

[Max Planck Institute for Molecular Genetics \(MPI-MG\)](#).

[14195 Berlin, Germany](#)

[JOB POST](#)

- [**PhD candidate - the neurodevelopmental disorder PURA Syndrome \(f/m/x\)**](#)

[Helmholtz Zentrum München - German Research Center for Environmental Health \(HMGU\)](#).

[Neuherberg \(bei München\), Germany](#)

[JOB POST](#)

-

PhD in Molecular Obesity Research within the Collaborative Research Center 1052 "Obesity Mechanisms" (f/m/x).

Helmholtz Zentrum München - German Research Center for Environmental Health (HMGU).

Leipzig, Germany.

JOB POST

Download PDF

Subjects

- Astronomy and astrophysics
- SARS-CoV-2

This article was downloaded by **calibre** from <https://www.nature.com/articles/d41586-021-01748-8>

| [Section menu](#) | [Main menu](#) |

- NEWS
- 22 June 2021

Astronomers victimized colleagues — and put historic Swedish department in turmoil

Investigations at Lund University found the high-ranking pair guilty of bullying, but staff members say stronger action is needed to repair the damage.

- [Alexandra Witze](#)
 1. Alexandra Witze
[View author publications](#)

You can also search for this author in [PubMed](#) [Google Scholar](#)





•

[Download PDF](#)



An observatory tower at Lund University in Sweden. Credit: Michael Persson/Alamy

Two astronomers at one of Sweden's top research institutions, Lund University, have victimized, discriminated against or bullied colleagues, according to two independent investigations commissioned in 2020 by the university. The cases have thrown the institution's historic astronomy research division, the Lund Observatory, into uproar.

The complaints that launched the investigations allege that the pair — Sofia Feltzing and Melvyn Davies — bullied colleagues using their positions of power, and that Lund University officials failed to act strongly enough following multiple reports over the years. Although bullying and harassment are rife in academia, this case is unusual because it pits many members of an academic division against two of its most senior professors, alleging long-lasting and widespread harm.



[Stress, anxiety, harassment: huge survey reveals pressures of scientists' working lives](#)

Feltzing is an observational astronomer who holds several influential roles across Europe, including chair of Sweden's National Committee for Astronomy. She denies some of the allegations from the investigation findings against her but agrees with those concerning two instances of what she says could be regarded as victimization. Davies, a theoretical astrophysicist who studies planetary systems and star clusters, denies all the allegations in the findings against him.

Both say they are actively working towards improving the working environment at the observatory. They also note that in January, lawyers for the university declined to pursue legal disciplinary action against them, citing a lack of evidence. Feltzing has since filed complaints against two of her managers; investigations into those complaints are ongoing.

Because of the case, Davies moved to Lund's mathematics department in January; Feltzing has been working from home, but is expected to be reintegrated into the observatory. The plan to bring Feltzing back has not gone down well with many there. Over the past year and a half, representatives of PhD and master's student groups have sent letters to Lund's dean of science and vice-chancellor, requesting that they take additional action. Faculty members have also weighed in: "Insisting on a

reintegration plan of a factual harasser without taking the safety and concerns of victims seriously puts astronomy [at Lund] at risk of collapse,” reads a January 2021 protest letter signed by 11 senior staff members and addressed to Erik Renström, the university’s vice-chancellor.



[Max Planck astrophysicist at centre of bullying allegations speaks up](#)

Renström says the university is taking steps towards fixing the situation, including bringing in another top administrator to supervise Feltzing's reintegration into the observatory. “In this case, we can observe that earlier, clearer and more robust measures would have been desirable and probably saved many people from a lot of suffering,” he wrote in an e-mail to *Nature*. “At the same time, the department must now look ahead, and robust and long-term work environment management is currently in progress.”

Lund University has a policy stating that it does not tolerate victimization or harassment. Yet “this was a problem of serial harassment”, says Anders Johansen, an astronomer who was head of the department of astronomy and theoretical physics, of which Lund Observatory is a part, from 2016 to 2020. He is moving to the University of Copenhagen, in part because of the stress of the case. Johansen says he received and tried to act on multiple complaints when he was department head, but failed to make headway; he compiled an informal tally from his own experience, and from speaking to past observatory leaders, which added up to a total of at least 36 complaints

since 2008. Feltzing and Davies confirmed to *Nature* that they knew of several complaints, in addition to the ones that prompted last year's investigations, but they declined to comment on the whole list.

Tumult at Lund

The investigations were triggered last September, when two staff members at the observatory filed separate complaints against both Feltzing and Davies. In the complaints, the astronomers describe situations ranging from Feltzing belittling students and other speakers during scientific talks, to Davies criticizing others' research and intentionally excluding colleagues from scientific opportunities.

Follow-up investigations concluded in November and December that Feltzing had committed 16 acts of victimization or offensive discrimination, and that Davies had committed two acts of victimization. All are violations of Sweden's Work Environment Act. These are the first complaints against Feltzing and Davies to result in findings against them.

Last December, Feltzing herself filed formal complaints against observatory head David Hobbs and Leif Lönnblad, head of the department of astronomy and theoretical physics. The resulting investigation is examining actions they took regarding the complaints against Feltzing, and is ongoing. Hobbs and Lönnblad declined a request from *Nature* for comment.



[Prominent palaeontologist loses £1-million grant following bullying investigation](#)

A number of sources at the observatory told *Nature* they believe the university has allowed problems to fester, damaging scientific output and causing anxiety. “Science activities are hugely affected,” says an astronomer who asked to remain anonymous for fear of reprisal. “We spend a lot of time denouncing and documenting the situation, and all our activities suffer from this.” The observatory has interrupted its seminar series to avoid bringing external speakers into a tense situation. Some employees have taken extensive sick leave because of the stress.

Renström says there is no evidence that scientific output has declined.

Bullying and victimization can have far-reaching and long-lasting impacts in academia, says Christina Björklund, an economic psychologist at the Karolinska Institute in Stockholm who studies workplace bullying. She emphasized that she was speaking generally, and not specifically about the Lund Observatory case. “You should be able to go to your workplace without being attacked by your co-worker,” she says. “Everybody should have a chance to be successful.” She notes that rates of stress, depression and mental illness can be high not only among people who are bullied, but also among bystanders.

Problems fester

Lund University is routinely ranked among Sweden's top research centres. Astronomy in the city of Lund goes back for nearly three and a half centuries; the first observatory there was built in 1672, by the grandfather of astronomer Anders Celsius — after whom the temperature scale is named.

Many of the people who previously reported harassment by Feltzing and Davies were students or postdocs who cycled out of the department while the professors remained. One was Guido Moyano Loyola, a former astronomy postdoc at Lund. In 2018, he alleged that Feltzing and Davies had bullied him and some of the other students; Moyano ended up leaving astronomy altogether, returning to his home country of Argentina and working as a data scientist. “I was really heartbroken,” he says. An investigation into Moyano’s claim by the university’s human-resources representatives culminated in supervised meetings with him and Feltzing and Davies; the pair say they thought the situation had been resolved through these meetings.



[Sexual harassment is rife in the sciences, finds landmark US study](#)

Anna Arnadottir, a graduate student of Feltzing’s between 2004 and 2009, says that her working relationship with Feltzing was “quite unhealthy”, to

the point that Arnadottir asked the department's director of graduate studies to intervene. In the last year of Arnadottir's PhD, all of her meetings with Feltzing had to have a third person present in them, says Arnadottir, who today is a research engineer at the observatory. Feltzing says that she worked on changing her behaviour towards Arnadottir.

The controversy is spilling over into Swedish astronomy more broadly. Feltzing technically remains chair of Sweden's National Committee for Astronomy, but the vice-chair of the committee has been leading its work since January, after the committee learnt of the complaints against Feltzing. In June, the committee established a working group to review policies regarding its chairship.

Feltzing is also principal investigator on a 20-million-kronor (US\$2.3-million) grant to study galaxy formation awarded last year by the Knut and Alice Wallenberg Foundation in Stockholm, one of Sweden's most prestigious sources of science funding. The foundation's executive director, Göran Sandberg, says the grant was awarded to the university, and "it is therefore up to the university to handle the situation that has arisen, including deciding on leadership for the project". The grant is the subject of tense discussions within the observatory over what role Feltzing should play in the project, given the findings against her.

Alarm bells ignored

Problems at the observatory burst into broad view in May 2020, when a survey commissioned by the university to probe workplace climate found that "two senior professors ... are described to control the department through behaviour such as verbal aggressiveness, rude tone, control of employees, capriciousness and offensive behaviours". The survey included interviews with all 49 employees at the observatory. The final report does not name the two senior professors involved, but Feltzing, Davies and Johansen were the only senior professors at the observatory at the time. The report concludes that 70% of observatory employees said there had been harassment or bullying.



Elite US science academy expels astronomer Geoff Marcy following harassment complaints

“The content of the report that was delivered at the end of May last year was alarming, and yet it didn’t set alarm bells ringing,” says Colin Carlile, a Lund Observatory master’s student who is an experienced international research programme manager and was previously director-general of the European Spallation Source, a physics research facility under construction in Lund. “Swift and decisive action is always called for in such circumstances, but clearly it does not always happen.”

Jesper Nielsen, a representative of the master’s students at the observatory, says that things might go relatively smoothly if Feltzing is brought back into the department in such a way as to avoid those in direct conflict with her. “But if it is being handled sloppily, and if her victims come into contact with her, then that’s where the big problems will arise,” he says. “I don’t know if it’s possible to reintegrate her nicely enough.”

Others say that the Lund Observatory experience is one that other institutions should not repeat. “If there is a zero-tolerance policy,” says Johansen, “there has to be some form of consequences or accountability.”

Nature **595**, 15-16 (2021)

doi: <https://doi.org/10.1038/d41586-021-01621-8>

Related Articles

-  [Stress, anxiety, harassment: huge survey reveals pressures of scientists' working lives](#)
 -  [Elite US science academy expels astronomer Geoff Marcy following harassment complaints](#)
 -  [Max Planck astrophysicist at centre of bullying allegations speaks up](#)
 -  [Prominent palaeontologist loses £1-million grant following bullying investigation](#)
 -  [Sexual harassment is rife in the sciences, finds landmark US study](#)
- ## Subjects
- [Scientific community](#)
 - [Institutions](#)
 - [Lab life](#)
 - [Law](#)

- [Astronomy and astrophysics](#)

Jobs from Nature Careers

- - - [All jobs](#)
 -
 - [**PhD Student \(m/f/div\) in Bioinformatics**](#)

[Max Planck Institute for Molecular Genetics \(MPI-MG\)](#)

[14195 Berlin, Germany](#)

[JOB POST](#)

- [**PhD Student \(m/f/div\) in Bioinformatics**](#)

[Max Planck Institute for Molecular Genetics \(MPI-MG\)](#)

[14195 Berlin, Germany](#)

[JOB POST](#)

- [**PhD candidate - the neurodevelopmental disorder PURA Syndrome \(f/m/x\)**](#)

[Helmholtz Zentrum München - German Research Center for Environmental Health \(HMGU\)](#)

[Neuherberg \(bei München\), Germany](#)

[JOB POST](#)

- [**PhD in Molecular Obesity Research within the Collaborative Research Center 1052 "Obesity"**](#)

Mechanisms" (f/m/x).

Helmholtz Zentrum München - German Research Center for Environmental Health (HMGU).

Leipzig, Germany.

JOB POST

Download PDF

Related Articles



- Stress, anxiety, harassment: huge survey reveals pressures of scientists' working lives



- Elite US science academy expels astronomer Geoff Marcy following harassment complaints



- Max Planck astrophysicist at centre of bullying allegations speaks up



- Prominent palaeontologist loses £1-million grant following bullying investigation



- [Sexual harassment is rife in the sciences, finds landmark US study](#)

Subjects

- [Scientific community](#)
- [Institutions](#)
- [Lab life](#)
- [Law](#)
- [Astronomy and astrophysics](#)

This article was downloaded by **calibre** from <https://www.nature.com/articles/d41586-021-01621-8>

| [Section menu](#) | [Main menu](#) |

- NEWS
- 22 June 2021

Delta coronavirus variant: scientists brace for impact

The rapid rise of the highly transmissible strain in the United Kingdom has put countries in Europe, North America and Africa on watch.

- [Ewen Callaway](#)
 1. Ewen Callaway
[View author publications](#)

You can also search for this author in [PubMed](#) [Google Scholar](#)





•

[Download PDF](#)



A traveller checks in at a KLM counter at Amsterdam's Schiphol Airport. Credit: Koen van Weel/ANP/AFP/Getty

When the first cases of the SARS-CoV-2 Delta variant were detected in the United Kingdom in mid-April, the nation was getting ready to open up. COVID-19 case numbers, hospitalizations and deaths were plummeting, thanks to months of lockdown and one of the world's fastest vaccination programmes. Two months later, the variant, which was first detected in India, has catalysed a third UK wave and forced the government to delay the full reopening of society it had originally slated for 21 June.

After observing the startlingly swift rise of the Delta variant in the United Kingdom, [other countries are bracing for the variant's impact](#) — if they aren't feeling it already. Nations with ample access to vaccines, such as those in Europe and North America, are hopeful that the shots can dampen the inevitable rise of Delta. But in countries without large vaccine stocks, particularly in Africa, some scientists worry that the variant could be devastating.

“In my mind, it will be really hard to keep out this variant,” says Tom Wenseleers, an evolutionary biologist and biostatistician at the Catholic University of Leuven (KU Leuven) in Belgium. “It’s very likely it will take over altogether on a worldwide basis.”

Delta, also known as B.1.617.2, belongs to a viral lineage first identified in India during a ferocious wave of infections there in April and May. The lineage grew rapidly in some parts of the country, and showed signs of partial resistance to vaccines. But it was difficult for researchers to disentangle these intrinsic properties of the variant from other factors driving India’s confirmed cases past 400,000 per day, such as mass gatherings.

Delta data

The Delta variant has been linked to a resurgence of COVID-19 in Nepal, southeast Asia and elsewhere, but its UK spread has given scientists a clear picture of the threat it poses. Delta seems to be around 60% more transmissible than the already highly infectious Alpha variant (also called B.1.1.7) identified in the United Kingdom in late 2020.

Delta is moderately resistant to vaccines, particularly in people who have received just a single dose. A [Public Health England study](#) published on 22 May found that a single dose of either AstraZeneca’s or Pfizer’s vaccine reduced a person’s risk of developing COVID-19 symptoms caused by the Delta variant by 33%, compared to 50% for the Alpha variant. A second dose of the AstraZeneca vaccine boosted protection against Delta to 60% (compared to 66% against Alpha), while two doses of Pfizer’s jab were 88% effective (compared to 93% against Alpha).

Preliminary evidence from England and Scotland suggests that people infected with Delta are about twice as likely to end up in hospital, compared with those infected with Alpha.

“The data coming out of the UK is so good, that we have a really good idea about how the Delta variant is behaving,” says Mads Albertsen, a bioinformatician at Aalborg University in Denmark. “That’s been an eye-opener.”

Denmark, which, like the United Kingdom, is a world leader in genomic surveillance, has also seen a steady rise in cases caused by the Delta variant — although far fewer than most other European countries. It is only a matter of time before the variant becomes dominant in Denmark, says Albertsen, but the hope is that its expansion can be slowed through vaccination, surveillance and enhanced contact tracing. “It’s going to take over,” he says, but “hopefully in a few months and not too soon.”

Meanwhile, the Danish government is easing restrictions, not re-imposing them: restaurants and bars have been open for months to individuals who have been vaccinated or received a recent negative test, and, as of 14 June, masks are no longer required in most indoor settings. “It is looking good now in Denmark, and we are keeping a close eye on the Delta variant,” says Albertsen. “It can change quite fast, as it has done in the UK.”

Cases of the Delta variant in the United Kingdom are doubling roughly every 11 days. But countries with ample vaccine stocks should be reassured by the slower uptick in hospital admissions, says Wenseleers. [A recent Public Health England study¹](#) found that people who have had one vaccine dose are 75% less likely to be hospitalized, compared with unvaccinated individuals, and those who are fully protected are 94% less likely to be hospitalized.

US spread

Delta is also on the rise in the United States, particularly in the Midwest and southeast. The US Centers for Disease Control and Prevention declared it a variant of concern on 15 June. But patchy surveillance means the picture there is less clear. According to nationwide sampling conducted by the genomics company Helix in San Mateo, California, Delta is rising fast. Using a rapid genotyping test, the company has found that the proportion of cases caused by Alpha fell from more than 70% in late April to around 42% as of mid-June, with the rise of Delta driving much of the shift².

Jeremy Kamil, a virologist at Louisiana State University Health in Shreveport, expects Delta to eventually become dominant in the United States, “but to be somewhat blunted by vaccination”. However, vast

disparities in vaccination rates could lead to regional and local variation in cases and hospitalizations caused by Delta, says Jennifer Surtees, a biochemist at the University at Buffalo, New York, who is conducting regional surveillance.

She notes that 70% of eligible New Yorkers have received at least one dose of vaccine — a milestone that triggered the lifting of most COVID-19 restrictions last week — but that figure is below 40% in some parts of the state. Communities with high proportions of African American and Hispanic individuals, where vaccination rates tend to be low, could be especially hard hit by Delta. “These are populations that are really at risk of a localized outbreak from Delta, so I think it’s really important to still keep tracking and watch this as much as possible,” Surtees says.

Data from Helix² on nearly 20,000 samples sequenced since April suggest that the Delta variant is spreading faster in US counties where less than 30% of residents have been fully vaccinated, compared to the counties with vaccination rates above that threshold.

Africa at risk

Delta poses the biggest risk, scientists say, to countries that have limited access to vaccines, particularly those in Africa, where most nations have vaccinated less than 5% of their populations. “The vaccines will never come in time,” says Wenseleers. “If these kinds of new variant arrive, it can be very devastating.”

Surveillance in African countries is extremely limited, but there are hints that the variant is already causing cases there to surge. Several sequences of the variant have been reported in the Democratic Republic of the Congo, where an outbreak in the capital city of Kinshasa has filled hospitals. The variant has also been detected in Malawi, Uganda and South Africa.

Countries that have close economic links to India, such as those in East Africa, are probably at the greatest risk of seeing a surge in cases caused by Delta, says Tulio de Oliveira, a bioinformatician and director of the KwaZulu-Natal Research and Innovation Sequencing Platform in Durban,

South Africa. In his country, all of the Delta cases have been detected in shipping crews at commercial ports, with no signs yet of spread in the general community.

De Oliveira expects it to stay this way. South Africa is in the middle of a third wave of infections caused by the Beta variant (also known as B.1.351) identified there last year. This, combined with a lack travel from countries affected by Delta, should make it harder for a new variant to take hold.

Similar factors could be keeping Delta at bay in Brazil, which is battling another immune-evading variant called P.1, or Gamma, says Gonzalo Bello, a virologist at the Oswaldo Cruz Institute in Rio de Janeiro, who is part of a team conducting national surveillance. So far, Brazil has sequenced just four cases of the Delta variant in the country.

While countries gird themselves against the Delta variant — or hope that it passes them by — researchers say we need to watch for even greater threats. “What most people are concerned about are the next variants — if we start to see variants that can really challenge the vaccines,” says Albertsen.

Nature **595**, 17-18 (2021)

doi: <https://doi.org/10.1038/d41586-021-01696-3>

References

1. 1.

Stowe, J. *et al.* Preprint at <https://go.nature.com/3gnqwxr> (2021).

2. 2.

Bolze, A. *et al.* Preprint at medRxiv
<https://doi.org/10.1101/2021.06.20.21259195> (2021).

[Download references](#)

Related Articles



- [Coronavirus variants get Greek names — but will scientists use them?](#)
- [COVID-19: A mammoth task for Africa's public health agencies](#)
- [How a rampant coronavirus variant blunts our immune defences](#)

Subjects

- [SARS-CoV-2](#)
- [Public health](#)
- [Virology](#)

Jobs from Nature Careers

- - - [All jobs](#)
 - - [PhD Student \(m/f/div\) in Bioinformatics](#)

[Max Planck Institute for Molecular Genetics \(MPI-MG\)](#)

[14195 Berlin, Germany](#)

[JOB POST](#)

- [PhD Student \(m/f/div\) in Bioinformatics](#)

[Max Planck Institute for Molecular Genetics \(MPI-MG\)](#)

[14195 Berlin, Germany](#)

[JOB POST](#)

- [56868: 3 Engineering Scientists, physicists or similar \(f/m/x\) - Development of an optical frequency reference for the project COMPASSO](#)

[German Aerospace Center \(DLR\)](#)

[Bremen, Germany](#)

[JOB POST](#)

- [PhD candidate - the neurodevelopmental disorder PURA Syndrome \(f/m/x\).](#)

[Helmholtz Zentrum München - German Research Center for Environmental Health \(HMGU\)](#)

[Neuherberg \(bei München\), Germany](#)

[JOB POST](#)

[Download PDF](#)

Related Articles



- [Coronavirus variants get Greek names — but will scientists use them?](#)
- [COVID-19: A mammoth task for Africa's public health agencies](#)

- [How a rampant coronavirus variant blunts our immune defences](#)

Subjects

- [SARS-CoV-2](#)
- [Public health](#)
- [Virology](#)

This article was downloaded by **calibre** from <https://www.nature.com/articles/d41586-021-01696-3>

| [Section menu](#) | [Main menu](#) |

- NEWS
- 18 June 2021

Mathematicians welcome computer-assisted proof in ‘grand unification’ theory

Proof-assistant software handles an abstract concept at the cutting edge of research, revealing a bigger role for software in mathematics.

- [Davide Castelvecchi](#)

1. Davide Castelvecchi
[View author publications](#)

You can also search for this author in [PubMed](#) [Google Scholar](#)





•

[Download PDF](#)



Efforts to verify a complex mathematical proof using computers have been successful. Credit: Fadel Senna/AFP via Getty

Peter Scholze wants to rebuild much of modern mathematics, starting from one of its cornerstones. Now, he has received validation for a proof at the heart of his quest from an unlikely source: a computer.

Although most mathematicians doubt that machines will replace the creative aspects of their profession any time soon, some acknowledge that technology will have an increasingly important role in their research — and this particular feat could be a turning point towards its acceptance.

Scholze, a number theorist, set forth the ambitious plan — which he co-created with his collaborator Dustin Clausen from the University of Copenhagen — in a series of lectures in 2019 at the University of Bonn, Germany, where he is based. The two researchers dubbed it ‘condensed mathematics’, and they say it promises to bring new insights and connections between fields ranging from geometry to number theory.

Other researchers are paying attention: Scholze is considered one of mathematics' brightest stars and has a track record of introducing revolutionary concepts. Emily Riehl, a mathematician at Johns Hopkins University in Baltimore, Maryland, says that if Scholze and Clausen's vision is realized, the way mathematics is taught to graduate students in 50 years' time could be very different than it is today. "There are a lot of areas of mathematics that I think in the future will be affected by his ideas," she says.

Until now, much of that vision rested on a technical proof so involved that even Scholze and Clausen couldn't be sure it was correct. But earlier this month, Scholze announced that a project to check the heart of the proof using specialized computer software had been successful.

Computer assistance

Mathematicians have long used computers to do numerical calculations or manipulate complex formulas. In some cases, they have proved major results by making computers do massive amounts of repetitive work — the most famous being a proof in the 1970s that any map can be coloured with just four different colours, and without filling any two adjacent countries with the same colour.



Number-theory prodigy among winners of most coveted prize in mathematics

But systems known as proof assistants go deeper. The user enters statements into the system to teach it the definition of a mathematical concept — an object — based on simpler objects that the machine already knows about. A statement can also just refer to known objects, and the proof assistant will answer whether the fact is ‘obviously’ true or false on the basis of its current knowledge. If the answer is not obvious, the user has to enter more details. Proof assistants thus force the user to lay out the logic of their arguments in a rigorous way, and they fill in simpler steps that human mathematicians had consciously or unconsciously skipped.

Once researchers have done the hard work of translating a set of mathematical concepts into a proof assistant, the program generates a library of computer code that can be built on by other researchers and used to define higher-level mathematical objects. In this way, proof assistants can help to verify mathematical proofs that would otherwise be time-consuming and difficult, perhaps even practically impossible, for a human to check.

Proof assistants have long had their fans, but this is the first time that they have had a major role at the cutting edge of a field, says Kevin Buzzard, a mathematician at Imperial College London who was part of a collaboration that checked Scholze and Clausen’s result. “The big remaining question was: can they handle complex mathematics?” says Buzzard. “We showed that they can.”

And it all happened much faster than anyone had imagined. Scholze [laid out his challenge](#) to proof-assistant experts in December 2020, and it was taken up by a group of volunteers led by Johan Commelin, a mathematician at the University of Freiburg in Germany. On 5 June — less than six months later — [Scholze posted on Buzzard’s blog](#) that the main part of the experiment had succeeded. “I find it absolutely insane that interactive proof assistants are now at the level that, within a very reasonable time span, they can formally verify difficult original research,” Scholze wrote.

[AI maths whiz creates tough new problems for humans to solve](#)

The crucial point of condensed mathematics, according to Scholze and Clausen, is to redefine the concept of topology, one of the cornerstones of modern maths. A lot of the objects that mathematicians study have a topology — a type of structure that determines which of the object's parts are close together and which aren't. Topology provides an idea of shape, but one that is more malleable than those of familiar, school-level geometry: in topology, any transformation that does not tear an object apart is admissible. For example, any triangle is topologically equivalent to any other triangle — or even to a circle — but not to a straight line.

Topology plays a crucial part not only in geometry, but also in functional analysis, the study of functions. Functions typically ‘live’ in spaces with an infinite number of dimensions (such as wavefunctions, which are foundational to quantum mechanics). It is also important for number systems called p -adic numbers, which have an exotic, ‘fractal’ topology.

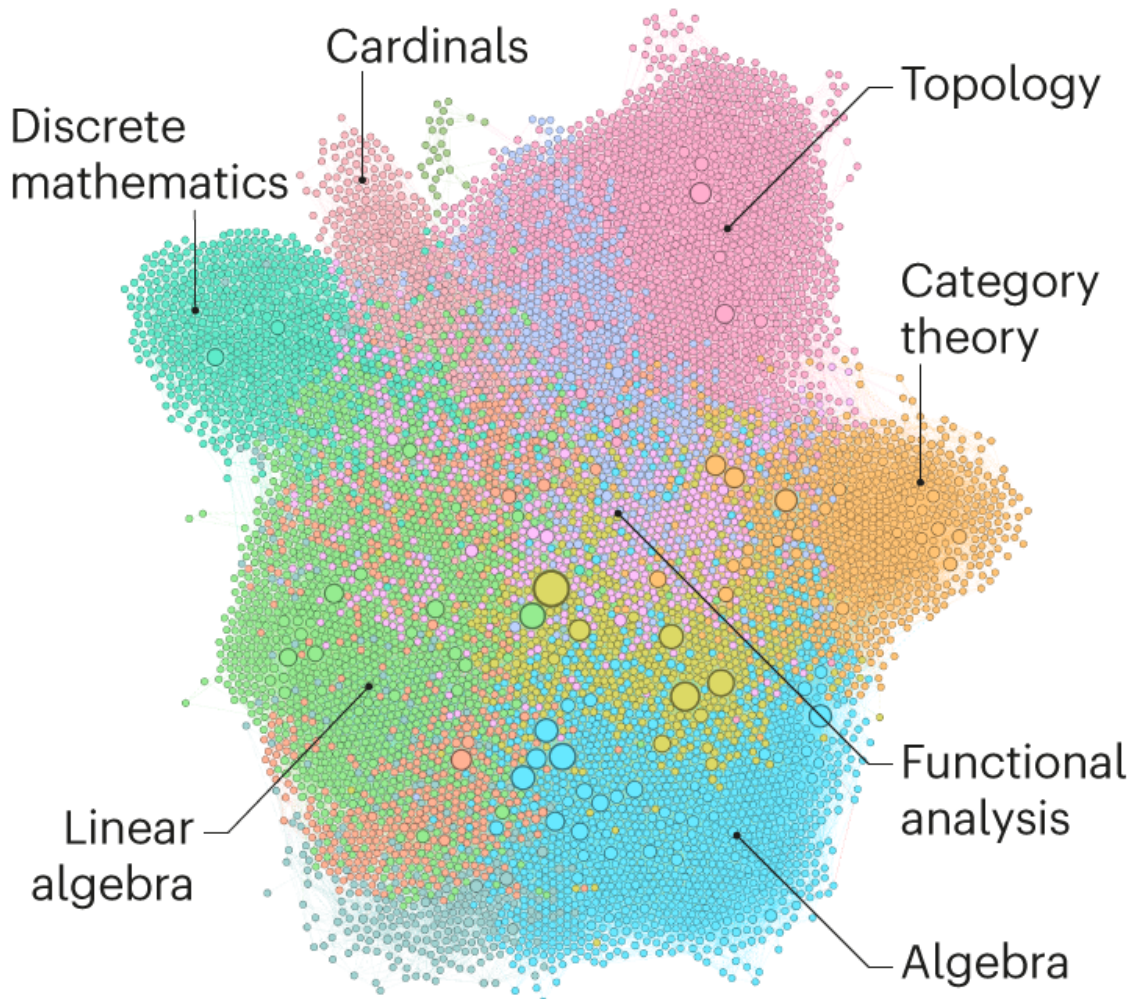
A grand unification

Around 2018, Scholze and Clausen began to realize that the conventional approach to the concept of topology led to incompatibilities between these three mathematical universes — geometry, functional analysis and p -adic numbers — but that alternative foundations could bridge those gaps. Many results in each of those fields seem to have analogues in the others, even though they apparently deal with completely different concepts. But once topology is defined in the ‘correct’ way, the analogies between the theories are revealed to be instances of the same ‘condensed mathematics’, the two researchers proposed. “It is some kind of grand unification” of the three fields, Clausen says.

Scholze and Clausen say they have already found simpler, ‘condensed’ proofs of a number of profound geometry facts, and that they can now prove theorems that were previously unknown. They have not yet made these public.

There was one catch, however: to show that geometry fits into this picture, Scholze and Clausen had to prove one highly technical theorem about the set of ordinary real numbers, which has the topology of a straight line. “It’s like

the foundational theorem that allows the real numbers to enter this new framework,” Commelin explains.



In the proof-assistant package Lean, users enter mathematical statements based on simpler statements and concepts that are already in the Lean library. The output, seen here in the case of Scholze and Clausen’s key result, is a complex network. The statements have been colour-coded and grouped by subfield of maths.Credit: Patrick Massot

Clausen recalls how Scholze worked relentlessly on the proof until it was completed ‘through force of will’, producing many original ideas in the process. “It was the most amazing mathematical feat I’ve ever witnessed,” Clausen recalls. But the argument was so complex that Scholze himself

worried there could be some subtle gap that invalidated the whole enterprise. “It looked convincing, but it was simply too novel,” says Clausen.

For help checking that work, Scholze turned to Buzzard, a fellow number theorist who is an expert in Lean, a proof-assistant software package. Lean was originally created by a computer scientist at Microsoft Research in Redmond, Washington, for the purpose of rigorously checking computer code for bugs.

Buzzard had been running a multi-year programme to encode the entire undergraduate maths curriculum at Imperial into Lean. He had also experimented with entering more-advanced mathematics into the system, including the concept of perfectoid spaces, which helped to earn Scholze a Fields Medal in 2018.

Commelin, who is also a number theorist, took the lead in the effort to verify Scholze and Clausen’s proof. Commelin and Scholze decided to call their Lean project the Liquid Tensor Experiment, in an *homage* to progressive-rock band Liquid Tension Experiment, of which both mathematicians are fans.

A febrile online collaboration ensued. A dozen or so mathematicians with experience in Lean joined in, and the researchers got help from computer scientists along the way. By early June, the team had fully translated the heart of Scholze’s proof — the part that worried him the most — into Lean. And it all checked out — the software was able to verify this part of the proof.

Better understanding

The Lean version of Scholze’s proof comprises tens of thousands of lines of code, 100 times longer than the original version, Commelin says. “If you just look at the Lean code, you will have a very hard time understanding the proof, especially the way it is now.” But the researchers say that the effort of getting the proof to work in the computer has helped them to understand it better, too.

AI Copernicus ‘discovers’ that Earth orbits the Sun

Riehl is among the mathematicians who have experimented with proof assistants, and even teaches them in some of her undergraduate classes. She says that, although she doesn’t systematically use them in her research, they have begun to change the very way she thinks of the practices of constructing mathematical concepts and stating and proving theorems about them. “Previously, I thought of proving and constructing as of two different things, and now I think of them as the same.”

Many researchers say that mathematicians are unlikely to be replaced by machines any time soon. Proof assistants can’t read a maths textbook, they need continuous input from humans, and they can’t decide whether a mathematical statement is interesting or profound — only whether it is correct, Buzzard says. Still, computers might soon be able to point out consequences of the known facts that mathematicians had failed to notice, he adds.

Scholze says he was surprised by how far proof assistants could go, but that he is unsure whether they will continue to have a major role in his research. “For now, I can’t really see how they would help me in my creative work as a mathematician.”

Nature **595**, 18-19 (2021)

doi: <https://doi.org/10.1038/d41586-021-01627-2>

Related Articles



- [Number-theory prodigy among winners of most coveted prize in mathematics](#)
- [AI Copernicus ‘discovers’ that Earth orbits the Sun](#)

- [AI maths whiz creates tough new problems for humans to solve](#)

Subjects

- [Mathematics and computing](#)

Jobs from Nature Careers

- - - [All jobs](#)
 - - [PhD Student \(m/f/div\) in Bioinformatics](#)
[Max Planck Institute for Molecular Genetics \(MPI-MG\)](#).
[14195 Berlin, Germany](#)
[JOB POST](#)
 - [PhD Student \(m/f/div\) in Bioinformatics](#)
[Max Planck Institute for Molecular Genetics \(MPI-MG\)](#).
[14195 Berlin, Germany](#)
[JOB POST](#)
 - [PhD candidate - the neurodevelopmental disorder PURA Syndrome \(f/m/x\)](#)
[Helmholtz Zentrum München - German Research Center for Environmental Health \(HMGU\)](#).

Neuherberg (bei München), Germany

JOB POST

- **PhD in Molecular Obesity Research within the Collaborative Research Center 1052 "Obesity Mechanisms" (f/m/x)**

Helmholtz Zentrum München - German Research Center for Environmental Health (HMGU)

Leipzig, Germany

JOB POST

Download PDF

Related Articles



- **Number-theory prodigy among winners of most coveted prize in mathematics**
- **AI Copernicus ‘discovers’ that Earth orbits the Sun**
- **AI maths whiz creates tough new problems for humans to solve**

Subjects

- **Mathematics and computing**

| [Section menu](#) | [Main menu](#) |

- NEWS
- 25 June 2021

Mysterious skull fossils expand human family tree — but questions remain

Fossilized bones found in Israel and China, including a specimen named ‘Dragon Man’, could belong to new types of ancient human. But the findings have sparked debate.

- [Nicola Jones](#) 0

1. Nicola Jones

1. Nicola Jones is a science journalist based in Pemberton, British Columbia

[View author publications](#)

You can also search for this author in [PubMed](#) [Google Scholar](#)





•

[Download PDF](#)



Excavation site near Nesher Ramla in central Israel.Credit: Yossi Zaidner

Fossils found in China and Israel dating from around 140,000 years ago are adding to the ranks of hominins that mixed and mingled with early modern humans.

The fossils from Israel hint that a previously unknown group of hominins, proposed to be the direct ancestors of Neanderthals, might have dominated life in the Levant and lived alongside *Homo sapiens*^{1,2}. Meanwhile, researchers studying an extremely well-preserved ancient human skull found in China in the 1930s have controversially classified it as a new species — dubbed Dragon Man — which might be an even closer relative to modern humans than are Neanderthals^{3,4}.



Crowdsourcing digs up an early human species

But both findings have sparked debate among scientists. The studies are based on analyses of the size, shape and structure of fossilized bones — methods that are subject to individual judgement and interpretation. As is often the case for fossil finds, there is no DNA evidence.

Separating early hominin specimens into unique species, working out if and how they interacted with others, and tracing their evolution are all difficult and contentious: “It’s very messy,” says Jeffrey Schwartz, an anthropologist and evolutionary biologist at the University of Pittsburgh in Pennsylvania.

Ancestor to Neanderthals

Since 2000, the view of human evolution during the past half a million years has become ever-more complicated as researchers have added to the list of species in the genus *Homo* that lived in the Middle and Late Pleistocene. The family tree now includes the Indonesian *H. floresiensis*, discovered in 2003; Siberian Denisovans, identified in 2010; South African *H. naledi*, described in 2015; and Filipino *H. luzonensis*, detailed in 2019.

These species overlapped in time with modern humans (*H. sapiens*), which are thought to have emerged from Africa and spread into Israel and other

regions some 200,000 years ago, and Neanderthals (*H. neanderthalis*), which had a stronghold in Europe 300,000 years ago and were outcompeted by, or subsumed into, modern humans by around 40,000 years ago.



[Ancient-human species mingled in Siberia's hottest property for 300,000 years](#)

However, some hominin fossils from this time period still don't fit neatly into any existing categories. Now, researchers studying some of these odd-ball fossils, found in Israel, think they might have identified a new group of hominins. Physical anthropologist Israel Hershkovitz at Tel Aviv University and his colleagues focused on skull fragments found at the site of Nesher Ramla in central Israel — parts of parietal bones and a jaw, probably belonging to the same individual — that date to between 140,000 and 120,000 years ago.

Conventional thinking is that only *H. sapiens* lived in the Levant at this time, the team says; the earliest conclusive evidence of Neanderthals being there is from 70,000 years ago. “What we expected to find was *Homo sapiens*,” says co-author Hila May, also at Tel Aviv University. “At first glance, for sure it wasn’t.” The jaw and teeth were Neanderthal-like, but the skull shape was more archaic — an unusual combination.

The oddity seems to match up with a handful of other fossils found around Israel, some dating back 400,000 years, none of which had previously been classified. “We couldn’t assign them to any *Homo* group,” says May. “It was a mystery.” In a pair of studies^{1,2} published in *Science* on 24 June, the group proposes that all of these fossils belong to a newly named hominin population — the Nesher Ramla people — who might have dominated this region for hundreds of thousands of years. The team says the Nesher Ramla people belonged to an unknown umbrella species, rather than constituting a new species themselves.



A mandible and skull found at Nesher Ramla. Researchers suggest these specimens belonged to a previously unknown group of ancient hominins. Credit: Avi Levin and Ilan Theiler, Sackler Faculty of Medicine, Tel Aviv University

The Nesher Ramla population seems to have mastered the same stone tools as *H. sapiens* living in the area. Artefacts found near the fossils suggest that these people napped flints, bringing in material from up to 10 kilometres away, and re-sharpened the tools when needed. Their use of similar technology hints that they lived together with modern humans and perhaps interbred.

But not all researchers agree with the team's findings. To palaeoanthropologist Philip Rightmire at Harvard University in Cambridge, Massachusetts, the skull looks like an "early, rather archaic-looking, Neanderthal". Rightmire says he would not be surprised to see Neanderthals in this region at this time.

Hershkovitz and colleagues argue that the Nesher Ramla people could have established early, pre-Neanderthal communities in Europe, injecting archaic genes from Africa or Asia into a species that has conventionally been thought of as evolving in Europe. "Neanderthals are no longer an exclusive European story," says Hershkovitz.

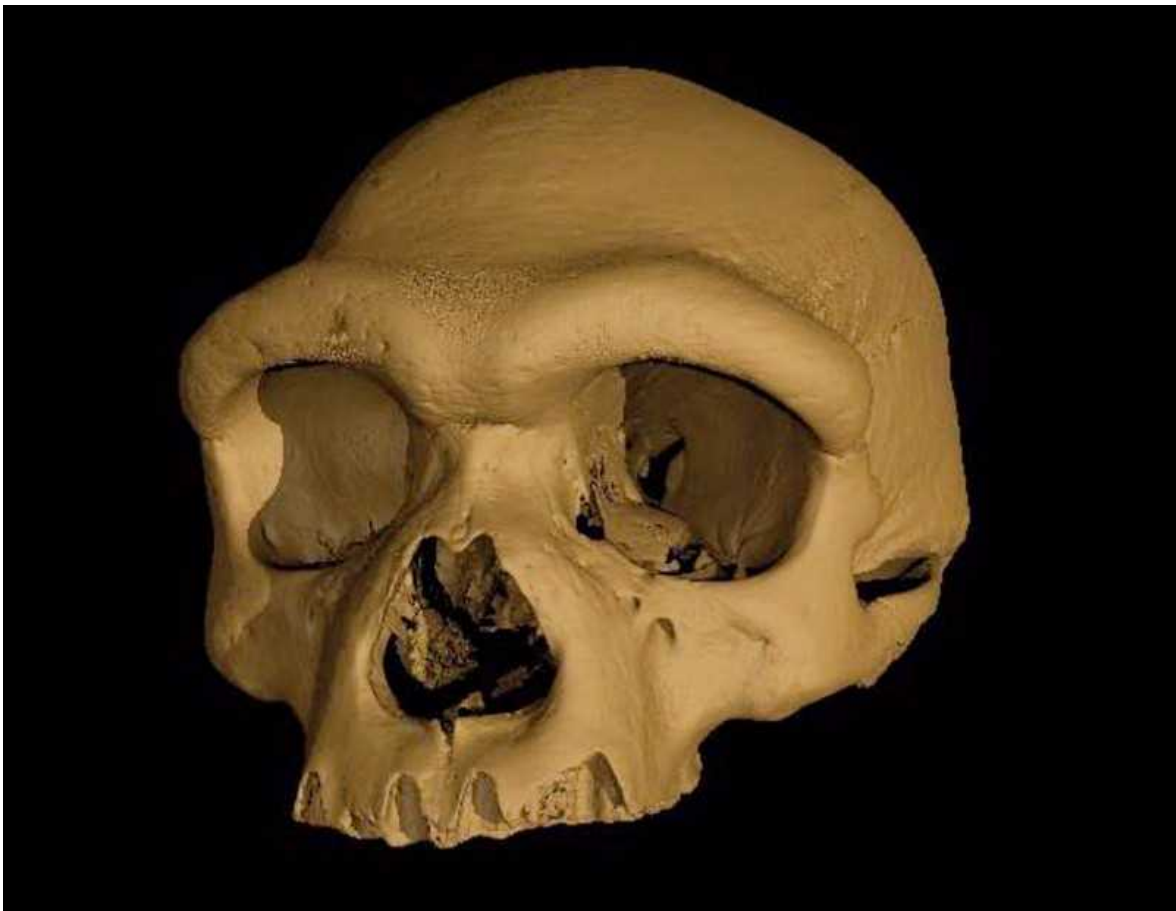
But Rightmire argues that the flow could have gone in the other direction. "I don't see any reason why these early Neanderthals, if that's what they are, couldn't have come from Europe," he says.

Dragon Man

In China, an assessment of a Middle Pleistocene hominin skull that was unearthed decades ago could also shed new light on our ancestors.

The Harbin skull is an extremely well-preserved cranium that dates to about 140,000 years ago and is thought to belong to a 50-year-old male. The skull was originally dug up in 1933 before being hidden from the Japanese army in a well, and was donated to Hebei GEO University in Shijiazhuang in 2018. The skull is particularly large and thick, with big, squarish eye sockets, low cheek bones, large teeth and a wide pallet.

In work published in *The Innovation* on 25 June, palaeontologist Ji Qiang at Hebei GEO University and colleagues propose that the unique features of the Harbin skull are enough to classify it as a new species^{3,4}. They suggest the species name *Homo longi* (Dragon Man) after the common name of Heilongjiang Province, Long Jiang (Dragon River), where the fossil was found.



A virtual reconstruction of the Harbin skull (still from video). Credit: Xijun Ni

However, naming a new species on the back of a single skull — particularly one that has been removed from its original context and comes with no artefacts — is controversial. “I think that there were more species running around Asia than people have allowed themselves to think about,” says Schwartz. But there isn’t enough evidence to convince him that this skull represents a new species.

The Harbin fossil is one of several odd Middle Pleistocene *Homo* skulls found in China over the years. In Rightmire’s view, these skulls probably represent what became of some of the early Neanderthals who marched from Europe through the Middle East, China and Siberia, eventually becoming the Denisovans. “These Asian bits and pieces probably belong to the same group as Denisovans,” he says. “I bet that’s what we’re talking about here.”

Hershkovitz argues that some of these Asian skulls might better fit into the Nesher Ramla group.



Mum's a Neanderthal, Dad's a Denisovan: First discovery of an ancient-human hybrid

In the study, Qiang and colleagues say that, given the Harbin skull's similarity to some early *H. sapiens* fossils, *H. longi* might be an even closer relative to modern humans than Neanderthals are. But Schwartz thinks some of these fossils have been inappropriately lumped into the *H. sapiens* category. "Many of these fossils are very, very different from each other," he says.

Overall, the current hominin classifications make little sense, argues Schwartz, because they bundle too much diversity together into species such as *H. sapiens*. "I think we should start from scratch," he says. "Some people aren't bold enough to say: 'let's look at everything from the beginning.'"

Nature 595, 20 (2021)

doi: <https://doi.org/10.1038/d41586-021-01738-w>

References

1. 1.

Hershkovitz, I. *et al.* *Science* **372**, 1424–1428 (2021).

[Article](#) [Google Scholar](#)

2. 2.

Zaidner, Y. *et al.* *Science* **372**, 1429–1433 (2021).

[Article](#) [Google Scholar](#)

3. 3.

Ji, Q. *et al.* *The Innovation* <https://doi.org/10.1016/j.xinn.2021.100132> (2021).

[Article](#) [Google Scholar](#)

4. 4.

Ni, X. *et al.* *The Innovation* <https://doi.org/10.1016/j.xinn.2021.100130> (2021).

[Article](#) [Google Scholar](#)

[Download references](#)

Related Articles

-  [Ancient-human species mingled in Siberia's hottest property for 300,000 years](#)



- [Ancient African genomes offer glimpse into early human history](#)



- [Mum's a Neanderthal, Dad's a Denisovan: First discovery of an ancient-human hybrid](#)



- [Lost Denisovan bone reveals surprisingly human-like finger](#)



- [Crowdsourcing digs up an early human species](#)



- [New species of early human discovered near fossil of 'Lucy'](#)
- [Oldest ancient-human DNA details dawn of Neanderthals](#)

Subjects

- [Palaeontology](#)
- [Evolution](#)

[Jobs from Nature Careers](#)

- - - [All jobs](#)
 - - [**PhD Student \(m/f/div\) in Bioinformatics**](#)
[Max Planck Institute for Molecular Genetics \(MPI-MG\)](#).
[14195 Berlin, Germany](#)
[JOB POST](#)
 - [**PhD Student \(m/f/div\) in Bioinformatics**](#)
[Max Planck Institute for Molecular Genetics \(MPI-MG\)](#).
[14195 Berlin, Germany](#)
[JOB POST](#)
 - [**56868: 3 Engineering Scientists, physicists or similar \(f/m/x\) - Development of an optical frequency reference for the project COMPASSO**](#)
[German Aerospace Center \(DLR\)](#).
[Bremen, Germany](#)
[JOB POST](#)
 - [**PhD candidate - the neurodevelopmental disorder PURA Syndrome \(f/m/x\)**](#)
[Helmholtz Zentrum München - German Research Center for Environmental Health \(HMGU\)](#).

[Neuherberg \(bei München\), Germany](#)

[JOB POST](#)

[Download PDF](#)

Related Articles



- [Ancient-human species mingled in Siberia's hottest property for 300,000 years](#)



- [Ancient African genomes offer glimpse into early human history](#)



- [Mum's a Neanderthal, Dad's a Denisovan: First discovery of an ancient-human hybrid](#)



- [Lost Denisovan bone reveals surprisingly human-like finger](#)



- [Crowdsourcing digs up an early human species](#)



- New species of early human discovered near fossil of 'Lucy'
- Oldest ancient-human DNA details dawn of Neanderthals

Subjects

- Palaeontology
- Evolution

This article was downloaded by **calibre** from <https://www.nature.com/articles/d41586-021-01738-w>

| [Section menu](#) | [Main menu](#) |

- NEWS
- 25 June 2021

Why Uruguay lost control of COVID

Complacency and a coronavirus variant help to explain why the country, once a pandemic success story, couldn't withstand the surge now rocking South America.

- [Luke Taylor](#)
 1. Luke Taylor
[View author publications](#)

You can also search for this author in [PubMed](#) [Google Scholar](#)





•

[Download PDF](#)



A doctor checks on a person infected with COVID-19 at his home in Montevideo, Uruguay. Credit: Matilde Campodonico/AP/Shutterstock

Once looked to as a global model for how to respond to the COVID-19 pandemic, Uruguay has in recent months lost its grip on the coronavirus SARS-CoV-2. It's now one of several countries in South America struggling to control a wave of infections.

Uruguayan scientists say a mix of complacency — fuelled by the country's early success at controlling the virus — and the challenges posed by a particularly transmissible SARS-CoV-2 variant are to blame.

“We were a model in 2020,” says Rafael Radi, a biochemist at the University of the Republic in Montevideo. “Unfortunately, things are not following the same path in 2021.”



[‘We are being ignored’: Brazil’s researchers blame anti-science government for devastating COVID surge](#)

For all of last year, the 3.5-million-person country recorded only about 19,100 cases of COVID-19 and 180 deaths from the disease. But it has already reported more than 341,000 infections and 5,100 deaths this year, according to the online publication [Our World in Data](#), maintained by researchers at the University of Oxford, UK (see ‘Uruguay’s surge’). On several occasions in May and June, it recorded the world’s highest number of COVID-19 deaths per capita.

In the past week, however, new infections and deaths have dropped, thanks to the country’s swift vaccine roll-out, says Radi — giving hope that the country can rein in the virus once more.

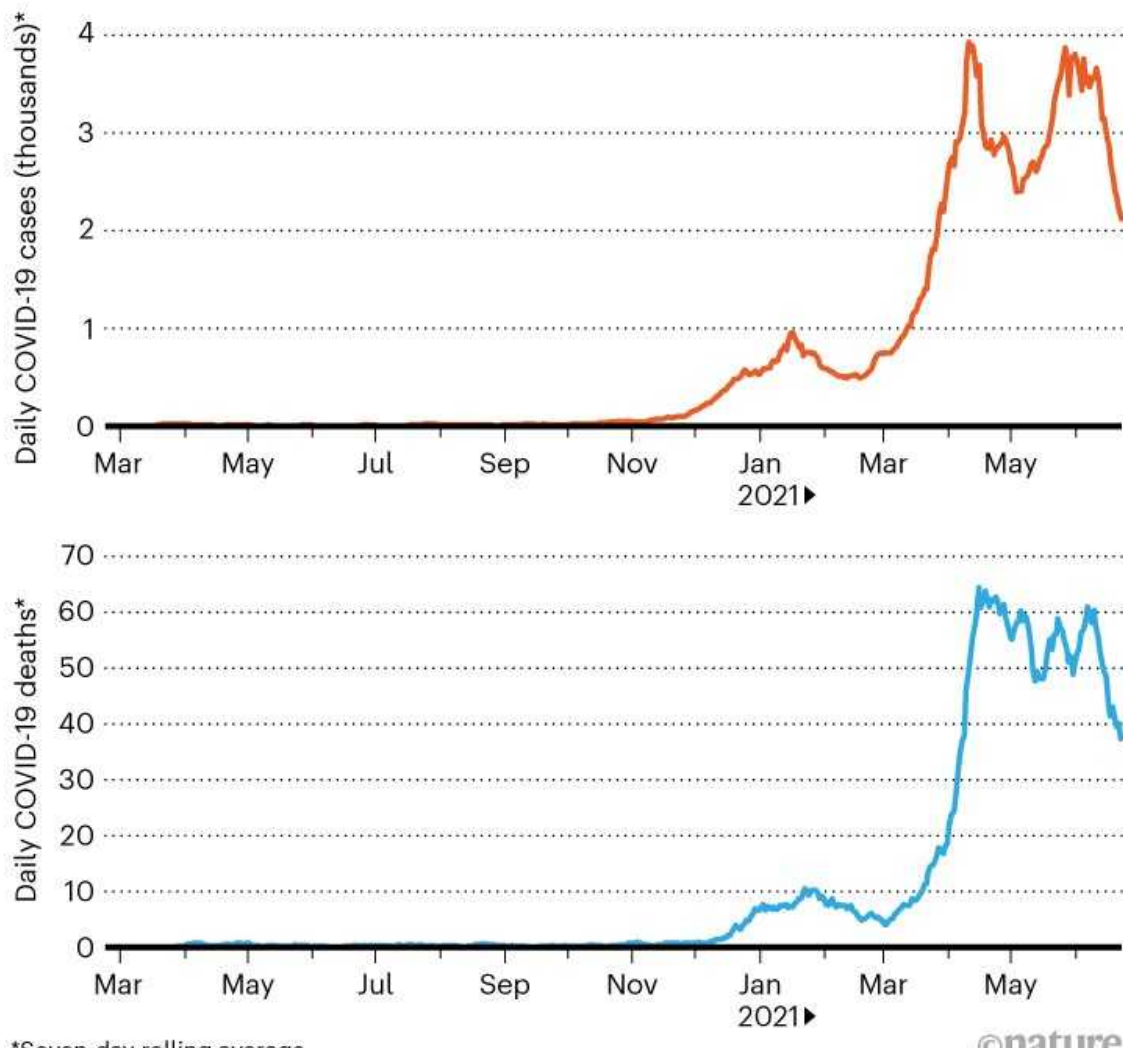
Early success

Uruguayan scientists and representatives attributed the country’s early success at keeping the pandemic in check to government officials following the advice of the Honorary Scientific Advisory Group (GACH), a team of 55 multidisciplinary science experts led by Radi. In March 2020, after the country confirmed its first COVID-19 cases, the government swiftly shut

down businesses and schools, and restricted travel at its borders, on the basis of the group's recommendations.

URUGUAY'S SURGE

The country managed to keep COVID-19 under control for most of 2020, but infections and deaths began to rise late in the year, and skyrocketed in March.



*Seven-day rolling average

©nature

Source: Our World in Data.

“We got many things right,” says Radi. “The coupling of health, science, government and society in 2020 was almost perfect.”

At the same time, [scientists — including Gonzalo Moratorio](#), a virologist at the Pasteur Institute and the University of the Republic, both in Montevideo

— realized that Uruguay would need COVID-19 tests to identify and then isolate people who are infected, and that the country couldn't rely on purchasing those kits from other nations. So the researchers developed their own, and eventually achieved one of the highest testing rates per capita in Latin America — second only to Chile. Thanks to widespread testing, and an aggressive contact-tracing system put in place by Uruguay's Ministry of Health, the country was able to break transmission chains before they could grow exponentially¹. On several occasions in 2020, Uruguay reported no new daily infections.



[Latin American scientists join the coronavirus vaccine race: ‘No one’s coming to rescue us’](#)

But all of that changed in 2021. COVID-19 cases began climbing in December. The GACH once again recommended restrictions, such as border closings, but government officials did not implement all of them. For instance, they did not close restaurants because it would have harmed the economy, says Radi.

As the number of infections continued to grow, Uruguay's test, trace, isolate (Tetris) programme faltered. Once more than 4% of tests come back positive, says Moratorio, Tetris cannot identify and isolate COVID-19 cases quickly enough to contain the virus.

“This really persistent first wave we are suffering is way beyond the Tetris strategy,” says Radi. “We have lost track of a large proportion of cases.”

Stuck in the middle

Another reason for Uruguay’s recent spike is the country’s geography, researchers say.

Although COVID-19 has receded in some parts of the world, it is raging in South America. The continent is currently reporting the five highest rates of weekly COVID-19 deaths per capita in the world.



[Scandal over COVID vaccine trial at Peruvian universities prompts outrage](#)

Uruguay is wedged between two of the region’s hotspots — Argentina and Brazil — where infections have been driven in part by a highly transmissible variant of SARS-CoV-2 called P.1, or Gamma. Some Uruguayan cities, such as Rivera, press against the border with Brazil, making travel restrictions between the countries ineffective there.

In February, less than 15% of all viruses sequenced in Uruguay were the Gamma variant — but in Rivera, that figure stood at 80%, says Rodney Colina, head of the molecular-virology laboratory at the University of the Republic in Salto, Uruguay.

Leakage of the Gamma variant into Uruguay was especially bad during the summer holidays, held early in the year, when family and friends came together rather than staying socially distanced. Scientists now detect the variant in nine of every ten sequenced virus samples nationwide, says Radi.

Relaxed vigilance

But the Gamma variant is only one part of the equation, Uruguay's scientists say. Paradoxically, the country's early success in containing the pandemic probably played a part in the loss of control in 2021.

"National authorities claimed victory too early," says Moratorio. "Fear of the virus was lost because of all the good things we had done before."



How the world failed to curb COVID

When case numbers surged, Uruguay should have locked down to bring them back to manageable levels, says Zaida Arteta, secretary of the Medical Union of Uruguay and a member of the Uruguayan Interdisciplinary COVID-19 Data Analysis Group, which monitors the pandemic.

"We had several opportunities to get back on track with our epidemiological tracing, but instead we continued opening up and moved from a strategy of containment to mitigation," she says.

The office of the Uruguayan president and the Ministry of Public Health did not respond to *Nature*'s queries about why they chose to not follow the GACH's recommendations to enact restrictions the second time around.

Government officials weren't the only ones to let their guard down when it came to COVID-19. Researchers say that compliance with social-distancing recommendations waned in 2021 because the people of Uruguay were confident in how the pandemic had been managed, and in the COVID-19 vaccines. The first shots were administered in Uruguay on 1 March.

Research [published by the GACH that month](#) found that, although the majority of Uruguayans think that COVID-19 is a severe disease, only one in three thought they themselves would get infected within the next six months.



['The perfect storm': lax social distancing fuelled a coronavirus variant's Brazilian surge](#)

“Though infections were increasing, there was a general sense that things were under control or getting better,” says Radi. “In fact, they were getting worse.”

So far, about 43% of Uruguayans have been fully vaccinated, and 63% have received at least one dose of a COVID-19 vaccine. The country has the second-fastest vaccination programme in South America, and on 9 June began administering jabs to people aged 12 to 17.

Positive COVID-19 cases have decreased by more than one-third in the past week. For those who have been vaccinated, admissions to intensive-care units have dropped by more than 92%, and deaths have plummeted by more than 95%, according to a study by Uruguay's Ministry of Public Health.

So experts remain cautiously hopeful. “It’s not over yet, we still have dozens of serious cases and expect more deaths,” says Arteta. “But the vaccine roll-out is one of Uruguay’s strengths. They are efficacious, and we are vaccinating very well and quickly. I hope the trend continues.”

Nature **595**, 21 (2021)

doi: <https://doi.org/10.1038/d41586-021-01714-4>

References

1. 1.

Moreno, P. *et al.* Preprint at medRxiv
<https://doi.org/10.1101/2020.07.24.20161802> (2020).

[Download references](#)

Related Articles

-  [**‘We are being ignored’: Brazil’s researchers blame anti-science government for devastating COVID surge**](#)
-  [**‘The perfect storm’: lax social distancing fuelled a coronavirus variant’s Brazilian surge**](#)

-  [India's massive COVID surge puzzles scientists](#)
-  [Scandal over COVID vaccine trial at Peruvian universities prompts outrage](#)
-  [Latin American scientists join the coronavirus vaccine race: 'No one's coming to rescue us'](#)
-  [How the world failed to curb COVID](#)

Subjects

- [Public health](#)
- [SARS-CoV-2](#)

Jobs from Nature Careers

- - - [All jobs](#)
 - - [PhD Student \(m/f/div\) in Bioinformatics](#)

[Max Planck Institute for Molecular Genetics \(MPI-MG\)](#)

[14195 Berlin, Germany](#)

[JOB POST](#)

- [PhD Student \(m/f/div\) in Bioinformatics](#)

[Max Planck Institute for Molecular Genetics \(MPI-MG\)](#)

[14195 Berlin, Germany](#)

[JOB POST](#)

- [56868: 3 Engineering Scientists, physicists or similar \(f/m/x\) - Development of an optical frequency reference for the project COMPASSO](#)

[German Aerospace Center \(DLR\)](#)

[Bremen, Germany](#)

[JOB POST](#)

- [PhD candidate - the neurodevelopmental disorder PURA Syndrome \(f/m/x\)](#)

[Helmholtz Zentrum München - German Research Center for Environmental Health \(HMGU\)](#)

[Neuherberg \(bei München\), Germany](#)

[JOB POST](#)

[Download PDF](#)

Related Articles

-  [‘We are being ignored’: Brazil’s researchers blame anti-science government for devastating COVID surge](#)
-  [‘The perfect storm’: lax social distancing fuelled a coronavirus variant’s Brazilian surge](#)
-  [India’s massive COVID surge puzzles scientists](#)
-  [Scandal over COVID vaccine trial at Peruvian universities prompts outrage](#)
-  [Latin American scientists join the coronavirus vaccine race: ‘No one’s coming to rescue us’](#)
-  [How the world failed to curb COVID](#)

Subjects

- [Public health](#)
- [SARS-CoV-2](#)

This article was downloaded by **calibre** from <https://www.nature.com/articles/d41586-021-01714-4>

| [Section menu](#) | [Main menu](#) |

- NEWS FEATURE
- 30 June 2021

Beyond coronavirus: the virus discoveries transforming biology

SARS-CoV-2 is just one of nonillions of viruses on our planet, and scientists are rapidly identifying legions of new species.

- [Amber Dance](#) ⁰
 1. Amber Dance is a science journalist in Los Angeles, California.
[View author publications](#)
You can also search for this author in [PubMed](#) [Google Scholar](#)





•



Viruses come in all shapes and sizes, such as the giant mimivirus (top right) and the lunar-lander-shaped bacteriophage (centre). Credit: False-colour electron micrographs (not to same scale). Top row L–R: Smallpox virus; *Acidianus* bottle-shaped virus; *Acanthamoeba polyphaga* mimivirus. centre row L–R: Rabies virus; T4 bacteriophage; rotavirus. Bottom row L–R: Ebola virus; Tobacco rattle virus; HIV-2. SPL; M. Häring *et al./J. Virol.*; E. Ghigo *et al./PLOS Pathog.*; Frederick A. Murphy/CDC Global

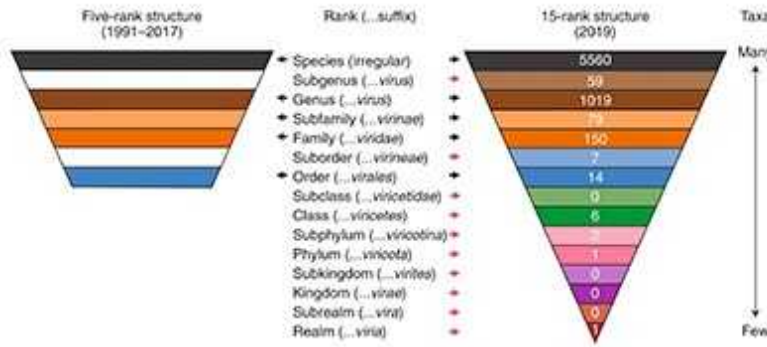
[Download PDF](#)

Mya Breitbart has hunted novel viruses in African termite mounds, Antarctic seals and water from the Red Sea. But to hit pay dirt, she has only to step into her back garden in Florida. Hanging around her swimming pool are spiny-backed orbweavers (*Gasteracantha cancriformis*) — striking spiders with bulbous white bodies, black speckles and six scarlet spikes that make them look like a piece of medieval weaponry. Even more striking for Breitbart, a viral ecologist at the University of South Florida in St Petersburg, was what was inside. When she and her colleagues collected a few spiders and ground them up, they found two viruses previously unknown to science¹.

Although we humans have been focused on one particularly nasty virus since early 2020, there are legions of other viruses out there waiting to be discovered. Scientists estimate that there are about 10^{31} individual viral particles inhabiting the oceans alone at any given time — 10 billion times the estimated number of stars in the known Universe.

It's becoming clear that ecosystems and organisms rely on viruses. Tiny but mighty, they have fuelled evolution for millions of years by shuttling genes between hosts. In the oceans, they slice open microorganisms, spilling their contents into the sea and flooding the food web with nutrients. "Without viruses," says Curtis Suttle, a virologist at the University of British Columbia in Vancouver, Canada, "we would not be alive."

There are just 9,110 named species listed by the International Committee on Taxonomy of Viruses (ICTV), but that's obviously a pitiful fraction of the total. In part, that's because officially classifying a virus used to require scientists to culture a virus in its host or host cells — a time-consuming if not impossible process. It's also because the search has been biased towards viruses that cause diseases in humans or organisms we care about, such as farm animals and crop plants. Yet, as the COVID-19 pandemic has reminded us, it's important to understand viruses that might jump from one host to another, threatening us, our animals or our crops.



The new scope of virus taxonomy: partitioning the virosphere into 15 hierarchical ranks

Over the past ten years, the number of known and named viruses has exploded, owing to advances in the technology for finding them, plus a recent change to the rules for identifying new species, to allow naming without having to culture virus and host. One of the most influential techniques is metagenomics, which allows researchers to sample the genomes in an environment without having to culture individual viruses. Newer technologies, such as single-virus sequencing, are adding even more viruses to the list, including some that are surprisingly common yet remained hidden until now. It's an exciting time to be doing this kind of research, says Breitbart. "I think, in many ways, now is the time of the virome."

In 2020 alone, the ICTV added 1,044 species to its official list, and thousands more await description and naming. This proliferation of genomes prompted virologists to rethink the way they classify viruses and helped to clarify their evolution. There is strong evidence that viruses emerged multiple times, rather than sprouting from a single origin.

Even so, the true range of the viral world remains mostly uncharted, says Jens Kuhn, a virologist at the US National Institute of Allergy and Infectious

Diseases facility at Fort Detrick, Maryland. “We really have absolutely no idea what’s out there.”

Here, there and everywhere

All viruses have two things in common: each encases its genome in a protein-based shell, and each relies on its host — be it a person, spider or plant — to reproduce itself. But beyond that general pattern lie endless variations.

There are minuscule circoviruses with only two or three genes, and massive mimiviruses that are bigger than some bacteria and carry hundreds of genes. There are lunar-lander-looking phage that infect bacteria and, of course, the killer spiky balls the world is now painfully familiar with. There are viruses that store their genes as DNA, and others that use RNA; there’s even a phage that uses an alternative genetic alphabet, replacing the chemical base A in the standard ACGT system with a different molecule, designated Z.



Studies of the spiny-backed orbweaver found two viruses previously unknown to science.Credit: Scott Leslie/Minden Pictures/Alamy

Viruses are so ubiquitous that they can turn up even when scientists aren't looking for them. Frederik Schulz did not intend to study viruses as he pored over genome sequences from waste water. As a graduate student at the University of Vienna, in 2015 he was using metagenomics to hunt for bacteria. This involves isolating DNA from a whole mix of organisms, chopping it into bits and sequencing all of them. A computer program then assembles the bits into individual genomes; it's like solving hundreds of jigsaw puzzles whose pieces have been jumbled up.

Among the bacterial genomes, Schulz couldn't help but notice a whopper of a virus genome — obvious because it carried genes for a viral shell — with a remarkable 1.57 million base pairs². It turned out to be a giant virus, part of a group whose members are large in terms of both genome size and absolute size (typically, 200 nanometres or more across). These viruses infect amoebae, algae and other protists, putting them in a position to influence ecosystems both aquatic and terrestrial.

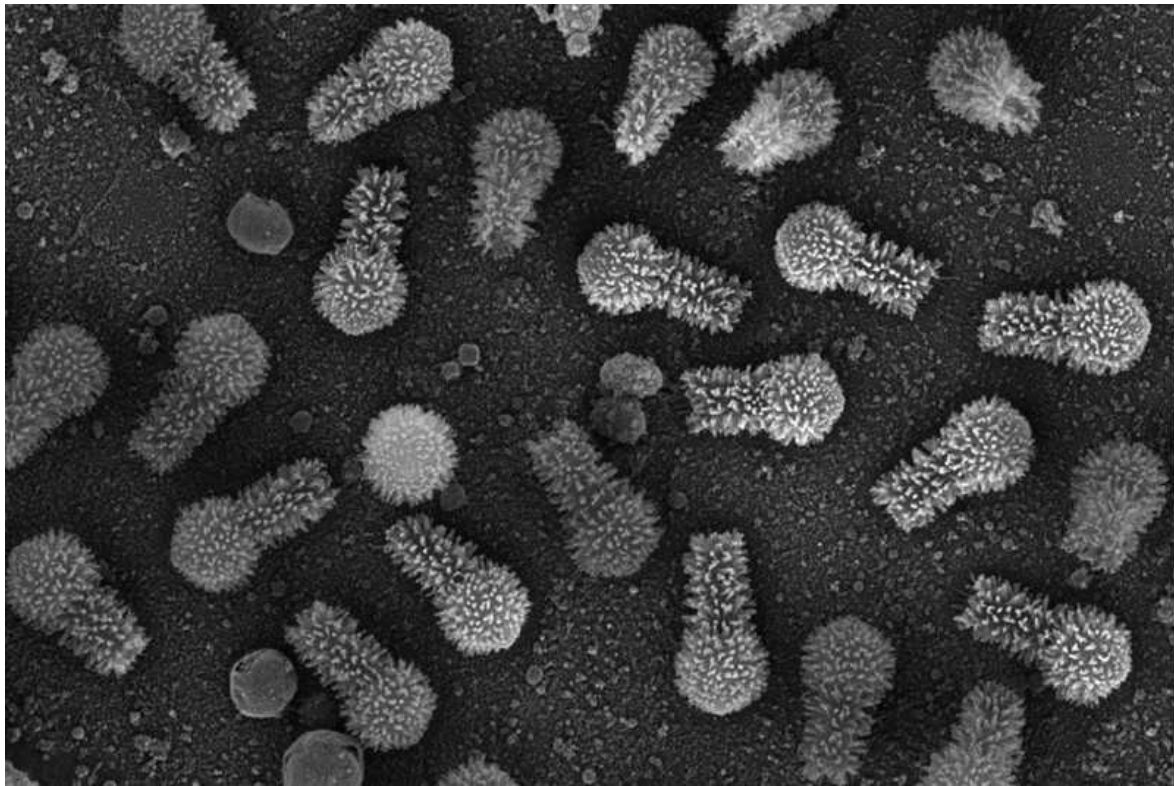


[Profile of a killer: the complex biology powering the coronavirus pandemic](#)

Schulz, now a microbiologist at the US Department of Energy Joint Genome Institute in Berkeley, California, decided to search for related viruses in metagenome data sets. In 2020, in a single paper³, he and his colleagues described more than 2,000 genomes from the group that contains giant viruses; before that, just 205 such genomes had been deposited in public databases.

Virologists have also looked inwards to find new species. Viral bioinformatician Luis Camarillo-Guerrero worked with colleagues at the Wellcome Sanger Institute in Hinxton, UK, to analyse metagenomes from the human gut, and built a database containing more than 140,000 kinds of phage. More than half of these were new to science. Their study⁴, published in February, matched others' findings that one of the most common viruses to infect the bacteria in our guts is a group known as crAssphage (named after the cross-assembly software that picked it up in 2014). Despite its abundance, not much is known about how it contributes to our microbiome, says Camarillo-Guerrero, who now works at DNA-sequencing company Illumina in Cambridge, UK.

Metagenomics has turned up a wealth of viruses, but it ignores many, too. RNA viruses aren't sequenced in typical metagenomes, so microbiologist Colin Hill at University College Cork, Ireland, and his colleagues looked for them in databases of RNAs, called metatranscriptomes. Scientists normally use these data to understand the genes in a population that are actively being turned into messenger RNA in to make proteins, but RNA virus genomes can show up, too. Using computational techniques to pull sequences out of the data, the team found 1,015 viral genomes in metatranscriptomes from sludge and water samples⁵. Again, they'd massively increased the number of known viruses with a single paper.



The giant tupanvirus, found in amoebae, is more than 1,000 nanometres long and has the largest set of protein-coding genes of any known virus. Credit: J. Abrahão *et al./Nature Commun.*

Although it's possible for these techniques to accidentally assemble genomes that aren't real, researchers have quality-control techniques to guard against this. But there are other blind spots. For instance, viral species whose members are very diverse are fiendishly difficult to find because it's hard for computer programs to piece together the disparate sequences.

The alternative is to sequence viral genomes one at a time, as microbiologist Manuel Martinez-Garcia does at the University of Alicante, Spain. He decided to try trickling seawater through a sorting machine to isolate single viruses, amplified their DNA, and got down to sequencing.

On his first attempt, he found 44 genomes. One turned out to represent some of the most abundant viruses in the ocean⁶. This virus is so diverse — its genetic jigsaw pieces so varied from one virus particle to the next — that its genome had never popped up in metagenomics studies. The team calls it 37-F6, for its location on the original laboratory dish, but Martinez-Garcia jokes

that, given its ability to hide in plain sight, it should have been named 007, after fictional superspy James Bond.

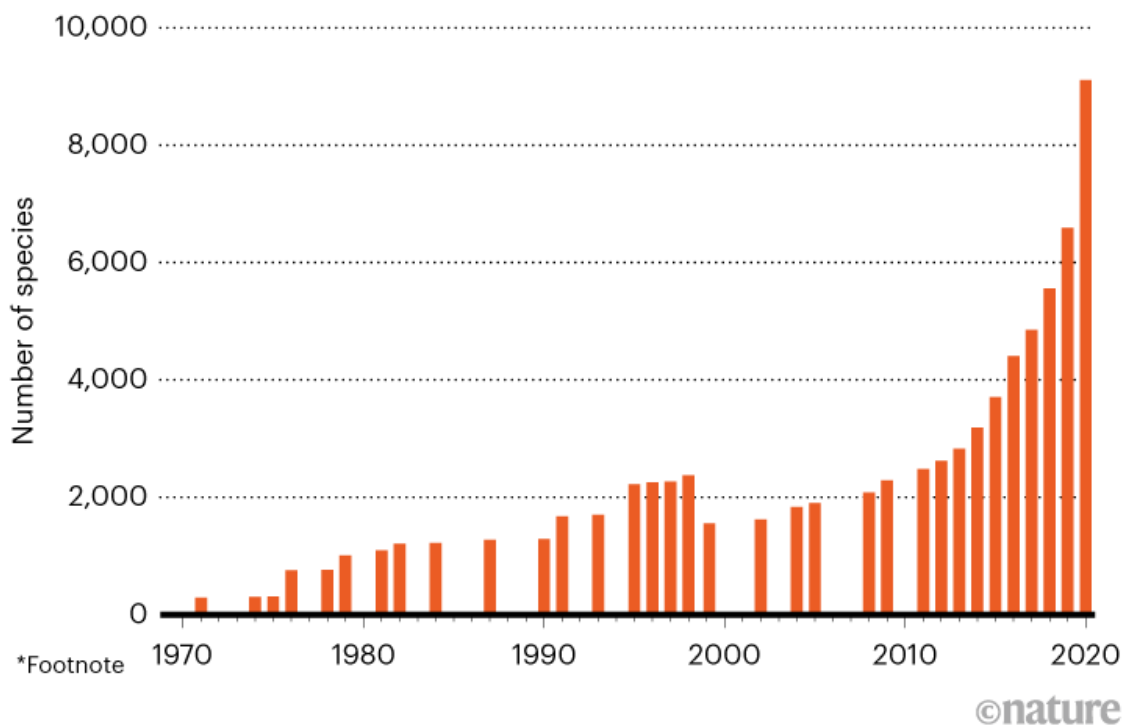
Virus family trees

The James Bond of ocean viruses lacks an official Latin species name, and so do most of the thousands of viral genomes discovered by metagenomics over the past decade. Those sequences presented the ICTV with a dilemma: is a genome enough to name a virus? Until 2016, proposing a new virus or taxonomic group to the ICTV required scientists to have that virus and its host in culture, with rare exceptions. But that year, after a contentious but cordial debate, virologists agreed that a genome was sufficient⁷.

Proposals for new viruses and groups poured in (see ‘Adding to the family’). But the evolutionary relationships between these viruses were often unclear. Virologists usually categorize viruses on the basis of their shapes (long and thin, say, or a head with a tail) or their genomes (DNA or RNA, single- or double-stranded), but this says surprisingly little about shared ancestry. For example, viruses with double-stranded DNA genomes seem to have arisen on at least four separate occasions.

ADDING TO THE FAMILY

Scientists have found and logged viruses in huge numbers in recent years, thanks to technological advances and a change in the way viruses can be named. Viruses can now be classified on the basis of just their genome, instead of researchers having to culture the virus and its host.



Source: ICTV

The original ICTV viral classification, which is entirely separate from the tree of cellular life, included only the lower rungs of the evolutionary hierarchy, from species and genus up to the order level — a tier equivalent to primates or trees with cones in the classification of multicellular life. There were no higher levels. And many viral families floated alone, with no links to other kinds of virus. So in 2018, the ICTV added higher-order levels: classes, phyla and kingdoms⁸.

At the very top, it invented ‘realms’, intended as counterparts to the ‘domains’ of cellular life — Bacteria, Archaea and Eukaryota — but using a different word to differentiate between the two trees. (Several years ago, some scientists suggested that certain viruses might fit into the cell-based evolutionary tree, but that idea has not gained widespread favour.)

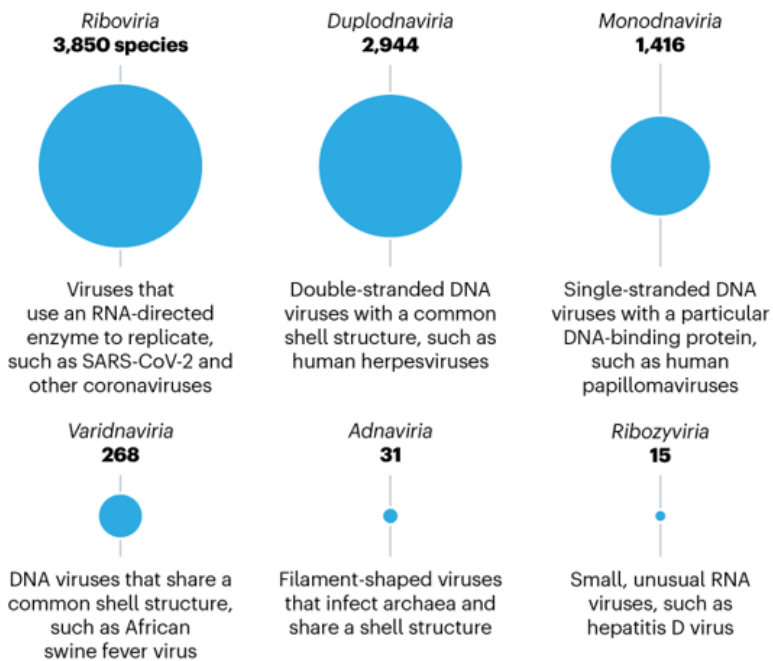
The ICTV outlined the branches of the tree, and grouped RNA-based viruses into a realm called *Riboviria*. SARS-CoV-2 and other coronaviruses, which have single-stranded RNA genomes, are part of this realm. But then it was up to the broader community of virologists to propose further taxonomic groups. As it happened, Eugene Koonin, an evolutionary biologist at the National Center for Biotechnology Information in Bethesda, Maryland, had assembled a team to analyse all the viral genomes, as well as the latest research on viral proteins, to create a first-draft taxonomy⁹.

They reorganized *Riboviria* and proposed three more realms (see ‘Virus realms’). There was some quibbling over the details, Koonin says, but the taxonomy was ratified without much trouble by ICTV members in 2020. Two further realms got the green light in 2021, but the original four realms will probably remain the largest, he says. Eventually, Koonin speculates, the realms might number up to 25.

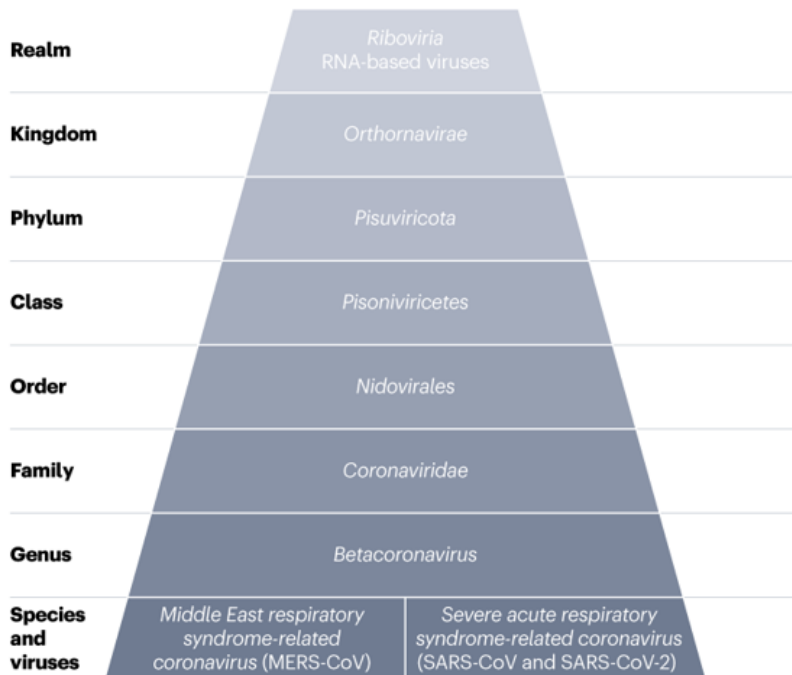
VIRUS REALMS

Unlike cell-based life forms, viruses don't have a single common ancestor, which makes it impossible to create a phylogenetic tree. Instead, as of 2021, the International Committee on Taxonomy of Viruses recognizes six realms, defined by similarities in their members' genes and proteins, each arising from a different common ancestor.

Realms by number of species



The realm of SARS-CoV-2 and its relatives



Source: ICTV (talk.ictvonline.org/taxonomy); ICTV Coronaviridae Study Group. *Nature Microbiol.* **5**, 536–544 (2020)

That number supports many scientists' suspicion that there's no one common ancestor for virus-kind. "There is no single root for all viruses," says Koonin. "It simply does not exist." That means that viruses probably arose several times in the history of life on Earth — and there's no reason to think such emergence can't happen again. "The *de novo* origin of new viruses, it's still ongoing," says Mart Krupovic, a virologist at the Pasteur Institute in Paris who was involved in both the ICTV decisions and Koonin's taxonomy team.

As to how the realms arose, virologists have several ideas. Perhaps they descended from independent genetic elements at the dawn of life on Earth, before cells even took shape. Maybe they escaped or 'devolved' from whole cells, ditching most of the cellular machinery for a minimal lifestyle. Koonin and Krupovic favour a hybrid hypothesis in which those primordial genetic elements stole genes from cellular life to build their virus particles. Because there are multiple origins for viruses, it's possible there are multiple ways they've originated, says Kuhn, who also served on the ICTV committee and worked on the new taxonomy proposal.

Thus, although the viral and cellular trees of life are distinct, the branches touch, and genes pass between the two. Whether viruses count as being 'alive' depends on your personal definition of life. Many researchers do not consider them to be living things, but others disagree. "I tend to believe that they are living," says Hiroyuki Ogata, a bioinformatician working on viruses at Kyoto University in Japan. "They are evolving, they have genetic material composed of DNA and RNA, and they are very important in the evolution of all life."

The current classification is widely recognized as just the first attempt, and some virologists say it's a bit of a mess. A score of families still lack links to any realm. "The good point is, we are trying to put some order in that mess," says Martinez-Garcia.

World changers

With the total mass of viruses on Earth equivalent to that of 75 million blue whales, scientists are certain they make a difference to food webs, ecosystems and even the planet's atmosphere. The accelerating discovery of new viruses "has revealed a watershed of new ways viruses directly impact ecosystems", says Matthew Sullivan, an environmental virologist at Ohio State University in Columbus. But scientists are still struggling to quantify how much of an impact they have.

"We don't have a very simple story around here at the moment," says Ogata. In the ocean, viruses can burst out of their microbial hosts, releasing carbon to be recycled by others that eat the host's innards and then produce carbon dioxide. But, more recently, scientists have also come to appreciate that popped cells often clump together and sink to the bottom of the ocean, sequestering carbon away from the atmosphere.



Viral genomes collected from thawing permafrost at Stordalen Mire in Sweden have genes that could help break down and release carbon. Credit: Bob Gibbons/Alamy

On land, thawing [permafrost is a major source of carbon](#), says Sullivan, and viruses seem to be instrumental in carbon release from microbes in that environment. In 2018, he and his colleagues described 1,907 viral genomes and fragments collected from thawing permafrost in Sweden, including genes for proteins that might influence how carbon compounds break down and, potentially, become greenhouse gases¹⁰.

Viruses can also influence other organisms by stirring up their genomes. For example, when viruses transfer antibiotic-resistance genes from one bacterium to another, drug-resistant strains can take over. Over time, this kind of transfer can create major evolutionary shifts in a population, says Camarillo-Guerrero. And not just in bacteria — an estimated 8% of human DNA is of viral origin. For example, our mammalian ancestors acquired a gene essential for placental development from a virus.

For many questions about viral lifestyles, scientists will need more than just genomes. They will need to find the virus's hosts. A virus itself might carry clues: it could be toting a recognizable bit of host genetic material in its own genome, for example.

Martinez-Garcia and his colleagues used single-cell genomics to identify the microbes that contained the newly discovered 37-F6 virus. The host, too, is one of the most abundant and diverse organisms in the sea, a bacterium known as *Pelagibacter*¹¹. In some waters, *Pelagibacter* makes up half the cells present. If just this one type of virus were to suddenly disappear, says Martinez-Garcia, ocean life would be thrown wildly off balance.

To understand a virus's full impact, scientists need to work out how it changes its host, says Alexandra Worden, an evolutionary ecologist at the GEOMAR Helmholtz Centre for Ocean Research in Kiel, Germany. She's studying giant viruses that carry genes for light-harvesting proteins called rhodopsins. Theoretically, these genes could be useful to the hosts — for purposes such as energy transfer or signalling — but the sequences can't confirm that. To find out what's going on with these rhodopsin genes, Worden plans to culture the host and virus together, and study how the pair function in the combined, 'virocell' state. "Cell biology is the only way you can say what that true role is, how does this really affect the carbon cycle," she says.

Back in Florida, Breitbart hasn't cultured her spider viruses, but she's learnt some more about them. The pair of viruses belong to a category Breitbart calls mind-boggling for their tiny, circular genomes, encoding just one gene for their protein coat and one for their replication protein. One of the viruses is found only in the spider's body, never its legs, so she thinks it's actually infecting some creature the spider eats. The other virus is found throughout the spider's body, and in its eggs and spiderlings, so she thinks it's transmitted from parent to offspring^{[12](#)}. It doesn't seem to be doing them any harm, as far as Breitbart can tell.

With viruses, "finding them's actually the easy part", she says. Picking apart how viruses influence host life cycles and ecology is much trickier. But first, virologists must answer one of the toughest questions of all, Breitbart says: "How do you pick which one to study?"

Nature **595**, 22-25 (2021)

doi: <https://doi.org/10.1038/d41586-021-01749-7>

References

1. 1.

Rosario, K. *et al.* *PeerJ* **6**, e5761 (2018).

[PubMed](#) [Article](#) [Google Scholar](#)

2. 2.

Schulz, F. *et al.* *Science* **356**, 85–85 (2017).

[PubMed](#) [Article](#) [Google Scholar](#)

3. 3.

Schulz, F. *et al.* *Nature* **578**, 432–436 (2020).

[PubMed](#) [Article](#) [Google Scholar](#)

4. 4.

Camarillo-Guerrero, L. F., Almeida, A., Rangel-Pineros, G., Finn, R. D. & Lawley, T. D. *Cell* **184**, 1098–1109.e9 (2021).

[PubMed](#) [Article](#) [Google Scholar](#)

5. 5.

Callanan, J. *et al.* *Sci. Adv.* **6**, eaay591 (2020).

[Article](#) [Google Scholar](#)

6. 6.

Martinez-Hernandez, F. *et al.* *Nature Commun.* **8**, 15892 (2017).

[PubMed](#) [Article](#) [Google Scholar](#)

7. 7.

Simmonds, P. *et al.* *Nature Rev. Microbiol.* **15**, 161–168 (2017).

[PubMed](#) [Article](#) [Google Scholar](#)

8. 8.

International Committee on Taxonomy of Viruses Executive Committee. *Nature Microbiol.* **5**, 668–674 (2020).

[PubMed](#) [Article](#) [Google Scholar](#)

9. 9.

Koonin, E. V. *et al.* *Microbiol. Mol. Biol. Rev.* **84**, e00061-19 (2020).

[PubMed](#) [Article](#) [Google Scholar](#)

10. 10.

Emerson, J. B. *et al.* *Nature Microbiol.* **3**, 870–770 (2018).

[PubMed](#) [Article](#) [Google Scholar](#)

11. 11.

Martinez-Hernandez, F. *et al.* *ISME J.* **13**, 232–236 (2019).

[PubMed](#) [Article](#) [Google Scholar](#)

12. 12.

Rosario, K., Mettel, K. A., Greco, A. M. & Breitbart, M. *J. Gen. Virol.* **100**, 1253–1265 (2019).

[PubMed](#) [Article](#) [Google Scholar](#)

[Download references](#)

Related Articles



- [**Profile of a killer: the complex biology powering the coronavirus pandemic**](#)



- [**Should virus-naming rules change during a pandemic? The question divides virologists**](#)



- [**The new scope of virus taxonomy: partitioning the virosphere into 15 hierarchical ranks**](#)

Subjects

- [Virology](#)
- [Evolution](#)
- [Ecology](#)

Jobs from Nature Careers

- - - [All jobs](#)
 -
 - **PhD Student (m/f/div) in Bioinformatics**

[Max Planck Institute for Molecular Genetics \(MPI-MG\)](#)

[14195 Berlin, Germany](#)

[JOB POST](#)

- **PhD Student (m/f/div) in Bioinformatics**

[Max Planck Institute for Molecular Genetics \(MPI-MG\)](#)

[14195 Berlin, Germany](#)

[JOB POST](#)

- **PhD candidate - the neurodevelopmental disorder PURA Syndrome (f/m/x)**

[Helmholtz Zentrum München - German Research Center for Environmental Health \(HMGU\)](#)

[Neuherberg \(bei München\), Germany](#)

JOB POST

- **PhD in Molecular Obesity Research within the Collaborative Research Center 1052 "Obesity Mechanisms" (f/m/x)**

Helmholtz Zentrum München - German Research Center for Environmental Health (HMGU)

Leipzig, Germany

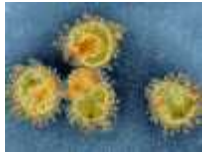
JOB POST

[Download PDF](#)

Related Articles



- **Profile of a killer: the complex biology powering the coronavirus pandemic**



- **Should virus-naming rules change during a pandemic? The question divides virologists**



- **The new scope of virus taxonomy: partitioning the virosphere into 15 hierarchical ranks**

Subjects

- [Virology](#)
 - [Evolution](#)
 - [Ecology](#)
-

This article was downloaded by **calibre** from <https://www.nature.com/articles/d41586-021-01749-7>

| [Section menu](#) | [Main menu](#) |

Opinion

- **[Yuan Longping \(1930–2021\)](#)** [24 June 2021]
Obituary • Crop scientist whose high-yield hybrid rice fed billions.
- **[Five ways to ensure flood-risk research helps the most vulnerable](#)** [29 June 2021]
Comment • Studies are skewed towards resilient places and people: improve data, metrics, inclusion and more.
- **[Boost vaccine confidence with trust, not ire](#)** [29 June 2021]
Correspondence •
- **[Cameroon: doubt could mean vaccine doses expire](#)** [29 June 2021]
Correspondence •
- **[It is dangerous to normalize solar geoengineering research](#)** [29 June 2021]
Correspondence •
- **[Notice who the science system honours, and how](#)** [29 June 2021]
Correspondence •

- OBITUARY
- 24 June 2021

Yuan Longping (1930–2021)

Crop scientist whose high-yield hybrid rice fed billions.

- [Shellen X. Wu](#) 9

1. [Shellen X. Wu](#)

1. Shellen X. Wu is associate professor of history at the University of Tennessee, Knoxville. Her second book will cover Chinese geopolitics and agricultural development.

[View author publications](#)

You can also search for this author in [PubMed](#) [Google Scholar](#)





•

[Download PDF](#)



Credit: Xinhua via Zuma Press

Chinese children recite a Tang dynasty poem that credits the farmer's sweat and toil for the rice on their plates. They should also acknowledge crop scientist Yuan Longping, the 'father of hybrid rice', the higher-yielding crop that feeds billions. He died on 22 May, aged 90.

As a key player in the Green Revolution, Yuan became one of China's most famous scientists, rising to direct the China National Hybrid Rice Research and Development Center in Changsha. When the Olympics came to China in 2008, he carried the torch.

Asked about the secret to his success, he listed four factors: knowledge, hard work, intuition and opportunity, quoting Louis Pasteur's saying that "chance favours the prepared mind". His life reflected the fortuitous conjunction of all four factors against the backdrop of a turbulent century.

Yuan Longping was born on 7 September 1930 in Beiping, as Beijing was called at the time. On the eve of the Communist Party of China's victory in 1949, he entered a college on the outskirts of Chongqing in Sichuan province, which later became Southwest University, to study agriculture and crop genetics.



Bellagio 1969: The green revolution

In the 1950s, China looked to the Soviet Union for guidance in science and technology. Many Chinese biologists adopted the erroneous ideas of Soviet agronomist Trofim Lysenko. One of Yuan's teachers at the college, Guan Xianghuan, continued to follow Gregor Mendel and US evolutionary biologist Thomas Hunt Morgan's theory of heredity and genetics. Because of this, Guan was labelled an enemy of the Communist Party in 1957 and took his own life in the early years of the Cultural Revolution in the 1960s. One of Yuan's later mentors, the geneticist Bao Wenkui, who did his PhD at the California Institute of Technology in Pasadena, was similarly persecuted and imprisoned for long periods.

On graduating in 1953, Yuan was assigned to teach agronomy at Anjiang Agricultural School in Hunan province, a place so small that he struggled to find it on a map. During the Great Leap Forward (1958–60) and the resulting famine, Yuan lived in the Hunan countryside. Nationwide, tens of millions died; some ate tree bark and grass. Yuan saw the bodies of those who had starved to death in the road. The memory of hunger never left him.

From 1960, Yuan focused on rice, China's most important staple crop, working in the fields around his school. In the West, research into the hybridization of wheat and maize (corn) led to the breakthroughs of the Green Revolution. The first generation of hybrid plants is typically more vigorous and productive than either parent, a phenomenon known as heterosis. As a self-pollinating crop, however, rice presented a unique challenge.

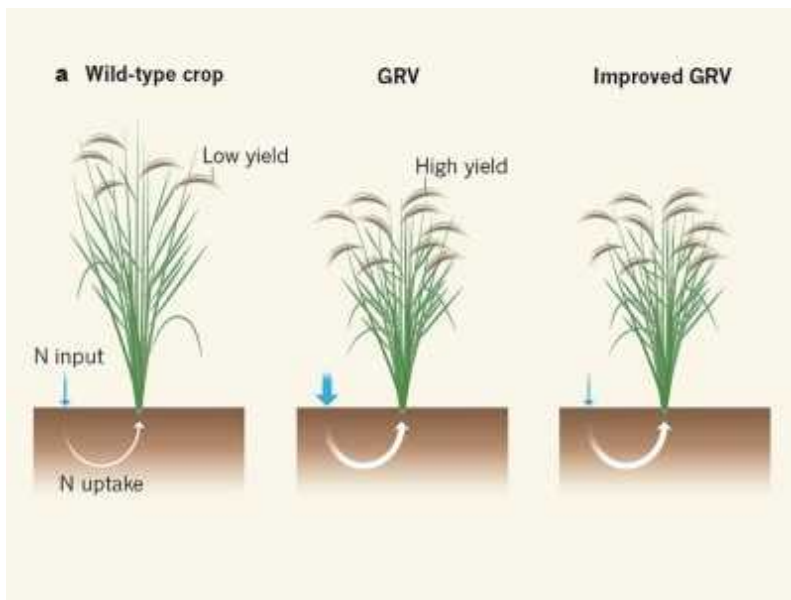


[Norman E. Borlaug \(1914–2009\)](#)

In the summer of 1961, Yuan discovered a stalk of hybrid rice in the wild. In 1964, he and a student spent the summer scouring miles of fields for naturally occurring male-sterile plants. In an article in the April 1966 issue of the premier science journal, Chinese Science Bulletin, Yuan reported his discovery of male-sterile rice plants. It might have saved his life.

With the start of the Cultural Revolution in 1966, the country descended into political chaos. Posters denouncing Yuan as a counter-revolutionary went up around campus, and a spot was reserved for him in the ‘cowshed’, or prison for intellectuals. School officials were stumped when a letter arrived from provincial and national leaders who had seen Yuan’s article, expressing support for his promising research. The dreaded counter-revolutionary designation went to another teacher, and Yuan was allowed to continue working.

Scientists of Yuan’s generation were asked to make enormous sacrifices for their country. In his 2010 memoir, he recalled how one year he spent just a day with his family. Particularly in the 1970s, Yuan spent much of his time on Hainan Island off the southern Chinese coast, where he and his team hunted for the wild strains needed to produce hybrid seed.



Improved nutrient use gives cereal crops a boost

The scientific ethos of the Mao era emphasized teamwork and learning from peasants. Yuan mentored numerous students on the importance of fieldwork. Many of these went on to make their own contributions to agricultural science. Until the late 1970s, aside from his 1966 article, Yuan’s name did not appear on the hybrid rice research he supervised.

Yuan's success inspired hybrid rice production in India, Vietnam and the Philippines. When Japanese geneticist Hiroshi Ikehashi identified a gene that promotes fertility in hybrids in the mid-1980s, Yuan was able to cross diverse plant strains. As a result, rice yields continued to rise when those of hybrid maize and wheat had plateaued. In 1999, it was estimated that the production increases brought about by hybrid rice fed an additional 100 million Chinese people each year ([D. Normile *Science* 283, 313; 1999](#)).

Elected an international member of the US National Academy of Science in 2006, Yuan never made it into the Chinese Academy of Sciences despite being nominated three times. He regularly expressed disinterest in politics: unusually for someone of his prominence, he never joined the Communist Party.

Yuan saw agriculture as his vocation and continued visiting the Hainan research station until he had a fall in March. The only concession he made to old age was driving to the fields, instead of walking or bicycling as earlier in life. To the last, he expressed optimism in the endless possibilities of science and technology, and that the next yield increase, with the potential to contribute to world food security and peace, is within reach.

Nature 595, 26 (2021)

doi: <https://doi.org/10.1038/d41586-021-01732-2>

Competing Interests

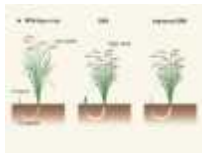
The author declares no competing interests.

Related Articles

-  [Bellagio 1969: The green revolution](#)
- [Genes from wild rice improve yield](#)



- [Norman E. Borlaug \(1914–2009\)](#)



- [Improved nutrient use gives cereal crops a boost](#)

Subjects

- [Plant sciences](#)
- [Agriculture](#)
- [Genetics](#)
- [History](#)

[Jobs from Nature Careers](#)

- - - [All jobs](#)
 - - [PhD Student \(m/f/div\) in Bioinformatics](#)

[Max Planck Institute for Molecular Genetics \(MPI-MG\)](#)

[14195 Berlin, Germany](#)

[JOB POST](#)

- [PhD Student \(m/f/div\) in Bioinformatics](#)

[Max Planck Institute for Molecular Genetics \(MPI-MG\)](#)

14195 Berlin, Germany

JOB POST

- **PhD candidate - the neurodevelopmental disorder PURA Syndrome (f/m/x).**

Helmholtz Zentrum München - German Research Center for Environmental Health (HMGU).

Neuherberg (bei München), Germany.

JOB POST

- **PhD in Molecular Obesity Research within the Collaborative Research Center 1052 "Obesity Mechanisms" (f/m/x).**

Helmholtz Zentrum München - German Research Center for Environmental Health (HMGU).

Leipzig, Germany.

JOB POST

Download PDF

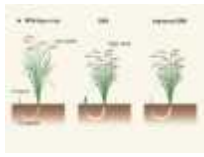
Related Articles



- **Bellagio 1969: The green revolution**
- **Genes from wild rice improve yield**



- [Norman E. Borlaug \(1914–2009\)](#)



- [Improved nutrient use gives cereal crops a boost](#)

Subjects

- [Plant sciences](#)
- [Agriculture](#)
- [Genetics](#)
- [History](#)

This article was downloaded by **calibre** from <https://www.nature.com/articles/d41586-021-01732-2>

- COMMENT
- 29 June 2021

Five ways to ensure flood-risk research helps the most vulnerable

Studies are skewed towards resilient places and people: improve data, metrics, inclusion and more.

- [Miyuki Hino](#) ⁰ &
- [Earthea Nance](#) ¹

1. [Miyuki Hino](#)

1. Miyuki Hino is an associate professor at the University of North Carolina at Chapel Hill, USA.

[View author publications](#)

You can also search for this author in [PubMed](#) [Google Scholar](#)

2. [Earthea Nance](#)

1. Earthea Nance is an assistant professor at Texas Southern University, Houston, USA.

[View author publications](#)

You can also search for this author in [PubMed](#) [Google Scholar](#)





•

[Download PDF](#)



A man carries a mattress salvaged from his home submerged by flooding in southwest Nigeria in 2016.Credit: Pius Utomi Ekpei/AFP via Getty

The year 2020 saw further devastating floods, caused by storms such as Cyclone Amphan in South Asia and a record-breaking hurricane season in the Atlantic Ocean. It is now clear that the changing climate is making coastal flooding more frequent, downpours heavier and storms wetter. Less appreciated is that the impacts of increased flooding are distributed unequally and unfairly. The greatest burdens fall on the most vulnerable.

Global damage from floods and storms has been trending steadily upwards, from US\$94 billion in the 1980s to more than \$1 trillion in the 2010s, according to the emergency-events database EM-DAT (www.emdat.be). This increased economic burden is driven in part by changing climate patterns, alongside increased settlement and development in areas of higher hazard.

Decades of research on environmental justice and social vulnerability have shown that the risks and impacts from flooding are disproportionately borne by marginalized households^{1,2}. Over the past few years, researchers have

begun to quantify this effect. For example, from 1999 to 2013, white residents of US counties with extensive damage from natural hazards, including flooding, on average gained \$126,000 in wealth over this period; Black and Latinx residents on average lost \$27,000 and \$29,000, respectively³. Communities with higher incomes often receive more aid after disasters⁴.

The problem is complex. Climate change not only shifts the weather we experience; it also reshapes the health and extent of natural resources such as forests and wetland ecosystems, financial markets, migration patterns, and the availability and affordability of safe housing. These cascading effects intersect with flood hazards to present new, complicated challenges for research.

Economic, political and social systems distribute climate risk unevenly, and policies designed to help people recover leave out many of the people most in need. Actions that fail to recognize this will reinforce, rather than mitigate, today's large and growing inequities. As communities around the world pay more attention to systemic racism and discrimination, those who study flood risk should similarly question how inequity is embedded in past and current practice.

Five challenges

Researchers can and should step up in five key ways.

Collect the right data. Current hazard models can mask real differences in exposure to flooding. This problem is particularly acute in developing countries, where fewer resources are available for mapping and modelling. For instance, on the basis of coarse elevation data in developing countries, the global population exposed to sea-level rise by 2100 was originally estimated at around 48 million people. After an effort to improve the resolution of the elevation data, that figure nearly quadrupled to 190 million people⁵.

Data gaps and concerns persist in developed countries as well. Most models capture riverine and coastal floods, not the urban flooding that occurs when

drainage systems are overwhelmed. This type of inundation is known to be a threat in older, often low-income and racially segregated parts of cities. Data on when and where this happens are not systematically collected. Residents of underserved communities where mistrust of government is high are less likely to file complaints and report flooding; or they file complaints to no avail. As a result, these areas can seem safe on paper when they are not⁶.

Approaches that engage local institutions and community members in combination with other data sources have been shown to improve flood-risk mapping in diverse places including Nepal⁷, the United States⁸ and Brazil⁹. In Nepal, for example, local residents filled data gaps by documenting the locations of key infrastructure, the elevations of houses, high-water marks, and characteristics that made households socially vulnerable.



Families in Houston, Texas, rescued from their flooded homes after Hurricane Harvey in 2017.Credit: Erich Schlegel/Getty

Choose the right metrics. Most assessments of flood risk and impact rely heavily on the metric of property damage. This practice typically treats each dollar of damage equally. Yet one dollar of damage has a much greater effect

on quality of life and well-being for low-income households than for wealthier ones. For example, after floods in Mumbai, India in 2005, the lowest-income families lost more than six times their monthly household income; middle-income families lost just two to three times^{[10](#)}.

Relying on estimates of property damage as a metric for evaluating the benefits of proposed mitigation methods systematically favours wealthier areas that have more to lose. Simply put, it is currently harder to protect a poor household than a rich one.

One way to correct this would be to adjust for differences in income and wealth, such as measuring risk and loss as relative metrics (damage as a percentage of total value, or losses as a share of household wealth). For example, in Ho Chi Minh City, Vietnam, research shows that considering differences in income and financial protection can lead to dramatically higher assessments of the benefits of protecting low-income populations^{[11](#)}.



Will COVID force public health to confront America's epic inequality?

A second way to shift the balance would be to focus more on the broad benefits to be gained by flood prevention (which everyone can experience) than on the avoided financial damage to property (which depends on existing wealth). A ‘benefits gained’ approach is theoretically more

equitable than the current ‘damages avoided’ method used in the United States.

Choosing metrics that capture aspects of well-being helps to ensure that projects do not simply swap flood stress for other financial or health stresses. This problem can arise when people are relocated out of floodplains. Compensation for relocation is often profoundly inadequate, and new homes can be offered in places that are far removed from jobs, friends and family. In Lagos, Nigeria, and Manila in the Philippines, for example, forced and voluntary relocations led to only temporary moves. People went back home for lack of livelihoods and social connections^{[12](#)}. In Fiji, sea walls built in 2015 to protect from higher sea levels reduced productivity in vegetable gardens and cut people off from the beach — and did not actually prevent flooding^{[13](#)}.

Many countries require some form of cost–benefit analysis for government expenditures, so data on the estimated costs and benefits of specific projects are broadly available. Researchers should mine this information to determine the extent to which cost–benefit analyses have encouraged investments in wealthy neighbourhoods and to examine more-equitable ways of evaluating projects intended to manage flood risk.

More research is also needed to assess the severity and distribution of flood impacts that are often unquantified, such as effects on mental and physical health, loss of employment or lack of access to education. Often severe in low-income populations, these effects are rarely measured.

Probe mechanisms that perpetuate inequality. Vulnerability does not begin with the hazard. For example, marginalized groups and informal settlements often locate in the most flood-prone places because of lack of access to safer land. Requirements for extensive paperwork can cut off access to post-disaster recovery funds for the poor or those facing a language barrier. Such conditions can create and perpetuate divisions across lines of race and class.



More floods, fires and cyclones — plan for domino effects on sustainability goals

These conditions can be very hard to counteract. Take, for example, Harris County, Texas, which includes the city of Houston. It uses the Centers for Disease Control and Prevention's Social Vulnerability Index (SVI) to prioritize flood-infrastructure investments. By scoring higher on the SVI, marginalized areas theoretically gain higher priority in spending on flood infrastructure. This policy of equity prioritization was part of a \$2.5-billion infrastructure bond supported by 85% of voters. However, the public learnt in March 2021 (see go.nature.com/3gduehe) that discretionary actions had undermined the equity goals. Instead of using bond money, which was secure, officials had tied investments in marginalized areas to unreliable matching funds from the federal government. When those monies did not come through, most of the projects in underserved areas were left unfunded.

Harris County had the data, the metrics, the policy, the votes and the money. These were not enough to overcome systemic inequity in the management of flood risk. As a result, the watersheds that contain the highest percentages of people of colour, the highest poverty rates, and the highest risk are now 75% unfunded for flood protection.

Research is needed to uncover how types of governance, organizational cultures, discretionary decisions and different actors — from politicians to

engineers to researchers — contribute to benefits for wealthy and privileged groups.



Heavy rains lashed Mumbai, India, in 2020, disrupting everyday life for its residents. Credit: Ashish Vaishnav/SOPA Images/LightRocket via Getty

Examine those who profit from the current system. Many current efforts to address inequity rely entirely on community consultation. This practice is necessary, but not sufficient. It can, perversely, place the burden of overcoming problems on the shoulders of marginalized people themselves. And it ignores the role of those with power and resources — the people who can investigate and reform policies and practices.

Research that elucidates the advantages and experiences of those with power is important to making progress. Affluent homeowners, for example, can choose to fill in and raise their lots, modifying the topography and pushing water towards the properties of low-income renters who cannot afford to live elsewhere.



The Flint water crisis: how citizen scientists exposed poisonous politics

As the impacts of climate change become more pronounced, there will be opportunities for profit for some and new threats to vulnerable groups. For example, ventures that create proprietary models for high-resolution predictions of climate risk could create a more uneven playing field, allowing those with resources to take advantage of cutting-edge technology while leaving others in the dark.

Policy reform can also create new concerns. The cost of flood insurance jumped in the United States between 2012 and 2014. Those trying to sell houses in low-income and minority neighbourhoods had to lower their prices more frequently to find a willing buyer¹⁴. Reforms aimed at understanding and reducing climate risk could cause similar disparities. Research can illuminate the distribution of the impacts of new policies, focusing on who benefits and who doesn't.

Broaden participation in research. The extent of these research gaps raises the question of why progress has been so slow. The problems are not new. Lack of incentives for the research community from institutions, funders and publishers is one key challenge. For example, research based on building strong relationships with local partners and practitioners is time-consuming. That hinders the inclusion of these people in research funded by grants with short timelines. Appreciation of the importance of this kind of work will

motivate more engagement and, ultimately, provide a stronger evidence base for policy.

Addressing these gaps and biases requires recognition of the value of diverse modes of research, and of outputs that leverage different types of data and different ways of knowing. Research that advances equity in flood-risk management is likely to be highly specific to individual places and communities, and not necessarily generalizable. This is an opportunity to elevate pioneers in the field and bring in and magnify under-represented voices, such as local experts in developing countries.

Sustained investment in a better understanding of the intersection of flood risk and social justice is long overdue.

Nature **595**, 27-29 (2021)

doi: <https://doi.org/10.1038/d41586-021-01750-0>

References

1. 1.

Fothergill, A., Maestas, E. G. M. & DeRouen Darlington, J. A. *Disasters* **23**, 156–173 (1999).

[PubMed](#) [Article](#) [Google Scholar](#)

2. 2.

Hallegatte, S., Vogt-Schilb, A., Rozenberg, J., Bangalore, M. & Beaudet, C. *Econ. Disasters Clim. Change* **4**, 223–247 (2020).

[Article](#) [Google Scholar](#)

3. 3.

Howell, J. & Elliott, J. R. *Social Probl.* **412**, 1–20 (2018).

[Article](#) [Google Scholar](#)

4. 4.

Drakes, O., Tate, E., Rainey, J. & Brody, S. *Int. J. Disaster Risk Reduction* **53**, 102010 (2021).

[Article](#) [Google Scholar](#)

5. 5.

Kulp, S. A. & Strauss, B. H. *Nature Commun.* **10**, 4844 (2019).

[PubMed](#) [Article](#) [Google Scholar](#)

6. 6.

Galloway, G. E. *et al.* *The Growing Threat of Urban Flooding* (Univ. Maryland and Texas A&M Univ., 2018). Available at go.nature.com/3czgkyw

[Google Scholar](#)

7. 7.

Liu, W. *et al.* *ISPRS Int. J. Geo-Inf.* **7**, 1–23 (2018).

[Article](#) [Google Scholar](#)

8. 8.

Gharaibeh, N., Oti, I., Meyer, M., Hendricks, M. & Van Zandt, S. *Risk Analysis* <https://doi.org/10.1111/risa.13256> (2019).

[Article](#) [Google Scholar](#)

9. 9.

Bustillos Ardaya, A., Evers, M. & Ribbe, L. *Land Use Pol.* **88**, 104103 (2019).

[Article](#) [Google Scholar](#)

10. 10.

Patankar, A. & Patwardhan, A. *Nat. Hazards* **80**, 285–310 (2016).

[Article](#) [Google Scholar](#)

11. 11.

Kind, J., Botzen, W. J. W. & Aerts, J. C. J. H. *Environ. Dev. Econ.* **25**, 115–134 (2020).

[Article](#) [Google Scholar](#)

12. 12.

Ajibade, I. *Clim. Change* **157**, 299–317 (2019).

[Article](#) [Google Scholar](#)

13. 13.

Piggott-McKellar, A. E., Nunn, P. D., McNamara, K. E. & Sekinini, S. T. in *Managing Climate Change in the Pacific Region* (ed. Leal Filho, W.) 69–84 (Springer, 2020).

[Google Scholar](#)

14. 14.

Nance, E. *Int. J. Disaster Risk Reduction* **13**, 20–36 (2015).

[Article](#) [Google Scholar](#)

[Download references](#)

Competing Interests

E.N. is a pro-bono member of the Harris County Community Flood Resilience Task Force.

Related Articles

-  [More floods, fires and cyclones — plan for domino effects on sustainability goals](#)
-  [Will COVID force public health to confront America's epic inequality?](#)
-  [How environmental racism is fuelling the coronavirus pandemic](#)
-  [The Flint water crisis: how citizen scientists exposed poisonous politics](#)
-  [India: a turbulent tale of rivers, floods and monsoons](#)

Subjects

- [Climate change](#)

- [Sustainability](#)

Jobs from Nature Careers

- - - [All jobs](#)
 - - **[PhD Student \(m/f/div\) in Bioinformatics](#)**

[Max Planck Institute for Molecular Genetics \(MPI-MG\)](#)

[14195 Berlin, Germany](#)

[JOB POST](#)

- **[PhD Student \(m/f/div\) in Bioinformatics](#)**

[Max Planck Institute for Molecular Genetics \(MPI-MG\)](#)

[14195 Berlin, Germany](#)

[JOB POST](#)

- **[PhD candidate - the neurodevelopmental disorder PURA Syndrome \(f/m/x\)](#)**

[Helmholtz Zentrum München - German Research Center for Environmental Health \(HMGU\)](#)

[Neuherberg \(bei München\), Germany](#)

[JOB POST](#)

- **[PhD in Molecular Obesity Research within the Collaborative Research Center 1052 "Obesity](#)**

Mechanisms" (f/m/x)

Helmholtz Zentrum München - German Research Center for Environmental Health (HMGU)

Leipzig, Germany

JOB POST

Download PDF

Related Articles



- More floods, fires and cyclones — plan for domino effects on sustainability goals



- Will COVID force public health to confront America's epic inequality?



- How environmental racism is fuelling the coronavirus pandemic



- The Flint water crisis: how citizen scientists exposed poisonous politics



- [India: a turbulent tale of rivers, floods and monsoons](#)

Subjects

- [Climate change](#)
- [Sustainability](#)

This article was downloaded by **calibre** from <https://www.nature.com/articles/d41586-021-01750-0>

| [Section menu](#) | [Main menu](#) |

- CORRESPONDENCE
- 29 June 2021

Boost vaccine confidence with trust, not ire

- [Hari McGrath](#) ORCID: <http://orcid.org/0000-0002-0037-4761> ✉
 1. [Hari McGrath](#)
 1. King's College London, UK.

[View author publications](#)

You can also search for this author in [PubMed](#) [Google Scholar](#)





•

[Download PDF](#)

Peter Hotez offers a counteroffensive to aggressive anti-vaccine disinformation ([Nature 592, 661; 2021](#)). However, vaccine hesitancy, rather than outright resistance, is a more important contributor to low COVID-vaccine uptake in certain communities. The concerns of vaccine-hesitant individuals are less polarized and so call for thoughtful handling.

In a large representative UK sample, the proportion of vaccine-hesitant respondents was four times greater than the proportion who were vaccine-resistant ([J. Murphy et al. Nature Commun. 12, 29; 2021](#)). COVID vaccine

hesitancy includes reservations around safety, efficacy and the speed of the vaccine release ([K. Pogue *et al. Vaccines* 8, 582; 2020](#)).

A forceful counteroffensive risks widening the divide between those open to being vaccinated and those who are not, as well as alienating those with reasonable concerns about COVID vaccines. To avert a dwindling of trust in government and scientific authorities and promote the well-being of society, we must enact constructive ways to deal with vaccine hesitancy that are centred around respect, openness and empathy.

Nature **595**, 30 (2021)

doi: <https://doi.org/10.1038/d41586-021-01783-5>

Competing Interests

The author declares no competing interests.

Related Articles

- [See more letters to the editor](#)

Subjects

- [Vaccines](#)
- [Society](#)
- [Psychology](#)

[Jobs from Nature Careers](#)

- - - [All jobs](#)
 - - [PhD Student \(m/f/div\) in Bioinformatics](#)

Max Planck Institute for Molecular Genetics (MPI-MG)

14195 Berlin, Germany

JOB POST

▪ **PhD Student (m/f/div) in Bioinformatics**

Max Planck Institute for Molecular Genetics (MPI-MG)

14195 Berlin, Germany

JOB POST

▪ **PhD candidate - the neurodevelopmental disorder PURA Syndrome (f/m/x)**

Helmholtz Zentrum München - German Research Center for Environmental Health (HMGU)

Neuherberg (bei München), Germany

JOB POST

▪ **PhD in Molecular Obesity Research within the Collaborative Research Center 1052 "Obesity Mechanisms" (f/m/x)**

Helmholtz Zentrum München - German Research Center for Environmental Health (HMGU)

Leipzig, Germany

JOB POST

Download PDF

Related Articles

- [See more letters to the editor](#)

Subjects

- [Vaccines](#)
- [Society](#)
- [Psychology](#)

This article was downloaded by **calibre** from <https://www.nature.com/articles/d41586-021-01783-5>

| [Section menu](#) | [Main menu](#) |

- CORRESPONDENCE
- 29 June 2021

Cameroon: doubt could mean vaccine doses expire

- [Amani Adidja](#)⁰,
- [Yap Boum](#)¹ &
- [Pierre Ongolo-Zogo](#)²

1. [Amani Adidja](#)

1. University of Yaoundé I, Yaoundé, Cameroon.

[View author publications](#)

You can also search for this author in [PubMed](#) [Google Scholar](#)

2. Yap Boum

1. University of Yaoundé I, Yaoundé, Cameroon.

[View author publications](#)

You can also search for this author in [PubMed](#) [Google Scholar](#)

3. Pierre Ongolo-Zogo

1. University of Yaoundé I, Yaoundé, Cameroon.

[View author publications](#)

You can also search for this author in [PubMed](#) [Google Scholar](#)





•

[Download PDF](#)

A huge global effort to increase the number of vaccines reaching low-income countries is necessary, but not sufficient. Working in Cameroon's vaccine roll-out against COVID-19, we've seen a level of hesitancy that we fear could mean that many doses will expire before people can benefit from them. Urgent investment is needed to counter misinformation in community-specific ways. Doses can then reach the most at-risk populations as soon as they arrive.

Cameroon, a nation of 25 million, has enough vaccine for 72% of those at high risk (812,300 people). By mid-June, just 2.3% of them had been fully vaccinated. Only around one in five health workers had accepted shots. Some people even refused polio vaccines, fearing that they were COVID-19 vaccines. At this rate, many of the allocated doses could go to waste.

Introducing a vaccine requires significant preparation to ensure optimal uptake (see, for example, go.nature.com/3wmd3vn). However, one month after the launch of the COVID-19 vaccination campaign in Cameroon, the communication strategy was neither validated nor implemented. Fears about extremely rare adverse events are widespread; fear of the pandemic is not.

Low-income countries must act now to boost confidence in vaccines.

Nature **595**, 30 (2021)

doi: <https://doi.org/10.1038/d41586-021-01784-4>

Competing Interests

The authors declare no competing interests.

Related Articles

- [See more letters to the editor](#)

Subjects

- [Public health](#)
- [Government](#)
- [Developing world](#)

[Jobs from Nature Careers](#)

-

- - [All jobs](#)
 - - **[PhD Student \(m/f/div\) in Bioinformatics](#)**
- [Max Planck Institute for Molecular Genetics \(MPI-MG\)](#)
[14195 Berlin, Germany](#)
[JOB POST](#)
- **[PhD Student \(m/f/div\) in Bioinformatics](#)**
- [Max Planck Institute for Molecular Genetics \(MPI-MG\)](#)
[14195 Berlin, Germany](#)
[JOB POST](#)
- **[PhD candidate - the neurodevelopmental disorder PURA Syndrome \(f/m/x\)](#)**
- [Helmholtz Zentrum München - German Research Center for Environmental Health \(HMGU\)](#)
[Neuherberg \(bei München\), Germany](#)
[JOB POST](#)
- **[PhD in Molecular Obesity Research within the Collaborative Research Center 1052 "Obesity Mechanisms" \(f/m/x\)](#)**
- [Helmholtz Zentrum München - German Research Center for Environmental Health \(HMGU\)](#)

[Leipzig, Germany](#)

[JOB POST](#)

[Download PDF](#)

Related Articles

- [See more letters to the editor](#)

Subjects

- [Public health](#)
- [Government](#)
- [Developing world](#)

This article was downloaded by **calibre** from <https://www.nature.com/articles/d41586-021-01784-4>

| [Section menu](#) | [Main menu](#) |

- CORRESPONDENCE
- 29 June 2021

It is dangerous to normalize solar geoengineering research

- [Frank Biermann](#) 0

1. [Frank Biermann](#)

1. Copernicus Institute of Sustainable Development, Utrecht University, the Netherlands. On behalf of 17 signatories.

[View author publications](#)

You can also search for this author in [PubMed](#) [Google Scholar](#)





•

[Download PDF](#)

We disagree with your view that research into solar geoengineering as a means to cool the planet should be given “a chance” ([Nature 593, 167; 2021](#)).

Your position aligns with those who seek to validate such research as a potential climate-policy option (see go.nature.com/3jfqrbr). However, much climate-governance scholarship opposes these untested technologies as a dangerous distraction from decarbonization policies.

Many social scientists argue that democratic and fair global governance of solar geoengineering is unattainable. Any future use of the approach would require complex decisions at a planetary scale on where, how and for how long it would be deployed, and on who would take responsibility for any harm caused.

In our view, the current world order is unfit to devise and implement such far-reaching agreements on planetary management. In the absence of effective global control, the geopolitics of solar geoengineering would be complex and frightening.

We call on our governments and funding agencies to halt the normalization of research into planetary solar-geoengineering technologies.

Decarbonization of our economies is feasible if the right steps are taken.

Solar geoengineering is neither necessary nor desirable. A global moratorium is needed.

Nature **595**, 30 (2021)

doi: <https://doi.org/10.1038/d41586-021-01724-2>

A full list of co-signatories to this letter appears in Supplementary Information.

Supplementary Information

1. [List of co-signatories](#)

Competing Interests

The author declares no competing interests.

Related Articles

- [See more letters to the editor](#)

Subjects

- [Climate change](#)
- [Funding](#)
- [Government](#)

[Jobs from Nature Careers](#)

- - - [All jobs](#)
 - - [PhD Student \(m/f/div\) in Bioinformatics](#)

[Max Planck Institute for Molecular Genetics \(MPI-MG\)](#)

[14195 Berlin, Germany](#)

[JOB POST](#)

- [PhD Student \(m/f/div\) in Bioinformatics](#)

[Max Planck Institute for Molecular Genetics \(MPI-MG\)](#)

[14195 Berlin, Germany](#)

[JOB POST](#)

- [PhD candidate - the neurodevelopmental disorder PURA Syndrome \(f/m/x\)](#)

[Helmholtz Zentrum München - German Research Center for Environmental Health \(HMGU\)](#)

[Neuherberg \(bei München\), Germany](#)

JOB POST

- **PhD in Molecular Obesity Research within the Collaborative Research Center 1052 "Obesity Mechanisms" (f/m/x)**

Helmholtz Zentrum München - German Research Center for Environmental Health (HMGU)

Leipzig, Germany

JOB POST

Download PDF

Related Articles

- See more letters to the editor

Subjects

- Climate change
- Funding
- Government

This article was downloaded by **calibre** from <https://www.nature.com/articles/d41586-021-01724-2>

- CORRESPONDENCE
- 29 June 2021

Notice who the science system honours, and how

- [Jason R. Dwyer](#) 9

1. [Jason R. Dwyer](#)

1. University of Rhode Island, Kingston, Rhode Island, USA.

[View author publications](#)

You can also search for this author in [PubMed](#) [Google Scholar](#)





•

[Download PDF](#)

As your Editorial points out, “Racism in science is endemic because the systems that produce and teach scientific knowledge have, for centuries, misrepresented, marginalized and mistreated people of colour and under-represented communities” ([Nature 593, 313; 2021](#)). It is also because these systems are selective in whom they honour and how.

In the same issue, a book review on Nobel prizewinner Fred Reines notes his creation of a neutrino laboratory “deep in a gold mine in South Africa in the 1960s, in defiance of academic sanctions against the apartheid state”. It

later states: “The man who rises off the page is an inspiring, supportive colleague ...” ([Nature 593, 334–335; 2021](#)). I understand that this could be representative of the framing offered by the book itself. But why did the crucial questions “inspiring to whom?” and “supportive of whom?” not capture editorial attention? The problems that arise from this kind of framing are much less elusive to detection than the neutrinos under discussion.

Nature **595**, 30 (2021)

doi: <https://doi.org/10.1038/d41586-021-01785-3>

Competing Interests

The author declares no competing interests.

Related Articles

- [See more letters to the editor](#)

Subjects

- [Ethics](#)
- [History](#)

[Jobs from Nature Careers](#)

- - - [All jobs](#)
 - - [PhD Student \(m/f/div\) in Bioinformatics](#)

[Max Planck Institute for Molecular Genetics \(MPI-MG\)](#)

14195 Berlin, Germany

JOB POST

- **PhD Student (m/f/div) in Bioinformatics**

Max Planck Institute for Molecular Genetics (MPI-MG)

14195 Berlin, Germany

JOB POST

- **56868: 3 Engineering Scientists, physicists or similar (f/m/x) - Development of an optical frequency reference for the project COMPASSO**

German Aerospace Center (DLR)

Bremen, Germany

JOB POST

- **PhD candidate - the neurodevelopmental disorder PURA Syndrome (f/m/x).**

Helmholtz Zentrum München - German Research Center for Environmental Health (HMGU)

Neuherberg (bei München), Germany

JOB POST

Download PDF

Related Articles

- **See more letters to the editor**

Subjects

- [Ethics](#)
- [History](#)

This article was downloaded by **calibre** from <https://www.nature.com/articles/d41586-021-01785-3>

| [Section menu](#) | [Main menu](#) |

Work

- **Mental health of graduate students sorely overlooked** [28 June 2021]
Career Feature • Too few resources exist to help early-career scientists deal with the stresses encountered in today's 'publish or perish' culture.
- **Digital secrets of successful lab management** [28 June 2021]
Technology Feature • Group leaders say these tools keep their research groups running smoothly.
- **Breeding heat-tolerant corals to save the Great Barrier Reef** [28 June 2021]
Where I Work • Kate Quigley is part of an Australian collaboration that aims to create corals that can survive warming ocean waters.

- CAREER FEATURE
- 28 June 2021

Mental health of graduate students sorely overlooked

Too few resources exist to help early-career scientists deal with the stresses encountered in today's 'publish or perish' culture.

- [Nikki Forrester](#) 0

1. Nikki Forrester

1. Nikki Forrester is a science journalist based in Davis, West Virginia.

[View author publications](#)

You can also search for this author in [PubMed](#) [Google Scholar](#)





•

[Find a new job](#)

[Download PDF](#)



Many graduate students feel overwhelmed by their work situation, and don't know where to turn for help.Credit: Getty

Graduate students around the world need more support to manage the mental-health issues, such as depression and anxiety, that they are experiencing at worrying rates, according to a report¹ from two US non-profit organizations.

The study was co-produced by the Council of Graduate Schools (CGS) in Washington DC and the Jed Foundation (JED) in New York City. Nance Roy, JED's chief clinical officer, says that the foundation, which works to protect emotional health in teenagers and young adults, wanted to examine the rise in mental-health problems among US graduate students. There are few targeted programmes or policies to mitigate those problems, she says. “We wanted to include the graduate-student voice in our report, but not place the burden of change on them.”

CGS president Suzanne Ortega says that when the organization — which represents about 500 universities in the United States, Canada and elsewhere — realized that its member institutions were noticing mental-health struggles among students, it sought to address the problem. Those institutions “were looking for resources and guidance”, says Ortega.

The CGS–JED report identifies challenges faced by graduate students, such as poor mentorship, the inability to access counselling services and a lack of training for non-academic careers. It also urges university administrators and members of campus communities to improve mental-health support services, revise leave-of-absence policies, and provide mentorship training for faculty members.

Mental-health problems among junior researchers are not specific to the United States, and are driven, in part, by the immense pressure on academic scientists to win funding, publish and land jobs in a brutally competitive market, says Katia Levecque, a psychology and law researcher at Ghent University in Belgium. “The mindset in academia is very often one in which failure is not an option and where non-academic jobs are not an option,” she says. The pandemic has exacerbated the problem, but it existed well before that. A 2017 study² that Levecque co-authored found that one in three PhD students is at risk of developing a mental-health disorder, especially depression.

Other studies have corroborated these findings. A 2020 mental-health survey³ of 13,000 junior researchers conducted by Cactus Communications, a scientific-communications company based in Mumbai, India, found that more than one-third (38%) of respondents often felt overwhelmed by their work situation. In a follow-up survey⁴ by Cactus, one anonymous PhD student in Europe said in a free-text response that being honest and open about mental-health struggles in academia is an important step towards tackling them.

Graduate students worldwide are starting to add their own voices to discussions on mental health: they are talking about their personal challenges, and saying that they can’t master them alone.

Pervasive pressures

Arildo Dias is one of many junior scientists who are struggling with anxiety in uncertain times. He received his PhD in 2013 in plant biology from the State University of Campinas in Brazil, and in 2019 started an unpaid position as a guest researcher at Goethe University Frankfurt in Germany, where his wife had secured a postdoctoral placement. He still has that post now. “It’s quite difficult to find a place where we can both stay and find paying jobs,” he says, noting that the pandemic has constrained work opportunities. “This has interfered with our personal lives because we had planned to have a family.”

The career uncertainty has caused a cascade of mental and personal struggles. “We are always thinking about the future. We don’t have security. We always have temporary contracts,” he says. “We always have the anxiety and stress that we’re not doing enough or should be doing more.”



Plant biologist Arildo Dias is one of many junior scientists who are struggling with anxiety in uncertain times. Credit: Somayeh Shadkam

These worries often drive early-career researchers to work long hours and prioritize their work at the expense of leisure pursuits and other aspects of their lives outside the laboratory. In a 2019 *Nature* survey⁵ of PhD students worldwide, 76% said they worked more than 40 hours per week, and nearly 40% were unsatisfied with their work–life balance.

Anindya Ganguly, a PhD student who studies mental-health issues in work environments at the Indian Institute of Management Calcutta in Kolkata, put his own health at risk by sometimes studying for 18 straight hours to prepare presentations for his two graduate courses. “For the first two years of your PhD, it’s really difficult to do anything other than studying because you know that at any moment, if you slack, you are out,” he says.

The anxiety that he felt about progressing in his PhD programme, combined with a lack of sleep, took a toll on Ganguly’s mental health. “I would call my dad and cry, ‘I cannot take this pressure any more. This is affecting my health. I’m not getting sleep.’ But at the same time, I love research. I want to be a PhD.”

In March 2020, Ganguly says, he faced extreme isolation and loneliness, a common experience of researchers worldwide during the pandemic. As COVID-19 cases rose in India, his university closed and Ganguly returned home to Haroa, where he had no Internet access. Because of travel restrictions, Internet services couldn’t be installed in his home area until June 2020. And, during the lockdown, a severe storm in Ganguly’s home region severed mobile-phone services, preventing him from reaching out to friends and family. “I wouldn’t get out of bed because I was totally shattered from within. I didn’t know what to do,” he says.

When power and phone connections were restored six days later, Ganguly contacted his supervisor, who helped him through the lockdown. “On the days I wouldn’t feel well, he would give me moral support and ask me to exercise and get some sun,” says Ganguly. “I was not very comfortable opening up to anyone, not even my adviser. But over time, I came to know that this is a person I could trust and rely on.”



Pandemic burnout is rampant in academia

Although some researchers have supportive mentors and colleagues with whom they can share their struggles, others experience further mental-health challenges owing to hostile work environments. In the 2019 *Nature* survey of PhD researchers worldwide, 21% of respondents said they had experienced harassment or discrimination in their programmes. Female respondents and those from minority ethnic groups were the most likely to report such behaviour. Scientists from sexual and gender minorities (LGBT+) are also more likely to experience harassment and career obstacles, according to a survey of US scientists (see [Nature](https://doi.org/gjqq) <https://doi.org/gjqq>; 2021).

Clara Giachetti earned her PhD in 2020 at the CONICET Institute of Marine Organisms Biology in Puerto Madryn, Argentina. During her time at graduate school, Giachetti worked with a group of women at her university, from all career stages, to raise awareness of the psychological violence, bias and other difficulties that women at her institution faced. The group conducted a survey asking female respondents to comment on and describe situations in which they felt unsafe at work, then printed the responses and hung them on walls throughout the institute.

Giachetti and her peers organized a safe space where women could discuss frightening experiences, launched a kindergarten and set aside a

breastfeeding room for scientists with babies. “All that begins with this action of visualizing what we are suffering,” says Giachetti.

Doctoral disturbance

Although often born of an intense desire to succeed, the types of mental-health struggle and how they manifest can vary drastically among junior researchers. Fara Rigolle, a PhD student studying psychology at Ghent University, who also mentors master’s students, often finds herself comparing her progress with that of colleagues who are further along in their doctoral programme. “I don’t think others put the expectation on me that I know everything and I’m an expert, but sometimes I do it to myself,” she says.

When a colleague described the symptoms of impostor syndrome to Rigolle, she realized that she was experiencing it herself. “The problem is that you always doubt yourself,” she says. “It’s a constant fight.”



Ewa Pluciennicka, a cognitive psychologist, is the founder of PhD Success, an online platform that provides counselling and peer support for PhD students worldwide. Credit: Anna Zhang

Impostor syndrome can also cause burnout among early-career researchers (see [Nature 591, 489–491; 2021](#)). At the beginning of her PhD programme in 2018, Mariana Murillo Roos questioned whether she was capable of being in the programme or belonged there. To overcome worries about falling behind and loneliness, Murillo Roos worked 12-hour days and at weekends. “Work was kind of a refuge because it was something I could control and set my mind on, rather than feeling sad,” she says. “I also wanted to feel that the sacrifice I was making was worth it.”

Murillo Roos moved from Costa Rica in 2018 to pursue a PhD at the Jena School for Microbial Communication in Germany. She doesn’t speak fluent German and it was tough adjusting to a new culture. As a visa holder, Murillo Roos also felt increased pressure to perform. “It’s truly just one shot,” she says, describing her hope that earning a PhD in Germany will make it easier for her to find opportunities in other European countries. “But you still need a visa — and it’s dependent on your progress.”

Even though she’s been encouraged to take holidays, Murillo Roos works overtime and rarely takes breaks. However, she doesn’t recommend this approach. “I’ve screwed up so many times because I’m tired or because I’m not thinking straight. It’s OK if you want to work a lot, but there’s also a risk. There’s a breaking point,” she says.

Keerti Pendyal, who was diagnosed with clinical depression in 2007, also experienced breaking points during his PhD at the Indian Institute of Management Calcutta. “I was getting divorced during the first year and it took a massive mental toll on my health,” he says, leading him to take a year of medical leave.

He returned to campus mainly because he had a room available there and nowhere else to go. “I was still in a very dark place even after I came back,” he recalls. “Sometimes I slept up to 20 hours a day.” A representative from the student body and his partner supported him through this time, often sitting by his side without pressuring him to talk. He also got a dog.

After returning to his university, Pendyal immediately asked his adviser for a recommended psychiatrist, whom he started seeing. “That was one of the best things I did,” he says. “I realized I can’t ignore my mental health and that I need to balance it along with other aspects of my life” (see ‘Managing mental health’).

Managing mental health

Some PhD students have found ways to cope with their mental-health struggles during graduate school. Here are some of their suggestions.

Take time away from work. When Belgium implemented a lockdown owing to the pandemic, Fara Rigolle, a PhD student studying psychology at the University of Ghent, started going on daily runs. At first, she worried that exercising was taking time away from her research and slowing progress in her PhD. “But in the long term, it really helps to have these moments away from my work,” Rigolle says.

Compare yourself with yourself. PhD students often struggle with impostor syndrome, which can include feelings that they are lagging behind their peers or progressing too slowly in their programmes. Although Rigolle still deals with impostor syndrome as a PhD student, she tries to compare herself only with where she was a year ago. “I can look back on myself and see that I made progress,” says Rigolle.

Talk to people who understand you. In 2018, Mariana Murillo Roos moved from Costa Rica to Germany to pursue a PhD in plant biology. She felt fortunate in having German friends who could help her to navigate the cultural norms and education system in Germany, but acknowledges that cultural barriers can be challenging for researchers who pursue PhDs in countries away from home. “Talking to someone is really important, but it depends a lot on who you talk to,” she says. Finding a person who understood her background helped Murillo Roos to stay motivated through the difficult times during her PhD.

Seek out support networks. “Don’t hide your struggles and don’t be ashamed of them. Be a problem solver and take action for your mental health,” says Ewa Pluciennicka, a cognitive psychologist and founder of

PhD Success, an online platform that provides counselling and peer support for PhD students worldwide. Pluciennicka encourages graduate students to seek out peer-support networks, where they can share their experiences and advice.

Problems of access

But not all researchers seek support for their mental-health struggles, in part because of the perceived stigma and a lack of awareness of the resources that exist. “I wish that universities and colleges were much more open about the resources that are available,” says Pendyal. “Even at my institute, we had to engage with the administration for quite some time to get them to circulate a document that mentioned there is a counsellor available. Students were not aware of this fact.”

In the CGS–JED report, many PhD students described problems accessing care. Counselling centres are often closed after 5 p.m. and at weekends, limiting access for those busy with classes, teaching and research. Some students were also apprehensive about going to a counselling centre where they could potentially encounter undergraduates whom they teach or work with. Financial limitations also prevent some graduate students from seeking care, JED’s Roy says.

Institutions and scientific organizations could offer graduate students classes on self-care, say advocates. “Often, the boundaries between work and life are blurred, and that’s fine — as long as you can handle it,” says Gábor Kismihók, who chairs the Researcher Mental Health Observatory (ReMO) COST Action, an initiative of 120 researchers, based in 31 European countries, to address mental-health issues in academia. “We have to know how to take care of ourselves, but this is not something you automatically know.”

Structural causes

Some institutions have implemented individually focused programmes for graduate students, such as yoga, meditation and time-management workshops, but these initiatives address only the symptoms while

overlooking the drivers of mental-health issues in academia, argues Levecque. “You have the danger of ‘mopping with the tap open’,” she says. “The individual might build up more resilience, regain motivation, and plan her or his work better, but in essence the health-damaging structural causes are not tackled.”

Individually focused programmes can also create a mindset of ‘blaming the victim’, Levecque says. Dias agrees that many mental-health problems are caused by structural problems in academia. “We think that it is an individual’s problem, but that’s just a very small part of the story,” he says. “The problems are with the culture and how the system is set up.”

If institutions and academic stakeholders ignore the structural drivers of mental-health issues among early-career researchers, they will fail to retain those people, warns Levecque. “They will lose the war of talents — it’s as simple as that,” she says. “If other jobs are better paid, have more prospects and enable work–life balance, why should you stay?”

Cactus’s 2020 mental-health survey found that scientists wanted organizations in academia and other stakeholders to foster a more inclusive environment, ensure a good work–life balance and move away from the ‘publish or perish’ culture⁴. “We need to normalize that it’s OK to need holidays and time off, it’s OK to retire, it’s OK to be unproductive for a while,” says Giachetti.



Science careers and mental health

For instance, lab leaders can give graduate students and postdocs greater flexibility in terms of working hours and time off, say advocates. Institutions, they say, can also implement policies that allow graduate students to take leave without being financially burdened. Because graduate students are often on teaching or research stipends, their income is connected to their student status, says Roy. The CGS–JED report recommends that institutions revise graduate-leave policies by allowing students to remain partially engaged with their programmes if they are away from the institution to address their mental-health struggles.

Mentoring for junior researchers often comes up short, according to the CGS–JED report, which recommends focusing on the individual instead of on their scientific output. “This is essential because people are not machines,” says Dias. He suggests that, instead of just looking at research production, lab leaders should ask their trainees how they are feeling and what their career goals are.

“We’ve created a hyper-competitive environment without much guidance about what comes next, and without much thought about how to prepare people for a full range of careers,” says Ortega. The CGS calls for career-development programmes that help junior researchers to acquire skills in communication, leadership, conflict resolution and entrepreneurship^{6,7}.

Institutions, say advocates, also need to enact policies that address harassment and discrimination, which can cause profound mental-health problems among academic researchers. In the Cactus follow-up survey, nearly one-quarter of respondents (23%) wanted academic organizations to implement measures to promote equality and prevent harassment, discrimination and bullying.

As awareness of the prevalence of mental-health issues and potential ways forward grows, so, too, does the desire for lasting structural change. “We keep talking about what is wrong with academia and how we must improve,” says Giachetti. “We need to put into practice all the things that we are discussing.”

Nature **595**, 135–137 (2021)

doi: <https://doi.org/10.1038/d41586-021-01751-z>

References

1. 1.

Council of Graduate Schools & the Jed Foundation. *Supporting Graduate Student Mental Health and Well-being* (CGS, 2021).

[Google Scholar](#)

2. 2.

Levecque, K., Anseel, F., De Beuckelaer, A., Van der Heyden, J. & Gisle, L. *Res. Policy* **46**, 868–879 (2017).

[Article](#) [Google Scholar](#)

3. 3.

Cactus Foundation. *Joy and Stress Triggers: A Global Survey on Mental Health Among Researchers* (Cactus Communications, 2020).

[Google Scholar](#)

4. 4.

Cactus Foundation. *How to Foster a Supportive Research Environment* (Cactus Communications, 2020).

[Google Scholar](#)

5. 5.

Woolston, C. *Nature* **575**, 403–406 (2019).

[PubMed](#) [Article](#) [Google Scholar](#)

6. 6.

Hayter, C. S. & Parker, M. A. *Res. Policy* **48**, 556–570 (2019).

[Article](#) [Google Scholar](#)

7. 7.

Fuhrmann, C. N., Halme, D. G., O'Sullivan, P. S. & Lindstaedt, B. *CBE Life Sci. Educ.* **10**, 239–249 (2017).

[Article](#) [Google Scholar](#)

[Download references](#)

Related Articles

-  [Pandemic burnout is rampant in academia](#)
-  ['The problem is greater than it's ever been': US universities urged to invest in mental-health resources](#)
-  [Science careers and mental health](#)

Subjects

- [Careers](#)
- [Policy](#)
- [Lab life](#)

Jobs from Nature Careers

- - - [All jobs](#)
 - - [PhD Student \(m/f/div\) in Bioinformatics](#)
[Max Planck Institute for Molecular Genetics \(MPI-MG\)](#)
[14195 Berlin, Germany](#)
[JOB POST](#)
 - [PhD Student \(m/f/div\) in Bioinformatics](#)
[Max Planck Institute for Molecular Genetics \(MPI-MG\)](#)
[14195 Berlin, Germany](#)
[JOB POST](#)
 - [56868: 3 Engineering Scientists, physicists or similar \(f/m/x\) - Development of an optical frequency reference for the project COMPASSO](#)
[German Aerospace Center \(DLR\)](#)
[Bremen, Germany](#)
[JOB POST](#)
 - [PhD candidate - the neurodevelopmental disorder PURA Syndrome \(f/m/x\)](#)

Helmholtz Zentrum München - German Research Center for Environmental Health (HMGU)

Neuherberg (bei München), Germany

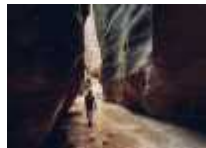
JOB POST

[Download PDF](#)

Related Articles



- [Pandemic burnout is rampant in academia](#)



- [‘The problem is greater than it’s ever been’: US universities urged to invest in mental-health resources](#)



- [Science careers and mental health](#)

Subjects

- [Careers](#)
- [Policy](#)
- [Lab life](#)

This article was downloaded by **calibre** from <https://www.nature.com/articles/d41586-021-01751-z>

- TECHNOLOGY FEATURE
- 28 June 2021

Digital secrets of successful lab management

Group leaders say these tools keep their research groups running smoothly.

- [Kendall Powell 0](#)

1. Kendall Powell

1. Kendall Powell is a freelance writer in Boulder, Colorado.

[View author publications](#)

You can also search for this author in [PubMed](#) [Google Scholar](#)





•

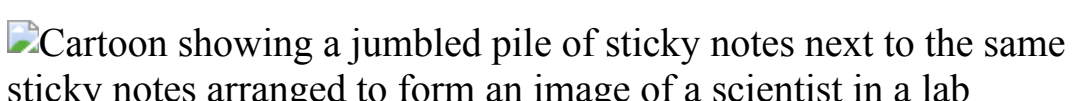


Illustration by The Project Twins

[Download PDF](#)

Christie Bahlai felt as if she was buried under a pile of virtual sticky notes. Like many group leaders, the computational ecologist appreciates that her team uses the messaging app Slack for virtual ‘water-cooler talk’. But she finds the app lacking when it comes to managing the various projects her

laboratory is working on — threads, ideas and long-term goals get lost as conversations and memes rush on.

“Slack is not a great way to record anything for posterity,” says Bahlai, who runs a seven-member group at Kent State University in Ohio. So in May, she decided to “lay down the hammer and invite everyone to a [Trello board](#)”. The project-management software acts like a shareable, virtual bulletin board, and Bahlai hopes it will give team members a tangible way to keep their research moving towards common goals.

“It’s the digitization of my yellow legal-sized notepad,” she says of her analog approach to tracking projects. And, importantly, she can’t misplace it, unlike her notepad.

When it comes to streamlining communications, organizing inventory and general project and lab management, group leaders often seek digital tools that go beyond the usual suspects of Google Docs, Zoom, Slack and GitHub. These tools especially help investigators who lead groups in the range of 5–15 people, that do not have a full-time lab manager or administrative help and who need inexpensive software solutions (see ‘Six tools group leaders love’). (Unless otherwise noted, the software applications highlighted here have a free option for academic and non-profit researchers.)

Six tools group leaders love

- [AnyDesk](#) is free software for accessing and controlling computers remotely.
- Google’s [Apps Script](#) automates actions across the Google application suite.
- [Benchling](#) is a suite of life-sciences apps, with tools for DNA design.
- [Google Keep](#) is a great way to share short, shareable lists of reagents or lab to-do’s, and can be accessed on a mobile phone.
- [Quartzy](#) centralizes lab orders and maps inventories.

- [Voice Dream](#) converts text into voice, and can be used to listen to PDFs of papers in the same way as an audiobook.

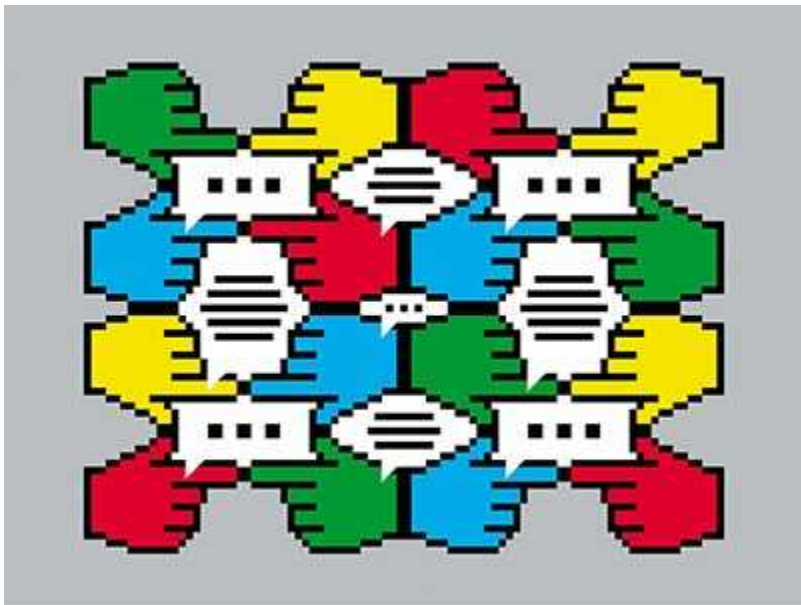
“Ironically, a lot of these tools are about not having people sit in front of a screen all the time,” says computational biologist Mark Gerstein at Yale University in New Haven, Connecticut. “I don’t think that helps people think.” Instead, he says, researchers spawn creativity when talking and scribbling down ideas together, be that on a phone, tablet, laptop or in person.

Big-picture project management

Bahlai’s group investigates insect communities, including using sound to estimate population size. The team navigated the pandemic using a combination of Zoom and Google Docs to talk about the tasks that were ‘on fire’, but longer-term goals were continually falling through the cracks. Trello, she hopes, can help seal those gaps.

Using Trello, Bahlai can break tasks into steps and assign each one to a lab member. For example, for a fieldwork project to record songs of grasshoppers and katydids, her team needs to deploy audio recording devices. The units have rechargeable batteries, so one task on the board is to assign someone to find, test and charge the batteries.

Trello also lets Bahlai get a ‘30,000-foot view’ of her group’s research. It provides a place to store lab ‘stream-of-consciousness’ Google Doc links. And it keeps her accountable, she says. Team members “will be able to say to me, ‘You haven’t reviewed Katie’s paper yet’”.



Tech tools to make research more open and inclusive

Similarly, Mary-Anne Lea, a marine-predator ecologist at the University of Tasmania in Hobart, Australia, is test-driving [Miro](#), an online ‘whiteboard’ app, both for her own group and to integrate interdisciplinary work across several groups and institutions.

Many of Lea’s group’s projects funnel into the South Eastern Australia Sentinels project, a collaboration of eight teams drawn from academic, government and non-profit organizations, which tracks the health, behaviour and human interactions of seabirds and marine mammals, as well as how marine heatwaves affect the animals.

With so many moving parts, it’s hard for everyone to “see how their bit of the puzzle fits into the whole”, says Lea. She wants a tool that handles project management, idea generation and planning consolidation. “I think Miro can do these things for us.”

Lea expects Miro will be especially helpful for students who have a 1–2-year project to have a place where they can outline their tasks, and she is beta-testing the idea with one of her undergraduate honours students, who studies penguins. They have each set up their own Miro boards and share them with each other. “She can see my big-picture thinking and where her project fits into that, and I can see what she is planning,” Lea says.

Digital aids for communication

For C. Titus Brown, a bioinformatician who spends most of his days at the University of California, Davis, in front of a screen, there's value in good old-fashioned conversations with his lab members.

But Brown hates meetings — particularly recurring events. “I'm philosophically against having weekly meetings where people who are stuck on things have to talk about them,” he says. Still, he wants the members of his 15-strong Laboratory for Data-Intensive Biology to be able to reach him easily for one-to-one catch-ups.

When Brown had weeks on the “rollercoaster of faculty time commitments”, he found that he spent more time on e-mail and Doodle polls trying to schedule a meeting than the meeting would actually take. Now, he's turned to the scheduling app [Calendly](#) to ensure he's available when team members need him.



[Four tools that help researchers working in collaborations to see the big picture](#)

Calendly has free and low-cost subscriptions (US\$8–15 per month), and integrates with Google, iCloud and Outlook calendars and with meeting

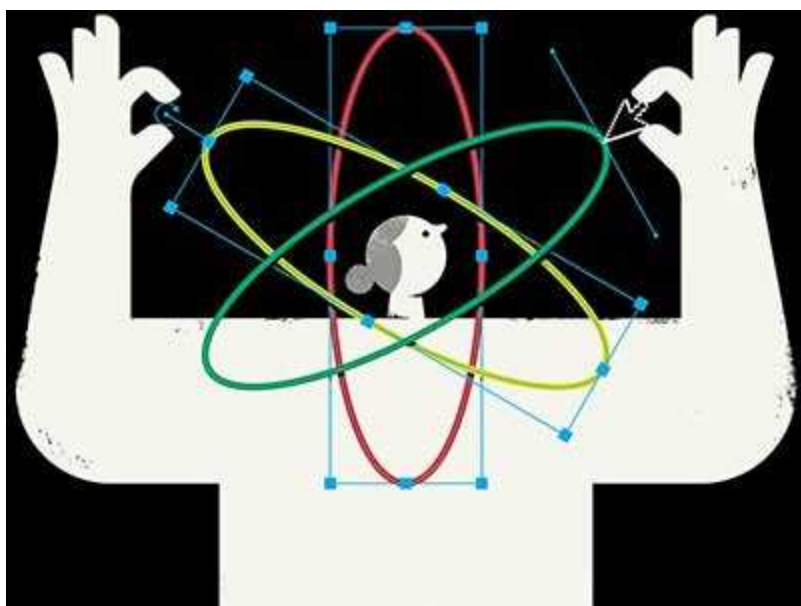
programs such as Zoom, Google Meet and Microsoft Teams, without sacrificing privacy. “It integrates with my calendar in a way that no one can see why I’m busy at a particular time,” says Brown.

Users can create public Calendly pages that allow anyone with the link to request an appointment in prespecified time blocks. When someone books a time slot, the program sends the user a notification and updates their calendar.

Users can also opt for ‘secret’ events that are not available for everyone, such as early-morning or late-night slots for international collaborators. Brown reserves one of these for doctoral students who need to schedule three-hour thesis meetings.

“I’d rather be meeting with my lab members than other people,” says Brown, and Calendly gives them a nice window into his calendar and availability.

Like Brown, Gerstein prizes face-to-face conversation and collaboration in his group, which works on large-scale analyses of biosensor and wearable data. As such, it attracts “hard-core computer geeks”, he says, so he’s thought deeply about how to entice them out from behind their screens.



[The software that powers scientific illustration](#)

“Computers now let us dictate, write and draw with our hands in much more relaxing and natural ways,” he says. Gerstein sets his phone on a nearby table, then uses [Google Recorder](#) to capture discussions, and the app (which is available only on Pixel phones) transcribes it in real time. The transcript is coupled to the audio and can be searched by keyword. Another dictation app, known as [Rev](#), offers quick-turnaround manual transcriptions for \$1.25 per minute of recording. Gerstein also uses the app Grammarly to “take the yucky voice-to-text transcript and fix the language up quickly”.

Gerstein describes his group’s use of these tools together as a “stack” to go from conversation to a rough draft of a manuscript in just a few clicks, he says. He estimates that the tools cut the time they spent on that task in half.

Gerstein has also investigated tools that digitally recreate the experience of scientists gathered around a whiteboard. Zoom’s Annotate feature is one option, which he has deployed during remote meetings both before and during the pandemic. Another is [Rocketbook](#), a reusable physical notebook (\$16–45) that has whiteboard-like paper paired with a mobile-phone app that converts photos of notebook scribbles, cartoons and diagrams into digital files. Both Rocketbook and [Google Lens](#) use optical character recognition to interpret handwriting and translate it into searchable text. “I’ve saved thousands of sheets of paper this way,” says Gerstein.

Taking stock

At the University of New Mexico in Albuquerque, immunologist Irene Salinas’ lab-management challenge was all about inventory. Members of her group had grown frustrated by the disorganized lab supplies and chaotic lab supply chain, made worse by pandemic disruptions. “We would have one million e-mails about who ordered it, did it arrive, who received it, was it aliquoted and where was it stored?” Salinas recalls.

What she needed was a way to track the entire chain from when a reagent needed ordering to its final storage on the lab’s shelves or in refrigerators or freezers. Luckily, one of her postdoctoral researchers was married to a freelance software engineer, and he agreed to develop an app for them and customize it to their needs.

[Lab Inventory](#) automates the workflow so that the team members can access and check on orders at any point. It embeds photos of the items and PDFs of order forms to make reordering easier. Developer Christian Bullo says that such customized web applications cost \$3,000–5,000 to build, and require about a month to develop. The app works for labs of up to 30 people, but could be scaled up for larger groups, he says.



[NatureTech hub](#)

For labs whose hardware is in high demand, [Bookkit](#) streamlines equipment booking and management. “Bookkit is like AirBnB for research facilities,” says Raif Yuecel, head of the Centre for Cytomics at the University of Exeter, UK.

With more than 40 people trying to access 10 pieces of equipment, Yuecel needed a way to manage use in an efficient and controlled way. Through Bookkit, he can advertise the instruments and services that his flow-cytometry core facility provides. Potential clients, both internal and external, can book immediately if there is availability and they have permission, or they can send a request to Yuecel’s team. On the Bookkit dashboard, Yuecel can see the daily, weekly or monthly calendars for all of the instruments and can control access on a per-user basis.

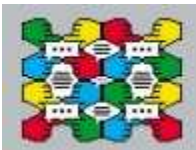
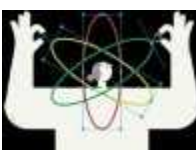
Yuecel accesses Bookkit through his university's subscription, but a free option is available for individual academic groups. Group leaders can generate a report each month to see who used each piece of equipment, how often and for which projects, as well as the associated costs. "We can do optimum resource management by tracking the usage of our instrumentation," says Yuecel.

Group leaders must find the digital tools that make their labs more streamlined, effective and creative. Apps that can do those things, leaders say, are worth their learning curves. Between in-house software, social media for outreach and other tools, researchers can become overwhelmed by platform fatigue, Lea says. "However, there's joy and excitement for learning new software if it makes your life easier."

Nature **595**, 138-139 (2021)

doi: <https://doi.org/10.1038/d41586-021-01752-y>

Related Articles

-  • [**Four tools that help researchers working in collaborations to see the big picture**](#)
-  • [**Tech tools to make research more open and inclusive**](#)
-  • [**The software that powers scientific illustration**](#)



- [NatureTech hub](#)

Subjects

- [Lab life](#)
- [Research management](#)
- [Communication](#)
- [Careers](#)

Jobs from Nature Careers

- - - [All jobs](#)
 - - **[PhD Student \(m/f/div\) in Bioinformatics](#)**
[Max Planck Institute for Molecular Genetics \(MPI-MG\)](#)
[14195 Berlin, Germany](#)
[JOB POST](#)
 - **[PhD Student \(m/f/div\) in Bioinformatics](#)**
[Max Planck Institute for Molecular Genetics \(MPI-MG\)](#)
[14195 Berlin, Germany](#)
[JOB POST](#)
 - **[56868: 3 Engineering Scientists, physicists or similar \(f/m/x\) - Development of an optical](#)**

frequency reference for the project COMPASSO

German Aerospace Center (DLR)

Bremen, Germany

JOB POST

- PhD candidate - the neurodevelopmental disorder PURA Syndrome (f/m/x).

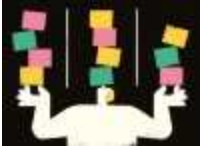
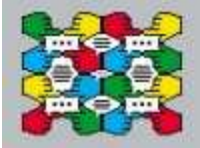
Helmholtz Zentrum München - German Research Center for Environmental Health (HMGU)

Neuherberg (bei München), Germany

JOB POST

Download PDF

Related Articles

-  Four tools that help researchers working in collaborations to see the big picture
-  Tech tools to make research more open and inclusive

-  [The software that powers scientific illustration](#)
-  [NatureTech hub](#)

Subjects

- [Lab life](#)
- [Research management](#)
- [Communication](#)
- [Careers](#)

This article was downloaded by **calibre** from <https://www.nature.com/articles/d41586-021-01752-y>.

| [Section menu](#) | [Main menu](#) |

- WHERE I WORK
- 28 June 2021

Breeding heat-tolerant corals to save the Great Barrier Reef

Kate Quigley is part of an Australian collaboration that aims to create corals that can survive warming ocean waters.

- [James Mitchell Crow](#) ⁰

1. James Mitchell Crow

1. James Mitchell Crow is a freelance science writer in Melbourne, Australia.

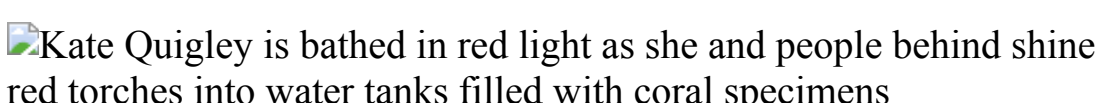
[View author publications](#)

You can also search for this author in [PubMed](#) [Google Scholar](#)





•



Kate Quigley is a research scientist at the Australian Institute of Marine Science outside Townsville, Queensland. Credit: Juergen Freund

[Download PDF](#)

Every October or November, over a few specific nights, corals in the Great Barrier Reef release many millions of eggs and sperm into the waters off Queensland, Australia, during a mass spawning event. My research brings this action indoors to Australia's national sea simulator. In this photo, taken

in November 2019, I am eagerly peering into the tank because the big dance is about to happen. We use red light to watch the spawning, because it doesn't disturb the coral.

I'm part of a multi-institute collaboration called the Reef Restoration and Adaptation Program. I study selective breeding of corals for heat tolerance in the face of climate change.

In the far north of the Great Barrier Reef (GBR), where the water is hottest, we find superstar corals that survive the high temperatures. These corals breed naturally with ones from farther south during spawning, but that is not happening fast enough to keep pace with rising temperatures. Through selective breeding, we can introduce heat tolerance into populations that don't have it — such as those in this tank, collected from the Keppel Islands in the southern GBR.

The GBR is the size of Italy. Can we scale up the seeding process by selectively breeding in land-based nurseries, before transferring baby heat-tolerant corals to the reef? Or is it better for tanker ships to put coral reproductive cells directly onto reefs?

Corals have a rich diversity of symbionts — single-celled algae — living inside them. Breeding the host coral for good heat tolerance can get us about a 10-fold increase in survival when temperatures rise. But if we combine that with heat-tolerant symbionts, we get a 26-fold increase.

Selective breeding can buy us time to get the reef's problem under control, but it is no silver bullet. Heat tolerance from natural genetic variation will run out if the temperature continues to spiral upward.

Nature **595**, 142 (2021)

doi: <https://doi.org/10.1038/d41586-021-01753-x>

Related Articles

-  [Unpicking the rhythms of the Amazon rainforest](#)
-  [Catching a wave to study coral](#)
-  [Charting ice from above](#)

Subjects

- [Careers](#)
- [Climate sciences](#)
- [Ocean sciences](#)

Jobs from Nature Careers

- - - [All jobs](#)
 - - [PhD Student \(m/f/div\) in Bioinformatics](#)

[Max Planck Institute for Molecular Genetics \(MPI-MG\)](#)

[14195 Berlin, Germany](#)

[JOB POST](#)

PhD Student (m/f/div) in Bioinformatics

Max Planck Institute for Molecular Genetics (MPI-MG)

14195 Berlin, Germany

JOB POST

- **PhD candidate - the neurodevelopmental disorder PURA Syndrome (f/m/x).**

Helmholtz Zentrum München - German Research Center for Environmental Health (HMGU)

Neuherberg (bei München), Germany

JOB POST

- **PhD in Molecular Obesity Research within the Collaborative Research Center 1052 "Obesity Mechanisms" (f/m/x)**

Helmholtz Zentrum München - German Research Center for Environmental Health (HMGU)

Leipzig, Germany

JOB POST

Download PDF

Related Articles

-  [Unpicking the rhythms of the Amazon rainforest](#)
-  [Catching a wave to study coral](#)
-  [Charting ice from above](#)

Subjects

- [Careers](#)
- [Climate sciences](#)
- [Ocean sciences](#)

This article was downloaded by **calibre** from <https://www.nature.com/articles/d41586-021-01753-x>

| [Section menu](#) | [Main menu](#) |

Research

- **[Programmable capillary action controls fluid flows](#)** [30 June 2021]

News & Views • A technological platform has been developed in which millimetre-scale cubes are assembled into 3D structures that control capillary action — enabling programmable fluid flows and modelling of a range of fluidic processes.

- **[Designer fibre meals sway human gut microbes](#)** [23 June 2021]

News & Views • Understanding how diet affects gut microbes and thereby influences human health might lead to targeted dietary strategies. A clinical trial now provides some steps on the path towards this goal.

- **[Migratory birds aid the redistribution of plants to new climates](#)** [23 June 2021]

News & Views • Birds that travel long distances can disperse seeds far and wide. An assessment of the timing and direction of European bird migration reveals how these patterns might affect seed dispersal as the planet warms.

- **[A base-pair view of interactions between genes and their enhancers](#)** [09 June 2021]

News & Views • A technique reveals how folded chromosomal DNA interacts in the nucleus, providing information at the level of single base pairs. The achievement offers an unprecedented level of detail about how gene activity is regulated.

- **[A highly magnetized and rapidly rotating white dwarf as small as the Moon](#)** [30 June 2021]

Article • A binary star merger has produced a white dwarf with a spin period of under 7 minutes, a magnetic field of 600 to 900 million gauss and a radius only slightly larger than that of our Moon.

- **[Demonstration of a trapped-ion atomic clock in space](#)** [30 June 2021]

Article • Operating in space, NASA's Deep Space Atomic Clock, a trapped-ion clock, is shown to have long-term stability and drift that are an order of magnitude better than current space clocks.

- **[Bilayer Wigner crystals in a transition metal dichalcogenide heterostructure](#)** [30 June 2021]

Article • Optical signatures reveal correlated insulating Wigner crystals—electron solids—in a bilayer of a two-dimensional transition metal dichalcogenide, MoSe₂, with hexagonal boron nitride between the layers.

- **Signatures of Wigner crystal of electrons in a monolayer semiconductor** [30 June 2021]
Article • The signature of a Wigner crystal—the analogue of a solid phase for electrons—is observed via the optical reflection spectrum in a monolayer transition metal dichalcogenide.
- **Cellular fluidics** [30 June 2021]
Article • Cellular fluidics provides a platform of unit-cell-based, three-dimensional structures for the deterministic control of multiphase flow, transport and reaction processes.
- **Precise date for the Laacher See eruption synchronizes the Younger Dryas** [30 June 2021]
Article • A revised date for the Laacher See eruption using measurements of subfossil trees shifts the chronology of European varved lakes relative to the Greenland ice core record, synchronizing the onset of the Younger Dryas across the North Atlantic–European sector.
- **Ridgecrest aftershocks at Coso suppressed by thermal destressing** [30 June 2021]
Article • Thirty years of geothermal heat production at Coso in California depleted shear stresses within the geothermal reservoir, which changed its faulting style and inhibited aftershocks from the 2019 Ridgecrest earthquake.
- **Limited potential for bird migration to disperse plants to cooler latitudes** [23 June 2021]
Article • Interactions between European bird and plant species show that fruiting period has a major effect on seed dispersal by migrating birds, which will influence plant adaptations to climate change through latitudinal dispersal.
- **Geometry of abstract learned knowledge in the hippocampus** [16 June 2021]
Article • The hippocampus geometrically represents both physical location and abstract variables on a neural manifold in mice performing a decision-making task in virtual reality.
- **Lineage tracing of human development through somatic mutations** [12 May 2021]
Article • Whole-genome sequencing of haematopoietic colonies from human fetuses reveals the somatic mutations acquired by individual progenitors, which are used as barcodes to construct a phylogenetic tree of blood development.
- **Evaluating microbiome-directed fibre snacks in gnotobiotic mice and humans** [23 June 2021]

Article • Fibre snacks that target distinct features of the microbiomes of donors with obesity transplanted into gnotobiotic mice also lead to fibre-specific changes in the microbiome and physiology when used in controlled-diet human studies.

- **An invariant Trypanosoma vivax vaccine antigen induces protective immunity** [26 May 2021]

Article • Systemic genome-led vaccinology and a mouse model of Trypanosoma vivax infection identify protective invariant subunit vaccine antigens, and demonstrate the possibility of generating effective vaccines that induce long-lasting protection against trypanosome infections.

- **TIM-3 restrains anti-tumour immunity by regulating inflammasome activation** [09 June 2021]

Article • Mouse genetic studies and single-cell transcriptome analysis demonstrate that TIM-3 on dendritic cells has a key role in regulating antitumour immunity via inflammasome activation and is a potential target for anticancer therapy.

- **COVID-19 tissue atlases reveal SARS-CoV-2 pathology and cellular targets** [29 April 2021]

Article • Single-cell analysis of lung, heart, kidney and liver autopsy samples shows the molecular and cellular changes and immune response resulting from severe COVID-19 infection.

- **A molecular single-cell lung atlas of lethal COVID-19** [29 April 2021]

Article • Lung samples collected soon after death from COVID-19 are used to provide a single-cell atlas of SARS-CoV-2 infection and the ensuing molecular changes.

- **A proximity-dependent biotinylation map of a human cell** [02 June 2021]

Article • A proximity-dependent biotinylation technique defines the location of more than 4,000 proteins in a human cell, and almost 36,000 proximal interactions between proteins, including those at the interface of the mitochondria and ER.

- **Defining genome architecture at base-pair resolution** [09 June 2021]

Article • Micro Capture-C allows physical contacts to be determined at base-pair resolution, revealing that transcription factors have an important role in the maintenance of the contacts between enhancers and promoters.

- **Structural basis of antifolate recognition and transport by PCFT** [26 May 2021]

Article • Cryo-electron microscopy structures of PCFT in a substrate-free state and bound to the antifolate drug pemetrexed provide insights into how this protein recognizes folates and mediates their transport into cells.

| [Next section](#) | [Main menu](#) | [Previous section](#) |

- NEWS AND VIEWS
- 30 June 2021

Programmable capillary action controls fluid flows

A technological platform has been developed in which millimetre-scale cubes are assembled into 3D structures that control capillary action — enabling programmable fluid flows and modelling of a range of fluidic processes.

- [Tammi L. van Neel](#) ORCID: <http://orcid.org/0000-0002-3626-8418>⁰
&
 - [Ashleigh B. Theberge](#) ¹
1. [Tammi L. van Neel](#)

1. Tammi L. van Neel is in the Department of Chemistry, University of Washington, Seattle, Washington 98195, USA.

[View author publications](#)

You can also search for this author in [PubMed](#) [Google Scholar](#)

2. [Ashleigh B. Theberge](#)

1. Ashleigh B. Theberge is in the Department of Chemistry, University of Washington, Seattle, Washington 98195, USA, and in the Department of Urology, University of Washington.

[View author publications](#)

You can also search for this author in [PubMed](#) [Google Scholar](#)



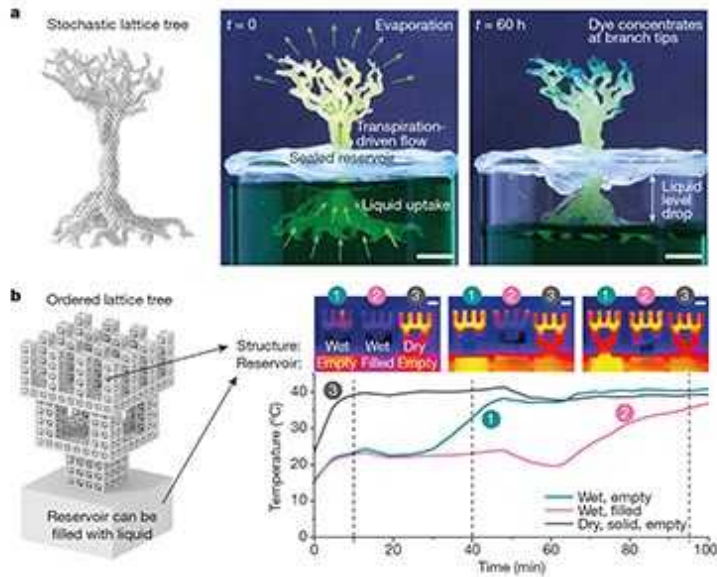


•

[Download PDF](#)

Scientists often draw inspiration from the world around them. In a [paper in *Nature*](#), inspired by nature's ability to efficiently perform processes involving multiple phases of matter, Dudukovic *et al.*¹ present cellular fluidics: a technological platform in which many cubic building blocks with complex internal structures are assembled to guide fluid flow using capillary action. The authors use this platform to construct a variety of fluidic structures, and demonstrate that it can model important multiphase processes such as transpiration — by which trees absorb water through their roots and transport it to leaves at the tips of their branches, where it evaporates.

Cellular fluidics also enables the fabrication of patterned multi-material structures, including objects that contain alternating electrically conducting and insulating regions.



[Read the paper: Cellular fluidics](#)

Capillary action drives many processes, such as the wetting of hairs on a paint brush and eyes tearing up. It enables the flow of liquid in small spaces — in the gaps between fibres in a paper towel, for example, or in capillary tubes used to collect blood — without the need for external forces such as pumps. For this reason, it has found use in the field of microfluidics, which studies the movement of small volumes of fluid through spaces of submillimetre dimensions. Capillary action underpins many microfluidic technologies, such as at-home pregnancy tests and portable glucose monitors. By combining engineering, chemistry and physics, miniature ‘lab-on-a-chip’ devices such as these have been developed for use in many fields².

Conventional microfluidic systems are closed (the fluid is completely confined within channels), require external pumps to push the fluid and are accessible only through sealed-off ports. The field of open microfluidics was therefore conceived to make microfluidic systems more accessible, for example to pipettes^{3–5}. In open microfluidics, at least one boundary of the flowing fluid is exposed to the air, creating an air–liquid interface.

Dudukovic *et al.* have drawn on the growing body of open-microfluidics theory to come up with a refined concept for this field: a unit cell from which complex 3D architectures can be built. Unit cells are usually thought of in the context of crystal lattices — they are the smallest repeating unit of a lattice. The unit cells in Dudukovic and colleagues' fluidics system are similarly used as the smallest building blocks of their fluidics platform. Each of these unit cells is a millimetre-scale cube with internal empty spaces that are open to the surrounding atmosphere (Fig. 1a).

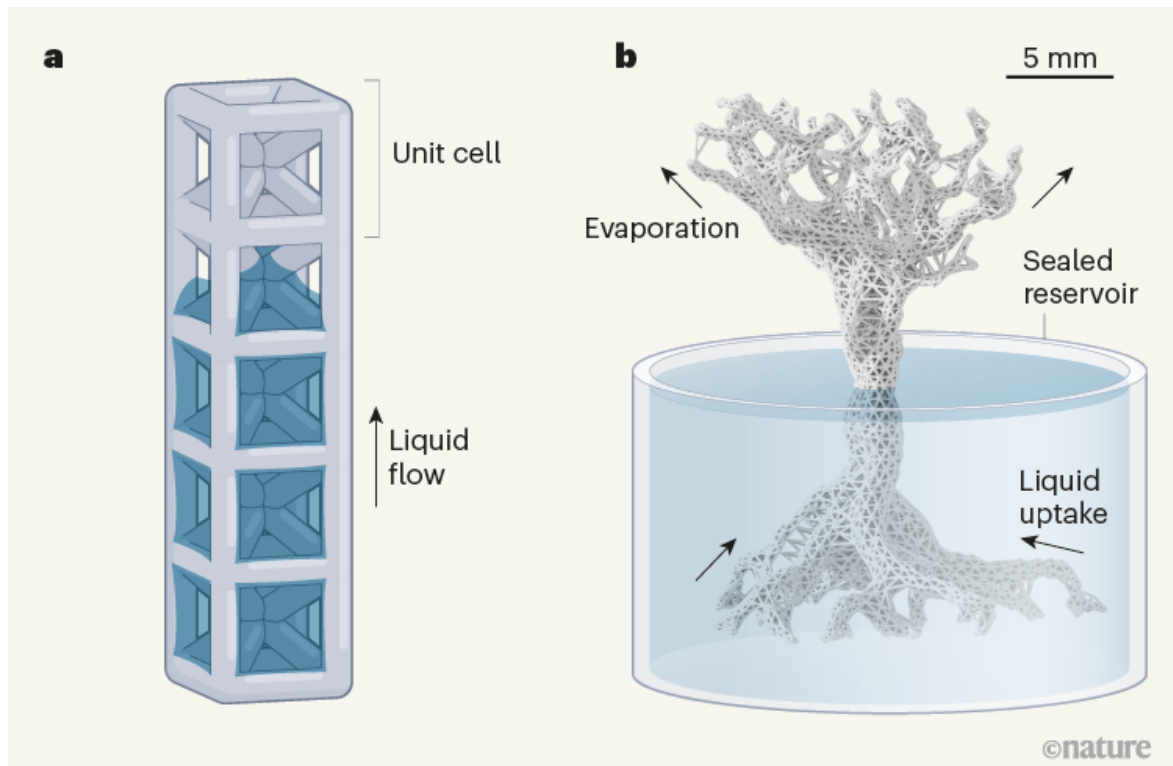
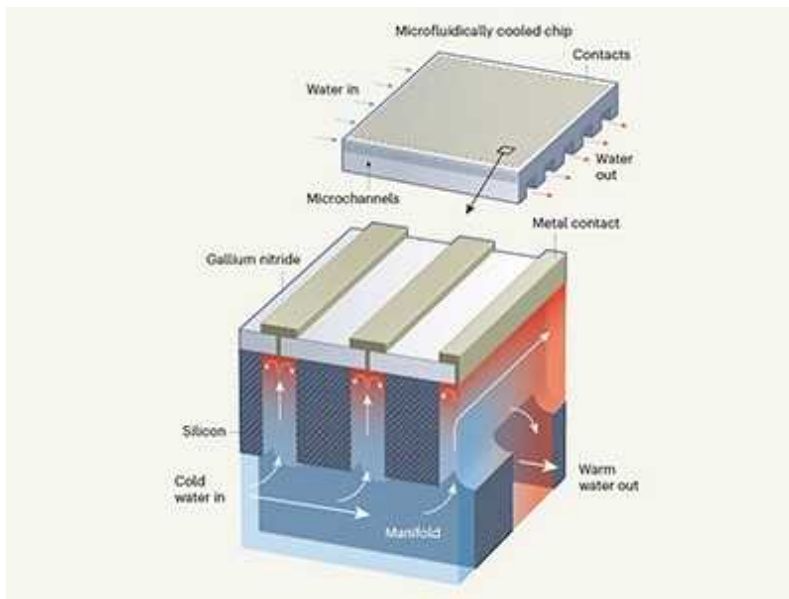


Figure 1 | Capillary flow and a transpiration-like process in cellular fluidic systems. Dudukovic *et al.*¹ report a technological platform called cellular fluidics. **a**, In this platform, millimetre-scale cubes known as unit cells have internal architectures that draw up fluids through capillary action. The combined capillary action of stacked unit cells produces a vertical flow of fluid. **b**, The authors report that a tree-like structure built from the unit cells continuously delivers liquid from a reservoir to the tips of the branches, where the liquid evaporates — a process that mimics transpiration in natural trees. (Tree image adapted from Fig. 4a of ref. 1.)

The spaces are delineated by struts, which partly act as supports to prevent the unit cells from collapsing. By tuning the shape and size of the struts, the authors can control capillary action in the cells. Moreover, when the cells are coupled together, the combined capillary action of each cell produces a controllable path through which the fluid flows. Impressively, by building a tree-like structure (tens of millimetres in height) from the unit cells, they demonstrate that the combined capillary action of the cells enables a multi-phase process similar to transpiration (Fig. 1b). If an analogous tree-like structure were made from similarly sized, hollow unit cells lacking internal struts, the water from the roots would not make it very far through the tree (see Extended Data Fig. 6 of the paper¹).

The flow of liquid in natural structures, such as tree leaves or soil, depends on the arrangement of the components in those structures³. Cellular fluidics is therefore the perfect tool with which to mimic such liquid flow, because the unit cells can be arranged in the same way as can the building blocks of the natural structures.



All-in-one design integrates microfluidic cooling into electronic chips

Capillary action occurs when the cohesive forces that hold molecules together in a fluid work together with the adhesive forces that cause the fluid to cling to a solid surface (such as the wall of a tube), thereby pulling the liquid in a given direction. Gravitational forces act against capillary action

when fluid rises vertically. Capillary flow in simple systems, such as tubes, can be described mathematically by considering the interplay between these various forces. The capillary rise in Dudukovic and colleagues' unit cells is more complex than that in tubes, and so the authors derived a theoretical model that describes how strut diameter and the number of cells coupled together influence the overall capillary action of a cellular fluidics system.

The fabrication of open structures, such as Dudukovic and co-workers' unit cells, can be difficult to achieve using many of the methods typically used in microfluidics. The authors therefore used 3D printing to build up their unit cells layer by layer. This is an attractive option because one can think of a design in the morning, then draw a model using computer-aided design programs, upload the file to a 3D printer and simply press 'start'. A working prototype can be ready by the end of the day. 3D printing is also appealing because of the range of materials that can be printed, from hard resins for prototypes of diagnostic devices to biocompatible gels for tissue engineering. However, in many applications it is necessary to produce structures that are fabricated from multiple materials.

Cellular fluidics provides a solution to this problem. Dudukovic *et al.* show that, by adjusting the size, shape and density of the unit cells in a 3D structure, fluid flow can be controlled and guided along a chosen path (Fig. 2). This provides a way to coat specific unit cells in a structure with metal: when solutions of appropriate catalysts and reagents were channelled along a particular pathway, only the cells in that pathway were metallized when the whole structure was subsequently immersed in a plating solution. The authors used this approach to coat selected regions of a cylinder-shaped structure with metal, producing concentric rings that alternated between being electrically conductive and non-conductive (see Fig. 6e of the paper¹). The researchers also suggest that the ability to channel fluids to specific areas of a structure could be used to deliver fluids within artificial organs.

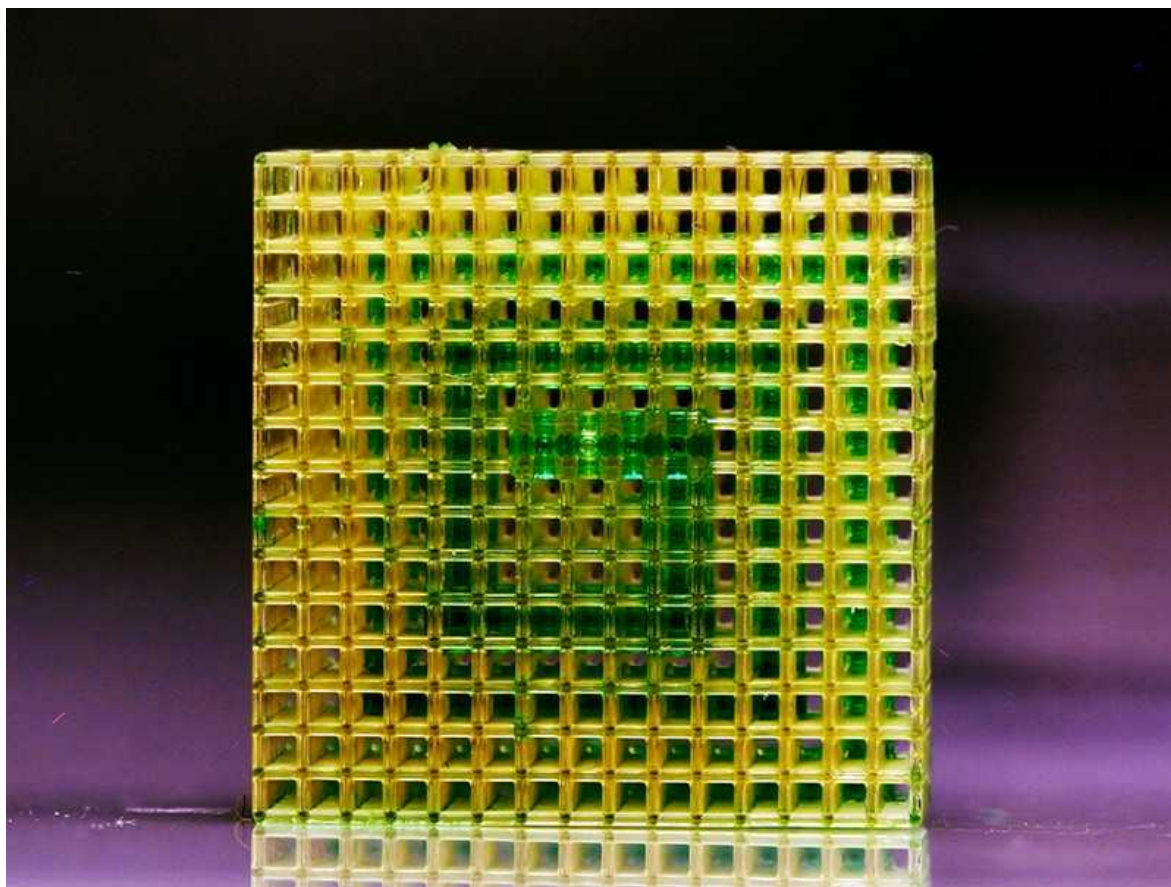


Figure 2 | Selective fluid flow in 3D structures. Dudukovic *et al.*¹ demonstrate that the flow path of a fluid through 3D cellular fluidics structures can be precisely controlled by altering the size, shape and density of unit cells. Here, a green fluid passes along a spiral path. Credit: Hawi Gemedo

Fluidic systems based on unit cells have been developed previously^{6,7}, and a limitation of Dudukovic and colleagues' work is that it largely reports known physical phenomena. However, a key advance of the present study is that it considerably increases our understanding of fluid flow in coupled unit-cell structures. We look forward to future applications in which cellular fluidics is used to investigate unknown physical principles or to fabricate novel multi-material structures. This technological platform opens up many exciting opportunities for research and is a valuable addition to the open-microfluidics toolkit.

doi: <https://doi.org/10.1038/d41586-021-01708-2>

References

1. 1.

Dudukovic, N. A. *et al. Nature* **595**, 58–65 (2021).

[Article](#) [Google Scholar](#)

2. 2.

Sackmann, E. K., Fulton, A. L. & Beebe, D. J. *Nature* **507**, 181–189 (2014).

[PubMed](#) [Article](#) [Google Scholar](#)

3. 3.

Berthier, J., Brakke, K. A. & Berthier, E. *Open Microfluidics* (Wiley-Scrivener, 2016).

[Google Scholar](#)

4. 4.

Delamarche, E. & Kaigala, G. V. *Open-Space Microfluidics: Concepts, Implementations, Applications* (Wiley, 2018).

[Google Scholar](#)

5. 5.

Berthier, E., Dostie, A. M., Lee, U. N., Berthier, J. & Theberge, A. B. *Anal. Chem.* **91**, 8739–8750 (2019).

[PubMed](#) [Article](#) [Google Scholar](#)

6. 6.

Jesus Esarte, J., Blanco, J. M., Bernardini, A. & Sancibrián, R. *Appl. Sci.* **9**, 2905 (2019).

[Article](#) [Google Scholar](#)

7. 7.

Fink, K. D., Kolodziejska, J. A., Jacobsen, A. J. & Roper, C. S. *AIChE J.* **57**, 2636–2646 (2011).

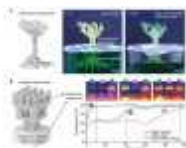
[Article](#) [Google Scholar](#)

[Download references](#)

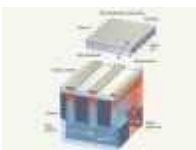
Competing Interests

A.B.T. declares ownership in Stacks to the Future, LLC, a company pursuing open microfluidic technologies. However, this technology is not featured in this publication.

Related Articles



- [Read the paper: Cellular fluidics](#)



- [All-in-one design integrates microfluidic cooling into electronic chips](#)



- [Micro-engineered liquid flow dissolves solids without dispersing them](#)

- [See all News & Views](#)

Subjects

- [Engineering](#)
- [Fluid dynamics](#)
- [Materials science](#)

[Jobs from Nature Careers](#)

- - - [All jobs](#)
 - - [PhD Student \(m/f/div\) in Bioinformatics](#)
[Max Planck Institute for Molecular Genetics \(MPI-MG\)](#)
[14195 Berlin, Germany](#)
[JOB POST](#)
 - [PhD Student \(m/f/div\) in Bioinformatics](#)
[Max Planck Institute for Molecular Genetics \(MPI-MG\)](#)
[14195 Berlin, Germany](#)
[JOB POST](#)
 - [56868: 3 Engineering Scientists, physicists or similar \(f/m/x\) - Development of an optical frequency reference for the project COMPASSO](#)
[German Aerospace Center \(DLR\)](#)

[Bremen, Germany](#)

[JOB POST](#)

- [PhD candidate - the neurodevelopmental disorder PURA Syndrome \(f/m/x\).](#)

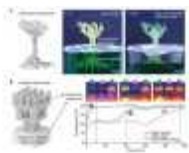
[Helmholtz Zentrum München - German Research Center for Environmental Health \(HMGU\)](#)

[Neuherberg \(bei München\), Germany](#)

[JOB POST](#)

[Download PDF](#)

Related Articles



- [Read the paper: Cellular fluidics](#)



- [All-in-one design integrates microfluidic cooling into electronic chips](#)



- [Micro-engineered liquid flow dissolves solids without dispersing them](#)
- [See all News & Views](#)

Subjects

- [Engineering](#)
 - [Fluid dynamics](#)
 - [Materials science](#)
-

This article was downloaded by **calibre** from <https://www.nature.com/articles/d41586-021-01708-2>

| [Section menu](#) | [Main menu](#) |

- NEWS AND VIEWS
- 23 June 2021

Designer fibre meals sway human gut microbes

Understanding how diet affects gut microbes and thereby influences human health might lead to targeted dietary strategies. A clinical trial now provides some steps on the path towards this goal.

- [Avner Leshem](#) ORCID: <http://orcid.org/0000-0003-4082-2036>⁰ &
- [Eran Elinav](#) ORCID: <http://orcid.org/0000-0002-5775-2110>¹

1. Avner Leshem

1. Avner Leshem is in the Department of Immunology, Weizmann Institute of Science, Rehovot, 7610001, Israel, and in the Department of Surgery, Tel Aviv Sourasky Medical Center, Tel Aviv, Israel.

[View author publications](#)

You can also search for this author in [PubMed](#) [Google Scholar](#)

2. Eran Elinav

1. Eran Elinav is in the Department of Immunology, Weizmann Institute of Science, Rehovot, 7610001, Israel, and in the Division of Microbiome and Cancer, German Cancer Research Center (DKFZ), Heidelberg, Germany.

[View author publications](#)

You can also search for this author in [PubMed](#) [Google Scholar](#)





•

[Download PDF](#)

There is growing evidence that our normal resident gut microorganisms, termed commensal microbes, can affect human health. Promoting beneficial commensal microbes through a type of nutritional supplement called a prebiotic is an area of intensive scientific and medical research. However, trying to harness a diet with the desired effect is challenging because the gut microbial community (also known as the microbiome) is highly complex, and because dietary responses are modulated by multiple hereditary and non-hereditary factors. [Writing in Nature](#), Delannoy-Bruno *et al.*¹ fill an essential gap in our mechanistic understanding of diet–microbiome

interactions by focusing on dietary fibre, a family of substances of pronounced physiological virtues that are predominantly metabolized by commensal microbes. This provides a sequel to the team's previous work on the development of microbiome-targeting foods^{2–6}.

To characterize the effect of dietary-fibre supplementation in overweight individuals, Delannoy-Bruno and colleagues used germ-free mice — animals raised and maintained in a sterile environment that are therefore devoid of the usual resident microbes of any sort. The team colonized the gut of each of nine mouse groups with the microbiome of one of nine women classed as obese. The mice were continuously fed a low-fibre, high-fat diet, coupled with periodic fibre supplementation (Fig. 1). Their microbiome was characterized to assess gene content (the level of particular genes present) before, during and after each episode of fibre supplementation. Building on previous work by this team⁵, which identified fibres that promote the growth of certain intestinal bacteria (those of the genus *Bacteroides*, which are less prevalent than normal in obese individuals), Delannoy-Bruno *et al.* chose three types of fibre that were fed sequentially to the mice. Each supplementation cycle was followed by a ‘washout’ period to enable intestinal clearing of the fibres, thereby allowing the authors to discern the effect of every individual type of fibre as distinct from the other fibres.

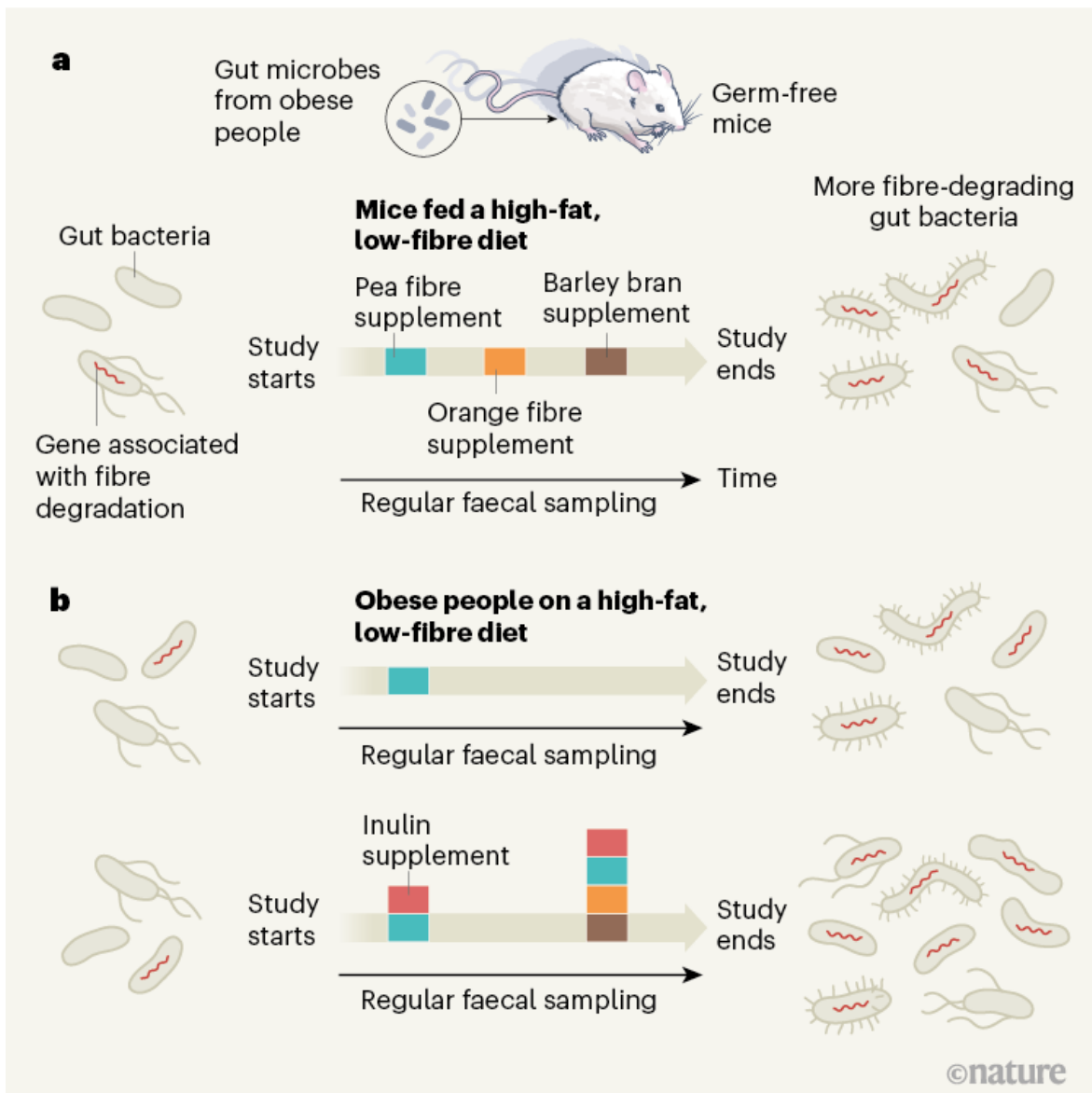
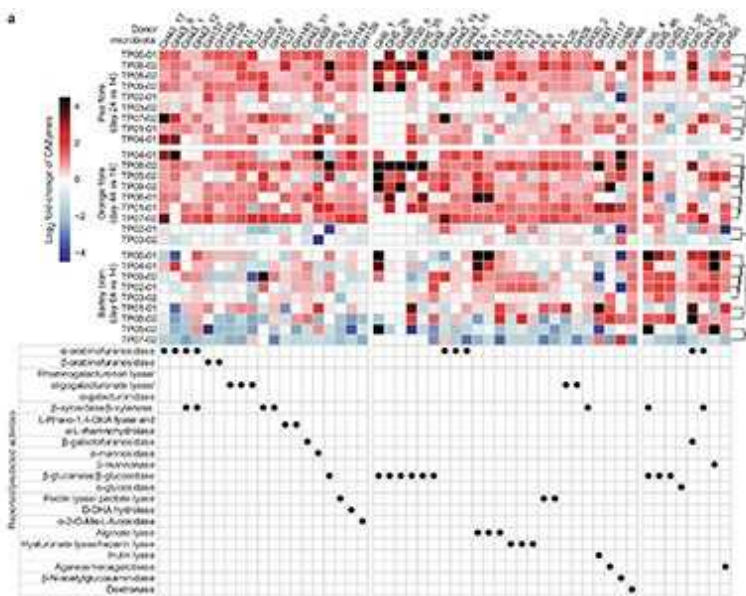


Figure 1 | Assessing the response to dietary fibres. Evidence-based dietary interventions to target gut microbes might offer a way to boost human health. **a**, Delannoy-Bruno *et al.*¹ analysed germ-free mice, which lack their natural gut microbes. These animals had their gut colonized with microbes from obese individuals. The animals received the type of diet associated with obesity, plus fibre snacks (pea fibre, orange fibre and barley bran) as indicated. The authors tracked the genes associated with intake of a particular type of dietary fibre by analysing microbial DNA in faecal samples. Each period of fibre supplementation resulted in an increase in the abundance of genes related to degradation of the fibre, presumably because the presence of the fibre gave a competitive advantage to bacterial species

harbouring those genes. **b**, The authors carried out a similar type of experiment in a human clinical trial, which corroborated the results of pea-fibre consumption in mice. A dietary-supplement regime that combined multiple types of fibre (including inulin) led to a substantial increase in the number of genes present that were associated with fibre degradation.

Human-microbiome-inoculated mice showed pronounced compositional shifts in their gut microbes in response to fibre supplementation. To identify fibre–microbe interactions and subtract irrelevant ‘noise’ in the data arising from normal fluctuations in the microbiome profile, the authors used a feature-reduction approach termed higher-order singular value decomposition. This revealed that exposure of the microbial population to a particular fibre resulted in a greater presence of genes that encode proteins needed for the metabolism of that fibre. For example, consumption of cellulose-containing pea and orange fibre led to a higher representation of genes encoding the β -glucosidase enzymes that hydrolyse such fibre, probably owing to the proliferation of bacteria that can use cellulose as an energy source. Interestingly, in mice inoculated with human microbiomes, similar signatures of fibre-responsive genes became highly abundant through the expansion of various bacterial taxa including, but not limited to, *Bacteroides*. The bacterial taxa that rose to dominance shared a competitive advantage in their response to the presence of the respective fibre. This highlights that a shift in microbial gene abundance, rather than a shift to a particular community structure in terms of the species present, is a common denominator in the response pattern to dietary interventions across individuals.

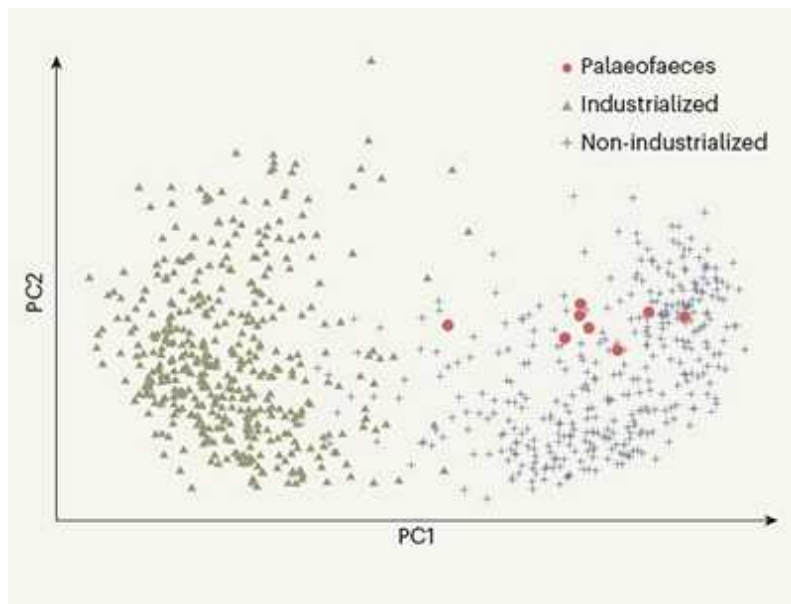


[Read the paper: Evaluating microbiome-directed fibre snacks in gnotobiotic mice and humans](#)

The authors then examined whether these findings have relevance to human biology. They characterized the microbiome of 12 overweight or obese study participants before, during and after pea-fibre dietary supplementation. To minimize the effect of microbiome variations stemming from dietary differences between individuals, participants were given meals consisting of a uniform high-saturated-fat, low-fibre diet (equivalent to the type of diet the mice were placed on). The microbial gene responses to fibre supplementation in humans largely resembled those observed in mice.

The authors also tested whether consumption of multiple fibre types results in a greater microbiome shift than was observed upon consumption of pea fibre alone as a supplement. For this study, a group of 14 individuals received a diet supplemented with a combination of two and then four types of fibre. The results indicate that the more types of fibre an individual consumes, the greater the rise in the number of microbial genes present that are involved in fibre metabolism. Changes in fibre-responsive enzymes closely correlated with changes in the plasma levels of proteins that are associated with specific metabolic and immune functions, as revealed by the analysis of blood samples from participants.

The emerging concept of precision nutrition proposes that human dietary responses are specific to food components, and that these components might be tailored to the individual to optimize their dietary response. Such responses are quantifiable and driven by a number of variables, including features of the food components (such as protein, carbohydrate and fat), the individual's physiological traits, and gut microbiome composition and function. Indeed, it has been suggested that the gut microbiome is a key modulator of physiological food responses and associated differences in such responses between individuals^{7,8}. Current US dietary guidelines recommend that healthy adults ingest at least 14 grams of fibre per 1,000 calories consumed⁹, with no individualization specified in terms of the fibre type or intake in grams. Delannoy-Bruno and colleagues' findings provide a framework that paves the way for optimizing an individual's fibre consumption, based on fibre type and their microbiome fibre-degradation signatures.



Ancient human faeces reveal gut microbes of the past

The authors' results underscore the considerable plasticity of the gut microbiome and its amenability to manipulation by prebiotics. Fibre-degradation capacity in individuals with habitual low levels of fibre consumption is not necessarily irreversibly diminished, but rather might be recovered by increasing their fibre consumption through combinatorial fibre selection^{10–13}. Furthermore, the findings by Delannoy-Bruno *et al.*

demonstrate that dietary responses might be mainly determined by the levels of relatively sparse microbiome genes (that become predominant after a dietary intervention), stressing the importance of studying diet–microbiome interactions at the level of genes. Different microbial communities in individuals contributed to these distinct functional capacities, highlighting the possibility that microbiome function (genes), rather than species composition, might correlate with personalized human physiological responses to food.

In some situations, the metabolic and immune-system characteristics of germ-free mice harbouring human microbiomes might affect the validity of using these animals as human surrogates in an experimental context^{14,15}. Nevertheless, the fibre-degrading properties of the mice analysed by Delannoy-Bruno *et al.* were strikingly similar to those of humans. This suggests that human microbiome colonization in germ-free mice might be a relevant tool for studying the causal drivers of diet–microbiome interactions and their effect on the mammalian host.

Such studies would greatly benefit from the development of computational-analysis tools that can identify temporal trajectories of microbial genes in response to dietary interventions, in both human donors and mice who receive microbial transplants. In this study, the authors used one such tool, higher-order singular value decomposition, which uncovered a profound microbiome gene response to dietary-fibre supplementation despite the modest sample size. Further refinement of such analytical pipelines, by the expansion of microbiome genome-level databases of gene functions and the incorporation of protein-level features, will probably aid further decoding of the contributions of the dietary–microbiome axis to host physiology.

Delannoy-Bruno and colleagues' findings provide valuable mechanistic insights into the microbial contributions to human dietary responses. This will probably lead to long-term, randomized clinical trials that assess causal links between distinct food ingredients, microbiome modulation and downstream health-related outcomes for humans. Indeed, this research team recently reported² that a data-driven dietary intervention targeting the microbiome helped to promote growth in undernourished children. The advances made by Delannoy-Bruno *et al.* bring us closer to the integration of precise microbiome engineering with evidence-based dietary sciences.

Nature **595**, 32-34 (2021)

doi: <https://doi.org/10.1038/d41586-021-01601-y>

References

1. 1.

Delannoy-Bruno, O. *et al.* *Nature* **595**, 91–95 (2021).

[Article](#) [Google Scholar](#)

2. 2.

Chen, R. Y. *et al.* *N. Engl. J. Med.* **384**, 1517–1528 (2021).

[PubMed](#) [Article](#) [Google Scholar](#)

3. 3.

Chen, R. Y. *et al.* *N. Engl. J. Med.* **383**, 321–333 (2020).

[PubMed](#) [Article](#) [Google Scholar](#)

4. 4.

Mostafa, I. *et al.* *BMC Public Health* **20**, 242 (2020).

[PubMed](#) [Article](#) [Google Scholar](#)

5. 5.

Patnode, M. L. *et al.* *Cell* **179**, 59–73 (2019).

[PubMed](#) [Article](#) [Google Scholar](#)

6. 6.

Gehrig, J. L. *et al.* *Science* **365**, 139 (2019).

[Article](#) [Google Scholar](#)

7. 7.

Zeevi, D. *et al.* *Cell* **163**, 1079–1094 (2015).

[PubMed](#) [Article](#) [Google Scholar](#)

8. 8.

Berry, S. E. *et al.* *Nature Med.* **26**, 964–973 (2020).

[PubMed](#) [Article](#) [Google Scholar](#)

9. 9.

US Department of Health and Human Services and US Department of Agriculture. *2015–2020 Dietary Guidelines for Americans* (HHS/USDA, 2015).

[Google Scholar](#)

10. 10.

Sonnenburg, E. D. *et al.* *Nature* **529**, 212–215 (2016).

[PubMed](#) [Article](#) [Google Scholar](#)

11. 11.

Eilam, O. *et al.* *mBio* **5**, e01526-14 (2014).

[PubMed](#) [Article](#) [Google Scholar](#)

12. 12.

Healey, G. *et al.* *Br. J. Nutr.* **119**, 176–189 (2018).

[PubMed](#) [Article](#) [Google Scholar](#)

13. 13.

Deehan, E. C. *et al.* *Cell Host Microbe* **27**, 389–404 (2020).

[PubMed](#) [Article](#) [Google Scholar](#)

14. 14.

Al-Asmakh, M. & Zadali, F. *J. Microbiol. Biotechnol.* **25**, 1583–1588 (2015).

[PubMed](#) [Article](#) [Google Scholar](#)

15. 15.

Lundberg, R., Toft, M. F., August, B., Hansen, A. K. & Hansen, C. H. *F. Gut Microbes* **7**, 68–74 (2016).

[PubMed](#) [Article](#) [Google Scholar](#)

[Download references](#)

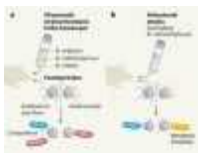
Competing Interests

E.E. is the scientific founder of DayTwo and BiomX.

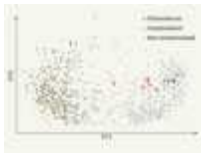
Related Articles



- [Read the paper: Evaluating microbiome-directed fibre snacks in gnotobiotic mice and humans](#)



- [Food for thought about manipulating gut bacteria](#)



- [Ancient human faeces reveal gut microbes of the past](#)
- [See all News & Views](#)

Subjects

- [Microbiology](#)
- [Nutrition](#)
- [Medical research](#)

Jobs from Nature Careers

- - - [All jobs](#)
 - - [PhD Student \(m/f/div\) in Bioinformatics](#)

[Max Planck Institute for Molecular Genetics \(MPI-MG\)](#)

[14195 Berlin, Germany](#)

[JOB POST](#)

- [PhD Student \(m/f/div\) in Bioinformatics](#)

[Max Planck Institute for Molecular Genetics \(MPI-MG\)](#)

[14195 Berlin, Germany](#)

[JOB POST](#)

- **PhD candidate - the neurodevelopmental disorder PURA Syndrome (f/m/x)**

Helmholtz Zentrum München - German Research Center for Environmental Health (HMGU)

Neuherberg (bei München), Germany

JOB POST

- **PhD in Molecular Obesity Research within the Collaborative Research Center 1052 "Obesity Mechanisms" (f/m/x)**

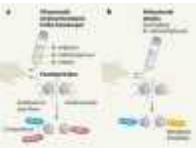
Helmholtz Zentrum München - German Research Center for Environmental Health (HMGU)

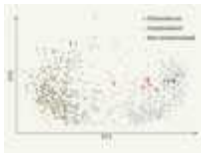
Leipzig, Germany

JOB POST

Download PDF

Related Articles

-  **Read the paper: Evaluating microbiome-directed fibre snacks in gnotobiotic mice and humans**
-  **Food for thought about manipulating gut bacteria**



- [Ancient human faeces reveal gut microbes of the past](#)
- [See all News & Views](#)

Subjects

- [Microbiology](#)
- [Nutrition](#)
- [Medical research](#)

This article was downloaded by **calibre** from <https://www.nature.com/articles/d41586-021-01601-y>.

| [Section menu](#) | [Main menu](#) |

- NEWS AND VIEWS
- 23 June 2021

Migratory birds aid the redistribution of plants to new climates

Birds that travel long distances can disperse seeds far and wide. An assessment of the timing and direction of European bird migration reveals how these patterns might affect seed dispersal as the planet warms.

- [Barnabas H. Daru](#) ORCID: <http://orcid.org/0000-0002-2115-0257> ⁰

1. [Barnabas H. Daru](#)

1. Barnabas H. Daru is in the Department of Life Sciences, Texas A&M University-Corpus Christi, Corpus Christi, Texas 78412, USA.

[View author publications](#)

You can also search for this author in [PubMed](#) [Google Scholar](#)





•

[Download PDF](#)

The rapid pace of global warming and its effects on habitats raise the question of whether species are able to keep up so that they remain in suitable living conditions. Some animals can move fast to adjust to a swiftly changing climate. Plants, being less mobile, rely on means such as seed dispersal by animals, wind or water to move to new areas, but this redistribution typically occurs within one kilometre of the original plant¹. [Writing in Nature](#), González-Varo *et al.*² shed light on the potential capacity of migratory birds to aid seed dispersal.

When the climate in a plant's usual range becomes hotter than it can tolerate, it must colonize new, cooler areas that might lie many kilometres away. It is not fully clear how plants distribute their seeds across great distances, let alone how they cross geographical barriers. One explanation for long-distance seed dispersal is through transport by migratory birds. Such birds ingest viable seeds when eating fruit (Fig. 1) and can move them tens or hundreds of kilometres outside the range of a plant species³. In this mode of dispersal, the seeds pass through the bird's digestive tract unharmed^{4,5} and are deposited in faeces, which provides fertilizer that aids plant growth. In the case of European migratory birds, for example, the direction of seed dispersal will depend on whether the timing of fruit production coincides with a bird's southward trip to warmer regions around the Equator, or northward to cooler regions. Many aspects of this process have been a mystery until now.



Figure 1 | A young blackcap bird (*Sylvia atricapilla*) eating elderberries. Credit: Getty

González-Varo and colleagues report how plants might be able to keep pace with rapid climate change through the help of migrating birds. The authors analysed the fruiting times of plants, patterns of bird migration and the interactions between fruit-eating birds and fleshy-fruited plants across Europe. Plants with fleshy fruits were chosen for this study because most of their seed transport is by migratory birds⁶, and because fleshy-fruited plants are an important component of the woody-plant community in Europe. The common approach until now has been to predict plant dispersal and colonization using models fitted to abiotic factors, such as the current climate. González-Varo *et al.* instead analysed an impressive data set of 949 different seed-dispersal interactions between bird and plant communities, together with data on entire fruiting times and migratory patterns of birds across Europe. The researchers also analysed DNA traces from bird faeces to identify the plants and birds responsible for seed dispersal.



[Read the paper: Limited potential for bird migration to disperse plants to cooler latitudes](#)

The authors hypothesized that the direction of seed migration depends on how the plants interact with migratory birds, the frequency of these interactions or the number of bird species that might transport seeds from each plant species. González-Varo and colleagues found that 86% of plant species studied might have seeds dispersed by birds during their southward trip towards drier and hotter equatorial regions in autumn, whereas only

about one-third of the plant species might be dispersed by birds migrating north in spring. This dispersal trend was more pronounced in temperate plants than in the Mediterranean plant communities examined. These results are in general agreement with well-known patterns of fruiting times and bird migrations. For example, the fruit of most fleshy-fruited plants in Europe ripens at a time that coincides with when birds migrate south towards the Equator⁷.

Perhaps the most striking feature of these inferred seed movements is the observation that 35% of plant species across European communities, which are closely related on the evolutionary tree (phylogenetically related), might benefit from long-distance dispersal by the northward journey of migratory birds. This particular subset of plants tends to fruit over a long period of time, or has fruits that persist over the winter. This means that the ability of plants to keep up with climate change could be shaped by their evolutionary history — implying that future plant communities in the Northern Hemisphere will probably come from plant species that are phylogenetically closely related and that have migrated from the south. Or, to put it another way, the overwhelming majority of plant species that are dispersed south towards drier and hotter regions at the Equator will probably be less able to keep pace with rapid climate change in their new locations than will the few ‘winners’ that are instead dispersed north to cooler climates. This has implications for understanding how plants will respond to climate change, and for assessing ecosystem functions and community assembly at higher levels of the food chain. However, for seeds of a given plant species, more evidence is needed to assess whether passing through the guts of birds affects germination success.

To determine which birds might be responsible for the plant redistributions to cooler climates in the north, the authors categorized European bird migrants into Palaearctic (those that fly to southern Europe and northern Africa during their non-breeding season) and Afro-Palaearctic (those that winter in sub-Saharan Africa). Only a few common Palaearctic migrants, such as the blackcap (*Sylvia atricapilla*; Fig. 1) or blackbird (*Turdus merula*), provide most of this crucial dispersal service northwards to cooler regions across Europe. Because migratory birds are able to relocate a small, non-random subset of plants, this could well have a strong influence on the types of plant community that will form under climate-change conditions.



A bird's migration decoded

A major problem, however, is that the role of these birds in dispersing seeds over long distances is already at risk from human pressures and environmental changes⁸. Understanding these large-scale seed-dispersal interactions offers a way for targeted conservation actions to protect the areas that are most vulnerable to climate change. This could include boosting protection efforts in and around the wintering grounds of migratory birds — locations that are already experiencing a rise in human pressures, such as illegal bird hunting.

González-Varo and colleagues' focus on seed dispersal across a Northern Hemisphere region means that, as with most ecological analyses, the results are dependent on scale, which can cause issues when interpreting data⁹. Because the Northern Hemisphere has more land area and steeper seasonal temperature gradients than the Southern Hemisphere does, seed-dispersal interactions might have different patterns from those occurring in the Southern Hemisphere or in aquatic systems.

For example, seed-eating birds from the genus *Quelea* migrate from the Southern Hemisphere to spend the dry season in equatorial West Africa, then move southwards again when the rains arrive. Their arrival in southern Africa usually coincides with the end of the wet season in this region, when annual grass seeds are in abundance. It will be worth investigating whether

migratory birds in the Southern Hemisphere also influence the redistribution of plant communities during global warming. Likewise, exploring the long-distance dispersal of seeds of aquatic plants, such as seagrasses¹⁰ by water birds, is another area for future research that might benefit from González-Varo and colleagues' methods.

This study provides a great example of how migratory birds might assist plant redistribution to new locations that would normally be difficult for them to reach on their own, and which might offer a suitable climate. As the planet warms, understanding how such biological mechanisms reorganize plant communities complements the information available from climate-projection models, which offer predictions of future species distributions.

Nature **595**, 34–36 (2021)

doi: <https://doi.org/10.1038/d41586-021-01547-1>

References

1. 1.

Jordano, P., García, C., Godoy, J. A. & García-Castaño, J. L. *Proc. Natl Acad. Sci. USA* **104**, 3278–3282 (2007).

[PubMed](#) [Article](#) [Google Scholar](#)

2. 2.

González-Varo, J. P. *et al.* *Nature* **595**, 75–79 (2021).

[Article](#) [Google Scholar](#)

3. 3.

Viana, D. S., Santamaría, L. & Figuerola, J. *Trends Ecol. Evol.* **31**, 763–775 (2016).

[PubMed](#) [Article](#) [Google Scholar](#)

4. 4.

Lehouck, V., Spanhove, T. & Lens, L. *Plant Ecol. Evol.* **144**, 96–100 (2011).

[Article](#) [Google Scholar](#)

5. 5.

Shikang, S., Fuqin, W. & Yuehua, W. *Sci. Rep.* **5**, 11615 (2015).

[PubMed](#) [Article](#) [Google Scholar](#)

6. 6.

Jordano, P. in *Seeds: The Ecology of Regeneration in Plant Communities* 3rd edn (ed. Gallagher, R. S.) 18–61 (CAB Int., 2014).

[Google Scholar](#)

7. 7.

Dingle, H. *Migration: The Biology of Life on the Move* (Oxford Univ. Press, 2014).

[Google Scholar](#)

8. 8.

Bairlein, F. *Science* **354**, 547–548 (2016).

[PubMed](#) [Article](#) [Google Scholar](#)

9. 9.

Daru, B. H., Farooq, H., Antonelli, A. & Faurby, S. *Nature Commun.* **11**, 2115 (2020).

[PubMed](#) [Article](#) [Google Scholar](#)

10. 10.

Rock, B. M. & Daru B. H. *Front. Mar. Sci.* **8**, 608867 (2021).

[Article](#) [Google Scholar](#)

[Download references](#)

Competing Interests

The author declares no competing interests.

Related Articles



- [Read the paper: Limited potential for bird migration to disperse plants to cooler latitudes](#)



- [A bird's migration decoded](#)



- [African forest maps reveal areas vulnerable to the effects of climate change](#)

- [See all News & Views](#)

Subjects

- [Ecology](#)
- [Climate change](#)

Jobs from Nature Careers

- - - [All jobs](#)
 - - [PhD Student \(m/f/div\) in Bioinformatics](#)
[Max Planck Institute for Molecular Genetics \(MPI-MG\)](#)
[14195 Berlin, Germany](#)
[JOB POST](#)
 - [PhD Student \(m/f/div\) in Bioinformatics](#)
[Max Planck Institute for Molecular Genetics \(MPI-MG\)](#)
[14195 Berlin, Germany](#)
[JOB POST](#)
 - [PhD candidate - the neurodevelopmental disorder PURA Syndrome \(f/m/x\)](#)
[Helmholtz Zentrum München - German Research Center for Environmental Health \(HMGU\)](#)
[Neuherberg \(bei München\), Germany](#)
[JOB POST](#)
 - [PhD in Molecular Obesity Research within the Collaborative Research Center 1052 "Obesity Mechanisms" \(f/m/x\)](#)

[Helmholtz Zentrum München - German Research Center for Environmental Health \(HMGU\)](#)

[Leipzig, Germany](#)

[JOB POST](#)

[Download PDF](#)

Related Articles



- [Read the paper: Limited potential for bird migration to disperse plants to cooler latitudes](#)



- [A bird's migration decoded](#)



- [African forest maps reveal areas vulnerable to the effects of climate change](#)

- [See all News & Views](#)

Subjects

- [Ecology](#)
- [Climate change](#)

| [Section menu](#) | [Main menu](#) |

- NEWS AND VIEWS
- 09 June 2021

A base-pair view of interactions between genes and their enhancers

A technique reveals how folded chromosomal DNA interacts in the nucleus, providing information at the level of single base pairs. The achievement offers an unprecedented level of detail about how gene activity is regulated.

- [Anne van Schoonhoven](#) ⁰ &
- [Ralph Stadhouders](#) ¹

1. Anne van Schoonhoven

1. Anne van Schoonhoven is in the Departments of Pulmonary Medicine and of Cell Biology, Erasmus University Medical Center, Rotterdam 3015 GD, the Netherlands.

[View author publications](#)

You can also search for this author in [PubMed](#) [Google Scholar](#)

2. Ralph Stadhouders

1. Ralph Stadhouders is in the Departments of Pulmonary Medicine and of Cell Biology, Erasmus University Medical Center, Rotterdam 3015 GD, the Netherlands.

[View author publications](#)

You can also search for this author in [PubMed](#) [Google Scholar](#)



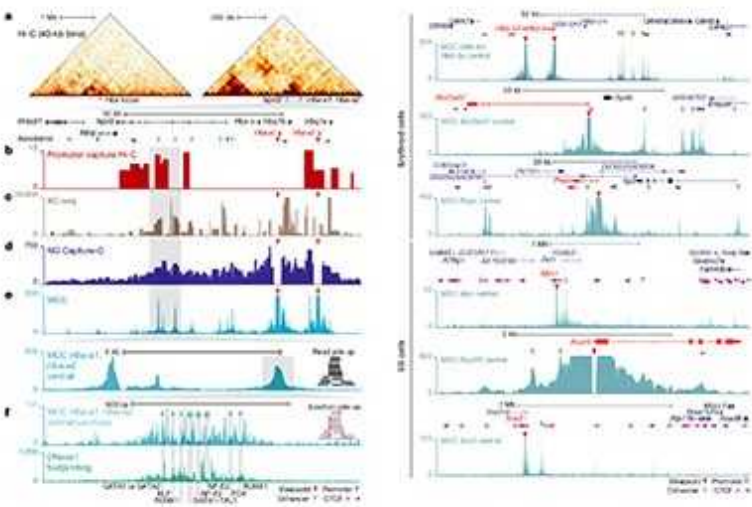


•

[Download PDF](#)

How can 2 metres of DNA fit into a nucleus that has an average diameter of only 10 micrometres? Almost all the cells in our body face this storage conundrum, which has intrigued scientists for decades. Moreover, this compaction tour de force folds DNA in the nucleus in a way that is far from random. The pattern of DNA folding is important for many processes that involve our genome, including the regulation of expression of our approximately 20,000 genes. [Writing in Nature](#), Hua *et al.*¹ describe a method they have developed to monitor 3D genome architecture. This information can pinpoint genomic interactions at the level of single base

pairs of DNA. It suggests new ways of thinking about how gene expression is controlled, and opens up exciting possibilities for future research.



[Read the paper: Defining genome architecture at base-pair resolution](#)

Humans and other organisms have evolved complex mechanisms to precisely regulate gene expression. Different types of cell express different sets of genes, and these expression patterns might depend on a cell's function, or arise in response to environmental cues, such as viral infection. Central to the control of gene expression are short regulatory sequences of DNA, termed enhancers, which are highly abundant in our genomes. According to current estimates², there are up to 810,000 enhancers across the human genome.

Enhancers are bound by the ‘bookkeepers’ of gene expression: DNA-binding proteins called transcription factors, which bind to short motifs of DNA sequences corresponding to 6–12 base pairs³. Enhancers can be located far from the gene(s) that they regulate, and how they stimulate gene expression is a major topic of research⁴. The current leading model is that enhancers and genes are brought into closer spatial proximity by specific patterns of DNA folding, enabling transcription factors to stimulate gene expression despite large intervening genomic distances between an enhancer and a particular gene^{5–7}.

Study of the 3D organization of genomes has been revolutionized by an approach called chromosome conformation capture (3C), which enables researchers to infer the frequencies of interactions between different DNA regions⁸. Such approaches indicate that enhancer–gene interactions occur preferentially in ‘insulated’ genomic neighbourhoods in the nucleus called topologically associating domains (TADs)⁹. Most TADs are formed by the cooperative action of a DNA-binding protein termed CTCF and a ring-shaped protein complex called cohesin, which is a type of molecular motor that drives a process known as loop extrusion¹⁰. In this process, cohesin engages DNA and extrudes it, in a similar way to how threading yarn through the eye of a needle forms a loop (Fig. 1). This extrusion continues until cohesin encounters DNA bound to CTCF, which forms a ‘roadblock’ for loop extrusion, stopping it.

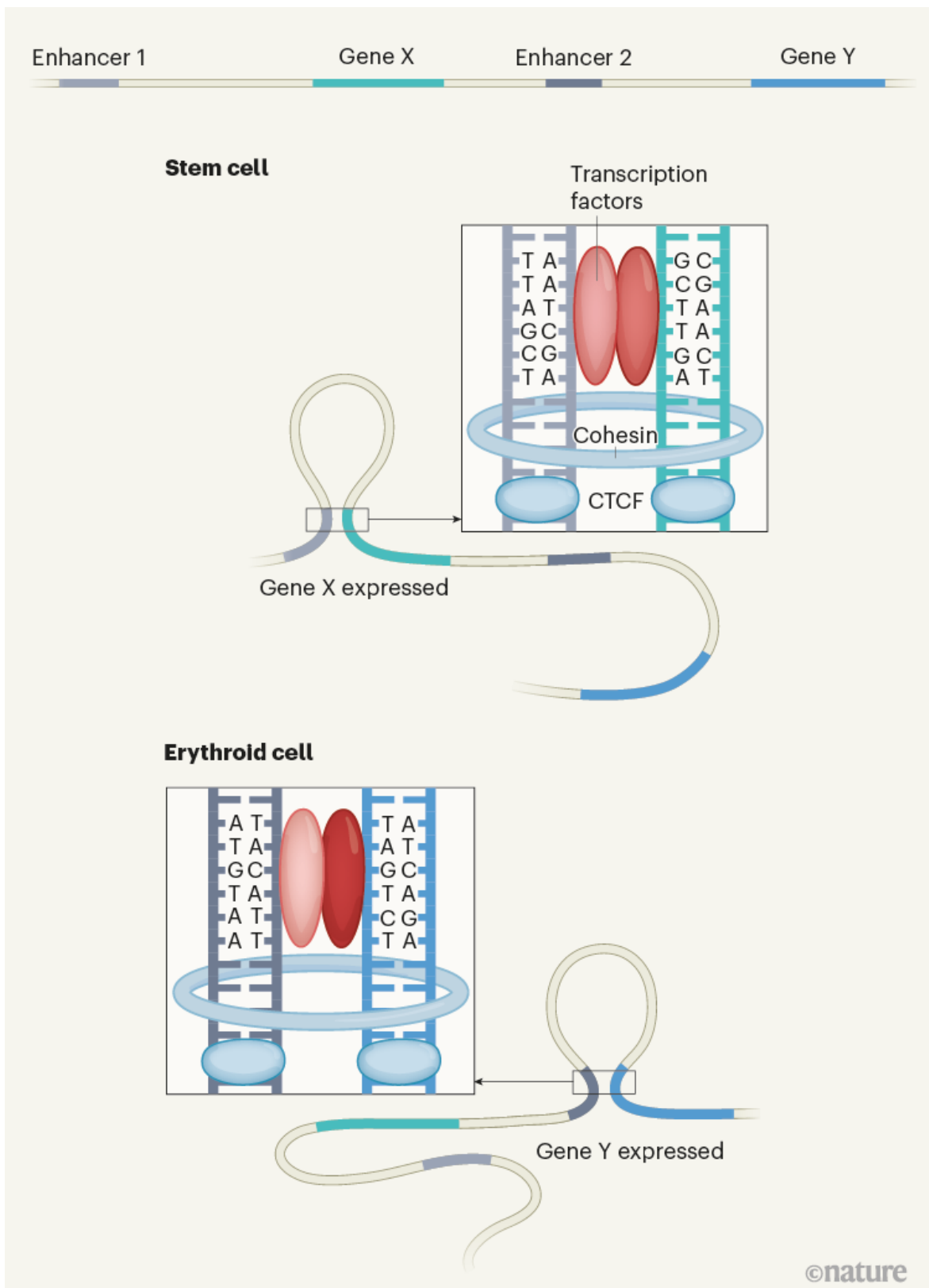
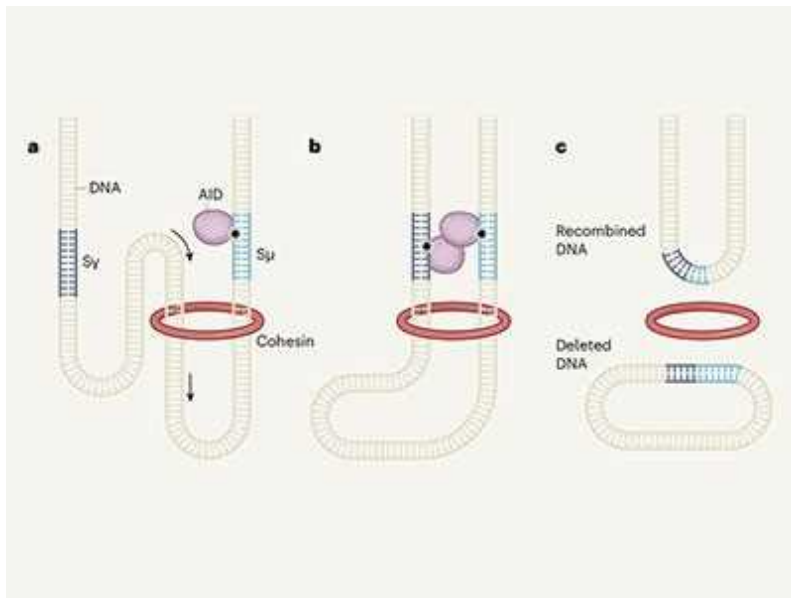


Figure 1 | Monitoring genomic folding. Hua *et al.*¹ have developed a new version of a method termed chromosome conformation capture (3C), called Micro-Capture-C (MCC). This method can identify regions of interacting DNA that are far apart in the linear genome sequence, such as enhancers (regulatory sequences that can promote gene expression) and genes. MCC can pinpoint interactions between base pairs of DNA from different parts of the genome, which is substantially more precise than was previously possible for other types of 3C. The authors used MCC to study stem cells and erythroid cells (precursor red blood cells) in mice. Their findings provide evidence for distinct base-pair patterns of gene and enhancer interactions in different cell types. The results are consistent with a model in which DNA from distant genomic locations is brought into close proximity by a ring-shaped protein complex called cohesin, which helps to generate DNA loops¹⁰. The DNA-binding protein CTCF organizes these loops into ‘insulated’ genomic neighbourhoods, within which interactions occur¹⁰. The ability to identify sites of DNA interactions at the level of individual bases — adenine (A), thymine (T), guanine (G) or cytosine (C) — sheds light on how DNA-binding proteins called transcription factors control gene expression.

TADs are thought to ‘trap’ genes and enhancers by thwarting DNA interactions across TAD borders, thereby increasing the probability that matching enhancer–gene pairs find each other. However, until now, 3C technology has been unable to define the nature of the physical contacts between genes and enhancers on the base-pair scale — this would be on a par with the precision with which interactions between DNA and the key transcription factors influencing gene expression have been determined. Hua *et al.* now close this resolution gap by developing a version of 3C that the authors call Micro-Capture-C (MCC).

Building on their previously developed version of 3C methodology¹¹, the authors made key technical refinements that strikingly improved the resolution of the DNA interactions that could be identified. Like all 3C techniques, MCC captures interactions through chemical crosslinking, which generates bonds between interacting regions of DNA. The crosslinked DNA is then cut into smaller fragments, after which the interactions are captured

by gluing together (ligating) interacting DNA strands that are close to each other in the nuclear space.



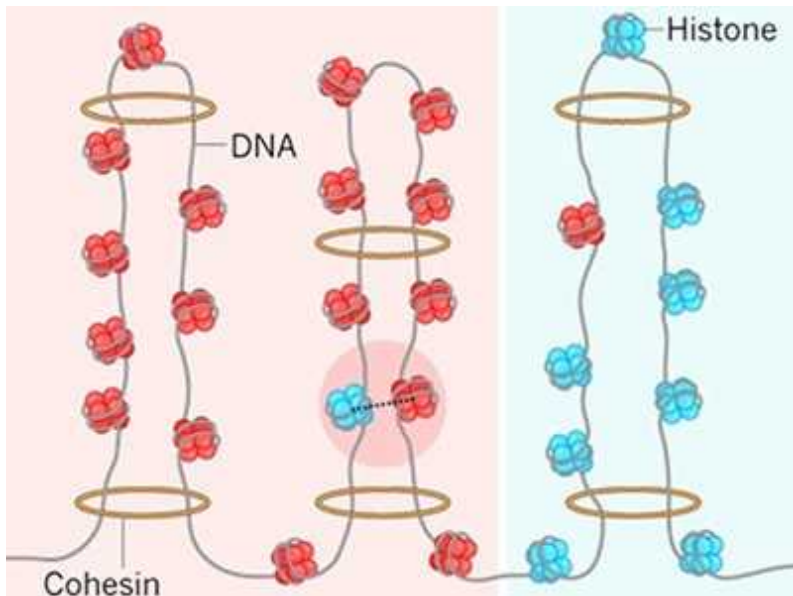
One ring to rule them all

For the pair of molecular ‘scissors’ that cuts DNA into small fragments, MCC uses the enzyme micrococcal nuclease (MNase), which fragments DNA in a mainly random fashion, independently of DNA sequences. This enables the generation of much smaller DNA fragments than those obtained using sequence-specific enzymes for DNA digestion. The approach helps to increase the resolution — as previously shown for another version of 3C technology¹². Crucially, Hua and colleagues show that DNA fragmentation by MNase does not have any major biases in terms of the DNA that is digested, with a minor preference for less-condensed DNA (characteristic of regions containing genes being expressed) over more-condensed DNA.

The DNA fragments corresponding to the ligated regions of interacting DNA are short and the full sequence of the fragment can be determined, which means that the exact position of the ligation junction is known for each captured interaction. MCC therefore enables the base pairs exactly at the ligation junction to be identified as the interacting regions. This offers a huge leap forward in terms of resolution. Hua and colleagues’ approach also enables DNA-binding-protein ‘footprints’ (the DNA sites to which such

proteins bind) to be detected because DNA that is bound to proteins is protected from digestion by MNase.

In addition to introducing us to this exciting technique, the authors immediately put MCC to use in investigating several fundamental aspects of 3D genome folding using embryonic stem cells and precursor red blood cells from mice. Remarkably, interactions between enhancers, genes and CTCF-binding sites occurred as highly localized signals (sharp peaks) in the data for DNA-interaction sites, rather than as broader regions of interaction, as is typical for earlier forms of 3C. Consistent with previous observations¹³, such discrete interactions involving genes almost always (around 87% of the time) occurred in TADs. The precise contacts revealed by MCC were often cell-type-specific, and were associated with the binding of transcription factors that are important for shaping the identity of particular cell lineages. If the authors mutated a transcription-factor binding site at the centre of an enhancer–gene interaction site, this resulted in localized loss of an interaction detected by MCC and reduced expression of the gene, compared with cells in which the transcription-factor binding site was intact. These findings suggest that transcription factors are responsible for maintaining highly specific 3D genome-folding patterns that are involved in transcriptional control.



How to build a cohesive genome in 3D

The genomic locations of the binding sites for CTCF are mostly the same in different cell types. This raises the question of how loop extrusion orchestrated by CTCF and cohesin contributes to tissue-specific DNA interactions. Hua *et al.* report that contacts between CTCF-bound DNA regions were increased when the intervening regions of DNA had greater numbers of actively transcribed genes and enhancers. The authors demonstrate that both cohesin and a protein called Nipbl, which can load cohesin onto DNA, were enriched at active genes and their enhancers, compared with their presence at less active genes and their enhancers. These data support a model in which cell-type-specific loading of cohesin onto active genes and enhancers aids loop extrusion towards cell-type-invariant CTCF ‘roadblock’ sites — an idea that fits well with previous observations^{14–16} that cohesin aids enhancer–gene interactions.

Although, at first glance, the individual technological innovations in the MCC method might not seem revolutionary, when combined, they offer something the field has long been waiting for: a way to precisely detect which DNA bases mediate long-range genomic interactions. This level of detail will enable high-resolution dissection of processes involving gene regulation, including those found in complex genomic regions containing multiple genes and regulatory elements, and where enhancer–gene interactions occur over short ranges (less than 20 kilobases of DNA). Although Hua and colleagues’ method does not allow genome-scale analyses, the approach might be adapted to make this possible in the future. Moreover, the base-pair resolution that MCC offers makes it an attractive tool for investigating how regulatory proteins set up and maintain 3D genome architecture.

MCC is also ideally suited to the search for links between disease-associated genetic-sequence variants in regulatory elements and their target genes. Given that such variation can disrupt the binding of transcription factors and often has subtle effects on gene expression, the quantitative nature and footprinting capacity of MCC would be extremely valuable for investigations of this kind.

Nature **595**, 36–37 (2021)

doi: <https://doi.org/10.1038/d41586-021-01494-x>

References

1. 1.

Hua, P. *et al.* *Nature* **595**, 125–129 (2021).

[Article](#) [Google Scholar](#)

2. 2.

The ENCODE Project Consortium *et al.* *Nature* **583**, 699–710 (2020).

[PubMed](#) [Article](#) [Google Scholar](#)

3. 3.

Lambert, S. A. *et al.* *Cell* **172**, 650–665 (2018).

[PubMed](#) [Article](#) [Google Scholar](#)

4. 4.

de Laat, W. & Duboule, D. *Nature* **502**, 499–506 (2013).

[PubMed](#) [Article](#) [Google Scholar](#)

5. 5.

Stadhouders, R., Filion, G. J. & Graf, T. *Nature* **569**, 345–354 (2019).

[PubMed](#) [Article](#) [Google Scholar](#)

6. 6.

Furlong, E. E. M. & Levine, M. *Science* **361**, 1341–1345 (2018).

[PubMed](#) [Article](#) [Google Scholar](#)

7. 7.

Schoenfelder, S. & Fraser, P. *Nature Rev. Genet.* **20**, 437–455 (2019).

[PubMed](#) [Article](#) [Google Scholar](#)

8. 8.

de Wit, E. & de Laat, W. *Genes Dev.* **26**, 11–24 (2012).

[PubMed](#) [Article](#) [Google Scholar](#)

9. 9.

Bonev, B. & Cavalli, G. *Nature Rev. Genet.* **17**, 661–678 (2016).

[PubMed](#) [Article](#) [Google Scholar](#)

10. 10.

Fudenberg, G., Abdennur, N., Imakaev, M., Goloborodko, A. & Mirny, L. A. *Cold Spring Harb. Symp. Quant. Biol.* **82**, 45–55 (2017).

[PubMed](#) [Article](#) [Google Scholar](#)

11. 11.

Davies, J. O. J. *et al.* *Nature Methods* **13**, 74–80 (2016).

[PubMed](#) [Article](#) [Google Scholar](#)

12. 12.

Krietenstein, N. *et al.* *Mol. Cell* **78**, 554–565 (2020).

[PubMed](#) [Article](#) [Google Scholar](#)

13. 13.

Dowen, J. M. *et al.* *Cell* **159**, 374–387 (2014).

[PubMed](#) [Article](#) [Google Scholar](#)

14. 14.

Kagey, M. H. *et al. Nature* **467**, 430–435 (2010).

[PubMed](#) [Article](#) [Google Scholar](#)

15. 15.

Chien, R. *et al. J. Biol. Chem.* **286**, 17870–17878 (2011).

[PubMed](#) [Article](#) [Google Scholar](#)

16. 16.

Liu, N. Q. *et al. Nature Genet.* **53**, 100–109 (2021).

[PubMed](#) [Article](#) [Google Scholar](#)

[Download references](#)

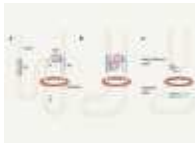
Competing Interests

The authors declare no competing interests.

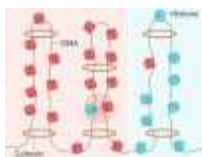
Related Articles



- [Read the paper: Defining genome architecture at base-pair resolution](#)



- [One ring to rule them all](#)



- [**How to build a cohesive genome in 3D**](#)
- [**See all News & Views**](#)

Subjects

- [Genomics](#)
- [Biotechnology](#)

[**Jobs from Nature Careers**](#)

- - - [**All jobs**](#)
 - - [**PhD Student \(m/f/div\) in Bioinformatics**](#)
[Max Planck Institute for Molecular Genetics \(MPI-MG\)](#)
[14195 Berlin, Germany](#)
[JOB POST](#)
 - [**PhD Student \(m/f/div\) in Bioinformatics**](#)
[Max Planck Institute for Molecular Genetics \(MPI-MG\)](#)
[14195 Berlin, Germany](#)
[JOB POST](#)
 - [**PhD candidate - the neurodevelopmental disorder PURA Syndrome \(f/m/x\)**](#)

Helmholtz Zentrum München - German Research Center for Environmental Health (HMGU)

Neuherberg (bei München), Germany

JOB POST

- **PhD in Molecular Obesity Research within the Collaborative Research Center 1052 "Obesity Mechanisms" (f/m/x)**

Helmholtz Zentrum München - German Research Center for Environmental Health (HMGU)

Leipzig, Germany

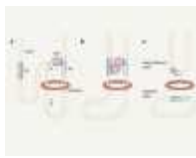
JOB POST

Download PDF

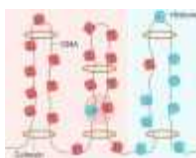
Related Articles



- **Read the paper: Defining genome architecture at base-pair resolution**



- **One ring to rule them all**



- **How to build a cohesive genome in 3D**

- [See all News & Views](#)

Subjects

- [Genomics](#)
- [Biotechnology](#)

This article was downloaded by **calibre** from <https://www.nature.com/articles/d41586-021-01494-x>

| [Section menu](#) | [Main menu](#) |

- Article
- [Published: 30 June 2021](#)

A highly magnetized and rapidly rotating white dwarf as small as the Moon

- [Ilaria Caiazzo](#) [ORCID: orcid.org/0000-0002-4770-5388¹](#),
- [Kevin B. Burdge](#) [ORCID: orcid.org/0000-0002-7226-836X¹](#),
- [James Fuller](#) [ORCID: orcid.org/0000-0002-4544-0750¹](#),
- [Jeremy Heyl](#) [ORCID: orcid.org/0000-0001-9739-367X²](#),
- [S. R. Kulkarni¹](#),
- [Thomas A. Prince](#) [ORCID: orcid.org/0000-0002-8850-3627¹](#),
- [Harvey B. Richer²](#),
- [Josiah Schwab³](#),
- [Igor Andreoni¹](#),
- [Eric C. Bellm](#) [ORCID: orcid.org/0000-0001-8018-5348⁴](#),
- [Andrew Drake¹](#),
- [Dmitry A. Duev](#) [ORCID: orcid.org/0000-0001-5060-8733¹](#),
- [Matthew J. Graham](#) [ORCID: orcid.org/0000-0002-3168-0139¹](#),
- [George Helou](#) [ORCID: orcid.org/0000-0003-3367-3415⁵](#),
- [Ashish A. Mahabal](#) [ORCID: orcid.org/0000-0003-2242-0244^{1,6}](#),
- [Frank J. Masci](#) [ORCID: orcid.org/0000-0002-8532-9395⁵](#),
- [Roger Smith⁷](#) &
- [Maayane T. Soumagnac^{8,9}](#)

Nature volume **595**, pages 39–42 (2021) [Cite this article](#)

- 226 Accesses

- 580 Altmetric
- [Metrics details](#)

Subjects

- [Astrophysical magnetic fields](#)
- [Compact astrophysical objects](#)
- [Stellar evolution](#)

Abstract

White dwarfs represent the last stage of evolution of stars with mass less than about eight times that of the Sun and, like other stars, are often found in binaries^{1,2}. If the orbital period of the binary is short enough, energy losses from gravitational-wave radiation can shrink the orbit until the two white dwarfs come into contact and merge³. Depending on the component masses, the merger can lead to a supernova of type Ia or result in a massive white dwarf⁴. In the latter case, the white dwarf remnant is expected to be highly magnetized^{5,6} because of the strong magnetic dynamo that should arise during the merger, and be rapidly spinning from the conservation of the orbital angular momentum⁷. Here we report observations of a white dwarf, ZTF J190132.9+145808.7, that exhibits these properties, but to an extreme: a rotation period of 6.94 minutes, a magnetic field ranging between 600 megagauss and 900 megagauss over its surface, and a stellar radius of $\sqrt{2140^2 - 230^2} \approx 160$ km, only slightly larger than the radius of the Moon. Such a small radius implies that the star's mass is close to the maximum white dwarf mass, or Chandrasekhar mass. ZTF J190132.9+145808.7 is likely to be cooling through the Urca processes (neutrino emission from electron capture on sodium) because of the high densities reached in its core.

Access options

Subscribe to Journal

Get full journal access for 1 year

\$199.00

only \$3.90 per issue

[Subscribe](#)

All prices are NET prices.

VAT will be added later in the checkout.

Tax calculation will be finalised during checkout.

Rent or Buy article

Get time limited or full article access on ReadCube.

from \$8.99

[Rent or Buy](#)

All prices are NET prices.

Additional access options:

- [Log in](#)
- [Access through your institution](#)
- [Learn about institutional subscriptions](#)

Fig. 1: Gaia colour–magnitude diagram.

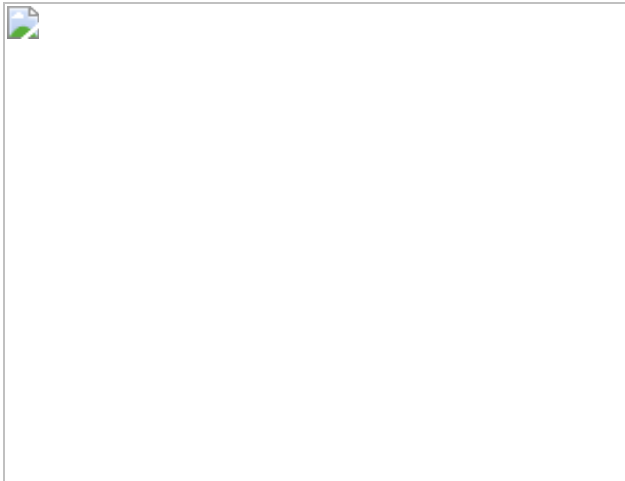


Fig. 2: ZTF J1901+1458 lightcurve.

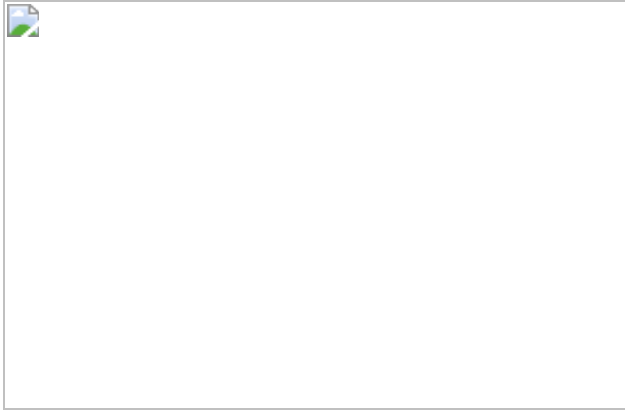
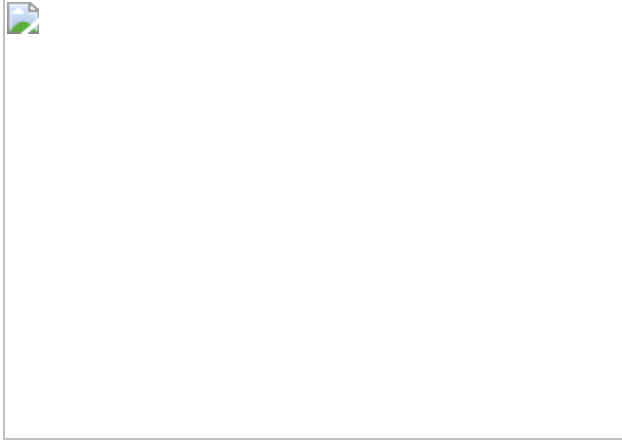


Fig. 3: ZTF J1901+1458 optical spectrum.



Fig. 4: Mass–radius relation.



Data availability

Upon request, I.C. will provide the reduced photometric lightcurves and spectroscopic data, and available ZTF data for the object. The spectroscopic data and photometric lightcurves are also available in the GitHub repository <https://github.com/ilac/ZTF-J1901-1458>. ZTF data are accessible in the ZTF database. The astrometric and photometric data are already in the public domain, and they are readily accessible in the Gaia and Pan-STARRSS catalogues and in the Swift database.

Code availability

We used the pyphot package (<https://mfouesneau.github.io/docs/pyphot/>) and the corner.py package⁷⁰. The LRIS spectra were reduced using the Lpipe pipeline⁷¹. Upon request, I.C. will provide the code used to analyse the spectroscopic and photometric data.

References

1. 1.

Brown, W. R. et al. The ELM Survey. VIII. Ninety-eight double white dwarf binaries. *Astrophys. J.* **889**, 49 (2020).

[ADS](#) [CAS](#) [Google Scholar](#)

2. 2.

Burke, K. B. et al. A systematic search of Zwicky Transient Facility data for ultracompact binary LISA-detectable gravitational-wave sources. *Astrophys. J.* **905**, 32 (2020).

[ADS](#) [CAS](#) [Google Scholar](#)

3. 3.

Shen, K. J. Every interacting double white dwarf binary may merge. *Astrophys. J. Lett.* **805**, L6 (2015).

[ADS](#) [Google Scholar](#)

4. 4.

Dan, M., Rosswog, S., Brüggen, M. & Podsiadlowski, P. The structure and fate of white dwarf merger remnants. *Mon. Not. R. Astron. Soc.* **438**, 14–34 (2014).

[ADS](#) [CAS](#) [Google Scholar](#)

5. 5.

Tout, C. A. et al. Binary star origin of high field magnetic white dwarfs. *Mon. Not. R. Astron. Soc.* **387**, 897–901 (2008).

[ADS](#) [Google Scholar](#)

6. 6.

Garca-Berro, E. et al. Double degenerate mergers as progenitors of high-field magnetic white dwarfs. *Astrophys. J.* **749**, 25 (2012).

[ADS](#) [Google Scholar](#)

7. 7.

Schwab, J. Evolutionary models for the remnant of the merger of two carbon-oxygen core white dwarfs. *Astrophys. J.* **906**, 53 (2021).

[ADS](#) [CAS](#) [Google Scholar](#)

8. 8.

Bellm, E. C. et al. The Zwicky Transient Facility: system overview, performance, and first results. *Publ. Astron. Soc. Pacif.* **131**, 018002 (2019).

[ADS](#) [Google Scholar](#)

9. 9.

Gaia Collaboration et al. The Gaia mission. *Astron. Astrophys.* **595**, A1 (2016).

[Google Scholar](#)

10. 10.

Harding, L. K. et al. CHIMERA: a wide-field, multi-colour, high-speed photometer at the prime focus of the Hale telescope. *Mon. Not. R. Astron. Soc.* **457**, 3036–3049 (2016).

[ADS](#) [Google Scholar](#)

11. 11.

Hermes, J. J. et al. White dwarf rotation as a function of mass and a dichotomy of mode line widths: Kepler observations of 27 pulsating DA white dwarfs through K2 Campaign 8. *Astrophys. J. Suppl.* **232**, 23 (2017).

[ADS](#) [Google Scholar](#)

12. 12.

Oke, J. B. et al. The Keck Low-Resolution Imaging Spectrometer. *Publ. Astron. Soc. Pacif.* **107**, 375 (1995).

[ADS](#) [Google Scholar](#)

13. 13.

Ruder, H., Wunner, G., Herold, H. & Geyer, F. *Atoms in Strong Magnetic Fields. Quantum Mechanical Treatment and Applications in Astrophysics and Quantum Chaos* (Springer, 1994).

14. 14.

Ferrario, L., de Martino, D. & Gänsicke, B. T. Magnetic white dwarfs. *Space Sci. Rev.* **191**, 111–169 (2015).

[ADS](#) [Google Scholar](#)

15. 15.

Ferrario, L. et al. EUVE J0317–855: a rapidly rotating, high-field magnetic white dwarf. *Mon. Not. R. Astron. Soc.* **292**, 205–217 (1997).

[ADS](#) [CAS](#) [Google Scholar](#)

16. 16.

Roming, P. W. A. et al. The Swift Ultra-Violet/Optical Telescope. *Space Sci. Rev.* **120**, 95–142 (2005).

[ADS](#) [Google Scholar](#)

17. 17.

Gehrels, N. et al. The Swift Gamma-Ray Burst Mission. *Astrophys. J.* **611**, 1005–1020 (2004).

[ADS](#) [CAS](#) [Google Scholar](#)

18. 18.

Chambers, K. C. et al. The Pan-STARRS1 Surveys. Preprint at <https://arxiv.org/abs/1612.05560> (2016).

19. 19.

Camisassa, M. E. et al. The evolution of ultra-massive white dwarfs. *Astron. Astrophys.* **625**, A87 (2019).

[CAS](#) [Google Scholar](#)

20. 20.

Siess, L. Evolution of massive AGB stars. II. Model properties at non-solar metallicity and the fate of super-AGB stars. *Astron. Astrophys.* **476**, 893–909 (2007).

[ADS](#) [CAS](#) [Google Scholar](#)

21. 21.

Shen, K. J., Bildsten, L., Kasen, D. & Quataert, E. The long-term evolution of double white dwarf mergers. *Astrophys. J.* **748**, 35 (2012).

[ADS](#) [Google Scholar](#)

22. 22.

Külebi, B., Jordan, S., Nelan, E., Bastian, U. & Altmann, M. Constraints on the origin of the massive, hot, and rapidly rotating magnetic white dwarf RE J 0317–853 from an HST parallax measurement. *Astron. Astrophys.* **524**, A36 (2010).

[ADS](#) [Google Scholar](#)

23. 23.

Pshirkov, M. S. et al. Discovery of a hot ultramassive rapidly rotating DBA white dwarf. *Mon. Not. R. Astron. Soc.* **499**, L21–L25 (2020).

[ADS](#) [Google Scholar](#)

24. 24.

Tsuruta, S. & Cameron, A. G. W. URCA shells in dense stellar interiors. *Astrophys. Space Sci.* **7**, 374–406 (1970).

[ADS](#) [CAS](#) [Google Scholar](#)

25. 25.

Schwab, J., Bildsten, L. & Quataert, E. The importance of Urca-process cooling in accreting ONe white dwarfs. *Mon. Not. R. Astron. Soc.* **472**, 3390–3406 (2017).

[ADS](#) [CAS](#) [Google Scholar](#)

26. 26.

Schwab, J. Cooling models for the most massive white dwarfs. *Astrophys. J.* (in the press).

27. 27.

Deloye, C. J. & Bildsten, L. Gravitational settling of ^{22}Ne in liquid white dwarf interiors: cooling and seismological effects. *Astrophys. J.* **580**, 1077–1090 (2002).

[ADS](#) [CAS](#) [Google Scholar](#)

28. 28.

Kilic, M. et al. The 100 pc white dwarf sample in the SDSS footprint. *Astrophys. J.* **898**, 84 (2020).

[ADS](#) [CAS](#) [Google Scholar](#)

29. 29.

Holberg, J. B. & Bergeron, P. Calibration of synthetic photometry using DA white dwarfs. *Astron. J.* **132**, 1221–1233 (2006).

[ADS](#) [CAS](#) [Google Scholar](#)

30. 30.

Fontaine, G., Brassard, P. & Bergeron, P. The potential of white dwarf cosmochronology. *Publ. Astron. Soc. Jpn* **113**, 409–435 (2001).

[ADS](#) [Google Scholar](#)

31. 31.

Van Grootel, V. et al. The instability strip of ZZ Ceti white dwarfs. I. Introduction of time-dependent convection. *Astron. Astrophys.* **539**, A87 (2012).

[Google Scholar](#)

32. 32.

Maeda, K. & Shibahashi, H. Pulsations of pre-white dwarfs with hydrogen-dominated atmospheres. *Publ. Astron. Soc. Pacif.* **66**, 76 (2014).

[ADS](#) [Google Scholar](#)

33. 33.

Quirion, P. O., Fontaine, G. & Brassard, P. Wind competing against settling: a coherent model of the GW Virginis instability domain. *Astrophys. J.* **755**, 128 (2012).

[ADS](#) [Google Scholar](#)

34. 34.

Burdge, K. B. et al. General relativistic orbital decay in a seven-minute-orbital-period eclipsing binary system. *Nature* **571**, 528–531 (2019).

[ADS](#) [CAS](#) [Google Scholar](#)

35. 35.

Burdge, K. B. et al. Orbital decay in a 20 minute orbital period detached binary with a hydrogen-poor low-mass white dwarf. *Astrophys. J. Lett.* **886**, L12 (2019).

[ADS](#) [CAS](#) [Google Scholar](#)

36. 36.

Gentile Fusillo, N. P. & et al. A Gaia Data Release 2 catalogue of white dwarfs and a comparison with SDSS. *Mon. Not. R. Astron. Soc.* **482**, 4570–4591 (2019).

[ADS](#) [Google Scholar](#)

37. 37.

Graham, M. J., Drake, A. J., Djorgovski, S. G., Mahabal, A. A. & Donalek, C. Using conditional entropy to identify periodicity. *Mon. Not. R. Astron. Soc.* **434**, 2629–2635 (2013).

[ADS](#) [Google Scholar](#)

38. 38.

Gaia Collaboration et al. Gaia Data Release 2. Summary of the contents and survey properties. *Astron. Astrophys.* **616**, A1 (2018).

[Google Scholar](#)

39. 39.

Rosner, W., Wunner, G., Herold, H. & Ruder, H. Hydrogen atoms in arbitrary magnetic fields. I. Energy levels and wavefunctions. *J. Phys. B* **17**, 29–52 (1984).

[ADS](#) [Google Scholar](#)

40. 40.

Forster, H. et al. Hydrogen atoms in arbitrary magnetic fields. II. Bound–bound transitions. *J. Phys. B* **17**, 1301–1319 (1984).

[ADS](#) [CAS](#) [Google Scholar](#)

41. 41.

Henry, R. J. W. & Oconnell, R. F. Hydrogen spectrum in magnetic white dwarfs: H alpha, H beta and H gamma transitions. *Publ. Astron. Soc. Pacif.* **97**, 333–339 (1985).

[ADS](#) [CAS](#) [Google Scholar](#)

42. 42.

Wunner, G., Roesner, W., Herold, H. & Ruder, H. Stationary hydrogen lines in white dwarf magnetic fields and the spectrum of the magnetic degenerate GRW + 70 8247. *Astron. Astrophys.* **149**, 102–108 (1985).

[ADS](#) [CAS](#) [Google Scholar](#)

43. 43.

Tremblay, P. E., Bergeron, P. & Gianninas, A. An improved spectroscopic analysis of DA white dwarfs from the Sloan Digital Sky Survey Data Release 4. *Astrophys. J.* **730**, 128 (2011).

[ADS](#) [Google Scholar](#)

44. 44.

Cardelli, J. A., Clayton, G. C. & Mathis, J. S. The relationship between infrared, optical, and ultraviolet extinction. *Astrophys. J.* **345**, 245 (1989).

[ADS](#) [CAS](#) [Google Scholar](#)

45. 45.

Bohlin, R. C., Hubeny, I. & Rauch, T. New grids of pure-hydrogen white dwarf NLTE model atmospheres and the HST/STIS flux calibration. *Astron. J.* **160**, 21 (2020).

[ADS](#) [CAS](#) [Google Scholar](#)

46. 46.

Timmes, F. X. & Swesty, F. D. The accuracy, consistency, and speed of an electron–positron equation of state based on table interpolation of the Helmholtz free energy. *Astrophys. J.* **126** (Suppl.), 501–516 (2000).

[Google Scholar](#)

47. 47.

Schwab, J. python-helmholtz: Python bindings for Frank Timmes' Helmholtz EoS. <https://doi.org/10.5281/zenodo.4056084> (2020).

48. 48.

Hamada, T. & Salpeter, E. E. Models for zero-temperature stars. *Astrophys. J.* **134**, 683 (1961).

[ADS](#) [MathSciNet](#) [CAS](#) [Google Scholar](#)

49. 49.

Tolman, R. C. Static solutions of Einstein's field equations for spheres of fluid. *Phys. Rev.* **55**, 364–373 (1939).

[ADS](#) [MATH](#) [Google Scholar](#)

50. 50.

Oppenheimer, J. R. & Volkoff, G. M. On massive neutron cores. *Phys. Rev.* **55**, 374–381 (1939).

[ADS](#) [CAS](#) [MATH](#) [Google Scholar](#)

51. 51.

Miyaji, S., Nomoto, K., Yokoi, K. & Sugimoto, D. Supernova triggered by electron captures. *Publ. Astron. Soc. Jpn* **32**, 303–329 (1980).

[ADS](#) [CAS](#) [Google Scholar](#)

52. 52.

Paxton, B. et al. Modules for Experiments in Stellar Astrophysics (MESA). *Astrophys. J. Suppl.* **192**, 3 (2011).

[ADS](#) [Google Scholar](#)

53. 53.

Paxton, B. et al. Modules for Experiments in Stellar Astrophysics (MESA): Planets, oscillations, rotation, and massive stars. *Astrophys. J. Suppl.* **208**, 4 (2013).

[ADS](#) [Google Scholar](#)

54. 54.

Paxton, B. et al. Modules for Experiments in Stellar Astrophysics (MESA): Binaries, pulsations, and explosions. *Astrophys. J. Suppl.* **220**, 15 (2015).

[ADS](#) [Google Scholar](#)

55. 55.

Paxton, B. et al. Modules for Experiments in Stellar Astrophysics (MESA): Convective boundaries, element diffusion, and massive star explosions. *Astrophys. J. Suppl.* **234**, 34 (2018).

[ADS](#) [Google Scholar](#)

56. 56.

Paxton, B. et al. Modules for Experiments in Stellar Astrophysics (MESA): Pulsating variable stars, rotation, convective boundaries, and energy conservation. *Astrophys. J. Suppl.* **243**, 10 (2019).

[ADS](#) [CAS](#) [Google Scholar](#)

57. 57.

Williams, K. A., Montgomery, M. H., Winget, D. E., Falcon, R. E. & Bierwagen, M. Variability in hot carbon-dominated atmosphere (hot DQ) white dwarfs: rapid rotation? *Astrophys. J.* **817**, 27 (2016).

[ADS](#) [Google Scholar](#)

58. 58.

Ferrario, L., Wickramasinghe, D. & Kawka, A. Magnetic fields in isolated and interacting white dwarfs. *Adv. Space Res.* **66**, 1025–1056 (2020).

[ADS](#) [CAS](#) [Google Scholar](#)

59. 59.

Montgomery, M. H. et al. SDSS J142625.71 + 575218.3: a prototype for a new class of variable white dwarf. *Astrophys. J. Lett.* **678**, L51 (2008).

[ADS](#) [Google Scholar](#)

60. 60.

Dufour, P., Fontaine, G., Liebert, J., Williams, K. & Lai, D. K. SDSS J142625.71 + 575218.3: the first pulsating white dwarf with a large detectable magnetic field. *Astrophys. J. Lett.* **683**, L167 (2008).

[ADS](#) [CAS](#) [Google Scholar](#)

61. 61.

Green, E. M., Dufour, P., Fontaine, G. & Brassard, P. Follow-up studies of the pulsating magnetic white dwarf SDSS J142625.71 + 575218.3. *Astrophys. J.* **702**, 1593–1603 (2009).

[ADS](#) [CAS](#) [Google Scholar](#)

62. 62.

Córsico, A. H., Althaus, L. G., Miller Bertolami, M. M. & Kepler, S. O. Pulsating white dwarfs: new insights. *Astron. Astrophys. Rev.* **27**, 7 (2019).

[ADS](#) [Google Scholar](#)

63. 63.

Beauchamp, A. et al. Spectroscopic studies of DB white dwarfs: the instability strip of the pulsating DB (V777 Herculis) stars. *Astrophys. J.* **516**, 887–891 (1999).

[ADS](#) [Google Scholar](#)

64. 64.

Fuller, J., Cantiello, M., Stello, D., Garcia, R. A. & Bildsten, L. Asteroseismology can reveal strong internal magnetic fields in red giant stars. *Science* **350**, 423–426 (2015).

[ADS](#) [MathSciNet](#) [CAS](#) [PubMed](#) [PubMed Central](#) [MATH](#) [Google Scholar](#)

65. 65.

Lecoanet, D., Vasil, G. M., Fuller, J., Cantiello, M. & Burns, K. J. Conversion of internal gravity waves into magnetic waves. *Mon. Not. R. Astron. Soc.* **466**, 2181–2193 (2017).

[ADS](#) [Google Scholar](#)

66. 66.

Loi, S. T. & Papaloizou, J. C. B. Effects of a strong magnetic field on internal gravity waves: trapping, phase mixing, reflection, and dynamical chaos. *Mon. Not. R. Astron. Soc.* **477**, 5338–5357 (2018).

[ADS](#) [CAS](#) [Google Scholar](#)

67. 67.

Loi, S. T. Magneto-gravity wave packet dynamics in strongly magnetized cores of evolved stars. *Mon. Not. R. Astron. Soc.* **493**, 5726–5742 (2020).

[ADS](#) [Google Scholar](#)

68. 68.

Stello, D. et al. A prevalence of dynamo-generated magnetic fields in the cores of intermediate-mass stars. *Nature* **529**, 364–367 (2016).

[ADS](#) [CAS](#) [PubMed](#) [PubMed Central](#) [Google Scholar](#)

69. 69.

Cantiello, M., Fuller, J. & Bildsten, L. Asteroseismic signatures of evolving internal stellar magnetic fields. *Astrophys. J.* **824**, 14 (2016).

[ADS](#) [Google Scholar](#)

70. 70.

Foreman-Mackey, D. corner.py: Scatterplot matrices in python. *J. Open Source Softw.* **1**, 24 (2016); <https://doi.org/10.21105/joss.00024>.

[ADS](#) [Article](#) [Google Scholar](#)

71. 71.

Perley, D. A. Fully automated reduction of longslit spectroscopy with the Low Resolution Imaging Spectrometer at the Keck Observatory. *Publ. Astron. Soc. Pacif.* **131**, 084503 (2019).

[ADS](#) [Google Scholar](#)

[Download references](#)

Acknowledgements

The authors thank S.-C. Leung and S. Phinney for discussions, and N. Reindl and M. Kilic for comments. I.C. is a Sherman Fairchild Fellow at Caltech and thanks the Burke Institute at Caltech for supporting her research. J.F. acknowledges support through an Innovator Grant from the Rose Hills Foundation, and the Sloan Foundation through grant FG-2018-10515. K.B.B. thanks NASA and the Heising Simons Foundation for supporting his research. J.S. is supported by the A. F. Morrison Fellowship in Lick Observatory and by the US National Science Foundation (NSF) through grant ACI-1663688. This work is based on observations obtained with the Samuel Oschin 48-inch telescope and the Palomar Observatory 60-inch telescope as part of the ZTF project. ZTF is supported by the NSF under grant no. AST-1440341 and a collaboration including Caltech, IPAC, the Weizmann Institute for Science, the Oskar Klein Center at Stockholm University, the University of Maryland, the University of Washington, Deutsches Elektronen-Synchrotron and Humboldt University, Los Alamos National Laboratories, the TANGO Consortium of Taiwan, the University

of Wisconsin at Milwaukee, and Lawrence Berkeley National Laboratories. Operations are conducted by Caltech Optical Observatories, IPAC and the University of Washington. Some of the data presented herein were obtained at the W. M. Keck Observatory, which is operated as a scientific partnership among the California Institute of Technology, the University of California and NASA. This work has made use of data from the European Space Agency (ESA) mission Gaia (<https://www.cosmos.esa.int/gaia>), processed by the Gaia Data Processing and Analysis Consortium (DPAC; <https://www.cosmos.esa.int/web/gaia/dpac/consortium>). Funding for the DPAC has been provided by national institutions, in particular the institutions participating in the Gaia Multilateral Agreement. The Pan-STARRS1 Surveys (PS1) and the PS1 public science archive have been made possible through contributions by the Institute for Astronomy, the University of Hawaii, the Pan-STARRS Project Office, the Max Planck Society and its participating institutes, the Max Planck Institute for Astronomy, Heidelberg and the Max Planck Institute for Extraterrestrial Physics, Garching, The Johns Hopkins University, Durham University, the University of Edinburgh, the Queen's University Belfast, the Harvard-Smithsonian Center for Astrophysics, the Las Cumbres Observatory Global Telescope Network Incorporated, the National Central University of Taiwan, the Space Telescope Science Institute, NASA under grant no. NNX08AR22G issued through the Planetary Science Division of the NASA Science Mission Directorate, NSF grant no. AST-1238877, the University of Maryland, Eotvos Lorand University (ELTE), Los Alamos National Laboratory, and the Gordon and Betty Moore Foundation. This work was supported by the Natural Sciences and Engineering Research Council of Canada.

Author information

Affiliations

1. Division of Physics, Mathematics and Astronomy, California Institute of Technology, Pasadena, CA, USA

Ilaria Caiazzo, Kevin B. Burge, James Fuller, S. R. Kulkarni, Thomas A. Prince, Igor Andreoni, Andrew Drake, Dmitry A. Duev, Matthew J.

Graham & Ashish A. Mahabal

2. Department of Physics and Astronomy, University of British Columbia, Vancouver, British Columbia, Canada

Jeremy Heyl & Harvey B. Richer

3. Department of Astronomy and Astrophysics, University of California, Santa Cruz, CA, USA

Josiah Schwab

4. Department of Astronomy, University of Washington, Seattle, WA, USA

Eric C. Bellm

5. IPAC, California Institute of Technology, Pasadena, CA, USA

George Helou & Frank J. Masci

6. Center for Data Driven Discovery, California Institute of Technology, Pasadena, CA, USA

Ashish A. Mahabal

7. Caltech Optical Observatories, California Institute of Technology, Pasadena, CA, USA

Roger Smith

8. Lawrence Berkeley National Laboratory, Berkeley, CA, USA

Maayane T. Soumagnac

9. Department of Particle Physics and Astrophysics, Weizmann Institute of Science, Rehovot, Israel

Maayane T. Soumagnac

Authors

1. Ilaria Caiazzo

[View author publications](#)

You can also search for this author in [PubMed](#) [Google Scholar](#)

2. Kevin B. Burdge

[View author publications](#)

You can also search for this author in [PubMed](#) [Google Scholar](#)

3. James Fuller

[View author publications](#)

You can also search for this author in [PubMed](#) [Google Scholar](#)

4. Jeremy Heyl

[View author publications](#)

You can also search for this author in [PubMed](#) [Google Scholar](#)

5. S. R. Kulkarni

[View author publications](#)

You can also search for this author in [PubMed](#) [Google Scholar](#)

6. Thomas A. Prince

[View author publications](#)

You can also search for this author in [PubMed](#) [Google Scholar](#)

7. Harvey B. Richer

[View author publications](#)

You can also search for this author in [PubMed](#) [Google Scholar](#)

8. Josiah Schwab

[View author publications](#)

You can also search for this author in [PubMed](#) [Google Scholar](#)

9. Igor Andreoni

[View author publications](#)

You can also search for this author in [PubMed](#) [Google Scholar](#)

10. Eric C. Bellm

[View author publications](#)

You can also search for this author in [PubMed](#) [Google Scholar](#)

11. Andrew Drake

[View author publications](#)

You can also search for this author in [PubMed](#) [Google Scholar](#)

12. Dmitry A. Duev

[View author publications](#)

You can also search for this author in [PubMed](#) [Google Scholar](#)

13. Matthew J. Graham

[View author publications](#)

You can also search for this author in [PubMed](#) [Google Scholar](#)

14. George Helou

[View author publications](#)

You can also search for this author in [PubMed](#) [Google Scholar](#)

15. Ashish A. Mahabal

[View author publications](#)

You can also search for this author in [PubMed](#) [Google Scholar](#)

16. Frank J. Masci

[View author publications](#)

You can also search for this author in [PubMed](#) [Google Scholar](#)

17. Roger Smith

[View author publications](#)

You can also search for this author in [PubMed](#) [Google Scholar](#)

18. Maayane T. Soumagnac

[View author publications](#)

You can also search for this author in [PubMed](#) [Google Scholar](#)

Contributions

I.C. reduced the ultraviolet data, conducted the spectral and photometric analysis, identified the magnetic field and is the primary author of the manuscript. K.B.B. performed the period search on ZTF data and reduced the optical data. I.C. and J.H. conducted the mass–radius analysis. I.C., K.B.B., J.F., J.H., S.R.K., T.A.P., H.B.R. and J.S. contributed to the physical interpretation of the object. J.S. constructed preliminary MESA models for the object. I.A., A.D., D.A.D., A.A.M., F.J.M., R.S. and M.T.S. contributed to the implementation of ZTF. G.H. is a co-PI of the ZTF Mid-Scale Innovations Program (MSIP). M.J.G. is the project scientist, E.C.B. is the survey scientist, T.A.P. is the co-PI and S.R.K. is the PI of ZTF.

Corresponding author

Correspondence to [Ilaria Caiazzo](#).

Ethics declarations

Competing interests

The authors declare no competing interests.

Additional information

Peer review information *Nature* thanks the anonymous reviewers for their contribution to the peer review of this work.

Publisher's note Springer Nature remains neutral with regard to jurisdictional claims in published maps and institutional affiliations.

Extended data figures and tables

Extended Data Fig. 1 Photometric fit.

The blue solid line shows the best-fitting model spectrum, fitted to Pan-STARRS and Swift photometry to determine T_{eff} , R_* and $E(B - V)$. The synthetic photometric values (obtained from the black line) are shown in red. The Swift values are shown in green with 1σ error bars and the Pan-STARRS values in blue with the error that we chose to account for the photometric variability (0.02 mag).

Extended Data Fig. 2 Gaia $E(B - V)$ of the closest stars.

The plot shows the extinction A_G as measured by Gaia of the stars within 5 degrees of ZTF 1901+1458 as a function of distance and converted to $E(B - V)$ assuming a reddening law with $R_V = 3.1$. We use the average reddening of the closest stars as a prior for the fitting. The error bars show 1σ errors.

Extended Data Fig. 3 Corner plots.

Corner plots for the photometric fitting: results for the model atmospheres of Tremblay et al.⁴³ (left) and Bohlin et al.⁴⁵ (right).

Extended Data Fig. 4 Phase-resolved spectra, blue side.

The LRIS phase-resolved spectra of ZTF J1901+1458 in the blue side. Some small variations can be observed in the spectral features with phase, especially in features at $\sim 4,600 \text{ \AA}$ and at $\sim 3,800 \text{ \AA}$.

Extended Data Fig. 5 Phase-resolved spectra, red side.

The LRIS phase-resolved spectra of ZTF J1901+1458 in the red side. Some small variations can be observed in the spectral features with phase: in particular, the feature at \sim 6,620 Å becomes broader and narrower with phase.

Extended Data Table 1 Photometric data for ZTF J1901+1458

[Full size table](#)

Extended Data Table 2 Identified Balmer transitions

[Full size table](#)

Rights and permissions

[Reprints and Permissions](#)

About this article



Check for
updates

Cite this article

Caiazzo, I., Burdge, K.B., Fuller, J. *et al.* A highly magnetized and rapidly rotating white dwarf as small as the Moon. *Nature* **595**, 39–42 (2021).
<https://doi.org/10.1038/s41586-021-03615-y>

[Download citation](#)

- Received: 27 October 2020
- Accepted: 05 May 2021
- Published: 30 June 2021

- Issue Date: 01 July 2021
- DOI: <https://doi.org/10.1038/s41586-021-03615-y>

[Access through your institution](#)

[Change institution](#)

[Buy or subscribe](#)

Advertisement

This article was downloaded by **calibre** from <https://www.nature.com/articles/s41586-021-03615-y>.

| [Section menu](#) | [Main menu](#) |

- Article
- [Published: 30 June 2021](#)

Demonstration of a trapped-ion atomic clock in space

- [E. A. Burt](#) [ORCID: orcid.org/0000-0002-2486-9021](#)¹ na1,
- [J. D. Prestage](#)¹ na1,
- [R. L. Tjoelker](#)¹ na1,
- [D. G. Enzer](#) [ORCID: orcid.org/0000-0002-8074-0150](#)¹,
- [D. Kuang](#)¹,
- [D. W. Murphy](#)¹,
- [D. E. Robison](#)¹,
- [J. M. Seubert](#)¹,
- [R. T. Wang](#)¹ &
- [T. A. Ely](#) [ORCID: orcid.org/0000-0001-8832-0399](#)¹

[Nature](#) volume 595, pages 43–47 (2021) [Cite this article](#)

- 333 Accesses
- 184 Altmetric
- [Metrics details](#)

Subjects

- [Astronomical instrumentation](#)
- [Atomic and molecular physics](#)
- [Quantum metrology](#)

Abstract

Atomic clocks, which lock the frequency of an oscillator to the extremely stable quantized energy levels of atoms, are essential for navigation applications such as deep space exploration¹ and global navigation satellite systems², and are useful tools with which to address questions in fundamental physics^{3,4,5,6}. Such satellite systems use precise measurement of signal propagation times determined by atomic clocks, together with propagation speed, to calculate position. Although space atomic clocks with low instability are an enabling technology for global navigation, they have not yet been applied to deep space navigation and have seen only limited application to space-based fundamental physics, owing to performance constraints imposed by the rigours of space operation⁷. Methods of electromagnetically trapping and cooling ions have revolutionized atomic clock performance^{8,9,10,11,12,13}. Terrestrial trapped-ion clocks operating in the optical domain have achieved orders-of-magnitude improvements in performance over their predecessors and have become a key component in national metrology laboratory research programmes¹³, but transporting this new technology into space has remained challenging. Here we show the results from a trapped-ion atomic clock operating in space. On the ground, NASA's Deep Space Atomic Clock demonstrated a short-term fractional frequency stability of $1.5 \times 10^{-13}/\tau^{1/2}$ (where τ is the averaging time)¹⁴. Launched in 2019, the clock has operated for more than 12 months in space and demonstrated there a long-term stability of 3×10^{-15} at 23 days (no drift removal), and an estimated drift of $3.0(0.7) \times 10^{-16}$ per day. Each of these exceeds current space clock performance by up to an order of magnitude^{15,16,17}. The Deep Space Atomic Clock is particularly amenable to the space environment because of its low sensitivity to variations in radiation, temperature and magnetic fields. This level of space clock performance will enable one-way navigation in which signal delay times are measured in situ, making near-real-time navigation of deep space probes possible¹⁸.

Access options

Subscribe to Journal

Get full journal access for 1 year

\$199.00

only \$3.90 per issue

[Subscribe](#)

All prices are NET prices.

VAT will be added later in the checkout.

Tax calculation will be finalised during checkout.

Rent or Buy article

Get time limited or full article access on ReadCube.

from \$8.99

[Rent or Buy](#)

All prices are NET prices.

Additional access options:

- [Log in](#)
- [Access through your institution](#)
- [Learn about institutional subscriptions](#)

Fig. 1: The Deep Space Atomic Clock launch.

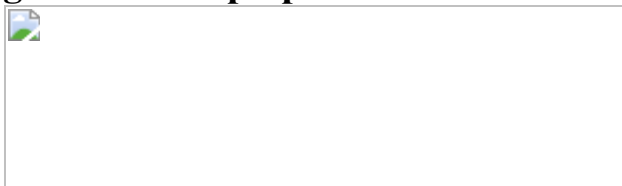


Fig. 2: Clock vacuum chamber and traps.



Fig. 3: Clock frequency offsets in space.

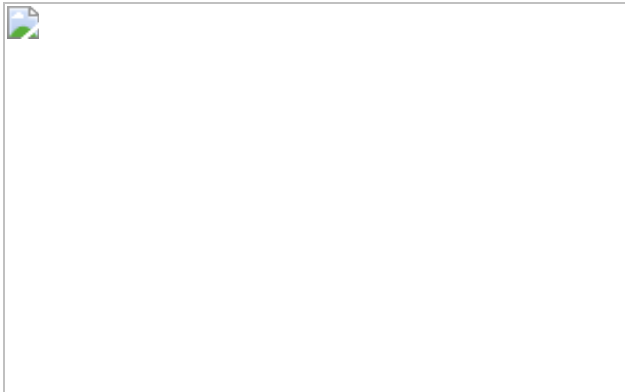
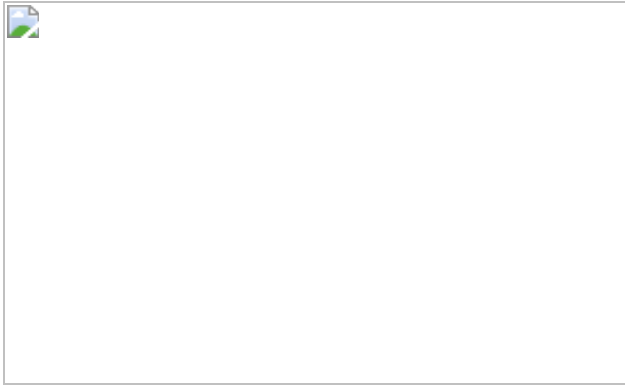


Fig. 4: Clock stability in space.



Data availability

Full data for Fig. 4 and Extended Data Fig. 3 are available from the corresponding author on reasonable request.

References

1. 1.

Thornton, C. L. & Border, J. S. *Radiometric Tracking Techniques for Deep-Space Navigation* (Wiley-Interscience, 2003).

2. 2.

Mallette, L. A., White, J. & Rochat, P. Space qualified frequency sources (clocks) for current and future GNSS applications. *IEEE/ION Position Locat. Navig. Symp. (Online)*, <https://doi.org/10.1109/PLANS.2010.5507225> (2010).

[Article](#) [Google Scholar](#)

3. 3.

Prestage, J. D., Tjoelker, R. L. & Maleki, L. Atomic clocks and variations of the fine structure constant. *Phys. Rev. Lett.* **74**, 3511 (1995).

[CAS](#) [Article](#) [ADS](#) [Google Scholar](#)

4. 4.

Safronova, M. S. The search for variation of fundamental constants with clocks. *Ann. Phys.* **531**, 1800364 (2019).

[Article](#) [Google Scholar](#)

5. 5.

McGrew, D. et al. Atomic clock performance enabling geodesy below the centimetre level. *Nature* **564**, 87 (2018).

[CAS](#) [Article](#) [ADS](#) [Google Scholar](#)

6. 6.

Hees, A., Guéna, J., Abgrall, M., Bize, S. & Wolf, P. Searching for an oscillating massive scalar field as a dark matter candidate using atomic hyperfine frequency comparisons. *Phys. Rev. Lett.* **117**, 061301 (2016).

[CAS](#) [Article](#) [ADS](#) [Google Scholar](#)

7. 7.

Vessot, R. F. C. et al. Test of relativistic gravitation with a space-borne hydrogen maser. *Phys. Rev. Lett.* **45**, 2081 (1980).

[Article](#) [ADS](#) [Google Scholar](#)

8. 8.

Prestage, J. D., Dick, G. J. & Maleki, L. Linear ion trap based atomic frequency standard. *IEEE Trans. Instrum. Meas.* **40**, 132 (1991).

[CAS Article](#) [ADS](#) [Google Scholar](#)

9. 9.

Cutler, L. S., Giffard, R. P. & McGuire, M. D. A trapped mercury 199 ion frequency standard. In *Proc. 13th Annual Precise Time and Time Interval (PTTI) Applications and Planning Meeting*, 563–577 (Institute of Navigation, 1981).

10. 10.

Tjoelker, R. L. et al. A mercury ion frequency standard engineering prototype for the NASA deep space network. In *Proc. 50th IEEE International Frequency Control Symposium*, 1073–1081 (IEEE, 1996).

11. 11.

Burt, E. A., Diener, W. A. & Tjoelker, R. L. A compensated multi-pole linear ion trap mercury frequency standard for ultra-stable timekeeping. *IEEE Trans. Ultrason. Ferroelectr. Freq. Control* **55**, 2586 (2008).

[Article](#) [Google Scholar](#)

12. 12.

Hinkley, N. et al. An atomic clock with 10^{-18} instability. *Science* **341**, 1215 (2013).

[CAS Article](#) [ADS](#) [Google Scholar](#)

13. 13.

Brewer, S. M. et al. $^{27}\text{Al}^+$ quantum-logic clock with a systematic uncertainty below 10^{-18} . *Phys. Rev. Lett.* **123**, 033201 (2019).

[CAS Article](#) [ADS](#) [Google Scholar](#)

14. 14.

Tjoelker, R. L. et al. Deep Space Atomic Clock (DSAC) for a NASA Technology Demonstration Mission. *IEEE Trans. Ultrason. Ferroelectr. Freq. Control* **63**, 1034–1043 (2016).

[Article](#) [ADS](#) [Google Scholar](#)

15. 15.

Lutwak, R., Emmons, D., Garvey, R. M. & Vlitas, P. Optically pumped cesium-beam frequency standard for GPS-III. In *Proc. 33rd Annual Precise Time and Time Interval (PTTI) Applications and Planning Meeting*, 19–30 (Institute of Navigation, 2001).

16. 16.

Riley, W. J. Rubidium atomic frequency standards for GPS block IIR. In *Proc. 22nd Annual Precise Time and Time Interval (PTTI)*, 221–230 (Institute of Navigation, 1990).

17. 17.

Droz, F. et al. Space passive hydrogen maser—performances and lifetime data. In *Proc. 2009 IEEE International Frequency Control Symposium Joint with the 22nd European Frequency and Time Forum*, 393–398 (IEEE, 2009).

18. 18.

Seubert, J., Ely, T. & Stuart, J. Results of the deep space atomic clock deep space navigation analog experiment. In *Proc. AAS/AIAA*

Astrodynamic Specialist Conference (American Astronomical Society, in the press).

19. 19.

Codik, A. Autonomous navigation of GPS satellites: a challenge for the future. *J. Inst. Navig.* **32**, 221–232 (1985).

[Article](#) [Google Scholar](#)

20. 20.

Dehmelt, H. G. Monoion oscillator as potential ultimate laser frequency standard. *IEEE Trans. Instrum. Meas.* **IM-31**, 83–87 (1982).

[CAS Article](#) [ADS](#) [Google Scholar](#)

21. 21.

Liu, L. et al. In-orbit operation of an atomic clock based on laser-cooled ^{87}Rb atoms. *Nat. Commun.* **9**, 2760 (2018).

[Article](#) [ADS](#) [Google Scholar](#)

22. 22.

Tjoelker, R. L. et al. Mercury atomic frequency standards for space-based navigation and timekeeping. In *Proc. 43rd annual Precise Time and Time Interval (PTTI) Systems and Applications Meeting*, 209–304 (Institute of Navigation, 2011).

23. 23.

Prestage, J.D., Chung, S., Le, T., Lim, L., and Maleki, L. Liter sized ion clock with 10^{-15} stability. In *Proc. Joint IEEE IFCS and PTTI*, 472–476 (IEEE, 2005).

24. 24.

Prestage, J. D. & Weaver, G. L. Atomic clocks and oscillators for deep-space navigation and radio science. *Proc. IEEE* **95**, 2235–2247 (2007).

[Article](#) [Google Scholar](#)

25. 25.

Ely, T. A., Seubert, J. & Bell, J. in *Space Operations: Innovations, Inventions, and Discoveries*, 105–138 (American Institute of Aeronautics and Astronautics, Inc., 2015).

26. 26.

Ely, T. A., Burt, E. A., Prestage, J. D., Seubert, J. M. & Tjoelker, R. L. Using the Deep Space Atomic Clock for navigation and science. *IEEE Trans. Ultrason. Ferroelectr. Freq. Control* **65**, 950–961 (2018).

[Article](#) [Google Scholar](#)

27. 27.

Prestage, J. D., Dick, G. J. & Maleki, L. New ion trap for frequency standard applications. *J. Appl. Phys.* **66**, 1013 (1989).

[Article](#) [ADS](#) [Google Scholar](#)

28. 28.

Prestage, J. D., Tjoelker, R. L. & Maleki, L. Higher pole linear traps for atomic clock applications. In *Proc. 1999 Joint European Frequency and Time Forum and IEEE International Frequency Control Symposium*, 121–124 (IEEE< 1999).

29. 29.

Dicke, R. H. The effect of collisions upon the Doppler width of spectral lines. *Phys. Rev.* **89**, 472 (1953).

[CAS](#) [Article](#) [ADS](#) [Google Scholar](#)

30. 30.

Enzer, D., Diener, W., Murphy, D., Rao, S. & Tjoelker, R. L. Drifts and environmental disturbances in atomic clock subsystem: quantifying local oscillator, control loop, & ion resonance interactions. *IEEE Trans. Ultrason. Ferroelectr. Freq. Control* **64**, 623–633 (2017).

[Article](#) [Google Scholar](#)

31. 31.

Ely, T. A., Murphy, D., Seubert, J., Bell, J. & Kuang, D. Expected performance of the Deep Space Atomic Clock Mission. In *Proc. AAS/AIAA Space Flight Mechanics Meeting*, 807–826 (American Astronomical Society, 2014).

32. 32.

Howe, D. A., Allan, D. W. & Barnes, J. A. Properties of signal sources and measurement methods. In *Proc. 35th Annual IEEE Symposium on Frequency Control*, 1–47 (IEEE, 1981).

33. 33.

Dick, G. J. Local oscillator induced instabilities in trapped ion frequency standards. In *Proc. 19th Precise Time and Time Interval Symposium*, 133–147 (Institute of Navigation, 1987).

34. 34.

Larson, K. M. & Levine, J. Time transfer using the phase of the GPS carrier. In *Proc. 1998 IEEE International Frequency Control Symposium*, 292–297 (IEEE, 1998).

35. 35.

Bertiger, W. et al. Single receiver phase ambiguity resolution with GPS data. *J. Geod.* **84**, 327–337 (2010).

[Article](#) [ADS](#) [Google Scholar](#)

36. 36.

Petit, G. Sub- 10^{-16} accuracy GNSS frequency transfer with IPPP. *GPS Solut.* **25**, 22 (2021).

[Article](#) [Google Scholar](#)

37. 37.

Larson, K. M., Ashby, N., Hackman, C. & Bertiger, W. An assessment of relativistic effects for low earth orbiters: the GRACE satellites. *Metrologia* **44**, 484 (2007).

[Article](#) [ADS](#) [Google Scholar](#)

38. 38.

Prestage, J. D., Tjoelker, R. L., Dick, G. J. & Maleki, L. Doppler sideband spectra for ions in a linear trap. In *Proc. IEEE International Frequency Control Symposium*, 148–154 (IEEE, 1993).

39. 39.

Tjoelker, R. L., Prestage, J. D., Dick, G. J. & Maleki, L. Long term stability of Hg⁺ trapped ion frequency standards. In *Proc. 1993 IEEE International Frequency Control Symposium*, 132–138 (IEEE, 1993).

40. 40.

Burt, E. A. & Tjoelker, R. L. Prospects for ultra-stable timekeeping with sealed vacuum operation in multi-pole linear ion trap standards. In *Proc. 39th Annual Precise Time and Time Interval Systems and Applications Meeting*, 309–316 (Institute of Navigation, 2008).

41. 41.

Chung, S. K., Prestage, J. D. & Tjoelker, R. L. Buffer gas experiments in mercury (Hg^+) ion clock. In *Proc. IEEE International Frequency Control Symposium*, 130–133 (IEEE, 2004).

42. 42.

Yi, L., Taghavi-Larigani, S., Burt, E. A. & Tjoelker, R. L. Progress towards a dual-isotope trapped mercury ion atomic clock: further studies of background gas collision shifts. In *Proc. 2012 IEEE International Frequency Control Symposium*, 1–5 (IEEE, 2012).

43. 43.

Shen, G. L. The pumping of methane by an ionization assisted Zr/Al getter pump. *J. Vac. Sci. Technol. A* **5**, 2580 (1987).

[CAS](#) [Article](#) [ADS](#) [Google Scholar](#)

44. 44.

Konradi, A., Badhwar, G. D. & Braby, L. A. Recent space shuttle observations of the South Atlantic Anomaly and the radiation belt models. *Adv. Space Res.* **14**, 911–921 (1994).

[CAS](#) [Article](#) [ADS](#) [Google Scholar](#)

45. 45.

Ginet, G. P., Madden, D., Dichter, B. K. & Brautigam, D. H. Energetic Proton Maps for the South Atlantic Anomaly. In *Proc. 2007 IEEE Radiation Effects Data Workshop*, 1–8 (IEEE, 2007).

46. 46.

Jerde, R. L., Peterson, L. E. & Stein, W. Effects of high energy radiations on noise pulses from photomultiplier tubes. *Rev. Sci. Instrum.* **38**, 1387 (1967).

[CAS Article](#) [ADS](#) [Google Scholar](#)

[Download references](#)

Acknowledgements

This work is jointly funded by NASA's Space Technology Mission Directorate (STMD) office and the office of Space Communications and Navigation (SCaN). The research was carried out at the Jet Propulsion Laboratory, California Institute of Technology, under a contract with the National Aeronautics and Space Administration (80NM0018D0004). Copyright 2020, California Institute of Technology. Government sponsorship acknowledged.

Author information

Author notes

1. These authors contributed equally: Eric A. Burt, John D. Prestage, Robert L. Tjoelker

Affiliations

1. Jet Propulsion Laboratory, California Institute of Technology, Pasadena, CA, USA
E. A. Burt, J. D. Prestage, R. L. Tjoelker, D. G. Enzer, D. Kuang, D. W. Murphy, D. E. Robison, J. M. Seubert, R. T. Wang & T. A. Ely

Authors

1. E. A. Burt
[View author publications](#)

You can also search for this author in [PubMed](#) [Google Scholar](#)

2. J. D. Prestage

[View author publications](#)

You can also search for this author in [PubMed](#) [Google Scholar](#)

3. R. L. Tjoelker

[View author publications](#)

You can also search for this author in [PubMed](#) [Google Scholar](#)

4. D. G. Enzer

[View author publications](#)

You can also search for this author in [PubMed](#) [Google Scholar](#)

5. D. Kuang

[View author publications](#)

You can also search for this author in [PubMed](#) [Google Scholar](#)

6. D. W. Murphy

[View author publications](#)

You can also search for this author in [PubMed](#) [Google Scholar](#)

7. D. E. Robison

[View author publications](#)

You can also search for this author in [PubMed](#) [Google Scholar](#)

8. J. M. Seubert

[View author publications](#)

You can also search for this author in [PubMed](#) [Google Scholar](#)

9. R. T. Wang

[View author publications](#)

You can also search for this author in [PubMed](#) [Google Scholar](#)

10. T. A. Ely

[View author publications](#)

You can also search for this author in [PubMed](#) [Google Scholar](#)

Contributions

E.A.B., J.D.P. and R.L.T. contributed equally. E.A.B. led DSAC clock preparation and optimization, determined operation modes and parameters, characterized the clock and payload before launch and in space, and led manuscript preparation activity. J.D.P. is the DSAC clock co-investigator, led the vacuum tube, ion trap, optics and magnetic design, and consulted on all other aspects of clock preparation, characterization and data analysis. R.L.T. is the DSAC clock co-investigator, consulted on all aspects of clock and payload design, preparation, characterization and data analysis, and led efforts to resolve several technical challenges with the instrument. D.G.E. led the development of telemetry processing and analysis tools, characterized local oscillator and system performance, and performed USO and control loop modelling. D.K. contributed GPS data processing, modelling and analysis. D.W.M. led the GPS data processing, modelling and analysis, including relativistic calculations and orbital parameter analysis, and wrote telemetry processing and display software. D.E.R. led controller algorithm implementation and data acquisition, and coordinated clock commanding through the spacecraft provider. J.M.S. was the DSAC deputy principal investigator and led technical and programmatic planning and performed the new one-way navigation experiments enabled by DSAC. T.A.E. is the DSAC principal investigator, led technical and programmatic planning and performed the new one-way navigation experiments enabled by DSAC, and with D.W.M. devised new methods to perform GPS receiver thermal calibrations. R.T.W led USO characterizations, instrument integration into the payload and payload integration into the spacecraft. All authors read, edited and approved the final manuscript.

Corresponding author

Correspondence to [E. A. Burt](#).

Ethics declarations

Competing interests

The authors declare no competing interests.

Additional information

Peer review information *Nature* thanks Pascale Defraigne, Ekkehard Peik and the other, anonymous, reviewer(s) for their contribution to the peer review of this work.

Publisher's note Springer Nature remains neutral with regard to jurisdictional claims in published maps and institutional affiliations.

Extended data figures and tables

[Extended Data Fig. 1 System-level block diagram of the DSAC payload.](#)

The GPS receiver (Rcv.) is not shown.

[Extended Data Fig. 2 Level diagram for \$^{199}\text{Hg\(II\)}\$.](#)

The $S_{1/2}, F = 1$ to $P_{1/2}, F = 1$ optical electric dipole transition used for state preparation and readout is shown in purple (note that the source of this light is broad enough to not resolve Zeeman sublevels, so the line is meant to indicate any transition between the $S_{1/2} F = 1$ and $P_{1/2} F = 1$ manifolds that is consistent with selection rules). Also shown are the $S_{1/2}, F = 0, m_F = 0$ to $S_{1/2}, F = 1, m_F = 0$ magnetic-field-insensitive 40.5-GHz hyperfine clock transition (thick black arrow), and the $\Delta m_F = \pm 1$ field-sensitive Zeeman lines at ± 140 kHz (thin black arrows).

[Extended Data Fig. 3 Measured Allan deviation.](#)

Allan deviation without any corrections (red), with relativity corrections but no temperature corrections (green), and with both relativity and temperature corrections (black). Simulated expected clock performance with clock parameters during the run with environmental perturbations (solid blue) and without (dashed blue) is shown for comparison. All traces except the blue are overlapping Allan deviation. For reference, the orbital period of about $T = 6,000$ s will result in expected peaks in the Allan deviation at $0.37T \approx 2,200$ s (ref. [30](#)).

Extended Data Fig. 4 Variations in the Earth's magnetic field observed on the DSAC spacecraft as a function of time.

The orbital period is approximately 6,000 s at an altitude of 720 km. The component of the field in the weakest shielding direction is plotted. Shielding in the other two directions is over an order of magnitude higher so that the impact of variations on the clock is dominated by the component shown.

Extended Data Fig. 5 Impact of magnetic field variations on the clock.

The Allan deviation of the frequency shift associated with measured magnetic field variations on board the DSAC spacecraft is shown (red) assuming a worst-case sensitivity of $7 \times 10^{-16} \mu\text{T}^{-1}$. Reference lines are also shown for expected multipole trap (dashed blue) and load trap (dashed black) operation noise floors (without LO noise aliasing effects for the multipole trap line). Error bars represent 68% confidence intervals.

Extended Data Fig. 6 Fractional frequency versus signal size in the load trap.

Signal size is the number of PMT counts measured at the line centre minus the counts at a detuning of one linewidth corresponding to the first minimum in a Rabi line trace. The slope gives an estimate of the number-dependent second-order Doppler shift while operating in the load trap. As a

point of reference, the corresponding shift in the multipole trap would be 10–20 times smaller.

Extended Data Fig. 7 Residuals from a fit to frequency versus signal size.

Residuals are now plotted against temperature in the load trap. A linear fit gives a total temperature sensitivity of $-2.3(1.1) \times 10^{-15} \text{ }^{\circ}\text{C}^{-1}$.

Extended Data Fig. 8 Temperature data.

Temperature data shown for the 52-day dataset described in the main text. **a**, Long-term temperature variation in the load trap over 52 days correlated with changes in Sun beta angle. **b**, A 5-day subset showing 24-h temperature variations. **c**, A 1-day subset showing orbital temperature variation.

Extended Data Fig. 9 Trace-gas evolution.

Frequency data with the temperature effect removed (black dots) and fitted to a straight line (blue line), so as to place a limit of 4.6×10^{-16} per day on frequency shifts due to trace-gas evolution in the clock vacuum chamber.

Extended Data Fig. 10 Passage through the SAA.

Total PMT counts in 8.1-s portions of each clock cycle as a function of time, showing excess counts due to passage through the SAA. Each passage is approximately 20 min, as shown for the expanded view (inset). The varying peak amplitude is due to spacecraft orbital precession, which varies the trajectory of the spacecraft in and out of the SAA on a daily timescale.

Rights and permissions

Reprints and Permissions

About this article



Check for
updates

Cite this article

Burt, E.A., Prestage, J.D., Tjoelker, R.L. *et al.* Demonstration of a trapped-ion atomic clock in space. *Nature* **595**, 43–47 (2021).
<https://doi.org/10.1038/s41586-021-03571-7>

[Download citation](#)

- Received: 04 December 2020
- Accepted: 21 April 2021
- Published: 30 June 2021
- Issue Date: 01 July 2021
- DOI: <https://doi.org/10.1038/s41586-021-03571-7>

[Access through your institution](#)

[Change institution](#)

[Buy or subscribe](#)

Associated Content

[A trapped ion atomic clock in space](#)

- Iulia Georgescu

Advertisement

This article was downloaded by **calibre** from <https://www.nature.com/articles/s41586-021-03571-7>

| [Section menu](#) | [Main menu](#) |

- Article
- [Published: 30 June 2021](#)

Bilayer Wigner crystals in a transition metal dichalcogenide heterostructure

- [You Zhou](#) ORCID: [orcid.org/0000-0002-9854-545X^{1,2}](https://orcid.org/0000-0002-9854-545X) nAff⁹,
- [Jiho Sung](#) ORCID: [orcid.org/0000-0002-7390-4567^{1,2}](https://orcid.org/0000-0002-7390-4567),
- [Elise Brutschea](#) ORCID: [orcid.org/0000-0001-9096-7482¹](https://orcid.org/0000-0001-9096-7482),
- [Ilya Esterlis](#)²,
- [Yao Wang](#) ORCID: [orcid.org/0000-0003-1736-0187^{2,3}](https://orcid.org/0000-0003-1736-0187),
- [Giovanni Scuri](#) ORCID: [orcid.org/0000-0003-1050-3114²](https://orcid.org/0000-0003-1050-3114),
- [Ryan J. Gelly](#)²,
- [Hoseok Heo](#)^{1,2},
- [Takashi Taniguchi](#) ORCID: [orcid.org/0000-0002-1467-3105⁴](https://orcid.org/0000-0002-1467-3105),
- [Kenji Watanabe](#) ORCID: [orcid.org/0000-0003-3701-8119⁵](https://orcid.org/0000-0003-3701-8119),
- [Gergely Zaránd](#)⁶,
- [Mikhail D. Lukin](#) ORCID: [orcid.org/0000-0002-8658-1007²](https://orcid.org/0000-0002-8658-1007),
- [Philip Kim](#)^{2,7},
- [Eugene Demler](#) ORCID: [orcid.org/0000-0002-2499-632X^{2,8}](https://orcid.org/0000-0002-2499-632X) &
- [Hongkun Park](#) ORCID: [orcid.org/0000-0001-9576-8829^{1,2}](https://orcid.org/0000-0001-9576-8829)

[Nature](#) volume **595**, pages 48–52 (2021) [Cite this article](#)

- 408 Accesses
- 51 Altmetric
- [Metrics details](#)

Subjects

- [Electronic properties and materials](#)
- [Phase transitions and critical phenomena](#)
- [Quantum fluids and solids](#)
- [Two-dimensional materials](#)

Abstract

One of the first theoretically predicted manifestations of strong interactions in many-electron systems was the Wigner crystal^{1,2,3}, in which electrons crystallize into a regular lattice. The crystal can melt via either thermal or quantum fluctuations⁴. Quantum melting of the Wigner crystal is predicted to produce exotic intermediate phases^{5,6} and quantum magnetism^{7,8} because of the intricate interplay of Coulomb interactions and kinetic energy. However, studying two-dimensional Wigner crystals in the quantum regime has often required a strong magnetic field^{9,10,11} or a moiré superlattice potential^{12,13,14,15}, thus limiting access to the full phase diagram of the interacting electron liquid. Here we report the observation of bilayer Wigner crystals without magnetic fields or moiré potentials in an atomically thin transition metal dichalcogenide heterostructure, which consists of two MoSe₂ monolayers separated by hexagonal boron nitride. We observe optical signatures of robust correlated insulating states at symmetric (1:1) and asymmetric (3:1, 4:1 and 7:1) electron doping of the two MoSe₂ layers at cryogenic temperatures. We attribute these features to bilayer Wigner crystals composed of two interlocked commensurate triangular electron lattices, stabilized by inter-layer interaction¹⁶. The Wigner crystal phases are remarkably stable, and undergo quantum and thermal melting transitions at electron densities of up to 6×10^{12} per square centimetre and at temperatures of up to about 40 kelvin. Our results demonstrate that an atomically thin heterostructure is a highly tunable platform for realizing many-body electronic states and probing their liquid–solid and magnetic quantum phase transitions^{4,5,6,7,8,17}.

Access options

[Subscribe to Journal](#)

Get full journal access for 1 year

\$199.00

only \$3.90 per issue

[Subscribe](#)

All prices are NET prices.

VAT will be added later in the checkout.

Tax calculation will be finalised during checkout.

Rent or Buy article

Get time limited or full article access on ReadCube.

from \$8.99

[Rent or Buy](#)

All prices are NET prices.

Additional access options:

- [Log in](#)
- [Access through your institution](#)
- [Learn about institutional subscriptions](#)

Fig. 1: Device structure and full control of carrier density in device D1.

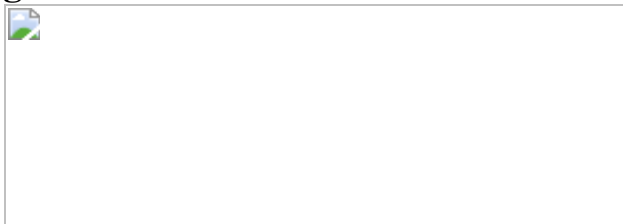


Fig. 2: Voltage-dependent reflectance and PL spectra of device D1 in the electron-doped regime at 4 K.

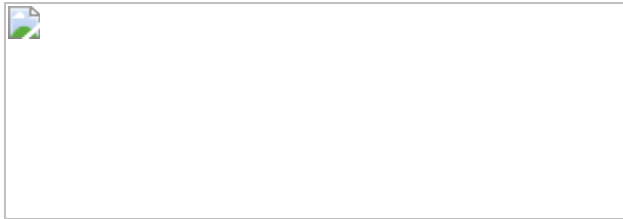


Fig. 3: Density and temperature dependence of the interaction-induced insulating states in device D1.

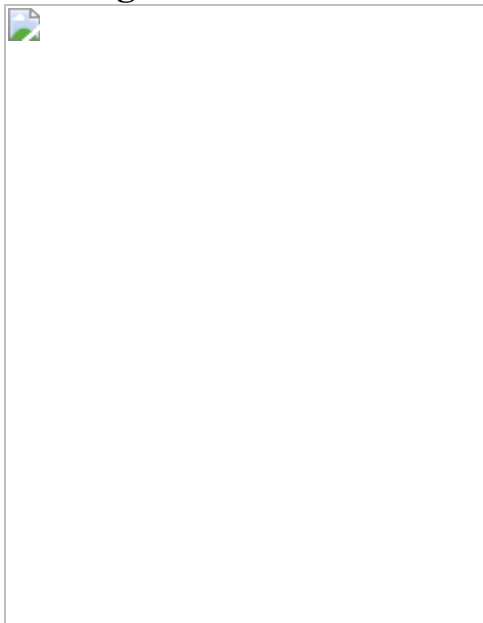
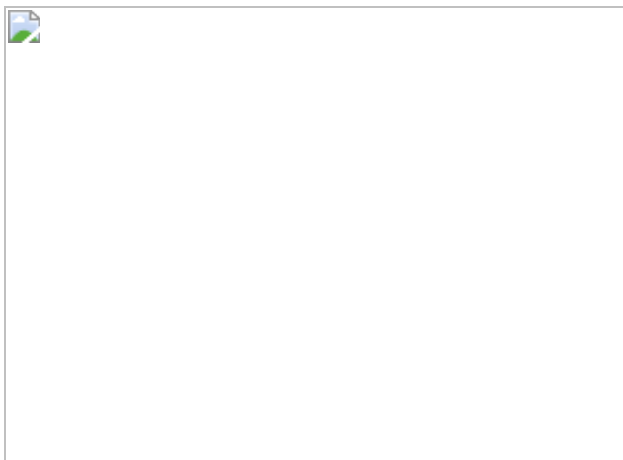


Fig. 4: Bilayer Wigner crystals and their quantum and thermal phase transitions.



Data availability

The data that support the plots within this paper and other findings of this study are available from the corresponding authors upon reasonable request.

References

1. 1.

Wigner, E. On the interaction of electrons in metals. *Phys. Rev.* **46**, 1002–1011 (1934).

[ADS](#) [CAS](#) [MATH](#) [Google Scholar](#)

2. 2.

Grimes, C. C. & Adams, G. Evidence for a liquid-to-crystal phase transition in a classical, two-dimensional sheet of electrons. *Phys. Rev. Lett.* **42**, 795–798 (1979).

[ADS](#) [CAS](#) [Google Scholar](#)

3. 3.

Shapir, I. et al. Imaging the electronic Wigner crystal in one dimension. *Science* **364**, 870–875 (2019).

[ADS](#) [CAS](#) [PubMed](#) [PubMed Central](#) [Google Scholar](#)

4. 4.

Monarkha, Y. P. & Syvokon, V. E. A two-dimensional Wigner crystal (Review Article). *Low Temp. Phys.* **38**, 1067–1095 (2012).

[ADS](#) [CAS](#) [Google Scholar](#)

5. 5.

Spivak, B. & Kivelson, S. A. Phases intermediate between a two-dimensional electron liquid and Wigner crystal. *Phys. Rev. B* **70**,

155114 (2004).

[ADS](#) [Google Scholar](#)

6. 6.

Spivak, B., Kravchenko, S. V., Kivelson, S. A. & Gao, X. P. A. Colloquium: Transport in strongly correlated two dimensional electron fluids. *Rev. Mod. Phys.* **82**, 1743–1766 (2010).

[ADS](#) [CAS](#) [Google Scholar](#)

7. 7.

Ortiz, G., Harris, M. & Ballone, P. Zero temperature phases of the electron gas. *Phys. Rev. Lett.* **82**, 5317 (1999).

[ADS](#) [CAS](#) [Google Scholar](#)

8. 8.

Chakravarty, S., Kivelson, S., Nayak, C. & Voelker, K. Wigner glass, spin liquids and the metal-insulator transition. *Phil. Mag. B* **79**, 859–868 (1999).

[ADS](#) [CAS](#) [Google Scholar](#)

9. 9.

Andrei, E. Y. et al. Observation of a magnetically induced Wigner solid. *Phys. Rev. Lett.* **60**, 2765–2768 (1988).

[ADS](#) [CAS](#) [Google Scholar](#)

10. 10.

Jiang, H. W. et al. Quantum liquid versus electron solid around $\nu = 1/5$ Landau-level filling. *Phys. Rev. Lett.* **65**, 633–636 (1990).

[ADS](#) [CAS](#) [Google Scholar](#)

11. 11.

Ma, M. K. et al. Thermal and quantum melting phase diagrams for a magnetic-field-induced Wigner solid. *Phys. Rev. Lett.* **125**, 036601 (2020).

[ADS](#) [CAS](#) [Google Scholar](#)

12. 12.

Regan, E. C. et al. Mott and generalized Wigner crystal states in WSe₂/WS₂ moiré superlattices. *Nature* **579**, 359–363 (2020).

[ADS](#) [CAS](#) [PubMed](#) [PubMed Central](#) [Google Scholar](#)

13. 13.

Xu, Y. et al. Correlated insulating states at fractional fillings of moiré superlattices. *Nature* **587**, 214–218 (2020).

[ADS](#) [CAS](#) [PubMed](#) [PubMed Central](#) [Google Scholar](#)

14. 14.

Huang, X. et al. Correlated insulating states at fractional fillings of the WS₂/WSe₂ moiré lattice. *Nat. Phys.* **17**, 715–719 (2021).

15. 15.

Jin, C. et al. Stripe phases in WSe₂/WS₂ moiré superlattices. *Nat. Mater.* <https://doi.org/10.1038/s41563-021-00959-8> (2021).

16. 16.

Świerkowski, L., Neilson, D. & Szymański, J. Enhancement of Wigner crystallization in multiple-quantum-well structures. *Phys. Rev. Lett.* **67**, 240 (1991).

[ADS](#) [PubMed](#) [PubMed Central](#) [Google Scholar](#)

17. 17.

Benenti, G., Waintal, X. & Pichard, J.-L. New quantum phase between the Fermi glass and the Wigner crystal in two dimensions. *Phys. Rev. Lett.* **83**, 1826–1829 (1999).

[ADS](#) [CAS](#) [Google Scholar](#)

18. 18.

Yoon, J., Li, C. C., Shahar, D., Tsui, D. C. & Shayegan, M. Wigner crystallization and metal-insulator transition of two-dimensional holes in GaAs at $B = 0$. *Phys. Rev. Lett.* **82**, 1744–1747 (1999).

[ADS](#) [CAS](#) [Google Scholar](#)

19. 19.

Hossain, M. S. et al. Observation of spontaneous ferromagnetism in a two-dimensional electron system. *Proc. Natl Acad. Sci.* **117**, 32244–32250 (2020).

[ADS](#) [CAS](#) [PubMed](#) [PubMed Central](#) [Google Scholar](#)

20. 20.

Scuri, G. et al. Large excitonic reflectivity of monolayer MoSe₂ encapsulated in hexagonal boron nitride. *Phys. Rev. Lett.* **120**, 037402 (2018).

[ADS](#) [CAS](#) [PubMed](#) [PubMed Central](#) [Google Scholar](#)

21. 21.

Back, P., Zeytinoglu, S., Ijaz, A., Kroner, M. & Imamoğlu, A. Realization of an electrically tunable narrow-bandwidth atomically

thin mirror using monolayer MoSe₂. *Phys. Rev. Lett.* **120**, 037401 (2018).

[ADS](#) [CAS](#) [PubMed](#) [PubMed Central](#) [Google Scholar](#)

22. 22.

Kormányos, A. et al. k·p theory for two-dimensional transition metal dichalcogenide semiconductors. *2D Mater.* **2**, 022001 (2015).

[Google Scholar](#)

23. 23.

Larentis, S. et al. Large effective mass and interaction-enhanced Zeeman splitting of K-valley electrons in MoSe₂. *Phys. Rev. B* **97**, 201407 (2018).

[ADS](#) [CAS](#) [Google Scholar](#)

24. 24.

Tang, Y. et al. Simulation of Hubbard model physics in WSe₂/WS₂ moiré superlattices. *Nature* **579**, 353–358 (2020).

[ADS](#) [CAS](#) [PubMed](#) [PubMed Central](#) [Google Scholar](#)

25. 25.

Shimazaki, Y. et al. Strongly correlated electrons and hybrid excitons in a moiré heterostructure. *Nature* **580**, 472–477 (2020).

[ADS](#) [CAS](#) [PubMed](#) [PubMed Central](#) [Google Scholar](#)

26. 26.

Ross, J. S. et al. Electrical control of neutral and charged excitons in a monolayer semiconductor. *Nat. Commun.* **4**, 1474 (2013).

[ADS](#) [PubMed](#) [PubMed Central](#) [Google Scholar](#)

27. 27.

Hubbard, J. Generalized Wigner lattices in one dimension and some applications to tetracyanoquinodimethane (TCNQ) salts. *Phys. Rev. B* **17**, 494–505 (1978).

[ADS](#) [CAS](#) [Google Scholar](#)

28. 28.

Zhou, Y. et al. Controlling excitons in an atomically thin membrane with a mirror. *Phys. Rev. Lett.* **124**, 027401 (2020).

[ADS](#) [CAS](#) [Google Scholar](#)

29. 29.

Sung, J. et al. Broken mirror symmetry in excitonic response of reconstructed domains in twisted MoSe₂/MoSe₂ bilayers. *Nat. Nanotechnol.* **15**, 750–754 (2020).

[ADS](#) [CAS](#) [Google Scholar](#)

30. 30.

Geick, R., Perry, C. H. & Rupprecht, G. Normal modes in hexagonal boron nitride. *Phys. Rev.* **146**, 543–547 (1966).

[ADS](#) [CAS](#) [Google Scholar](#)

31. 31.

Van der Donck, M. & Peeters, F. M. Interlayer excitons in transition metal dichalcogenide heterostructures. *Phys. Rev. B* **98**, 115104 (2018).

[ADS](#) [Google Scholar](#)

32. 32.

Smoleński, T. et al. Observation of Wigner crystal of electrons in a monolayer semiconductor. Preprint at <https://arxiv.org/abs/2010.03078> (2020).

33. 33.

Platzman, P. M. & Fukuyama, H. Phase diagram of the two-dimensional electron liquid. *Phys. Rev. B* **10**, 3150–3158 (1974).

[ADS](#) [CAS](#) [Google Scholar](#)

34. 34.

Goldoni, G. & Peeters, F. M. Stability, dynamical properties, and melting of a classical bilayer Wigner crystal. *Phys. Rev. B* **53**, 4591–4603 (1996).

[ADS](#) [CAS](#) [Google Scholar](#)

35. 35.

Schweigert, I. V., Schweigert, V. A. & Peeters, F. M. Enhanced stability of the square lattice of a classical bilayer Wigner crystal. *Phys. Rev. B* **60**, 14665–14674 (1999).

[ADS](#) [CAS](#) [Google Scholar](#)

36. 36.

Bedanov, V. M., Gadiyak, G. V. & Lozovik, Y. E. On a modified Lindemann-like criterion for 2D melting. *Phys. Rev. A* **109**, 289–291 (1985).

[Google Scholar](#)

37. 37.

Imry, Y. & Ma, S.-k. Random-field instability of the ordered state of continuous symmetry. *Phys. Rev. Lett.* **35**, 1399–1401 (1975).

[ADS](#) [CAS](#) [Google Scholar](#)

38. 38.

Ruzin, I. M., Marianer, S. & Shklovskii, B. I. Pinning of a two-dimensional Wigner crystal by charged impurities. *Phys. Rev. B* **46**, 3999–4008 (1992).

[ADS](#) [CAS](#) [Google Scholar](#)

39. 39.

Chitra, R. & Giamarchi, T. Zero field Wigner crystal. *Eur. Phys. J. B* **44**, 455–467 (2005).

[ADS](#) [CAS](#) [Google Scholar](#)

40. 40.

Waintal, X. On the quantum melting of the two-dimensional Wigner crystal. *Phys. Rev. B* **73**, 075417 (2006).

[ADS](#) [Google Scholar](#)

41. 41.

Bonsall, L. & Maradudin, A. A. Some static and dynamical properties of a two-dimensional Wigner crystal. *Phys. Rev. B* **15**, 1959–1973 (1977).

[ADS](#) [CAS](#) [Google Scholar](#)

42. 42.

Tanatar, B. & Ceperley, D. M. Ground state of the two-dimensional electron gas. *Phys. Rev. B* **39**, 5005–5016 (1989).

[ADS](#) [CAS](#) [Google Scholar](#)

43. 43.

Knörzer, J. et al. Wigner crystals in two-dimensional transition-metal dichalcogenides: spin physics and readout. *Phys. Rev. B* **101**, 125101 (2020).

[ADS](#) [Google Scholar](#)

44. 44.

Chen, Y. P. Pinned bilayer Wigner crystals with pseudospin magnetism. *Phys. Rev. B* **73**, 115314 (2006).

[ADS](#) [Google Scholar](#)

45. 45.

Dayal, S., Clay, R. T., Li, H. & Mazumdar, S. Paired electron crystal: order from frustration in the quarter-filled band. *Phys. Rev. B* **83**, 245106 (2011).

[ADS](#) [Google Scholar](#)

46. 46.

Monarkha, Y. & Kono, K. *Two-Dimensional Coulomb Liquids and Solids* (Springer, 2004).

47. 47.

Cevallos, F. A. et al. Liquid salt transport growth of single crystals of the layered dichalcogenides MoS₂ and WS₂. *Cryst. Growth Des.* **19**, 5762–5767 (2019).

[CAS](#) [Google Scholar](#)

48. 48.

Kim, K. et al. van der Waals heterostructures with high accuracy rotational alignment. *Nano Lett.* **16**, 1989–1995 (2016).

[ADS](#) [CAS](#) [PubMed](#) [PubMed Central](#) [Google Scholar](#)

49. 49.

Kim, K. et al. Band alignment in WSe₂–graphene heterostructures. *ACS Nano* **9**, 4527–4532 (2015).

[CAS](#) [PubMed](#) [PubMed Central](#) [Google Scholar](#)

50. 50.

Smoleński, T. et al. Interaction-induced Shubnikov–de Haas oscillations in optical conductivity of monolayer MoSe₂. *Phys. Rev. Lett.* **123**, 097403 (2019).

[ADS](#) [PubMed](#) [PubMed Central](#) [Google Scholar](#)

[Download references](#)

Acknowledgements

We acknowledge support from the DoD Vannevar Bush Faculty Fellowship (N00014-16-1-2825 for H.P., N00014-18-1-2877 for P.K.), NSF CUA (PHY-1125846 for H.P., E.D. and M.D.L.), Samsung Electronics (for H.P. and P.K.), NSF (PHY-1506284 for H.P. and M.D.L., DGE-1745303 for E.B., DMR-2038011 for Y.W.), AFOSR MURI (FA9550-17-1-0002), ARL (W911NF1520067 for H.P. and M.D.L.), DOE (DE-SC0020115 for H.P. and M.D.L.), AFOSR (FA9550-21-1-0216 for E.D.) and BME’s TKP 2020 Nanotechnology grant (G.Z.). Device fabrication was carried out at the Harvard Center for Nanoscale Systems. Y.W. acknowledges Frontera computing system at the Texas Advanced Computing Center for geometric optimization of crystal structures. I.E. and E.D. acknowledge resources of the National Energy Research Scientific Computing Center (NERSC) for phase transition calculations. NERSC is a US Department of Energy Office

of Science User Facility operated under contract no. DE-AC02-05CH11231.

Author information

Author notes

1. You Zhou

Present address: Department of Materials Science and Engineering,
University of Maryland, College Park, MD, USA

Affiliations

1. Department of Chemistry and Chemical Biology, Harvard University, Cambridge, MA, USA

You Zhou, Jiho Sung, Elise Brutschea, Hoseok Heo & Hongkun Park

2. Department of Physics, Harvard University, Cambridge, MA, USA

You Zhou, Jiho Sung, Ilya Esterlis, Yao Wang, Giovanni Scuri, Ryan J. Gelly, Hoseok Heo, Mikhail D. Lukin, Philip Kim, Eugene Demler & Hongkun Park

3. Department of Physics and Astronomy, Clemson University, Clemson, SC, USA

Yao Wang

4. International Center for Materials Nanoarchitectonics, National Institute for Materials Science, Tsukuba, Japan

Takashi Taniguchi

5. Research Center for Functional Materials, National Institute for Materials Science, Tsukuba, Japan

Kenji Watanabe

6. MTA-BME Quantum Dynamics and Correlations Research Group,
Institute of Physics, Budapest University of Technology and
Economics, Budapest, Hungary

Gergely Zarand

7. John A. Paulson School of Engineering and Applied Sciences, Harvard
University, Cambridge, MA, USA

Philip Kim

8. Institute for Theoretical Physics, ETH Zrich, Zrich, Switzerland

Eugene Demler

Authors

1. You Zhou

[View author publications](#)

You can also search for this author in [PubMed](#) [Google Scholar](#)

2. Jiho Sung

[View author publications](#)

You can also search for this author in [PubMed](#) [Google Scholar](#)

3. Elise Brutschea

[View author publications](#)

You can also search for this author in [PubMed](#) [Google Scholar](#)

4. Ilya Esterlis

[View author publications](#)

You can also search for this author in [PubMed](#) [Google Scholar](#)

5. Yao Wang
[View author publications](#)

You can also search for this author in [PubMed](#) [Google Scholar](#)

6. Giovanni Scuri
[View author publications](#)

You can also search for this author in [PubMed](#) [Google Scholar](#)

7. Ryan J. Gelly
[View author publications](#)

You can also search for this author in [PubMed](#) [Google Scholar](#)

8. Hoseok Heo
[View author publications](#)

You can also search for this author in [PubMed](#) [Google Scholar](#)

9. Takashi Taniguchi
[View author publications](#)

You can also search for this author in [PubMed](#) [Google Scholar](#)

10. Kenji Watanabe
[View author publications](#)

You can also search for this author in [PubMed](#) [Google Scholar](#)

11. Gergely Zaránd
[View author publications](#)

You can also search for this author in [PubMed](#) [Google Scholar](#)

12. Mikhail D. Lukin
[View author publications](#)

You can also search for this author in [PubMed](#) [Google Scholar](#)

13. Philip Kim

[View author publications](#)

You can also search for this author in [PubMed](#) [Google Scholar](#)

14. Eugene Demler

[View author publications](#)

You can also search for this author in [PubMed](#) [Google Scholar](#)

15. Hongkun Park

[View author publications](#)

You can also search for this author in [PubMed](#) [Google Scholar](#)

Contributions

H.P. and Y.Z. conceived the project. Y.Z., J.S. and E.B. fabricated the samples, and designed and performed the experiments. I.E., Y.W., G.Z. and E.D. developed the theoretical model, and Y.Z., J.S., E.B., I.E. and Y.W. analysed the data. G.S. assisted with optical measurements, G.S. and R.J.G. assisted with sample fabrication, and H.H. grew the MoSe₂ crystals. T.T. and K.W. provided hBN samples. Y.Z., J.S., E.B., I.E., Y.W., G.S., E.D. and H.P. wrote the manuscript with extensive input from the other authors. H.P., E.D., P.K. and M.D.L. supervised the project.

Corresponding authors

Correspondence to [Eugene Demler](#) or [Hongkun Park](#).

Ethics declarations

Competing interests

The authors declare no competing interests.

Additional information

Peer review information *Nature* thanks the anonymous reviewers for their contribution to the peer review of this work.

Publisher's note Springer Nature remains neutral with regard to jurisdictional claims in published maps and institutional affiliations.

Extended data figures and tables

Extended Data Fig. 1 Optical spectroscopic characterization of device D1 at $T = 4$ K.

a, A spatial map of integrated PL intensity at (0 V, 0 V). The PL intensity from the MoSe₂/hBN/MoSe₂, which is quite uniform throughout the entire region, is stronger than that from the monolayer regions, suggesting that both MoSe₂ layers maintain their direct bandgap. **b**, Reflection contrast R/R_0 at (0 V, 0 V). **c**, Representative PL spectra taken from the gated region of device D1 at 4 K. We find the standard deviation of the exciton energy across the gated region to be about 1 meV, much less than the exciton linewidth. The inset shows the spots where the PL spectra were collected, with the colour of the dot and of the spectrum curve matching each other. The dashed line encloses the bilayer region covered by both top and bottom gates. **d**, The linewidth of the neutral exciton X_0 as a function of total electron density n , measured along $n_t:n_b = 1:1$ and $2:1$, compared with a monolayer MoSe₂. **e**, 2D maps of X_0 linewidth as a function of V_{tg}/d_{tg} and V_{bg}/d_{bg} . Free charge carriers in MoSe₂ can interact with X_0 by introducing additional scattering, which leads to the broadening of X_0 (refs. [20,21](#)). The features I, II and IV are defined in the same way as in Fig. [2](#). Along the $n_t:n_b = 1:1$ and $4:1$ features (I and II), we observe narrower X_0 linewidth. This is further corroboration that the system is in insulating states along these density ratios. The blue, red and yellow dashed lines represent the linecuts where we extract data shown in the same colour in **d**. For large V_{tg} and V_{bg} (top right corner of the graph), the intensity of X_0 becomes very

weak and therefore the linewidth cannot be reliably extracted. **f**, 2D maps of integrated charged exciton emission (X_T) as a function of V_{tg}/d_{tg} and V_{bg}/d_{bg} . The features I–IV are defined in the same way as in Fig. 2. We observe reduced X_T emission along features I and II (Fig. 2b).

Extended Data Fig. 2 Gate dependence of PL spectra from device D1 at 4 K.

a–c, PL spectra as a function of V_{bg} with a fixed V_{tg} of 0 V (**a**), 2.5 V (**b**) and 5 V (**c**). **d–f**, PL spectra as a function of V_{tg} with a fixed V_{bg} of 0 V (**d**), 1.5 V (**e**) and 4 V (**f**). When the top (bottom) MoSe₂ is intrinsic or highly doped, the application of V_{bg} (V_{tg}) mainly modifies the response of the bottom (top) layer. Here X_{0b} and X_{0t} represent the neutral exciton from the bottom and the top layer, respectively, while X_{Tb} and X_{Tt} represent the charged exciton from the bottom and the top layer, respectively. On the basis of such gate dependence, we can distinguish the contributions from the top versus the bottom layer when they have non-degenerate optical response (when the filling ratio is not 1:1). At intermediate gate voltage (**b**, **e**), however, the total PL of the neutral exciton is enhanced at a particular voltage configuration (denoted as I), corresponding to the feature I observed in Fig. 2.

Extended Data Fig. 3 Gate dependence of reflectance spectra from device D1 at 4 K.

a–f, As for Extended Data Fig. 2 but for normalized reflectance, R/R_0 ; the spectra are normalized to the background reflectance when both MoSe₂ layers are highly doped with electrons.

Extended Data Fig. 4 Optical characterization of device D1 at 100 mK.

a, b, 2D maps of integrated neutral exciton X_0 PL (**a**) and the second derivative of X_0 PL intensity with respect to the electric field (**b**), as a

function of V_{tg}/d_{tg} and V_{bg}/d_{bg} . The density ratios can be determined from the troughs in **b**. We added guide lines I, II, III and V, which correspond to constant density ratio $n_t:n_b$ of 1:1, 4:1, 7:1 and 3:1, respectively.

Extended Data Fig. 5 Observation of bilayer Wigner crystals in another MoSe₂/hBN/MoSe₂ device, D2, at 4 K.

a, PL spectrum of D2 at zero gate bias. Inset, a microscope image of D2. In this device, the inter-layer hBN thickness is 1.6 nm. The white and yellow dashed lines indicate top and bottom monolayer MoSe₂, respectively. Scale bar, 10 μm. **b, c**, 2D maps of neutral exciton X₀ reflectance contrast R/R_0 (**b**) and integrated X₀ PL (**c**), as a function of V_{tg}/d_{tg} and V_{bg}/d_{bg} . The emerging insulating feature I corresponds to a density ratio of $n_t:n_b = 1:1$, with a lower critical density than found in device D1; we did not observe insulating states at other density ratios. Taken together, this suggests that bilayer Wigner crystals are less stable for this larger inter-layer separation. **d–f**, Gate-dependence of PL spectra from device D2 at 4 K with a fixed V_{tg} of 0 V (**d**), 0.8 V (**e**) and 2 V (**f**). **g–i**, As **d–f** but with a fixed V_{bg} of 0 V (**g**), 0.725 V (**h**) and 2 V (**i**). Such gate-dependent behaviours are similar to those of D1.

Extended Data Fig. 6 Optically detected resistance and capacitance measurements of device D1 at 4 K.

a, Schematic of the optically detected resistance and capacitance measurements of device D1 with a partial top gate and a global back gate (grey area at top and bottom, respectively). The green layers are hBN dielectrics. A d.c. bias is applied to the top and bottom gates (V_{tg} and V_{bg} , respectively) and a small a.c. bias ($\Delta \tilde{V}$) is superimposed on the top gate voltage. When the frequency of the a.c. voltage is high (typically a few kHz in our experiment), no charge can be injected from the metal contact into MoSe₂, but there is charge redistribution between region 1 and region 2. The dynamics of such charge redistribution provide information on the quantum capacitance and resistance of the gated region, which can be probed by the reflectance change of excitons in the ungated

region 2 (here we represent the incident probe light using the red arrow). **b**, A spatial map of integrated PL intensity showing the extent of the t-MoSe₂ and b-MoSe₂ layers as yellow and white dashed lines, respectively. The green circle represents the detection spot. The solid red lines show the outline of the partial top gates. **c**, Reflection spectra from the spot indicated by the green circle in **b** at (0 V, 0 V). The red dashed line represents the continuous wave laser centred at 1.637 eV for probing resistance and capacitance. **d**, A 2D map of neutral exciton reflectance contrast at 1.637 eV as a function of V_{tg}/d_{tg} and V_{bg}/d_{bg} . Reflectance contrast is not affected by the d.c. bias applied to the local top gate, V_{tg} , as expected. **e**, **f**, 2D maps of the reflectance contrast change ΔOC which is in-phase (**e**) and out-of-phase (**f**) with the a.c. modulation voltage. We observe a reduction in the in-phase component X and an increase in the out-of-phase component Y along the 1:1 feature. The magnitude of $|\Delta OC|$ is reduced along this feature. **g**, **h**, Extracted capacitance (**g**) and resistance (**h**) of region 1 based on the effective a.c. circuit model and equation presented in Methods. The coloured dashed lines indicate the bottom-gate voltages for the line profiles in Fig. [2d](#) in the main text.

Extended Data Fig. 7 Examples of procedures for estimating $I_t(n_t)$, $I_b(n_b)$ and δ .

a, b, The integrated PL intensity from X_0 , I_0 , as a function of V_{bg} (V_{tg}) while keeping V_{tg} (V_{bg}) at a large value. Because the X_0 emission from the heavily doped layer can be omitted, these values can be used to estimate $I_t(n_t)$ and $I_b(n_b)$: that is, $I_0(n_t, n_b^+) = I_t(n_t) + I_b(n_b^+) = I_t(n_t)$, and $I_0(n_t^+, n_b) = I_t(n_t^+) + I_b(n_b) = I_b(n_b)$. Here n_t^+ and n_b^+ denote the heavily electron-doped top and bottom layer, respectively. We note the value of I_0 only begins to decrease above a finite gate voltage, which corresponds to the conduction band minimum. On the basis of this, we can estimate the carrier density using ΔV_{tg} (ΔV_{bg}), which is the applied top (bottom) gate voltage relative to the onset voltage corresponding to the conduction band edge. **c**, The value of I_0 as function of V_{bg} while keeping V_{tg} at 2.5 V (yellow curve). To calculate δ , we first subtract $I_t(2.5 \text{ V})$ from the raw I_0 data (red curve).

The relative enhancement of the red curve with respect to the $I_b(V_{bg})$ curve (blue) represents the enhancement due to bilayer Wigner crystal formation. **d**, The value of δ at $V_{tg} = 2.5$ V determined using this method. We note that near the band edge δ becomes less than zero because of the MoSe₂ layer's weak screening and the difficulties in estimating $I_t(n_t)$ or $I_b(n_b)$ when the layer is intrinsic.

Extended Data Fig. 8 2D maps of integrated X₀ PL intensity of device D1 as a function of V_{tg}/d_{tg} and V_{bg}/d_{bg} at various temperatures.

a–i, 2D maps measured at temperatures (in K) of 4, 15, 17, 23, 30, 35, 40, 45 and 50, respectively. The insulating features become weaker and broader at higher temperatures and eventually disappear.

Extended Data Fig. 9 2D maps of γ and Γ as a function of total density n and temperature T .

a, 2D map of Lindemann parameter γ . The dashed black and yellow line represents the contour of $\gamma = 0.56$, the phase boundary between the classical bilayer Wigner crystal and the electron liquid, estimated from the experimentally determined critical density at 4 K (see Supplementary Information for details). The white dashed line represents the density at which theory predicts the staggered triangular lattice structure becomes unstable, giving way to a sequence of structural transitions³⁴. **b**, 2D map of Γ , which is the ratio of the average Coulomb energy to the thermally averaged kinetic energy per electron. The black dashed line represents $\Gamma = 17$, also estimated from the experimentally determined critical density at 4 K. The black arrows along the x and y directions indicate respectively thermal melting and quantum melting of the bilayer Wigner crystal. We note that at finite temperatures Γ is not equivalent to the interaction parameter r_s , which is the ratio of the Coulomb energy to the Fermi energy at 0 K (see Supplementary Information).

Extended Data Fig. 10 Umklapp scattering from Wigner crystals measured in device D1 at 4 K.

a, The derivative of the reflectance contrast R/R_0 with respect to photon energy E , as a function of bottom-layer carrier density n_b , measured along $n_t \cdot n_b = 1$ in device D1 at 4 K. In addition to the neutral exciton X_0 , an umklapp scattering peak may be seen, whose energy shifts linearly with carrier density. **b**, To further enhance the contrast of the features, we take the derivative of the reflectance contrast R/R_0 with respect to V_{bg} ; this clearly shows the evolution of both exciton X_0 and its umklapp scattering. In the weak coupling regime, the exciton scattering will probably be dominated by the electrons from the same layer. In addition, for a bilayer Wigner crystal with the same density in each layer, the primitive unit cell is the same as that of each individual layer. On the basis of these considerations, we can estimate the exciton mass from the density dependence of the splitting between X_0 and the umklapp peak. We estimate the exciton mass to be about $1.8m_e$, which is in agreement with literature²², given the uncertainties in determining the slope of the energy shift and electron densities.

Supplementary information

Supplementary Information

This file contains the Supplementary Methods and Discussion and Supplementary Figures 1–7.

Rights and permissions

Reprints and Permissions

About this article



Cite this article

Zhou, Y., Sung, J., Brutschea, E. *et al.* Bilayer Wigner crystals in a transition metal dichalcogenide heterostructure. *Nature* **595**, 48–52 (2021). <https://doi.org/10.1038/s41586-021-03560-w>

[Download citation](#)

- Received: 04 October 2020
- Accepted: 15 April 2021
- Published: 30 June 2021
- Issue Date: 01 July 2021
- DOI: <https://doi.org/10.1038/s41586-021-03560-w>

[Access through your institution](#)

[Change institution](#)

[Buy or subscribe](#)

Advertisement

This article was downloaded by **calibre** from <https://www.nature.com/articles/s41586-021-03560-w>

- Article
- [Published: 30 June 2021](#)

Signatures of Wigner crystal of electrons in a monolayer semiconductor

- [Tomasz Smołński](#) [ORCID: orcid.org/0000-0002-4706-7777](#)¹,
- [Pavel E. Dolgirev](#)²,
- [Clemens Kuhlenkamp](#)^{1,3,4},
- [Alexander Popert](#)¹,
- [Yuya Shimazaki](#) [ORCID: orcid.org/0000-0002-5315-6813](#)¹,
- [Patrick Back](#)¹,
- [Xiaobo Lu](#) [ORCID: orcid.org/0000-0003-3149-4755](#)¹,
- [Martin Kroner](#)¹,
- [Kenji Watanabe](#) [ORCID: orcid.org/0000-0003-3701-8119](#)⁵,
- [Takashi Taniguchi](#) [ORCID: orcid.org/0000-0002-1467-3105](#)⁶,
- [Ilya Esterlis](#)²,
- [Eugene Demler](#) [2,7](#) &
- [Ataç Imamoğlu](#) [ORCID: orcid.org/0000-0002-0641-1631](#)¹

[Nature](#) volume **595**, pages 53–57 (2021) [Cite this article](#)

- 377 Accesses
- 117 Altmetric
- [Metrics details](#)

Subjects

- [Electronic properties and materials](#)
- [Quantum fluids and solids](#)

Abstract

When the Coulomb repulsion between electrons dominates over their kinetic energy, electrons in two-dimensional systems are predicted to spontaneously break continuous-translation symmetry and form a quantum crystal¹. Efforts to observe^{2,3,4,5,6,7,8,9,10,11,12} this elusive state of matter, termed a Wigner crystal, in two-dimensional extended systems have primarily focused on conductivity measurements on electrons confined to a single Landau level at high magnetic fields. Here we use optical spectroscopy to demonstrate that electrons in a monolayer semiconductor with density lower than 3×10^{11} per centimetre squared form a Wigner crystal. The combination of a high electron effective mass and reduced dielectric screening enables us to observe electronic charge order even in the absence of a moiré potential or an external magnetic field. The interactions between a resonantly injected exciton and electrons arranged in a periodic lattice modify the exciton bandstructure so that an umklapp resonance arises in the optical reflection spectrum, heralding the presence of charge order¹³. Our findings demonstrate that charge-tunable transition metal dichalcogenide monolayers¹⁴ enable the investigation of previously uncharted territory for many-body physics where interaction energy dominates over kinetic energy.

Access options

Subscribe to Journal

Get full journal access for 1 year

\$199.00

only \$3.90 per issue

[Subscribe](#)

All prices are NET prices.
VAT will be added later in the checkout.
Tax calculation will be finalised during checkout.

Rent or Buy article

Get time limited or full article access on ReadCube.

from \$8.99

[Rent or Buy](#)

All prices are NET prices.

Additional access options:

- [Log in](#)
- [Access through your institution](#)
- [Learn about institutional subscriptions](#)

Fig. 1: Optical signatures of a Wigner crystal at zero magnetic field and millikelvin temperatures.



Fig. 2: Phase transition between the Wigner crystal and electron liquid states at $B = 0$.

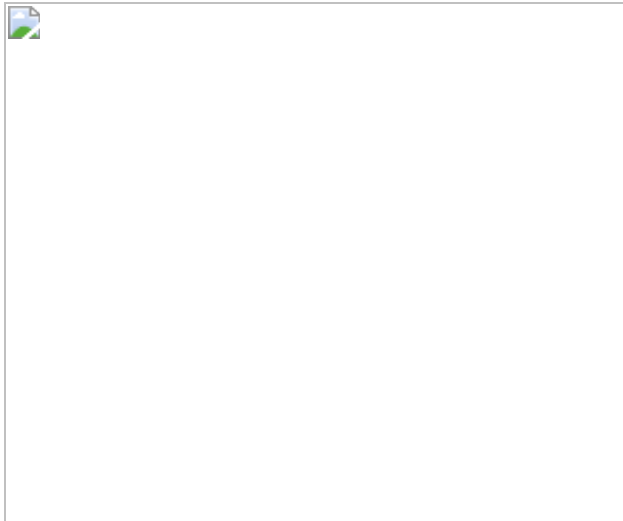


Fig. 3: Enhanced Wigner crystal signatures at $B > 0$.

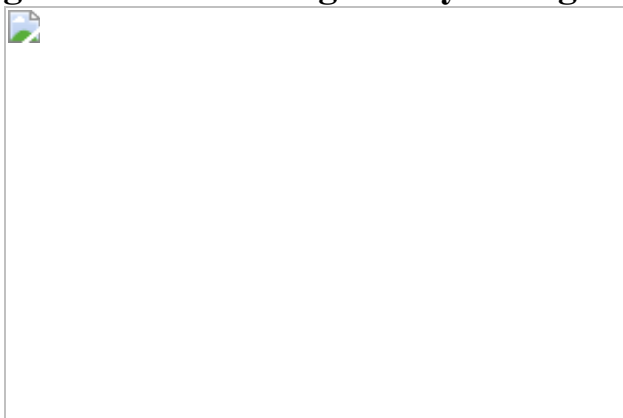
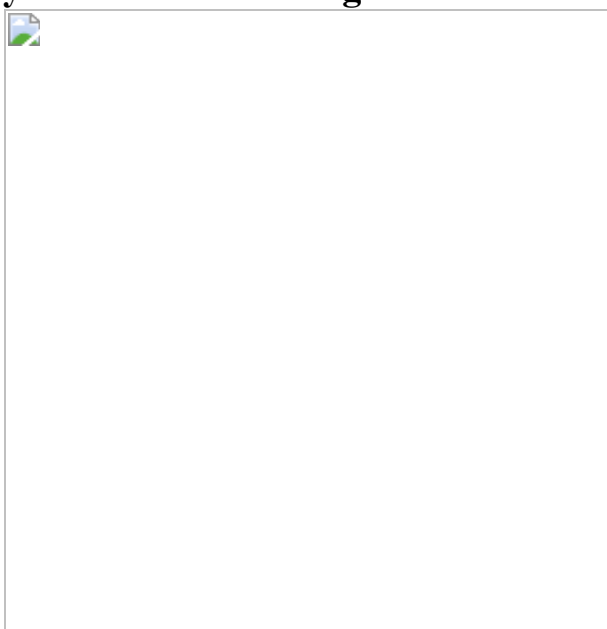


Fig. 4: Theoretical analysis of magnetoroton scattering and Wigner crystal correlation length.



Data availability

The data that support the findings of this study are available at the ETH Research Collection (<https://doi.org/10.3929/ethz-b-000478739>).

References

1. 1.

Wigner, E. On the interaction of electrons in metals. *Phys. Rev.* **46**, 1002–1011 (1934).

[ADS](#) [CAS](#) [MATH](#) [Google Scholar](#)

2. 2.

Lozovik, Y. E. & Yudson, V. I. Crystallization of a two-dimensional electron gas in a magnetic field. *J. Exp. Theor. Phys. Lett.* **22**, 11–12 (1975).

[Google Scholar](#)

3. 3.

Grimes, C. C. & Adams, G. Evidence for a liquid-to-crystal phase transition in a classical, two-dimensional sheet of electrons. *Phys. Rev. Lett.* **42**, 795–798 (1979).

[ADS](#) [CAS](#) [Google Scholar](#)

4. 4.

Andrei, E. Y. et al. Observation of a magnetically induced Wigner solid. *Phys. Rev. Lett.* **60**, 2765–2768 (1988).

[ADS](#) [CAS](#) [Google Scholar](#)

5. 5.

Goldman, V. J., Santos, M., Shayegan, M. & Cunningham, J. E. Evidence for two-dimensional quantum Wigner crystal. *Phys. Rev. Lett.* **65**, 2189–2192 (1990).

[ADS](#) [CAS](#) [Google Scholar](#)

6. 6.

Williams, F. I. B. et al. Conduction threshold and pinning frequency of magnetically induced Wigner solid. *Phys. Rev. Lett.* **66**, 3285–3288 (1991).

[ADS](#) [CAS](#) [Google Scholar](#)

7. 7.

Buhmann, H. et al. Novel magneto-optical behavior in the Wigner-solid regime. *Phys. Rev. Lett.* **66**, 926–929 (1991).

[ADS](#) [CAS](#) [Google Scholar](#)

8. 8.

Goldys, E. M. et al. Magneto-optical probe of two-dimensional electron liquid and solid phases. *Phys. Rev. B* **46**, 7957–7960 (1992).

[ADS](#) [CAS](#) [Google Scholar](#)

9. 9.

Ye, P. D. et al. Correlation lengths of the Wigner-crystal order in a two-dimensional electron system at high magnetic fields. *Phys. Rev. Lett.* **89**, 176802 (2002).

[ADS](#) [CAS](#) [Google Scholar](#)

10. 10.

Chen, Y. P. et al. Melting of a 2D quantum electron solid in high magnetic field. *Nat. Phys.* **2**, 452–455 (2006).

[CAS](#) [Google Scholar](#)

11. 11.

Tiemann, L., Rhone, T. D., Shibata, N. & Muraki, K. NMR profiling of quantum electron solids in high magnetic fields. *Nat. Phys.* **10**, 648–652 (2014).

[CAS](#) [Google Scholar](#)

12. 12.

Deng, H. et al. Commensurability oscillations of composite fermions induced by the periodic potential of a Wigner crystal. *Phys. Rev. Lett.* **117**, 096601 (2016).

[ADS](#) [CAS](#) [PubMed](#) [PubMed Central](#) [Google Scholar](#)

13. 13.

Shimazaki, Y. et al. Optical signatures of periodic charge distribution in a Mott-like correlated insulator state. *Phys. Rev. X* **11**, 021027 (2021).

[Google Scholar](#)

14. 14.

Xu, X., Yao, W., Xiao, D. & Heinz, T. F. Spin and pseudospins in layered transition metal dichalcogenides. *Nat. Phys.* **10**, 343–350 (2014).

[CAS](#) [Google Scholar](#)

15. 15.

Drummond, N. D. & Needs, R. J. Phase diagram of the low-density two-dimensional homogeneous electron gas. *Phys. Rev. Lett.* **102**, 126402 (2009).

[ADS](#) [CAS](#) [PubMed](#) [PubMed Central](#) [Google Scholar](#)

16. 16.

Yoon, J., Li, C. C., Shahar, D., Tsui, D. C. & Shayegan, M. Wigner crystallization and metal–insulator transition of two-dimensional holes in GaAs at $B = 0$. *Phys. Rev. Lett.* **82**, 1744–1747 (1999).

[ADS](#) [CAS](#) [Google Scholar](#)

17. 17.

Shapir, I. et al. Imaging the electronic Wigner crystal in one dimension. *Science* **364**, 870–875 (2019).

[ADS](#) [CAS](#) [PubMed](#) [PubMed Central](#) [Google Scholar](#)

18. 18.

Hossain, M. S. et al. Observation of spontaneous ferromagnetism in a two-dimensional electron system. *Proc. Natl Acad. Sci. USA* **117**, 32244–32250 (2020).

[ADS](#) [CAS](#) [PubMed](#) [PubMed Central](#) [Google Scholar](#)

19. 19.

Zarenia, M., Neilson, D., Partoens, B. & Peeters, F. M. Wigner crystallization in transition metal dichalcogenides: a new approach to correlation energy. *Phys. Rev. B* **95**, 115438 (2017).

[ADS](#) [Google Scholar](#)

20. 20.

Regan, E. C. et al. Mott and generalized Wigner crystal states in WSe₂/WS₂ moiré superlattices. *Nature* **579**, 359–363 (2020).

[ADS](#) [CAS](#) [PubMed](#) [PubMed Central](#) [Google Scholar](#)

21. 21.

Tang, Y. et al. Simulation of Hubbard model physics in WSe₂/WS₂ moiré superlattices. *Nature* **579**, 353–358 (2020).

[ADS](#) [CAS](#) [PubMed](#) [PubMed Central](#) [Google Scholar](#)

22. 22.

Shimazaki, Y. et al. Strongly correlated electrons and hybrid excitons in a moiré heterostructure. *Nature* **580**, 472–477 (2020).

[ADS](#) [CAS](#) [PubMed](#) [PubMed Central](#) [Google Scholar](#)

23. 23.

Wang, L. et al. Correlated electronic phases in twisted bilayer transition metal dichalcogenides. *Nat. Mater.* **19**, 861–866 (2020).

[CAS](#) [PubMed](#) [PubMed Central](#) [Google Scholar](#)

24. 24.

Xu, Y. et al. Correlated insulating states at fractional fillings of moiré superlattices. *Nature* **587**, 214–218 (2020).

[ADS](#) [CAS](#) [PubMed](#) [PubMed Central](#) [Google Scholar](#)

25. 25.

Padhi, B., Chitra, R. & Phillips, P. W. Generalized Wigner crystallization in moiré materials. *Phys. Rev. B* **103**, 125146 (2021).

[ADS](#) [CAS](#) [Google Scholar](#)

26. 26.

Smoleński, T. et al. Interaction-induced Shubnikov–de Haas oscillations in optical conductivity of monolayer MoSe₂. *Phys. Rev. Lett.* **123**, 097403 (2019).

[ADS](#) [PubMed](#) [PubMed Central](#) [Google Scholar](#)

27. 27.

Sidler, M. et al. Fermi polaron-polaritons in charge-tunable atomically thin semiconductors. *Nat. Phys.* **13**, 255–261 (2017).

[CAS](#) [Google Scholar](#)

28. 28.

Efimkin, D. K. & MacDonald, A. H. Many-body theory of trion absorption features in two-dimensional semiconductors. *Phys. Rev. B* **95**, 035417 (2017).

[ADS](#) [Google Scholar](#)

29. 29.

Zhang, Y. et al. Direct observation of the transition from indirect to direct bandgap in atomically thin epitaxial MoSe₂. *Nat. Nanotech.* **9**, 111–115 (2014).

[ADS](#) [CAS](#) [Google Scholar](#)

30. 30.

Larentis, S. et al. Large effective mass and interaction-enhanced Zeeman splitting of *K*-valley electrons in MoSe₂. *Phys. Rev. B* **97**, 201407 (2018).

[ADS](#) [CAS](#) [Google Scholar](#)

31. 31.

Li, Y. et al. Valley splitting and polarization by the Zeeman effect in monolayer MoSe₂. *Phys. Rev. Lett.* **113**, 266804 (2014).

[ADS](#) [Google Scholar](#)

32. 32.

Glazov, M. M. et al. Exciton fine structure and spin decoherence in monolayers of transition metal dichalcogenides. *Phys. Rev. B* **89**, 201302 (2014).

[ADS](#) [Google Scholar](#)

33. 33.

Spivak, B., Kravchenko, S. V., Kivelson, S. A. & Gao, X. P. A. Transport in strongly correlated two dimensional electron fluids. *Rev. Mod. Phys.* **82**, 1743–1766 (2010).

[ADS](#) [CAS](#) [Google Scholar](#)

34. 34.

Tešanović, Z., Axel, F. & Halperin, B. I. “Hall crystal” versus Wigner crystal. *Phys. Rev. B* **39**, 8525–8551 (1989).

[ADS](#) [MathSciNet](#) [Google Scholar](#)

35. 35.

Ruzin, I. M., Marianer, S. & Shklovskii, B. I. Pinning of a two-dimensional Wigner crystal by charged impurities. *Phys. Rev. B* **46**, 3999–4008 (1992).

[ADS](#) [CAS](#) [Google Scholar](#)

36. 36.

Zhu, X., Littlewood, P. B. & Millis, A. J. Sliding motion of a two-dimensional Wigner crystal in a strong magnetic field. *Phys. Rev. B* **50**, 4600–4621 (1994).

[ADS](#) [CAS](#) [Google Scholar](#)

37. 37.

Fogler, M. M. & Huse, D. A. Dynamical response of a pinned two-dimensional Wigner crystal. *Phys. Rev. B* **62**, 7553–7570 (2000).

[ADS](#) [CAS](#) [Google Scholar](#)

38. 38.

Chitra, R. & Giamarchi, T. Zero field Wigner crystal. *Eur. Phys. J. B* **44**, 455–467 (2005).

[ADS](#) [CAS](#) [Google Scholar](#)

39. 39.

Koulakov, A. A., Fogler, M. M. & Shklovskii, B. I. Charge density wave in two-dimensional electron liquid in weak magnetic field. *Phys. Rev. Lett.* **76**, 499–502 (1996).

[ADS](#) [CAS](#) [Google Scholar](#)

40. 40.

Bernu, B., Cândido, L. & Ceperley, D. M. Exchange frequencies in the 2D Wigner crystal. *Phys. Rev. Lett.* **86**, 870–873 (2001).

[ADS](#) [CAS](#) [Google Scholar](#)

41. 41.

Zomer, P. J., Guimarães, M. H. D., Brant, J. C., Tombros, N. & van Wees, B. J. Fast pick up technique for high quality heterostructures of

bilayer graphene and hexagonal boron nitride. *Appl. Phys. Lett.* **105**, 013101 (2014).

[ADS](#) [Google Scholar](#)

42. 42.

Knüppel, P. et al. Nonlinear optics in the fractional quantum Hall regime. *Nature* **572**, 91–94 (2019).

[ADS](#) [Google Scholar](#)

43. 43.

Back, P., Zeytinoglu, S., Ijaz, A., Kroner, M. & Imamoğlu, A. Realization of an electrically tunable narrow-bandwidth atomically thin mirror using monolayer MoSe₂. *Phys. Rev. Lett.* **120**, 037401 (2018).

[ADS](#) [CAS](#) [PubMed](#) [PubMed Central](#) [Google Scholar](#)

44. 44.

Lee, S.-Y., Jeong, T.-Y., Jung, S. & Yee, K.-J. Refractive index dispersion of hexagonal boron nitride in the visible and near-infrared. *Phys. Status Solidi B* **256**, 1800417 (2019).

[ADS](#) [Google Scholar](#)

45. 45.

Rah, Y., Jin, Y., Kim, S. & Yu, K. Optical analysis of the refractive index and birefringence of hexagonal boron nitride from the visible to near-infrared. *Opt. Lett.* **44**, 3797–3800 (2019).

[ADS](#) [CAS](#) [PubMed](#) [PubMed Central](#) [Google Scholar](#)

46. 46.

Srivastava, A. et al. Valley Zeeman effect in elementary optical excitations of monolayer WSe₂. *Nat. Phys.* **11**, 141–147 (2015).

[CAS](#) [Google Scholar](#)

47. 47.

Aivazian, G. et al. Magnetic control of valley pseudospin in monolayer WSe₂. *Nat. Phys.* **11**, 148–152 (2015).

[CAS](#) [Google Scholar](#)

48. 48.

Kim, K. K. et al. Synthesis and characterization of hexagonal boron nitride film as a dielectric layer for graphene devices. *ACS Nano* **6**, 8583–8590 (2012).

[CAS](#) [PubMed](#) [PubMed Central](#) [Google Scholar](#)

49. 49.

Laturia, A., Van de Put, M. L. & Vandenberghe, W. G. Dielectric properties of hexagonal boron nitride and transition metal dichalcogenides: from monolayer to bulk. *npj 2D Mater. Appl.* **2**, 6 (2018); correction **4**, 28 (2020).

[Google Scholar](#)

50. 50.

Monarkha, Y. P. & Syvokon, V. E. A two-dimensional Wigner crystal. *Low Temp. Phys.* **38**, 1067–1095 (2012).

[ADS](#) [CAS](#) [Google Scholar](#)

51. 51.

Bruun, G. M. & Nelson, D. R. Quantum hexatic order in two-dimensional dipolar and charged fluids. *Phys. Rev. B* **89**, 094112 (2014).

[ADS](#) [Google Scholar](#)

52. 52.

Yu, H., Liu, G.-B., Gong, P., Xu, X. & Yao, W. Dirac cones and Dirac saddle points of bright excitons in monolayer transition metal dichalcogenides. *Nat. Commun.* **5**, 3876 (2014).

[ADS](#) [CAS](#) [PubMed](#) [PubMed Central](#) [Google Scholar](#)

53. 53.

Qiu, D. Y., Cao, T. & Louie, S. G. Nonanalyticity, valley quantum phases, and lightlike exciton dispersion in monolayer transition metal dichalcogenides: theory and first-principles calculations. *Phys. Rev. Lett.* **115**, 176801 (2015).

[ADS](#) [PubMed](#) [PubMed Central](#) [Google Scholar](#)

54. 54.

Scuri, G. et al. Large excitonic reflectivity of monolayer MoSe₂ encapsulated in hexagonal boron nitride. *Phys. Rev. Lett.* **120**, 037402 (2018).

[ADS](#) [CAS](#) [PubMed](#) [PubMed Central](#) [Google Scholar](#)

55. 55.

Efimkin, D. K. & MacDonald, A. H. Exciton-polarons in doped semiconductors in a strong magnetic field. *Phys. Rev. B* **97**, 235432 (2018).

[ADS](#) [CAS](#) [Google Scholar](#)

56. 56.

Goryca, M. et al. Revealing exciton masses and dielectric properties of monolayer semiconductors with high magnetic fields. *Nat. Commun.* **10**, 4172 (2019).

[ADS](#) [CAS](#) [PubMed](#) [PubMed Central](#) [Google Scholar](#)

[Download references](#)

Acknowledgements

C.K. and A.I. thank M. Knap for discussions. This work was supported by the Swiss National Science Foundation (SNSF) under grant no. 200021-178909/1. K.W. and T.T. acknowledge support from the Elemental Strategy Initiative conducted by MEXT, Japan, A3 Foresight by JSPS and CREST (grant no. JPMJCR15F3) and JST. P.E.D., I.E. and E.D. were supported by Harvard-MIT CUA, AFOSR-MURI: Photonic Quantum Matter award FA95501610323, Harvard Quantum Initiative.

Author information

Affiliations

1. Institute for Quantum Electronics, ETH Zürich, Zürich, Switzerland

Tomasz Smołeński, Clemens Kuhlenkamp, Alexander Popert, Yuya Shimazaki, Patrick Back, Xiaobo Lu, Martin Kroner & Ataç Imamoğlu

2. Department of Physics, Harvard University, Cambridge, MA, USA

Pavel E. Dolgirev, Ilya Esterlis & Eugene Demler

3. Department of Physics and Institute for Advanced Study, Technical University of Munich, Garching, Germany

Clemens Kuhlenkamp

4. München Center for Quantum Science and Technology, Munich, Germany

Clemens Kuhlenkamp

5. Research Center for Functional Materials, National Institute for Materials Science, Tsukuba, Japan

Kenji Watanabe

6. International Center for Materials Nanoarchitectonics, National Institute for Materials Science, Tsukuba, Japan

Takashi Taniguchi

7. Institute for Theoretical Physics, ETH Zürich, Zürich, Switzerland

Eugene Demler

Authors

1. Tomasz Smołeński

[View author publications](#)

You can also search for this author in [PubMed](#) [Google Scholar](#)

2. Pavel E. Dolgirev

[View author publications](#)

You can also search for this author in [PubMed](#) [Google Scholar](#)

3. Clemens Kuhlenkamp

[View author publications](#)

You can also search for this author in [PubMed](#) [Google Scholar](#)

4. Alexander Popert

[View author publications](#)

You can also search for this author in [PubMed](#) [Google Scholar](#)

5. Yuya Shimazaki

[View author publications](#)

You can also search for this author in [PubMed](#) [Google Scholar](#)

6. Patrick Back

[View author publications](#)

You can also search for this author in [PubMed](#) [Google Scholar](#)

7. Xiaobo Lu

[View author publications](#)

You can also search for this author in [PubMed](#) [Google Scholar](#)

8. Martin Kroner

[View author publications](#)

You can also search for this author in [PubMed](#) [Google Scholar](#)

9. Kenji Watanabe

[View author publications](#)

You can also search for this author in [PubMed](#) [Google Scholar](#)

10. Takashi Taniguchi

[View author publications](#)

You can also search for this author in [PubMed](#) [Google Scholar](#)

11. Ilya Esterlis

[View author publications](#)

You can also search for this author in [PubMed](#) [Google Scholar](#)

12. Eugene Demler

[View author publications](#)

You can also search for this author in [PubMed](#) [Google Scholar](#)

13. Ataç Imamoğlu

[View author publications](#)

You can also search for this author in [PubMed](#) [Google Scholar](#)

Contributions

T.S. and A.I. conceived the experiments. T.S. carried out the measurements and analysed the data. M.K. and Y.S. helped with the experimental setup and the data analysis. K.W. and T.T. grew the hBN crystals. A.P., P.B. and X.L. fabricated the samples. P.E.D., C.K. and I.E. did the theoretical modelling and carried out the calculations under the guidance of E.D. T.S., P.E.D., E.D. and A.I. wrote the manuscript. T.S., E.D. and A.I. supervised the project.

Corresponding authors

Correspondence to [Tomasz Smołeński](#) or [Eugene Demler](#) or [Ataç Imamoğlu](#).

Ethics declarations

Competing interests

The authors declare no competing interests.

Additional information

Peer review information *Nature* thanks the anonymous reviewers for their contribution to the peer review of this work.

Publisher's note Springer Nature remains neutral with regard to jurisdictional claims in published maps and institutional affiliations.

Extended data figures and tables

Extended Data Fig. 1 Device structure and the experimental setup.

a, Illustration of the structure of the device investigated in the main text. **b**, Simplified schematic of the experimental setup used for magneto-optical, mK-temperature measurements. FLG, few-layer graphene; NA, numerical aperture.

Extended Data Fig. 2 Normalization and differentiation of the reflectance data.

a, Reflectance spectra acquired for the main device at $T = 80$ mK at two different spots: one in the MoSe₂ monolayer region (blue) and one off the MoSe₂ monolayer (red). Both spectra were obtained at charge neutrality ($V_t = -1$ V) and in the absence of the magnetic field. **b**, The reflectance contrast spectrum $R_c \equiv \Delta R/R_0$ determined based on the two spectra from **a**. **c, d**, Colour plots showing zero-field top-gate voltage evolutions of the derivative of reflectance contrast $\langle\{R\}_{\{\{\backslash rm{c}\}\}}^{\{\{\prime\}\}}=\{\backslash rm{d}\}\{R\}_{\{\{\backslash rm{c}\}\}}/\{\backslash rm{d}\}\{V\}_{\{\{\backslash rm{t}\}\}}\rangle$ with respect to the V_t (dashed lines mark the exciton and umklapp energies). The left panel presents a derivative evaluated numerically using standard, symmetric difference quotient method as $\langle\{R\}_{\{\{\backslash rm{c}\}\}}^{\{\{\prime\}\}}(\{V\}_{\{\{\backslash rm{t}\}\},n})=[\{R\}_{\{\{\backslash rm{c}\}\}}(\{V\}_{\{\{\backslash rm{t}\}\},n+1})-\{R\}_{\{\{\backslash rm{c}\}\}}(\{V\}_{\{\{\backslash rm{t}\}\},n-1})]/[\{V\}_{\{\{\backslash rm{t}\}\},n+1}-\{V\}_{\{\{\backslash rm{t}\}\},n-1}]\rangle$. The right panel shows a derivative of the same data obtained using the other method, in which dR_c/dV_t is computed as a difference quotient between symmetric data points separated not by two, but by four gate-voltage steps, that is, $\langle\{R\}_{\{\{\backslash rm{c}\}\}}^{\{\{\prime\}\}}(\{V\}_{\{\{\backslash rm{t}\}\},n})=[\{R\}_{\{\{\backslash rm{c}\}\}}(\{V\}_{\{\{\backslash rm{t}\}\},n+2})-\{R\}_{\{\{\backslash rm{c}\}\}}(\{V\}_{\{\{\backslash rm{t}\}\},n-2})]/[\{V\}_{\{\{\backslash rm{t}\}\},n+2}-\{V\}_{\{\{\backslash rm{t}\}\},n-2}]\rangle$. This method was used to plot the gate-voltage derivatives in Figs. 1–3.

Extended Data Fig. 3 Fitting the exciton and umklapp peaks with dispersive Lorentzian spectral profiles.

a, Colour map showing top-gate voltage evolution of the reflectance contrast R_c spectra measured at $T = 80$ mK for the main device, at zero magnetic field, for low electron doping densities, and in the spectral vicinity of the exciton peak. **b**, Similar map presenting evolution of the reflectance contrast R_c upon subtraction of the fitted exciton spectral profile R_X as well as a smooth Gaussian-like background B (independent of the voltage). The dashed lines in both panels indicate the energies of the exciton and umklapp peaks. **c**, **d**, Cross-sections through the maps in **a**, **b** at $V_t = 0.8$ V showing, respectively, bare and background-corrected reflectance contrast spectra. The solid lines indicate the fits to the experimental data with dispersive Lorentzian spectral profiles, based on which we determined the exciton and umklapp energies (marked by vertical dashed lines). In the case of the umklapp peak, the fitting was carried out only in the energy region covered by the data points shown in green, in order to avoid spurious contribution around the energy of the main exciton (of about 1,635.5 meV at the selected $V_t = 0.8$ V) that originates from the residual of the exciton resonance fitting.

Extended Data Fig. 4 Calibration of the electron density for the dilution refrigerator experiments based on the Shubnikov–de Haas oscillations in the exciton linewidth.

a, Colour map presenting σ^- -polarized reflectance contrast spectra measured at $T = 80$ mK for the main device as a function of the top-gate voltage at $B = 16$ T. **b**, Gate-voltage dependence of the exciton linewidth extracted from the data in **a** by fitting the exciton resonance with a dispersive Lorentzian spectral profile. Dashed lines in both panels indicate the positions of integer filling factors. **c**, Gate voltages $V_t(v, B)$ corresponding to the positions of the exciton linewidth minima extracted from the reflectance measurements carried out at different magnetic fields. All of the presented data points were obtained in the regime where the Fermi level does not exceed the valley Zeeman splitting in the conduction band. Solid lines represent the fit of the data points with a set of linear

dependencies corresponding to subsequent integer filling factors, which form a Landau level fan chart.

Extended Data Fig. 5 Comparison of the zero-field Wigner crystal signatures at $T = 80$ mK and $T = 4$ K.

a, b, Colour maps showing zero-field top-gate voltage evolution of the derivative of reflectance contrast spectra with respect to V_t measured in the dilution refrigerator for the main device at two different temperatures: $T = 80$ mK (**a**) and $T = 4$ K (**b**). Black dashed lines mark the fitted energy E_X of the exciton resonance, and the green lines indicate the expected position of the umklapp peak $E_X + \Delta E_U$ for $\Delta E_U = \frac{h^2 n}{m \sqrt{3}}$ corresponding to a triangular Wigner crystal and $m_X = 1.1 m_e$.

Extended Data Fig. 6 Melting of the Wigner crystal at elevated temperatures.

a, Colour maps displaying back-gate voltage evolution of the derivative of reflectance contrast spectra with respect to V_b measured in the VTI-based setup at zero magnetic field and different temperatures of the main device (as indicated). In each map, the black dashed lines mark the fitted energy E_X of the main exciton peak, while the green line in the map at $T = 4.5$ K represents the expected position of the umklapp resonance $E_X + \frac{h^2 n}{m \sqrt{3}}$ corresponding to a triangular Wigner crystal and $m_X = 1.3 m_e$. **b-d**, Cross-sections through the maps in **a** (as well as through a similar map measured at $T = 15.2$ K) at $V_b = -0.6$ V (**b**), $V_b = -0.45$ V (**c**), and $V_b = -0.35$ V (**d**) corresponding to electron densities $n_e/10^{11} \text{ cm}^{-2}$ of, respectively, 1.2, 1.6 and 1.9. **e**, Relative amplitude of the umklapp transition determined as a function of the temperature as the average value of $d(\Delta R/R_0)/dV_b$ in a 0.8-meV-wide energy window around the umklapp energy (marked by shaded regions in **b-d**) at different electron densities (as indicated). The error bar for each data point is estimated as a standard error (that is, standard deviation of the mean) of all points within the aforementioned energy

window for a given n_e and T . The solid lines represent the fits of the temperature dependence for each n_e with a linear decrease $a(T_m - T) + b$ at $T < T_m$ and a flat background level b at $T > T_m$, with a melting temperatures $T_m = 11 \pm 1$ K of the Wigner crystal being found to be the same for all investigated values of n_e within the experimental uncertainty. **f**, The same cross-sections as in **c** (determined at $V_b = -0.45$ V) together with the solid lines representing the fits of the umklapp lineshapes at different temperatures with a phenomenological Lorentzian profile overlaid on a (fixed) polynomial background. **g**, Temperature-dependent relative amplitude of the umklapp peak at $n_e \approx 1.6 \times 10^{11}$ cm⁻² extracted based on the Lorentzian fits from **f** (as well as based on similar fits of the data taken at different temperatures; the error bars correspond to standard errors increased by a temperature-independent term that is introduced to account for systematic uncertainty stemming from determination of the background profile). Solid line indicates a linear fit to the data points with non-zero amplitude corresponding to the same Wigner crystal melting temperature of $T_m = 11 \pm 1$ K.

Extended Data Fig. 7 Analysis of disorder-induced broadening of the umklapp peak.

a, b, Colour maps showing top-gate voltage evolution of the differentiated reflectance contrast $d(\Delta R/R_0)/dE$ (**a**) and the bare reflectance contrast $\Delta R/R_0$ (**b**) acquired for the main device at $B = 14$ T, $T = 80$ mK, and in σ^- polarization of detection (note that these results were obtained in a different measurement than that shown in Fig. 3e,f). Grey horizontal dashed lines mark the voltages corresponding to filling factors of $v = 0, 0.34$, and 1 . White (black) dashed (dotted) line indicates the fitted energy $E_X(\sigma^-)$ ($E_X(\sigma^+)$) of the σ^- -polarized (σ^+ -polarized) main exciton resonance. The green dashed line represents the expected energy of the umklapp peak determined as $\sqrt{E_X^2 + \Delta^2}$, where $\Delta = \sqrt{h^2 + 2m_eV_b^2} - \sqrt{s_k^2 + \sqrt{3m_eV_b^2 + s_k^2}}$. The expression for E_X is $E_X = \sqrt{h^2 + 2m_eV_b^2}$.

detuning calculated within the frame the model from Supplementary Information section 3 using the exciton mass of $m_X = 1.3m_e$, the strength of the electron–hole exchange $s|K| = 300$ meV (with $|K|$ representing the valley momentum), and experimentally determined main exciton Zeeman splitting $\Delta_Z = 3.6$ meV. **c, d**, Cross-sections through the maps in **a, b** at $V_t = 0.45$ V corresponding to the electron density $n_e \approx 1.16 \times 10^{11}$ cm $^{-2}$ and Landau level filling factor $\nu \approx 0.34$. The solid line in **c** shows the fit of the experimental data with a sum of two differentiated dispersive Lorentzian spectral profiles $\langle\{R\}_{\{\{\rm{X}\}\}}^{\{\prime\}}(E) + \langle\{R\}_{\{\{\rm{U}\}\}}^{\{\prime\}}(E)\rangle$ representing the main and umklapp resonances. The solid line in **d** in turn depicts the fit of the main exciton resonance in the bare reflectance spectrum with a transfer-matrix model, allowing us to extract the nonradiative broadening of the exciton $\langle\{\gamma_{\{\rm{X}\}}\}^{\{\rm{nrad}\}}\rangle = 0.78\langle\{\rm{meV}\}\rangle$. **e**, The fits of the differentiated reflectance spectrum at $\nu \approx 0.34$ with the sum of two differentiated dispersive Lorentzians $\langle\{R\}_{\{\{\rm{X}\}\}}^{\{\prime\}}(E) + \langle\{R\}_{\{\{\rm{U}\}\}}^{\{\prime\}}(E)\rangle$ corresponding to different correlation lengths of the Wigner crystal (as indicated). For each fit the parameters of the main exciton resonance (that is, amplitude A_X , linewidth γ_X , energy E_X and phase φ_X) as well as the phase φ_0 and the energy E_U of the umklapp peak are fixed at the values obtained from the fit in **c**. The linewidth and amplitude of the umklapp resonance are assumed to be given by $\langle\{\gamma_{\{\rm{U}\}}\}\rangle = \langle\{\gamma_{\{\rm{X}\}}\}^{\{\rm{nrad}\}}\rangle + \langle\{\gamma_{\{\rm{U}\}}\}^{\{\rm{dis}\}}\rangle$ and $A_U = \alpha_U A_X$, where the disorder-induced broadening $\langle\{\gamma_{\{\rm{U}\}}\}^{\{\rm{dis}\}}\rangle$ and the relative amplitude α_U are fitted based on the predictions of the theoretical model from Supplementary Information section 6 describing the umklapp lineshape for a Wigner crystal with a given correlation length. For all fits α_U is assumed to be smaller than 5%. **f**, The coefficient of determination R^2 evaluated for the fits corresponding to different Wigner crystal correlation lengths based on the data points in a 2-meV-wide energy window around the umklapp resonance (marked by shaded region). The dashed line indicates the value of R^2 obtained in the same way for an unconstrained fit in **c**.

Extended Data Fig. 8 Observation of zero-magnetic-field Wigner crystal signatures for the second device.

a, Colour map showing reflectance contrast spectra measured as a function of the top-gate voltage V_t for the second device. The data were acquired at $T = 4$ K and in the absence of the magnetic field. **b**, Gate-voltage evolution of the derivative of the spectra from **a** with respect to V_t . Black dashed lines in both panels indicate the energy of the exciton peak E_X obtained by fitting its spectral profile with dispersive Lorentzian lineshape. Green lines mark the expected position $E_X + \Delta E_U$ of the umklapp peak, where $\Delta E_U = \frac{h^2 n}{m_e} \sqrt{3}$ is computed under an assumption of a triangular Wigner crystal and for the value of exciton mass $m_X = 1.3 m_e$.

Supplementary information

Supplementary Information

This file contains Supplementary Information Sections 1-6, including Supplementary Figures 1-12 and additional references.

Rights and permissions

Reprints and Permissions

About this article



Cite this article

Smoleński, T., Dolgirev, P.E., Kuhlenkamp, C. *et al.* Signatures of Wigner crystal of electrons in a monolayer semiconductor. *Nature* **595**, 53–57 (2021). <https://doi.org/10.1038/s41586-021-03590-4>

[Download citation](#)

- Received: 06 October 2020
- Accepted: 28 April 2021
- Published: 30 June 2021
- Issue Date: 01 July 2021
- DOI: <https://doi.org/10.1038/s41586-021-03590-4>

[Access through your institution](#)

[Change institution](#)

[Buy or subscribe](#)

Advertisement

This article was downloaded by **calibre** from <https://www.nature.com/articles/s41586-021-03590-4>

- Article
- [Published: 30 June 2021](#)

Cellular fluidics

- [Nikola A. Dudukovic](#) [ORCID: orcid.org/0000-0002-0852-7080¹](#),
- [Erika J. Fong](#) [ORCID: orcid.org/0000-0003-1890-473X¹](#),
- [Hawi B. Gemedo](#) [ORCID: orcid.org/0000-0001-6801-7317¹](#),
- [Joshua R. DeOtte](#) [ORCID: orcid.org/0000-0002-4388-7129¹](#),
- [Maira R. Cerón](#) [ORCID: orcid.org/0000-0002-5151-0479¹](#),
- [Bryan D. Moran¹](#),
- [Jonathan T. Davis](#) [ORCID: orcid.org/0000-0001-8573-9354¹](#),
- [Sarah E. Baker¹](#) &
- [Eric B. Duoss](#) [ORCID: orcid.org/0000-0002-5473-2528¹](#)

[Nature](#) volume **595**, pages 58–65 (2021) [Cite this article](#)

- 582 Accesses
- 50 Altmetric
- [Metrics details](#)

Subjects

- [Chemical engineering](#)
- [Climate sciences](#)
- [Design, synthesis and processing](#)
- [Fluid dynamics](#)
- [Structural materials](#)

Abstract

The natural world provides many examples of multiphase transport and reaction processes that have been optimized by evolution. These phenomena take place at multiple length and time scales and typically include gas–liquid–solid interfaces and capillary phenomena in porous media^{1,2}. Many biological and living systems have evolved to optimize fluidic transport. However, living things are exceptionally complex and very difficult to replicate^{3,4,5}, and human-made microfluidic devices (which are typically planar and enclosed) are highly limited for multiphase process engineering^{6,7,8}. Here we introduce the concept of cellular fluidics: a platform of unit-cell-based, three-dimensional structures—enabled by emerging 3D printing methods^{9,10}—for the deterministic control of multiphase flow, transport and reaction processes. We show that flow in these structures can be ‘programmed’ through architected design of cell type, size and relative density. We demonstrate gas–liquid transport processes such as transpiration and absorption, using evaporative cooling and CO₂ capture as examples. We design and demonstrate preferential liquid and gas transport pathways in three-dimensional cellular fluidic devices with capillary-driven and actively pumped liquid flow, and present examples of selective metallization of pre-programmed patterns. Our results show that the design and fabrication of architected cellular materials, coupled with analytical and numerical predictions of steady-state and dynamic behaviour of multiphase interfaces, provide deterministic control of fluidic transport in three dimensions. Cellular fluidics may transform the design space for spatial and temporal control of multiphase transport and reaction processes.

Access options

Subscribe to Journal

Get full journal access for 1 year

\$199.00

only \$3.90 per issue

[Subscribe](#)

All prices are NET prices.
VAT will be added later in the checkout.
Tax calculation will be finalised during checkout.

Rent or Buy article

Get time limited or full article access on ReadCube.

from \$8.99

[Rent or Buy](#)

All prices are NET prices.

Additional access options:

- [Log in](#)
- [Access through your institution](#)
- [Learn about institutional subscriptions](#)

Fig. 1: Cellular fluidics: a nature-inspired, unit-cell-based platform.

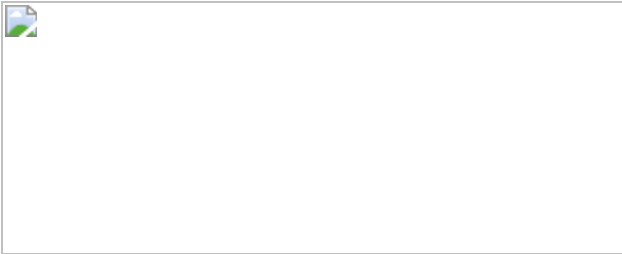


Fig. 2: Architected design for predictable capillary rise.

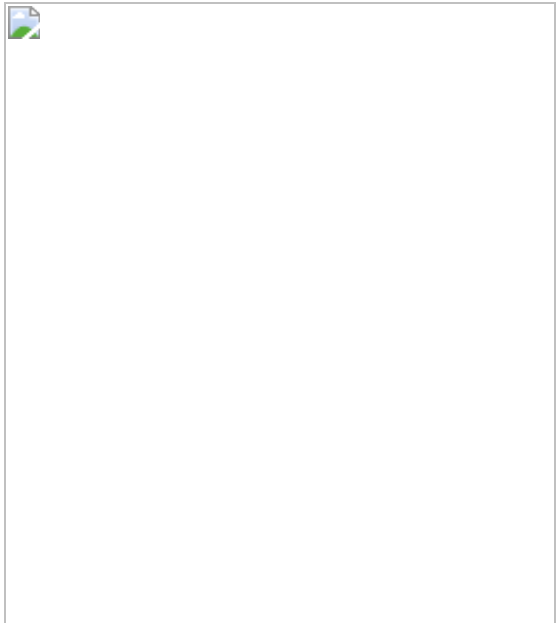


Fig. 3: Numerical simulations and high-speed videography reveal dynamics.

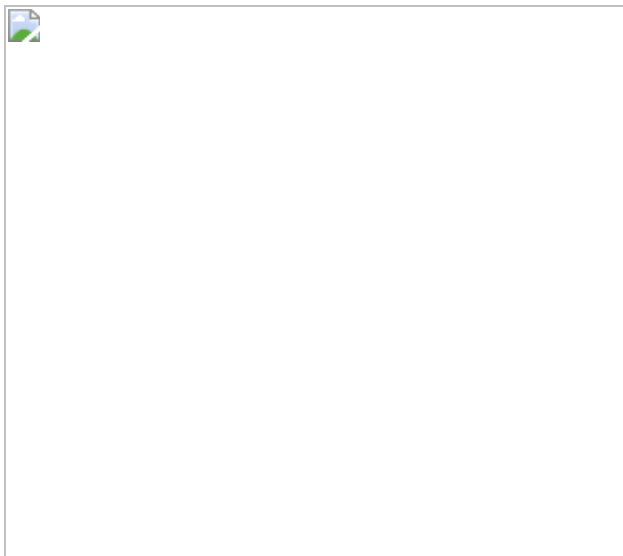


Fig. 4: Transpiration in cellular fluidics.

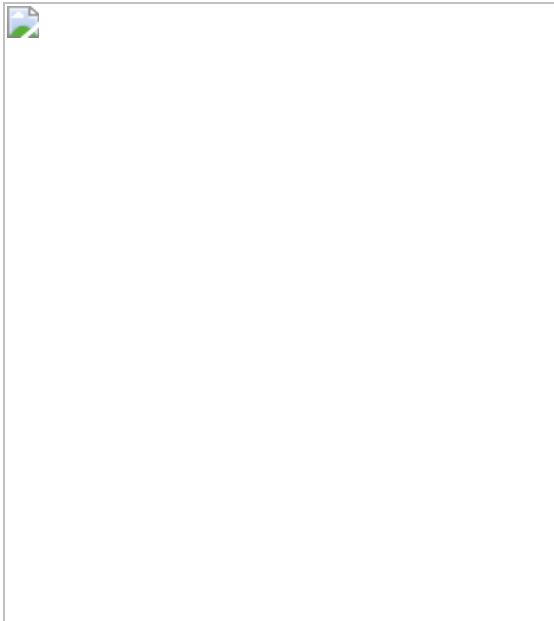


Fig. 5: Gas absorption in cellular fluidics.

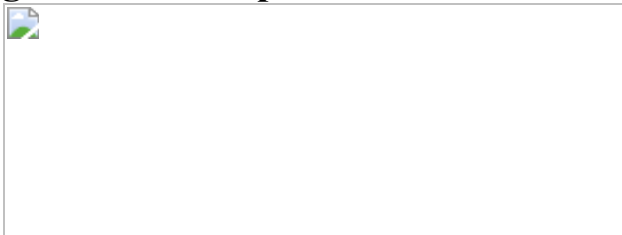
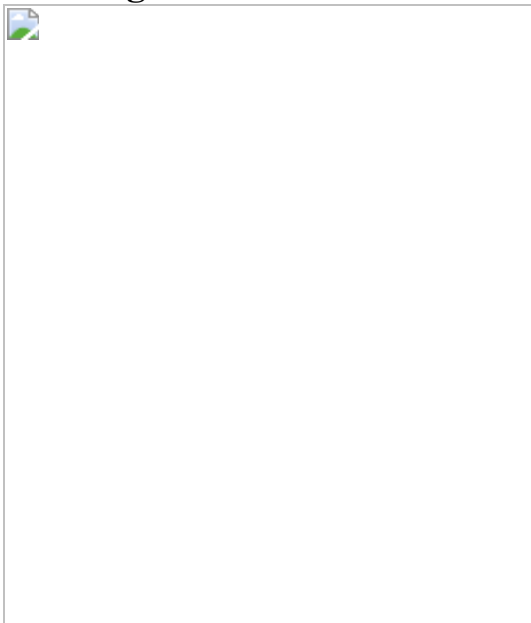


Fig. 6: Preferential fluid pathways for continuous flow and selective patterning.



Data availability

Source data for calculated porosities and interfacial areas of different unit cells are included with the paper. Reasonable requests for additional data that support the findings of this study will be honoured upon securing release approval from the Lawrence Livermore National Laboratory and the US Department of Energy. [Source data](#) are provided with this paper.

Code availability

Reasonable requests for the code that support the findings of this study will be honoured upon securing release approval from the Lawrence Livermore National Laboratory and the US Department of Energy.

References

1. 1.

Kirkham, M. B. in *Principles of Soil and Plant Water Relations* 2nd edn (ed. Kirkham, M. B.) Ch. 15, 243–266 (Academic, 2014).

2. 2.

Grigoryan, B. et al. Multivascular networks and functional intravascular topologies within biocompatible hydrogels. *Science* **364**, 458–464 (2019).

[ADS](#) [CAS](#) [PubMed](#) [PubMed Central](#) [Google Scholar](#)

3. 3.

Yaraghi, N. A. & Kisailus, D. Biomimetic structural materials: inspiration from design and assembly. *Annu. Rev. Phys. Chem.* **69**, 23–57 (2018).

[ADS](#) [CAS](#) [PubMed](#) [Google Scholar](#)

4. 4.

Huang, W. et al. Multiscale toughening mechanisms in biological materials and bioinspired designs. *Adv. Mater.* **31**, 1901561 (2019).

[CAS](#) [Google Scholar](#)

5. 5.

Torres, A. M. et al. Bone-inspired microarchitectures achieve enhanced fatigue life. *Proc. Natl Acad. Sci. USA* **116**, 24457–24462 (2019).

[ADS](#) [CAS](#) [PubMed](#) [PubMed Central](#) [Google Scholar](#)

6. 6.

Whitesides, G. M. The origins and the future of microfluidics. *Nature* **442**, 368–373 (2006).

[ADS](#) [CAS](#) [Google Scholar](#)

7. 7.

Shui, L., Pennathur, S., Eijkel, J. C. & van den Berg, A. Multiphase flow in lab on chip devices: a real tool for the future? *Lab Chip* **8**, 1010–1014 (2008).

[CAS](#) [PubMed](#) [Google Scholar](#)

8. 8.

Pennathur, S. Flow control in microfluidics: are the workhorse flows adequate? *Lab Chip* **8**, 383–387 (2008).

[CAS](#) [PubMed](#) [Google Scholar](#)

9. 9.

Zheng, X. et al. Ultralight, ultrastiff mechanical metamaterials. *Science* **344**, 1373–1377 (2014).

[ADS](#) [CAS](#) [PubMed](#) [Google Scholar](#)

10. 10.

Zheng, X. et al. Multiscale metallic metamaterials. *Nat. Mater.* **15**, 1100–1106 (2016).

[ADS](#) [CAS](#) [PubMed](#) [Google Scholar](#)

11. 11.

Piorek, B. D. et al. Free-surface microfluidic control of surface-enhanced Raman spectroscopy for the optimized detection of airborne molecules. *Proc. Natl Acad. Sci. USA* **104**, 18898–18901 (2007).

[ADS](#) [CAS](#) [PubMed](#) [PubMed Central](#) [Google Scholar](#)

12. 12.

Delamarche, E. & Kaigala, G. V. (eds) *Open-Space Microfluidics: Concepts, Implementations, Applications* (John Wiley & Sons, 2018).

13. 13.

Olanrewaju, A., Beaugrand, M., Yafia, M. & Juncker, D. Capillary microfluidics in microchannels: from microfluidic networks to capillaric circuits. *Lab Chip* **18**, 2323–2347 (2018).

[CAS](#) [PubMed](#) [Google Scholar](#)

14. 14.

Martinez, A. W., Phillips, S. T. & Whitesides, G. M. Three-dimensional microfluidic devices fabricated in layered paper and tape. *Proc. Natl Acad. Sci. USA* **105**, 19606–19611 (2008).

[ADS](#) [CAS](#) [PubMed](#) [PubMed Central](#) [Google Scholar](#)

15. 15.

Martinez, A. W., Phillips, S. T., Whitesides, G. M. & Carrilho, E. Diagnostics for the developing world: microfluidic paper-based analytical devices. *Anal. Chem.* **82**, 3–10 (2010).

[CAS](#) [PubMed](#) [Google Scholar](#)

16. 16.

Kotz, F. et al. Fabrication of arbitrary three-dimensional suspended hollow microstructures in transparent fused silica glass. *Nat. Commun.* **10**, 1439 (2019).

[ADS](#) [PubMed](#) [PubMed Central](#) [Google Scholar](#)

17. 17.

Schaedler, T. A. et al. Ultralight metallic microlattices. *Science* **334**, 962–965 (2011).

[ADS](#) [CAS](#) [PubMed](#) [Google Scholar](#)

18. 18.

Cui, H., Hensleigh, R., Chen, H. & Zheng, X. Additive manufacturing and size-dependent mechanical properties of three-dimensional microarchitected, high-temperature ceramic metamaterials. *J. Mater. Res.* **33**, 360–371 (2018).

[ADS](#) [CAS](#) [Google Scholar](#)

19. 19.

Jackson, J. A. et al. Field responsive mechanical metamaterials. *Sci. Adv.* **4**, eaau6419 (2018).

[ADS](#) [CAS](#) [PubMed](#) [PubMed Central](#) [Google Scholar](#)

20. 20.

Wang, Q. et al. Lightweight mechanical metamaterials with tunable negative thermal expansion. *Phys. Rev. Lett.* **117**, 175901 (2016).

[ADS](#) [PubMed](#) [Google Scholar](#)

21. 21.

Farzinazar, S., Schaedler, T., Valdevit, L. & Lee, J. Thermal transport in hollow metallic microlattices. *APL Mater.* **7**, 101108 (2019).

[ADS](#) [Google Scholar](#)

22. 22.

Xu, H. & Pasini, D. Structurally efficient three-dimensional metamaterials with controllable thermal expansion. *Sci. Rep.* **6**, 34924 (2016).

[ADS](#) [CAS](#) [PubMed](#) [PubMed Central](#) [Google Scholar](#)

23. 23.

Dudukovic, N. A. et al. Predicting nanoparticle suspension viscoelasticity for multimaterial 3D printing of silica–titania glass. *ACS Appl. Nano Mater.* **1**, 4038–4044 (2018).

[CAS](#) [Google Scholar](#)

24. 24.

Dylla-Spears, R. et al. 3D printed gradient index glass optics. *Sci. Adv.* **6**, eabc7429 (2020).

[ADS](#) [CAS](#) [PubMed](#) [PubMed Central](#) [Google Scholar](#)

25. 25.

Zhu, C. et al. Highly compressible 3D periodic graphene aerogel microlattices. *Nat. Commun.* **6**, 6962 (2015).

[ADS](#) [CAS](#) [PubMed](#) [Google Scholar](#)

26. 26.

Golobic, A. M. et al. Active mixing of reactive materials for 3D printing. *Adv. Eng. Mater.* **21**, 1900147 (2019).

[Google Scholar](#)

27. 27.

Xia, X. et al. Electrochemically reconfigurable architected materials. *Nature* **573**, 205–213 (2019).

[ADS](#) [CAS](#) [PubMed](#) [Google Scholar](#)

28. 28.

Hensleigh, R. et al. Charge-programmed three-dimensional printing for multi-material electronic devices. *Nat. Electron.* **3**, 216–224 (2020).

[CAS](#) [Google Scholar](#)

29. 29.

Zhu, C. et al. Toward digitally controlled catalyst architectures: hierarchical nanoporous gold via 3D printing. *Sci. Adv.* **4**, eaas9459 (2018).

[ADS](#) [CAS](#) [PubMed](#) [PubMed Central](#) [Google Scholar](#)

30. 30.

Fink, K. D., Kolodziejska, J. A., Jacobsen, A. J. & Roper, C. S. Fluid dynamics of flow through microscale lattice structures formed from self-propagating photopolymer waveguides. *AICHE J.* **57**, 2636–2646 (2011).

[CAS](#) [Google Scholar](#)

31. 31.

Li, C. et al. Bioinspired inner microstructured tube controlled capillary rise. *Proc. Natl Acad. Sci. USA* **116**, 12704–12709 (2019).

[ADS](#) [CAS](#) [PubMed](#) [PubMed Central](#) [Google Scholar](#)

32. 32.

Ragelle, H. et al. Surface tension-assisted additive manufacturing. *Nat. Commun.* **9**, 1184 (2018).

[ADS](#) [PubMed](#) [PubMed Central](#) [Google Scholar](#)

33. 33.

Esarte, J., Blanco, J. M., Bernardini, A. & Sancibrián, R. Performance assessment of a three-dimensional printed porous media produced by selective laser melting technology for the optimization of loop heat pipe wicks. *Appl. Sci.* **9**, 2905 (2019).

[CAS](#) [Google Scholar](#)

34. 34.

Rapp, B. E. *Microfluidics: Modeling, Mechanics and Mathematics* (Elsevier, 2016).

35. 35.

Watts, S., Arrighi, W., Kudo, J., Tortorelli, D. A. & White, D. A. Simple, accurate surrogate models of the elastic response of three-

dimensional open truss micro-architectures with applications to multiscale topology design. *Struct. Multidiscipl. Optim.* **60**, 1887–1920 (2019).

[MathSciNet](#) [Google Scholar](#)

36. 36.

Nguyen, P. Q., Dorval Courchesne, N.-M., Duraj-Thatte, A., Praveschotinunt, P. & Joshi, N. S. Engineered living materials: prospects and challenges for using biological systems to direct the assembly of smart materials. *Adv. Mater.* **30**, 1704847 (2018).

[Google Scholar](#)

37. 37.

Huang, G., Zhu, Y., Liao, Z., Xu, R. & Jiang, P.-X. Biomimetic self-pumping transpiration cooling for additive manufactured porous module with tree-like micro-channel. *Int. J. Heat Mass Transf.* **131**, 403–410 (2019).

[Google Scholar](#)

38. 38.

Hanks, D. F. et al. High heat flux evaporation of low surface tension liquids from nanoporous membranes. *ACS Appl. Mater. Interfaces* **12**, 7232–7238 (2020).

[CAS](#) [PubMed](#) [Google Scholar](#)

39. 39.

Vericella, J. J. et al. Encapsulated liquid sorbents for carbon dioxide capture. *Nat. Commun.* **6**, 6124 (2015).

[ADS](#) [CAS](#) [PubMed](#) [Google Scholar](#)

40. 40.

Tsunazawa, Y., Yokoyama, T. & Nishiyama, N. An experimental study on the rate and mechanism of capillary rise in sandstone. *Prog. Earth Planet. Sci.* **3**, 8 (2016).

[ADS](#) [Google Scholar](#)

41. 41.

So, J.-H. et al. Reversibly deformable and mechanically tunable fluidic antennas. *Adv. Funct. Mater.* **19**, 3632–3637 (2009).

[CAS](#) [Google Scholar](#)

42. 42.

Vafaei, S., Tuck, C., Wildman, R. & Ashcroft, I. Spreading of the nanofluid triple line in ink jet printed electronics tracks. *Addit. Manuf.* **11**, 77–84 (2016).

[CAS](#) [Google Scholar](#)

43. 43.

Tumbleston, J. R. et al. Continuous liquid interface production of 3D objects. *Science* **347**, 1349–1352 (2015).

[ADS](#) [CAS](#) [PubMed](#) [Google Scholar](#)

44. 44.

Saha, S. K. et al. Scalable submicrometer additive manufacturing. *Science* **366**, 105–109 (2019).

[ADS](#) [CAS](#) [PubMed](#) [Google Scholar](#)

45. 45.

Kelly, B. E. et al. Volumetric additive manufacturing via tomographic reconstruction. *Science* **363**, 1075–1079 (2019).

[ADS](#) [CAS](#) [PubMed](#) [Google Scholar](#)

46. 46.

Walker, D. A., Hedrick, J. L. & Mirkin, C. A. Rapid, large-volume, thermally controlled 3D printing using a mobile liquid interface. *Science* **366**, 360–364 (2019).

[ADS](#) [CAS](#) [PubMed](#) [PubMed Central](#) [Google Scholar](#)

47. 47.

Suss, M. E. et al. Capacitive desalination with flow-through electrodes. *Energy Environ. Sci.* **5**, 9511–9519 (2012).

[CAS](#) [Google Scholar](#)

48. 48.

Wu, L. et al. Highly efficient three-dimensional solar evaporator for high salinity desalination by localized crystallization. *Nat. Commun.* **11**, 521 (2020).

[ADS](#) [PubMed](#) [PubMed Central](#) [Google Scholar](#)

49. 49.

Dinh, C.-T. et al. CO₂ electroreduction to ethylene via hydroxide-mediated copper catalysis at an abrupt interface. *Science* **360**, 783–787 (2018).

[CAS](#) [PubMed](#) [PubMed Central](#) [Google Scholar](#)

50. 50.

Weislogel, M. M. et al. The capillary flow experiments aboard the International Space Station: Status. *Acta Astronaut.* **65**, 861–869 (2009).

[ADS](#) [Google Scholar](#)

51. 51.

Stewart, A. Woman tree roots digital design. *Thingiverse* <https://www.thingiverse.com/thing:2513453> (2017).

52. 52.

Kinstlinger, I. S. & Miller, J. S. 3D-printed fluidic networks as vasculature for engineered tissue. *Lab Chip* **16**, 2025–2043 (2016).

[CAS](#) [PubMed](#) [Google Scholar](#)

53. 53.

Rosàs-Canyelles, E., Modzelewski, A. J., Geldert, A., He, L. & Herr, A. E. Assessing heterogeneity among single embryos and single blastomeres using open microfluidic design. *Sci. Adv.* **6**, eaay1751 (2020).

[ADS](#) [PubMed](#) [PubMed Central](#) [Google Scholar](#)

54. 54.

Nguyen, D. T. et al. 3D-printed transparent glass. *Adv. Mater.* **29**, 1701181 (2017).

[Google Scholar](#)

55. 55.

Kotz, F. et al. Three-dimensional printing of transparent fused silica glass. *Nature* **544**, 337–339 (2017).

[ADS](#) [CAS](#) [PubMed](#) [Google Scholar](#)

56. 56.

Helmer, D. & Rapp, B. E. Divide and print. *Nat. Mater.* **19**, 131–133 (2020).

[ADS](#) [CAS](#) [PubMed](#) [Google Scholar](#)

57. 57.

Gao, L. & McCarthy, T. J. Contact angle hysteresis explained. *Langmuir* **22**, 6234–6237 (2006).

[CAS](#) [PubMed](#) [Google Scholar](#)

58. 58.

Rodríguez-Valverde, M. Á. & Miranda, M. T. Derivation of Jurin’s law revisited. *Eur. J. Phys.* **32**, 49–54 (2011).

[MATH](#) [Google Scholar](#)

59. 59.

Messner, M. C. Optimal lattice-structured materials. *J. Mech. Phys. Solids* **96**, 162–183 (2016).

[ADS](#) [MathSciNet](#) [Google Scholar](#)

60. 60.

NASA Johnson. Capillary flow experiments on Space Station.
<https://www.youtube.com/watch?v=3lwY8xxJxKo> (2014).

61. 61.

de Gennes, P. G. Wetting: statics and dynamics. *Rev. Mod. Phys.* **57**, 827–863 (1985).

[ADS](#) [MathSciNet](#) [Google Scholar](#)

62. 62.

Leger, L. & Joanny, J. F. Liquid spreading. *Rep. Prog. Phys.* **55**, 431–486 (1992).

[ADS](#) [CAS](#) [Google Scholar](#)

63. 63.

Hubbe, M. A., Gardner, D. J. & Shen, W. Contact angles and wettability of cellulosic surfaces: a review of proposed mechanisms and test strategies. *BioResources* **10**, 8657–8749 (2015).

[CAS](#) [Google Scholar](#)

64. 64.

Shusteff, M. et al. One-step volumetric additive manufacturing of complex polymer structures. *Sci. Adv.* **3**, eaao5496 (2017).

[PubMed](#) [PubMed Central](#) [Google Scholar](#)

[Download references](#)

Acknowledgements

We are grateful to the late J. J. Vericella for his contributions to the CO₂ capture technologies that enabled this work. We thank R. Goldsberry and J. Long for support with figure illustrations and artwork; D. Macknelly for providing guidance on lattice generation; C. Ye and J. Mancini for assistance with high-speed video experiments; and J. Knipe, S. Pang, X. Xia, V. Beck and C. Spadaccini for discussions. This work was performed under the auspices of the US Department of Energy by the Lawrence Livermore National Laboratory under contract DE-AC52-07NA27344 and LDRD 19-SI-005 with information management number LLNL-JRNL-811671.

Author information

Affiliations

1. Lawrence Livermore National Laboratory, Livermore, CA, USA

Nikola A. Dudukovic, Erika J. Fong, Hawi B. Gemedo, Joshua R. DeOtte, Maira R. Cerón, Bryan D. Moran, Jonathan T. Davis, Sarah E. Baker & Eric B. Duoss

Authors

1. Nikola A. Dudukovic

[View author publications](#)

You can also search for this author in [PubMed](#) [Google Scholar](#)

2. Erika J. Fong

[View author publications](#)

You can also search for this author in [PubMed](#) [Google Scholar](#)

3. Hawi B. Gemedo

[View author publications](#)

You can also search for this author in [PubMed](#) [Google Scholar](#)

4. Joshua R. DeOtte

[View author publications](#)

You can also search for this author in [PubMed](#) [Google Scholar](#)

5. Maira R. Cerón

[View author publications](#)

You can also search for this author in [PubMed](#) [Google Scholar](#)

6. Bryan D. Moran

[View author publications](#)

You can also search for this author in [PubMed](#) [Google Scholar](#)

7. Jonathan T. Davis

[View author publications](#)

You can also search for this author in [PubMed](#) [Google Scholar](#)

8. Sarah E. Baker

[View author publications](#)

You can also search for this author in [PubMed](#) [Google Scholar](#)

9. Eric B. Duoss

[View author publications](#)

You can also search for this author in [PubMed](#) [Google Scholar](#)

Contributions

N.A.D. designed structures, devices and experiments, performed 3D printing, capillary rise tests and analytical calculations, recorded images and videos, and wrote the manuscript. E.J.F. designed and fabricated devices, performed capillary rise, transpiration, and active gas and liquid flow experiments, recorded images and videos, carried out thermal and Schlieren imaging and analysis, and colorimetric analysis of CO₂ absorption. H.B.G. fabricated structures, performed capillary rise, active flow, transpiration and CO₂ absorption experiments and analysis, performed selective metallization, recorded images and videos. J.R.D. designed structures, carried out numerical simulations and analysis, performed high-speed videography experiments and analysis. M.C.R. performed CO₂ absorption experiments and analysis. B.D.M. designed and assembled the Schlieren imaging set-up and participated in data collection. J.T.D. fabricated structures and carried out electroless plating. S.E.B. proposed and supervised the project. E.B.D. conceived the idea, proposed and supervised

the project, and wrote the manuscript. All authors participated in discussions of the research and revisions of the manuscript.

Corresponding author

Correspondence to [Eric B. Duoss](#).

Ethics declarations

Competing interests

A patent application has been filed by the Lawrence Livermore National Security LLC on the basis of the cellular fluidics concept described here (US Patent Application Serial No. 16/549,543), on which N.A.D., S.E.B., V. Beck, S. Chandrasekaran, J.R.D., E.B.D., J. Feaster, J. Knipe, J. Mancini, J. Oakdale, F. Qian and M. Worsley are listed as inventors.

Additional information

Peer review information *Nature* thanks Sung Kang, Abraham D. Stroock and the other, anonymous, reviewer(s) for their contribution to the peer review of this work. Peer reviewer reports are available.

Publisher's note Springer Nature remains neutral with regard to jurisdictional claims in published maps and institutional affiliations.

Extended data figures and tables

[Extended Data Fig. 1 Effects of cellular architecture on fluid transport.](#)

a, Unit cell types used in this study. **b**, Porosity as a function of relative strut diameter D^* can be used to determine the liquid-holding capacity of a given cell type. **c**, The cell design can be optimized for a desired liquid–solid and gas–liquid interfacial area by choosing an optimal D^* . **d**,

Illustration of the repeating structural motif in BCC arrays. Owing to the symmetry of the BCC unit cell, the structure defined by the green control volume ($0, 0, 0$) is also repeated in the magenta control volume, offset by a half-cell distance ($L/2, L/2, L/2$). **e**, Geometric considerations for a simplified analysis of capillary rise in BCC structures. Assuming the force equilibrium always occurs at the central node where F_{adh} is at a minimum (Fig. 2a), the contact perimeter can be approximated by a circle circumscribing the elliptical cross-section. The capillary height is explicitly solved for from the force equilibrium at the node. For an array of cells, the contact perimeter in the control volume can be approximated by the dashed lines, resulting in a greater contact perimeter and higher capillary rise.

[Source data](#)

[Extended Data Fig. 2 Numerical simulations of surface-tension-driven and actively pumped liquid flow.](#)

a, Simulations of capillary rise in an array of BCC cells. Similar trends in the spatiotemporal evolution of the gas–liquid and liquid–solid interfaces are observed as for a single column of cells (Fig. 3c). The liquid fronts at the outer corners accelerate and decelerate in an alternating manner. The overall velocity decreases over time. See Supplementary Video 1. **b**, Simulations of flow through a channel of simple cubic structures of different strut diameters were carried out on the outlined domain of 1.5 mm cells using quarter symmetry. The gas–liquid interface evolution and pressure map along the central cross-section plane are shown at time steps of 2, 10 and 20 ms. The white circles represent the cross-sections of the cell struts. For a cell with 500- μm struts, the gas–liquid interface initially advances, then recedes. **c**, Flow rate variation over time for cubic cells with different strut diameters. The negative magnitude of the flow rate (black line) corresponds to the receding interface in a cell with 500 μm . **d**, Average pressure variation over time. In cells with 500- μm struts, the average pressure becomes positive, indicating that the interface will not propagate in the desired direction and suggesting a potential leak scenario. In cells with 600- μm struts, the pressure hovers around zero, indicating that this strut thickness can be considered as the minimum critical value, and that slightly thicker struts are needed to ensure flow in the desired direction. **e**, The

maximum pressure at the interface across the first cell (0 to L) corresponds to the swelling of the liquid in the cell before it propagates into the subsequent cell. Exceeding the Laplace pressure of the advancing interface indicates a leak can occur (Supplementary Fig. 6).

Extended Data Fig. 3 Gas–liquid transport under different environmental conditions.

a, Illustration of water evaporation for cellular fluidics with and without a liquid reservoir and filter paper (left). Evaporative mass loss of the test structures at different relative humidity (middle). When supplied with a liquid reservoir, the evaporation rate of cellular fluidics is comparable to filter paper (right). **b**, Flow cell used for measurements of humidification and pressure drop for gas flow across wetted devices (left). Comparable levels of humidification are achieved between cellular fluidic devices and filter paper (middle); Data are mean \pm s.d.; $n = 6$. However, significant pressure drops were observed across filter paper, whereas no appreciable pressure drop could be detected for the cellular fluidics. Gas-driven liquid ejection was observed for both the filter paper ($11\text{--}15 \text{ ml min}^{-1}$) and a cellular fluidic device ($>25 \text{ ml min}^{-1}$) with no gas pores (right). Incorporating open (non-liquid-filled) gas pores allowed robust operation with no liquid ejection at all tested flow rates. **c**, Flow cell used for measurements of pressure drop of liquid flow across a uniform isotruss lattice (left). The data agree well with calculations from the Ergun equation, implying that pressure drop due to inertial effects is significant at higher flow rates (middle). Pressure drops calculated for lattices of different cell types at a liquid velocity of 10 cm s^{-1} (right). The circle symbol in the right plot corresponds to the circle symbol data point in the middle plot.

Extended Data Fig. 4 Effect of unit cell coordination number on CO₂ absorption rate.

a, Images (top) of the hierarchical lattice filled with a solution of Na_2CO_3 and a pH-sensitive colour indicator that changes from blue to yellow upon CO_2 saturation. The rate of absorption in the lattice is significantly faster than a liquid pool of the same sorbent volume. **b**, Hierarchical structure

750 s after exposure to CO₂, with analysed regions of interest outlined. Scale bar, 5 mm. **c**, Colorimetric map depicting the reaction rate during the first 500 s. The extent of CO₂ absorption is estimated by the colour change from blue to yellow (the sum of green and red channels minus the blue channel for each pixel). Higher reaction rates occur at cells with a lower coordination number—that is, more gas–liquid interfaces (blue arrows)—compared to cells with a higher coordination number (black arrows). The enlarged images of the outlined regions show high rates of reaction occurring at interfaces in the centre of each unit cell. Although it is expected that the reaction will occur more rapidly at struts and corners, where the liquid layer is the thinnest and has the highest surface-area-to-volume ratio, the thin liquid layer results in high reflectivity and low levels of pH indicator, which limits the measurement accuracy in these regions. The cell at the intersection with a higher coordination number shows a slower reaction rate than adjacent cells. **d**, The extent of reaction progression for cells selected in **b**. Cells with a coordination number 5 (black) show lower levels of reaction than cells with coordination number 2 (blue and pink).

Extended Data Fig. 5 Actively driven flow in channels of simple cubic cells with uniform and graded density structure.

a, In the uniform density structure, the pressure drop across the channel causes the liquid to halt its propagation in the desired direction and break the surface tension at a gas–liquid interface facing an undesirable direction, which results in a leak. **b**, In the graded density structure, the retaining capillary force along the desired flow direction better matches pressure drop across the channel, which results in uniform and leak-free flow through the entire structure. Scale bars, 5 mm.

Extended Data Fig. 6 Capillary rise in $N_x \times N_y \times N_z$ arrays of isotruss and simple cubic cells.

a, For isotruss cells, similar to BCC cells (Fig. 2), capillary rise of $N_x \times N_y \times N_z$ arrays is higher compared to a single column of the same relative density. **b**, The same effect is not observed in arrays of simple cubic

cells, where there is no strut structure that is internal to the cubic cell. Scale bars, 5 mm.

Extended Data Fig. 7 Transpiration experiments comparing cellular fluidic structures with filter paper.

Transpiration was observed by the water level drop in the reservoir and the concentration of green dye at the tip of the structures. **a**, A cellular fluidic structure and filter paper with an equivalent surface area exhibit similar evaporation rates, plotted as the decrease in liquid level in the reservoir over time. **b**, Filter paper was cut to match the shape of the cellular fluidic structure, but the filter paper collapsed under its own weight after 90 min of use. Conversely, the cellular fluidic component is a mechanically robust structure that exhibits no sign of collapse or deformation. **c**, Transpiration from the stochastic tree structure and filter paper holding equivalent volumes of liquid. Scale bars, 5 mm.

Extended Data Table 1 Dimensionless parameters derived for cellular fluidics

[Full size table](#)

Extended Data Table 2 Parameter values of cellular fluidic structures

[Full size table](#)

Supplementary information

Supplementary Information

This file contains Supplementary Methods (analytical calculations) and Supplementary Figures (unmodified images from Figs. 2d, 2f and 6c, evaporation front analysis from Fig. 4c, simulated velocity from Fig. 3c and thermal imaging data from Fig. 4b without smoothing, microscopy of micro-roughness effects, illustration of filter paper testing cell).

Peer Review File

Supplementary Video 1

Capillary rise – simulations and experiments. Simulation (left) and high-speed video (right) of single cell filling and capillary rise in a $1 \times 1 \times N_z$ cell column shown in Fig. 3. High-speed video of capillary rise in a column. Simulation of capillary rise in a $N_x \times N_y \times N_z$ array (Extended Data Fig. 2a). High-speed video of capillary rise in an array.

Supplementary Video 2

Multiphase processes in cellular fluidics. Video of transpiration of green-dyed ethanol through a stochastic tree structure. Infrared videos corresponding to data in Figs. 4b and 4c. Schlieren imaging used to calculate evaporative flux shown in Fig. 4d. Temporal color change of the hierarchical structure is used to estimate CO₂ absorption in Extended Data Fig. 4.

Supplementary Video 3

Active flow. Videos of active flow through 1D and 2D cellular fluidic structures, and demonstration of programmed fluidic and selectively metallized pathways in 3D.

Source data

Source Data Extended Data Fig. 1

Rights and permissions

Reprints and Permissions

About this article



Check for
updates

Cite this article

Dudukovic, N.A., Fong, E.J., Gemedo, H.B. *et al.* Cellular fluidics. *Nature* **595**, 58–65 (2021). <https://doi.org/10.1038/s41586-021-03603-2>

[Download citation](#)

- Received: 29 June 2020
- Accepted: 30 April 2021
- Published: 30 June 2021
- Issue Date: 01 July 2021
- DOI: <https://doi.org/10.1038/s41586-021-03603-2>

[Access through your institution](#)

[Change institution](#)

[Buy or subscribe](#)

Associated Content

[Programmable capillary action controls fluid flows](#)

- Tammi L. van Neel
- Ashleigh B. Theberge

[Why leaky pipes can be better for moving water](#)

- Ellie Mackay

Advertisement

| [Section menu](#) | [Main menu](#) |

- Article
- [Published: 30 June 2021](#)

Precise date for the Laacher See eruption synchronizes the Younger Dryas

- [Frederick Reinig](#) ORCID: [orcid.org/0000-0001-6839-8340¹](https://orcid.org/0000-0001-6839-8340),
- [Lukas Wacker²](#),
- [Olaf Jöris](#) ORCID: [orcid.org/0000-0002-6360-5096^{3,4,5}](https://orcid.org/0000-0002-6360-5096),
- [Clive Oppenheimer](#) ORCID: [orcid.org/0000-0003-4506-7260⁶](https://orcid.org/0000-0003-4506-7260),
- [Giulia Guidobaldi](#) ORCID: [orcid.org/0000-0002-8742-1996⁷](https://orcid.org/0000-0002-8742-1996),
- [Daniel Nievergelt⁷](#),
- [Florian Adolphi](#) ORCID: [orcid.org/0000-0003-0014-8753^{8,9}](https://orcid.org/0000-0003-0014-8753),
- [Paolo Cherubini^{7,10}](#),
- [Stefan Engels](#) ORCID: [orcid.org/0000-0002-2078-0361¹¹](https://orcid.org/0000-0002-2078-0361),
- [Jan Esper^{1,12}](#),
- [Alexander Land](#) ORCID: [orcid.org/0000-0002-8579-9880^{13,14}](https://orcid.org/0000-0002-8579-9880),
- [Christine Lane](#) ORCID: [orcid.org/0000-0001-9206-3903⁶](https://orcid.org/0000-0001-9206-3903),
- [Hardy Pfanz¹⁵](#),
- [Sabine Remmele¹³](#),
- [Michael Sigl](#) ORCID: [orcid.org/0000-0002-9028-9703¹⁶](https://orcid.org/0000-0002-9028-9703),
- [Adam Sookdeo²](#) &
- [Ulf Büntgen](#) ORCID: [orcid.org/0000-0002-3821-0818^{6,7,12,17}](https://orcid.org/0000-0002-3821-0818)

[Nature](#) volume 595, pages 66–69 (2021) [Cite this article](#)

- 174 Accesses
- 108 Altmetric

- [Metrics details](#)

Subjects

- [Climate and Earth system modelling](#)
- [Environmental impact](#)
- [Geography](#)
- [Palaeoclimate](#)
- [Volcanology](#)

Abstract

The Laacher See eruption (LSE) in Germany ranks among Europe's largest volcanic events of the Upper Pleistocene^{1,2}. Although tephra deposits of the LSE represent an important isochron for the synchronization of proxy archives at the Late Glacial to Early Holocene transition³, uncertainty in the age of the eruption has prevailed⁴. Here we present dendrochronological and radiocarbon measurements of subfossil trees that were buried by pyroclastic deposits that firmly date the LSE to $13,006 \pm 9$ calibrated years before present (bp; taken as ad 1950), which is more than a century earlier than previously accepted. The revised age of the LSE necessarily shifts the chronology of European varved lakes^{5,6} relative to the Greenland ice core record, thereby dating the onset of the Younger Dryas to $12,807 \pm 12$ calibrated years bp, which is around 130 years earlier than thought. Our results synchronize the onset of the Younger Dryas across the North Atlantic–European sector, preclude a direct link between the LSE and Greenland Stadial-1 cooling⁷, and suggest a large-scale common mechanism of a weakened Atlantic Meridional Overturning Circulation under warming conditions^{8,9,10}.

Access options

Subscribe to Journal

Get full journal access for 1 year

\$199.00

only \$3.90 per issue

[Subscribe](#)

All prices are NET prices.

VAT will be added later in the checkout.

Tax calculation will be finalised during checkout.

Rent or Buy article

Get time limited or full article access on ReadCube.

from \$8.99

[Rent or Buy](#)

All prices are NET prices.

Additional access options:

- [Log in](#)
- [Access through your institution](#)
- [Learn about institutional subscriptions](#)

Fig. 1: LSE wood finds.

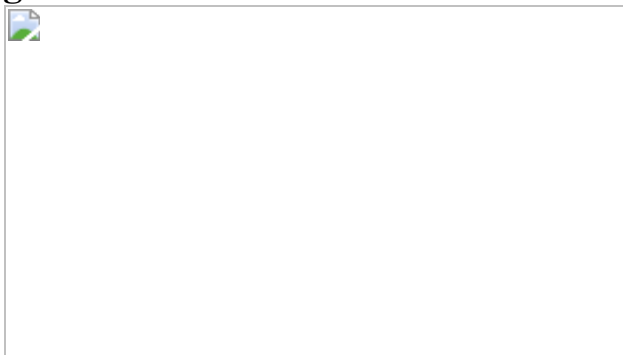


Fig. 2: Dendrochronological cross-dating of pre-LSE tree-ring width measurements.

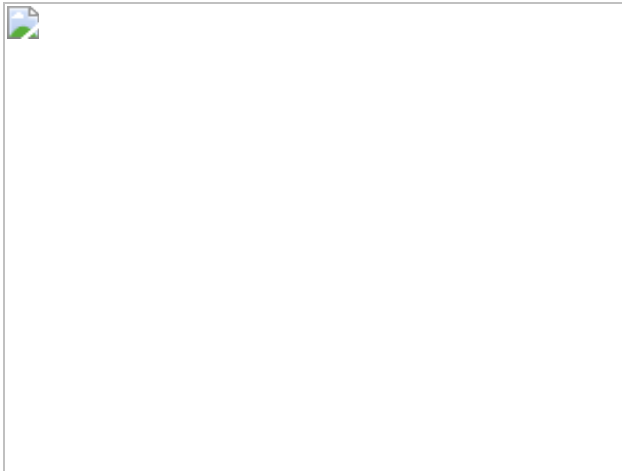


Fig. 3: Dating of the LSE.

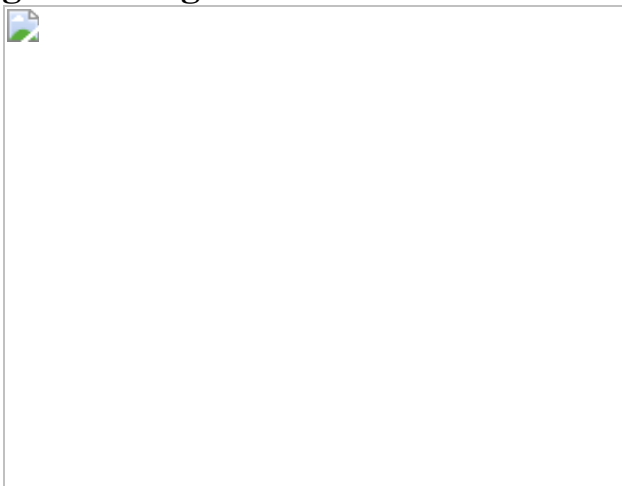
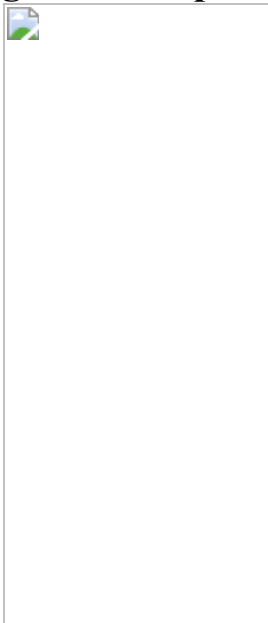


Fig. 4: Multi-proxy alignment of circum-Atlantic records.



Data availability

Data that support the findings of this study are available from the NOAA/World Data Service for Paleoclimatology data (<https://www.ncdc.noaa.gov/paleo/study/33194>). [Source data](#) are provided with this paper.

References

1. 1.

Schmincke, H.-U. in *Mantle Plumes* (eds Ritter, J. R. R. & Christensen, U. R.) 241–322 (Springer, 2007).

2. 2.

Schmincke, H.-U., Park, C. & Harms, E. Evolution and environmental impacts of the eruption of Laacher See Volcano (Germany) 12,900 a BP. *Quat. Int.* **61**, 61–72 (1999).

[Google Scholar](#)

3. 3.

Lane, C. S., Blockley, S. P. E., Bronk Ramsey, C. & Lotter, A. F. Tephrochronology and absolute centennial scale synchronisation of European and Greenland records for the last glacial to interglacial transition: a case study of Soppensee and NGRIP. *Quat. Int.* **246**, 145–156 (2011).

[Google Scholar](#)

4. 4.

Reinig, F. et al. Towards a dendrochronologically refined date of the Laacher See eruption around 13,000 years ago. *Quat. Sci. Rev.* **229**, 106128 (2020).

[Google Scholar](#)

5. 5.

Brauer, A., Endres, C. & Negendank, J. F. W. Lateglacial calendar year chronology based on annually laminated sediments from Lake Meerfelder Maar, Germany. *Quat. Int.* **61**, 17–25 (1999).

[Google Scholar](#)

6. 6.

Rach, O., Brauer, A., Wilkes, H. & Sachse, D. Delayed hydrological response to Greenland cooling at the onset of the Younger Dryas in western Europe. *Nat. Geosci.* **7**, 109–112 (2014).

[ADS](#) [CAS](#) [Google Scholar](#)

7. 7.

Baldini, J. U. L., Brown, R. J. & Mawdsley, N. Evaluating the link between the sulfur-rich Laacher See volcanic eruption and the Younger Dryas climate anomaly. *Clim. Past* **14**, 969–990 (2018).

[Google Scholar](#)

8. 8.

Broecker, W. S., Peteet, D. M. & Rind, D. Does the ocean–atmosphere system have more than one stable mode of operation? *Nature* **315**, 21–26 (1985).

[ADS](#) [CAS](#) [Google Scholar](#)

9. 9.

Rahmstorf, S. et al. Exceptional twentieth-century slowdown in Atlantic Ocean overturning circulation. *Nat. Clim. Change* **5**, 475–480 (2015).

[ADS](#) [Google Scholar](#)

10. 10.

Caesar, L., Rahmstorf, S., Robinson, A., Feulner, G. & Saba, V. Observed fingerprint of a weakening Atlantic Ocean overturning circulation. *Nature* **556**, 191–196 (2018).

[ADS](#) [CAS](#) [PubMed](#) [PubMed Central](#) [Google Scholar](#)

11. 11.

Holasek, R. E., Self, S. & Woods, A. W. Satellite observations and interpretation of the 1991 Mount Pinatubo eruption plumes. *J. Geophys. Res.* **101**, 27635–27655 (1996).

[ADS](#) [Google Scholar](#)

12. 12.

Baales, M. et al. Impact of the Late Glacial eruption of the Laacher See volcano, central Rhineland, Germany. *Quat. Res.* **58**, 273–288 (2002).

[Google Scholar](#)

13. 13.

van den Bogaard, P. $^{40}\text{Ar}/^{39}\text{Ar}$ ages of sanidine phenocrysts from Laacher See tephra (12,900 yr BP): chronostratigraphic and petrological significance. *Earth Planet. Sci. Lett.* **133**, 163–174 (1995).

[ADS](#) [Google Scholar](#)

14. 14.

Textor, C., Sachs, P. M., Graf, H.-F. & Hansteen, T. H. The 12 900 years BP Laacher See eruption: estimation of volatile yields and

simulation of their fate in the plume. *Geol. Soc. Lon. Spec. Pub.* **213**, 307–328 (2003).

[ADS](#) [CAS](#) [Google Scholar](#)

15. 15.

Reinig, F. et al. New tree-ring evidence for the Late Glacial period from the northern pre-Alps in eastern Switzerland. *Quat. Sci. Rev.* **186**, 215–224 (2018).

[ADS](#) [Google Scholar](#)

16. 16.

Reinig, F. et al. Introducing anatomical techniques to subfossil wood. *Dendrochronologia* **52**, 146–151 (2018).

[Google Scholar](#)

17. 17.

Schweingruber, F. H. *Tree Rings: Basics and Applications of Dendrochronology* (Kluwer Academic Publishers, 1988).

18. 18.

Reimer, P. J. et al. The IntCal20 Northern Hemisphere radiocarbon age calibration curve (0–55 cal kBP). *Radiocarbon* **62** 725–757 (2020).

[CAS](#) [Google Scholar](#)

19. 19.

Brauer, A., Haug, G. H., Dulski, P., Sigman, D. M. & Negendank, J. F. W. An abrupt wind shift in western Europe at the onset of the Younger Dryas cold period. *Nat. Geosci.* **1**, 520–523 (2008).

[ADS](#) [CAS](#) [Google Scholar](#)

20. 20.

Hafstadson, H., Sejrup, H. P., Klitgaard Kristensen, D. & Johnsen, S. Coupled response of the late glacial climatic shifts of northwest Europe reflected in Greenland ice cores: evidence from the northern North Sea. *Geology* **23**, 1059–1062 (1995).

[ADS](#) [Google Scholar](#)

21. 21.

Hughen, K. A., Southon, J. R., Lehman, S. J. & Overpeck, J. T. Synchronous radiocarbon and climate shifts during the last deglaciation. *Science* **290**, 1951–1955 (2000).

[ADS](#) [CAS](#) [PubMed](#) [PubMed Central](#) [Google Scholar](#)

22. 22.

Johnsen, S. J. et al. Irregular glacial interstadials recorded in a new Greenland ice core. *Nature* **359**, 311–313 (1992).

[ADS](#) [Google Scholar](#)

23. 23.

Rasmussen, S. O. et al. A stratigraphic framework for abrupt climatic changes during the Last Glacial period based on three synchronized Greenland ice-core records: refining and extending the INTIMATE event stratigraphy. *Quat. Sci. Rev.* **106**, 14–28 (2014).

[ADS](#) [Google Scholar](#)

24. 24.

Lane, C. S., Brauer, A., Blockley, S. P. E. & Dulski, P. Volcanic ash reveals time-transgressive abrupt climate change during the Younger Dryas. *Geology* **41**, 1251–1254 (2013).

[ADS](#) [Google Scholar](#)

25. 25.

Muschitiello, F. et al. Fennoscandian freshwater control on Greenland hydroclimate shifts at the onset of the Younger Dryas. *Nat. Commun.* **6**, 8939 (2015).

[ADS](#) [CAS](#) [PubMed](#) [PubMed Central](#) [Google Scholar](#)

26. 26.

Obreht, I. et al. An annually resolved record of Western European vegetation response to Younger Dryas cooling. *Quat. Sci. Rev.* **231**, 106198 (2020).

[Google Scholar](#)

27. 27.

Lohne, Ø. S., Mangerud, J. & Birks, H. H. Precise ^{14}C ages of the Vedde and Saksunarvatn ashes and the Younger Dryas boundaries from western Norway and their comparison with the Greenland Ice Core (GICC05) chronology. *J. Quat. Sci.* **28**, 490–500 (2013).

[Google Scholar](#)

28. 28.

Brauer, A. et al. High resolution sediment and vegetation responses to Younger Dryas climate change in varved lake sediments from Meerfelder Maar, Germany. *Quat. Sci. Rev.* **18**, 321–329 (1999).

[ADS](#) [Google Scholar](#)

29. 29.

Neugebauer, I. et al. A Younger Dryas varve chronology from the Rehwiese palaeolake record in NE-Germany. *Quat. Sci. Rev.* **36**, 91–

102 (2012).

[ADS](#) [Google Scholar](#)

30. 30.

Lotter, A. F., Eicher, U., Siegenthaler, U. & Birks, H. J. B. Late-glacial climatic oscillations as recorded in Swiss lake sediments. *J. Quat. Sci.* **7**, 187–204 (1992).

[Google Scholar](#)

31. 31.

Merkt, J. & Müller, H. Varve chronology and palynology of the Lateglacial in Northwest Germany from lacustrine sediments of Hämelsee in Lower Saxony. *Quat. Int.* **61**, 41–59 (1999).

[Google Scholar](#)

32. 32.

Steffensen, J. P. et al. High-resolution Greenland ice core data show abrupt climate change happens in few years. *Science* **321**, 680–684 (2008).

[ADS](#) [CAS](#) [PubMed](#) [PubMed Central](#) [Google Scholar](#)

33. 33.

Adolphi, F. et al. Connecting the Greenland ice-core and U/Th timescales via cosmogenic radionuclides: testing the synchronicity of Dansgaard–Oeschger events. *Clim. Past* **14**, 1755–1781 (2018).

[Google Scholar](#)

34. 34.

von Grafenstein, U., Erlenkeuser, H., Brauer, A., Jouzel, J., & Johnsen, S. J. A mid-European decadal isotope-climate record from 15,500 to 5000 years B.P. *Science* **284**, 1654–1657 (1999).

[ADS](#) [Google Scholar](#)

35. 35.

Lauterbach, S. et al. Environmental responses to Lateglacial climatic fluctuations recorded in the sediments of pre-Alpine Lake Mondsee (northeastern Alps). *J. Quat. Sci.* **26**, 253–267 (2011).

[Google Scholar](#)

36. 36.

Lohne, Ø. S., Mangerud, J. & Birks, H. H. IntCal13 calibrated ages of the Vedde and Saksunarvatn ashes and the Younger Dryas boundaries from Kråkenes, western Norway. *J. Quat. Sci.* **29**, 506–507 (2014).

[Google Scholar](#)

37. 37.

Condron, A. & Winsor, P. Meltwater routing and the Younger Dryas. *Proc. Natl Acad. Sci. USA* **109**, 19928–19933 (2012).

[ADS](#) [CAS](#) [PubMed](#) [PubMed Central](#) [Google Scholar](#)

38. 38.

Renssen, H. et al. Multiple causes of the Younger Dryas cold period. *Nat. Geosci.* **8**, 946–949 (2015).

[ADS](#) [CAS](#) [Google Scholar](#)

39. 39.

Hajdas, I. et al. AMS radiocarbon dating and varve chronology of Lake Soppensee: 6000 to 12000 ^{14}C years BP. *Clim. Dyn.* **9**, 107–116 (1993).

[Google Scholar](#)

40. 40.

Wulf, S. et al. Tracing the Laacher See tephra in the varved sediment record of the Trzecowskie palaeolake in central Northern Poland. *Quat. Sci. Rev.* **76**, 129–139 (2013).

[ADS](#) [Google Scholar](#)

41. 41.

Park, C. & Schmincke, H.-U. Multistage damming of the Rhine River by tephra fallout during the 12,900 BP Plinian Laacher See Eruption (Germany). Syn-eruptive Rhine damming I. *J. Volcanol. Geotherm. Res.* **389**, 106688 (2020).

[CAS](#) [Google Scholar](#)

42. 42.

Waldmann, G. *Vulkanfossilien im Laacher Bims* (Gregor and Unger, 1996).

43. 43.

Frechen, J. Die Tuffe des Laacher Vulkangebietes als quartärgeologische Leitgesteine und Zeitmarken. *Fortschr. Geol. Rheinl. Westfal.* **4**, 363–370 (1959).

[Google Scholar](#)

44. 44.

Schweitzer, H.-J. Entstehung und Flora des Trasses im nördlichen Laachersee-Gebiet. *E&G Quat. Sci. J.* **9**, 28–56 (1958).

[Google Scholar](#)

45. 45.

Street, M. *Analysis of Late Palaeolithic and Mesolithic Faunal Assemblages in the Northern Rhineland, Germany*. PhD thesis, Univ. Birmingham (1993).

46. 46.

Street, M. Ein Wald der Allerodzeit bei Miesenheim, Stadt Andernach (Neuwieder Becken). *Archäologisches Korrespondenzblatt* **16**, 13–22 (1986).

[Google Scholar](#)

47. 47.

Baales, M., Bittmann, F. & Kromer, B. Verkohlte Bäume im Trass der Laacher See-Tephra bei Kruft (Neuwieder Becken): ein Beitrag zur Datierung des Laacher See-Ereignisses und zur Vegetation der Allerød-Zeit am Mittelrhein. *Archäologisches Korrespondenzblatt* **28**, 191–204 (1998).

[Google Scholar](#)

48. 48.

Brunnacker, K., Fruth, H.-J., Juvigné, E. & Urban, B. Spätpaläolithische Funde aus Thür, Kreis Mayen-Koblenz. *Archäologisches Korrespondenzblatt Mainz* **12**, 417–427 (1982).

[Google Scholar](#)

49. 49.

Rinn, F. *TSAP: time series analyses presentation*. Reference manual v.3.0 (RinnTech, 1996).

50. 50.

Synal, H.-A., Stocker, M. & Suter, M. MICADAS: a new compact radiocarbon AMS system. *Nucl. Instrum. Methods Phys. Res. B* **259**, 7–13 (2007).

[ADS](#) [CAS](#) [Google Scholar](#)

51. 51.

Wacker, L. et al. MICADAS: routine and high-precision radiocarbon dating. *Radiocarbon* **52**, 252–262 (2010).

[CAS](#) [Google Scholar](#)

52. 52.

Wacker, L. et al. Radiocarbon dating to a single year by means of rapid atmospheric ^{14}C changes. *Radiocarbon* **56**, 573–579 (2014).

[CAS](#) [Google Scholar](#)

53. 53.

Němec, M., Wacker, L. & Gäggeler, H. Optimization of the graphitization process at age-1. *Radiocarbon* **52**, 1380–1393 (2010).

[Google Scholar](#)

54. 54.

Sookdeo, A. et al. Quality dating: a well-defined protocol implemented at ETH for high-precision ^{14}C -dates tested on Late Glacial wood. *Radiocarbon* **62**, 891–899 (2020).

[CAS](#) [Google Scholar](#)

55. 55.

Kaiser, K. F. *Beiträge zur Klimageschichte vom späten Hochglazial bis ins frühe Holozän: rekonstruiert mit Jahrringen und Molluskenschalen aus verschiedenen Vereisungsgebieten* (Ziegler, 1993).

56. 56.

Bronk Ramsey, C. Deposition models for chronological records. *Quat. Sci. Rev.* **27**, 42–60 (2008).

[ADS](#) [Google Scholar](#)

57. 57.

Bronk Ramsey, C. Dealing with outliers and offsets in radiocarbon dating. *Radiocarbon* **51**, 1023–1045 (2009).

[Google Scholar](#)

58. 58.

Bird, M. I. in *Encyclopedia of Quaternary Science* (ed. Elias S.A.) 353–360 (Elsevier, 2013).

59. 59.

Holdaway, R. N., Duffy, B. & Kennedy, B. Evidence for magmatic carbon bias in ^{14}C dating of the Taupo and other major eruptions. *Nat. Commun.* **9**, 4110 (2018).

[ADS](#) [PubMed](#) [PubMed Central](#) [Google Scholar](#)

60. 60.

Kromer, B., Spurk, M., Remmele, S., Barbetti, M. & Joniello, V. Segments of atmospheric ^{14}C change as derived from Late Glacial and Early Holocene floating tree-ring series. *Radiocarbon* **40**, 351–358 (1997).

[Google Scholar](#)

61. 61.

Muschitiello, F. & Wohlfarth, B. Time-transgressive environmental shifts across Northern Europe at the onset of the Younger Dryas. *Quat. Sci. Rev.* **109**, 49–56 (2015).

[Google Scholar](#)

62. 62.

Engels, S. et al. Subdecadal-scale vegetation responses to a previously unknown late-Allerød climate fluctuation and Younger Dryas cooling at Lake Meerfelder Maar (Germany). *J. Quat. Sci.* **31**, 741–752 (2016).

[Google Scholar](#)

63. 63.

Sigl, M. et al. Timing and climate forcing of volcanic eruptions for the past 2,500 years. *Nature* **523**, 543–549 (2015).

[ADS](#) [CAS](#) [PubMed](#) [PubMed Central](#) [Google Scholar](#)

64. 64.

Svensson, A. et al. Bipolar volcanic synchronization of abrupt climate change in Greenland and Antarctic ice cores during the last glacial period. *Clim. Past* **16**, 1565–1580 (2020).

[Google Scholar](#)

65. 65.

Adolphi, F. & Muscheler, R. Synchronizing the Greenland ice core and radiocarbon timescales over the Holocene – Bayesian wiggle-matching of cosmogenic radionuclide records. *Clim. Past* **12**, 15–30 (2016).

[Google Scholar](#)

66. 66.

Adolphi, F. et al. Radiocarbon calibration uncertainties during the last deglaciation: insights from new floating tree-ring chronologies. *Quat. Sci. Rev.* **170**, 98–108 (2017).

[ADS](#) [Google Scholar](#)

67. 67.

Muscheler, R., Adolphi, F. & Knudsen, M. F. Assessing the differences between the IntCal and Greenland ice-core time scales for the last 14,000 years via the common cosmogenic radionuclide variations. *Quat. Sci. Rev.* **106**, 81–87 (2014).

[ADS](#) [Google Scholar](#)

68. 68.

Ruth, U., Wagenbach, D., Steffensen, J. P. & Bigler, M. Continuous record of microparticle concentration and size distribution in the central Greenland NGRIP ice core during the last glacial period. *J. Geophys. Res.* **108**, 4098 (2003).

[Google Scholar](#)

69. 69.

Bigler, M. et al. Optimization of high-resolution continuous flow analysis for transient climate signals in ice cores. *Environ. Sci. Technol.* **45**, 4483–4489 (2011).

[ADS](#) [CAS](#) [PubMed](#) [PubMed Central](#) [Google Scholar](#)

70. 70.

Mortensen, A. K., Bigler, M., Grönvold, K., Steffensen, J. P. & Johnsen, S. J. Volcanic ash layers from the Last Glacial Termination in the NGRIP ice core. *J. Quat. Sci.* **20**, 209–219 (2005).

[Google Scholar](#)

71. 71.

Reimer, P. J. et al. IntCal13 and Marine13 radiocarbon age calibration curves 0–50,000 years cal BP. *Radiocarbon* **55**, 1869–1887 (2013).

[ADS](#) [CAS](#) [PubMed](#) [PubMed Central](#) [Google Scholar](#)

72. 72.

Buizert, C. et al. Abrupt ice-age shifts in southern westerly winds and Antarctic climate forced from the north. *Nature* **563**, 681–685 (2018).

[ADS](#) [CAS](#) [PubMed](#) [PubMed Central](#) [Google Scholar](#)

73. 73.

Seierstad, I. K. et al. Consistently dated records from the Greenland GRIP, GISP2 and NGRIP ice cores for the past 104 ka reveal regional millennial-scale $\delta^{18}\text{O}$ gradients with possible Heinrich event imprint. *Quat. Sci. Rev.* **106**, 29–46 (2014).

[ADS](#) [Google Scholar](#)

74. 74.

Sigl, M. et al. The WAIS Divide deep ice core WD2014 chronology – part 2: annual-layer counting (0–31 ka BP). *Clim. Past* **12**, 769–786 (2016).

[Google Scholar](#)

75. 75.

Litt, T., Behre, K.-E., Meyer, K.-D., Stephan, H.-J. & Wansa, S. Stratigraphische Begriffe für das Quartär des norddeutschen Vereisungsgebietes. *Eiszeitalt. Ggw. Quat. Sci. J.* **56**, 7–65 (2007).

[Google Scholar](#)

76. 76.

Riede, F. Past-forwarding ancient calamities. Pathways for making archaeology relevant in disaster risk reduction research. *Humanities* **6**, 79 (2017).

[Google Scholar](#)

77. 77.

Patton, H. et al. Deglaciation of the Eurasian ice sheet complex. *Quat. Sci. Rev.* **169**, 148–172 (2017).

[ADS](#) [Google Scholar](#)

78. 78.

Zielinski, G. A., Mayewski, P. A., Meeker, L. D., Whitlow, S. & Twickler, M. S. A. 110,000-yr record of explosive volcanism from the GISP2 (Greenland) ice core. *Quat. Res.* **45**, 109–118 (1996).

[CAS](#) [Google Scholar](#)

79. 79.

Severi, M. et al. Synchronisation of the EDML and EDC ice cores for the last 52 kyr by volcanic signature matching. *Clim. Past* **3**, 367–374 (2007).

[Google Scholar](#)

[Download references](#)

Acknowledgements

This study was supported by the WSL-internal project ‘LSD’ and the Swiss National Science Foundation (SNF Grant 200021L_157187/1). U.B. and J.E. received funding from SustES: Adaptation strategies for sustainable ecosystem services and food security under adverse environmental conditions (CZ.02.1.01/0.0/0.0/16_019/0000797). M.S. received funding from the European Research Council under the European Union’s Horizon 2020 research and innovation programme (grant agreement no. 820047). We thank A. Hunold, H. Schaaf and B. Streubel for assistance during fieldwork, the University of Hohenheim and M. Friedrich for initial investigations during a DEKLIM-project; and D. Dahl-Jensen and P. Reimer for their constructive feedback that further improved the quality of the manuscript.

Author information

Affiliations

1. Department of Geography, Johannes Gutenberg University, Mainz, Germany

Frederick Reinig & Jan Esper

2. Laboratory of Ion Beam Physics, ETH Zurich, Zurich, Switzerland

Lukas Wacker & Adam Sookdeo

3. Römisch-Germanisches Zentralmuseum–MONREPOS Archaeological Research Centre and Museum for Human Behavioural Evolution, Neuwied, Germany

Olaf Jöris

4. Institute of Ancient Studies, Department of Prehistoric and Protohistoric Archaeology, Johannes Gutenberg University, Mainz, Germany

Olaf Jöris

5. Key Laboratory of Western China's Environmental Systems (Ministry of Education), College of Earth and Environmental Sciences, Lanzhou University, Lanzhou, China

Olaf Jöris

6. Department of Geography, University of Cambridge, Cambridge, UK

Clive Oppenheimer, Christine Lane & Ulf Büntgen

7. Swiss Federal Research Institute WSL, Birmensdorf, Switzerland

Giulia Guidobaldi, Daniel Nievergelt, Paolo Cherubini & Ulf Büntgen

8. Alfred Wegener Institute, Helmholtz Center for Polar and Marine Research, Bremerhaven, Germany

Florian Adolphi

9. Department of Geosciences, University of Bremen, Bremen, Germany

Florian Adolphi

10. Department of Forest and Conservation Sciences, University of British Columbia, Vancouver, British Columbia, Canada

Paolo Cherubini

11. Department of Geography, Birkbeck University of London, London, UK

Stefan Engels

12. Global Change Research Institute of the Czech Academy of Sciences (CzechGlobe), Brno, Czech Republic

Jan Esper & Ulf Büntgen

13. Institute of Biology (190a), University of Hohenheim, Stuttgart, Germany

Alexander Land & Sabine Remmeli

14. Silviculture & Forest Growth and Yield, University of Applied Forest Sciences, Rottenburg am Neckar, Germany

Alexander Land

15. Institute of Applied Botanics and Volcanic Biology, Universität Duisburg-Essen, Essen, Germany

Hardy Pfanz

16. Climate and Environmental Physics, Physics Institute, Oeschger Centre for Climate Change Research, University of Bern, Bern, Switzerland

Michael Sigl

17. Department of Geography, Faculty of Science, Masaryk University, Brno, Czech Republic

Ulf Büntgen

Authors

1. Frederick Reinig

[View author publications](#)

You can also search for this author in [PubMed](#) [Google Scholar](#)

2. Lukas Wacker

[View author publications](#)

You can also search for this author in [PubMed](#) [Google Scholar](#)

3. Olaf Jöris

[View author publications](#)

You can also search for this author in [PubMed](#) [Google Scholar](#)

4. Clive Oppenheimer

[View author publications](#)

You can also search for this author in [PubMed](#) [Google Scholar](#)

5. Giulia Guidobaldi

[View author publications](#)

You can also search for this author in [PubMed](#) [Google Scholar](#)

6. Daniel Nievergelt

[View author publications](#)

You can also search for this author in [PubMed](#) [Google Scholar](#)

7. Florian Adolphi

[View author publications](#)

You can also search for this author in [PubMed](#) [Google Scholar](#)

8. Paolo Cherubini

[View author publications](#)

You can also search for this author in [PubMed](#) [Google Scholar](#)

9. Stefan Engels

[View author publications](#)

You can also search for this author in [PubMed](#) [Google Scholar](#)

10. Jan Esper

[View author publications](#)

You can also search for this author in [PubMed](#) [Google Scholar](#)

11. Alexander Land

[View author publications](#)

You can also search for this author in [PubMed](#) [Google Scholar](#)

12. Christine Lane

[View author publications](#)

You can also search for this author in [PubMed](#) [Google Scholar](#)

13. Hardy Pfanz

[View author publications](#)

You can also search for this author in [PubMed](#) [Google Scholar](#)

14. Sabine Remmele

[View author publications](#)

You can also search for this author in [PubMed](#) [Google Scholar](#)

15. Michael Sigl

[View author publications](#)

You can also search for this author in [PubMed](#) [Google Scholar](#)

16. Adam Sookdeo

[View author publications](#)

You can also search for this author in [PubMed](#) [Google Scholar](#)

17. Ulf Büntgen

[View author publications](#)

You can also search for this author in [PubMed](#) [Google Scholar](#)

Contributions

F.R., U.B., O.J. and L.W. designed the study with input from D.N. Tree-ring width measurements were performed by F.R., G.G. and D.N. Radiocarbon

measurements and analyses were performed by G.G. and L.W., with the involvement of F.R. L.W. modelled the ^{14}C . The paper was written by F.R., together with U.B., O.J., J.E., C.O., M.S. and L.W. Further editorial contributions were made by F.A., P.C., S.E., C.L. and A.S. Wood samples were prepared and provided by O.J., H.P., A.L. and S.R. Ice core data were provided and discussed by M.S. and F.A.

Corresponding author

Correspondence to [Frederick Reinig](#).

Ethics declarations

Competing interests

The authors declare no competing interests.

Additional information

Peer review information *Nature* thanks Paula Reimer and the other, anonymous, reviewer(s) for their contribution to the peer review of this work.

Publisher's note Springer Nature remains neutral with regard to jurisdictional claims in published maps and institutional affiliations.

Extended data figures and tables

[Extended Data Fig. 1 Temporal and spatial setting of the Laacher See eruption.](#)

a, Climatic development of the past 15,000 years according to the NGRIP Greenland $\delta^{18}\text{O}$ ice core record²³ (blue), covering the Late Glacial and Holocene periods, shown together with the LST $^{40}\text{Ar}/^{39}\text{Ar}$ age determination¹³ at $12,900 \pm 560$ bp (mean $\pm 1\sigma$; red). INTIMATE event

stratigraphy²³ of the Late Glacial is outlined left of the NGRIP record, with the European palaeobotanical subdivision of this period⁷⁵ aligned on the right. BØ, Bølling interstadial; MEI, Meiendorf interstadial; YD, YD cold interval. Offsets between both schemes are the topic of intensive and ongoing discussion. **b**, Geospatial distribution of LST fallout deposits (orange dots; modified from a previously published study⁷⁶) with locations of Laacher See (red triangle) and the source of the tree stems used to build the Swiss Late Glacial tree-ring and ^{14}C records¹⁸ (green dot; SWILM- ^{14}C). The light blue line indicates the extent of the late AL Fennoscandian ice sheet (modified from a previously published study⁷⁷). The map was produced using QGIS.

Extended Data Fig. 2 Examples of LSE wood finds.

a, Locations of archived (circles with black borders) and newly excavated (in 2019, circles with orange borders) subfossil wood samples within the MLST deposits in the Neuwied Basin (modified from a previously published study¹²). Isopachs for LST fallout are shown in red, and grey shading indicates the extent of MLST ignimbrite deposits. **b–f** Subfossil trees from the Brohltal (1986, photograph by E. Turner) (**b**), from an excavated forest at Miesenheim (1986, photograph by M. Street)⁴⁶ (**c**), from Kruft (1996, photograph by M. Baales)⁴⁷ (**d**); from Meurin (**e**) and an excavation at a new locality in Miesenheim (**f**). Note that only the samples from Brohltahl and Meurin are included in this study, as other materials were exhausted during previous analyses or unsuitable for the performed measurements (see [Methods](#)). The map was produced using QGIS. All photographs are provided by the MONREPOS picture archive.

Extended Data Fig. 3 Reduced χ^2 test results.

a–h, Most likely ^{14}C calendar placement⁵² of the last ring of Poplar 1 matched to SWILM- ^{14}C with an offset of 11 cal. years (yrs) (**a**); Poplar 1 matched to SWILM- $^{14}\text{C}_{\text{plus}}$ with an offset of 22 cal. years (**b**); Poplar 2 matched to SWILM- ^{14}C with an offset of 18 cal. years (**c**); Birch 1 matched to SWILM- ^{14}C with an offset of 36 cal. years (**d**); Birch 1 matched to

SWILM- $^{14}\text{C}_{\text{plus}}$ with an offset of 46 cal. years (**e**); all pre-LSE samples matched to SWILM- ^{14}C with an offset of 20 cal. years (**f**); Daettnau 3 matched to SWILM- ^{14}C with an offset of 13 cal. years (**g**); and Poplar 1 matched to Daettnau 3 with an offset of 25 cal. years (**h**). Black lines denote to the 95% confidence interval.

Extended Data Fig. 4 Multi-proxy alignment of North Atlantic and European records.

a, NGRIP (grey) and Greenland Ice Sheet Project Two (GISP2) (black) oxygen isotopes ($\delta^{18}\text{O}$) at 20-year resolution from Greenland on the GICC05 timescale²³, Alpine $\delta^{18}\text{O}$ records from Lake Ammersee³⁴ (yellow) and Lake Mondsee³⁵ (red), and MFM⁵ (blue) varve thickness plotted as 10-year running means, dated to the MFM timescale with a LSE date of 12,880 bp_{MFM} (± 40 years; red dotted vertical line) indicating time-transgressive GS-1 and the YD cooling between 13,200 and 12,400 bp_{GICC05}. **b**, The same European proxy records shifted 126 years according to the new LSE date of 13,006 cal.bp (red vertical line)²⁸ now outlining a synchronized cooling into the GS-1 and YD across the North Atlantic. Blue shading denotes the period of strongest cooling evident in the Greenland ice core isotope records.

Extended Data Fig. 5 Non-sea-salt sulfate and particle records from polar ice cores around the time of the LSE.

a, Ice-core records of sulfate from the Greenland Ice Sheet Project Two (GISP2)⁷⁸ and NGRIP⁶⁹ records. **b**, High-resolution (1 cm depth) record of sulfate and dust⁶⁸ from the NGRIP ice-core record⁶⁹ between 13,015 and 12,975 bp_{GICC05} with three volcanic anomalies at 12,980 bp_{GICC05} (1), 12,982 bp_{GICC05} (2) and 12,994 bp_{GICC05} (3; see Extended Data Table 3). Black arrows indicate additional obtained sulfate peaks; the cyan bar denotes the 17-cm sampling range in which tephra shards were previously detected and characterized⁷⁰ encompassing two distinct volcanic signals (1 and 2). **c**, Ice-core records of sulfate (calculated from sulfur measurements) from West Antarctic Ice Sheet Divide (WD)⁷⁴ and Dronning Maud Land

(EDML)⁷⁹ ice core. All ice cores are synchronized^{65,72,73} on the GICC05 chronology²³ timescale with respect to ad 1950. Grey horizontal lines represent the accumulated age error in 13,000 bp with ± 105 years for WD2014⁷⁴ and ± 140 years for GICC05²³, which has been further reduced ($-12/+21$ years; 2σ) based on the synchronization of tree-ring ^{14}C and ice-core ^{10}Be ³³. Red horizontal lines outline the added LSE ^{14}C uncertainty (± 9 years). Yellow dots denote the obtained bipolar sulfate anomalies.

Source data

Extended Data Fig. 6 D Sequence wiggle-matching results with OxCal.

a–c, All radiocarbon (^{14}C) modelled LSE ages obtained from Poplar 1 (**a**), Birch 1 (**b**) and Poplar 2 (**c**), applying the extended Swiss Late Glacial Reference (SWILM- $^{14}\text{C}_{\text{plus}}$) point to a similar eruption date. Whereas the long-lived Poplar 1 and Birch 1 exceed the ^{14}C plateau with the initial ^{14}C dates, Poplar 2 provide three possible wiggle-match placements; however, under the constraint that this sample was also found within the MLST deposits, the two younger ^{14}C results need to be excluded.

Extended Data Table 1 Pre-LSE chronology

[Full size table](#)

Extended Data Table 2 Annually varved layer estimate of the YD onset relative to the LST

[Full size table](#)

Extended Data Table 3 Volcanic sulfate depositions in Greenland and Antarctica around the new LSE date

[Full size table](#)

Extended Data Table 4 OxCal calibration results of ^{14}C -dated events from the Kråkenes core chronologies

[Full size table](#)

Source data

Source Data Extended Data Fig. 5

Source Data Extended Data Table. 3

Rights and permissions

[Reprints and Permissions](#)

About this article



Check for
updates

Cite this article

Reinig, F., Wacker, L., Jöris, O. *et al.* Precise date for the Laacher See eruption synchronizes the Younger Dryas. *Nature* **595**, 66–69 (2021). <https://doi.org/10.1038/s41586-021-03608-x>

[Download citation](#)

- Received: 29 August 2020
- Accepted: 04 May 2021
- Published: 30 June 2021
- Issue Date: 01 July 2021
- DOI: <https://doi.org/10.1038/s41586-021-03608-x>

[Access through your institution](#)

[Change institution](#)

[Buy or subscribe](#)

Advertisement

This article was downloaded by **calibre** from <https://www.nature.com/articles/s41586-021-03608-x>

| [Section menu](#) | [Main menu](#) |

- Article
- [Published: 30 June 2021](#)

Ridgecrest aftershocks at Coso suppressed by thermal destressing

- [Kyungjae Im](#) ORCID: [orcid.org/0000-0003-0057-3119¹](https://orcid.org/0000-0003-0057-3119),
- [Jean-Philippe Avouac](#) ORCID: [orcid.org/0000-0002-3060-8442¹](https://orcid.org/0000-0002-3060-8442),
- [Elías R. Heimisson](#) ORCID: [orcid.org/0000-0001-8342-7226¹](https://orcid.org/0000-0001-8342-7226) nAff⁴ &
- [Derek Elsworth^{2,3}](#)

[Nature](#) volume 595, pages 70–74 (2021) [Cite this article](#)

- 103 Accesses
- 33 Altmetric
- [Metrics details](#)

Subjects

- [Natural hazards](#)
- [Seismology](#)

Abstract

Geothermal and volcanic areas are prone to earthquake triggering^{1,2}. The Coso geothermal field in California lies just north of the surface ruptures driven by the 2019 Ridgecrest earthquake (moment magnitude $M_w = 7.1$), in an area where changes in coseismic stress should have triggered aftershocks^{3,4}. However, no aftershocks were observed there⁴. Here we show that 30 years of geothermal heat production at Coso depleted shear

stresses within the geothermal reservoir. Thermal contraction of the reservoir initially induced substantial seismicity, as observed in the Coso geothermal reservoir, but subsequently depleted the stress available to drive the aftershocks during the Ridgecrest sequence. This destressing changed the faulting style of the reservoir and impeded aftershock triggering. Although unlikely to have been the case for the Ridgecrest earthquake, such a destressed zone could, in principle, impede the propagation of a large earthquake.

Access options

Subscribe to Journal

Get full journal access for 1 year

\$199.00

only \$3.90 per issue

[Subscribe](#)

All prices are NET prices.

VAT will be added later in the checkout.

Tax calculation will be finalised during checkout.

Rent or Buy article

Get time limited or full article access on ReadCube.

from \$8.99

[Rent or Buy](#)

All prices are NET prices.

Additional access options:

- [Log in](#)

- [Access through your institution](#)
- [Learn about institutional subscriptions](#)

Fig. 1: Ridgecrest aftershock and prior seismicity in the Coso area.



Fig. 2: Production, power generation and surface subsidence for our reference simulation.

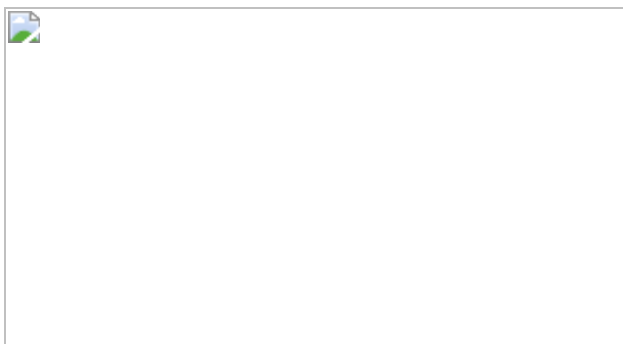


Fig. 3: Simulation of stress changes due to thermal contraction, pore pressure changes and anelastic failure of the reservoir.



Data availability

The seismic catalogue¹⁰ is publicly available from the Southern California Earthquake Data Center (<https://scedc.caltech.edu/data/alt-2011-dd-hauksson-yang-shearer.html>). The Coso field well location and flow rate

data are available from the California Department of Conservation (<https://maps.conervation.ca.gov/doggr/wellfinder>, <https://www.conervation.ca.gov/calgem/geothermal/manual/Pages/producton.aspx>). Simulation data are available in the Caltech data repository (<https://doi.org/10.22002/D1.1455>). [Source data](#) are provided with this paper.

Code availability

The TOUGH–FLAC coupled simulator and all input files are available in the Caltech data repository (<https://doi.org/10.22002/D1.1455>).

References

1. 1.

Zang, A. et al. Analysis of induced seismicity in geothermal reservoirs – an overview. *Geothermics* **52**, 6–21 (2014).

[Google Scholar](#)

2. 2.

Kim, K.-H. et al. Assessing whether the 2017 M_w 5.4 Pohang earthquake in South Korea was an induced event. *Science* **360**, 1007–1009 (2018).

[ADS](#) [CAS](#) [PubMed](#) [PubMed Central](#) [Google Scholar](#)

3. 3.

Ross, Z. E. et al. Hierarchical interlocked orthogonal faulting in the 2019 Ridgecrest earthquake sequence. *Science* **366**, 346–351 (2019).

[ADS](#) [CAS](#) [PubMed](#) [PubMed Central](#) [Google Scholar](#)

4. 4.

Hardebeck, J. L. A stress-similarity triggering model for aftershocks of the M_w 6.4 and 7.1 Ridgecrest earthquakes. *Bull. Seismol. Soc. Am.* **110**, 1716–1727 (2020).

[Google Scholar](#)

5. 5.

Chen, K. et al. Cascading and pulse-like ruptures during the 2019 Ridgecrest earthquakes in the Eastern California Shear Zone. *Nat. Commun.* **11**, 22 (2020).

[ADS](#) [CAS](#) [PubMed](#) [PubMed Central](#) [Google Scholar](#)

6. 6.

Hill, D. P. et al. Seismicity remotely triggered by the magnitude 7.3 Landers, California, earthquake. *Science* **260**, 1617–1623 (1993).

[ADS](#) [CAS](#) [PubMed](#) [PubMed Central](#) [Google Scholar](#)

7. 7.

Grigoli, F. et al. The November 2017 M_w 5.5 Pohang earthquake: a possible case of induced seismicity in South Korea. *Science* **360**, 1003–1006 (2018).

[ADS](#) [CAS](#) [PubMed](#) [PubMed Central](#) [Google Scholar](#)

8. 8.

Deichmann, N. & Giardini, D. Earthquakes induced by the stimulation of an enhanced geothermal system below Basel (Switzerland). *Seismol. Res. Lett.* **80**, 784–798 (2009).

[Google Scholar](#)

9. 9.

Hauksson, E. & Unruh, J. Regional tectonics of the Coso geothermal area along the intracontinental plate boundary in central eastern California: three-dimensional V_p and V_p/V_s models, spatial-temporal seismicity patterns, and seismogenic deformation. *J. Geophys. Res. Solid Earth* **112**, B06309 (2007).

[ADS](#) [Google Scholar](#)

10. 10.

Hauksson, E., Yang, W. & Shearer, P. M. Waveform relocated earthquake catalog for Southern California (1981 to June 2011). *Bull. Seismol. Soc. Am.* **102**, 2239–2244 (2012).

[Google Scholar](#)

11. 11.

Kaven, J. O. Seismicity rate change at the Coso geothermal field following the July 2019 Ridgecrest earthquakes. *Bull. Seismol. Soc. Am.* **110**, 1728–1735 (2020).

[Google Scholar](#)

12. 12.

Blake, K. et al. Updated shallow temperature survey and resource evolution for the Coso geothermal field. In *Proc. World Geotherm. Congr.* (2020).

13. 13.

Bertani, R. World geothermal power generation in the period 2001–2005. *Geothermics* **34**, 651–690 (2005).

[Google Scholar](#)

14. 14.

Fialko, Y. & Simons, M. Deformation and seismicity in the Coso geothermal area, Inyo County, California: observations and modeling using satellite radar interferometry. *J. Geophys. Res. Solid Earth* **105**, 21781–21793 (2000).

[Google Scholar](#)

15. 15.

Reinisch, E. C., Cardiff, M., Kreemer, C., Akerley, J. & Feigl, K. L. Time-series analysis of volume change at Brady Hot Springs, Nevada, USA, using geodetic data from 2003–2018. *J. Geophys. Res. Solid Earth* **125**, B017816 (2020).

[Google Scholar](#)

16. 16.

Wicks, C. W., Thatcher, W., Monastero, F. C. & Hasting, M. A. Steady state deformation of the Coso Range, east central California, inferred from satellite radar interferometry. *J. Geophys. Res. Solid Earth* **106**, 13769–13780 (2001).

[Google Scholar](#)

17. 17.

Blankenship, D. A. et al. *Frontier Observatory for Research in Geothermal Energy: Phase 1 Topical Report West Flank of Coso, CA*. Report No. 1455367, <https://doi.org/10.2172/1455367> (US Department of Energy, 2016).

18. 18.

Goebel, T. H. W. & Brodsky, E. E. The spatial footprint of injection wells in a global compilation of induced earthquake sequences. *Science* **361**, 899–904 (2018).

[ADS](#) [MathSciNet](#) [CAS](#) [PubMed](#) [PubMed Central](#) [MATH](#) [Google Scholar](#)

19. 19.

Goebel, T. H. W., Weingarten, M., Chen, X., Haffener, J. & Brodsky, E. E. The 2016 M_w 5.1 Fairview, Oklahoma earthquakes: evidence for long-range poroelastic triggering at >40 km from fluid disposal wells. *Earth Planet. Sci. Lett.* **472**, 50–61 (2017).

[ADS](#) [CAS](#) [Google Scholar](#)

20. 20.

Sanyal, S., Menzies, A., Granados, E., Sugine, S. & Gentner, R. Long term testing of geothermal wells in the Coso hot springs KGRA. In *Proc. 12th Work. Geotherm. Reserv. Eng.* 37–44 (1987).

21. 21.

Im, K., Elsworth, D., Guglielmi, Y. & Mattioli, G. S. Geodetic imaging of thermal deformation in geothermal reservoirs - production, depletion and fault reactivation. *J. Volcanol. Geotherm. Res.* **338**, 79–91 (2017).

[ADS](#) [CAS](#) [Google Scholar](#)

22. 22.

Rutqvist, J., Wu, Y.-S., Tsang, C.-F. & Bodvarsson, G. A modeling approach for analysis of coupled multiphase fluid flow, heat transfer, and deformation in fractured porous rock. *Int. J. Rock Mech. Min. Sci.* **39**, 429–442 (2002).

[Google Scholar](#)

23. 23.

Segall, P. & Fitzgerald, S. D. A note on induced stress changes in hydrocarbon and geothermal reservoirs. *Tectonophysics* **289**, 117–128 (1998).

[ADS](#) [Google Scholar](#)

24. 24.

Yang, W., Hauksson, E. & Shearer, P. M. Computing a large refined catalog of focal mechanisms for southern California (1981–2010): temporal stability of the style of faulting. *Bull. Seismol. Soc. Am.* **102**, 1179–1194 (2012).

[Google Scholar](#)

25. 25.

Taron, J., Elsworth, D. & Min, K.-B. Numerical simulation of thermal-hydrologic-mechanical-chemical processes in deformable, fractured porous media. *Int. J. Rock Mech. Min. Sci.* **46**, 842–854 (2009).

[Google Scholar](#)

26. 26.

Feng, Q. & Lees, J. M. Microseismicity, stress, and fracture in the Coso geothermal field, California. *Tectonophysics* **289**, 221–238 (1998).

[ADS](#) [Google Scholar](#)

27. 27.

Davatzes, N. C. & Hickman, S. H. Stress and Faulting in the Coso Geothermal Field: Update and Recent Results from the East Flank and Coso Wash. In *Proc. 31st Work. Geotherm. Reserv. Eng.* (2006).

28. 28.

Rose, P. et al. An enhanced geothermal system at Coso, California — recent accomplishments. In *Proc. World Geotherm. Congr.* (2005).

29. 29.

Cooper, H. W. & Simmons, G. The effect of cracks on the thermal expansion of rocks. *Earth Planet. Sci. Lett.* **36**, 404–412 (1977).

[ADS](#) [CAS](#) [Google Scholar](#)

30. 30.

Spane, F. Jr. *Hydrogeologic Investigation of Coso Hot Springs, Inyo County, California*. Report No. 6025, <https://www.ekcrcd.org/files/bcdf564af/Hydrogeologic+Investigation+of+Coso+Hot+Springs.pdf> (Naval Weapons Center, 1978).

31. 31.

MHA Environmental Consulting. *Coso Operating Company Hay Ranch Water Extraction and Delivery System. Conditional Use Permit (CUP 2007-003) Application*. Report No. SCH 2007101002, https://www.inyowater.org/wp-content/uploads/legacy/INDEX_DOCS/Coso%20Hay%20Ranch_FEI_R_Doc_30_08.pdf (2008).

32. 32.

Zarrouk, S. J. & Moon, H. Efficiency of geothermal power plants: a worldwide review. *Geothermics* **51**, 142–153 (2014).

[Google Scholar](#)

33. 33.

Ali, S. T. et al. Geodetic measurements and numerical models of deformation: examples from geothermal fields in the western United States. In *Proc. 41st Work. Geotherm. Reserv. Eng.* (2016).

34. 34.

Wang, K. & Bürgmann, R. Co- and early postseismic deformation due to the 2019 Ridgecrest earthquake sequence constrained by Sentinel-1 and COSMO-SkyMed SAR data. *Seismol. Res. Lett.* **91**, 1998–2009 (2020).

[Google Scholar](#)

35. 35.

Reinisch, E. C., Ali, S. T., Cardiff, M., Kaven, J. O. & Feigl, K. L. Geodetic measurements and numerical models of deformation at Coso geothermal field, California, 2004–2016. *Remote Sens.* **12**, 225 (2020).

[ADS](#) [Google Scholar](#)

36. 36.

Ader, T. J., Lapusta, N., Avouac, J.-P. & Ampuero, J.-P. Response of rate-and-state seismogenic faults to harmonic shear-stress perturbations. *Geophys. J. Int.* **198**, 385–413 (2014).

[ADS](#) [Google Scholar](#)

37. 37.

Dieterich, J. A constitutive law for rate of earthquake production and its application to earthquake clustering. *J. Geophys. Res. Solid Earth* **99**, 2601–2618 (1994).

[Google Scholar](#)

38. 38.

Zhang, Q. et al. Absence of remote earthquake triggering within the Coso and Salton Sea geothermal production fields. *Geophys. Res. Lett.* **44**, 726–733 (2017).

[ADS](#) [Google Scholar](#)

39. 39.

Alfaro-Diaz, R., Velasco, A. A., Pankow, K. L. & Kilb, D. Optimally oriented remote triggering in the Coso geothermal region. *J. Geophys. Res. Solid Earth* **125**, B019131 (2020).

[Google Scholar](#)

40. 40.

Hauksson, E. & Jones, L. M. Seismicity, stress state, and style of faulting of the Ridgecrest-Coso region from the 1930s to 2019: seismotectonics of an evolving plate boundary segment. *Bull. Seismol. Soc. Am.* **110**, 1457–1473 (2020).

[Google Scholar](#)

41. 41.

Kostrov, V. Seismic moment and energy of earthquakes, and seismic flow of rock. *Izv. Acad. Sci. USSR Phys. Solid Earth* **1**, 23–44 (1974).

[MathSciNet](#) [Google Scholar](#)

42. 42.

Cornet, F. H., Helm, J., Poitrenaud, H. & Etchecopar, A. Seismic and aseismic slips induced by large-scale fluid injections. *Pure Appl. Geophys.* **150**, 563–583 (1997).

[ADS](#) [Google Scholar](#)

43. 43.

Guglielmi, Y., Cappa, F., Avouac, J.-P., Henry, P. & Elsworth, D. Seismicity triggered by fluid injection-induced aseismic slip. *Science* **348**, 1224–1226 (2015).

[ADS](#) [CAS](#) [PubMed](#) [PubMed Central](#) [Google Scholar](#)

44. 44.

Wei, S. et al. The 2012 Brawley swarm triggered by injection-induced aseismic slip. *Earth Planet. Sci. Lett.* **422**, 115–125 (2015).

[ADS](#) [CAS](#) [Google Scholar](#)

45. 45.

Cappa, F., Scuderi, M. M., Collettini, C., Guglielmi, Y. & Avouac, J.-P. Stabilization of fault slip by fluid injection in the laboratory and in situ. *Sci. Adv.* **5**, eaau4065 (2019).

[ADS](#) [CAS](#) [PubMed](#) [PubMed Central](#) [Google Scholar](#)

46. 46.

Kwiatek, G. et al. Controlling fluid-induced seismicity during a 6.1-km-deep geothermal stimulation in Finland. *Sci. Adv.* **5**, eaav7224 (2019).

[ADS](#) [PubMed](#) [PubMed Central](#) [Google Scholar](#)

47. 47.

Hillers, G. et al. Noise-based monitoring and imaging of aseismic transient deformation induced by the 2006 Basel reservoir stimulation. *Geophysics* **80**, KS51–KS68 (2015).

[ADS](#) [Google Scholar](#)

48. 48.

Häring, M. O., Schanz, U., Ladner, F. & Dyer, B. C. Characterisation of the Basel 1 enhanced geothermal system. *Geothermics* **37**, 469–495 (2008).

[Google Scholar](#)

49. 49.

Gan, Q. & Elsworth, D. Thermal drawdown and late-stage seismic-slip fault reactivation in enhanced geothermal reservoirs. *J. Geophys. Res. Solid Earth* **119**, 8936–8949 (2014).

[ADS](#) [Google Scholar](#)

50. 50.

Eshelby, J. D. The determination of the elastic field of an ellipsoidal inclusion, and related problems. *Proc. R. Soc. Lond. Ser. A.* **241**, 376–396 (1957)

[ADS](#) [MathSciNet](#) [MATH](#) [Google Scholar](#)

51. 51.

Peaceman, D. W. Interpretation of well-block pressures in numerical reservoir simulation with nonsquare grid blocks and anisotropic permeability. *Soc. Pet. Eng. J.* **23**, 531–543 (1983).

[Google Scholar](#)

52. 52.

Cappa, F. & Rutqvist, J. Modeling of coupled deformation and permeability evolution during fault reactivation induced by deep underground injection of CO₂. *Int. J. Greenh. Gas Control* **5**, 336–346 (2011).

[Google Scholar](#)

53. 53.

Frohlich, C. Triangle diagrams: ternary graphs to display similarity and diversity of earthquake focal mechanisms. *Phys. Earth Planet.*

Inter. **75**, 193–198 (1992).

[ADS](#) [Google Scholar](#)

[Download references](#)

Acknowledgements

This study was supported by the National Science Foundation via the IUCR center Geomechanics and Mitigation of Geohazards (award number 1822214) and via the Southern California Earthquake Center (SCEC). The SCEC is funded by NSF Cooperative Agreement EAR-1600087 and USGS Cooperative Agreement G17AC00047.

Author information

Author notes

1. Elías R. Heimisson

Present address: Swiss Seismological Service, ETH Zurich, Zurich, Switzerland

Affiliations

1. Geology and Planetary Science Division, California Institute of Technology, Pasadena, CA, USA

Kyungjae Im, Jean-Philippe Avouac & Elías R. Heimisson

2. Energy and Mineral Engineering and Geosciences, EMS Energy Institute, Pennsylvania State University, University Park, PA, USA

Derek Elsworth

3. G3 Center, Pennsylvania State University, University Park, PA, USA

Derek Elsworth

Authors

1. Kyungjae Im

[View author publications](#)

You can also search for this author in [PubMed](#) [Google Scholar](#)

2. Jean-Philippe Avouac

[View author publications](#)

You can also search for this author in [PubMed](#) [Google Scholar](#)

3. Elías R. Heimisson

[View author publications](#)

You can also search for this author in [PubMed](#) [Google Scholar](#)

4. Derek Elsworth

[View author publications](#)

You can also search for this author in [PubMed](#) [Google Scholar](#)

Contributions

K.I. carried out the data analysis and numerical simulations. E.R.H. computed the coseismic Coulomb stress changes. D.E. provided the simulator TOUGH–FLAC. K.I. and J.-P.A. designed the study and wrote the Article. All authors edited the manuscript.

Corresponding author

Correspondence to [Kyungjae Im](#).

Ethics declarations

Competing interests

The authors declare no competing interests.

Additional information

Peer review information *Nature* thanks Roland Burgmann, J. Ole Kaven and the other, anonymous, reviewer(s) for their contribution to the peer review of this work.

Publisher's note Springer Nature remains neutral with regard to jurisdictional claims in published maps and institutional affiliations.

Extended data figures and tables

[Extended Data Fig. 1 Seismicity before and after the Ridgecrest mainshock \(5 July 2019\) in and around the Coso area.](#)

We divided the area into different domains. **a–d**, Relocated seismicity¹⁰ of all magnitude, before (2010 to the $M_w = 7.1$ mainshock; grey circles) and after ($M_w = 7.1$ mainshock to the end of 2019; blue circles) the Ridgecrest earthquake. **a–h**, We compare the spatial distribution (**a–d**) and cumulative magnitude–frequency distribution (**e–h**) of earthquakes before (black) and after (blue) the mainshock for the Coso volcanic area (**a, e**), Cactus flat (**b, f**), Coso geothermal field (**c, g**) and the northwest edge of the $M_w = 7.1$ event (**d, h**). Red rectangles in **a** define the areas for each plot. Black triangles in **c** indicate the locations of geothermal wells. The density of aftershocks above the detection threshold ($M_w > 1$) is about two orders of magnitude lower in the Coso geothermal field (**c**) than in the surrounding areas (**b, d**). A similar result has been reported previously⁴.

[Extended Data Fig. 2 History of seismicity in the Coso area.](#)

a, Distribution of seismicity ($M_w > 1$)¹⁰. **b**, Seismicity history over the entire Coso area. **c–f**, Seismicity history of event magnitude (circles; left axis) and annual rate (black line; right axis) for each fault zone (**c–e**, Coso main field; **f**, east flank area), as indicated in **a**. The fault zones are selected on the basis of the expression of the seismic cloud.

Extended Data Fig. 3 Change of focal mechanism in the Coso main field area and effective stress changes predicted by the simulation.

a, The rake angle shows that the proportion of normal faulting (-120° to about -60°) increases with time. **b**, **c**, Ternary plots⁵³ show that the formal mechanism is more diverse, with increased normal faulting in the later operation period (2001–2019; **c**) than in the earlier period (1981–2000; **b**). **d–f**, Time-dependent maximum horizontal (red), minimum horizontal (blue) and vertical (black) stress at different depths, calculated as an average along a 1-km baseline at the centre of the reservoir at each depth (**d**, 1,000 m; **e**, 1,500 m; **f**, 1,750 m). The stresses within the reservoir (**e**, **f**) decline with time, but the rate of decline in vertical stress is lower than that in maximum horizontal stress. The simulation predicts an increase in the proportion of normal faulting and diversity of focal mechanism, as observed in **a–c**.

Extended Data Fig. 4 Model description.

Blue, dark green and light green blocks represent the reservoir, upper host and lower host elements, respectively. The right-hand side shows the repeating five-spot pattern of injectors (triangles) and producers (circles). Inset, initial horizontal stresses (σ_1 , maximum; σ_3 , minimum) calculated from Coso field data (Fig. 1a, inset). Vertical stress (σ_v) is calculated as gravitational stress for an effective density of $1,400 \text{ kg m}^{-3}$ at every time step. The x axis is chosen to be parallel to the dominant fault orientation in the main field (Fig. 1a, inset), which is parallel to the main fault ruptured in the $M_w = 7.1$ Ridgecrest earthquake. Roller and shear stress boundaries are applied corresponding to the initial stress, as shown in the inset. The ground surface is stress-free.

Extended Data Fig. 5 Simulation results with lower flow rate.

This simulation result is identical to that shown in Fig. 2, but with a lower flow rate, set to match the injection rate via permeability reduction. Other parameters are identical to our reference simulation (Fig. 2). **a**, Reported injection and production flow rates from the Coso field (thin lines) and simulation (bold lines). **b**, Ground deformation recovered from InSAR measurements between May 1996 and June 1998¹⁴. Image adapted with permission from ref. ¹⁴, American Geophysical Union. **c**, Cumulative line-of-sight (LOS) surface displacement at the end of the simulation (year 30). The white arrow shows the line-of-sight unit vector (0.38, -0.09, 0.92)¹⁴. **d**, Time evolution of maximum line-of-sight displacement (black line) and observations (blue solid lines)^{14,33,34}, along with their extrapolations (blue dashed lines). **e**, Shear stress at the end of the simulation (year 30) in the orientation parallel to the $M_w = 7.1$ rupture in the reservoir area (inset).

Extended Data Fig. 6 Well bore and reservoir pressure.

a, Pressure change at well bores (black straight line) and well blocks (the block where the imaginary well bore is embedded; coloured lines). The pressure gap between the well bore and well block is larger at injection than at production, owing to the low temperature and consequent low fluid viscosity. **b**, Pressure drop distribution at the end of the simulation. The white rectangle indicates the $4 \text{ km} \times 4 \text{ km} \times 3 \text{ km}$ reservoir area. The pressure drops by around 5.5 MPa in the reservoir, and the halo of pressure drop extends beyond the reservoir area.

Extended Data Fig. 7 Predicted surface displacements at the end of the reference simulation.

a-d, Displacement along the x (**a**), y (**b**) and z (**c**) axes and line-of-sight displacement (**d**; identical to Fig. 2e). The white arrow denotes the azimuth of the line-of-sight vector (0.38, -0.09, 0.92)¹⁴.

Extended Data Fig. 8 Predicted surface deformation due to changes in pore pressure alone.

a, Line-of-sight surface displacement recovered from InSAR measurements between May 1996 and June 1998 (identical to Fig. 2d). Image adapted with permission from ref. 14, American Geophysical Union. **b**, Predicted line-of-sight surface displacement at the end of the isothermal simulation. All parameters are identical to those for the reference simulation (Fig. 2), which accounts for thermal strain. **c**, Time evolution of maximum line-of-sight displacement of the isothermal (red) and non-isothermal (black; Fig. 2f) simulations, together with observations (blue solid lines)^{14,33,34} and their interpolations (blue dashed lines). The ‘no thermal stress case’ represents the subsidence from pressure depletion alone. **d**, Observed and predicted ground displacements projected along the line of sight (arrow in b) of the InSAR images^{14,33}. The black solid line are from our reference simulation (Fig. 2); the red solid line is from the isothermal simulation (no thermal strain). The curves are normalized by the maximum displacement of about 65 cm and about 35 cm for the reference and no-thermal-stress cases, respectively (c). The case from ref. 14 is measured between September 1993 and May 1996, with a maximum displacement of about 8 cm (west–east) and about 5 cm (south–north); the case from ref. 33 is measured between February 2008 and October 2009, with a maximum displacement of around 2 cm.

Extended Data Fig. 9 Predicted stress changes in a simulation with reduced friction.

The simulation geometry and parameters are identical to those for the reference simulation (Fig. 3), except for a lower internal friction coefficient of 0.3. **a**, Change in Coulomb stress at the end of the simulation (year 30), calculated for faults parallel to the main rupture (inset). **b**, Shear stress at the end of the simulation (year 30). Shear stress in the reservoir area (white rectangle) is strongly depleted owing to rock failure. **c**, Mohr circle representation of stress changes during the simulation. Maximum and minimum effective normal stress are calculated at the centre of the reservoir (stresses averaged along the yellow line in b). The Mohr circle at year 0 is smaller than for the higher friction cases (Fig. 3c) owing to initial failure. The grey dashed line indicates the input failure criteria in this simulation. **d**,

Change in shear stress at the centre of the reservoir (averaged along the yellow line in **b**).

Extended Data Fig. 10 Comparison between fully elastic and Mohr–Coulomb failure models.

a, As in Fig. 3c. **b**, As in **a**, except that the reservoir is fully elastic (no failure). When the reservoir is fully elastic (that is, when failure and the resulting drop in stress are neglected), normal stresses become impossibly large in tension. **c**, **d** Evolution of normal and shear stress relative to the orientation of the Ridgecrest fault (Extended Data Fig. 4, inset) at a depth of 1,500 m, for the Mohr–Coulomb failure model (**c**) the fully elastic model (**d**). With the failure model (**c**), the stresses naturally approach zero over time, as a result of shear and tensile failure; in the fully elastic case (**d**), normal stresses transit through zero and become highly tensile when the shear stress drops, as a result of failure being ignored. The wiggles in the well pattern area of the reservoir are due to the non-uniform distribution of temperature driving differential thermal stresses.

Extended Data Fig. 11 Cumulative shear strain at the conclusion of the reference simulation (after 30 years of production).

The largest change in strain occurs in the well pattern area, where the change in temperature is largest. The maximum shear strain is about 1.1×10^{-3} , which is approximately two orders of magnitude larger than the strain released by seismicity, as estimated from the sum of all seismic moments (see text).

Extended Data Table 1 Simulation model parameters [Full size table](#)

Source data

[Source Data Fig. 1](#)

Source Data Fig. 2

Source Data Fig. 3

Rights and permissions

Reprints and Permissions

About this article



Check for
updates

Cite this article

Im, K., Avouac, JP., Heimisson, E.R. *et al.* Ridgecrest aftershocks at Coso suppressed by thermal destressing. *Nature* **595**, 70–74 (2021).
<https://doi.org/10.1038/s41586-021-03601-4>

Download citation

- Received: 28 June 2020
- Accepted: 30 April 2021
- Published: 30 June 2021
- Issue Date: 01 July 2021
- DOI: <https://doi.org/10.1038/s41586-021-03601-4>

Access through your institution

Change institution

Buy or subscribe

Advertisement

This article was downloaded by **calibre** from <https://www.nature.com/articles/s41586-021-03601-4>

| [Section menu](#) | [Main menu](#) |

- Article
- [Published: 23 June 2021](#)

Limited potential for bird migration to disperse plants to cooler latitudes

- [Juan P. González-Varo](#) [ORCID: orcid.org/0000-0003-1439-6475¹](#),
- [Beatrix Rumeu¹](#),
- [Jörg Albrecht](#) [ORCID: orcid.org/0000-0002-9708-9413²](#),
- [Juan M. Arroyo³](#),
- [Rafael S. Bueno](#) [ORCID: orcid.org/0000-0001-8964-8572⁴](#),
- [Tamara Burgos⁵](#),
- [Luís P. da Silva](#) [ORCID: orcid.org/0000-0003-2358-1277⁶](#),
- [Gema Escribano-Ávila⁷](#),
- [Nina Farwig⁸](#),
- [Daniel García⁹](#),
- [Ruben H. Heleno¹⁰](#),
- [Juan C. Illera⁹](#),
- [Pedro Jordano](#) [ORCID: orcid.org/0000-0003-2142-9116³](#),
- [Przemysław Kurek¹¹](#),
- [Benno I. Simmons](#) [ORCID: orcid.org/0000-0002-2751-9430¹²](#),
- [Emilio Virgós⁵](#),
- [William J. Sutherland¹³](#) &
- [Anna Traveset⁷](#)

Nature volume 595, pages 75–79 (2021) [Cite this article](#)

- 2391 Accesses

- 400 Altmetric
- [Metrics details](#)

Subjects

- [Climate-change ecology](#)
- [Community ecology](#)
- [Ecological networks](#)

Abstract

Climate change is forcing the redistribution of life on Earth at an unprecedented velocity^{1,2}. Migratory birds are thought to help plants to track climate change through long-distance seed dispersal^{3,4}. However, seeds may be consistently dispersed towards cooler or warmer latitudes depending on whether the fruiting period of a plant species coincides with northward or southward migrations. Here we assess the potential of plant communities to keep pace with climate change through long-distance seed dispersal by migratory birds. To do so, we combine phenological and migration information with data on 949 seed-dispersal interactions between 46 bird and 81 plant species from 13 woodland communities across Europe. Most of the plant species (86%) in these communities are dispersed by birds migrating south, whereas only 35% are dispersed by birds migrating north; the latter subset is phylogenetically clustered in lineages that have fruiting periods that overlap with the spring migration. Moreover, the majority of this critical dispersal service northwards is provided by only a few Palaearctic migrant species. The potential of migratory birds to assist a small, non-random sample of plants to track climate change latitudinally is expected to strongly influence the formation of novel plant communities, and thus affect their ecosystem functions and community assembly at higher trophic levels.

Access options

Subscribe to Journal

Get full journal access for 1 year

\$199.00

only \$3.90 per issue

[Subscribe](#)

All prices are NET prices.

VAT will be added later in the checkout.

Tax calculation will be finalised during checkout.

Rent or Buy article

Get time limited or full article access on ReadCube.

from \$8.99

[Rent or Buy](#)

All prices are NET prices.

Additional access options:

- [Log in](#)
- [Access through your institution](#)
- [Learn about institutional subscriptions](#)

Fig. 1: Location of the 13 European seed-dispersal networks we studied, and network with bird–plant interactions in relation to bird migration.

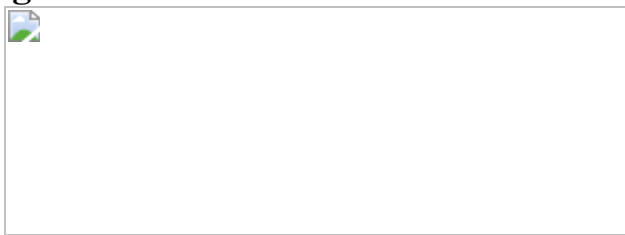


Fig. 2: Seed-dispersal interactions of plants with migratory birds in relation to southward and northward migration and Mediterranean or

temperate biome.

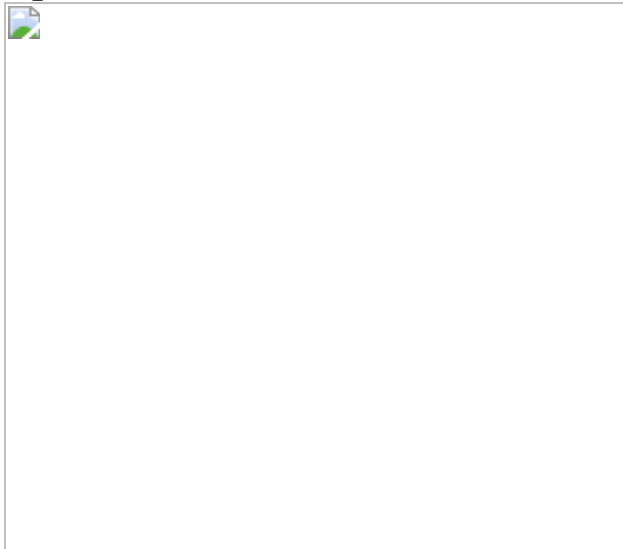
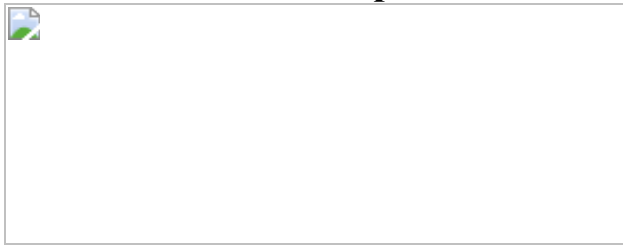


Fig. 3: Relevance of Palaearctic and Afro-Palaearctic migratory birds dispersing seeds during their southward and northward migration in Mediterranean and temperate communities.



Data availability

All data used in the analyses are available through the Dryad Digital Repository (<https://doi.org/10.5061/dryad.15dv41nx3>). The dated phylogeny of seed plants (Spermatophyta) used to obtain our phylogenetic tree is available through GitHub (https://github.com/FePhyFoFum/big_seed_plant_trees/releases). Data on bird body weight used for size classification (Supplementary Fig. 2) were obtained from EltonTraits 1.0 available through Figshare (<https://doi.org/10.6084/m9.figshare.c.3306933>).

Code availability

The R scripts used to generate all results and figures are available through the Dryad Digital Repository (<https://doi.org/10.5061/dryad.15dv41nx3>).

References

1. 1.

Pecl, G. T. et al. Biodiversity redistribution under climate change: impacts on ecosystems and human well-being. *Science* **355**, eaai9214 (2017).

[Google Scholar](#)

2. 2.

Diffenbaugh, N. S. & Field, C. B. Changes in ecologically critical terrestrial climate conditions. *Science* **341**, 486–492 (2013).

[ADS](#) [CAS](#) [Google Scholar](#)

3. 3.

Viana, D. S., Santamaría, L. & Figuerola, J. Migratory birds as global dispersal vectors. *Trends Ecol. Evol.* **31**, 763–775 (2016).

[Google Scholar](#)

4. 4.

Bauer, S. & Hoyer, B. J. Migratory animals couple biodiversity and ecosystem functioning worldwide. *Science* **344**, 1242552 (2014).

[CAS](#) [Google Scholar](#)

5. 5.

Corlett, R. T. & Westcott, D. A. Will plant movements keep up with climate change? *Trends Ecol. Evol.* **28**, 482–488 (2013).

[Google Scholar](#)

6. 6.

Lenoir, J. & Svenning, J. C. Climate-related range shifts – a global multidimensional synthesis and new research directions. *Ecography* **38**, 15–28 (2015).

[Google Scholar](#)

7. 7.

Lenoir, J. et al. Species better track climate warming in the oceans than on land. *Nat. Ecol. Evol.* **4**, 1044–1059 (2020).

[Google Scholar](#)

8. 8.

Loarie, S. R. et al. The velocity of climate change. *Nature* **462**, 1052–1055 (2009).

[ADS](#) [CAS](#) [Google Scholar](#)

9. 9.

Chen, I.-C., Hill, J. K., Ohlemüller, R., Roy, D. B. & Thomas, C. D. Rapid range shifts of species associated with high levels of climate warming. *Science* **333**, 1024–1026 (2011).

[ADS](#) [CAS](#) [Google Scholar](#)

10. 10.

González-Varo, J. P., López-Bao, J. V. & Guitián, J. Seed dispersers help plants to escape global warming. *Oikos* **126**, 1600–1606 (2017).

[Google Scholar](#)

11. 11.

Urban, M. C. et al. Improving the forecast for biodiversity under climate change. *Science* **353**, aad8466 (2016).

[PubMed](#) [PubMed Central](#) [Google Scholar](#)

12. 12.

Thuiller, W. et al. Predicting global change impacts on plant species' distributions: future challenges. *Perspect. Plant Ecol. Evol. Syst.* **9**, 137–152 (2008).

[Google Scholar](#)

13. 13.

Nadeau, C. P. & Urban, M. C. Eco-evolution on the edge during climate change. *EcoGraphy* **42**, 1280–1297 (2019).

[Google Scholar](#)

14. 14.

Bacles, C. F. E., Lowe, A. J. & Ennos, R. A. Effective seed dispersal across a fragmented landscape. *Science* **311**, 628 (2006).

[Google Scholar](#)

15. 15.

Jordano, P., García, C., Godoy, J. A. & García-Castaño, J. L. Differential contribution of frugivores to complex seed dispersal patterns. *Proc. Natl Acad. Sci. USA* **104**, 3278–3282 (2007).

[ADS](#) [CAS](#) [PubMed](#) [PubMed Central](#) [Google Scholar](#)

16. 16.

Breitbach, N., Böhning-Gaese, K., Laube, I. & Schleuning, M. Short seed-dispersal distances and low seedling recruitment in farmland populations of bird-dispersed cherry trees. *J. Ecol.* **100**, 1349–1358 (2012).

[Google Scholar](#)

17. 17.

Cain, M. L., Damman, H. & Muir, A. Seed dispersal and the Holocene migration of woodland herbs. *Ecol. Monogr.* **68**, 325–347 (1998).

[Google Scholar](#)

18. 18.

Nathan, R. et al. Spread of North American wind-dispersed trees in future environments. *Ecol. Lett.* **14**, 211–219 (2011).

[Google Scholar](#)

19. 19.

Nathan, R. et al. Mechanisms of long-distance seed dispersal. *Trends Ecol. Evol.* **23**, 638–647 (2008).

[Google Scholar](#)

20. 20.

Viana, D. S., Gangoso, L., Bouten, W. & Figuerola, J. Overseas seed dispersal by migratory birds. *Proc. R. Soc. Lond. B* **283**, 20152406 (2016).

[Google Scholar](#)

21. 21.

Viana, D. S., Santamaría, L., Michot, T. C. & Figuerola, J. Migratory strategies of waterbirds shape the continental-scale dispersal of aquatic organisms. *Ecography* **36**, 430–438 (2013).

[Google Scholar](#)

22. 22.

Carlquist, S. The biota of long-distance dispersal. V. Plant dispersal to Pacific islands. *Bull. Torrey Bot. Club* **94**, 129–162 (1967).

[Google Scholar](#)

23. 23.

Esteves, C. F., Costa, J. M., Vargas, P., Freitas, H. & Heleno, R. H. On the limited potential of Azorean fleshy fruits for oceanic dispersal. *PLoS ONE* **10**, e0138882 (2015).

[PubMed](#) [PubMed Central](#) [Google Scholar](#)

24. 24.

Viana, D. S., Santamaría, L., Michot, T. C. & Figuerola, J. Allometric scaling of long-distance seed dispersal by migratory birds. *Am. Nat.* **181**, 649–662 (2013).

[Google Scholar](#)

25. 25.

Martínez-López, V., García, C., Zapata, V., Robledano, F. & De la Rúa, P. Intercontinental long-distance seed dispersal across the Mediterranean basin explains population genetic structure of a bird-dispersed shrub. *Mol. Ecol.* **29**, 1408–1420 (2020).

[Google Scholar](#)

26. 26.

Newton, I. *The Migration Ecology of Birds* (Elsevier, 2010).

27. 27.

Sorensen, A. E. Interactions between birds and fruit in a temperate woodland. *Oecologia* **50**, 242–249 (1981).

[ADS](#) [CAS](#) [Google Scholar](#)

28. 28.

González-Varo, J. P., Arroyo, J. M. & Jordano, P. The timing of frugivore-mediated seed dispersal effectiveness. *Mol. Ecol.* **28**, 219–231 (2019).

[PubMed](#) [PubMed Central](#) [Google Scholar](#)

29. 29.

Jordano, P. in *Seeds: The Ecology of Regeneration of Plant Communities* (ed. Gallagher, R. S.) 18–61 (CABI, 2014).

30. 30.

Bascompte, J. & Jordano, P. *Mutualistic Networks* (Princeton Univ. Press, 2013).

31. 31.

Gallinat, A. S. et al. Patterns and predictors of fleshy fruit phenology at five international botanical gardens. *Am. J. Bot.* **105**, 1824–1834 (2018).

[Google Scholar](#)

32. 32.

Cadotte, M. W. Experimental evidence that evolutionarily diverse assemblages result in higher productivity. *Proc. Natl Acad. Sci. USA*

110, 8996–9000 (2013).

[ADS](#) [CAS](#) [PubMed](#) [PubMed Central](#) [Google Scholar](#)

33. 33.

Mitter, C., Farrell, B. & Futuyma, D. J. Phylogenetic studies of insect–plant interactions: insights into the genesis of diversity. *Trends Ecol. Evol.* **6**, 290–293 (1991).

[CAS](#) [PubMed](#) [PubMed Central](#) [Google Scholar](#)

34. 34.

Siemann, E., Tilman, D., Haarstad, J. & Ritchie, M. Experimental tests of the dependence of arthropod diversity on plant diversity. *Am. Nat.* **152**, 738–750 (1998).

[CAS](#) [PubMed](#) [PubMed Central](#) [Google Scholar](#)

35. 35.

Sanderson, F. J., Donald, P. F., Pain, D. J., Burfield, I. J. & van Bommel, F. P. J. Long-term population declines in Afro-Palearctic migrant birds. *Biol. Conserv.* **131**, 93–105 (2006).

[Google Scholar](#)

36. 36.

Beresford, A. E. et al. Phenology and climate change in Africa and the decline of Afro-Palearctic migratory bird populations. *Remote Sens. Ecol. Conserv.* **5**, 55–69 (2019).

[Google Scholar](#)

37. 37.

Nilsson, C., Bäckman, J. & Alerstam, T. Seasonal modulation of flight speed among nocturnal passerine migrants: differences between short- and long-distance migrants. *Behav. Ecol. Sociobiol.* **68**, 1799–1807 (2014).

[Google Scholar](#)

38. 38.

Gaston, K. J. Valuing common species. *Science* **327**, 154–155 (2010).

[ADS](#) [CAS](#) [PubMed](#) [PubMed Central](#) [Google Scholar](#)

39. 39.

Horton, K. G. et al. Phenology of nocturnal avian migration has shifted at the continental scale. *Nat. Clim. Change* **10**, 63–68 (2020).

[ADS](#) [Google Scholar](#)

40. 40.

Miller-Rushing, A. J., Lloyd-Evans, T. L., Primack, R. B. & Satzinger, P. Bird migration times, climate change, and changing population sizes. *Glob. Change Biol.* **14**, 1959–1972 (2008).

[ADS](#) [Google Scholar](#)

41. 41.

Brochet, A.-L. et al. Preliminary assessment of the scope and scale of illegal killing and taking of birds in the Mediterranean. *Bird Conserv. Int.* **26**, 1–28 (2016).

[Google Scholar](#)

42. 42.

Kays, R., Crofoot, M. C., Jetz, W. & Wikelski, M. Terrestrial animal tracking as an eye on life and planet. *Science* **348**, aaa2478 (2015).

[Google Scholar](#)

43. 43.

Stiles, E. W. Patterns of fruit presentation and seed dispersal in bird-disseminated woody plants in the eastern deciduous forest. *Am. Nat.* **116**, 670–688 (1980).

[Google Scholar](#)

44. 44.

Noma, N. & Yumoto, T. Fruiting phenology of animal-dispersed plants in response to winter migration of frugivores in a warm temperate forest on Yakushima Island, Japan. *Ecol. Res.* **12**, 119–129 (1997).

[Google Scholar](#)

45. 45.

Lovas-Kiss, Á. et al. Shorebirds as important vectors for plant dispersal in Europe. *Ecography* **42**, 956–967 (2019).

[Google Scholar](#)

46. 46.

Coughlan, N. E., Kelly, T. C., Davenport, J. & Jansen, M. A. K. Up, up and away: bird-mediated ectozoochorous dispersal between aquatic environments. *Freshw. Biol.* **62**, 631–648 (2017).

[Google Scholar](#)

47. 47.

Olson, D. M. et al. Terrestrial ecoregions of the world: a new map of life on Earth: a new global map of terrestrial ecoregions provides an innovative tool for conserving biodiversity. *Bioscience* **51**, 933–938 (2001).

[Google Scholar](#)

48. 48.

Rivas-Martínez, S., Penas, A. & Díaz, T. *Bioclimatic Map of Europe, Thermoclimatic Belts* (Cartographic Service, Univ. León, 2004).

49. 49.

Olesen, J. M. et al. Missing and forbidden links in mutualistic networks. *Proc. R. Soc. Lond. B* **278**, 725–732 (2011).

[Google Scholar](#)

50. 50.

Snow, B. & Snow, D. *Birds and Berries* (T. and A. D. Poyser, 1988).

51. 51.

Stiebel, H. & Bairlein, F. Frugivory in central European birds I: diet selection and foraging. *Vogelwarte* **46**, 1–23 (2008).

[Google Scholar](#)

52. 52.

González-Varo, J. P., Arroyo, J. M. & Jordano, P. Who dispersed the seeds? The use of DNA barcoding in frugivory and seed dispersal studies. *Methods Ecol. Evol.* **5**, 806–814 (2014).

[Google Scholar](#)

53. 53.

Simmons, B. I. et al. Moving from frugivory to seed dispersal: incorporating the functional outcomes of interactions in plant–frugivore networks. *J. Anim. Ecol.* **87**, 995–1007 (2018).

[PubMed](#) [PubMed Central](#) [Google Scholar](#)

54. 54.

Plein, M. et al. Constant properties of plant–frugivore networks despite fluctuations in fruit and bird communities in space and time. *Ecology* **94**, 1296–1306 (2013).

[PubMed](#) [PubMed Central](#) [Google Scholar](#)

55. 55.

Albrecht, J. et al. Variation in neighbourhood context shapes frugivore-mediated facilitation and competition among co-dispersed plant species. *J. Ecol.* **103**, 526–536 (2015).

[Google Scholar](#)

56. 56.

García, D. Birds in ecological networks: insights from bird–plant mutualistic interactions. *Ardeola* **63**, 151–180 (2016).

[Google Scholar](#)

57. 57.

Farwig, N., Schabo, D. G. & Albrecht, J. Trait-associated loss of frugivores in fragmented forest does not affect seed removal rates. *J. Ecol.* **105**, 20–28 (2017).

[Google Scholar](#)

58. 58.

Torroba Balmori, P., Zaldívar García, P. & Hernández Lázaro, Á.
Semillas de Frutos Carnosos del Norte Ibérico: Guía de Identificación
(Ediciones Univ. Valladolid, 2013).

59. 59.

Stiebel, H. *Frugivorie bei Mitteleuropäischen Vögeln*. PhD thesis,
Univ. Oldenburg (2003).

60. 60.

Jordano, P. Data from: Angiosperm fleshy fruits and seed dispersers: a comparative analysis of adaptation and constraints in plant-animal interactions. *Dryad* <https://doi.org/10.5061/dryad.9tb73> (2013).

61. 61.

González-Varo, J. P., Carvalho, C. S., Arroyo, J. M. & Jordano, P. Unravelling seed dispersal through fragmented landscapes: frugivore species operate unevenly as mobile links. *Mol. Ecol.* **26**, 4309–4321 (2017).

[Google Scholar](#)

62. 62.

Ratnasingham, S. & Hebert, P. D. N. bold: the Barcode of Life data system (<http://www.barcodinglife.org>). *Mol. Ecol. Notes* **7**, 355–364 (2007).

[CAS](#) [PubMed](#) [PubMed Central](#) [Google Scholar](#)

63. 63.

CBOL Plant Working Group et al. A DNA barcode for land plants. *Proc. Natl Acad. Sci. USA* **106**, 12794–12797 (2009).

[PubMed](#) [PubMed Central](#) [Google Scholar](#)

64. 64.

Altschul, S. F. et al. Gapped BLAST and PSI-BLAST: a new generation of protein database search programs. *Nucleic Acids Res.* **25**, 3389–3402 (1997).

[CAS](#) [PubMed](#) [PubMed Central](#) [Google Scholar](#)

65. 65.

González-Varo, J. P., Díaz-García, S., Arroyo, J. M. & Jordano, P. Seed dispersal by dispersing juvenile animals: a source of functional connectivity in fragmented landscapes. *Biol. Lett.* **15**, 20190264 (2019).

[PubMed](#) [PubMed Central](#) [Google Scholar](#)

66. 66.

Fuentes, M. Latitudinal and elevational variation in fruiting phenology among western European bird-dispersed plants. *Ecography* **15**, 177–183 (1992).

[Google Scholar](#)

67. 67.

Herrera, C. M. A study of avian frugivores, bird-dispersed plants, and their interaction in Mediterranean scrublands. *Ecol. Monogr.* **54**, 1–23 (1984).

[Google Scholar](#)

68. 68.

Hampe, A. & Bairlein, F. Modified dispersal-related traits in disjunct populations of bird-dispersed *Frangula alnus* (Rhamnaceae): a result of its Quaternary distribution shifts? *Ecography* **23**, 603–613 (2000).

[Google Scholar](#)

69. 69.

Thomas, P. A. & Mukassabi, T. A. Biological flora of the British Isles: *Ruscus aculeatus*. *J. Ecol.* **102**, 1083–1100 (2014).

[Google Scholar](#)

70. 70.

Jordano, P. Biología de la reproducción de tres especies del género *Lonicera* (Caprifoliaceae) en la Sierra de Cazorla. *An. Jardín Botánico Madr.* 1979 **48**, 31–52 (1990).

[Google Scholar](#)

71. 71.

Debussche, M. & Isenmann, P. A Mediterranean bird disperser assemblage: composition and phenology in relation to fruit availability. *Rev. Ecol.* **47**, 411–432 (1992).

[Google Scholar](#)

72. 72.

Jordano, P. Diet, fruit choice and variation in body condition of frugivorous warblers in Mediterranean scrubland. *Ardea* **76**, 193–209 (1988).

[Google Scholar](#)

73. 73.

Barroso, Á., Amor, F., Cerdá, X. & Boulay, R. Dispersal of non-myrmecochorous plants by a “keystone disperser” ant in a Mediterranean habitat reveals asymmetric interdependence. *Insectes Soc.* **60**, 75–86 (2013).

[Google Scholar](#)

74. 74.

González-Varo, J. P. Fragmentation, habitat composition and the dispersal/predation balance in interactions between the Mediterranean myrtle and avian frugivores. *Ecography* **33**, 185–197 (2010).

[Google Scholar](#)

75. 75.

Sánchez-Salcedo, E. M., Martínez-Nicolás, J. J. & Hernández, F. Phenological growth stages of mulberry tree (*Morus* sp.) codification and description according to the BBCH scale. *Ann. Appl. Biol.* **171**, 441–450 (2017).

[Google Scholar](#)

76. 76.

García-Castaño, J. L. *Consecuencias Demográficas de la Dispersión de Semillas por Aves y Mamíferos Frugívoros en la Vegetación Mediterránea de Montaña*. PhD thesis, Univ. Sevilla (2001).

77. 77.

Gilbert, O. L. *Symporicarpos albus* (L.) S. F. Blake (*S. rivularis* Suksd., *S. racemosus* Michaux). *J. Ecol.* **83**, 159–166 (1995).

[Google Scholar](#)

78. 78.

Billerman, S. M. et al. (eds) *Birds of the World* (Cornell Laboratory of Ornithology, 2020).

79. 79.

Tellería, J., Asensio, B. & Díaz, M. *Aves Ibéricas: II. Paseriformes* (J. M. Reyero Editor, 1999).

80. 80.

Díaz, M., Asensio, B. & Tellería, J. L. *Aves Ibéricas: I. No paseriformes* (J. M. Reyero Editor, 1996).

81. 81.

SEO/Birdlife. *La Enciclopedia de las Aves de España* (SEO/Birdlife-Fundación BBVA, 2019).

82. 82.

Spina, F. & Volponi, S. *Atlante della Migrazione degli Uccelli in Italia. 2. Passeriformi* (Ministero dell'Ambiente e della Tutela del Territorio e del Mare, Istituto Superiore per la Protezione e la Ricerca Ambientale (ISPRA), Tipografia SCR-Roma, 2008).

83. 83.

Spina, F. & Volponi, S. *Atlante della Migrazione degli Uccelli in Italia. 1. Non-Passeriformi* (Ministero dell'Ambiente e della Tutela del Territorio e del Mare, Istituto Superiore per la Protezione e la Ricerca Ambientale (ISPRA), Tipografia CSR-Roma, 2008).

84. 84.

Wernham, C. et al. *The Migration Atlas: Movements of the Birds of Britain and Ireland* (T. & A. D. Poyser, 2002).

85. 85.

Cramp, S. *The Complete Birds of the Western Palearctic (CD-ROM)* (Oxford Univ. Press, 1998).

86. 86.

Bairlein, F. et al. *Atlas des Vogelzugs - Ringfunde deutscher Brut- und Gastvögel* (Aula, 2014).

87. 87.

Tomiałojć, L. & Stawarczyk, T. *Awifauna Polski: Rozmieszczenie, Liczebność i Zmiany* (PTPP pro. Natura, 2003).

88. 88.

Busse, P., Gromadzki, M. & Szulc, B. Obserwacje przelotu jesiennego ptaków w roku 1960 w Górkach Wschodnich koło Gdańska
(Observations on bird migration at Górkach Wschodnich near Gdańsk Autumn 1960). *Acta Ornithologica* **7**, 305–336 (1963).

[Google Scholar](#)

89. 89.

Bobrek, R. et al. Międzysezonowa powtarzalność dynamiki jesiennej migracji wróblowych Passeriformes nad Jeziorem Rakutowskim. *Ornis Polonica* **57**, 39–57 (2016).

[Google Scholar](#)

90. 90.

Keller, M. et al. *Ptaki Środkowej Wisły* (M-ŚTO, 2017).

91. 91.

Bocheński, M. et al. Awifauna przelotna i zimująca środkowego odcinka doliny Odry. *Ptaki Śląska* **16**, 123–161 (2006).

[Google Scholar](#)

92. 92.

BTO. BirdTrack. <http://www.birdtrack.net> (accessed October 2018).

93. 93.

Brooks, M. E. et al. glmmTMB balances speed and flexibility among packages for zero-inflated generalized linear mixed modeling. *R J.* **9**, 378–400 (2017).

[Google Scholar](#)

94. 94.

Fox, J. & Weisberg, S. *An R Companion to Applied Regression* 2nd edn (SAGE, 2011).

95. 95.

Douma, J. C. & Weedon, J. T. Analysing continuous proportions in ecology and evolution: a practical introduction to beta and Dirichlet regression. *Methods Ecol. Evol.* **10**, 1412–1430 (2019).

[Google Scholar](#)

96. 96.

Smith, S. A. & Brown, J. W. Constructing a broadly inclusive seed plant phylogeny. *Am. J. Bot.* **105**, 302–314 (2018).

[Google Scholar](#)

97. 97.

Magallón, S., Gómez-Acevedo, S., Sánchez-Reyes, L. L. & Hernández-Hernández, T. A metacalibrated time-tree documents the early rise of flowering plant phylogenetic diversity. *New Phytol.* **207**, 437–453 (2015).

[PubMed](#) [PubMed Central](#) [Google Scholar](#)

98. 98.

Paradis, E. & Schliep, K. ape 5.0: an environment for modern phylogenetics and evolutionary analyses in R. *Bioinformatics* **35**, 526–528 (2019).

[CAS](#) [PubMed](#) [PubMed Central](#) [Google Scholar](#)

99. 99.

Pagel, M. Inferring the historical patterns of biological evolution. *Nature* **401**, 877–884 (1999).

[ADS](#) [CAS](#) [Google Scholar](#)

100. 100.

Freckleton, R. P., Harvey, P. H. & Pagel, M. Phylogenetic analysis and comparative data: a test and review of evidence. *Am. Nat.* **160**, 712–726 (2002).

[CAS](#) [Google Scholar](#)

101. 101.

Molina-Venegas, R. & Rodríguez, M. Á. Revisiting phylogenetic signal; strong or negligible impacts of polytomies and branch length information? *BMC Evol. Biol.* **17**, 53 (2017).

[PubMed](#) [PubMed Central](#) [Google Scholar](#)

102. 102.

Revell, L. J. phytools: an R package for phylogenetic comparative biology (and other things). *Methods Ecol. Evol.* **3**, 217–223 (2012).

[Google Scholar](#)

103. 103.

Dormann, C. F., Fründ, J., Blüthgen, N. & Gruber, B. Indices, graphs and null models: analyzing bipartite ecological networks. *Open Ecol. J.* **2**, 7–24 (2009).

[Google Scholar](#)

104. 104.

Bascompte, J., Jordano, P. & Olesen, J. M. Asymmetric coevolutionary networks facilitate biodiversity maintenance. *Science* **312**, 431–433 (2006).

[ADS](#) [CAS](#) [Google Scholar](#)

105. 105.

Bates, D., Maechler, M. & Bolker, B. lme4: linear mixed-effects models using ‘Eigen’ and S4. R package version 1.1-19 <https://CRAN.R-project.org/package=lme4> (2013).

[Download references](#)

Acknowledgements

The ‘Molecular Ecology Laboratory’ (LEM–EBD–CSIC; ISO9001:2015 and ISO14001:2015 certifications) and the ‘Research Unit of Biodiversity’ (UO–CSIC–PA) provided logistical support for molecular analyses. We thank L. Viesca and E. Cires for laboratory assistance, and J. M. Varela for the bird illustrations. Barcoding data were obtained within an Individual Fellowship from the Marie Skłodowska-Curie Actions (H2020-MSCA-IF-2014-656572: MobileLinks) and supported by a GRUPIN grant from the Regional Government of Asturias (IDI/2018/000151). ‘King Jaume I’ awarded to A.T. supported data collation during two postdoctoral contracts. J.P.G.-V. is supported by a Spanish ‘Ramón y Cajal’ fellowship (RYC-2017-22095) and a grant from the Spanish MICINN (PID2019-104922GA-I00/AEI/10.13039/501100011033). B.R. is supported by a Spanish ‘Juan de la Cierva Incorporación’ fellowship (IJCI-2017-33475). R.H.H. is funded

by the Portuguese Foundation for Science and Technology (UID/BIA/04004/2020). B.I.S. is supported by a Royal Commission for the Exhibition of 1851 Research Fellowship. W.J.S. is funded by Arcadia.

Author information

Affiliations

1. Departamento de Biología, IVAGRO, Universidad de Cádiz, Puerto Real, Spain

Juan P. González-Varo & Beatriz Rumeu

2. Senckenberg Biodiversity and Climate Research Centre (BiK-F), Frankfurt am Main, Germany

Jörg Albrecht

3. Integrative Ecology Group, Estación Biológica de Doñana (EBD-CSIC), Sevilla, Spain

Juan M. Arroyo & Pedro Jordano

4. Dipartimento Scienze Agrarie, Alimentari e Forestali e Dipartimento di Scienze e Tecnologie Biologiche, Chimiche e Farmaceutiche, Università degli Studi di Palermo, Palermo, Italy

Rafael S. Bueno

5. Departamento de Biología y Geología, Física y Química Inorgánica, Universidad Rey Juan Carlos, Móstoles, Spain

Tamara Burgos & Emilio Virgós

6. CIBIO-InBIO, Research Center in Biodiversity and Genetic Resources, University of Porto, Vairão, Portugal

Luís P. da Silva

7. Global Change Research Group, Mediterranean Institute of Advanced Studies (CSIC-UIB), Esporles, Spain

Gema Escribano-Ávila & Anna Traveset

8. Conservation Ecology, Department of Biology, University of Marburg, Marburg, Germany

Nina Farwig

9. Research Unit of Biodiversity (UO-CSIC-PA), Oviedo University, Mieres, Spain

Daniel García & Juan C. Illera

10. CFE – Centre for Functional Ecology, Department of Life Sciences, University of Coimbra, Coimbra, Portugal

Ruben H. Heleno

11. Department of Plant Ecology and Environmental Protection, Adam Mickiewicz University, Poznań, Poland

Przemysław Kurek

12. Centre for Ecology and Conservation, College of Life and Environmental Sciences, University of Exeter, Penryn, UK

Benno I. Simmons

13. Conservation Science Group, Department of Zoology, University of Cambridge, Cambridge, UK

William J. Sutherland

Authors

1. Juan P. González-Varo
[View author publications](#)

You can also search for this author in [PubMed](#) [Google Scholar](#)

2. Beatriz Rumeu

[View author publications](#)

You can also search for this author in [PubMed](#) [Google Scholar](#)

3. Jörg Albrecht

[View author publications](#)

You can also search for this author in [PubMed](#) [Google Scholar](#)

4. Juan M. Arroyo

[View author publications](#)

You can also search for this author in [PubMed](#) [Google Scholar](#)

5. Rafael S. Bueno

[View author publications](#)

You can also search for this author in [PubMed](#) [Google Scholar](#)

6. Tamara Burgos

[View author publications](#)

You can also search for this author in [PubMed](#) [Google Scholar](#)

7. Luís P. da Silva

[View author publications](#)

You can also search for this author in [PubMed](#) [Google Scholar](#)

8. Gema Escribano-Ávila

[View author publications](#)

You can also search for this author in [PubMed](#) [Google Scholar](#)

9. Nina Farwig

[View author publications](#)

You can also search for this author in [PubMed](#) [Google Scholar](#)

10. Daniel García

[View author publications](#)

You can also search for this author in [PubMed](#) [Google Scholar](#)

11. Ruben H. Heleno

[View author publications](#)

You can also search for this author in [PubMed](#) [Google Scholar](#)

12. Juan C. Illera

[View author publications](#)

You can also search for this author in [PubMed](#) [Google Scholar](#)

13. Pedro Jordano

[View author publications](#)

You can also search for this author in [PubMed](#) [Google Scholar](#)

14. Przemysław Kurek

[View author publications](#)

You can also search for this author in [PubMed](#) [Google Scholar](#)

15. Benno I. Simmons

[View author publications](#)

You can also search for this author in [PubMed](#) [Google Scholar](#)

16. Emilio Virgós

[View author publications](#)

You can also search for this author in [PubMed](#) [Google Scholar](#)

17. William J. Sutherland

[View author publications](#)

You can also search for this author in [PubMed](#) [Google Scholar](#)

18. Anna Traveset

[View author publications](#)

You can also search for this author in [PubMed](#) [Google Scholar](#)

Contributions

J.P.G.-V. conceived the study. J.P.G.-V., J.A., J.M.A., R.S.B., T.B., G.E.-Á., N.F., D.G., J.C.I., P.J., P.K., W.J.S. and E.V. obtained data of seven new seed-dispersal networks within the EU project ‘MobileLinks’. J.M.A. and J.C.I. also conducted the molecular analyses for these networks. L.P.d.S. and R.H.H. provided data of one unpublished network. P.J. provided data of two published networks. B.R., J.P.G.-V. and A.T. gathered data on fruiting phenology and bird migrations; J.P.G.-V., B.R., J.A. and B.I.S. analysed the data; J.P.G.-V. wrote the first manuscript draft, and all authors worked on the final version.

Corresponding author

Correspondence to [Juan P. González-Varo](#).

Ethics declarations

Competing interests

The authors declare no competing interests.

Additional information

Peer review information *Nature* thanks Christiaan Both, Barnabas Daru, David Inouye, Duarte Viana and the other, anonymous, reviewer(s) for their contribution to the peer review of this work.

Publisher's note Springer Nature remains neutral with regard to jurisdictional claims in published maps and institutional affiliations.

Extended data figures and tables

Extended Data Fig. 1 Conceptual diagrams showing directional patterns of long-distance seed dispersal by migratory birds and phenological overlaps between seed-dispersal periods and bird migrations.

a, Yellow and black arrows denote long-distance seed dispersal within and beyond the current range of a plant species, respectively. Seed dispersal mediated by birds migrating south (left), non-migrating birds (centre) and birds migrating north (right). The colour gradient from red to blue represents a climatic gradient from warmer to cooler latitudes (from south to north in the Northern Hemisphere), respectively. In the diagram on the right, seed dispersal within the range is necessary for warm-adapted populations to colonize cooler areas that are warming owing to climate change, whereas seed dispersal beyond the range is necessary for range shifts. **b**, Three hypothetical examples of phenological overlap between the seed-dispersal period of plant species *i* and bird species *j* while the bird migrates northwards (top), southwards (middle) or during both migrations (bottom). The examples include a wintering migrant with a winter–spring fruiting plant (top); a summer migrant with a summer–autumn fruiting plant (middle); and a transient migrant with an autumn–winter fruiting plant (bottom). In some cases, there is also phenological overlap during non-migration periods. More details on phenological overlaps in relation to the migratory strategy of birds are provided in Supplementary Fig. 3.

Extended Data Fig. 2 Estimated interaction frequencies of plant species within each study network with birds migrating northwards, southwards or not migrating.

Blue, interactions during northward migration; red, interactions during southward migration; grey, non-migration interactions. Each panel

represents a seed-dispersal network. The left column of panels includes Mediterranean networks, whereas the right column includes temperate networks. DE, Germany; ES, Spain; IT, Italy; PL, Poland; PT, Portugal; UK, United Kingdom.

Extended Data Fig. 3 Variables of the seed-dispersal phenology across the phylogenetic tree of plants.

Phylogenetic signal was tested in plant-species means across networks in start and end dates (D_{start} and D_{end}), as well as in length ($D_{\text{length}} = D_{\text{end}} - D_{\text{start}}$) of the seed-dispersal period ($n = 81$ plant species) by means of Pagels' λ , as described in 'Phylogenetic signal in plants' in 'Statistical analyses' (Methods). The three phenological variables showed significant phylogenetic signal ($D_{\text{start}}, \lambda = 0.800, P = 0.0103$; $D_{\text{end}}, \lambda = 0.781, P = 0.0015$; and $D_{\text{length}}, \lambda = 0.419, P = 0.0343$). To test for phylogenetic signal, we previously calculated the species-level means for D_{start} , D_{end} and D_{length} across bioclimates (Extended Data Fig. 6). For this reason, we assessed the amount of variance in these phenological variables that is accounted for by bioclimate, as compared to that accounted for by species through linear-mixed models (LMMs) that included 'bioclimate' as fixed factor and 'plant species' as random factor to account for the repeated measures per species. Bioclimate accounted for only a minor fraction of variance (1–3%) in D_{start} , D_{end} and D_{length} , as shown by the marginal R^2 values (variance explained by fixed effects; $R^2_{\text{LMM}(m)} = 0.028, 0.01$ and 0.023, respectively). By contrast, the high conditional R^2 values (variance explained by both fixed and random effects; $R^2_{\text{LMM}(c)} = 0.780, 0.845$ and 0.643, respectively) indicated that plant species accounted for most variance in the three phenological variables. LMMs were fitted with the R package package lme4 (v.1.1-19)¹⁰⁵.

Extended Data Fig. 4 Number of migratory bird species interacting with plants during migration per network in relation to migration direction and biome.

Large dots and bars denote means \pm 95% confidence intervals estimated by a GLMM, whereas circles denote values for each seed-dispersal network ($n = 26$ observations, 13 networks \times 2 directions). Only migration direction had significant effects on the number of migratory bird species interacting with plants during migration in the GLMM (Poisson family and log-link function) testing the effects of migration direction (Wald $\chi^2 = 11.08$, $P = 0.0009$), biome (Wald $\chi^2 = 0.17$, $P = 0.6789$) and their interaction (Wald $\chi^2 = 0.02$, $P = 0.8921$). Model estimates \pm s.e.: intercept = 2.297 ± 0.156 ; direction (northward) = -0.500 ± 0.208 ; biome (temperate) = -0.091 ± 0.215 ; direction (northward) \times biome (temperate) = 0.039 ± 0.288 ; southward and Mediterranean were used as the reference categories (intercepts) for the factors direction and biome, respectively. A mean of 9.5 bird species per community dispersed plants during their southward migration, but only 5.9 species did so during the northward migration.

Extended Data Fig. 5 Individual and cumulative bird species strengths accumulated across seed-dispersal subnetworks.

a, Bird species strength accumulated across seed-dispersal subnetworks between plants and birds migrating southwards or northwards, and in Mediterranean and temperate biomes; species strength quantifies the relevance of a bird species across the entire fleshy-fruited plant community¹⁰⁴ ($n = 24$ species). Some bird species have stacked values from several subnetworks, whereas other species participated only in a single subnetwork. **b**, The cumulative species strength across the southward and northward subnetworks were significantly correlated in the Mediterranean (Kendall's $\tau = 0.396$, $P = 0.0129$) and the temperate biome ($\tau = 0.588$, $P = 0.0006$), indicating that bird species generally display a proportional role in both migrations. However, the cumulative species strength in the Mediterranean and temperate biome were not correlated, neither across the northward ($\tau = 0.276$, $P = 0.1089$) nor across the southward subnetworks ($\tau = 0.263$, $P = 0.0764$) (correlation between left and right panels in **a**). These results indicate discordance between biomes in the identity of bird species contributions to community-wide seed dispersal during each migration. Pearson's r yielded qualitatively similar results, with higher coefficient values in the significant correlations ($r = 0.946$ and 0.847).

[Extended Data Fig. 6 Bioclimate-level plant phenology from several sources.](#)

Subset of 16 out of the 81 plant species present in the study networks illustrating how, in many cases, we obtained data on seed-dispersal phenology from several sources for the same plant species–bioclimate combination. Colour codes denote different data sources. A vertical grey line divides the calendar year.

Extended Data Table 1 Characteristics of the European seed-dispersal networks that we studied

[Full size table](#)

Extended Data Table 2 List of bird and plant species of the 13 study networks

[Full size table](#)

Extended Data Table 3 Significance of the fixed factors migration direction and biome, and their interaction, in GLMMs testing effects on seed-dispersal interactions of plants with migrating birds

[Full size table](#)

Extended Data Table 4 Significance of the fixed factors migration direction and biome, and their interaction, in GLMMs testing effects on the proportion of migratory bird species that were Palaearctic migrants, and in the network-level frequency of seed-dispersal interactions with Palaearctic migrants

[Full size table](#)

Supplementary information

[Supplementary Information](#)

This file contains the Supplementary methods, Supplementary Discussions 1-2, Supplementary Figures 1-7 and Supplementary References.

[Reporting Summary](#)

Rights and permissions

[Reprints and Permissions](#)

About this article



Check for
updates

Cite this article

González-Varo, J.P., Rumeu, B., Albrecht, J. *et al.* Limited potential for bird migration to disperse plants to cooler latitudes. *Nature* **595**, 75–79 (2021). <https://doi.org/10.1038/s41586-021-03665-2>

[Download citation](#)

- Received: 15 July 2020
- Accepted: 21 May 2021
- Published: 23 June 2021
- Issue Date: 01 July 2021
- DOI: <https://doi.org/10.1038/s41586-021-03665-2>

[Access through your institution](#)

[Change institution](#)

[Buy or subscribe](#)

Associated Content

[Migratory birds aid the redistribution of plants to new climates](#)

- Barnabas H. Daru

Advertisement

This article was downloaded by **calibre** from <https://www.nature.com/articles/s41586-021-03665-2>

| [Section menu](#) | [Main menu](#) |

- Article
- [Published: 16 June 2021](#)

Geometry of abstract learned knowledge in the hippocampus

- [Edward H. Nieh](#) [ORCID: orcid.org/0000-0003-2154-6224](#)^{1 na1},
- [Manuel Schottdorf](#) [ORCID: orcid.org/0000-0002-5468-4255](#)^{1 na1},
- [Nicolas W. Freeman](#)¹,
- [Ryan J. Low](#)¹,
- [Sam Lewallen](#)¹,
- [Sue Ann Koay](#) [ORCID: orcid.org/0000-0002-9648-2475](#)¹,
- [Lucas Pinto](#) [ORCID: orcid.org/0000-0002-0471-9317](#)^{1 nAffs},
- [Jeffrey L. Gauthier](#) [ORCID: orcid.org/0000-0002-0509-8532](#)¹,
- [Carlos D. Brody](#) [ORCID: orcid.org/0000-0002-4201-561X](#)^{1,2,3 na2} &
- [David W. Tank](#) [ORCID: orcid.org/0000-0002-9423-4267](#)^{1,2,4 na2}

[Nature](#) volume 595, pages 80–84 (2021) [Cite this article](#)

- 9025 Accesses
- 153 Altmetric
- [Metrics details](#)

Subjects

- [Neural circuits](#)
- [Neuroscience](#)

Abstract

Hippocampal neurons encode physical variables^{1,2,3,4,5,6,7} such as space¹ or auditory frequency⁶ in cognitive maps⁸. In addition, functional magnetic resonance imaging studies in humans have shown that the hippocampus can also encode more abstract, learned variables^{9,10,11}. However, their integration into existing neural representations of physical variables^{12,13} is unknown. Here, using two-photon calcium imaging, we show that individual neurons in the dorsal hippocampus jointly encode accumulated evidence with spatial position in mice performing a decision-making task in virtual reality^{14,15,16}. Nonlinear dimensionality reduction¹³ showed that population activity was well-described by approximately four to six latent variables, which suggests that neural activity is constrained to a low-dimensional manifold. Within this low-dimensional space, both physical and abstract variables were jointly mapped in an orderly manner, creating a geometric representation that we show is similar across mice. The existence of conjoined cognitive maps suggests that the hippocampus performs a general computation—the creation of task-specific low-dimensional manifolds that contain a geometric representation of learned knowledge.

Access options

Subscribe to Journal

Get full journal access for 1 year

\$199.00

only \$3.90 per issue

[Subscribe](#)

All prices are NET prices.

VAT will be added later in the checkout.

Tax calculation will be finalised during checkout.

Rent or Buy article

Get time limited or full article access on ReadCube.

from \$8.99

[Rent or Buy](#)

All prices are NET prices.

Additional access options:

- [Log in](#)
- [Access through your institution](#)
- [Learn about institutional subscriptions](#)

Fig. 1: Imaging of CA1 neural activity in mice performing the accumulating towers task.



Fig. 2: CA1 neurons jointly encode the position of the mice and accumulated evidence in an evidence-accumulation task.

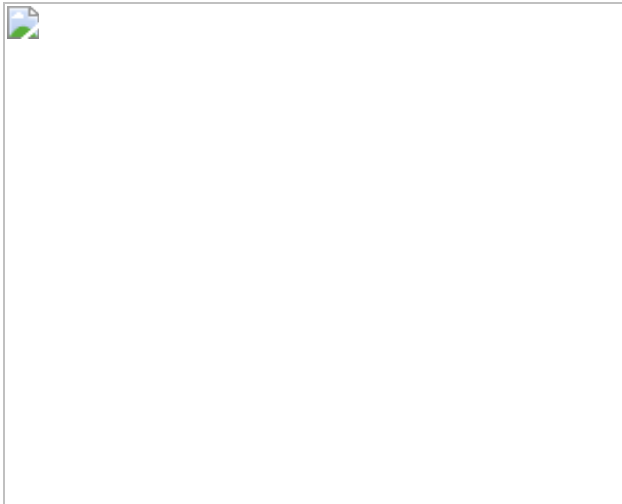


Fig. 3: Geometric representation of task variables on low-dimensional neural manifolds.

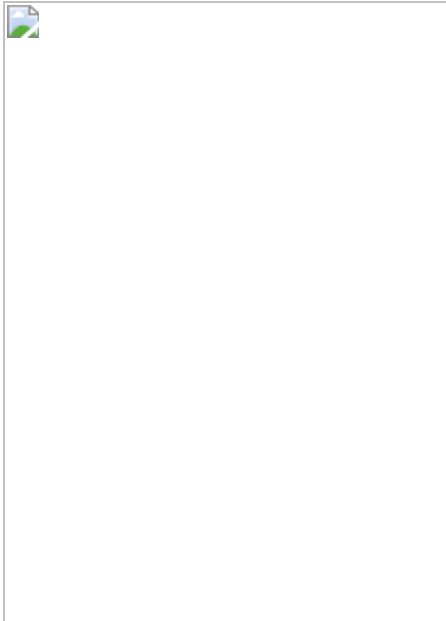
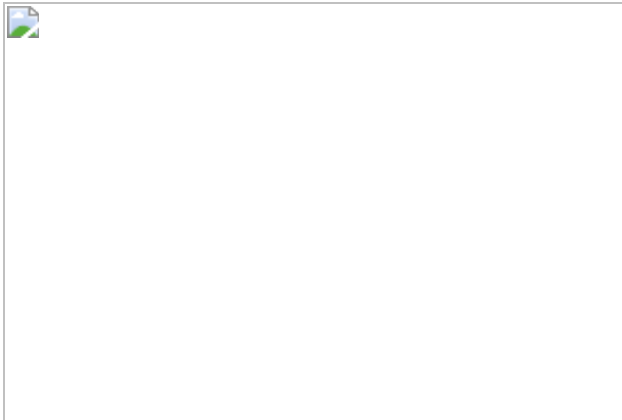


Fig. 4: Sequential activity of CA1 neurons in single trials is predictive of behaviour and explained by the manifold.



Data availability

The datasets generated in this study are available from the corresponding authors on reasonable request. [Source data](#) are provided with this paper.

Code availability

The code used for all analyses in this study is available on GitHub (https://github.com/BrainCOGS/HPC_manifolds). All other codes are available on reasonable request.

References

1. 1.

O'Keefe, J. & Dostrovsky, J. The hippocampus as a spatial map. Preliminary evidence from unit activity in the freely-moving rat. *Brain Res.* **34**, 171–175 (1971).

[PubMed](#) [Google Scholar](#)

2. 2.

Frank, L. M., Brown, E. N. & Wilson, M. Trajectory encoding in the hippocampus and entorhinal cortex. *Neuron* **27**, 169–178 (2000).

[CAS](#) [PubMed](#) [Google Scholar](#)

3. 3.

Wood, E. R., Dudchenko, P. A., Robitsek, R. J. & Eichenbaum, H. Hippocampal neurons encode information about different types of memory episodes occurring in the same location. *Neuron* **27**, 623–633 (2000).

[CAS](#) [PubMed](#) [Google Scholar](#)

4. 4.

Eichenbaum, H., Kuperstein, M., Fagan, A. & Nagode, J. Cue-sampling and goal-approach correlates of hippocampal unit activity in rats performing an odor-discrimination task. *J. Neurosci.* **7**, 716–732 (1987).

[CAS](#) [PubMed](#) [PubMed Central](#) [Google Scholar](#)

5. 5.

Herzog, L. E. et al. Interaction of taste and place coding in the hippocampus. *J. Neurosci.* **39**, 3057–3069 (2019).

[CAS](#) [PubMed](#) [PubMed Central](#) [Google Scholar](#)

6. 6.

Aronov, D., Nevers, R. & Tank, D. W. Mapping of a non-spatial dimension by the hippocampal–entorhinal circuit. *Nature* **543**, 719–722 (2017).

[ADS](#) [CAS](#) [PubMed](#) [PubMed Central](#) [Google Scholar](#)

7. 7.

Taxidis, J. et al. Differential emergence and stability of sensory and temporal representations in context-specific hippocampal sequences.

Neuron **108**, 984–998.e9 (2020).

[CAS](#) [PubMed](#) [Google Scholar](#)

8. 8.

O'Keefe, J. & Nadel, L. *The Hippocampus as a Cognitive Map* (Clarendon, 1978).

9. 9.

Schuck, N. W. & Niv, Y. Sequential replay of nonspatial task states in the human hippocampus. *Science* **364**, eaaw5181 (2019).

[ADS](#) [CAS](#) [PubMed](#) [PubMed Central](#) [Google Scholar](#)

10. 10.

Tavares, R. M. et al. A map for social navigation in the human brain. *Neuron* **87**, 231–243 (2015).

[CAS](#) [PubMed](#) [PubMed Central](#) [Google Scholar](#)

11. 11.

Park, S. A., Miller, D. S., Nili, H., Ranganath, C. & Boorman, E. D. Map making: constructing, combining, and inferring on abstract cognitive maps. *Neuron* **107**, 1226–1238.e8 (2020).

[CAS](#) [PubMed](#) [Google Scholar](#)

12. 12.

Rubin, A. et al. Revealing neural correlates of behavior without behavioral measurements. *Nat. Commun.* **10**, 4745 (2019).

[ADS](#) [PubMed](#) [PubMed Central](#) [Google Scholar](#)

13. 13.

Low, R. J., Lewallen, S., Aronov, D., Nevers, R. & Tank, D. W. Probing variability in a cognitive map using manifold inference from neural dynamics. Preprint at <https://doi.org/10.1101/418939> (2018).

14. 14.

Pinto, L. et al. An accumulation-of-evidence task using visual pulses for mice navigating in virtual reality. *Front. Behav. Neurosci.* **12**, 36 (2018).

[PubMed](#) [PubMed Central](#) [Google Scholar](#)

15. 15.

Koay, S. A., Thibierge, S., Brody, C. D. & Tank, D. W. Amplitude modulations of cortical sensory responses in pulsatile evidence accumulation. *eLife* **9**, e60628 (2020).

[CAS](#) [PubMed](#) [PubMed Central](#) [Google Scholar](#)

16. 16.

Engelhard, B. et al. Specialized coding of sensory, motor and cognitive variables in VTA dopamine neurons. *Nature* **570**, 509–513 (2019).

[ADS](#) [CAS](#) [PubMed](#) [PubMed Central](#) [Google Scholar](#)

17. 17.

MacDonald, C. J., Lepage, K. Q., Eden, U. T. & Eichenbaum, H. Hippocampal “time cells” bridge the gap in memory for discontiguous events. *Neuron* **71**, 737–749 (2011).

[CAS](#) [PubMed](#) [PubMed Central](#) [Google Scholar](#)

18. 18.

Pastalkova, E., Itskov, V., Amarasingham, A. & Buzsáki, G. Internally generated cell assembly sequences in the rat hippocampus. *Science*

321, 1322–1327 (2008).

[ADS](#) [CAS](#) [PubMed](#) [PubMed Central](#) [Google Scholar](#)

19. 19.

Tolman, E. C. Cognitive maps in rats and men. *Psychol. Rev.* **55**, 189–208 (1948).

[CAS](#) [PubMed](#) [Google Scholar](#)

20. 20.

Bellmund, J. L. S., Gärdenfors, P., Moser, E. I. & Doeller, C. F. Navigating cognition: spatial codes for human thinking. *Science* **362**, eaat6766 (2018).

[ADS](#) [PubMed](#) [Google Scholar](#)

21. 21.

Eichenbaum, H. in *Behavioral Neuroscience of Learning and Memory* (eds Clark, R. E. & Martin, S. J.) 101–117 (Springer, 2018).

22. 22.

Constantinescu, A. O., O'Reilly, J. X. & Behrens, T. E. J. Organizing conceptual knowledge in humans with a gridlike code. *Science* **352**, 1464–1468 (2016).

[ADS](#) [CAS](#) [PubMed](#) [PubMed Central](#) [Google Scholar](#)

23. 23.

Gallego, J. A., Perich, M. G., Miller, L. E. & Solla, S. A. Neural manifolds for the control of movement. *Neuron* **94**, 978–984 (2017).

[CAS](#) [PubMed](#) [PubMed Central](#) [Google Scholar](#)

24. 24.

Russo, A. A. et al. Motor cortex embeds muscle-like commands in an untangled population response. *Neuron* **97**, 953–966.e8 (2018).

[CAS](#) [PubMed](#) [PubMed Central](#) [Google Scholar](#)

25. 25.

Chaudhuri, R., Gercek, B., Pandey, B., Peyrache, A. & Fiete, I. The intrinsic attractor manifold and population dynamics of a canonical cognitive circuit across waking and sleep. *Nat. Neurosci.* **22**, 1512–1520 (2019).

[CAS](#) [PubMed](#) [Google Scholar](#)

26. 26.

Eichenbaum, H. & Cohen, N. J. Can we reconcile the declarative memory and spatial navigation views on hippocampal function? *Neuron* **83**, 764–770 (2014).

[CAS](#) [PubMed](#) [PubMed Central](#) [Google Scholar](#)

27. 27.

Recanatesi, S. et al. Predictive learning as a network mechanism for extracting low-dimensional latent space representations. *Nat. Commun.* **12**, 1417 (2021).

[ADS](#) [CAS](#) [PubMed](#) [PubMed Central](#) [Google Scholar](#)

28. 28.

Aronov, D. & Tank, D. W. Engagement of neural circuits underlying 2D spatial navigation in a rodent virtual reality system. *Neuron* **84**, 442–456 (2014).

[CAS](#) [PubMed](#) [PubMed Central](#) [Google Scholar](#)

29. 29.

Dombeck, D. A., Harvey, C. D., Tian, L., Looger, L. L. & Tank, D. W. Functional imaging of hippocampal place cells at cellular resolution during virtual navigation. *Nat. Neurosci.* **13**, 1433–1440 (2010).

[CAS](#) [PubMed](#) [PubMed Central](#) [Google Scholar](#)

30. 30.

Harvey, C. D., Coen, P. & Tank, D. W. Choice-specific sequences in parietal cortex during a virtual-navigation decision task. *Nature* **484**, 62–68 (2012).

[ADS](#) [CAS](#) [PubMed](#) [PubMed Central](#) [Google Scholar](#)

31. 31.

Brunton, B. W., Botvinick, M. M. & Brody, C. D. Rats and humans can optimally accumulate evidence for decision-making. *Science* **340**, 95–98 (2013).

[ADS](#) [CAS](#) [PubMed](#) [Google Scholar](#)

32. 32.

Gold, J. I. & Shadlen, M. N. The neural basis of decision making. *Annu. Rev. Neurosci.* **30**, 535–574 (2007).

[CAS](#) [Google Scholar](#)

33. 33.

Gill, P. R., Mizumori, S. J. Y. & Smith, D. M. Hippocampal episode fields develop with learning. *Hippocampus* **21**, 1240–1249 (2011).

[PubMed](#) [Google Scholar](#)

34. 34.

McKenzie, S. et al. Hippocampal representation of related and opposing memories develop within distinct, hierarchically organized neural schemas. *Neuron* **83**, 202–215 (2014).

[CAS](#) [PubMed](#) [PubMed Central](#) [Google Scholar](#)

35. 35.

Howard, M. W., Lizardo, A. & Tiganj, Z. Evidence accumulation in a Laplace domain decision space. *Comput. Brain Behav.* **1**, 237–251 (2018).

[PubMed](#) [PubMed Central](#) [Google Scholar](#)

36. 36.

Pnevmatikakis, E. A. et al. Simultaneous denoising, deconvolution, and demixing of calcium imaging data. *Neuron* **89**, 285–299 (2016).

[CAS](#) [PubMed](#) [PubMed Central](#) [Google Scholar](#)

37. 37.

Pnevmatikakis, E. A. & Giovannucci, A. NoRMCorre: an online algorithm for piecewise rigid motion correction of calcium imaging data. *J. Neurosci. Methods* **291**, 83–94 (2017).

[CAS](#) [PubMed](#) [Google Scholar](#)

38. 38.

Skaggs, W. E., McNaughton, B. L. & Gothard, K. M. An information-theoretic approach to deciphering the hippocampal code. In *Advances in Neural Information Processing Systems 5* (eds Hanson, S. J. et al.) 1030–1037 (Morgan-Kaufmann, 1993).

39. 39.

Grassberger, P. & Procaccia, I. Measuring the strangeness of strange attractors. *Physica D* **9**, 189–208 (1983).

[ADS](#) [MathSciNet](#) [MATH](#) [Google Scholar](#)

40. 40.

Stachenfeld, K. L., Botvinick, M. M. & Gershman, S. J. The hippocampus as a predictive map. *Nat. Neurosci.* **20**, 1643–1653 (2017).

[CAS](#) [PubMed](#) [Google Scholar](#)

41. 41.

Gauthier, J. L. & Tank, D. W. A dedicated population for reward coding in the hippocampus. *Neuron* **99**, 179–193.e7 (2018).

[CAS](#) [PubMed](#) [PubMed Central](#) [Google Scholar](#)

42. 42.

Pinto, L. et al. Task-dependent changes in the large-scale dynamics and necessity of cortical regions. *Neuron* **104**, 810–824.e9 (2019).

[CAS](#) [PubMed](#) [PubMed Central](#) [Google Scholar](#)

43. 43.

Domnisoru, C., Kinkhabwala, A. A. & Tank, D. W. Membrane potential dynamics of grid cells. *Nature* **495**, 199–204 (2013).

[ADS](#) [CAS](#) [PubMed](#) [PubMed Central](#) [Google Scholar](#)

44. 44.

Rich, P. D., Liaw, H.-P. & Lee, A. K. Large environments reveal the statistical structure governing hippocampal representations. *Science* **345**, 814–817 (2014).

[ADS](#) [CAS](#) [PubMed](#) [Google Scholar](#)

45. 45.

Tenenbaum, J. B., de Silva, V. & Langford, J. C. A global geometric framework for nonlinear dimensionality reduction. *Science* **290**, 2319–2323 (2000).

[ADS](#) [CAS](#) [PubMed](#) [Google Scholar](#)

46. 46.

Yu, B. M. et al. Gaussian-process factor analysis for low-dimensional single-trial analysis of neural population activity. *J. Neurophysiol.* **102**, 614–635 (2009).

[PubMed](#) [PubMed Central](#) [Google Scholar](#)

[Download references](#)

Acknowledgements

We thank A. Song and S. Thibierge for assistance with two-photon imaging, S. Stein and S. Baptista for technical support with animal training, M. L. Ioffe for providing code and E. M. Diamanti and B. Engelhard for discussions. This work was supported by NIH grants U01NS090541, U19NS104648 and F32MH119749, as well as the Simons Collaboration on the Global Brain.

Author information

Author notes

1. Lucas Pinto

Present address: Department of Physiology, Feinberg School of Medicine, Northwestern University, Chicago, IL, USA

2. These authors contributed equally: Edward H. Nieh, Manuel Schottdorf
3. These authors jointly supervised this work: Carlos D. Brody, David W. Tank

Affiliations

1. Princeton Neuroscience Institute, Princeton University, Princeton, NJ, USA
Edward H. Nieh, Manuel Schottdorf, Nicolas W. Freeman, Ryan J. Low, Sam Lewallen, Sue Ann Koay, Lucas Pinto, Jeffrey L. Gauthier, Carlos D. Brody & David W. Tank
2. Department of Molecular Biology, Princeton University, Princeton, NJ, USA
Carlos D. Brody & David W. Tank
3. Howard Hughes Medical Institute, Princeton University, Princeton, NJ, USA
Carlos D. Brody
4. Bezos Center for Neural Dynamics, Princeton University, Princeton, NJ, USA
David W. Tank

Authors

1. Edward H. Nieh
[View author publications](#)

You can also search for this author in [PubMed](#) [Google Scholar](#)

2. Manuel Schottdorf
[View author publications](#)

You can also search for this author in [PubMed](#) [Google Scholar](#)

3. Nicolas W. Freeman

[View author publications](#)

You can also search for this author in [PubMed](#) [Google Scholar](#)

4. Ryan J. Low

[View author publications](#)

You can also search for this author in [PubMed](#) [Google Scholar](#)

5. Sam Lewallen

[View author publications](#)

You can also search for this author in [PubMed](#) [Google Scholar](#)

6. Sue Ann Koay

[View author publications](#)

You can also search for this author in [PubMed](#) [Google Scholar](#)

7. Lucas Pinto

[View author publications](#)

You can also search for this author in [PubMed](#) [Google Scholar](#)

8. Jeffrey L. Gauthier

[View author publications](#)

You can also search for this author in [PubMed](#) [Google Scholar](#)

9. Carlos D. Brody

[View author publications](#)

You can also search for this author in [PubMed](#) [Google Scholar](#)

10. David W. Tank

[View author publications](#)

You can also search for this author in [PubMed](#) [Google Scholar](#)

Contributions

E.H.N., C.D.B. and D.W.T. designed the experiments. E.H.N. and N.W.F. performed the experiments. E.H.N., M.S. and N.W.F. analysed the data. S.A.K. wrote the code for the processing of the calcium-imaging data. L.P. provided the code for behavioural analysis. J.L.G. provided the code for mutual information calculations. M.S., R.J.L. and S.L. developed the MIND algorithm. E.H.N., M.S., C.D.B. and D.W.T. wrote the paper.

Corresponding authors

Correspondence to [Carlos D. Brody](#) or [David W. Tank](#).

Ethics declarations

Competing interests

The authors declare no competing interests.

Additional information

Peer review information *Nature* thanks the anonymous reviewers for their contribution to the peer review of this work.

Publisher's note Springer Nature remains neutral with regard to jurisdictional claims in published maps and institutional affiliations.

Extended data figures and tables

[Extended Data Fig. 1 Characterization of CA1 neural variability in the accumulating towers task.](#)

a, Each heat map represents one neuron and the trial-by-trial activity of that neuron in the towers task for left-choice trials. Each row in each heat map is the $\Delta F/F$ (normalized within each neuron) of the neuron in that trial. **b**, Same as in **a**, but for the alternation task. Note that the single-trial activity appears more variable in the towers task and more reliable in the alternation task, consistent with the results that evidence is also being represented by neurons in the towers task. **c**, Neural activity ($\Delta F/F$ normalized within each neuron) of cells significantly encoding evidence, sorted by activity in half the trials (top) and plotted using the same sorting in the other half of the trials (bottom).

[Source data](#)

[Extended Data Fig. 2 Place fields in evidence-by-position space.](#)

a, Each heat map shows the mean $\Delta F/F$ of a neuron with significant mutual information in $E \times Y$ space. **b**, Scatterplot of the mutual information in $R_E \times Y$ space versus $E \times Y$ space for each cell with significant information in $E \times Y$ space ($n = 917$ neurons). R_E is randomized evidence. **c**, Same as in **b**, but for $E \times R_Y$ space versus $E \times Y$ space. R_Y is randomized position. **d**, In total, 29% of imaged neurons had significant mutual information in $E \times Y$ space, whereas 16% had significant mutual information only for position and 6% had significant mutual information only for evidence. **e**, Of the cells with significant mutual information in $E \times Y$ space, 89.9% had significantly more information in $E \times Y$ space than just place or evidence information alone, whereas 9.8% could not be differentiated from place cells and 0.3% could not be differentiated from evidence cells ([Methods](#)). **f**, The probability of a cell having significant mutual information in $E \times Y$ space is significantly greater than the joint probability of a cell being a place cell and a cell being an evidence cell. Two-tailed Wilcoxon signed-rank test, $*P = 0.016$; $n = 7$ mice; data are mean \pm s.e.m. **g**, Cells with significant mutual information in $E \times Y$ space had 1.7 ± 0.03 (mean \pm s.e.m.) firing fields ($n = 917$ cells).

[Source data](#)

Extended Data Fig. 3 Dimensionality of an earlier training stage.

During the training of the towers task, mice proceed through various stages of training. In one of these training stages, mice perform a task nearly identical to the towers task, except that visual cues only show up on one side of the maze. **a**, The intrinsic dimensionality of the one-side cues task is approximately 4.2 (4.0–4.5; 95% bootstrapped confidence interval). $n = 4$ mice; data are mean \pm 95% bootstrapped confidence intervals. Grey dashed lines illustrate the slope expected for a four-dimensional manifold. **b**, Intrinsic dimensionality of the one-side cues task is significantly lower than the dimensionality of the towers task. Two-tailed Wilcoxon rank-sum test, * $P = 0.042$; $n = 7$ mice (towers task) and $n = 4$ mice (one-side cues task); data are mean \pm s.e.m. **c**, Choice-specific place cell sequences in the one-side cues task, similar to Fig. 2a. Sequences are divided into left-choice-preferring (top), right-choice-preferring (middle) and non-preferring (bottom) cells. Data are split between left-choice trials (left) and right-choice trials (right). Cells are shown in the same order within each row group. $\Delta F/F$ was normalized within each neuron.

[Source data](#)

Extended Data Fig. 4 Cross-validation methods and results demonstrating how neural activity from single neurons is captured by coordinated population activity.

a, Illustration of the cross-validation method to calculate the decoding index in Fig. 3c. Data are split for training (solid colours) and testing (shaded colours). With the training data, a map is obtained from $\Delta F/F$ to latent dimensions and back. This map is then evaluated on the test data. **b**, To assess the performance of the map, we concatenate the neuron \times time data in the test block and reconstructed test block into two vectors and calculate the correlation coefficient from the elementwise pairwise comparison of the vectors. The correlation coefficient was averaged across 10 individually held-out trials to yield the decoding index. **c**, Illustration of a similar analysis in which the activity of a single cell is decoded from a manifold fit

to the rest of the neural population. One neuron (red) is removed before using MIND to obtain a set of latents. Next, in the training data (solid green), a map is calculated from the manifold to the activity of the held-out neuron. The map is then used to predict the test data (shaded green). The correlation coefficient is calculated as in **b** and averaged over five folds across 10 individually held-out neurons as the decoding index. **d**, Example of neural activity from 40 individually reconstructed neurons, in which the activity of each neuron was decoded from the five-dimensional manifold fit to the other cells following procedures in **c** (comparable to Fig. 3b, for which the method in **a** and **b** was used). $\Delta F/F$ is normalized to the maximum $\Delta F/F$ in the window shown. **e**, Cross-validated correlation coefficients between the activity of individual neurons in the real and reconstructed data, in which the reconstruction was accomplished with d -dimensional embeddings of the neural manifold. The decoding index is the correlation coefficient between the predicted and real $\Delta F/F$ of the held-out ROIs. $n = 7$ mice; data are mean \pm s.e.m.

Source data

Extended Data Fig. 5 Task manifold and neural manifold encode different variables.

a, The visual space of the accumulating towers task across a representative session. Top, the mean luminance of the virtual-reality visual field as a function of position in the T-maze. Bottom, four example frames. Note the high variability of luminance during the cue period, where bright towers are randomly presented on the left and right walls. **b**, Performing dimensionality reduction on the time series of the pixel values in the raw video stream using MIND reveals a low-dimensional manifold, reflecting the visual sensory structure of the accumulating towers task. Plotting luminance (top) and evidence (bottom) on the manifold reveals that luminance is represented as a smooth gradient, whereas evidence requires memory and is thus absent on the task manifold. **c**, Same as in **b**, but showing the neural manifold obtained from the mouse that ran the session (Fig. 3f). Note the absence of a luminance representation, but the emergence of evidence.

Source data

Extended Data Fig. 6 Decoding other variables from the neural manifold.

a, Similar to Fig. 3f, the view angle is plotted as colour on the three-dimensional embedding of the manifold. **b**, The five latent variables of the neural manifold embedded in a five-dimensional Euclidean space are better predicted by GPR from view angle and evidence values than from view angle and shuffled evidence values. Two-tailed Wilcoxon signed-rank test, $*P = 0.016$; $n = 7$ mice; data are mean \pm s.e.m. Decoding index is the correlation coefficient between the predicted manifold values and true manifold values, averaged over the five dimensions of the manifold. **c**, Same as in **b**, but for decoding manifold values using position and velocity. The addition of velocity to position information significantly improves the decoding of manifold values. Two-tailed Wilcoxon signed-rank test, $*P = 0.016$; $n = 7$ mice; data are mean \pm s.e.m. **d**, Same as in **b**, but for decoding using position and time. The addition of time information does not significantly increase how well manifold values are decoded. Two-tailed Wilcoxon signed-rank test, $P = 0.30$ (ns, not significant); $n = 7$ mice; data are mean \pm s.e.m. **e**, We used PCA to separate the correlated and orthogonal dimensions between evidence and view angle and decoded both PC1 (correlated) and PC2 (orthogonal) from the five-dimensional embedding of the manifold. $n = 7$ mice; data are mean \pm s.e.m. The decoding index is the correlation coefficient between the predicted and true principal component values. **f**, The view angle is better decoded from the neural manifold (five-dimensional embedding) in the towers task ('Tow'), when evidence is also present, than in the alternation task ('Alt') when evidence is not present. Two-tailed Wilcoxon rank-sum test, $P = 0.07$; $n = 7$ mice (towers task) and $n = 7$ mice (alternation task); data are mean \pm s.e.m. The decoding index is the correlation coefficient between the predicted and true view angle values. **g**, Average view angle trajectories, separated between left- and right-choice trials, for the mice in the towers task ($n = 7$ mice; blue, thin lines) and the alternation task ($n = 7$ mice; red, thin lines). Thick lines represent averages across mice. **h**, Average view angle values in the towers task ($n = 7$ mice; blue, thin lines) and the alternation task ($n = 7$ mice; red, thin lines) over all trials. Thick lines and shaded area are mean \pm 95% bootstrapped confidence

interval. **i**, Accuracy in predicting the upcoming choice (left), the choice of the mouse in the previous trial (centre) and whether the previous trial was rewarded (right) from d -dimensional embeddings of the neural manifold. $n = 7$ mice; data are mean \pm s.e.m.

[Source data](#)

Extended Data Fig. 7 Examples of sequences in CA1 neural activity.

a, Schematic to describe how doublets were defined. Orange and green are calcium traces of the cells under consideration. Grey is the calcium trace of a third cell. **b**, Twenty-five examples of doublets in a single session from one mouse. Each panel shows traces for trials in which the doublet was present. Orange traces are the neural activity from the first cell in the doublet; green traces are the neural activity from the second cell in the doublet. Heat maps represent the normalized neural activity of each cell across all trials in the session.

[Source data](#)

Extended Data Fig. 8 Neural activity generated by trajectories through the task.

a, Trajectories through evidence and position in one session of the task. Each thin line represents a fit with a cubic spline to a single trial; thick lines represent fits over all trials in which the mouse was supposed to turn left or right. **b**, The average change in position and evidence over time across trials in a single session for a set of representative states in evidence and position space. **c**, Conceptual diagram showing four trajectories through the neural manifold in right-choice trials. Two different doublets are activated because the trajectories pass through their firing fields. **d**, Shuffling trial IDs within right-choice trials will disrupt doublet activity while maintaining trial-averaged place and choice preferences of each cell.

[Source data](#)

Extended Data Fig. 9 Choice-predictive sequences in CA1 neural activity.

a, Distribution of the values in Fig. 4b. **b**, Distribution of the values in Fig. 4c. **c**, Distribution of the values in Fig. 4f. **d**, ROC curves for sequential activity predicted from the five-dimensional embedding of the manifold compared to sequential activity in real data. $n = 7$ mice. **e**, Similar to a, but for triplets. Inset shows that triplets are significantly more likely to appear in the real data than in the shuffled dataset in which trial IDs were shuffled. Two-tailed paired Student's t -test, real versus shuffled data, $****P < 0.0001$; $n = 34,737$ triplets. **f**, Similar to c, but for triplets, showing that left- and right-choice-predictive triplets from real data are more predictive than triplets obtained from the shuffled dataset in which trial IDs were shuffled. Left inset, left-predictive, $n = 1,135$ triplets, two-tailed paired Student's t -test, real versus shuffled data, $****P < 0.0001$; right inset, right-predictive, $n = 1,755$ triplets, two-tailed paired Student's t -test, real versus shuffled data, $****P < 0.0001$. **g**, Left-choice-predictive triplets are significantly more predictive than instances in which the first two cells in the triplet fire, but the third does not, or when the third cell fires alone. $n = 1,135$ triplets; two-tailed paired Student's t -tests, Bonferroni corrected; $1 \rightarrow 2 \rightarrow 3$ versus $1 \rightarrow 2 \rightarrow \text{not } 3$, $****P < 0.0001$; $1 \rightarrow 2 \rightarrow 3$ versus $\text{not } 1 \rightarrow \text{not } 2 \rightarrow 3$, $****P < 0.0001$; $1 \rightarrow 2 \rightarrow \text{not } 3$ versus $\text{not } 1 \rightarrow \text{not } 2 \rightarrow 3$, $P = 0.78$. **h**, Notably, for left-choice-predictive triplets, in trials in which cells 1 and 2 fire, but cell 3 does not, significantly more trials end with the mouse turning right than the same instances in the shuffled dataset. $n = 1,135$ triplets, two-tailed paired Student's t -test, real versus shuffled data, $****P < 0.0001$. **i**, Same as in g, but for right-choice-predictive triplets. $n = 1,755$ triplets; two-tailed paired Student's t -tests, Bonferroni corrected; $1 \rightarrow 2 \rightarrow 3$ versus $1 \rightarrow 2 \rightarrow \text{not } 3$, $****P < 0.0001$; $1 \rightarrow 2 \rightarrow 3$ versus $\text{not } 1 \rightarrow \text{not } 2 \rightarrow 3$, $****P < 0.0001$; $1 \rightarrow 2 \rightarrow \text{not } 3$ versus $\text{not } 1 \rightarrow \text{not } 2 \rightarrow 3$, $P = 1.0$. **j**, Same as in h, but for right-choice-predictive triplets. $n = 1,755$ triplets; two-tailed paired Student's t -test, real versus shuffled data, $****P < 0.0001$. For box plots, boundaries: 25–75th percentiles; midline, median; whiskers, minimum–maximum.

[Source data](#)

Supplementary information

Supplementary Information

This file contains the Supplementary Discussion and Supplementary References.

Reporting Summary

Video 1 Example trials from the mouse's perspective

Videos from the viewpoint of a mouse showing behavioral trials from the accumulating towers task. The first trial shows an example of the navigational component of the task - the animal initially turns too early and has to correct itself before making it into the correct arm.

Video 2 Example manifold firing fields

Neural activity from 25 example cells recorded in the same imaging session and plotted on the 3-dimensional embedding of the manifold. Similar to Fig. 3d, we only show $\Delta F/F$ values that are 3 standard deviations above the mean activity for each cell.

Video 3 Example left- and right-choice trajectories through manifold space

Two trajectories (left-choice trial = blue; right-choice trial = red) through manifold space in one imaging session from one animal. Position (left) and evidence (right) are plotted as color on the 3-dimensional embedding of the manifold. The bar at the bottom represents the time elapsed in the trial (cue and delay periods).

Source data

Source Data Fig. 1

[Source Data Fig. 2](#)

[Source Data Fig. 3](#)

[Source Data Fig. 4](#)

[Source Data Extended Data Fig. 1](#)

[Source Data Extended Data Fig. 2](#)

[Source Data Extended Data Fig. 3](#)

[Source Data Extended Data Fig. 4](#)

[Source Data Extended Data Fig. 5](#)

[Source Data Extended Data Fig. 6](#)

[Source Data Extended Data Fig. 7](#)

[Source Data Extended Data Fig. 8](#)

[Source Data Extended Data Fig. 9](#)

Rights and permissions

[Reprints and Permissions](#)

About this article



Check for
updates

Cite this article

Nieh, E.H., Schottdorf, M., Freeman, N.W. *et al.* Geometry of abstract learned knowledge in the hippocampus. *Nature* **595**, 80–84 (2021). <https://doi.org/10.1038/s41586-021-03652-7>

[Download citation](#)

- Received: 05 February 2020
- Accepted: 18 May 2021
- Published: 16 June 2021
- Issue Date: 01 July 2021
- DOI: <https://doi.org/10.1038/s41586-021-03652-7>

[Access through your institution](#)

[Change institution](#)

[Buy or subscribe](#)

Advertisement

This article was downloaded by **calibre** from <https://www.nature.com/articles/s41586-021-03652-7>

| [Section menu](#) | [Main menu](#) |

- Article
- [Published: 12 May 2021](#)

Lineage tracing of human development through somatic mutations

- [Michael Spencer Chapman](#)^{1,2,3 na1},
- [Anna Maria Ranzoni](#) ORCID: orcid.org/0000-0002-2573-1382^{1,4,5 na1},
- [Brynelle Myers](#)^{1,4,5},
- [Nicholas Williams](#) ORCID: orcid.org/0000-0003-3989-9167¹,
- [Tim H. H. Coorens](#) ORCID: orcid.org/0000-0002-5826-3554¹,
- [Emily Mitchell](#)^{1,3,4},
- [Timothy Butler](#) ORCID: orcid.org/0000-0001-5803-1035¹,
- [Kevin J. Dawson](#)¹,
- [Yvette Hooks](#)¹,
- [Luiza Moore](#) ORCID: orcid.org/0000-0001-5315-516X^{1,6},
- [Jyoti Nangalia](#)^{1,4,5},
- [Philip S. Robinson](#) ORCID: orcid.org/0000-0002-6237-7159^{1,7},
- [Kenichi Yoshida](#)¹,
- [Elizabeth Hook](#)⁶,
- [Peter J. Campbell](#) ORCID: orcid.org/0000-0002-3921-0510^{1,4 na2} &
- [Ana Cvejic](#) ORCID: orcid.org/0000-0003-3204-9311^{1,4,5 na2}

[Nature](#) volume 595, pages 85–90 (2021) [Cite this article](#)

- 7781 Accesses
- 226 Altmetric
- [Metrics details](#)

Subjects

- [Genomics](#)
- [Haematopoiesis](#)

Abstract

The ontogeny of the human haematopoietic system during fetal development has previously been characterized mainly through careful microscopic observations¹. Here we reconstruct a phylogenetic tree of blood development using whole-genome sequencing of 511 single-cell-derived haematopoietic colonies from healthy human fetuses at 8 and 18 weeks after conception, coupled with deep targeted sequencing of tissues of known embryonic origin. We found that, in healthy fetuses, individual haematopoietic progenitors acquire tens of somatic mutations by 18 weeks after conception. We used these mutations as barcodes and timed the divergence of embryonic and extra-embryonic tissues during development, and estimated the number of blood antecedents at different stages of embryonic development. Our data support a hypoblast origin of the extra-embryonic mesoderm and primitive blood in humans.

Access options

Subscribe to Journal

Get full journal access for 1 year

\$199.00

only \$3.90 per issue

[Subscribe](#)

All prices are NET prices.

VAT will be added later in the checkout.

Tax calculation will be finalised during checkout.

Rent or Buy article

Get time limited or full article access on ReadCube.

from \$8.99

[Rent or Buy](#)

All prices are NET prices.

Additional access options:

- [Log in](#)
- [Access through your institution](#)
- [Learn about institutional subscriptions](#)

Fig. 1: Experimental workflow and phylogenetic trees.

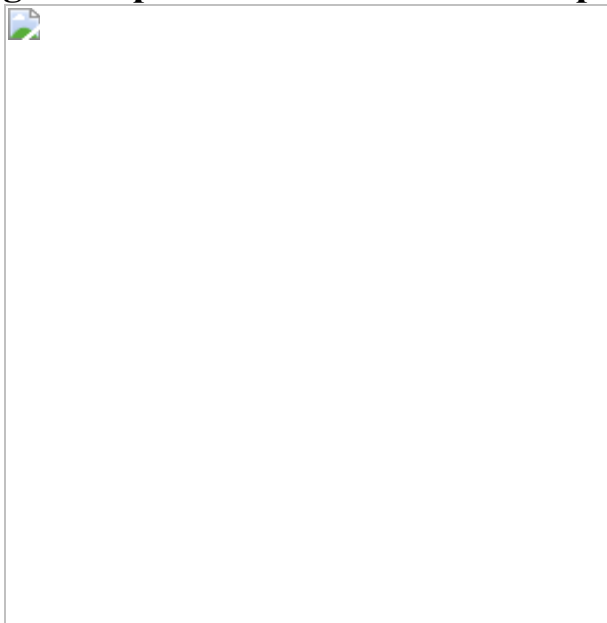


Fig. 2: Reconstructing lineage divergence through targeted sequencing.

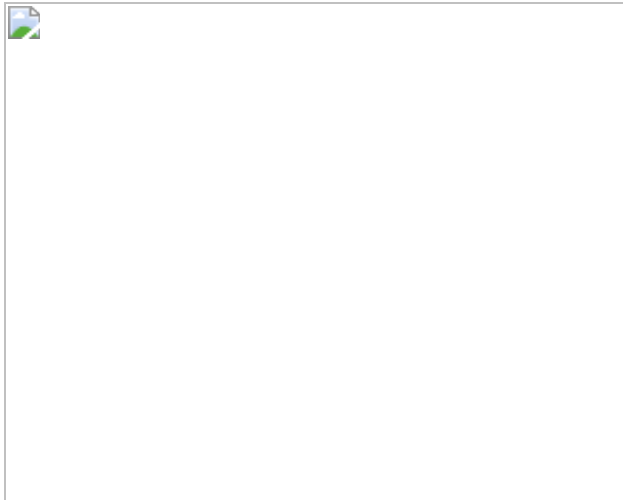


Fig. 3: Timing of divergence of embryonic and extra-embryonic lineages during development.

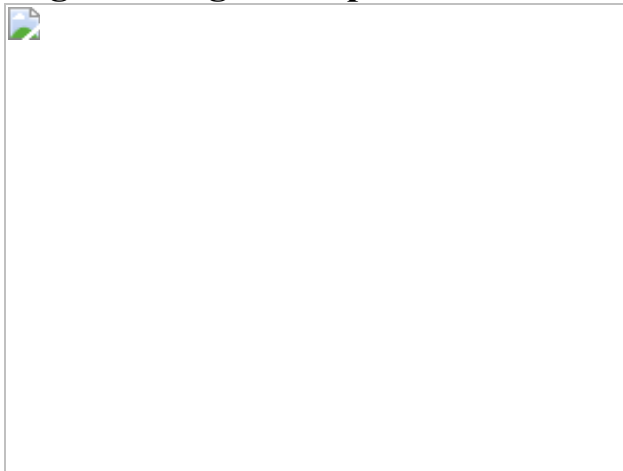
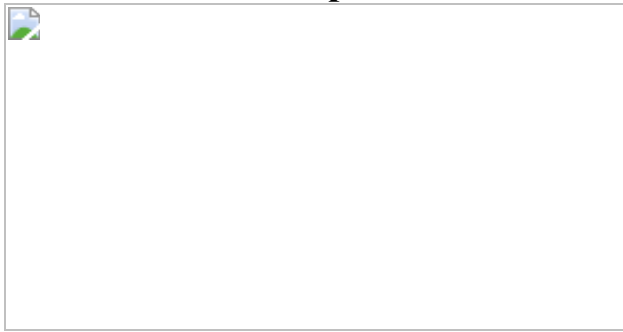


Fig. 4: Representation of haematopoietic lineages in developmentally defined non-haematopoietic tissues.



Data availability

Whole genomes and targeted sequencing data have been deposited in the European Genome–phenome Archive (EGA) (<https://www.ebi.ac.uk/ega/>). WGS data have been deposited with EGA accession number EGAD00001006162 and targeted sequencing data have been deposited with accession number EGAD00001006118. Data from the EGA are accessible for research use only to all bona fide researchers, as assessed by the Data Access Committee (<https://www.ebi.ac.uk/ega/about/access>). Data can be accessed by registering for an EGA account and contacting the Data Access Committee. All laser-capture microdissection images are deposited on Mendeley Data ('Phylogeny_of_foetal_hematopoiesis_2020_LCM_images', at <https://doi.org/10.17632/9b264dw38s.1>), and are accessible without restriction. Laser-capture microdissection images can be viewed using the free software NDP.view 2. More extensive derived datasets are available, together with the analysis code, without restriction at https://github.com/mspencerchapman/Phylogeny_of_foetal_hematopoiesis. Source data are provided with this paper.

Code availability

All scripts and some derived datasets are available at https://github.com/mspencerchapman/Phylogeny_of_foetal_hematopoiesis.

References

1. 1.

Ivanovs, A. et al. Human hematopoietic stem cell development: from the embryo to the dish. *Development* **144**, 2323–2337 (2017).

[CAS Article](#) [Google Scholar](#)

2. 2.

OpenStax. *Anatomy and Physiology* (2016).

3. 3.

Luckett, W. P. Origin and differentiation of the yolk sac and extraembryonic mesoderm in presomite human and rhesus monkey embryos. *Am. J. Anat.* **152**, 59–97 (1978).

[CAS](#) [Article](#) [Google Scholar](#)

4. 4.

Palis, J. & Yoder, M. C. Yolk-sac hematopoiesis: the first blood cells of mouse and man. *Exp. Hematol.* **29**, 927–936 (2001).

[CAS](#) [Article](#) [Google Scholar](#)

5. 5.

Silver, L. & Palis, J. Initiation of murine embryonic erythropoiesis: a spatial analysis. *Blood* **89**, 1154–1164 (1997).

[CAS](#) [Article](#) [Google Scholar](#)

6. 6.

Arnold, S. J. & Robertson, E. J. Making a commitment: cell lineage allocation and axis patterning in the early mouse embryo. *Nat. Rev. Mol. Cell Biol.* **10**, 91–103 (2009).

[CAS](#) [Article](#) [Google Scholar](#)

7. 7.

Rossant, J. & Tam, P. P. L. New insights into early human development: lessons for stem cell derivation and differentiation. *Cell Stem Cell* **20**, 18–28 (2017).

[CAS](#) [Article](#) [Google Scholar](#)

8. 8.

Enders, A. C. & King, B. F. Formation and differentiation of extraembryonic mesoderm in the rhesus monkey. *Am. J. Anat.* **181**, 327–340 (1988).

[CAS](#) [Article](#) [Google Scholar](#)

9. 9.

Kelemen, E., Calvo, W. & Fliedner, T. M. *Atlas of Human Hemopoietic Development* (1979).

10. 10.

Charbord, P., Tavian, M., Humeau, L. & Péault, B. Early ontogeny of the human marrow from long bones: an immunohistochemical study of hematopoiesis and its microenvironment. *Blood* **87**, 4109–4119 (1996).

[CAS](#) [Article](#) [Google Scholar](#)

11. 11.

Blokzijl, F. et al. Tissue-specific mutation accumulation in human adult stem cells during life. *Nature* **538**, 260–264 (2016).

[ADS](#) [CAS](#) [Article](#) [Google Scholar](#)

12. 12.

Baron, C. S. & van Oudenaarden, A. Unravelling cellular relationships during development and regeneration using genetic lineage tracing. *Nat. Rev. Mol. Cell Biol.* **20**, 753–765 (2019).

[CAS](#) [Article](#) [Google Scholar](#)

13. 13.

Lee-Six, H. et al. Population dynamics of normal human blood inferred from somatic mutations. *Nature* **561**, 473–478 (2018).

[ADS](#) [CAS](#) [Article](#) [Google Scholar](#)

14. 14.

Bárcena, A. et al. Human placenta and chorion: potential additional sources of hematopoietic stem cells for transplantation. *Transfusion* **51**, 94S–105S (2011).

[Article](#) [Google Scholar](#)

15. 15.

Hodgkinson, A. & Eyre-Walker, A. Variation in the mutation rate across mammalian genomes. *Nat. Rev. Genet.* **12**, 756–766 (2011).

[CAS](#) [Article](#) [Google Scholar](#)

16. 16.

Chapman, M. A. et al. Initial genome sequencing and analysis of multiple myeloma. *Nature* **471**, 467–472 (2011).

[ADS](#) [CAS](#) [Article](#) [Google Scholar](#)

17. 17.

Schuster-Böckler, B. & Lehner, B. Chromatin organization is a major influence on regional mutation rates in human cancer cells. *Nature* **488**, 504–507 (2012).

[ADS](#) [Article](#) [Google Scholar](#)

18. 18.

Ju, Y. S. et al. Somatic mutations reveal asymmetric cellular dynamics in the early human embryo. *Nature* **543**, 714–718 (2017).

[ADS](#) [CAS](#) [Article](#) [Google Scholar](#)

19. 19.

Yoshida, K. et al. Tobacco smoking and somatic mutations in human bronchial epithelium. *Nature* **578**, 266–272 (2020).

[ADS](#) [CAS](#) [Article](#) [Google Scholar](#)

20. 20.

Ye, A. Y. et al. A model for postzygotic mosaicism quantifies the allele fraction drift, mutation rate, and contribution to de novo mutations. *Genome Res.* **28**, 943–951 (2018).

[CAS](#) [Article](#) [Google Scholar](#)

21. 21.

Schulz, K. N. & Harrison, M. M. Mechanisms regulating zygotic genome activation. *Nat. Rev. Genet.* **20**, 221–234 (2019).

[CAS](#) [Article](#) [Google Scholar](#)

22. 22.

Molè, M. A., Weberling, A. & Zernicka-Goetz, M. Comparative analysis of human and mouse development: from zygote to pre-gastrulation. *Curr. Top. Dev. Biol.* **136**, 113–138 (2020).

[Article](#) [Google Scholar](#)

23. 23.

Xiang, L. et al. A developmental landscape of 3D-cultured human pre-gastrulation embryos. *Nature* **577**, 537–542 (2020).

[CAS](#) [Article](#) [Google Scholar](#)

24. 24.

Kuruppumullage Don, P., Ananda, G., Chiaromonte, F. & Makova, K. D. Segmenting the human genome based on states of neutral genetic divergence. *Proc. Natl Acad. Sci. USA* **110**, 14699–14704 (2013).

[ADS](#) [Article](#) [Google Scholar](#)

25. 25.

Wu, J. et al. Chromatin analysis in human early development reveals epigenetic transition during ZGA. *Nature* **557**, 256–260 (2018).

[ADS](#) [CAS](#) [Article](#) [Google Scholar](#)

26. 26.

Velten, L. et al. Human haematopoietic stem cell lineage commitment is a continuous process. *Nat. Cell Biol.* **19**, 271–281 (2017).

[CAS](#) [Article](#) [Google Scholar](#)

27. 27.

Ellis, P. et al. Reliable detection of somatic mutations in solid tissues by laser-capture microdissection and low-input DNA sequencing. *Nat. Protocols* **16**, 841–871 (2021).

[CAS](#) [Article](#) [Google Scholar](#)

28. 28.

Van Loo, P. et al. Allele-specific copy number analysis of tumors. *Proc. Natl Acad. Sci. USA* **107**, 16910–16915 (2010).

[ADS](#) [Article](#) [Google Scholar](#)

29. 29.

Conway, T. et al. Xenome—a tool for classifying reads from xenograft samples. *Bioinformatics* **28**, i172–i178 (2012).

[CAS](#) [Article](#) [Google Scholar](#)

30. 30.

Raine, K. M. et al. cgPindel: identifying somatically acquired insertion and deletion events from paired end sequencing. *Curr. Protoc. Bioinformatics* **52**, 15.7.1–15.7.12 (2015).

[Article](#) [Google Scholar](#)

31. 31.

Jones, D. et al. cgCaVEManWrapper: simple execution of CaVEMan in order to detect somatic single nucleotide variants in NGS data. *Curr. Protoc. Bioinformatics* **56**, 15.10.1–15.10.18 (2016).

[Article](#) [Google Scholar](#)

32. 32.

Coorens, T. H. H. et al. Embryonal precursors of Wilms tumor. *Science* **366**, 1247–1251 (2019).

[ADS](#) [CAS](#) [Article](#) [Google Scholar](#)

33. 33.

Hoang, D. T. et al. MPBoot: fast phylogenetic maximum parsimony tree inference and bootstrap approximation. *BMC Evol. Biol.* **18**, 11 (2018).

[Article](#) [Google Scholar](#)

[Download references](#)

Acknowledgements

The study was supported by European Research Council project 677501 – ZF_Blood (to A.C. and A.M.R.), an EMBO Young Investigator Award (to A.C.) and core support grants from the Wellcome Trust to the Wellcome Sanger Institute and both Wellcome and the MRC to the Wellcome Trust–Medical Research Council Cambridge Stem Cell Institute (203151/Z/16/Z). M.S.C. was supported by a Wellcome Clinical PhD Fellowship. We thank the Wellcome Sanger Institute (WSI) Cytometry Core Facility for their help with single-cell index sorting; the WSI DNA pipelines for their contribution to sequencing the data; the WSI Cancer, Ageing and Somatic Mutation programme IT and sample teams for their bioinformatic and logistical support; J. Eliasova (scientific illustrator, WSI) for her support and help with the illustrations; and the Human Developmental Biology Resource (HDBR) for providing samples.

Author information

Author notes

1. These authors contributed equally: Michael Spencer Chapman, Anna Maria Ranzoni
2. These authors jointly supervised this work: Peter J. Campbell, Ana Cvejic

Affiliations

1. Wellcome Trust Sanger Institute, Hinxton, UK

Michael Spencer Chapman, Anna Maria Ranzoni, Brynelle Myers, Nicholas Williams, Tim H. H. Coorens, Emily Mitchell, Timothy Butler, Kevin J. Dawson, Yvette Hooks, Luiza Moore, Jyoti Nangalia, Philip S. Robinson, Kenichi Yoshida, Peter J. Campbell & Ana Cvejic

2. Department of Haematology, Hammersmith Hospital, Imperial College Healthcare NHS Trust, London, UK

Michael Spencer Chapman

3. Department of Haematology, Cambridge University Hospitals NHS Foundation Trust, Cambridge, UK

Michael Spencer Chapman & Emily Mitchell

4. Wellcome Trust–Medical Research Council Cambridge Stem Cell Institute, Cambridge, UK

Anna Maria Ranzoni, Brynelle Myers, Emily Mitchell, Jyoti Nangalia, Peter J. Campbell & Ana Cvejic

5. Department of Haematology, University of Cambridge, Cambridge, UK

Anna Maria Ranzoni, Brynelle Myers, Jyoti Nangalia & Ana Cvejic

6. Department of Histopathology, Cambridge University Hospitals NHS Foundation Trust, Cambridge, UK

Luiza Moore & Elizabeth Hook

7. Department of Paediatrics, University of Cambridge, Cambridge, UK

Philip S. Robinson

Authors

1. Michael Spencer Chapman

[View author publications](#)

You can also search for this author in [PubMed](#) [Google Scholar](#)

2. Anna Maria Ranzoni

[View author publications](#)

You can also search for this author in [PubMed](#) [Google Scholar](#)

3. Brynelle Myers

[View author publications](#)

You can also search for this author in [PubMed](#) [Google Scholar](#)

4. Nicholas Williams

[View author publications](#)

You can also search for this author in [PubMed](#) [Google Scholar](#)

5. Tim H. H. Coorens

[View author publications](#)

You can also search for this author in [PubMed](#) [Google Scholar](#)

6. Emily Mitchell

[View author publications](#)

You can also search for this author in [PubMed](#) [Google Scholar](#)

7. Timothy Butler

[View author publications](#)

You can also search for this author in [PubMed](#) [Google Scholar](#)

8. Kevin J. Dawson

[View author publications](#)

You can also search for this author in [PubMed](#) [Google Scholar](#)

9. Yvette Hooks

[View author publications](#)

You can also search for this author in [PubMed](#) [Google Scholar](#)

10. Luiza Moore

[View author publications](#)

You can also search for this author in [PubMed](#) [Google Scholar](#)

11. Jyoti Nangalia

[View author publications](#)

You can also search for this author in [PubMed](#) [Google Scholar](#)

12. Philip S. Robinson

[View author publications](#)

You can also search for this author in [PubMed](#) [Google Scholar](#)

13. Kenichi Yoshida

[View author publications](#)

You can also search for this author in [PubMed](#) [Google Scholar](#)

14. Elizabeth Hook

[View author publications](#)

You can also search for this author in [PubMed](#) [Google Scholar](#)

15. Peter J. Campbell

[View author publications](#)

You can also search for this author in [PubMed](#) [Google Scholar](#)

16. Ana Cvejic

[View author publications](#)

You can also search for this author in [PubMed](#) [Google Scholar](#)

Contributions

A.C., A.M.R. and P.J.C. conceived the study; A.M.R. performed all the experiments with help from B.M.; M.S.C. carried out the computational analysis of the WGS data, under the supervision of P.J.C.; Y.H. prepared all histology sections for microdissection; T.B. assisted with the targeted sequencing strategy; T.B. and P.S.R. assisted with the laser-capture microdissections; K.Y. helped with the analysis of the bronchial epithelial

phylogeny data; E.H. and L.M. assisted with annotating histology slides; N.W., T.H.H.C. and E.M. assisted with somatic mutation calling from WGS data, the construction of the phylogeny and the assignment of mutations to the tree; N.W., J.N. and K.J.D. helped to design and implement population simulation models to help with interpreting the phylogenies; A.C., A.M.R. and M.S.C. designed the figures and wrote the manuscript with inputs from the other authors. All authors approved the final version of the manuscript.

Corresponding authors

Correspondence to [Peter J. Campbell](#) or [Ana Cvejic](#).

Ethics declarations

Competing interests

P.J.C. is a co-founder and stock-holder in Mu Genomics Ltd. The other authors declare no competing interests.

Additional information

Peer review information *Nature* thanks Fernando Camargo, Patrick Tam and the other, anonymous, reviewer(s) for their contribution to the peer review of this work. Peer reviewer reports are available.

Publisher's note Springer Nature remains neutral with regard to jurisdictional claims in published maps and institutional affiliations.

Extended data figures and tables

[Extended Data Fig. 1 Fluorescence-activated cell sorting strategy for haematopoietic progenitor cells from fetal liver and bone marrow.](#)

a, Following the exclusion of debris and cell doublets by gating and depletion of mature cells using a lineage antibody cocktail, we used anti-CD34 and anti-CD38 staining to sort single haematopoietic progenitor cells from the liver of an 8-pcw fetus. The sorting strategy for different stem and haematopoietic progenitor populations from matched liver and two femurs of a 18-pcw fetus. Following exclusion of debris and cell doublets and lineage depletion, anti-CD34, anti-CD38, anti-CD90, anti-CD45RA, anti-CD49f, anti-CD7, anti-CD10 and anti-CD123 staining was used to sort haematopoietic progenitor populations. **b**, Laser-capture microdissected tissues. Representative histological slides of tissue structures with different developmental origins. Between 9 and 18 sections were made for each tissue. Slides were stained with haematoxylin and eosin before microdissection. Structures microdissected from the 8-pcw sample included: mesodermal core and syncytiotrophoblast from the placenta, blood circulating in the heart, muscle from the heart, tubules from the kidney, epithelium from the gut, epidermis from the skin and vertebral disc from the vertebrae. Structures microdissected from the 18-pcw sample included: epidermis and peripheral nerves from the skin, muscle from the heart and glomeruli from the kidney. HSCs, haematopoietic stem cells; CMPs, common myeloid progenitors; MEPs, megakaryocyte–erythroid progenitors. $n = 20,000$ cells.

Extended Data Fig. 2 Sample contamination and sequencing coverage.

a, Box plot showing the percentage of human sequencing reads, before the exclusion of contaminating mouse reads from the feeder layer. The boxes indicate the median and interquartile range (IQR) and the whiskers extend to the largest and smallest values no more than $1.5 \times$ IQR from the box. Outlying points are plotted individually. **b**, Dot plot showing, for each colony of the two fetuses, the final sequencing coverage, after exclusion of mouse reads, against the percentage of human reads. The solid lines show the effect of human read percentage on the final sequencing coverage for each fetus, estimated using a linear model. The shaded area is the 95% confidence interval of this effect. **c**, Box plot showing final sample coverage for the two fetuses. The boxes indicate the median and IQR and the whiskers extend to the largest and smallest values no more than $1.5 \times$

IQR from the box. Outlying points are plotted individually. **d**, Dot plot showing the uncorrected SNV burden per colony against sample coverage (samples with $<4\times$ coverage are excluded). The solid lines show the effect of sequencing coverage on the uncorrected SNV burden for each fetus, estimated using a linear model. The shaded area is the 95% confidence interval of this effect. **e**, Dot plot showing the corrected SNV burden per colony against sequencing coverage (samples with $<4\times$ coverage excluded). The solid lines show the effect of sequencing coverage on the corrected SNV burden for each fetus, estimated using a linear model. The shaded area is the 95% confidence interval of this effect. **f**, Dot plot showing the uncorrected indel burden per colony against sequencing coverage (samples with $<4\times$ coverage excluded). The solid lines show the effect of sequencing coverage on the indel burden for each fetus, estimated using a linear model. The shaded area is the 95% confidence interval of this effect. **g**, ASCAT plot showing a normal male diploid karyotype for the 8-pcw and 18-pcw fetuses. **h**, Histograms showing variant allele fraction (VAF) of shared mutations with targeted sequencing depth $\geq 8\times$ in the 8-pcw fetus. **i**, Histograms showing VAF of private mutations with targeted sequencing depth $\geq 8\times$ in the 8-pcw fetus. **j**, Histograms showing VAF of shared mutations with targeted sequencing depth $\geq 8\times$ in the 18-pcw fetus. **k**, Histograms showing VAF of shared mutations with targeted sequencing depth $\geq 8\times$ in the 18-pcw fetus. **l**, Histograms showing SNV burden per single-HSPC derived colony for the 8-pcw and 18-pcw fetuses, corrected for both the proportion of private mutations that are acquired in vitro, and for sample sensitivity. **m**, Indel burden per single-HSPC derived colony for the 8-pcw and 18-pcw fetuses, with no correction applied. **n**, Mean numbers of private and shared SNVs per colony for each fetus.

Source data

Extended Data Fig. 3 Benchmarking and validation of the phylogenetic trees.

a, Heat maps of the genotype data used for tree-building. Owing to the lower average coverage, there are more missing values in the 18-pcw data. Dendograms are from hierarchical clustering of the data, and do not represent the phylogeny. **b**, Internal consistency of the shared mutation data

for each fetus as determined by the disagreement score. A perfect phylogeny has a score of zero. Scores for the data are compared with scores for random shuffles of the genotype data at each locus. **c**, Comparison of the phylogenetic trees built by MPBoot and those by alternative phylogeny-inference algorithms IQTree and SCITE for both the 8-pcw and 18-pcw fetuses. Clades present in one phylogeny that are absent in the other are highlighted in red. The Robinson–Foulds distance of the alternative tree as compared with the MPBoot tree is shown. **d**, Robustness of each clade in three alternative bootstrapping approaches: bootstrapping of the raw sequencing read count data, bootstrapping of the mutation matrix and the bootstrap approximation method implemented with MPBoot. The proportion of bootstraps in which a clade is retained is shown, ordered by decreasing robustness. Clades from the first three generations—which are particularly important for later analysis—are highlighted in red. **e, f**, Comparison of the sequencing read count bootstrap trees to the original trees by the quartet divergence and Robinson–Foulds similarity for the 8-pcw (**e**) and 18-pcw (**f**) fetuses. **g**, Bar plot showing the relative contribution of the two daughter cells of the first detected cell division in 14 phylogenies obtained by human adult bronchial epithelial cells. Original data obtained from ref. [19](#). MRCA, most recent common ancestor; R-F, Robinson–Foulds.

[Source data](#)

Extended Data Fig. 4 Sensitivity and specificity of targeted sequencing mutation calling in fetal tissues.

a, For the 8-pcw fetus, the sensitivity for detection of shared (top) and private (bottom) mutations at different cell fractions in each tissue. As the prior expectation for the presence of mutations is dependent on the position within the phylogeny, the sensitivity is lower for private mutations. Solid lines indicate median values, and shaded areas show 95% confidence intervals from simulations ($n = 1,000$). **b**, As in **a**, but for the 18-pcw fetus. **c**, Comparison of the cell fractions of called mutations in the 8-pcw data, and false-positive calls simulated from the error distribution. The overall call rate across tissues is printed on each panel. The data are split by mutations occurring at different generations from the zygote. Owing to the high prior expectation, early mutations are frequently called from the error

distribution, but at extremely low cell fractions that do not overlap those of the data. Later mutations have more overlap in the cell fractions of calls made from the data and the error distribution, but are rarely made from the error distribution. **d**, As in **c**, but for the 18-pcw fetus. Mutations on the minor branch are not included in this figure as none were called in the data and the generation of these mutations is uncertain.

[Source data](#)

Extended Data Fig. 5 Genomic distribution of identified somatic mutations.

a, Plot showing the proportion of variants mapping to different genomic features. The box-and-whisker plots show proportions of simulated mutations in different categories ($n = 524$), with the boxes indicating median and IQR and the whiskers denoting the range. **b**, Plot showing the proportion of variants within protein-coding sequences. The histograms show the distribution obtained by 500 simulations of random acquisition of mutations across the genome. **c**, Plot showing the proportion of variants within introns of protein-coding genes. The histograms show the distribution obtained by 500 simulations of random acquisition of mutations across the genome. **d**, Mutations in protein-coding sequences in the 18-pcw fetus, mapped on the branch of acquisition. Only those found in ≥ 2 colonies are shown. **e**, Mutations in protein-coding sequences in the 8-pcw fetus, mapped on the branch of acquisition. Only those found in ≥ 2 colonies are shown.

[Source data](#)

Extended Data Fig. 6 Mutational signatures.

a–c, Mutational signatures incorporating the trinucleotide context of shared mutations (**a**), private mutations assigned to the clonal peak in the binomial mixture model (that is, likely in vivo-acquired mutations) (**b**) and private mutations assigned to subclonal peaks in the binomial mixture (that is, likely in vitro-acquired mutations) (**c**). **d**, Mutations detected in WGS of two 8-pcw trophoblast microbiopsies.

[Source data](#)

Extended Data Fig. 7 Timing of divergence of embryonic and extra-embryonic lineages during development.

a, Heat map of the targeted sequencing data from the 8-pcw fetus. Each column and each row represents a single tissue. The colour shows the level of correlation. **b**, Density plots showing the distribution of variant allele fraction of mutations identified through WGS of specific microbiopsies. **c**, Heat map of the targeted sequencing data from the 18-pcw fetus. Each column represents an individual mutation, and each row a single tissue. The colour shows the variant allele fraction of the mutation in that tissue; grey indicates that the mutation was not detected. **d**, Heat map of the targeted sequencing data from the 18-pcw fetus. Each column and each row represents a single tissue. The colour shows the level of correlation. **e**, Line plot showing lineage loss of microdissected tissues in the 18-pcw fetus at different times (represented as cell generations from the zygote). Shaded areas represent confidence intervals. **f**, Phylogenetic tree showing the clonal relationships of 18-pcw HSPCs. Mutations identified in HSPCs by WGS that were also detected in non-haematopoietic tissues are coloured on the tree according to the earliest diverging tissue in which the mutation was reliably detected. Branch lengths are proportional to the number of mutations accumulated. The tree contains only those SNVs included in the bait set for targeted sequencing. In all heat maps, the tissues are clustered using soft cosine similarity (Methods). Vaf, variant allele fraction.

[Source data](#)

Extended Data Fig. 8 High level of intermixing of 18-pcw HSPCs among fetal liver and two sites of bone marrow.

a, Ultrametric phylogenetic tree of 18-pcw HSPCs with branches coloured by the tissue from which HSPCs bearing the mutations were isolated. Black branches indicate that cells were found in more than one tissue; coloured branches indicate cells were unique to one specific tissue. **b**, Analysis of molecular variance used to formally test for clustering on the phylogeny of HSPCs isolated from the same tissue. The histogram shows the null

distribution used to detect clustering. Distributions were obtained by randomly permuting which cells were assigned to which tissue ($n = 30,000$). The observed value of the phi statistic is shown as a red line, with the P value indicating no statistically significant clustering by tissue. **c**, Bar plot showing the number of new mutations identified through WGS in the 18 microbiopsies with coverage $>15\times$. **d**, Heat map showing the cell fractions of individual new mutations shared by more than one tissue, identified through WGS in the different tissues. **e**, Line plot showing the fraction of captured haematopoietic lineages shared by non-haematopoietic tissues in the 18-pcw phylogeny, grouped by germ layer and plotted over successive generations. **f, g**, Phylogenetic trees highlighting mutations detected in HSPCs that were shared with the ectoderm (**f**) and mesoderm (**g**) in the 18-pcw fetus. The fraction of cells deriving from each lineage is plotted on a pie chart. Trees were made ultrametric. VAF, variant allele fraction.

Source data

Extended Data Fig. 9 Inference of lineages.

a, Potential outcomes of cell division of a multipotent antecedent observed in the HSPC phylogeny, **b**, Top of the 8-pcw phylogeny. Mutations detected in trophectoderm tissues are highlighted in red. Dark blue circles represent antecedent cells that are committed to the inner cell mass, but with a direct ancestor that was multipotent (contributing to both inner cell mass and trophectoderm). **c**, Top of the 8-pcw phylogeny. Mutations detected in extra-embryonic-mesoderm-derived tissues are highlighted in orange. Dark blue circles represent the 20 antecedent cells that are committed to the epiblast, but with a direct ancestor that was multipotent (contributing to both epiblast and hypoblast).

Supplementary information

Supplementary Methods

This file contains further detailed methods not covered in the main Methods section.

Reporting Summary

Peer Review File

Supplementary Table 1

A list of antibodies used for the study, including clone and manufacturer.

Supplementary Table 2

Laser capture microdissection biopsies undergoing targeted sequencing for the 8 pcw foetus.

Supplementary Table 3

Laser capture microdissection biopsies undergoing targeted sequencing for the 18 pcw foetus.

Supplementary Table 4

Laser capture microdissection biopsies undergoing whole-genome sequencing (8 pcw foetus).

Source data

Source Data Fig. 1

Source Data Fig. 2

Source Data Fig. 3

Source Data Fig. 4

[Source Data Extended Data Fig. 2](#)

[Source Data Extended Data Fig. 3](#)

[Source Data Extended Data Fig. 4](#)

[Source Data Extended Data Fig. 5](#)

[Source Data Extended Data Fig. 6](#)

[Source Data Extended Data Fig. 7](#)

[Source Data Extended Data Fig. 8](#)

Rights and permissions

[Reprints and Permissions](#)

About this article



Check for
updates

Cite this article

Spencer Chapman, M., Ranzoni, A.M., Myers, B. *et al.* Lineage tracing of human development through somatic mutations. *Nature* **595**, 85–90 (2021). <https://doi.org/10.1038/s41586-021-03548-6>

[Download citation](#)

- Received: 29 May 2020
- Accepted: 13 April 2021

- Published: 12 May 2021
- Issue Date: 01 July 2021
- DOI: <https://doi.org/10.1038/s41586-021-03548-6>

[Access through your institution](#)

[Change institution](#)

[Buy or subscribe](#)

Advertisement

This article was downloaded by **calibre** from <https://www.nature.com/articles/s41586-021-03548-6>

| [Section menu](#) | [Main menu](#) |

- Article
- [Published: 23 June 2021](#)

Evaluating microbiome-directed fibre snacks in gnotobiotic mice and humans

- [Omar Delannoy-Bruno](#) ORCID: [orcid.org/0000-0002-6637-4609^{1,2}](https://orcid.org/0000-0002-6637-4609),
- [Chandani Desai](#) ORCID: [orcid.org/0000-0002-3708-3634^{1,2}](https://orcid.org/0000-0002-3708-3634),
- [Arjun S. Raman^{1,2,3}](#),
- [Robert Y. Chen^{1,2}](#),
- [Matthew C. Hibberd](#) ORCID: [orcid.org/0000-0001-6520-677X^{1,2,3}](https://orcid.org/0000-0001-6520-677X),
- [Jiye Cheng](#) ORCID: [orcid.org/0000-0002-0266-3997^{1,2,3}](https://orcid.org/0000-0002-0266-3997),
- [Nathan Han^{1,2}](#),
- [Juan J. Castillo](#) ORCID: [orcid.org/0000-0001-9680-5273⁴](https://orcid.org/0000-0001-9680-5273),
- [Garret Couture⁴](#),
- [Carlito B. Lebrilla](#) ORCID: [orcid.org/0000-0001-7190-5323⁴](https://orcid.org/0000-0001-7190-5323),
- [Ruteja A. Barve](#) ORCID: [orcid.org/0000-0002-1171-9761⁵](https://orcid.org/0000-0002-1171-9761),
- [Vincent Lombard](#) ORCID: [orcid.org/0000-0002-9684-7067⁶](https://orcid.org/0000-0002-9684-7067),
- [Bernard Henrissat](#) ORCID: [orcid.org/0000-0002-3434-8588^{6,7}](https://orcid.org/0000-0002-3434-8588),
- [Semen A. Leyn](#) ORCID: [orcid.org/0000-0002-9886-9120⁸](https://orcid.org/0000-0002-9886-9120),
- [Dmitry A. Rodionov^{8,9}](#),
- [Andrei L. Osterman⁸](#),
- [David K. Hayashi¹⁰](#),
- [Alexandra Meynier¹⁰](#),
- [Sophie Vinoy](#) ORCID: [orcid.org/0000-0002-1038-6985¹⁰](https://orcid.org/0000-0002-1038-6985),
- [Kyleigh Kirbach¹¹](#),
- [Tara Wilmot¹¹](#),
- [Andrew C. Heath¹²](#),
- [Samuel Klein¹¹](#),

- [Michael J. Barratt^{1,2,3}](#) &
- [Jeffrey I. Gordon](#) [ORCID: orcid.org/0000-0001-8304-3548^{1,2,3}](#)

Nature volume **595**, pages 91–95 (2021) [Cite this article](#)

- 3553 Accesses
- 72 Altmetric
- [Metrics details](#)

Subjects

- [Agriculture](#)
- [Experimental models of disease](#)
- [Microbiome](#)

Abstract

Changing food preferences brought about by westernization that have deleterious health effects^{1,2}—combined with myriad forces that are contributing to increased food insecurity—are catalysing efforts to identify more nutritious and affordable foods³. Consumption of dietary fibre can help to prevent cardiovascular disease, type 2 diabetes and obesity^{4,5,6}. A substantial number of reports have explored the effects of dietary fibre on the gut microbial community^{7,8,9}. However, the microbiome is complex, dynamic and exhibits considerable intra- and interpersonal variation in its composition and functions. The large number of potential interactions between the components of the microbiome makes it challenging to define the mechanisms by which food ingredients affect community properties. Here we address the question of how foods containing different fibre preparations can be designed to alter functions associated with specific components of the microbiome. Because a marked increase in snack consumption is associated with westernization, we formulated snack prototypes using plant fibres from different sustainable sources that targeted distinct features of the gut microbiomes of individuals with obesity when

transplanted into gnotobiotic mice. We used these snacks to supplement controlled diets that were consumed by adult individuals with obesity or who were overweight. Fibre-specific changes in their microbiomes were linked to changes in their plasma proteomes indicative of an altered physiological state.

Access options

Subscribe to Journal

Get full journal access for 1 year

\$199.00

only \$3.90 per issue

[Subscribe](#)

All prices are NET prices.

VAT will be added later in the checkout.

Tax calculation will be finalised during checkout.

Rent or Buy article

Get time limited or full article access on ReadCube.

from \$8.99

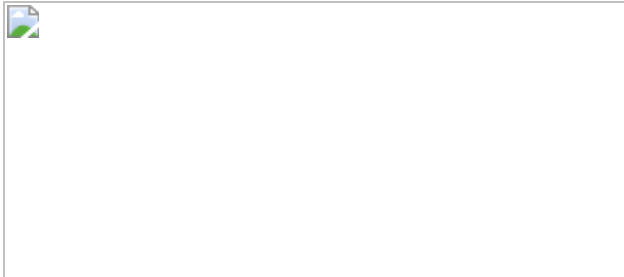
[Rent or Buy](#)

All prices are NET prices.

Additional access options:

- [Log in](#)
- [Access through your institution](#)
- [Learn about institutional subscriptions](#)

Fig. 1: Controlled-diet study of the effects of fibre snack prototypes on the faecal microbiomes of individuals with obesity or who are overweight.



Data availability

V4-16S rRNA sequences in raw format before post-processing and data analysis, plus shotgun sequencing datasets generated from faecal DNA, have been deposited at the European Nucleotide Archive under study accession [PRJEB38148](#). Raw proteomic datasets generated from the aptamer-based 1.3K SomaLogic platform have been deposited in the European Genome-Phenome Archive (EGA) under accession IDs EGAD00010002133 (pea fibre study) and EGAD00010002132 (fibre blends study). Any other relevant data are available from the corresponding author upon reasonable request. [Source data](#) are provided with this paper.

Code availability

Code for HOSVD (CP-ALS plus randomization code) and CC-SVD is available via Zenodo (<https://doi.org/10.5281/zenodo.4767887>).

References

1. 1.

NCD Risk Factor Collaboration (NCD-RisC). Trends in adult body-mass index in 200 countries from 1975 to 2014: a pooled analysis of 1698 population-based measurement studies with 19·2 million participants. *Lancet* **387**, 1377–1396 (2016).

[Google Scholar](#)

2. 2.

GBD 2017 Diet Collaborators. Health effects of dietary risks in 195 countries, 1990-2017: a systematic analysis for the Global Burden of Disease Study 2017. *Lancet* **393**, 1958–1972 (2019).

[Google Scholar](#)

3. 3.

Willett, W. et al. Food in the Anthropocene: the EAT-Lancet Commission on healthy diets from sustainable food systems. *Lancet* **393**, 447–492 (2019).

[PubMed](#) [Google Scholar](#)

4. 4.

Hauner, H. et al. Evidence-based guideline of the German Nutrition Society: carbohydrate intake and prevention of nutrition-related diseases. *Ann. Nutr. Metab.* **60** (Suppl 1), 1–58 (2012).

[ADS](#) [CAS](#) [Google Scholar](#)

5. 5.

Reynolds, A. et al. Carbohydrate quality and human health: a series of systematic reviews and meta-analyses. *Lancet* **393**, 434–445 (2019).

[CAS](#) [Google Scholar](#)

6. 6.

Zhao, L. et al. Gut bacteria selectively promoted by dietary fibers alleviate type 2 diabetes. *Science* **359**, 1151–1156 (2018).

[ADS](#) [CAS](#) [Google Scholar](#)

7. 7.

Asnicar, F. et al. Microbiome connections with host metabolism and habitual diet from 1,098 deeply phenotyped individuals. *Nat. Med.* **27**, 321–332 (2021).

[CAS](#) [Google Scholar](#)

8. 8.

Kovatcheva-Datchary, P. et al. Dietary fiber-induced improvement in glucose metabolism is associated with increased abundance of *Prevotella*. *Cell Metab.* **22**, 971–982 (2015).

[CAS](#) [Google Scholar](#)

9. 9.

Sonnenburg, E. D. et al. Specificity of polysaccharide use in intestinal *Bacteroides* species determines diet-induced microbiota alterations. *Cell* **141**, 1241–1252 (2010).

[CAS](#) [PubMed](#) [PubMed Central](#) [Google Scholar](#)

10. 10.

Ridaura, V. K. et al. Gut microbiota from twins discordant for obesity modulate metabolism in mice. *Science* **341**, 1241214 (2013).

[PubMed](#) [Google Scholar](#)

11. 11.

Patnode, M. L. et al. Interspecies competition impacts targeted manipulation of human gut bacteria by fiber-derived glycans. *Cell* **179**, 59–73.e13 (2019).

[CAS](#) [PubMed](#) [PubMed Central](#) [Google Scholar](#)

12. 12.

Lombard, V., Golaconda Ramulu, H., Drula, E., Coutinho, P. M. & Henrissat, B. The carbohydrate-active enzymes database (CAZy) in 2013. *Nucleic Acids Res.* **42**, D490–D495 (2014).

[CAS](#) [Google Scholar](#)

13. 13.

Overbeek, R. et al. The SEED and the Rapid Annotation of microbial genomes using Subsystems Technology (RAST). *Nucleic Acids Res.* **42**, D206–D214 (2014).

[CAS](#) [Google Scholar](#)

14. 14.

Martino, C. et al. Context-aware dimensionality reduction deconvolutes gut microbial community dynamics. *Nat. Biotechnol.* **39**, 165–168 (2021).

[CAS](#) [Google Scholar](#)

15. 15.

Wesener, D. A. et al. Microbiota functional activity biosensors for characterizing nutrient metabolism in vivo. *eLife* **10**, e64478 (2021).

[PubMed](#) [PubMed Central](#) [Google Scholar](#)

16. 16.

Temple, M. J. et al. A *Bacteroidetes* locus dedicated to fungal 1,6- β -glucan degradation: Unique substrate conformation drives specificity of the key endo-1,6- β -glucanase. *J. Biol. Chem.* **292**, 10639–10650 (2017).

[CAS](#) [PubMed](#) [PubMed Central](#) [Google Scholar](#)

17. 17.

Larsbrink, J. et al. A discrete genetic locus confers xyloglucan metabolism in select human gut *Bacteroidetes*. *Nature* **506**, 498–502 (2014).

[ADS](#) [CAS](#) [PubMed](#) [PubMed Central](#) [Google Scholar](#)

18. 18.

Schröder, C. et al. Characterization of a theme C glycoside hydrolase family 9 endo-beta-glucanase from a biogas reactor metagenome. *Protein J.* **37**, 454–460 (2018).

[Google Scholar](#)

19. 19.

Shimizu, H. et al. Characterization and structural analysis of a novel exo-type enzyme acting on β-1,2-glucooligosaccharides from *Parabacteroides distasonis*. *Biochemistry* **57**, 3849–3860 (2018).

[CAS](#) [Google Scholar](#)

20. 20.

Li, W. et al. PspAG97A: a halophilic α-glucoside hydrolase with wide substrate specificity from glycoside hydrolase family 97. *J. Microbiol. Biotechnol.* **26**, 1933–1942 (2016).

[CAS](#) [Google Scholar](#)

21. 21.

Gloster, T. M., Turkenburg, J. P., Potts, J. R., Henrissat, B. & Davies, G. J. Divergence of catalytic mechanism within a glycosidase family provides insight into evolution of carbohydrate metabolism by human gut flora. *Chem. Biol.* **15**, 1058–1067 (2008).

[CAS](#) [PubMed](#) [PubMed Central](#) [Google Scholar](#)

22. 22.

Helbert, W. et al. Discovery of novel carbohydrate-active enzymes through the rational exploration of the protein sequences space. *Proc. Natl Acad. Sci. USA* **116**, 6063–6068 (2019).

[CAS](#) [PubMed](#) [PubMed Central](#) [Google Scholar](#)

23. 23.

Ndeh, D. et al. Complex pectin metabolism by gut bacteria reveals novel catalytic functions. *Nature* **544**, 65–70 (2017).

[ADS](#) [CAS](#) [PubMed](#) [PubMed Central](#) [Google Scholar](#)

24. 24.

Hashimoto, W., Miyake, O., Ochiai, A. & Murata, K. Molecular identification of *Sphingomonas* sp. A1 alginate lyase (A1-IV') as a member of novel polysaccharide lyase family 15 and implications in alginate lyase evolution. *J. Biosci. Bioeng.* **99**, 48–54 (2005).

[CAS](#) [Google Scholar](#)

25. 25.

Ritchie, M. E. et al. limma powers differential expression analyses for RNA-sequencing and microarray studies. *Nucleic Acids Res.* **43**, e47 (2015).

[PubMed](#) [PubMed Central](#) [Google Scholar](#)

26. 26.

Derecka, M. et al. Tyk2 and Stat3 regulate brown adipose tissue differentiation and obesity. *Cell Metab.* **16**, 814–824 (2012).

[CAS](#) [PubMed](#) [PubMed Central](#) [Google Scholar](#)

27. 27.

Pedersen, L., Olsen, C. H., Pedersen, B. K. & Hojman, P. Muscle-derived expression of the chemokine CXCL1 attenuates diet-induced obesity and improves fatty acid oxidation in the muscle. *Am. J. Physiol. Endocrinol. Metab.* **302**, E831–E840 (2012).

[CAS](#) [Google Scholar](#)

28. 28.

Kraja, A. T. et al. Genetic analysis of 16 NMR-lipoprotein fractions in humans, the GOLDN study. *Lipids* **48**, 155–165 (2013).

[CAS](#) [Google Scholar](#)

29. 29.

ZhuGe, D. L., Javaid, H. M. A., Sahar, N. E., Zhao, Y. Z. & Huh, J. Y. Fibroblast growth factor 2 exacerbates inflammation in adipocytes through NLRP3 inflammasome activation. *Arch. Pharm. Res.* **43**, 1311–1324 (2020).

[Google Scholar](#)

30. 30.

Michalak, L. et al. Microbiota-directed fibre activates both targeted and secondary metabolic shifts in the distal gut. *Nat. Commun.* **11**, 5773 (2020).

[ADS](#) [CAS](#) [PubMed](#) [PubMed Central](#) [Google Scholar](#)

31. 31.

Bucholz, K. K., Heath, A. C. & Madden, P. A. Transitions in drinking in adolescent females: evidence from the Missouri adolescent female

twin study. *Alcohol. Clin. Exp. Res.* **24**, 914–923 (2000).

[CAS](#) [Google Scholar](#)

32. 32.

Mifflin, M. D. et al. A new predictive equation for resting energy expenditure in healthy individuals. *Am. J. Clin. Nutr.* **51**, 241–247 (1990).

[CAS](#) [Google Scholar](#)

33. 33.

Subar, A. F. et al. Comparative validation of the Block, Willett, and National Cancer Institute food frequency questionnaires: the Eating at America's Table Study. *Am. J. Epidemiol.* **154**, 1089–1099 (2001).

[CAS](#) [Google Scholar](#)

34. 34.

Caporaso, J. G. et al. Global patterns of 16S rRNA diversity at a depth of millions of sequences per sample. *Proc. Natl Acad. Sci. USA* **108** (Suppl 1), 4516–4522 (2011).

[ADS](#) [CAS](#) [Google Scholar](#)

35. 35.

Callahan, B. J. et al. DADA2: high-resolution sample inference from Illumina amplicon data. *Nat. Methods* **13**, 581–583 (2016).

[CAS](#) [PubMed](#) [PubMed Central](#) [Google Scholar](#)

36. 36.

R Core Team. *R: A Language and Environment for Statistical Computing* (R Foundation for Statistical Computing, 2017).

37. 37.

Di Luccia, B. et al. Combined prebiotic and microbial intervention improves oral cholera vaccination responses in a mouse model of childhood undernutrition. *Cell Host Microbe* **27**, 899–908.e5 (2020).

[PubMed](#) [PubMed Central](#) [Google Scholar](#)

38. 38.

Baym, M. et al. Inexpensive multiplexed library preparation for megabase-sized genomes. *PLoS ONE* **10**, e0128036 (2015).

[PubMed](#) [PubMed Central](#) [Google Scholar](#)

39. 39.

Martin, M. Cutadapt removes adapter sequences from high-throughput sequencing reads. *EMBnetJ.* **17**, 10–12 (2011)

[Google Scholar](#)

40. 40.

Joshi, N. A. & Fass, J. N. *Sickle: A Sliding-Window, Adaptive, Quality-based Trimming tool for FastQ Files (Version 1.33) Software* (2011).

41. 41.

Langmead, B. & Salzberg, S. L. Fast gapped-read alignment with Bowtie 2. *Nat. Methods* **9**, 357–359 (2012).

[CAS](#) [PubMed](#) [PubMed Central](#) [Google Scholar](#)

42. 42.

Peng, Y., Leung, H. C. M., Yiu, S. M. & Chin, F. Y. L. IDBA-UD: a de novo assembler for single-cell and metagenomic sequencing data with highly uneven depth. *Bioinformatics* **28**, 1420–1428 (2012).

[CAS](#) [PubMed](#) [Google Scholar](#)

43. 43.

Li, D., Liu, C.-M., Luo, R., Sadakane, K. & Lam, T.-W. MEGAHIT: an ultra-fast single-node solution for large and complex metagenomics assembly via succinct de Bruijn graph. *Bioinformatics* **31**, 1674–1676 (2015).

[CAS](#) [Google Scholar](#)

44. 44.

Seemann, T. Prokka: rapid prokaryotic genome annotation. *Bioinformatics* **30**, 2068–2069 (2014).

[CAS](#) [Google Scholar](#)

45. 45.

Liao, Y., Smyth, G. K. & Shi, W. featureCounts: an efficient general purpose program for assigning sequence reads to genomic features. *Bioinformatics* **30**, 923–930 (2014).

[CAS](#) [PubMed](#) [Google Scholar](#)

46. 46.

Buchfink, B., Xie, C. & Huson, D. H. Fast and sensitive protein alignment using DIAMOND. *Nat. Methods* **12**, 59–60 (2015).

[CAS](#) [PubMed](#) [Google Scholar](#)

47. 47.

Camacho, C. et al. BLAST+: architecture and applications. *BMC Bioinformatics* **10**, 421 (2009).

[PubMed](#) [PubMed Central](#) [Google Scholar](#)

48. 48.

Mistry, J., Finn, R. D., Eddy, S. R., Bateman, A. & Punta, M. Challenges in homology search: HMMER3 and convergent evolution of coiled-coil regions. *Nucleic Acids Res.* **41**, e121 (2013).

[CAS](#) [PubMed](#) [PubMed Central](#) [Google Scholar](#)

49. 49.

Chen, R. Y. et al. Duodenal microbiota in stunted undernourished children with enteropathy. *N. Engl. J. Med.* **383**, 321–333 (2020).

[CAS](#) [PubMed](#) [PubMed Central](#) [Google Scholar](#)

50. 50.

Plerou, V. et al. Random matrix approach to cross correlations in financial data. *Phys. Rev. E* **65**, 066126 (2002).

[ADS](#) [Google Scholar](#)

51. 51.

Winkler, E. S. et al. Human neutralizing antibodies against SARS-CoV-2 require intact Fc effector functions for optimal therapeutic protection. *Cell* **184**, 1804–1820.e16 (2021).

[CAS](#) [PubMed](#) [PubMed Central](#) [Google Scholar](#)

52. 52.

Zou, W. et al. Ablation of fat cells in adult mice induces massive bone gain. *Cell Metab.* **32**, 801–813.e6 (2020).

[CAS](#) [Google Scholar](#)

53. 53.

Adamo, L. et al. Proteomic signatures of heart failure in relation to left ventricular ejection fraction. *J. Am. Coll. Cardiol.* **76**, 1982–1994 (2020).

[CAS](#) [Google Scholar](#)

54. 54.

Tsingas, M. et al. *Sox9* deletion causes severe intervertebral disc degeneration characterized by apoptosis, matrix remodeling, and compartment-specific transcriptomic changes. *Matrix Biol.* **94**, 110–133 (2020).

[CAS](#) [Google Scholar](#)

55. 55.

Joly, J. H., Lowry, W. E. & Graham, N. A. Differential gene set enrichment analysis: a statistical approach to quantify the relative enrichment of two gene sets. *Bioinformatics* **36**, 5247–5254 (2020).

[CAS](#) [Google Scholar](#)

56. 56.

Wickham, H. *ggplot2: Elegant Graphics for Data Analysis* (Springer, 2009).

57. 57.

Blakeney, A. B., Harris, P. J., Henry, R. J. & Stone, B. A. A simple and rapid preparation of alditol acetates for monosaccharide analysis. *Carbohydr. Res.* **113**, 291–299 (1983).

[CAS](#) [Google Scholar](#)

58. 58.

Englyst, H. N. & Cummings, J. H. Improved method for measurement of dietary fiber as non-starch polysaccharides in plant foods. *J. Assoc. Off. Anal. Chem.* **71**, 808–814 (1988).

[CAS](#) [Google Scholar](#)

59. 59.

Blumenkrantz, N. & Asboe-Hansen, G. New method for quantitative determination of uronic acids. *Anal. Biochem.* **54**, 484–489 (1973).

[CAS](#) [Google Scholar](#)

60. 60.

Thibault, J.-F. Automatisation du dosage des substances pectiques par la méthode au métahydroxydiphényle. *Lebensm. Wiss. Technol.* **12**, 247–251 (1979).

[CAS](#) [Google Scholar](#)

61. 61.

Filisetti-Cozzi, T. M. C. C. & Carpita, N. C. Measurement of uronic acids without interference from neutral sugars. *Anal. Biochem.* **197**, 157–162 (1991).

[CAS](#) [Google Scholar](#)

62. 62.

Levigne, S., Thomas, M., Ralet, M.-C., Quemener, B. & Thibault, J.-F. Determination of the degrees of methylation and acetylation of pectins using a C18 column and internal standards. *Food Hydrocoll.* **16**, 547–550 (2002).

[CAS](#) [Google Scholar](#)

63. 63.

Pettolino, F. A., Walsh, C., Fincher, G. B. & Bacic, A. Determining the polysaccharide composition of plant cell walls. *Nat. Protoc.* **7**, 1590–1607 (2012).

[CAS](#) [Google Scholar](#)

64. 64.

Buffetto, F. et al. The deconstruction of pectic rhamnogalacturonan I unmasks the occurrence of a novel arabinogalactan oligosaccharide epitope. *Plant Cell Physiol.* **56**, 2181–2196 (2015).

[CAS](#) [Google Scholar](#)

65. 65.

Amicucci, M. J. et al. A rapid-throughput adaptable method for determining the monosaccharide composition of polysaccharides. *Int. J. Mass Spectrom.* **438**, 22–28 (2019).

[CAS](#) [Google Scholar](#)

66. 66.

Xu, G., Amicucci, M. J., Cheng, Z., Galermo, A. G. & Lebrilla, C. B. Revisiting monosaccharide analysis - quantitation of a comprehensive set of monosaccharides using dynamic multiple reaction monitoring. *Analyst* **143**, 200–207 (2018).

[ADS](#) [CAS](#) [Google Scholar](#)

67. 67.

Galermo, A. G. et al. Liquid chromatography-tandem mass spectrometry approach for determining glycosidic linkages. *Anal. Chem.* **90**, 13073–13080 (2018).

[CAS](#) [PubMed](#) [PubMed Central](#) [Google Scholar](#)

68. 68.

Galermo, A. G., Nandita, E., Castillo, J. J., Amicucci, M. J. & Lebrilla, C. B. Development of an extensive linkage library for characterization of carbohydrates. *Anal. Chem.* **91**, 13022–13031 (2019).

[CAS](#) [Google Scholar](#)

69. 69.

Cowardin, C. A. et al. Mechanisms by which sialylated milk oligosaccharides impact bone biology in a gnotobiotic mouse model of infant undernutrition. *Proc. Natl Acad. Sci. USA* **116**, 11988–11996 (2019).

[CAS](#) [PubMed](#) [PubMed Central](#) [Google Scholar](#)

[Download references](#)

Acknowledgements

We thank M. Karlsson and D. O’Donnell for their assistance with gnotobiotic mouse husbandry; S. Marion for her role in collecting clinical metadata and faecal samples from members of the MOAFTs study cohort with obesity, and the two human studies; S. Waller for design of the controlled diet study menus and oversight of the metabolic kitchen; S. Torbitzky for her assistance with coordination and planning of the human studies; M. Patnode for his input about the selection of lead fibres; S. Le Gall, L. Saulnier and B. Laillet for carbohydrate analysis of pea, orange and barley bran fibre preparations; G. Cesbron Lavau and M. Okoniewska for formulation and scale-up production of snack prototypes for human studies; S. Abdel-Hamid for production of the HiSF–LoFV diets given to gnotobiotic mice; L. Dimartino for analysis of the fibre ingredients in these diets; and L. Kyro for assistance with figure illustrations. Technical support was provided by S. Deng, J. Serugo, J. Lelwala-Guruge, K. Ahsan, S. Bale, J. Veitinger, J. Forman and S. Karlsson (archiving and processing mouse and human biospecimens), M. Meier, J. Hoisington-López and M. Crosby

(bacterial V4-16S rDNA amplicon and faecal microbiome shotgun sequencing), T. Juehne, A. Lutz and J. Yu (generating SOMAscan datasets), and R. Head and C. Storer (assistance with CompBio analyses). This work was funded by grants from the NIH (DK078669, DK70977, UL1-TR002345) and from Mondelēz Global LLC. Controlled diet studies of human participants were overseen by members of the Clinical Science Research Core of the Nutrition Obesity Research Center (NORC), which is supported by NIH grant P30 DK056341. Plasma proteomic data sets were generated by the Genome Technology Access Center at Washington University School of Medicine, which is supported in part by NIH Grants P30 CA91842 and UL1TR002345. O.D.-B. received support from NIH R25GM103757, T32GM007067 and T32HL130357 as a pre-doctoral trainee. J.I.G. is the recipient of a Thought Leader Award from Agilent Technologies.

Author information

Affiliations

1. Edison Family Center for Genome Sciences and Systems Biology, Washington University School of Medicine, St Louis, MO, USA

Omar Delannoy-Bruno, Chandani Desai, Arjun S. Raman, Robert Y. Chen, Matthew C. Hibberd, Jiye Cheng, Nathan Han, Michael J. Barratt & Jeffrey I. Gordon

2. Center for Gut Microbiome and Nutrition Research, Washington University School of Medicine, St Louis, MO, USA

Omar Delannoy-Bruno, Chandani Desai, Arjun S. Raman, Robert Y. Chen, Matthew C. Hibberd, Jiye Cheng, Nathan Han, Michael J. Barratt & Jeffrey I. Gordon

3. Department of Pathology and Immunology, Washington University School of Medicine, St Louis, MO, USA

Arjun S. Raman, Matthew C. Hibberd, Jiye Cheng, Michael J. Barratt & Jeffrey I. Gordon

4. Department of Chemistry, University of California, Davis, CA, USA

Juan J. Castillo, Garret Couture & Carlito B. Lebrilla

5. Department of Genetics, Washington University School of Medicine, St Louis, MO, USA

Ruteja A. Barve

6. Architecture et Fonction des Macromolécules Biologiques, Centre National de la Recherche Scientifique and Aix-Marseille Université, Marseille, France

Vincent Lombard & Bernard Henrissat

7. Department of Biological Sciences, King Abdulaziz University, Jeddah, Saudi Arabia

Bernard Henrissat

8. Infectious and Inflammatory Disease Center, Sanford Burnham Prebys Medical Discovery Institute, La Jolla, CA, USA

Semen A. Leyn, Dmitry A. Rodionov & Andrei L. Osterman

9. A. A. Kharkevich Institute for Information Transmission Problems, Russian Academy of Sciences, Moscow, Russia

Dmitry A. Rodionov

10. Mondelēz Global LLC, Chicago, IL, USA

David K. Hayashi, Alexandra Meynier & Sophie Vinoy

11. Department of Medicine, Washington University School of Medicine, St Louis, MO, USA

Kyleigh Kirbach, Tara Wilmot & Samuel Klein

12. Department of Psychiatry, Washington University School of Medicine,
St Louis, MO, USA

Andrew C. Heath

Authors

1. Omar Delannoy-Bruno

[View author publications](#)

You can also search for this author in [PubMed](#) [Google Scholar](#)

2. Chandani Desai

[View author publications](#)

You can also search for this author in [PubMed](#) [Google Scholar](#)

3. Arjun S. Raman

[View author publications](#)

You can also search for this author in [PubMed](#) [Google Scholar](#)

4. Robert Y. Chen

[View author publications](#)

You can also search for this author in [PubMed](#) [Google Scholar](#)

5. Matthew C. Hibberd

[View author publications](#)

You can also search for this author in [PubMed](#) [Google Scholar](#)

6. Jiye Cheng

[View author publications](#)

You can also search for this author in [PubMed](#) [Google Scholar](#)

7. Nathan Han

[View author publications](#)

You can also search for this author in [PubMed](#) [Google Scholar](#)

8. Juan J. Castillo

[View author publications](#)

You can also search for this author in [PubMed](#) [Google Scholar](#)

9. Garret Couture

[View author publications](#)

You can also search for this author in [PubMed](#) [Google Scholar](#)

10. Carlito B. Lebrilla

[View author publications](#)

You can also search for this author in [PubMed](#) [Google Scholar](#)

11. Ruteja A. Barve

[View author publications](#)

You can also search for this author in [PubMed](#) [Google Scholar](#)

12. Vincent Lombard

[View author publications](#)

You can also search for this author in [PubMed](#) [Google Scholar](#)

13. Bernard Henrissat

[View author publications](#)

You can also search for this author in [PubMed](#) [Google Scholar](#)

14. Semen A. Leyn

[View author publications](#)

You can also search for this author in [PubMed](#) [Google Scholar](#)

15. Dmitry A. Rodionov

[View author publications](#)

You can also search for this author in [PubMed](#) [Google Scholar](#)

16. Andrei L. Osterman

[View author publications](#)

You can also search for this author in [PubMed](#) [Google Scholar](#)

17. David K. Hayashi

[View author publications](#)

You can also search for this author in [PubMed](#) [Google Scholar](#)

18. Alexandra Meynier

[View author publications](#)

You can also search for this author in [PubMed](#) [Google Scholar](#)

19. Sophie Vinoy

[View author publications](#)

You can also search for this author in [PubMed](#) [Google Scholar](#)

20. Kyleigh Kirbach

[View author publications](#)

You can also search for this author in [PubMed](#) [Google Scholar](#)

21. Tara Wilmot

[View author publications](#)

You can also search for this author in [PubMed](#) [Google Scholar](#)

22. Andrew C. Heath

[View author publications](#)

You can also search for this author in [PubMed](#) [Google Scholar](#)

23. Samuel Klein

[View author publications](#)

You can also search for this author in [PubMed](#) [Google Scholar](#)

24. Michael J. Barratt

[View author publications](#)

You can also search for this author in [PubMed](#) [Google Scholar](#)

25. Jeffrey I. Gordon

[View author publications](#)

You can also search for this author in [PubMed](#) [Google Scholar](#)

Contributions

O.D.-B. and J.I.G. designed the gnotobiotic mouse studies. A.C.H. oversaw collection of faecal samples from human donors with obesity used to colonize germ-free mice. O.D.-B. and N.H. performed mouse studies. M.J.B., S.K., O.D.-B. and J.I.G. designed the human studies together with D.K.H., A.M. and S.V., who oversaw the design, manufacture and quality-control analysis of the fibre snack prototypes used in the two human studies. A.M. and S.V. organized carbohydrate and glycosidic linkage composition analysis of fibre preparations. Controlled diet studies of human participants were overseen by S.K. together with K.K. and T.W. J.J.C., G.C. and C.B.L. conducted mass spectrometric assays of mouse diets and faecal samples. J.C. performed LC–QTOF–MS analyses of human faecal samples collected from participants consuming the two- and four-fibre-containing snacks. O.D.-B. oversaw the archiving and processing of mouse and human biospecimens and generated the 16S rDNA and shotgun sequencing datasets from these samples. M.C.H. and C.D. implemented the metagenomic assembly and annotation pipeline. D.A.R., S.A.L. and A.O. performed mcSEED pathway reconstructions of faecal microbiomes, and V.L. and B.H. provided CAZyme annotations. A.S.R. developed the HOSVD and R.Y.C. the CC-SVD analytic platforms that were applied to datasets generated from mice and humans. O.D.-B. and R.A.B. performed CompBio analyses of plasma proteome datasets generated from human

studies. O.D.-B., C.D., M.J.B. and J.I.G. analysed the data. O.D.-B. and J.I.G. wrote the paper with assistance provided by the co-authors.

Corresponding author

Correspondence to [Jeffrey I. Gordon](#).

Ethics declarations

Competing interests

J.I.G. is a co-founder of Matatu, Inc., a company characterizing the role of diet-by-microbiota interactions in animal health. A.O. and D.R. are co-founders of Phenobiome Inc., a company pursuing development of computational tools for predictive phenotype profiling of microbial communities. C.B.L. is a co-founder of Evolve Biosystems, interVenn Bio and BCD Bioscience, companies involved in the characterization of glycans and developing carbohydrate applications for human health. D.K.H., A.M. and S.V. are employees of Mondelēz Global LLC, a multinational company engaged in production of snack foods. The remaining authors declare that they have no competing financial interests. A patent application related to the fibre-snack formulations described in this Article has been filed and published (WO 2021/016129).

Additional information

Peer review information *Nature* thanks David Bolam, Eran Elinav and the other, anonymous, reviewer(s) for their contribution to the peer review of this work.

Publisher's note Springer Nature remains neutral with regard to jurisdictional claims in published maps and institutional affiliations.

Extended data figures and tables

Extended Data Fig. 1 Monosaccharide content and glycosidic linkages present in the fibre preparations, and in the unsupplemented and fibre-supplemented HiSF–LoFV diets fed to gnotobiotic mice.

a, b, Monosaccharides and linkages, some represented by their methylated monosaccharide derivatives, in the fibre preparations. Stacked bars represent the mean for technical replicates ($n = 3$) for each glycosyl linkage determination. **c**, Monosaccharides in the unsupplemented and fibre-supplemented HiSF–LoFV diets. Bars represent the mean \pm s.d. for technical replicates ($n = 3$). * $P < 0.05$, ** $P < 0.01$, *** $P < 0.0001$ compared to the unsupplemented diet phase (one-way ANOVA with Holm–Šídák multiple comparison correction). **d**, Linkages, represented by their methylated monosaccharide derivatives in the unsupplemented and fibre-supplemented HiSF–LoFV diets. Stacked bars represent the mean for technical replicates ($n = 3$) for each glycosidic linkage determination. Glc, glucose; Gal, galactose; GalA, galacturonic acid; GlcA, glucuronic acid; Ara, arabinose; Xyl, xylose; Man, mannose; Fru, fructose; Fuc, fucose; Rha, rhamnose; Rib, ribose; Hex, hexose; dHex, deoxyhexose; T, terminal; f, furanose; p, pyranose; X, undefined linkage.

Source data

Extended Data Fig. 2 The effects of dietary fibres in gnotobiotic mice fed a HiSF-LoFV diet and colonized with faecal microbial communities of nine human donors with obesity.

a, Experimental design. **b**, HOSVD. Three-dimensional matrices are termed ‘tensors’. A tensor (O) with dimensions n , m and p , in which n represents subjects (mice or humans), m represents features (CAZymes, mcSEED metabolic pathways and ASVs) and p represents time, can be analysed by HOSVD in which a ‘core tensor’ (G) is created—a tensor in which the only non-zero values are along the diagonal (boxes shown in G). Each box represents a ‘tensor component’ (TC). Each tensor component relates the variation between each axis of the O tensor. Additionally, three new matrices are created that are related to each other through each tensor

component; for example, ‘Projection of variables onto TC1’ indicates that variation defined by tensor component 1 is defined by variation across the first row of n , the first column of m and the first column of p . **c–e**, HOSVD applied to CAZymes in faecal microbiomes of mice colonized with microbial communities of nine human donors with obesity ($n = 348$ faecal samples analysed) during each of the three dietary fibre interventions in the diet oscillation experiment. **f**, Heat map of discriminatory CAZymes with log₂-transformed fold changes in abundance that were defined as statistically significant during at least one dietary intervention. The grand mean of the data is shown for mice containing the nine different human donor microbiomes sampled at the indicated time points and normalized to day 14 values ($n = 6\text{--}10$ mice per group; $n = 232$ faecal samples analysed). The order of CAZymes from left to right is based on their function (rows below) and magnitude of their change within and across fibre treatments. $\ddagger q$ value < 0.10 ; $*$ q value < 0.05 (linear mixed-effects model, FDR-corrected).

[Source data](#)

[Extended Data Fig. 3 Responses of CAZymes and mcSEED metabolic pathways identified by HOSVD analysis as discriminatory for fibre snack consumption in gnotobiotic mice colonized with the faecal communities of nine human donors with obesity.](#)

a, b, Heat map of discriminatory CAZymes and mcSEED metabolic pathways with changes in abundance that were statistically significant during at least one dietary intervention. Data are averaged for mice containing a given human donor microbiota ($n = 6$ to 10 mice per group; $n = 232$ faecal samples analysed) sampled at the indicated time points and normalized to day-14 values. The order of CAZymes from left to right of the heat map in **a** follows the same order as in Extended Data Fig. [2f](#), and the order of mcSEED pathways from top to bottom in **b** follows the same order as shown in Fig. [1d](#). Hierarchical clustering (Euclidean distances) of CAZyme and mcSEED metabolic pathway profiles was used to group donor microbiomes.

[Source data](#)

Extended Data Fig. 4 HOSVD applied to mcSEED metabolic pathway and ASV datasets generated from the faecal microbial communities of mice containing microbial communities of human donors with obesity during the pea, orange and barley bran fibre phases of the diet oscillation.

a, Microbiome configurations as defined by the representation of mcSEED metabolic pathways on tensor component 1 and tensor component 2 during pea fibre, orange fibre and barley bran phase of diet oscillation. **b**, Projections of microbiota configuration as defined by the representation of bacterial taxa (ASVs) on tensor component 1 and tensor component 2 during pea fibre, orange fibre and barley bran phases of the diet oscillation protocol ($n = 9$ human microbiomes; $n = 6\text{--}10$ mouse recipients of each human microbiome; $n = 348$ faecal samples analysed for data presented in **a, b**).

[Source data](#)

Extended Data Fig. 5 Responses of bacterial taxa (ASVs) identified by HOSVD as discriminatory for dietary fibre consumption in gnotobiotic mice colonized with human donor microbiota, and in human participants enrolled in the controlled-diet studies.

a, Bray–Curtis dissimilarity distances calculated from the ASV content of communities sampled at all time points (days 4, 9, 14, 19, 24, 29, 34, 39, 44, 49, 54, 59 and 64 after colonization) from a given group of recipient mice compared to the ASV content of their corresponding human donor community before transplantation (Bray–Curtis distances calculated from ASV abundances in faecal samples collected from each group of mice ($n = 6\text{--}10$ mice; $n = 752$ faecal samples in total) compared to the abundances of these ASVs in each of their corresponding nine human-donor faecal communities). **** P value < 0.0001 (one-way ANOVA,

Šídák's correction). **b**, Heat map of statistically significant \log_2 -transformed fold changes in the abundances of discriminatory ASVs in gnotobiotic mice during at least one of the fibre interventions. The heat map on the left shows the grand mean for data obtained from all groups of mice and the heat map on the right shows averaged data for mice containing a given donor microbiota ($n = 6$ to 10 mice per group; $n = 232$ faecal samples obtained at the indicated time points with data normalized to day-14 values). Hierarchical clustering (Euclidean distances) of ASV profiles was used to group donor microbiota with similar responses to each fibre supplement. **c**, ASVs with \log_2 -transformed fold changes in abundance that were statistically significant in human participants after at least one of the fibre snack interventions. Left, mean values for participants enrolled in each study; the three panels to the right show changes in ASV abundances in individual participants after consumption of each of the fibre snacks. Data are normalized to pretreatment time points, that is, day 14 (study 1) and day 11 (study 2) ($n = 12$ and 14 participants for study 1 and 2, respectively, $n = 66$ faecal samples analysed). Hierarchical clustering (Euclidean distances) of ASV profiles was used to group participants with similar responses to a given fibre snack. $\ddagger q$ value < 0.1 , $*q$ value < 0.05 (linear mixed-effects model, FDR-corrected).

[Source data](#)

[Extended Data Fig. 6 Identification by HOSVD of fibre-snack-discriminatory CAZymes and mcSEED metabolic pathways in human participants in the controlled-diet studies.](#)

a, b, CAZymes and mcSEED metabolic pathways with \log_2 -transformed fold changes in abundance were statistically significant during at least one of the three fibre snack interventions. Data are shown for each participant after consumption of each fibre snack type and are normalized to pretreatment time points, that is, day 14 (study 1) and day 11 (study 2) ($n = 12$ and 14 participants for study 1 and 2, respectively, $n = 66$ faecal samples analysed). Hierarchical clustering (Euclidean distances) of CAZyme and mcSEED metabolic pathway profiles was used to group participants with similar responses to each fibre snack type. CAZymes

marked with a + were also fibre-treatment discriminatory in the gnotobiotic mouse studies.

Extended Data Fig. 7 Spearman-rank cross-correlation analysis of the representation of CAZymes, monosaccharides and glycosidic linkages in the faecal communities of participants consuming the pea-fibre snack prototype.

a, b, Correlations between the \log_2 -transformed fold change of statistically significant, HOSVD-defined discriminatory CAZyme gene abundances (matched by time and participant) to the \log_2 -transformed fold change in levels of monosaccharides and glycosidic linkages at days 25 and 35 (fibre snack consumption), and days 45 and 49 (post-intervention phase) normalized to day 14 (pre-intervention phase; $n = 60$ faecal samples analysed; 12 participants). Green boxes in **a** highlight a statistically significant positive correlation between GH43_37 (arabinofuranosidase) and arabinose, a prominent monosaccharide component of pea fibre. In **b**, evidence is provided that participant microbiomes contain CAZymes that cleave multiple branches of pea fibre arabinan, resulting in accumulation of its 1,5-arabinofuranose backbone in faeces. Further details are in [Supplementary Results](#). * $P < 0.05$; ** $P < 0.01$. Glucose (Glc), galacturonic acid (GalA), arabinose (Ara), xylose (Xyl), galactose (Gal), mannose (Man), rhamnose (Rha), fucose (Fuc), fructose (Fru), glucuronic acid (GlcA), *N*-acetylglucosamine (GlcNAc), *N*-acetylgalactosamine (GalNAc), allose (All), ribose (Rib), hexose (Hex), deoxyhexose (dHex); terminal (T), pyranose (p), furanose (f), undefined linkage (X).

Extended Data Fig. 8 Schematic of the analytic pipeline for identifying associations between changes in the plasma proteome and CAZyme responses after fibre snack consumption.

Step 1 shows cross-correlation analysis between plasma proteins and discriminatory CAZymes with changes in abundance that were statistically

significant. Step 2 shows SVD analysis of Spearman's rho values of the cross-correlation matrix. Proteins with projections along SV1 are plotted in a histogram to identify those proteins most correlated with discriminatory CAZymes (those within the 10th and 90th percentile, $\alpha < 0.1$). Step 3 represents a CompBio-based analysis of groups of proteins with SV1 projections within the 10th and 90th percentiles. Biological themes enriched in proteins binned in the 10th and 90th percentiles are generated (threshold cutoff for enrichment score (\log_2) > 14.8). Step 4 is a SVD analysis of protein profiles within each biological theme for all participants, followed by cross-correlation between SVD projections (SV1) of themed proteins and discriminatory CAZyme responses to treatment.

Extended Data Fig. 9 CAZyme-associated plasma proteome responses to consumption of the four-fibre snack prototype.

a–c, Contextual language processing literature analysis (CompBio) of proteins with abundances that were significantly correlated with treatment-discriminatory CAZymes in participants consuming the four-fibre snack. The analysis procedure is summarized in Extended Data Fig. 8. Treatment-responsive proteins, identified by CC-SVD as having projections at the extremes of SV1 (10th and 90th percentiles of the distribution), are grouped into biological themes identified by CompBio, on the basis of a conditional probability analysis, as being significantly enriched for contextually associated biological concepts (processes or pathways) over those that occur by random sampling of the literature. Themes with enrichment scores (\log_2 -transformed) > 14.8 in the plasma proteomes of participants who consumed the four-fibre snack are shown in **b, c** (Supplementary Table 10d–f provides a comprehensive list of themes associated with this and the other fibre snacks). **d, e**, Biological themes based on proteins positioned in 10th and 90th percentiles (**d** and **e**, respectively) are portrayed as spheres. The size of a sphere is related to its enrichment score in the plasma proteome after consumption of the four-fibre snack. The thickness of the blue lines connecting themes signifies the number of proteins shared between them. Component proteins of exemplary themes (orange spheres) are listed in boxes and coloured by their median \log_2 -transformed fold

change in response to consumption of the snack (blue, decrease; red, increase).

Extended Data Fig. 10 Connecting host responses defined by plasma proteomic features to microbiome responses defined by CAZyme features in participants consuming the four-fibre snack.

CC-SVD analysis of the plasma proteome with significantly changed discriminatory CAZymes in all participants after consuming the four-fibre snack. Two distinct groups of proteins with significant correlations with CAZymes are shown; one group with SV1 projections situated in the 10th percentile (top) and the other in the 90th percentile (bottom). CompBio analysis revealed biological themes that were significantly correlated with these CAZymes. Themes, their enrichment scores (\log_2 -transformed), the number of proteins comprising each theme and the cross-correlation (Spearman's rho) values between SV1 projections of themes and discriminatory CAZymes are presented. Each circle represents the correlation between a biological theme and a fibre-responsive CAZyme, with larger and darker circles indicating stronger correlations (positive correlations are coloured in red; negative correlations are coloured in blue).

Extended Data Fig. 11 Individual responses of the plasma proteome of participants consuming the four-fibre snack prototype.

a, b, Heat maps plotting the projections on SV1 of changes in the representation of biological themes during consumption of the four-fibre snack. **c**, Heat map plotting the \log_2 -transformed fold change in the levels of plasma proteins enriched in the glucose metabolism theme. Data for each participant are shown, normalized to the last day of the pretreatment phase on day 11. The four-fibre snack produced the greatest reduction in HOMA-IR among the three different snacks tested (Supplementary Table 5c). However, this reduction did not achieve statistical significance ($P = 0.078$, linear mixed-effects model) after the short period of snack consumption in this study. **d–f**, LC-QTOF-MS analysis of a biomarker of orange fibre

consumption present in faecal samples obtained from gnotobiotic mice and humans. **d**, Comparison of levels of the *m/z* 274.1442 analyte in colonized and germ-free mice fed the unsupplemented, orange-fibre-supplemented or pea-fibre-supplemented HiSF–LoFV diet for 10 days. The analyte is detectable only when orange fibre is consumed and is not dependent upon on the human donor microbiome for its generation. Bars represent mean values \pm s.d. for biological replicates ($n = 5$ mice per group). **d, e**, Comparisons of levels of the analyte in faecal samples obtained from participants in human study 2 on days 25 and 49 when they were consuming the maximum dose of the two-fibre (pea and inulin) and four-fibre (pea fibre, inulin, orange fibre plus barley bran) snack food prototypes. The bar graph in **e** represents mean values \pm s.d. for technical replicates ($n = 14$ participants). The difference documented between participants consuming the 2- versus 4-fibre snacks is statistically significant ($P = 0.0004$, paired two-tailed t-test). The horizontal dashed line in **f** denotes a baseline value operationally defined as the highest level of detection of the analyte in participants consuming the two-fibre snack food prototype lacking orange fibre.

[Source data](#)

[Extended Data Fig. 12 Plasma proteins with statistically significant changes in their abundances as a function of fibre treatment type and participant.](#)

Heat map plotting the \log_2 -transformed fold change in the abundances of plasma proteins in participants consuming the indicated fibre snack prototype. Data from the nine participants in study 1 (pea-fibre snack) who were also enrolled in study 2 (two- and four-fibre snacks) are shown. Changes in protein levels are referenced to their abundances on the last day of the pretreatment phase (day 14 and day 11 in study 1 and study 2, respectively) ($n = 66$ blood plasma samples analysed). * $P < 0.05$; ** $P < 0.01$; *** $P < 0.001$ (linear model, limma²⁵).

Supplementary information

Supplementary Information

This file contains the Supplementary Results and approved Study Protocols for NCT04159259 and NCT04101344.

Reporting Summary

Supplementary Tables

This file contains Supplementary Tables 1-10.

Source data

Source Data Fig. 1

Source Data Extended Data Fig. 1

Source Data Extended Data Fig. 2

Source Data Extended Data Fig. 3

Source Data Extended Data Fig. 4

Source Data Extended Data Fig. 5

Source Data Extended Data Fig. 11

Rights and permissions

Reprints and Permissions

About this article



Check for
updates

Cite this article

Delannoy-Bruno, O., Desai, C., Raman, A.S. *et al.* Evaluating microbiome-directed fibre snacks in gnotobiotic mice and humans. *Nature* **595**, 91–95 (2021). <https://doi.org/10.1038/s41586-021-03671-4>

[Download citation](#)

- Received: 01 July 2020
- Accepted: 25 May 2021
- Published: 23 June 2021
- Issue Date: 01 July 2021
- DOI: <https://doi.org/10.1038/s41586-021-03671-4>

[Access through your institution](#)

[Change institution](#)

[Buy or subscribe](#)

Associated Content

[Designer fibre meals sway human gut microbes](#)

- Avner Leshem
- Eran Elinav

Advertisement

This article was downloaded by **calibre** from <https://www.nature.com/articles/s41586-021-03671-4>

| [Section menu](#) | [Main menu](#) |

An invariant *Trypanosoma vivax* vaccine antigen induces protective immunity
[Download PDF](#)

- Article
- [Published: 26 May 2021](#)

An invariant *Trypanosoma vivax* vaccine antigen induces protective immunity

- [Delphine Autheman](#)¹,
- [Cécile Crosnier](#)¹,
- [Simon Clare](#)²,
- [David A. Goulding](#)³,
- [Cordelia Brandt](#)²,
- [Katherine Harcourt](#)²,
- [Charlotte Tolley](#) [ORCID: orcid.org/0000-0002-1119-7983](#)²,
- [Francis Galaway](#)¹,
- [Malhar Khushu](#)¹,
- [Han Ong](#)¹,
- [Alessandra Romero-Ramirez](#) [ORCID: orcid.org/0000-0002-8610-7815](#)⁴,
- [Craig W. Duffy](#) [ORCID: orcid.org/0000-0001-9359-4888](#)⁴,
- [Andrew P. Jackson](#)⁴ &
- [Gavin J. Wright](#) [ORCID: orcid.org/0000-0003-0537-0863](#)^{1,5,6,7}

[Nature](#) volume 595, pages 96–100 (2021) [Cite this article](#)

- 5744 Accesses
- 209 Altmetric
- [Metrics details](#)

Subjects

- [Parasitology](#)
- [Protein vaccines](#)

Abstract

Trypanosomes are protozoan parasites that cause infectious diseases, including African trypanosomiasis (sleeping sickness) in humans and nagana in economically important livestock^{1,2}. An effective vaccine against trypanosomes would be an important control tool, but the parasite has evolved sophisticated immunoprotective mechanisms—including antigenic variation³—that present an apparently insurmountable barrier to vaccination. Here we show, using a systematic genome-led vaccinology approach and a mouse model of *Trypanosoma vivax* infection⁴, that protective invariant subunit vaccine antigens can be identified. Vaccination with a single recombinant protein comprising the extracellular region of a conserved cell-surface protein that is localized to the flagellum membrane (which we term ‘invariant flagellum antigen from *T. vivax*’) induced long-lasting protection. Immunity was passively transferred with immune serum, and recombinant monoclonal antibodies to this protein could induce sterile protection and revealed several mechanisms of antibody-mediated immunity, including a major role for complement. Our discovery identifies a vaccine candidate for an important parasitic disease that has constrained socioeconomic development in countries in sub-Saharan Africa⁵, and provides evidence that highly protective vaccines against trypanosome infections can be achieved.

[Download PDF](#)

Main

African trypanosomiasis is an infectious disease that is caused by unicellular parasites of the genus *Trypanosoma*, which are transmitted by the bite of an infected tsetse fly. In humans, trypanosome infections cause sleeping sickness: a deadly disease that threatens the lives of millions of people who live in over 30 countries in sub-Saharan Africa⁶. Some species of trypanosome also infect important livestock animals (including cattle, goats and pigs) and cause the wasting disease nagana (animal African trypanosomiasis), which affects the livelihoods of people who rely on these animals for milk, food and draught power¹. Approximately three million cattle die from this disease every year, which results in an estimated direct annual economic cost of many hundreds of millions of dollars⁷ and represents a major barrier for the socioeconomic advancement of many countries in Africa. Nagana is primarily caused by *T. vivax* and *Trypanosoma congolense* and is currently managed with drugs, but resistance is increasing⁸. Previous attempts to develop subunit vaccines against African trypanosome infections have highlighted the difficulties in overcoming the immune evasion strategies that have been evolved by these parasites to enable them to survive in host blood⁹. These strategies include antigenic variation: the serial

expression of an abundant allelically excluded variable surface glycoprotein (VSG), and the rapid removal of surface-bound antibodies by hydrodynamic sorting^{3,10}. It is widely thought that the VSG forms a constantly changing, impenetrable surface coating that sterically shields other surface proteins from host antibodies, which leads to chronic infections characterized by oscillating parasitaemia; however, a careful analysis of recent structural information suggests that this model may not fully explain the protective role of the VSGs¹¹. We therefore hypothesized that the VSGs may also subvert natural immunity by preventing the acquisition of high-titre antibody responses to protective antigens, suggesting that eliciting prophylactic unnatural host immunity by vaccination could be achieved. Here we report the identification of a conserved cell-surface protein that—when used as a subunit vaccine in a mouse model of *T. vivax* infection—is capable of eliciting highly protective immunity.

A subunit vaccine induces immunity to *T. vivax*

To identify subunit vaccine candidates for *T. vivax*, we established a genome-led vaccinology approach using a bioluminescent mouse model of infection⁴ (Fig. 1a). We determined that adoptive transfer of about 100 parasites intravenously into BALB/c mouse hosts resulted in an acute, reproducible infection that permitted sensitive and accurate quantification of parasitaemia using light-based imaging¹². We selected subunit vaccine candidates by searching the *T. vivax* genome¹³ for genes that encode predicted cell-surface and secreted proteins that are likely to be accessible to vaccine-elicited antibodies. We selected 60 candidates using the following criteria: (1) they did not belong to paralogous gene families (to minimize the risk of functional redundancy in different mammalian hosts)¹⁴; (2) contained more than 300 amino acids in their predicted extracellular region (and so are likely to be accessible at the cell surface); and (3) had evidence of expression in the blood stages¹⁵ (Supplementary Table 1). We synthesized gene sequences encoding the entire predicted extracellular region, and cloned them into a mammalian protein expression plasmid that contained an exogenous secretion peptide and purification tags. We expressed the candidates as soluble recombinant proteins in HEK293 cells to increase the chance that structurally critical posttranslational modifications were appropriately added. Of the 60 expression plasmids we tested, 39 yielded sufficient protein after purification for vaccination trials (Extended Data Fig. 1a). For vaccination, we used a prime and two-boost regime that used alum as an adjuvant to bias host responses towards humoral immunity. To reduce any systemic adjuvant-elicited effects on disease progression, we rested the vaccinated mice for a minimum of four weeks following the final boost before parasite challenge (Extended Data Fig. 1b,c). *Trypanosoma vivax* loses virulence once removed from donor mice, and so, to avoid confounding effects due to the loss of parasite viability during the infection procedure, we ensured that infections were

comparable in control mice challenged before and after the vaccinated mice (Extended Data Fig. 1b).

Fig. 1: Candidate V23 (IFX) induces protective immunity in a mouse model of *T. vivax* infection.

 figure1

a, Schematic of the genome-led vaccinology approach. **b**, Summary of mean parasitaemia ($n \geq 3$ mice) quantified by bioluminescence in cohorts of vaccinated mice challenged with *T. vivax*. Although the V58 candidate had lower mean parasitaemia relative to controls on day 8, it rebounded on day 9 and so was not considered further. **c, d**, Bioluminescent images of adjuvant-only control (left panels) and mice vaccinated with V31 (**c** right) and V23 (**d** right); images were taken five (top panels) and eight (bottom panels) days after infection.

[Source data](#)

[Full size image](#)

We determined the elicited antibody titres to each antigen, and the vast majority (90%) had mean half-maximal responses at serum dilutions greater than 1:10,000 (Extended Data Fig. 1d). We found that, of the 39 antigens tested, 34 had no effect on the infection parameters relative to controls (Fig. 1b, Extended Data Fig. 2). We observed statistically significant effects on parasite growth with four antigens (Fig. 1b): two candidates (V2 and V8) exhibited a slight delay, and one candidate (V31) showed a longer delay, to the ascending phase of parasitaemia (Fig. 1b,c), and one candidate (V23) showed no detectable parasites in all five vaccinated mice (Fig. 1b,d). For each of the four candidates, we repeated the experiments using independent protein preparations and larger cohorts of mice. The two candidates that induced a slight delay

(V2 and V8) did not replicate, and so were not pursued further (Extended Data Fig. 3a). Candidate V31 reduced the rate of parasite multiplication once more and induced improved protection compared to the initial screen so that 9 out of 15 mice survived until day 16 after infection (Extended Data Fig. 3a). V23 vaccination again elicited robust protection, and longitudinal sampling of these mice showed that 10 out of the 15 mice were protected beyond at least day 170 (Extended Data Fig. 3a,b). We dissected protected mice several months after infection, which revealed no detectable extravascular reservoirs of parasites (Extended Data Fig. 4). On the basis of these and subsequent findings, we propose the name ‘invariant flagellum antigen from *T. vivax*’ (IFX) for the V23 candidate (TvY486_0807240).

IFX localizes to the flagellum

IFX is a previously uncharacterized type-I cell-surface glycoprotein that contains a short (18 amino acid) cytoplasmic region that does not include any known protein domains and has no paralogues (protein sequence identity greater than 25%) within *T. vivax*, nor homologues in other sequenced genomes of *Trypanosoma* species. To begin the functional characterization of IFX, we asked whether it had a specific localization in blood-stage parasites. Immunocytochemistry showed that staining was localized along the length of the flagellum and loosely concentrated in discrete puncta (Fig. 2a). Using immunogold electron microscopy, we found that IFX was enriched at the boundaries of where the flagellum is attached to the cell body; in different sections, these clusters were either unilaterally or bilaterally located (Fig. 2b). In mid-sagittal sections, IFX was located along the length of the flagellum membrane and concentrated in discrete clusters at the points at which the flagellum was in close apposition to the cell membrane; specifically, the gold particles were located between the flagellum and cell body membranes (Extended Data Fig. 5a–f). These data demonstrated that IFX was localized to the flagellum membrane and particularly enriched as continuous or punctuated bilateral stripes along the flagellum, and bordering the region where the flagellum is attached to the parasite cell body, which suggests a structural role in maintaining flagellar function.

Fig. 2: IFX is expressed on the flagellum membrane of *T. vivax* and concentrated at the periphery of the flagellum–cell-body contact.

figure2

a. Immunofluorescence staining of *T. vivax* with rabbit anti-IFX antiserum (red) (left) or control pre-immune serum (right) counterstained with DAPI (blue) demonstrates

localization of IFX to the flagellum. Scale bars, 5 µm. **b**, Immunogold electron microscopy using an anti-IFX mouse monoclonal antibody localized IFX to the borders of where the flagellum is in contact with the parasite cell body in transverse sections (black arrows in left and middle images) compared to isotype-matched control (right). Scale bars, 100 nm. Representative images of at least two independent experiments are shown.

[Full size image](#)

Passive protection by antibodies to IFX

To determine the immunological mechanisms of IFX-mediated protection, we first demonstrated that antibodies contributed to immunity by transferring immune serum from IFX-vaccinated mice to naive recipient mice, which inhibited parasite growth in a dose-dependent manner (Fig. 3a). Depletion of CD4- and CD8-positive T lymphocytes and NK1.1-positive natural killer cells in IFX-vaccinated mice did not affect protective efficacy, demonstrating that these cell types were not direct executors of immunity once it was established (Extended Data Fig. 6). To further investigate the role of antibodies in immunity using an independent approach, we selected six hybridomas that secreted monoclonal antibodies to IFX. Of the six monoclonal antibodies we selected, three affected parasite growth when used in passive protection experiments (Fig. 3b). We determined the approximate location of the monoclonal-antibody-binding sites on IFX and quantified their binding affinities, but did not observe a simple positive correlation between their protective efficacy and either the location of their epitope or binding affinity (Extended Data Fig. 7). The inhibitory effects of one antibody (designated 8E12) titrated with dose (Fig. 3c).

Fig. 3: Passive transfer of immunity to *T. vivax* infections with anti-IFX antibodies.

 figure3

a, Dose-dependent inhibition of *T. vivax* by adoptive transfer of sera from IFX-vaccinated mice relative to sera from unimmunized control mice. Groups of five mice

were compared by one-way analysis of variance (ANOVA) with Sidak post hoc test; * $P \leq 0.05$, **** $P \leq 0.0001$. **b**, Three out of six anti-IFX IgG1-isotype monoclonal antibodies (6B3, 8E12 and 3D12), each given at a dose of $3 \times 100 \mu\text{g}$, passively protect against *T. vivax* infection relative to an isotype-matched control. Groups of five mice were compared by one-way ANOVA with Sidak post hoc test; **** $P \leq 0.0001$. **c**, Passive protection of the 8E12–IgG1 monoclonal antibody is dose-dependent. Parasitaemia was quantified at day 5 using bioluminescence. Data points represent individual mice; bars indicate mean \pm s.d., groups of five mice were compared by one-way ANOVA with Sidak post hoc test; ** $P \leq 0.01$, **** $P \leq 0.0001$. The background bioluminescence threshold is indicated by grey shading.

[Source data](#)

[Full size image](#)

Several mechanisms of anti-IFX protection

Isotyping the monoclonal antibodies to IFX revealed that they were all of the IgG1 subclass, which, in mice, do not effectively recruit immune effector functions such as complement or bind activating Fc receptors with high affinity¹⁶; this suggests that direct antibody binding to IFX affected parasite viability. To establish the role of Fc-mediated immune effectors in anti-IFX antibody protection, we selected 8E12 (which gave intermediate protective effects) and, by cloning the rearranged antibody variable regions, switched the monoclonal antibody isotype from IgG1 to IgG2a (Extended Data Fig. 8). We observed that the 8E12–IgG2a monoclonal antibodies had a substantially increased potency compared to the 8E12–IgG1 when used in passive transfer experiments (Fig. 4a), and titrating this antibody showed that 3 doses of 50 micrograms or more conferred sterile protection (Fig. 4b, Extended Data Fig. 9a). This demonstrated that the recruitment of antibody-mediated immune effectors was important for parasite neutralization, and to quantify their relative contributions we engineered three further monoclonal antibodies, each of which lacked the binding sites for C1q (ΔC1q), FcRs (ΔFcR) or both ($\Delta\text{C1q}\Delta\text{FcR}$)¹⁷ (Extended Data Fig. 8c). When used in passive protection experiments, we observed that mutation of the C1q binding site almost completely reversed the inhibition of parasite growth, which demonstrates that C1q-mediated complement recruitment was a major protective mechanism (Fig. 4c, Extended Data Fig. 9b). Mutating the FcR binding site also relieved the inhibition of parasite growth (but to a lesser extent), whereas mutation of both C1q and FcR sites inhibited growth with a potency similar to that of the IgG1 isotype (Fig. 4c, Extended Data Fig. 9b). These experiments revealed that anti-IFX antibodies inhibited parasite multiplication by several immune mechanisms, dominated by the recruitment of complement.

Fig. 4: There are several mechanisms of antibody-mediated anti-IFX immunological protection, dominated by complement recruitment.

 [figure4](#)

a, Anti-IFX 8E12–IgG2a monoclonal antibodies passively protect against *T. vivax* infection more potently than do 8E12–IgG1 monoclonal antibodies. **b**, Dose titration of 8E12–IgG2a monoclonal antibody compared to isotype-matched control. **c**, Passive transfer of 8E12–IgG2a monoclonal antibodies containing mutations that prevent binding to C1q (Δ C1q), FcRs (Δ FcR) or both (Δ C1q Δ FcR) relieved the inhibition of parasite multiplication to differing degrees, demonstrating that there are several mechanisms of antibody-based immunological protection, including a major role for complement. Parasitaemia was quantified at day 5 using bioluminescence. Data points represent individual mice. Grey shading indicates background bioluminescence. Bars indicate mean \pm s.d. One of two independent experiments with very similar outcomes is shown.

[Source data](#)

[Full size image](#)

IFX is highly conserved across isolates

To further assess and develop IFX as a potential vaccine target, we tested appropriate routes of administration and other adjuvants that would bias antibody responses towards more-protective isotypes. Of two selected adjuvants that have previously been used in veterinary vaccines and can be delivered subcutaneously, we found that the saponin-based adjuvant Quil-A elicited consistent antibody titres equivalent to the protective responses induced by alum, of which a large proportion were of the IgG2 isotypes (Extended Data Fig. [10a, b](#)); these mice were potently protected against parasite challenge (Fig. [5a](#), Extended Data Fig. [10c](#)). One potential challenge with subunit vaccines is that the genes encoding antigens that elicit protective immune responses in natural infections can be subject to diversifying selection, which potentially leads to strain-specific immunity and limits the usefulness of the vaccine^{[18](#)}.

We therefore analysed the *IFX* gene sequence in 29 cosmopolitan *T. vivax* genomes and showed that it is highly conserved by comparison to other surface antigens. We observed only a single non-synonymous polymorphism in 2 out of 29 strains (Fig. 5b) and both of these were heterozygotes; the frequency of the mutation across all strains was therefore very low (0.058), demonstrating that *IFX* is almost completely invariant within the parasite population. This high level of sequence conservation across isolates suggests that the *IFX* protein is not a target of host immune responses and, consistent with this, sera from naturally infected cattle were not immunoreactive to *IFX* (Fig. 5c). Finally, a successful vaccine must be able to elicit long-lasting protection: we therefore repeatedly challenged *IFX*-vaccinated mice over 100 days after they received their final immunization. We observed that mice remained fully protected, including when parasites were delivered subcutaneously (Fig. 5d).

Fig. 5: IFX is highly conserved and can elicit long-lasting immunity to *T. vivax* infections.

 figure5

a, Comparing veterinary adjuvants using subcutaneous delivery demonstrates that Quil-A is as effective as the positive control (*IFX* adjuvanted in alum and delivered intraperitoneally). Parasitaemia was quantified at day 5 using bioluminescence. Data points represent individual mice. Grey shading indicates background bioluminescence. Bars indicate mean \pm s.d. Mont., montanide ISA 201 VG. **b**, Parasite population genetic analysis shows that *IFX* is highly conserved compared to other genes; mean synonymous (Ds) and nonsynonymous (Dn) substitution densities are shown (+s.d. where appropriate). **c**, *IFX* is not immunogenic in the context of a natural infection. Immunoreactivity to the indicated proteins in sera from Cameroonian (C) ($n = 10$) or Kenyan (K) ($n = 10$) cattle, or uninfected control cattle from the UK (U) ($n = 6$). Bar indicates median. **d**, Mice vaccinated with *IFX* adjuvanted in alum were protected from two intravenous (i.v.) and one final subcutaneous (s.c.) *T. vivax* challenge given over 100 days after the final booster immunization.

[Source data](#)

[Full size image](#)

Discussion

We have shown that it is possible to elicit apparently sterile protection to an experimental trypanosome infection with a subunit vaccine that corresponds to the ectodomain of the invariant cell-surface parasite protein IFX. The localization of IFX to the boundaries of where the flagellum is in contact with the parasite cell body suggests it performs a role in flagellar structure and function. Our demonstration that antibodies are required for immunity raises questions about the immunoprotective mechanisms used by trypanosomes, and, importantly, that their vulnerabilities that can be exploited to develop vaccines. The inhibition of parasite growth by antibodies to IFX suggest that the VSG surface coat of *T. vivax* cannot fully shield it from antibody binding, and that anti-IFX antibodies are not removed by endocytosis within the flagellar pocket from the parasite surface with sufficient rapidity to prevent immune effector recruitment mediated by antibodies. The findings that the *IFX* gene sequence was highly conserved across parasite isolates, and that sera from infected cattle living in nagana-endemic regions were not immunoreactive to IFX, suggest that natural parasite infections in some species can subvert host immunity to avoid eliciting protective antibody responses. These mechanisms could include perturbations of the B cell compartment, which have previously been described in experimental models of other trypanosome species^{19,20,21}, or that the IFX protein may not be suitably presented to the host immune system in the context of a natural infection. Preliminary experiments to translate these findings to goats did not show protection²² and highlighted the need to develop infection models that are suitable for vaccine testing, and a greater understanding of which antibody isotypes and adjuvants elicit the necessary mechanisms of immune effector recruitment. The discovery of an antigen that can elicit protection to a trypanosome infection provides optimism and a technical road map that could be followed to identify vaccine antigens not only for other trypanosome species, but also parasites that have thus far proven intractable to vaccine development. Finally, IFX represents a very attractive vaccine candidate for an important livestock disease that has been a major barrier to socioeconomic development in sub-Saharan Africa.

Methods

A group size of five mice was selected for the initial vaccine screening on the basis of the highly reproducible nature of the *T. vivax* infection between individual mice as quantified by bioluminescence, and the requirement for a strong effect size for an effective vaccine. In a typical vaccine test experiment, we calculate a mean and s.d. of $6 \times 10^7 \pm 1 \times 10^7$ photons per second ($n = 5$) in an adjuvant control cage on day five after infection. A sample size of five mice at 90% statistical power would be sufficient to allow us to detect a reduction in parasitaemia of $\geq 35\%$ using a one-sided *t*-test at

$P \leq 0.05$. Larger group sizes of up to 15 mice were used in replication studies. The experiments were not randomized, and investigators were not blinded to allocation during experiments and outcome assessment, although vaccination and parasite quantification were performed by independent researchers.

Mouse strains and ethical approvals

All mouse experiments were performed under UK Home Office governmental regulations (project licence numbers PD3DA8D1F and P98FFE489) and European directive 2010/63/EU. Research was ethically approved by the Sanger Institute Animal Welfare and Ethical Review Board. Mice were maintained under a 12-h light/dark cycle at a temperature of 19–24 °C and humidity between 40 and 65%. The mice used in this study were 6–14-week-old female *Mus musculus* strain BALB/c, which were obtained from a breeding colony at the Research Support Facility, Wellcome Sanger Institute.

Cell lines and antibodies

Recombinant proteins and antibodies used in this study were expressed in HEK293E²³ or HEK293-6E²⁴ provided by Y. Durocher. Neither cell line was authenticated but they were regularly tested for mycoplasma (Surrey Diagnostics) and found to be negative. The antibodies used in this study were as follows. Primary antibodies were: six anti-IFX mouse monoclonal antibodies were selected and validated in this study: 6B3, 8C9, 3D12, 2H3, 10E2 and 8E12 from hybridomas that all secreted IgG1 isotypes. A rabbit polyclonal antibody to the entire ectodomain of IFX was generated by Cambridge Research Biochemicals and validated by enzyme-linked immunosorbent assay (ELISA) against the recombinant IFX ectodomain. The 8E12 antibody was cloned and expressed recombinantly as a mouse IgG2a isotype as described in ‘Antibody cloning, isotype switching, mutagenesis and purification’. Mouse isotype control antibodies were: IgG1 (MOPC-21, BE0083, BioXcell) and IgG2a (C1.18.4, BE0085, BioXcell). Antibodies used for in vivo leukocyte cell depletion were: anti-mouse CD4 (clone GK1.5, BP0003-1, BioXcell), anti-mouse CD8 (clone 2.43, BP0061, BioXcell), anti-mouse NK1.1 (clone PK136, BE0036, BioXcell), and control anti-keyhole limpet haemocyanin (clone LTF-2, BP0090, BioXcell). Antibodies used for protein quantification for ELISAs were mouse monoclonal anti-His (His-Tag monoclonal antibody, 70796, EMD-Millipore), and biotinylated mouse anti-rat CD4 (clone OX68). OX68 was purified from the spent tissue culture medium from the hybridoma, which was a gift from N. Barclay. Secondary antibodies used were: goat anti-mouse alkaline phosphatase conjugated secondary (A3562, Sigma-Aldrich) and rabbit anti-bovine alkaline phosphatase conjugated secondary (A0705 Sigma-Aldrich). Mouse antibody isotypes were determined using the mouse monoclonal antibody isotyping kit (ISO2-KT Sigma-Aldrich).

Vaccine target identification and expression

The *T. vivax* genome was searched for genes encoding predicted type I, GPI-anchored and secreted proteins using protein feature searching in TriTrypDB²⁵. The regions corresponding to the entire predicted extracellular domains of *T. vivax* cell-surface and secreted proteins from the Y486 strain were determined by using transmembrane²⁶ and GPI-anchor²⁷ or signal peptide²⁸ prediction software. Protein sequences encoding the predicted extracellular domain and lacking their signal peptide were codon-optimized for expression in human cells and made by gene synthesis (Geneart and Twist Bioscience). The sequences were flanked by unique NotI and Ascl restriction enzyme sites and cloned into a pTT3-based mammalian expression vector²³ between an N-terminal signal peptide to direct protein secretion and a C-terminal tag that included a protein sequence that could be enzymatically biotinylated by the BirA protein–biotin ligase²⁹ and a 6-His tag for purification³⁰. The ectodomains were expressed as soluble recombinant proteins in HEK293 cells as previously described^{31,32}. To prepare purified proteins for immunization, between 50 ml and 1.2 l (depending on the level at which the protein was expressed) of spent culture medium containing the secreted ectodomain was collected from transfected cells, filtered and purified by Ni²⁺ immobilized metal-ion affinity chromatography using HisTRAP columns using an AKTAPure instrument (GEHealthcare). Proteins were eluted in 400 mM imidazole as previously described³³, and extensively dialysed into HEPES-buffered saline (HBS) before being quantified by spectrophotometry at 280 nm. Protein purity was determined by resolving one to two micrograms of purified protein by SDS–PAGE using NuPAGE 4–12% Bis Tris precast gels (ThermoFisher) for 50 min at 200 V. Where reducing conditions were required, NuPAGE reducing agent and anti-oxidant (Invitrogen) were added to the sample and the running buffer, respectively. The gels were stained with InstantBlue (Expedeon) and imaged using a c600 Ultimate Western System (Azure biosystems). Purified proteins were aliquoted and stored frozen at –20 °C until used. Where enzymatically monobiotinylated proteins were required to determine antibody titres by ELISA, proteins were co-transfected with a secreted version of the protein biotin ligase (BirA) as previously described³², and extensively dialysed against HBS and their level of expression determined by ELISA using a mouse monoclonal anti-His antibody (His-Tag monoclonal antibody, 70796, EMD Millipore) as primary antibody and a goat anti-mouse alkaline phosphatase-conjugated secondary (A3562, Sigma-Aldrich).

Vaccine formulation and administration

For the initial screening of antigens, aliquots of purified protein for immunization were thawed, diluted and mixed 50% v/v with alhydrogel adjuvant 2% (InvivoGen) for two hours at room temperature. For each antigen, groups of five 6–8-week-old

female BALB/c mice were immunized intraperitoneally using a prime and two-boost strategy using the amounts of protein documented in Supplementary Table 1. For retesting those antigens that had shown some effect in the preliminary screen, one group of 15 mice received three intraperitoneal immunizations of the query protein adjuvanted in alum using similar amounts as used in the initial screen (Supplementary Table 1); a control group, also of 15 mice, received the adjuvant alone. For evaluating different IFX vaccine–adjuvant formulations, groups of five mice received three immunizations of 50 µg IFX adjuvanted with either alhydrogel, montanide ISA 201 VG or Quil-A in a total volume of 200 µl. IFX was formulated with montanide ISA 201 VG according to the manufacturer’s instructions using a stirrer to create the water-in-oil emulsion. IFX was mixed in a 1:1 (v/v) ratio with Quil-A adjuvant using a 0.5 mg ml⁻¹ solution. IFX adjuvanted in montanide, or Quil-A were administered subcutaneously at two different injection sites (100 µl per site), whereas IFX adjuvanted in alhydrogel was administered intraperitoneally.

Quantification of serum antibody titres by ELISA

To determine the serum antibody responses to immunized proteins, blood biopsies were collected between ten to twelve days after the final immunization from the tail of each mouse and clotted for two hours at room temperature. Cells were removed by centrifugation, the serum collected, supplemented with sodium azide to a final concentration of 2 mM as a preservative and stored at –20 °C until use. Cattle sera were donated from archived material at the University of Liverpool, originally collected from natural *T. vivax* infections in Cameroon (northwest state), and Kenya (western state) where the infection was positively identified by thick blood smear and the parasite identified as *T. vivax* using the VerY Diag field test.

To determine the antibody titre against an antigen of interest, individual sera were initially diluted 1:1,000 and then six fourfold serial dilutions in PBST and 2% BSA were prepared. These dilutions were pre-incubated overnight at room temperature with 100 µg ml⁻¹ of purified rat CD4d3 + 4-BLH protein to adsorb any anti-biotin or His tag antibodies. Sera were transferred to streptavidin-coated ELISA plates on which the biotinylated target antigen was immobilized. To ensure that all anti-tag antibodies were adsorbed, binding of the lowest dilution of antisera was also tested against biotinylated rat CD4d3 + 4-BLH protein similarly immobilized on the ELISA plate to confirm the absence of any anti-tag immunoreactivity³⁴. Sera were incubated for one hour at room temperature followed by three washes with PBST before incubating with an anti-mouse IgG secondary antibody conjugated to alkaline phosphatase (Sigma-Aldrich) used as a 1:5,000 dilution for one hour. Following three further washes with PBST, 100 µl of 1 mg ml⁻¹ Sigma 104 phosphatase substrate was added and substrate hydrolysis quantified at 405 nm using a plate reader (Spark, Tecan). To quantify immunoreactivity to *T. vivax* antigens in the context of natural infections, cattle sera

were diluted 1:800 in PBST and 2% BSA and incubated for two hours at room temperature with biotinylated ectodomains of V2, V53, IFX or control rat CD200, adsorbed on the microtitre plate. Following three washes with PBST, a secondary rabbit anti-bovine IgG antibody (A0705, Sigma-Aldrich) diluted 1:20,000 was incubated for one hour and washed three times with PBST before adding colorimetric phosphatase substrate and acquiring absorbance readings.

Antibody isotyping

Isotyping of the monoclonal antibodies and polyclonal sera responses was performed using the Mouse Monoclonal Antibody Isotyping Kit (ISO2-KT, Sigma-Aldrich), according to the manufacturer's instructions. In brief, the biotinylated ectodomain of the IFX protein was immobilized on a streptavidin-coated plate, incubated with sera diluted 1:1,000 in PBST and 2% BSA or hybridoma supernatants, washed in PBST before adding isotype-specific goat anti-mouse secondary antibodies diluted 1:1,000. Binding was quantified with an alkaline-phosphatase-conjugated rabbit anti-goat tertiary antibody (1:5,000, Sigma-Aldrich) followed by a colorimetric phosphatase substrate, and hydrolysis products quantified by absorbance readings at 405 nm.

Trypanosoma parasite strain and maintenance

A transgenic form of *T. vivax* genetically engineered to ubiquitously express the firefly luciferase enzyme³⁵ was provided by P. Minoprio. The parental strain of this parasite is the IL1392 line derived from the Y486 strain used for genome sequencing¹³ and has previously been fully documented¹². Parasites were initially recovered from a frozen stabilate by intraperitoneal administration into two BALB/c female mice. Parasites were maintained by weekly serial blood passage in wild-type female BALB/c mice by taking a blood biopsy, quantifying living parasites in PBS and 20 mM d-glucose by microscopy and infecting four naive mice intravenously. During the course of the project, two further aliquots of frozen parasites were thawed and then used for infection challenges: no significant differences in the kinetics of infection were observed. Luciferase-expressing *T. congolense* parasites were a gift from B. Wickstead and C. Gadelha, and were maintained by weekly serial intravenous blood passage in wild-type female BALB/c mice.

Trypanosoma vivax infections

For infection challenges, bloodstream forms of *T. vivax* parasites were obtained from the blood of an infected donor mouse at the peak of parasitaemia, diluted in PBS and 20 mM d-glucose, quantified by microscopy and used to infect mice by intravenous injection. While establishing the infection model in our facility, we observed that the *T. vivax* parasite was labile and gradually lost virulence once removed from living

mice. To reduce the possibility of any artefactual protective effects being due to the loss of parasite virulence during the challenge procedure, we screened the protective effects of antigens in a cohort design. Each cohort contained six cages of five mice: four cages contained mice immunized with a different query subunit-vaccine candidate, and the other two cages contained control mice immunized with adjuvant alone. Vaccinated mice were rested for four to eight weeks after the final immunization to mitigate any possible non-specific protective effects elicited by the adjuvant. During the infection procedure, the mice in the control cages were challenged first and last, and the data from the cohort used only if the infections in the control mice from the two cages were comparable. During the infection procedures, parasites were outside of a living mouse for no more than 40 min. Mice were normally challenged by intravenous delivery of 10^2 (cohorts 1–7, 10 and 11) to 10^3 (cohorts 8 and 9) parasites for the initial screening and passive transfer protection experiments, but were also challenged intraperitoneally during the establishment of the model and subcutaneously when investigating the duration of protection. The mice were not randomized between cages and the operator was not blinded to the group condition. Occasionally, individual infected mice within a group unexpectedly exhibited only background levels of bioluminescence, which was attributed to the injected luciferin substrate not distributing from the site of delivery (possibly due to mislocalization of the injection bolus); in these instances, the mice were excluded from the analysis. This occurred 12 times out of 1,650 injections (0.7%) in screening cohorts 3, 5, 6 and 9. Groups were compared using bioluminescence quantification as a proxy for parasitaemia and one-way ANOVA with Dunnett's post hoc test unless specified.

Quantification of *T. vivax* infections by bioluminescent in vivo imaging

The luciferase substrate d-luciferin (potassium salt, Source BioScience) was reconstituted to 30 mg ml⁻¹ in Dulbecco's PBS (Hyclone), filter-sterilized (0.22 µm) and stored in aliquots at -20 °C. Aliquots were thawed and administered to animals at a dose of 200 mg kg⁻¹, by intraperitoneal injection ten minutes before bioluminescence acquisitions. The mice were given three minutes of free movement before being anaesthetized with 2.5% isoflurane and placed in the imaging chamber where anaesthesia was maintained for acquisition. An average background bioluminescence measurement was determined by luciferin administration in five female BALB/c mice and calculating the mean whole-body bioluminescence; where appropriate, this value is indicated as a light grey shading on bioluminescence plots. To determine long-term persistence of the parasites in different organs of infected mice, mice were administered with luciferin, imaged and then euthanized with an overdose of anaesthetic. Mice were then perfused with PBS until the perfusion fluid ran clear, the organs dissected, arranged on a Petri dish and bathed in PBS containing 20 mM glucose and 3.3 mg ml⁻¹ luciferin for imaging. Emitted photons were acquired by a charge coupled device (CCD) camera (IVIS Spectrum Imaging System, Perkin

Elmer). Regions of interest (ROIs) were drawn and total photons emitted from the image of each mouse were quantified using Living Image software version 4.7.4 (Xenogen), the results were expressed as the number of photons s⁻¹. Bioluminescence values were exported and plotted in Prism GraphPad version 8.0.2, which was also used for testing statistical significance where needed. Where necessary, peripheral parasitaemia was quantified by direct microscopic observation as previously described¹². In brief, five microlitres of blood obtained from the tail vein were appropriately diluted in PBS containing 20 mM glucose and parasite counts were expressed as number of parasites per blood millilitre.

Passive transfer of immunity

To obtain sufficient sera for adoptive transfer experiments, fifty 6–8-week-old female BALB/c mice were immunized intraperitoneally three times with 20 µg of purified IFX adjuvanted in alum, with each immunization separated by two weeks. Nine days after the final immunization, sera were collected as above, aliquoted and stored at -20 °C until use. For passive transfer experiments, groups of 10-to-14-week-old female BALB/c mice were dosed three times with either sera or purified monoclonal antibodies on three consecutive days; three hours after the second dosing, mice were challenged intravenously with 10² *T. vivax* parasites. When using immune serum for passive transfer protection experiments, doses of 100 and 200 µl of sera from either IFX-vaccinated mice or non-immunized control mice were administered. For monoclonal antibodies, the purified antibody was diluted to the required dose in PBS and 200 µl administered intravenously. Control isotypes antibodies used were MOPC-21 for the IgG1 isotype and C1.18.4 for the IgG2a isotype (both from BioXcell). The serum half-life for mouse IgG1 and IgG2a are known to be between 6 and 8 days³⁶.

In vivo cell depletion

Groups of five mice were immunized three times with 50-µg doses of purified IFX to induce protective immunity to *T. vivax*. To deplete immune mice of defined leucocyte lineages, mice within each group were depleted by intraperitoneal administration of lineage-specific monoclonal antibodies using standard procedures. In brief, natural killer cells were depleted by four injections of 500 µg of the PK136 monoclonal antibody that targets the NK1.1 glycoprotein at days -5, -1, 0 and 2 relative to *T. vivax* challenge. Mouse CD4 and CD8 T lymphocytes were depleted by one intraperitoneal 750-µg injection of the monoclonal antibodies targeting CD4 (clone GK1.5) or CD8 (clone 2.43) receptors, respectively, the day before the infection. The LFT-2 monoclonal antibody (750 µg) was used as an isotype-matched control antibody. Mice were challenged with 10² *T. vivax* parasites and parasitaemia quantified was using bioluminescent imaging as described in ‘Quantification of *T. vivax* infections by bioluminescent in vivo imaging’.

Trypanosome genomic sequence analysis

To identify whether IFX had any homologues in other *Trypanosome* species, the entire IFX sequence was analysed with Interproscan; this showed that it does not contain any known protein domains other than the predicted N-terminal signal peptide and transmembrane helix. Comparison of the predicted IFX protein sequence with all the other sequenced *Trypanosoma* species genomes in TriTrypDB²⁵ (<https://tritrypdb.org>) using tBLASTx returned no reliable matches; moreover, comparison of a hidden Markov model of the IFX protein sequence with all *Trypanosoma brucei*, *T. congolense* and *Trypanosoma cruzi* proteins using HMMER also produced no matches, demonstrating IFX is unique to *T. vivax*. To confirm that IFX is present in a single copy, the IFX protein sequence was compared with a six-frame translation of the genome sequence using tBLASTn to identify any sequence copies (annotated or not) with >98% amino acid identity typical of allelic variation.

Illumina sequencing reads from 29 clinical strains isolated from Nigeria, Togo, Burkina Faso, The Gambia, Ivory Coast, Uganda and Brazil were mapped to the *T. vivax* Y486 reference sequence using BWA³⁷ before single-nucleotide polymorphisms (SNPs) were called using the GATK4 analysis toolkit³⁸. Insertion and/or deletions (indels) and variant positions with QD < 2.0, FS > 60.0, MQ < 40.0, MQRankSum < -12.5 or ReadPosRankSum < -8.0 were excluded to produce a final list of 403,190 SNPs. Individuals were classified as missing if allele calls were supported by fewer than three reads. Coding SNPs and synonymous or non-synonymous codon alterations were identified by comparison to the reference annotation using a custom Biopython script; pi-values were calculated on a per site basis using vcftools³⁹. Genes selected for comparison were *V31* (TvY486_0003730), two VSGs (TvY486_0031620 and TvY486_0040490), *ISG* (TvY486_0503980), *HpHbR* (TvY486_0040690) and the ‘housekeeping’ gene *GAPDH* (TvY486_1006840).

Electron microscopy

Trypanosoma vivax parasites were resuspended in 1% formalin prepared using freshly dissolved paraformaldehyde in PBS for 30 min (all steps at room temperature), washed three times in PBS, blocked with PBS and glycine followed by 5% fetal calf serum for 30 min and then incubated with a mouse monoclonal antibody to IFX (clone 8E12) for 1 h. After rinsing, the parasites were incubated with goat anti-mouse IgG preadsorbed to 10 nm gold particles (ab27241 Abcam) for 30 min, washed and fixed in a mixture of 2% formalin and 2.5% glutaraldehyde in 0.1 M sodium cacodylate buffer for 30 min. After washing again, the parasites were post-fixed in 1% osmium tetroxide for 30 min, dehydrated in an ethanol series, embedded in epoxy resin and 60-nm ultrathin sections were cut on a Leica UC6 ultramicrotome, contrasted with uranyl acetate and lead citrate and examined on a 120 kV FEI Spirit Biotwin using a Tietz

F4.16 CCD camera. The density of anti-IFX gold particle staining was determined by counting the number of gold particles per μm of membrane on both sagittal and transverse sections. Membrane lengths were determined using the segmented line function in ImageJ version 1.45s and a known image scaling factor. To assign dorsal and ventral sectors, a line was drawn across (transverse) or along (sagittal) the flagellum midpoint.

Anti-IFX antibody selection and characterization

To raise polyclonal antisera against IFX, the entire ectodomain of IFX was expressed and purified and injected into rabbits (Cambridge Research Biochemicals). The sera were purified on Hi-Trap Protein G HP columns (GE Healthcare) according to the manufacturer's instructions. Hybridomas secreting monoclonal antibodies to IFX were selected using standard protocols, as previously described⁴⁰. In brief, the SP2/0 myeloma cell line was grown in advanced DMEM/F12 medium (Invitrogen) supplemented with 20% fetal bovine serum, penicillin (100 U ml^{-1}), streptomycin ($100 \mu\text{g ml}^{-1}$) and L-glutamine (2 mM). Following spleen dissection and dissociation, 10^8 splenocytes were fused to 10^7 SP2/0 myeloma in 50% PEG (PEG 1500, Roche), using standard procedures. The resulting hybridomas were plated over ten 96-well plates and initially grown in advanced DMEM and F12 medium (Invitrogen) supplemented with 20% fetal bovine serum, penicillin (100 U ml^{-1}), streptomycin ($100 \mu\text{g ml}^{-1}$) and L-glutamine (2 mM) before addition of hypoxanthine–aminopterin–thymidine (HAT) selection medium 24 h after the fusion. After 11 days, hybridoma supernatants were collected to determine the presence of antibodies reacting to the IFX protein using an ELISA-based method, as previously described⁴⁰. Seven wells (2H3, 3D12, 6B3, 8C9, 8E12, 8F10 and 10E2) containing hybridoma colonies secreting antibodies that reacted with IFX, but not to a control protein containing the same purification tags, were identified and cultured for a further four days in HAT-selection medium. Hybridoma cells from each of the positive wells were cloned by limiting dilution over two 96-well plates at a density of 0.5 cells per well and grown in HAT-free SP2/0 conditioned medium. Eleven days later, twelve wells corresponding to each of the seven clones were selected and tested again by ELISA for reactivity to the IFX protein. Hybridoma 8F10 was not successfully cloned but three positive wells from the remaining hybridomas were chosen for a second round of dilution cloning in the conditions described above. After a final test for reactivity to IFX, a single well from each of the positive clones was expanded and adapted to grow in Hybridoma-SFM serum-free medium (Thermo Fisher).

To determine the location of the anti-IFX monoclonal antibody epitopes, subfragments of the IFX ectodomain corresponding to the boundaries of predicted secondary structure (M1–T251, M1–S472, S135–T251 and N442–S535) were designed, produced by gene synthesis and cloned into a mammalian expression plasmid with an

enzymatically biotinylated C-terminal tag (Twist Biosciences). Biotinylated proteins were expressed as secreted recombinant proteins in HEK293 cells as described in ‘Vaccine target identification and expression’ and dialysed to remove free d-biotin. Biotinylated IFX fragments were immobilized on a streptavidin-coated plate and binding of the six mouse monoclonal antibodies was tested by ELISA and detected with an alkaline-phosphatase-conjugated anti-mouse secondary antibody (Sigma-Aldrich) as previously described⁴⁰. Binding of a rabbit polyclonal antibody raised to the entire ectodomains of IFX (Cambridge Research Biochemicals) was used as a positive control for each of the subdomains, and detected with an alkaline-phosphatase-conjugated anti-rabbit secondary antibody (Jackson Immunoresearch).

For affinity-purification of monoclonal antibodies from hybridoma culture supernatants, spent supernatants were supplemented with 0.1 M sodium acetate, pH 5.0 immediately before purification on a HiTrap Protein G HP 1 mL column (GE Healthcare) using an AKTA pure instrument. Elution was performed in 0.1 M glycine, pH 2.7 followed by immediate neutralization with 1 M Tris-HCl, pH 9.0. Purified antibodies were extensively dialysed against PBS and stored at 4 °C until use. To capture antibodies on streptavidin-coated sensor chips for biophysical interaction analysis, 300 µg of purified monoclonal antibodies were chemically biotinylated using a 20-fold molar excess of sulfo-NHS-biotin (ThermoFisher) for two hours at room temperature; to remove excess biotin the solutions were dialysed against 5 l PBS for 16 h.

Antibody affinity by surface plasmon resonance

Antibody affinities were determined by surface plasmon resonance (SPR) essentially as previously described⁴¹ using a Biacore 8K instrument (GE Healthcare). To measure antibody interaction affinity rather than avidity, between 400 to 600 RU of biotinylated anti-IFX monoclonal antibodies were immobilized on a streptavidin-coated sensor chip prepared using the Biotin CAPture kit (GE Healthcare); a biotinylated mouse monoclonal antibody (OX68) was used as a non-binding control in the reference flow cell. The entire ectodomain of IFX was used as the analyte, which was first purified and resolved by size-exclusion chromatography on a Superdex 200 Increase 10/300 column (GE Healthcare) in HBS-EP (10 mM HEPES, 150 mM NaCl, 3 mM EDTA, 0.05% v/v P20 surfactant) immediately before use in SPR experiments to remove any protein aggregates that might influence kinetic measurements. Increasing concentrations of twofold dilutions of the entire ectodomain of IFX as a soluble analyte were injected at 30 µl min⁻¹ for a contact time of 120 s and dissociation of 600 s. Both kinetic and equilibrium binding data were analysed in the manufacturer’s Biacore 8K evaluation software version 1.1 (GE Healthcare) and plotted in Prism GraphPad version 8.0.2. All experiments were performed at 37 °C in HBS-EP.

Antibody cloning, isotype switching, mutagenesis and purification

To switch the isotype of the 8E12 anti-IFX monoclonal antibody from IgG1, it was first necessary to amplify the genes encoding the rearranged light and heavy variable regions from the hybridoma; this was performed essentially as previously described⁴⁰. In brief, total RNAs were extracted from the cloned 8E12 hybridoma using the RNAqueous-micro total RNA isolation kit (Ambion) followed by reverse transcription with Superscript III (Thermo Fisher). PCR products encoding the rearranged heavy and light chain regions were individually amplified using sets of degenerate oligonucleotides and then assembled in a subsequent fusion PCR using a linker fragment to create a single PCR product containing both the rearranged light and heavy chains, as previously described⁴². The fusion PCR product was ligated using the NotI and AscI restriction sites into an expression plasmid obtained from Addgene (plasmid no. 114561) in frame with the mouse constant IgG2a heavy chain⁴³. Competent *Escherichia coli* were transformed and purified plasmids used in small-scale transfections of HEK293 cells to identify those plasmids encoding functional antibodies as previously described⁴⁴.

To perturb the recruitment of immune effectors in the mouse IgG2a recombinant antibody and retain serum half-life, we mutated the C1q and FcR binding sites in the IgG2a constant heavy chain by site-directed mutagenesis as previously described¹⁷. Mutation to the binding site of Fcy receptors (Δ FcR) was achieved by introducing the L234A and L235A substitutions using primers FcR sense 5'-GCACCTAACGCTGCAGGTGGACCATCCG-3' and FcR anti-sense 5'-TGGTCACCTGCAGCGTTAGGTGCTGGGC-3'. To abrogate C1q binding (Δ C1q), a single amino-acid change P329A was introduced using primers C1q sense 5'-CAAAGACCTCGCTGCGCCCATCGAGAGAAC-3' and C1q anti-sense 5'-GATGGCGCAGCGAGGTCTTGTTGACC-3'. In both cases, antibody mutagenesis was achieved by first amplifying 20 ng of an expression vector containing the mouse constant IgG2a heavy chain with each oligonucleotide separately for nine cycles (denaturation for 45 s at 94 °C; annealing for 40 s at 58 °C; elongation for 7 min and 30 s at 72 °C), using the KOD Hot Start DNA polymerase (Merck). Amplification reactions performed with complementary oligonucleotides were then mixed, 0.5 μ l KOD Hot Start DNA polymerase was added to the reaction, and the amplification was resumed for a further 18 cycles. At the end of the reaction, half of the PCR reaction was digested with 20 U DpnI enzyme (New England Biolabs), which specifically cleaves methylated strands from the parental plasmid, for 3 h at 37 °C before transforming 5 μ l into TOP 10 chemically competent bacteria (Invitrogen). Mutations were confirmed in selected clones by DNA sequencing. To generate a double mutant lacking both the C1q and FcR binding sites (Δ C1q Δ FcR), site-directed mutagenesis was performed on an expression plasmid containing the FcR mutation, using the set of oligonucleotides designed for C1q mutagenesis. Both single mutants and the double-

mutant backbones were doubly digested with NotI and AscI restriction enzymes and the fusion PCR product encoding the variable regions of the 8E12 recombinant antibody cloned into them, plasmids purified and verified by sequencing.

Antibodies were produced by transfecting HEK293 cells with plasmids encoding the recombinant 8E12–IgG2a monoclonal antibody with the wild-type IgG2a heavy chain, single mutants that lacked C1q and FcR binding, and the double mutant. Six days after transfection, the cell culture supernatant was collected and the recombinant antibodies were purified on a HiTrap Protein G HP 1-ml column, according to the manufacturer's instructions as previously described⁴⁰.

Reporting summary

Further information on research design is available in the [Nature Research Reporting Summary](#) linked to this paper.

Data availability

Annotated *T. vivax* genome data were obtained from TriTrypDB (<https://tritrypdb.org>). All data generated or analysed during this study are included in this Article, and/or are available from the corresponding author (G.J.W., who can also be contacted at gavin.wright@york.ac.uk) on reasonable request. [Source data](#) are provided with this paper.

References

1. 1.

Morrison, L. J., Vezza, L., Rowan, T. & Hope, J. C. Animal African trypanosomiasis: time to increase focus on clinically relevant parasite and host species. *Trends Parasitol.* **32**, 599–607 (2016).

[PubMed](#) [Google Scholar](#)

2. 2.

Büscher, P., Cecchi, G., Jamonneau, V. & Priotto, G. Human African trypanosomiasis. *Lancet* **390**, 2397–2409 (2017).

[PubMed](#) [Google Scholar](#)

3. 3.

Horn, D. Antigenic variation in African trypanosomes. *Mol. Biochem. Parasitol.* **195**, 123–129 (2014).

[CAS](#) [PubMed](#) [PubMed Central](#) [Google Scholar](#)

4. 4.

D'Archivio, S. et al. Non-invasive in vivo study of the *Trypanosoma vivax* infectious process consolidates the brain commitment in late infections. *PLoS Negl. Trop. Dis.* **7**, e1976 (2013).

[PubMed](#) [PubMed Central](#) [Google Scholar](#)

5. 5.

Budd, L. T. *DFID-funded Tsetse and Trypanosome Research and Development Since 1980. Vol. 2. Economic Analysis* (DFID Livestock Production, Animal Health and Natural Resources Systems Research Programmes, 1999).

6. 6.

Aksoy, S., Buscher, P., Lehane, M., Solano, P. & Van Den Abbeele, J. Human African trypanosomiasis control: achievements and challenges. *PLoS Negl. Trop. Dis.* **11**, e0005454 (2017).

[PubMed](#) [PubMed Central](#) [Google Scholar](#)

7. 7.

Kristjanson, P. M., Swallow, B. M., Rowlands, G. J., Kruska, R. L. & de Leeuw, P. N. Measuring the costs of African animal trypanosomosis, the potential benefits of control and returns to research. *Agric. Syst.* **59**, 79–98 (1999).

[Google Scholar](#)

8. 8.

Tsegaye, B., Dagnachew, S. & Terefe, G. Review on drug resistant animal trypanosomes in Africa and overseas. *Afr. J. Basic Appl. Sci.* **7**, 73–83 (2015).

[Google Scholar](#)

9. 9.

La Greca, F. & Magez, S. Vaccination against trypanosomiasis: can it be done or is the trypanosome truly the ultimate immune destroyer and escape artist? *Hum. Vaccin.* **7**, 1225–1233 (2011).

[PubMed](#) [PubMed Central](#) [Google Scholar](#)

10. 10.

Engstler, M. et al. Hydrodynamic flow-mediated protein sorting on the cell surface of trypanosomes. *Cell* **131**, 505–515 (2007).

[CAS](#) [PubMed](#) [Google Scholar](#)

11. 11.

Schwede, A., Macleod, O. J. S., MacGregor, P. & Carrington, M. How does the VSG coat of bloodstream form African trypanosomes interact with external proteins? *PLoS Pathog.* **11**, e1005259 (2015).

[PubMed](#) [PubMed Central](#) [Google Scholar](#)

12. 12.

Chamond, N. et al. *Trypanosoma vivax* infections: pushing ahead with mouse models for the study of nagana. I. Parasitological, hematological and pathological parameters. *PLoS Negl. Trop. Dis.* **4**, e792 (2010).

[PubMed](#) [PubMed Central](#) [Google Scholar](#)

13. 13.

Jackson, A. P. et al. Antigenic diversity is generated by distinct evolutionary mechanisms in African trypanosome species. *Proc. Natl Acad. Sci. USA* **109**, 3416–3421 (2012).

[ADS](#) [CAS](#) [PubMed](#) [PubMed Central](#) [Google Scholar](#)

14. 14.

Jackson, A. P. et al. A cell-surface phylome for African trypanosomes. *PLoS Negl. Trop. Dis.* **7**, e2121 (2013).

[CAS](#) [PubMed](#) [PubMed Central](#) [Google Scholar](#)

15. 15.

Jackson, A. P. et al. Global gene expression profiling through the complete life cycle of *Trypanosoma vivax*. *PLoS Negl. Trop. Dis.* **9**, e0003975 (2015).

[PubMed](#) [PubMed Central](#) [Google Scholar](#)

16. 16.

Collins, A. M. IgG subclass co-expression brings harmony to the quartet model of murine IgG function. *Immunol. Cell Biol.* **94**, 949–954 (2016).

[CAS](#) [PubMed](#) [Google Scholar](#)

17. 17.

Lo, M. et al. Effector-attenuating substitutions that maintain antibody stability and reduce toxicity in mice. *J. Biol. Chem.* **292**, 3900–3908 (2017).

[CAS](#) [PubMed](#) [PubMed Central](#) [Google Scholar](#)

18. 18.

Ouattara, A. et al. Designing malaria vaccines to circumvent antigen variability. *Vaccine* **33**, 7506–7512 (2015).

[CAS](#) [PubMed](#) [PubMed Central](#) [Google Scholar](#)

19. 19.

Frenkel, D. et al. *Trypanosoma brucei* co-opts NK cells to kill splenic B2 B cells. *PLoS Pathog.* **12**, e1005733 (2016).

[PubMed](#) [PubMed Central](#) [Google Scholar](#)

20. 20.

Radwanska, M. et al. Trypanosomiasis-induced B cell apoptosis results in loss of protective anti-parasite antibody responses and abolishment of vaccine-induced memory responses. *PLoS Pathog.* **4**, e1000078 (2008).

[PubMed](#) [PubMed Central](#) [Google Scholar](#)

21. 21.

Bockstal, V. et al. *T. brucei* infection reduces B lymphopoiesis in bone marrow and truncates compensatory splenic lymphopoiesis through transitional B-cell apoptosis. *PLoS Pathog.* **7**, e1002089 (2011).

[CAS](#) [PubMed](#) [PubMed Central](#) [Google Scholar](#)

22. 22.

Romero Ramirez, A. I. *Antigen Discovery in Trypanosoma vivax* (Univ. Liverpool, 2020).

23. 23.

Durocher, Y., Perret, S. & Kamen, A. High-level and high-throughput recombinant protein production by transient transfection of suspension-growing human 293-EBNA1 cells. *Nucleic Acids Res.* **30**, e9 (2002).

[PubMed](#) [PubMed Central](#) [Google Scholar](#)

24. 24.

Loignon, M. et al. Stable high volumetric production of glycosylated human recombinant IFNalpha2b in HEK293 cells. *BMC Biotechnol.* **8**, 65 (2008).

[PubMed](#) [PubMed Central](#) [Google Scholar](#)

25. 25.

Aslett, M. et al. TriTrypDB: a functional genomic resource for the Trypanosomatidae. *Nucleic Acids Res.* **38**, D457–D462 (2010).

[CAS](#) [PubMed](#) [Google Scholar](#)

26. 26.

Sonnhammer, E. L., von Heijne, G. & Krogh, A. A hidden Markov model for predicting transmembrane helices in protein sequences. *Proc. Int. Conf. Intell. Syst. Mol. Biol.* **6**, 175–182 (1998).

[CAS](#) [PubMed](#) [Google Scholar](#)

27. 27.

Eisenhaber, B., Bork, P. & Eisenhaber, F. Prediction of potential GPI-modification sites in proprotein sequences. *J. Mol. Biol.* **292**, 741–758 (1999).

[CAS](#) [PubMed](#) [Google Scholar](#)

28. 28.

Bendtsen, J. D., Nielsen, H., von Heijne, G. & Brunak, S. Improved prediction of signal peptides: SignalP 3.0. *J. Mol. Biol.* **340**, 783–795 (2004).

[PubMed](#) [Google Scholar](#)

29. 29.

Bushell, K. M., Söllner, C., Schuster-Boeckler, B., Bateman, A. & Wright, G. J. Large-scale screening for novel low-affinity extracellular protein interactions. *Genome Res.* **18**, 622–630 (2008).

[CAS](#) [PubMed](#) [PubMed Central](#) [Google Scholar](#)

30. 30.

Sun, Y., Gallagher-Jones, M., Barker, C. & Wright, G. J. A benchmarked protein microarray-based platform for the identification of novel low-affinity extracellular protein interactions. *Anal. Biochem.* **424**, 45–53 (2012).

[CAS](#) [PubMed](#) [PubMed Central](#) [Google Scholar](#)

31. 31.

Crosnier, C. et al. A library of functional recombinant cell-surface and secreted *P. falciparum* merozoite proteins. *Mol. Cell. Proteomics* **12**, 3976–3986 (2013).

[CAS](#) [PubMed](#) [PubMed Central](#) [Google Scholar](#)

32. 32.

Kerr, J. S. & Wright, G. J. Avidity-based extracellular interaction screening (AVEXIS) for the scalable detection of low-affinity extracellular receptor-ligand interactions. *J. Vis. Exp.* **61**, e3881 (2012).

[Google Scholar](#)

33. 33.

Bartholdson, S. J. et al. Semaphorin-7A is an erythrocyte receptor for *P. falciparum* merozoite-specific TRAP homolog, MTRAP. *PLoS Pathog.* **8**, e1003031 (2012).

[PubMed](#) [PubMed Central](#) [Google Scholar](#)

34. 34.

Crosnier, C. et al. Systematic screening of 96 *Schistosoma mansoni* cell-surface and secreted antigens does not identify any strongly protective vaccine candidates in a mouse model of infection. *Wellcome Open Res.* **4**, 159 (2019).

[PubMed](#) [PubMed Central](#) [Google Scholar](#)

35. 35.

D'Archivio, S. et al. Genetic engineering of *Trypanosoma (Duttonella) vivax* and in vitro differentiation under axenic conditions. *PLoS Negl. Trop. Dis.* **5**, e1461 (2011).

[PubMed](#) [PubMed Central](#) [Google Scholar](#)

36. 36.

Vieira, P. & Rajewsky, K. The half-lives of serum immunoglobulins in adult mice. *Eur. J. Immunol.* **18**, 313–316 (1988).

[CAS](#) [PubMed](#) [Google Scholar](#)

37. 37.

Li, H. & Durbin, R. Fast and accurate short read alignment with Burrows-Wheeler transform. *Bioinformatics* **25**, 1754–1760 (2009).

[CAS](#) [PubMed](#) [PubMed Central](#) [Google Scholar](#)

38. 38.

DePristo, M. A. et al. A framework for variation discovery and genotyping using next-generation DNA sequencing data. *Nat. Genet.* **43**, 491–498 (2011).

[CAS](#) [PubMed](#) [PubMed Central](#) [Google Scholar](#)

39. 39.

Danecek, P. et al. The variant call format and VCFtools. *Bioinformatics* **27**, 2156–2158 (2011).

[CAS](#) [PubMed](#) [PubMed Central](#) [Google Scholar](#)

40. 40.

Crosnier, C., Staudt, N. & Wright, G. J. A rapid and scalable method for selecting recombinant mouse monoclonal antibodies. *BMC Biol.* **8**, 76 (2010).

[PubMed](#) [PubMed Central](#) [Google Scholar](#)

41. 41.

Zenonos, Z. A. et al. Basigin is a druggable target for host-oriented antimalarial interventions. *J. Exp. Med.* **212**, 1145–1151 (2015).

[CAS](#) [PubMed](#) [PubMed Central](#) [Google Scholar](#)

42. 42.

Müller-Sienerth, N., Crosnier, C., Wright, G. J. & Staudt, N. Cloning of recombinant monoclonal antibodies from hybridomas in a single mammalian expression plasmid. *Methods Mol. Biol.* **1131**, 229–240 (2014).

[PubMed](#) [Google Scholar](#)

43. 43.

Andrews, N. P. et al. A toolbox of IgG subclass-switched recombinant monoclonal antibodies for enhanced multiplex immunolabeling of brain. *eLife* **8**, e43322 (2019).

[PubMed](#) [PubMed Central](#) [Google Scholar](#)

44. 44.

Staudt, N., Müller-Sienerth, N. & Wright, G. J. Development of an antigen microarray for high throughput monoclonal antibody selection. *Biochem. Biophys. Res. Commun.* **445**, 785–790 (2014).

[CAS](#) [PubMed](#) [PubMed Central](#) [Google Scholar](#)

[Download references](#)

Acknowledgements

This research was funded by the Wellcome Trust (grant 206194) and BBSRC (grant BB/S001980/1). A.R.-R. was supported by a PhD studentship funded by FONDECYT-CONCYTEC, the National Council of Science, Technology and Innovation from Peru (grant contract number 001-2016-FONDECYT). We are indebted to Institut Pasteur for providing us with the *T. vivax* luciferase line. We thank Sanger Institute animal technicians for their support with animal work, N. Karp for advice on experimental design, C. Mackenzie for preliminary work on anti-IFX monoclonal antibodies, E. Coomber for help with hybridoma tissue culture, and M. Carrington, L. Morrison and T. Rowan for helpful discussions.

Author information

Affiliations

1. Cell Surface Signalling Laboratory, Wellcome Sanger Institute, Hinxton, UK
Delphine Autheman, Cécile Crosnier, Francis Galaway, Malhar Khushu, Han Ong & Gavin J. Wright
2. Pathogen Support Team, Wellcome Sanger Institute, Hinxton, UK
Simon Clare, Cordelia Brandt, Katherine Harcourt & Charlotte Tolley
3. Electron and Advanced Light Microscopy, Wellcome Sanger Institute, Hinxton, UK
David A. Goulding
4. Department of Infection Biology and Microbiomes, University of Liverpool, Liverpool, UK
Alessandra Romero-Ramirez, Craig W. Duffy & Andrew P. Jackson
5. Department of Biology, University of York, York, UK
Gavin J. Wright
6. Hull York Medical School, University of York, York, UK
Gavin J. Wright

7. York Biomedical Research Institute, University of York, York, UK

Gavin J. Wright

Authors

1. Delphine Autheman

[View author publications](#)

You can also search for this author in [PubMed](#) [Google Scholar](#)

2. Cécile Crosnier

[View author publications](#)

You can also search for this author in [PubMed](#) [Google Scholar](#)

3. Simon Clare

[View author publications](#)

You can also search for this author in [PubMed](#) [Google Scholar](#)

4. David A. Goulding

[View author publications](#)

You can also search for this author in [PubMed](#) [Google Scholar](#)

5. Cordelia Brandt

[View author publications](#)

You can also search for this author in [PubMed](#) [Google Scholar](#)

6. Katherine Harcourt

[View author publications](#)

You can also search for this author in [PubMed](#) [Google Scholar](#)

7. Charlotte Tolley

[View author publications](#)

You can also search for this author in [PubMed](#) [Google Scholar](#)

8. Francis Galaway

[View author publications](#)

You can also search for this author in [PubMed](#) [Google Scholar](#)

9. Malhar Khushu

[View author publications](#)

You can also search for this author in [PubMed](#) [Google Scholar](#)

10. Han Ong

[View author publications](#)

You can also search for this author in [PubMed](#) [Google Scholar](#)

11. Alessandra Romero-Ramirez

[View author publications](#)

You can also search for this author in [PubMed](#) [Google Scholar](#)

12. Craig W. Duffy

[View author publications](#)

You can also search for this author in [PubMed](#) [Google Scholar](#)

13. Andrew P. Jackson

[View author publications](#)

You can also search for this author in [PubMed](#) [Google Scholar](#)

14. Gavin J. Wright

[View author publications](#)

You can also search for this author in [PubMed](#) [Google Scholar](#)

Contributions

D.A. and G.J.W. designed the study. D.A. prepared proteins, and performed immunizations and parasite challenges with help from S.C., C.B., H.O. and K.H. C.C. selected hybridomas, cloned the 8E12 monoclonal antibody, and did the isotype switching, mutagenesis and purification. D.A.G. performed immunogold labelling. C.T. generated hybridomas. F.G. and M.K. performed SPR experiments and analysis. A.R.-R., C.W.D. and A.P.J. provided and analysed *T. vivax* genome sequences and provided sera from infected cattle. D.A. and G.J.W. prepared the manuscript with comments from all co-authors.

Corresponding author

Correspondence to [Gavin J. Wright](#).

Ethics declarations

Competing interests

D.A. and G.J.W. are named inventors on two UK patent applications relating to this research.

Additional information

Peer review information *Nature* thanks Michael Ferguson and the other, anonymous, reviewer(s) for their contribution to the peer review of this work. Peer reviewer reports are available.

Publisher's note Springer Nature remains neutral with regard to jurisdictional claims in published maps and institutional affiliations.

Extended data figures and tables

[Extended Data Fig. 1 Trypanosoma vivax vaccine candidate antigens, organization of the protection screen and antibody titres.](#)

a, Vaccine candidates were expressed as soluble recombinant proteins in HEK293 cells, purified and resolved by SDS–PAGE to determine protein integrity and purity. For uncropped gel images, see Supplementary Fig. 1. **b**, Mice were vaccinated with a protein-in-alum formulation using a prime and two-boost regime and rested before challenge with the luciferase-expressing *T. vivax* parasite line and parasitaemia quantified using bioluminescent imaging. Vaccine candidates were tested in cohorts containing two control cages that were infected first and last to ensure any effect on the reduction of parasite multiplication was not confounded by the loss of parasite virulence. **c**, Parasite multiplication was identical in mice treated with adjuvant alone compared to naive mice. A group of five mice were immunized three times with alum alone (filled circles) and rested for six weeks and the infection with bioluminescent *T. vivax* was compared to naive mice (open circles). Data points represent individual mice; grey shading indicates background bioluminescence. **d**, Serum dilutions for the half-maximal responses for each antigen. Data points are individual mice and bars represent mean \pm s.d.; $n = 5$. ND, not determined. Grey stars indicate no detectable response.

[Source data](#)

Extended Data Fig. 2 Summary of systematic genome-led reverse vaccinology screen that identified subunit vaccine candidates for *T. vivax*.

Bioluminescence is used as a proxy for parasitaemia and is shown for each mouse in the indicated days post-challenge. Candidates are identified using their ‘V number’ and organized into their screening cohorts. The two cages of adjuvant-only controls for each cohort are highlighted in grey. The majority of candidates had no effect on the ascending phase of parasitaemia, and are left unshaded. Three candidates (V2, V8 and V31) that had a statistically significant effect on infection are highlighted in pale yellow, and the candidate that elicited strong protection (V23) is highlighted in pale green. Data points are bioluminescence readings from individual mice. The occasional reductions in parasitaemia followed by rebound after day 8 are likely to be due to protective anti-VSG responses and selection of an antigenically distinct variant.

[Source data](#)

Extended Data Fig. 3 Replication of strong protective effects in a larger group of mice vaccinated with candidate V23 (IFX).

a, Quantification of replicate vaccinations and *T. vivax* infections with four antigens showing protective effects in the initial screen. V23 and V31 vaccinations replicated, but not V2 and V8. Parasitaemia was quantified on day six using bioluminescence; data points represent individual mice and bars indicate mean \pm s.d. ns, not significant, $****P \leq 0.0001$ two-tailed *t*-test; grey shading indicates background bioluminescence thresholds. **b**, Fifteen mice were immunized with purified soluble IFX–V23 recombinant protein adjuvanted in alum and challenged with transgenic luciferase-expressing *T. vivax*. Parasitaemia was quantified on the indicated days after parasite challenge using bioluminescence; controls are a cohort of 15 mice treated with adjuvant only. Ten out of the 15 mice were protected until at least day 170. Data points represent individual mice and grey shading indicates bioluminescence thresholds of uninfected mice. Where mice had to be euthanized for health reasons thought to be unrelated to the infection, this is indicated by a cross.

[Source data](#)

Extended Data Fig. 4 Parasites do not detectably persist in the organs, adipose tissue or dermis of mice vaccinated with candidate V23 (IFX), challenged with *T. vivax*.

An IFX–V23-immunized mouse was challenged with luciferase-expressing transgenic *T. vivax* parasites and protection from infection relative to controls was established. The mouse was rested and, nine months later, injected with luciferin to detect residual parasites using bioluminescence. No bioluminescent signals above background were detected in vaccinated mice either when the whole mouse was imaged, or within the dissected organs, adipose deposits and dermis of IFX–V23-immunized mouse (top panels). An unimmunized mouse was used 8 days after parasite challenge as a positive control (bottom panels).

Extended Data Fig. 5 IFX staining is specific to *T. vivax* and concentrated at the boundary of the flagellum–cell body contact.

a, Immunogold electron microscopy using an anti-IFX mouse monoclonal antibody localized IFX to clusters along the length of the flagellum in mid-sagittal sections (white arrows and bars). **b**, Enlarged view of the box in **a**, showing IFX located between the flagellum and cell membranes. **c**, Anti-IFX particle staining density was quantified along the membrane interface of the ventral flagellum–cell body (IVC), dorsal flagellum (DF) and cell body area on sagittal and transverse sections. Individual data points are shown; bars represent means. **d, e**, Control electron micrographs of *T. vivax* parasites stained with an isotype-matched control mouse IgG1 antibody (**d**) or goat anti-mouse coated gold particles alone (**e**), showing no accumulation of gold particles. **f**, *Trypanosoma congolense* parasites were stained with anti-IFX rabbit polyclonal sera (top panels) or control preimmune sera (bottom panels) followed by fluorescently conjugated anti-rabbit secondary (red) and counterstained with DAPI (blue). No staining of the parasites was observed demonstrating antibody specificity. Flag., flagellum; fm, flagellar membrane; cm, parasite cell membrane. Scale bars, 100 nm (**a, b**), 150 nm (**d, e**), 8 μ m (**f**). Representative images of at least two independent experiments are shown.

[Source data](#)

Extended Data Fig. 6 Depletion of CD4- and CD8-positive T lymphocytes and natural killer cells in IFX-vaccinated mice before parasite challenge do not affect IFX-mediated protective efficacy.

Groups of mice were vaccinated with IFX, rested and then either natural killer (NK) cells ($n = 4$) or CD4- ($n = 5$) or CD8-positive ($n = 4$) T lymphocytes were depleted using lineage-specific monoclonal antibodies (antibody clone names indicated) before challenging with luciferase-expressing *T. vivax* parasites. Cell-depleted mice showed no significant difference to control mice treated with an isotype-matched control antibody (LTF-2). The virulence of parasites was confirmed by showing robust infections in naive mice in the same experiment. Parasitaemia was quantified on day 5

using bioluminescence, grey shading indicates bioluminescence thresholds of uninfected mice; data points represent individual mice and bars indicate mean ± s.d.

[Source data](#)

Extended Data Fig. 7 Identification of the binding epitopes and affinities of a panel of mouse monoclonal antibodies recognizing *T. vivax* IFX.

a, Schematic showing the N- and C-terminal boundaries of four fragments of the IFX ectodomain. **b**, Identification of the epitope locations for the anti-IFX monoclonal antibodies. The entire ectodomain (EE) ($n = 5$) and derived fragments (1 to 4) ($n = 3$) were expressed as enzymatically biotinylated soluble recombinant proteins in HEK293 cells, immobilized on streptavidin-coated microtitre plates, and the binding of each of the anti-IFX monoclonal antibodies was quantified by ELISA. The hybridoma secreting monoclonal antibody 8F10 was not successfully cloned and therefore not further investigated. Bars represent mean ± s.d. **c**, Schematic of the antibody binding data to the IFX ectodomain fragments, showing the approximate locations of the antibody epitopes. **d**, Quantification of the equilibrium binding affinity of the anti-IFX monoclonal antibodies by SPR. Five of the anti-IFX monoclonal antibodies were chemically biotinylated and immobilized on a streptavidin-coated sensor chip and the binding to serial dilutions of purified soluble IFX ectodomains was measured. The binding affinity for each of the antibodies at equilibrium (K_D) was calculated by fitting the binding data (inset) to a simple 1:1 binding isotherm. K_D values are mean ± s.d. using seven analyte dilutions from one experiment. There was no simple positive correlation between the antibody binding affinity and protective efficacy. Antibody affinities were plotted against percentage parasite inhibition in passive transfer experiments at day 5 after infection (mean ± s.d.; $n = 5$).

[Source data](#)

Extended Data Fig. 8 Recombinant antibody cloning, isotype switching and mutation of antibody effector recruitment sites of the anti-IFX 8E12 hybridoma.

a, The rearranged variable light and heavy regions of the anti-IFX 8E12 monoclonal antibody were amplified and assembled by fusion PCR using a ‘joining’ fragment before being subcloned into a mammalian protein expression plasmid containing the mouse IgG2a heavy chain. Twelve of fifteen colonies expressed functional anti-IFX antibodies and three selected clones contained identical V_H and V_L sequences. The 8E12–IgG2a antibody was produced by transfection of HEK293 cells. For uncropped gel images see Supplementary Fig. 1. **b**, The binding affinity of the 8E12 monoclonal

antibody for IFX is unaffected after isotype switching. The biophysical binding parameters of the 8E12 monoclonal antibody for IFX were determined by SPR as both the hybridoma-expressed IgG1 (left) and recombinant IgG2a (right). Serial dilutions of the purified complete ectodomain of IFX were injected for two minutes over the biotinylated antibodies immobilized on a streptavidin-coated sensor chip and left to dissociate. Equilibrium binding constants were calculated by fitting the binding data to a Langmuir binding isotherm and found to be essentially equivalent. **c**, Mutation of the C1q and FcR recruitment sites on the 8E12–IgG2a heavy chain. The specified mutations that are known to abrogate binding to either C1q or FcR were made on the recombinant 8E12–IgG2a plasmid using site-directed mutagenesis. Mutations were made individually (Δ C1q and Δ FcR) and together (Δ C1q Δ FcR). Each of the three mutant antibodies were expressed, purified and IFX-binding activity normalized to the parent 8E12–IgG2a and 8E12–IgG1 by ELISA.

[Source data](#)

Extended Data Fig. 9 The anti-IFX 8E12–IgG2a monoclonal antibody with abrogated immune effector recruitment sites reveals highly potent protection due to several mechanisms of immunological protection, including a major role for complement.

a, Groups of five mice were injected three times intravenously with the indicated doses of purified anti-IFX 8E12–IgG2a monoclonal antibody and challenged with the luciferase-expressing transgenic *T. vivax* parasites. Control is an isotype-matched mouse IgG2a monoclonal antibody. A cross indicates where a single mouse had to be removed from the study on day 16 for health reasons thought to be unrelated to the infection. **b**, Groups of five mice were administered three times intravenously with either 50 µg (left) or 100 µg (right) of purified anti-IFX 8E12–IgG2a monoclonal antibody containing mutations in immune effector recruitment binding sites and challenged with luciferase-expressing transgenic *T. vivax* parasites. Mutations prevented binding to C1q (Δ C1q), FcRs (Δ FcR) or both (Δ C1q Δ FcR) and were compared to non-mutated 8E12–IgG2a, 8E12–IgG1 and both isotype-matched IgG2a and IgG1 controls. In all panels, data points represent individual mice and grey shading indicates bioluminescence thresholds of uninfected mice; dashed lines indicate survival within each group. Reductions in parasitaemia followed by rebounds after day 8 post-infection are likely to be due to the development of protective host antibody responses directed to the dominant VSG within the parasite population and selection of an antigenically distinct variant. One of two independent experiments with very similar outcomes is shown.

[Source data](#)

Extended Data Fig. 10 IFX adjuvanted in Quil-A and delivered subcutaneously induces consistent and isotype-balanced anti-IFX titres that are highly protective.

a, Groups of five mice were immunized with the purified ectodomain of IFX adjuvanted in alum, Quil-A and montanide ISA 201 VG (mont.) using a prime and two-boost regime either intraperitoneally (alum i.p.) or subcutaneously (Quil-A and montanide s.c.). Half-maximal anti-IFX titres were determined by ELISA. Bars are mean ± s.d. IFX adjuvanted with Quil-A administered subcutaneously were able to elicit anti-IFX antibody titres that were as high as those elicited by IFX adjuvanted with alum delivered intraperitoneally. **b**, Quantification of different anti-IFX antibody isotypes elicited by the different adjuvants. IFX and Quil-A were able to induce a larger proportion of IgG2 isotype subclasses. Data points represent individual mice ($n = 5$) and bars are mean ± s.d. **c**, Increased protection to *T. vivax* challenge using Quil-A in a protein-in-adjuvant vaccine formulation. Fourteen mice were immunized subcutaneously with purified soluble IFX recombinant protein adjuvanted in Quil-A and challenged with transgenic luciferase-expressing *T. vivax*. Parasitaemia was quantified on the indicated days after parasite challenge using bioluminescence; controls are a cohort of 14 mice treated with adjuvant only. Data points represent individual mice and grey shading indicates bioluminescence thresholds of uninfected mice. Crosses indicate where individuals had to be removed from the study for health reasons thought to be unrelated to the infection. The smaller bioluminescence peaks in four mice corresponding to high bioluminescent readings between days 16 and 24 were caused by bleed-through of bioluminescence signal from the mouse that eventually succumbed to infection.

[Source data](#)

Supplementary information

Supplementary Figure 1

Original gels corresponding to Extended Data Figure 1a and Extended Data Figure 8a.

Reporting Summary

Supplementary Table 1

A table of the *Trypanosoma vivax* antigens tested in this study.

Peer Review File

Source data

[Source Data Fig. 1](#)

[Source Data Fig. 3](#)

[Source Data Fig. 4](#)

[Source Data Fig. 5](#)

[Source Data Extended Data Fig. 1](#)

[Source Data Extended Data Fig. 2](#)

[Source Data Extended Data Fig. 3](#)

[Source Data Extended Data Fig. 5](#)

[Source Data Extended Data Fig. 6](#)

[Source Data Extended Data Fig. 7](#)

[Source Data Extended Data Fig. 8](#)

[Source Data Extended Data Fig. 9](#)

[Source Data Extended Data Fig. 10](#)

Rights and permissions

[Reprints and Permissions](#)

About this article



Check for
updates

Cite this article

Autheman, D., Crosnier, C., Clare, S. *et al.* An invariant *Trypanosoma vivax* vaccine antigen induces protective immunity. *Nature* **595**, 96–100 (2021).
<https://doi.org/10.1038/s41586-021-03597-x>

[Download citation](#)

- Received: 28 January 2020
- Accepted: 29 April 2021
- Published: 26 May 2021
- Issue Date: 01 July 2021
- DOI: <https://doi.org/10.1038/s41586-021-03597-x>

[Download PDF](#)

Advertisement

This article was downloaded by **calibre** from <https://www.nature.com/articles/s41586-021-03597-x>

| [Section menu](#) | [Main menu](#) |

- Article
- [Published: 09 June 2021](#)

TIM-3 restrains anti-tumour immunity by regulating inflammasome activation

- [Karen O. Dixon](#) ORCID: [orcid.org/0000-0001-7811-5439^{1,2,3}](https://orcid.org/0000-0001-7811-5439),
- [Marcin Tabaka³](#),
- [Markus A. Schramm](#) ORCID: [orcid.org/0000-0003-3513-3842^{1,2 nAff6}](https://orcid.org/0000-0003-3513-3842),
- [Sheng Xiao^{1,2 nAff7}](#),
- [Ruihan Tang^{1,2}](#),
- [Danielle Dionne³](#),
- [Ana. C. Anderson](#) ORCID: [orcid.org/0000-0002-0877-2932^{1,2,3}](https://orcid.org/0000-0002-0877-2932),
- [Orit Rozenblatt-Rosen](#) ORCID: [orcid.org/0000-0001-6313-3570^{3 nAff8}](https://orcid.org/0000-0001-6313-3570),
- [Aviv Regev](#) ORCID: [orcid.org/0000-0003-3293-3158^{3,4,5 nAff8}](https://orcid.org/0000-0003-3293-3158) &
- [Vijay K. Kuchroo](#) ORCID: [orcid.org/0000-0001-7177-2110^{1,2,3}](https://orcid.org/0000-0001-7177-2110)

[Nature](#) volume 595, pages 101–106 (2021) [Cite this article](#)

- 11k Accesses
- 99 Altmetric
- [Metrics details](#)

Subjects

- [Dendritic cells](#)

- [Tumour immunology](#)

Abstract

T cell immunoglobulin and mucin-containing molecule 3 (TIM-3), first identified as a molecule expressed on interferon- γ producing T cells¹, is emerging as an important immune-checkpoint molecule, with therapeutic blockade of TIM-3 being investigated in multiple human malignancies. Expression of TIM-3 on CD8 $^{+}$ T cells in the tumour microenvironment is considered a cardinal sign of T cell dysfunction; however, TIM-3 is also expressed on several other types of immune cell, confounding interpretation of results following blockade using anti-TIM-3 monoclonal antibodies. Here, using conditional knockouts of TIM-3 together with single-cell RNA sequencing, we demonstrate the singular importance of TIM-3 on dendritic cells (DCs), whereby loss of TIM-3 on DCs—but not on CD4 $^{+}$ or CD8 $^{+}$ T cells—promotes strong anti-tumour immunity. Loss of TIM-3 prevented DCs from expressing a regulatory program and facilitated the maintenance of CD8 $^{+}$ effector and stem-like T cells. Conditional deletion of TIM-3 in DCs led to increased accumulation of reactive oxygen species resulting in NLRP3 inflammasome activation. Inhibition of inflammasome activation, or downstream effector cytokines interleukin-1 β (IL-1 β) and IL-18, completely abrogated the protective anti-tumour immunity observed with TIM-3 deletion in DCs. Together, our findings reveal an important role for TIM-3 in regulating DC function and underscore the potential of TIM-3 blockade in promoting anti-tumour immunity by regulating inflammasome activation.

Access options

Subscribe to Journal

Get full journal access for 1 year

\$199.00

only \$3.90 per issue

Subscribe

All prices are NET prices.

VAT will be added later in the checkout.

Tax calculation will be finalised during checkout.

Rent or Buy article

Get time limited or full article access on ReadCube.

from \$8.99

Rent or Buy

All prices are NET prices.

Additional access options:

- [Log in](#)
- [Access through your institution](#)
- [Learn about institutional subscriptions](#)

Fig. 1: Deletion of TIM-3 on DCs leads to reduced tumour burden.

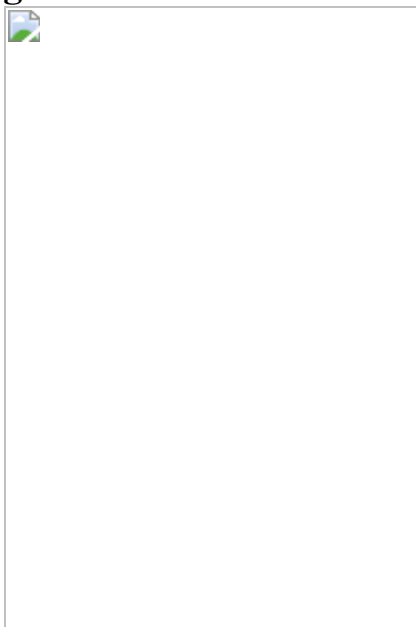


Fig. 2: Expansion of stem-like memory-precursor CD8⁺ T cells in *Havcr2*^{cko} tumours.

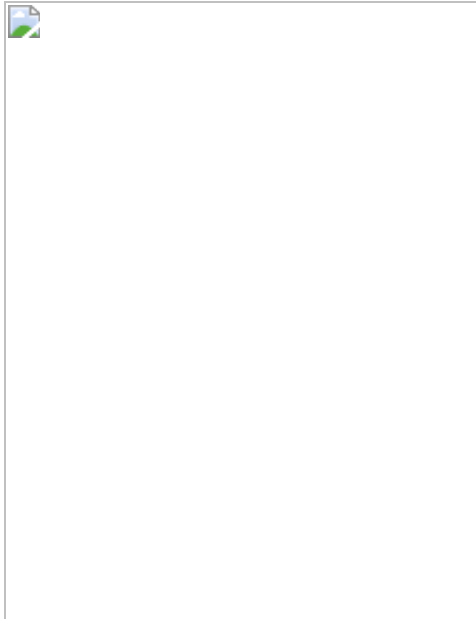


Fig. 3: TIM-3 deficiency promotes DC functionality and enhances antigen-specific anti-tumour immunity.

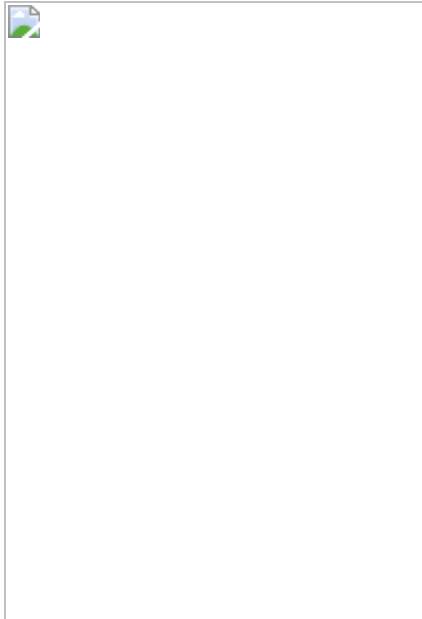
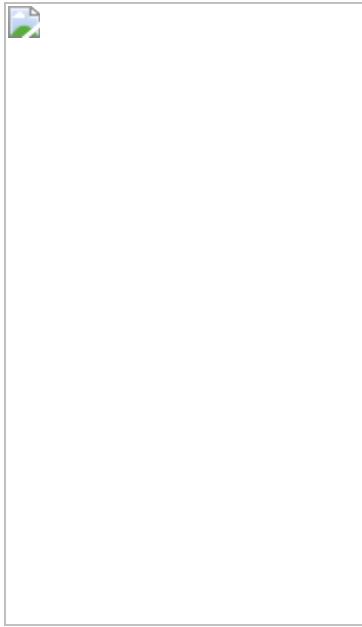


Fig. 4: Loss of TIM-3 on DCs promotes inflammasome activation.



Data availability

Data have been uploaded to NCBI Gene Expression Omnibus (<https://www.ncbi.nlm.nih.gov/geo/>) under data repository accession number [GSE151914](#). [Source data](#) are provided with this paper.

References

1. 1.

Monney, L. et al. Th1-specific cell surface protein Tim-3 regulates macrophage activation and severity of an autoimmune disease. *Nature* **415**, 536–541 (2002).

[CAS](#) [PubMed](#) [Google Scholar](#)

2. 2.

Sakuishi, K. et al. Targeting Tim-3 and PD-1 pathways to reverse T cell exhaustion and restore anti-tumor immunity. *J. Exp. Med.* **207**, 2187–2194 (2010).

[CAS](#) [PubMed](#) [PubMed Central](#) [Google Scholar](#)

3. 3.

Jin, H. T. et al. Cooperation of Tim-3 and PD-1 in CD8 T-cell exhaustion during chronic viral infection. *Proc. Natl Acad. Sci. USA* **107**, 14733–14738 (2010).

[ADS](#) [CAS](#) [PubMed](#) [PubMed Central](#) [Google Scholar](#)

4. 4.

Rangachari, M. et al. Bat3 promotes T cell responses and autoimmunity by repressing Tim-3-mediated cell death and exhaustion. *Nat. Med.* **18**, 1394–1400 (2012).

[CAS](#) [PubMed](#) [PubMed Central](#) [Google Scholar](#)

5. 5.

da Silva, I. P. et al. Reversal of NK-cell exhaustion in advanced melanoma by Tim-3 blockade. *Cancer Immunol. Res.* **2**, 410–422 (2014).

[PubMed](#) [PubMed Central](#) [Google Scholar](#)

6. 6.

Anderson, A. C. et al. Promotion of tissue inflammation by the immune receptor Tim-3 expressed on innate immune cells. *Science* **318**, 1141–1143 (2007).

[ADS](#) [CAS](#) [PubMed](#) [Google Scholar](#)

7. 7.

Liu, L. Z. et al. CCL15 recruits suppressive monocytes to facilitate immune escape and disease progression in hepatocellular carcinoma. *Hepatology* **69**, 143–159 (2019).

[CAS](#) [PubMed](#) [Google Scholar](#)

8. 8.

Broz, M. L. et al. Dissecting the tumor myeloid compartment reveals rare activating antigen-presenting cells critical for T cell immunity. *Cancer Cell* **26**, 638–652 (2014).

[CAS](#) [PubMed](#) [PubMed Central](#) [Google Scholar](#)

9. 9.

de Mingo Pulido, A. et al. TIM-3 regulates CD103⁺ dendritic cell function and response to chemotherapy in breast cancer. *Cancer Cell* **33**, 60–74 (2018).

[PubMed](#) [PubMed Central](#) [Google Scholar](#)

10. 10.

Chiba, S. et al. Tumor-infiltrating DCs suppress nucleic acid-mediated innate immune responses through interactions between the receptor TIM-3 and the alarmin HMGB1. *Nat. Immunol.* **13**, 832–842 (2012).

[CAS](#) [PubMed](#) [PubMed Central](#) [Google Scholar](#)

11. 11.

Gayden, T. et al. Germline *HAVCR2* mutations altering TIM-3 characterize subcutaneous panniculitis-like T cell lymphomas with hemophagocytic lymphohistiocytic syndrome. *Nat. Genet.* **50**, 1650–1657 (2018).

[CAS](#) [PubMed](#) [Google Scholar](#)

12. 12.

Kikushige, Y. et al. TIM-3 is a promising target to selectively kill acute myeloid leukemia stem cells. *Cell Stem Cell* **7**, 708–717 (2010).

[CAS](#) [PubMed](#) [Google Scholar](#)

13. 13.

Dama, P., Tang, M., Fulton, N., Kline, J. & Liu, H. Gal9/Tim-3 expression level is higher in AML patients who fail chemotherapy. *J. Immunother. Cancer* **7**, 175 (2019).

[PubMed](#) [PubMed Central](#) [Google Scholar](#)

14. 14.

Uma Borate, M. et al. Phase Ib study of the anti-TIM-3 antibody MBG453 in combination with decitabine in patients with high-risk myelodysplastic syndrome (MDS) and acute myeloid leukemia (AML). *Blood* **134**, 570 (2019).

[Google Scholar](#)

15. 15.

Roberts, E. W. et al. Critical role for CD103⁺/CD141⁺ dendritic cells bearing CCR7 for tumor antigen trafficking and priming of T cell immunity in melanoma. *Cancer Cell* **30**, 324–336 (2016).

[CAS](#) [PubMed](#) [PubMed Central](#) [Google Scholar](#)

16. 16.

Maier, B. et al. A conserved dendritic-cell regulatory program limits antitumour immunity. *Nature* **580**, 257–262 (2020).

[ADS](#) [CAS](#) [PubMed](#) [PubMed Central](#) [Google Scholar](#)

17. 17.

Polprasert, C. et al. Frequent germline mutations of *HAVCR2* in sporadic subcutaneous panniculitis-like T-cell lymphoma. *Blood Adv.* **3**, 588–595 (2019).

[CAS](#) [PubMed](#) [PubMed Central](#) [Google Scholar](#)

18. 18.

Pfirschke, C. et al. Immunogenic chemotherapy sensitizes tumors to checkpoint blockade therapy. *Immunity* **44**, 343–354 (2016).

[CAS](#) [PubMed](#) [PubMed Central](#) [Google Scholar](#)

19. 19.

Sade-Feldman, M. et al. Defining T cell states associated with response to checkpoint immunotherapy in melanoma. *Cell* **175**, 998–1013 (2018).

[CAS](#) [PubMed](#) [PubMed Central](#) [Google Scholar](#)

20. 20.

Best, J. A. et al. Transcriptional insights into the CD8⁺ T cell response to infection and memory T cell formation. *Nat. Immunol.* **14**, 404–412 (2013).

[CAS](#) [PubMed](#) [PubMed Central](#) [Google Scholar](#)

21. 21.

Kurtulus, S. et al. Checkpoint blockade immunotherapy induces dynamic changes in PD-1⁻CD8⁺ tumor-infiltrating T cells. *Immunity* **50**, 181–194 (2019).

[CAS](#) [PubMed](#) [PubMed Central](#) [Google Scholar](#)

22. 22.

Yost, K. E. et al. Clonal replacement of tumor-specific T cells following PD-1 blockade. *Nat. Med.* **25**, 1251–1259 (2019).

[CAS](#) [PubMed](#) [PubMed Central](#) [Google Scholar](#)

23. 23.

Thommen, D. S. et al. A transcriptionally and functionally distinct PD-1⁺CD8⁺ T cell pool with predictive potential in non-small-cell lung cancer treated with PD-1 blockade. *Nat. Med.* **24**, 994–1004 (2018).

[CAS](#) [PubMed](#) [PubMed Central](#) [Google Scholar](#)

24. 24.

Siddiqui, I. et al. Intratumoral Tcf1⁺PD-1⁺CD8⁺ T cells with stem-like properties promote tumor control in response to vaccination and checkpoint blockade immunotherapy. *Immunity* **50**, 195–211 (2019).

[CAS](#) [PubMed](#) [PubMed Central](#) [Google Scholar](#)

25. 25.

Miller, B. C. et al. Subsets of exhausted CD8⁺ T cells differentially mediate tumor control and respond to checkpoint blockade. *Nat. Immunol.* **20**, 326–336 (2019).

[CAS](#) [PubMed](#) [PubMed Central](#) [Google Scholar](#)

26. 26.

Im, S. J. et al. Defining CD8⁺ T cells that provide the proliferative burst after PD-1 therapy. *Nature* **537**, 417–421 (2016).

[ADS](#) [CAS](#) [PubMed](#) [PubMed Central](#) [Google Scholar](#)

27. 27.

Pauken, K. E. et al. Epigenetic stability of exhausted T cells limits durability of reinvigoration by PD-1 blockade. *Science* **354**, 1160–1165 (2016).

[ADS](#) [CAS](#) [PubMed](#) [PubMed Central](#) [Google Scholar](#)

28. 28.

Jadhav, R. R. et al. Epigenetic signature of PD-1⁺TCF1⁺ CD8 T cells that act as resource cells during chronic viral infection and respond to PD-1 blockade. *Proc. Natl Acad. Sci. USA* **116**, 14113–14118 (2019).

[CAS](#) [PubMed](#) [PubMed Central](#) [Google Scholar](#)

29. 29.

Bottcher, J. P. et al. NK cells stimulate recruitment of cDC1 into the tumor microenvironment promoting cancer immune control. *Cell* **172**, 1022–1037 (2018).

[CAS](#) [PubMed](#) [PubMed Central](#) [Google Scholar](#)

30. 30.

Spranger, S., Dai, D., Horton, B. & Gajewski, T. F. Tumor-residing Batf3 dendritic cells are required for effector T cell trafficking and adoptive T cell therapy. *Cancer Cell* **31**, 711–723 (2017).

[CAS](#) [PubMed](#) [PubMed Central](#) [Google Scholar](#)

31. 31.

Schiebinger, G. et al. Optimal-transport analysis of single-cell gene expression identifies developmental trajectories in reprogramming. *Cell* **176**, 928–943 (2019).

[CAS](#) [PubMed](#) [PubMed Central](#) [Google Scholar](#)

32. 32.

Martinon, F., Burns, K. & Tschoopp, J. The inflammasome: a molecular platform triggering activation of inflammatory caspases and processing of proIL-beta. *Mol. Cell* **10**, 417–426 (2002).

[CAS](#) [PubMed](#) [Google Scholar](#)

33. 33.

Zanoni, I. et al. An endogenous caspase-11 ligand elicits interleukin-1 release from living dendritic cells. *Science* **352**, 1232–1236 (2016).

[ADS](#) [CAS](#) [PubMed](#) [PubMed Central](#) [Google Scholar](#)

34. 34.

Masters, S. L. et al. Activation of the NLRP3 inflammasome by islet amyloid polypeptide provides a mechanism for enhanced IL-1 β in type 2 diabetes. *Nat. Immunol.* **11**, 897–904 (2010).

[CAS](#) [PubMed](#) [PubMed Central](#) [Google Scholar](#)

35. 35.

Martinon, F. Signaling by ROS drives inflammasome activation. *Eur. J. Immunol.* **40**, 616–619 (2010).

[CAS](#) [PubMed](#) [Google Scholar](#)

36. 36.

Schroder, K., Zhou, R. & Tschopp, J. The NLRP3 inflammasome: a sensor for metabolic danger? *Science* **327**, 296–300 (2010).

[ADS](#) [CAS](#) [PubMed](#) [Google Scholar](#)

37. 37.

Groß, C. J. et al. K⁺ efflux-independent NLRP3 inflammasome activation by small molecules targeting mitochondria. *Immunity* **45**, 761–773 (2016).

[PubMed](#) [Google Scholar](#)

38. 38.

Chakraborty, D. et al. Enhanced autophagic-lysosomal activity and increased BAG3-mediated selective macroautophagy as adaptive response of neuronal cells to chronic oxidative stress. *Redox Biol.* **24**, 101181 (2019).

[CAS](#) [PubMed](#) [PubMed Central](#) [Google Scholar](#)

39. 39.

Rosati, A., Graziano, V., De Laurenzi, V., Pascale, M. & Turco, M. C. BAG3: a multifaceted protein that regulates major cell pathways. *Cell Death Dis.* **2**, e141 (2011).

[CAS](#) [PubMed](#) [PubMed Central](#) [Google Scholar](#)

40. 40.

Coll, R. C. et al. A small-molecule inhibitor of the NLRP3 inflammasome for the treatment of inflammatory diseases. *Nat. Med.* **21**, 248–255 (2015).

[CAS](#) [PubMed](#) [PubMed Central](#) [Google Scholar](#)

41. 41.

Zhai, Y. et al. Opposing regulatory functions of the TIM3 (HAVCR2) signalosome in primary effector T cells as revealed by quantitative interactomics. *Cell. Mol. Immunol.* (2020).

42. 42.

Zeidan, A. M. et al. A multi-center phase I trial of ipilimumab in patients with myelodysplastic syndromes following hypomethylating agent failure. *Clin. Cancer Res.* **24**, 3519–3527 (2018).

[MathSciNet](#) [CAS](#) [PubMed](#) [PubMed Central](#) [Google Scholar](#)

43. 43.

Davids, M. S. et al. Ipilimumab for patients with relapse after allogeneic transplantation. *N. Engl. J. Med.* **375**, 143–153 (2016).

[CAS](#) [PubMed](#) [PubMed Central](#) [Google Scholar](#)

44. 44.

Daver, N. et al. Phase IB/II study of nivolumab in combination with azacytidine (AZA) in patients (pts) with relapsed acute myeloid leukemia (AML). *Blood* **128**, 763 (2016).

[Google Scholar](#)

45. 45.

Zhivaki, D. et al. Inflammasomes within hyperactive murine dendritic cells stimulate long-lived T cell-mediated anti-tumor immunity. *Cell Rep.* **33**, 108381 (2020).

[CAS](#) [PubMed](#) [PubMed Central](#) [Google Scholar](#)

46. 46.

Engblom, C. et al. Osteoblasts remotely supply lung tumors with cancer-promoting SiglecF^{high} neutrophils. *Science* **358**, eaal5081 (2017).

[PubMed](#) [PubMed Central](#) [Google Scholar](#)

47. 47.

Li, B. et al. Cumulus provides cloud-based data analysis for large-scale single-cell and single-nucleus RNA-seq. *Nat. Methods* **17**, 793–798 (2021).

[Google Scholar](#)

48. 48.

Butler, A., Hoffman, P., Smibert, P., Papalexi, E. & Satija, R. Integrating single-cell transcriptomic data across different conditions, technologies, and species. *Nat. Biotechnol.* **36**, 411–420 (2018).

[CAS](#) [PubMed](#) [PubMed Central](#) [Google Scholar](#)

49. 49.

Becht, E. et al. Dimensionality reduction for visualizing single-cell data using UMAP. *Nat. Biotechnol.* **37**, 38–44 (2019).

[CAS](#) [Google Scholar](#)

50. 50.

Zilionis, R. et al. Single-cell transcriptomics of human and mouse lung cancers reveals conserved myeloid populations across individuals and species. *Immunity* **50**, 1317–1334 (2019).

[CAS](#) [PubMed](#) [PubMed Central](#) [Google Scholar](#)

51. 51.

Gubin, M. M. et al. High-dimensional analysis delineates myeloid and lymphoid compartment remodeling during successful immune-checkpoint cancer therapy. *Cell* **175**, 1014–1030 (2018).

[CAS](#) [PubMed](#) [PubMed Central](#) [Google Scholar](#)

52. 52.

Lee, P. H. et al. Host conditioning with IL-1 β improves the antitumor function of adoptively transferred T cells. *J. Exp. Med.* **216**, 2619–2634 (2019).

[CAS](#) [PubMed](#) [PubMed Central](#) [Google Scholar](#)

53. 53.

Robinson, M. D., McCarthy, D. J. & Smyth, G. K. edgeR: a Bioconductor package for differential expression analysis of digital gene expression data. *Bioinformatics* **26**, 139–140 (2010).

[CAS](#) [Google Scholar](#)

54. 54.

Mertins, P. et al. An integrative framework reveals signaling-to-transcription events in Toll-like receptor signaling. *Cell Rep.* **19**, 2853–2866 (2017).

[CAS](#) [PubMed](#) [PubMed Central](#) [Google Scholar](#)

[Download references](#)

Acknowledgements

We thank all members of the Kuchroo lab, L. Apetoh, N. Acharya, M. Collins, A. Madi, Y. Wolf, J. Kagan and D. Zhivaki for insightful discussions, J. Xia, H. Stroh, S. Zaghouani, R. Kumar, C. Farmer and C. Lambden for laboratory support, and L. Gaffney for figure editing. The lung adenocarcinoma cell line KP1.9 was derived from lung tumours of C57BL/6 KP mice and was provided by A. Zippelius. The *Ncr1*^{cre} mice were provided by E. Vivier. We thank J. Gould for help with Cumulus pipelines. K.O.D. was supported by the European Commission, Excellent Science H2020 no. 708658 and no. 10130984. M.A.S. was supported by Deutsche Forschungsgemeinschaft (DFG grant SCHR 1481/1-1). This work was supported by grants from the National Institutes of Health (V.K.K.: P01AI073748, P01CA236749, P01 AI056299, P01 AI039671 and R01AI144166; A.C.A.: R01CA187975), Klarman Cell Observatory at Broad Institute and a CEGS grant from NIH (M.T. and A.R.), and a Brigham and Women's President's Scholar Award (A.C.A.).

Author information

Author notes

1. Markus A. Schramm

Present address: Department of Rheumatology and Clinical Immunology, Medical Center–University of Freiburg, Faculty of Medicine, University of Freiburg, Freiburg, Germany

2. Sheng Xiao

Present address: Celsius Therapeutics, Cambridge, MA, USA

3. Orit Rozenblatt-Rosen & Aviv Regev

Present address: Genentech, South San Francisco, CA, USA

Affiliations

1. Evergrande Center for Immunologic Diseases, Harvard Medical School, Brigham and Women's Hospital, Boston, MA, USA

Karen O. Dixon, Markus A. Schramm, Sheng Xiao, Ruihan Tang, Ana. C. Anderson & Vijay K. Kuchroo

2. Ann Romney Center for Neurologic Diseases, Harvard Medical School, Brigham and Women's Hospital, Boston, MA, USA

Karen O. Dixon, Markus A. Schramm, Sheng Xiao, Ruihan Tang, Ana. C. Anderson & Vijay K. Kuchroo

3. Klarman Cell Observatory, Broad Institute of MIT and Harvard, Cambridge, MA, USA

Karen O. Dixon, Marcin Tabaka, Danielle Dionne, Ana. C. Anderson, Orit Rozenblatt-Rosen, Aviv Regev & Vijay K. Kuchroo

4. Department of Biology, Koch Institute and Ludwig Center, Massachusetts Institute of Technology, Cambridge, MA, USA

Aviv Regev

5. Howard Hughes Medical Institute, Cambridge, MA, USA

Aviv Regev

Authors

1. Karen O. Dixon

[View author publications](#)

You can also search for this author in [PubMed](#) [Google Scholar](#)

2. Marcin Tabaka

[View author publications](#)

You can also search for this author in [PubMed](#) [Google Scholar](#)

3. Markus A. Schramm

[View author publications](#)

You can also search for this author in [PubMed](#) [Google Scholar](#)

4. Sheng Xiao

[View author publications](#)

You can also search for this author in [PubMed](#) [Google Scholar](#)

5. Ruihan Tang

[View author publications](#)

You can also search for this author in [PubMed](#) [Google Scholar](#)

6. Danielle Dionne

[View author publications](#)

You can also search for this author in [PubMed](#) [Google Scholar](#)

7. Ana. C. Anderson

[View author publications](#)

You can also search for this author in [PubMed](#) [Google Scholar](#)

8. Orit Rozenblatt-Rosen
[View author publications](#)

You can also search for this author in [PubMed](#) [Google Scholar](#)

9. Aviv Regev
[View author publications](#)

You can also search for this author in [PubMed](#) [Google Scholar](#)

10. Vijay K. Kuchroo
[View author publications](#)

You can also search for this author in [PubMed](#) [Google Scholar](#)

Contributions

K.O.D. performed experiments with help from M.A.S. M.T. performed computational analysis with guidance from A.R. S.X. generated the TIM-3 floxed mouse. R.T., D.D., A.C.A., O.R.-R. and A.R. provided input or other essential resources. K.O.D. and V.K.K. designed the experimental setup and conceived the study. K.O.D. wrote the manuscript and prepared figures with input and edits from V.K.K. and all authors.

Corresponding author

Correspondence to [Vijay K. Kuchroo](#).

Ethics declarations

Competing interests

V.K.K. has an ownership interest in and is a member of the scientific advisory board for Tizona Therapeutics, Bicara Therapeutics, Compass Therapeutics, Larkspur Biosciences and Trishula Therapeutics. V.K.K. and

A.C.A. are named inventors on patents related to TIM-3. K.O.D., V.K.K., M.T. and A.R. are named inventors on a provisional patent that has been filed including work from this study. A.R. and V.K.K. are co-founders of and have an ownership interest in Celsius Therapeutics. Additionally, A.R. is a co-founder and equity holder in Immunitas Therapeutics, and was a scientific advisory board member of Thermo Fisher Scientific, Syros Pharmaceuticals, Asimov, and Neogene Therapeutics until 31 July 2020. A.C.A. is a member of the advisory board for Tizona Therapeutics, Trishula Therapeutics, Compass Therapeutics, Zumutor Biologics and ImmuneOncia and is a paid consultant for Larkspur Biosciences and iTeos Therapeutics. A.R. and O.R.-R. are co-inventors on patent applications filed by the Broad Institute to inventions relating to single-cell genomics. The interests of V.K.K. were reviewed and managed by the Brigham and Women's Hospital and Partners Healthcare in accordance with their conflict-of-interest policies. The interests of A.R. were reviewed and managed by the Broad Institute and HHMI in accordance with their conflict-of-interest policies. Since 1 August 2020, A.R. has been an employee of Genentech, a member of the Roche group. O.R.-R. is currently an employee of Genentech. The authors declare no other competing interests.

Additional information

Peer review information *Nature* thanks Laurence Zitvogel and the other, anonymous, reviewer(s) for their contribution to the peer review of this work.

Publisher's note Springer Nature remains neutral with regard to jurisdictional claims in published maps and institutional affiliations.

Extended data figures and tables

[Extended Data Fig. 1 Generation of conditional knockout mice for TIM-3.](#)

a, Strategy for generating the *Havcr2*-targeting vector to target the *Havcr2* allele. Blue boxes represent exons (E). The 5' external probes for Southern

Blot are indicated by thick red line. Targeted events were identified by Southern blot analysis of *Afl2*-digested genomic ES cell DNAs with the 5' flanking probe as shown in A. **b**, MC38-OVA^{dim} (0.5×10^6 cells) were subcutaneously implanted into *Havcr2*^{fl/fl} and *Havcr2*^{fl/fl}*Cd11c*^{Cre} mice. On D14 dLNs were explanted followed by cell sorting for sc-RNA-seq of CD45+ cells. UMAPs of canonical cDC1 markers *Xcr1*, *Clec9a* and *Flt3*, (bottom) UMAP of *Havcr2* expression among clusters found in dLN, violin plot from scRNA-seq displaying normalized expression of *Havcr2* in each cluster. **c, d**, WT mice were implanted with MC38 cells (1.0×10^6). On D21 tumours were explanted followed by flow cytometric analysis of TIM-3 (gMFI) on tumour infiltrating immune cells ($n = 3-4$). **e**, MC38-OVA^{dim} (0.5×10^6 cells) tumour cells were subcutaneously implanted into *Havcr2*^{fl/fl}, *Havcr2*^{fl/fl}*LysM*^{Cre} ($n = 3$), *Havcr2*^{fl/fl}*Cx3cr1*^{Cre} ($n = 3$) and *Havcr2*^{fl/fl}*Zbtb46*^{Cre} ($n = 4$) animals. Representative Flow cytometric analysis of TIM-3 expression on DC1, DC2, migDCs, macrophages and monocytes. DCs were gated as in Ext Fig. 2: CD45+, CD3-CD19-NK1.1-, ClassII⁺CD11c⁺, Ly6c-CD64- and **DC1**: CD103⁺CD11b-, **DC2**: CD11b⁺CD103- **migDCs** CD11b⁺CD103⁺. Macrophages: CD45+, CD3-CD19-NK1.1-, ClassII^{lo} Ly6c^{lo}CD64⁺F480⁺CX3CR1⁺, monocytes ClassII^{lo} Ly6c^{hi}CD64^{lo}Ly6g-. (right) Percentage expression and gMFI of TIM-3. **f**, MC38-OVA^{dim} (0.5×10^6 cells) were subcutaneously implanted into *Havcr2*^{fl/fl} ($n = 5$), *Havcr2*^{fl/fl}*Cd4*^{Cre} ($n = 3$), *Havcr2*^{fl/fl}*Cd11c*^{Cre} ($n = 5$) and *Havcr2*^{fl/fl}*Zbtb46*^{Cre} ($n = 4$) mice. On D14 tumours were explanted followed by flow cytometric analysis of TIM-3 expression on CD4 TILs, CD8 TILs and tumour infiltrating DC1 from *Havcr2*^{fl/fl}, *Havcr2*^{fl/fl} × *CD4*^{Cre}, *Havcr2*^{fl/fl} × *CD11c*^{Cre} and *Havcr2*^{fl/fl} × *Zbtb46*^{Cre}. The results shown are from one experiment, representative of at least 3 independent experiments. *** $P < 0.001$; **** $P < 0.0001$ (One-Way ANOVA). Data shown (**f**) as mean ± s.e.m. * $P < 0.05$; *** $P < 0.0001$ (Student Two-Tailed *t*-test).

[Source data](#)

[Extended Data Fig. 2 Deletion of TIM-3 in cDC using Zbtb46 recapitulates findings using CD11c cre.](#)

a, Tumour growth curve of MC38-OVA^{dim} subcutaneously implanted into *Havcr2*^{fl/fl} and *Havcr2*^{fl/fl}*LysM*^{Cre} ($n = 6$). **b**, Tumour growth curve MC38-OVA^{dim} OVA subcutaneously implanted *Havcr2*^{fl/+} × *CD11c*^{Cre} and *Havcr2*^{fl/fl} × *CD11c*^{Cre} ($n = 5$). **c**, Tumour of *Havcr2*^{fl/fl} mice implanted with B16-OVA. On D3 XCR1+ BMDC1 were sorted, pulsed with OVA and injected into tumour bearing mice. **d**, Flow-cytometric analysis of frequency ($n = 9$), and absolute number ($n = 4$) of OVA specific CD8⁺ T cells from tumours injected with *Havcr2*^{fl/fl} or *Havcr2*^{cko} DC1. **e–h**, Flow-cytometric analysis of OVA specific CD8⁺ T cells from tumours injected with *Havcr2*^{fl/fl} or *Havcr2*^{cko} DC1 ($n = 4$). **i**, MC38-OVA^{dim} (0.5×10^6 cells) tumour cells were subcutaneously implanted into *Havcr2*^{fl/fl} and *Havcr2*^{fl/fl} × *Zbtb46*^{Cre} animals ($n = 4$ -5). Flow cytometric analysis (d14) of TIM-3 expression on tumour infiltrating DC1, DC2, migDCs and pDC from *Havcr2*^{fl/fl} and *Havcr2*^{fl/fl} × *Zbtb46*^{Cre}. **j**, Tumour weight and total CD45⁺ cells of MC38 subcutaneously implanted *Havcr2*^{fl/fl} and *Havcr2*^{fl/fl} × *Zbtb46*^{Cre} ($n = 5$). **k**, Tumour growth curve of B16 subcutaneously implanted *Havcr2*^{fl/fl} and *Havcr2*^{fl/fl} × *Zbtb46*^{Cre} ($n = 9$). **l, m**, Tumour growth curve of B16F10 melanoma (**l**) and B16-OVA (**m**) subcutaneously implanted *Havcr2*^{fl/fl}, *Havcr2*^{fl/fl} × *CD4*^{Cre} and *Havcr2*^{fl/fl} × *CD11c*^{Cre} cre in parallel ($n = 4$ -5). **n**, Weights of tumours from (Fig. 11). **o**, B16-OVA subcutaneously implanted *Havcr2*^{fl/fl}, *Havcr2*^{fl/fl} × *CD4*^{Cre} and *Havcr2*^{fl/fl} × *Zbtb46*^{Cre} in parallel ($n = 4$). The results shown are from one experiment, representative of at least three independent experiments. * $P < 0.05$; ** $P < 0.01$; *** $P < 0.001$; **** $P < 0.0001$ (Two-Way ANOVA). Data shown (**d–h**) as mean ± s.e.m. * $P < 0.05$; ** $P < 0.01$ (Student Two-Tailed *t*-test).

[Source data](#)

[Extended Data Fig. 3 Deficiency of TIM-3 on DC leads to increased numbers of tumour infiltrating CD8⁺ T cells.](#)

MC38-OVA^{dim} (0.5×10^6 cells) tumour cells were subcutaneously implanted into *Havcr2*^{fl/fl} and isolated at D14. **a**, Gating strategy and phenotype of intratumoral myeloid cells. **b–l**, Flow cytometric

quantification of immune cells in tumours from *Havcr2*^{fl/fl} and *Havcr2*^{fl/fl} × *CD11c*^{Cre} mice at d14 harvest. **m**, Flow cytometric analysis of DC1 and Mig DC from *Havcr2*^{fl/fl} and *Havcr2*^{cko} tumours at d14 harvest following in vitro stimulation for 4 h in the presence of Brefeldin A and Monensin. Data shown (**I**) as mean ± s.e.m. **P* < 0.05 (Student Two-Tailed *t*-test) *n* = 5–9/group.

Source data

Extended Data Fig. 4 scRNA-seq of *Havcr2*^{fl/fl} and *Havcr2*^{cko} total CD45⁺ cells.

a, UMAP scRNA-seq plot of annotated total cells from *Havcr2*^{fl/fl} and *Havcr2*^{fl/fl} × *CD11c*^{Cre} (*Havcr2*^{cko}) tumours. **b**, UMAP scRNA-seq plots showing select marker gene expression. **c**, Heat map from scRNA-seq displaying normalized expression of select genes in each cluster. **d**, UMAP scRNA-seq plot showing distribution of *Havcr2*^{fl/fl} (blue) and *Havcr2*^{cko} (orange) cells. **e**, Bar graph showing frequency of *Havcr2*^{fl/fl} (blue) and *Havcr2*^{cko} (orange) cells in each cluster.

Extended Data Fig. 5 Expansion of CD8⁺ PD1⁺ cells in *Havcr2*^{cko} tumours.

MC38-OVA^{dim} (0.5 × 10⁶ cells) were subcutaneously implanted into *Havcr2*^{fl/fl} and *Havcr2*^{fl/fl} × *CD11c*^{Cre} (*Havcr2*^{cko}) mice and harvested on D14. **a**, Frequency (*n* = 9–10) and absolute numbers (*n* = 4–5) of CD8+ PD1+ TILs from *Havcr2*^{fl/fl} and *Havcr2*^{cko} tumours. **b**, Analysis of expression of PD1 versus TIM-3, Lag3 and TIGIT in CD8+ TILs (*n* = 4–5). **c**, Flow cytometry (d14 harvest) of CD8 TILs from *Havcr2*^{fl/fl} and *Havcr2*^{cko} for expression of TIM-3 and CXCR5 (*n* = 4–5). **d**, Flow cytometry of CD8+ PD1+ TILs from *Havcr2*^{fl/fl} and *Havcr2*^{fl/fl} × *Zbtb46*^{Cre} for expression of IL-7R, SLAMF6 CX3CR1, IFNγ, IL-2, TCF1, Ki67 and T-bet (bottom right) Representative histograms of data in **d**. The results shown are from one experiment, representative of at least three independent

experiments, $n = 4\text{-}5$ group. * $P < 0.05$; ** $P < 0.01$; (Student Two-Tailed t -test).

[Source data](#)

Extended Data Fig. 6 Identification of tumour infiltrating myeloid cells in *Havcr2*^{f/f} and *Havcr2*^{cko} tumours.

a, UMAP scRNA-seq plot of annotated total myeloid cells from *Havcr2*^{f/f} and *Havcr2*^{f/f} × *CD11c*^{Cre} (*Havcr2*^{cko}) tumours. **b**, UMAP scRNA-seq plots showing select marker gene expression. **c**, Heat map from scRNA-seq displaying normalized expression of select genes in each cluster. **d**, UMAP scRNA-seq plot showing distribution of *Havcr2*^{f/f} (blue) and *Havcr2*^{cko} (orange) cells. **e**, Bar graph showing frequency of *Havcr2*^{f/f} (blue) and *Havcr2*^{cko} (orange) cells in each cluster.

Extended Data Fig. 7 Decreased expression of mregDC markers in TIM-3-deficient migDCs.

a, MC38-OVA^{dim} (0.5×10^6 cells) tumour cells were subcutaneously implanted into *Havcr2*^{f/f} and *Havcr2*^{f/f} × *CD11c*^{Cre} (*Havcr2*^{cko}) animals and Flow cytometric analysis of DC populations was performed on D14 to assess expression of described mregDC markers including CD200, CD83, IL4R and OX40. The results shown are from one experiment, $n = 5$ per group. * $P < 0.05$; ** $P < 0.01$; *** $P < 0.001$; (One-Way ANOVA). **b**, Tumour growth curves of MC38-OVA^{dim} (0.5×10^6 cells) subcutaneously implanted into *Havcr2*^{f/f} and *Havcr2*^{cko} mice treated with either Isotype control, anti-IL-12 (500μg/mouse) or anti-IL-4 (25μg/mouse). Treatment was initiated on D3 and antibodies were delivered i.p. every 3 days until experiment cessation. The results shown are from one experiment, $n = 4\text{-}5$ per group. *** $P < 0.001$; **** $P < 0.0001$ (Two-Way ANOVA). **c**, Splenic DC were sorted from *Havcr2*^{f/f} and *Havcr2*^{cko} animals and cultured with dead HLA mismatched splenocytes osmotically loaded with 10mg/ml Ova together with CTV labelled naïve OTI cells. Representative plots of CD44⁺ CTV^{lo} T cells after 72-h co-culture. Mean ± s.e.m. of 3 individual mice.

Alternatively, DC from *Havcr2*^{fl/fl} and *Havcr2*^{cko} animals, were cultured with beads passively adsorbed with Ova together with CTV labelled naïve OTI cells. Representative plots of CD44⁺ CTV^{lo} T cells after 72-h co-culture. Mean ± s.e.m. of 3 individual mice, *P < 0.0001 (Student Two-Tailed t-test). **d**, CFSE or CTV labelled splenocytes were pulsed with OVA₂₅₇₋₂₆₄ or MOG₃₇₋₄₆ (Irrelevant Antigen) and injected at 50:50 ratio into MC38-OVA^{dim} bearing *Havcr2*^{fl/fl} or *Havcr2*^{cko} mice. Percentage cytotoxicity calculated as 100-(CTV/CTV+CFSE) (n = 5). **e**, Bar plot of data from Fig. 4a, demonstrating unidirectional analysis of the fraction of DCs expressing ligand X and the fraction of T cells expressing the cognate Receptor; Ligand (migDCs): Receptor (CD8) interaction from *Havcr2*^{fl/fl} (grey) and *Havcr2*^{cko} (red) tumours. **f**, UMAP showing expression of *Il18rl* and *Il18rap* on cluster 7 (CD8⁺ T cells), with violin plots showing the differential expression of both receptor in of *Havcr2*^{fl/fl} (blue) and *Havcr2*^{cko} (orange) CD8⁺ T cells, *Havcr2*^{fl/fl} and *Havcr2*^{cko} (**e**) tumours were harvested and mechanically dissociated. Tissue supernatant was collected, and levels of cytokines were determined relative to mg protein per sample, n = 4/group, **P < 0.01; (Student Two-Tailed t-test).

Source data

Extended Data Fig. 8 Enhanced inflammasome activation in TIM-3-deficient *cko* DC.

BMDC were differentiated in the presence of FLT3L for 10 days. **a**, Flow cytometric analysis assessing typical DC1 and DC2 markers. XCR1⁺ cells were sorted after 10 days of differentiation and seeded at a density of 0.25 × 10⁶. Sorted cells were either unstimulated or primed with LPS (1µg/ml) for 3 h followed by the addition of oxidised phospholipids (ox-PAPC) (100µg/ml), pDA: dT (1µg/ml), Flagellin (1µg/ml), *C. difficile* (1µg/ml), or Nigericin (10mM). **b**, **c**, Following overnight cultures supernatants were harvested and ELISA was performed to detect IL-1β (**b**) and TNF (**c**) (non-inflammasome regulated control). The results shown are from one experiment (n = 3 per group), representative of at least 3 individual experiments, *P < 0.05 **P < 0.01; ***P < 0.001 (Student Two Tailed t-test). **d**, MC38-OVA^{dim} was subcutaneously implanted into *Havcr2*^{fl/fl} and

Havcr2^{cko} mice and on D14 mononuclear cells were isolated and incubated with DHR123 as a measure of ROS activity ($n = 4$). **e**, Tumour growth curve of MC38-OVA^{dim} subcutaneously implanted *Havcr2*^{f/f} and *Havcr2*^{cko} treated with control or anti-IL-1 β and anti-IL-18 ($n = 4$). **f**, Weights of B16-OVA (0.25×10^6 cells) subcutaneously implanted into *Havcr2*^{f/f} and *Havcr2*^{f/f} × *Zbtb46*^{Cre} and treated with either Isotype control (Hamster IgG and Rat IgG2a) or anti-IL-1 β and anti-IL-18 (Hamster IgG and Rat IgG2a respectively), all at a dose of 8mg/kg. **g–k**, Flow cytometric analysis of CD8 $^{+}$ TILs harvested from MC38-OVA^{dim} tumours subcutaneously implanted into *Havcr2*^{f/f} and *Havcr2*^{f/f} × *Zbtb46*^{Cre} and treated with either Isotype control upon termination of experiment (d15). The results shown are from one experiment, representative of at least two independent experiments $n = 4\text{--}5/\text{group}$. *** $P < 0.001$; **** $P < 0.0001$ (Two-Way ANOVA). **l–n**, *Havcr2*^{f/f} (**l**), *Havcr2*^{f/f} × *CD4*^{Cre} (**m**) and *Havcr2*^{f/f} × *Zbtb46*^{Cre} (**n**) mice were implanted with B16-OVA and monitored for development of a palpable tumour. On D6 when tumours reached ~30–50mm² mice were randomized and treated with either (i) Isotype controls (IgG2a and IgG2b), (ii) anti-TIM-3, (iii) anti PD-L1 and (iv) anti-TIM-3 + PD-L1. Anti-TIM-3 was administered at a dose of 200 $\mu\text{g}/\text{mouse}$ and anti-PDL1 at a dose of 50 $\mu\text{g}/\text{mouse}$. All tumours were measured daily for the duration of the experiment. Antibody treatment was initiated on D6 and administered again on D9 and D12. Area under the curve (AUC) was calculated from graphs in (**k–m**). The results shown are from one experiment, $n = 4$ per group. ** $P < 0.01$; *** $P < 0.001$; **** $P < 0.0001$ (Two-Way ANOVA). Area under curve data- ** $P < 0.01$; *** $P < 0.001$; **** $P < 0.0001$ (One-Way ANOVA).

[Source data](#)

Supplementary information

[Supplementary Table 1](#)

Summary of curated gene signatures constructed from various databases of gene signatures.

Reporting Summary

Source data

[Source Data Fig. 1](#)

[Source Data Fig. 2](#)

[Source Data Fig. 3](#)

[Source Data Fig. 4](#)

[Source Data Extended Data Fig. 1](#)

[Source Data Extended Data Fig. 2](#)

[Source Data Extended Data Fig. 3](#)

[Source Data Extended Data Fig. 5](#)

[Source Data Extended Data Fig. 7](#)

[Source Data Extended Data Fig. 8](#)

Rights and permissions

[Reprints and Permissions](#)

About this article



Check for
updates

Cite this article

Dixon, K.O., Tabaka, M., Schramm, M.A. *et al.* TIM-3 restrains anti-tumour immunity by regulating inflammasome activation. *Nature* **595**, 101–106 (2021). <https://doi.org/10.1038/s41586-021-03626-9>

[Download citation](#)

- Received: 14 July 2020
- Accepted: 11 May 2021
- Published: 09 June 2021
- Issue Date: 01 July 2021
- DOI: <https://doi.org/10.1038/s41586-021-03626-9>

[Access through your institution](#)

[Change institution](#)

[Buy or subscribe](#)

Advertisement

This article was downloaded by **calibre** from <https://www.nature.com/articles/s41586-021-03626-9>

| [Section menu](#) | [Main menu](#) |

COVID-19 tissue atlases reveal SARS-CoV-2 pathology and cellular targets
[Download PDF](#)

- Article
- [Published: 29 April 2021](#)

COVID-19 tissue atlases reveal SARS-CoV-2 pathology and cellular targets

- [Toni M. Delorey](#) [ORCID: orcid.org/0000-0001-6614-3803](#)^{1 na1},
- [Carly G. K. Ziegler](#)^{2,3,4,5,6,7 na1},
- [Graham Heimberg](#)^{1 na1},
- [Rachelly Normand](#)^{2,8,9,10,11 na1},
- [Yiming Yang](#) [ORCID: orcid.org/0000-0002-0386-9428](#)^{1,8 na1},
- [Åsa Segerstolpe](#)^{1 na1},
- [Domenic Abbondanza](#) [ORCID: orcid.org/0000-0002-7202-0225](#)^{1 na1},
- [Stephen J. Fleming](#) [ORCID: orcid.org/0000-0002-1885-4405](#)^{12,13 na1},
- [Ayshwarya Subramanian](#)^{1 na1},
- [Daniel T. Montoro](#)^{2 na1},
- [Karthik A. Jagadeesh](#)^{1 na1},
- [Kushal K. Dey](#)^{14 na1},
- [Pritha Sen](#)^{2,8,15,16 na1},
- [Michal Slyper](#)^{1 na1},
- [Yered H. Pita-Juárez](#)^{2,10,17,18,19 na1},
- [Devan Phillips](#)^{1 na1},
- [Jana Biermann](#) [ORCID: orcid.org/0000-0002-8907-4633](#)^{20,21 na1},
- [Zohar Bloom-Ackermann](#)²²,
- [Nikolaos Barkas](#) [ORCID: orcid.org/0000-0002-4675-0718](#)¹²,
- [Andrea Ganna](#)^{23,24},
- [James Gomez](#)²²,
- [Johannes C. Melms](#) [ORCID: orcid.org/0000-0002-5410-6586](#)^{20,21},
- [Igor Katsyv](#)²⁵,
- [Erica Normandin](#)^{2,10},
- [Pourya Naderi](#)^{10,17,18},
- [Yury V. Popov](#)^{10,26,27},
- [Siddharth S. Raju](#)^{2,28,29},

- [Sebastian Niezen](#) ORCID: orcid.org/0000-0002-9297-8828^{10,26,27},
- [Linus T.-Y. Tsai](#)^{2,10,26,30,31},
- [Katherine J. Siddle](#)^{2,32},
- [Malika Sud](#)¹,
- [Victoria M. Tran](#)²²,
- [Shamsudheen K. Vellarikkal](#)^{2,33},
- [Yiping Wang](#)^{20,21},
- [Liat Amir-Zilberstein](#)¹,
- [Deepak S. Atri](#) ORCID: orcid.org/0000-0001-8139-5419^{2,33},
- [Joseph Beechem](#)³⁴,
- [Olga R. Brook](#) ORCID: orcid.org/0000-0002-7074-8909³⁵,
- [Jonathan Chen](#)^{2,36},
- [Prajan Divakar](#)³⁴,
- [Phylicia Dorceus](#)¹,
- [Jesse M. Engreitz](#) ORCID: orcid.org/0000-0002-5754-1719^{2,37},
- [Adam Essene](#)^{26,30,31},
- [Donna M. Fitzgerald](#)³⁸,
- [Robin Fropf](#)³⁴,
- [Steven Gazal](#)³⁹,
- [Joshua Gould](#) ORCID: orcid.org/0000-0001-9581-5461^{1,12},
- [John Grzyb](#)⁴⁰,
- [Tyler Harvey](#)¹,
- [Jonathan Hecht](#)^{10,17},
- [Tyler Hether](#)³⁴,
- [Judit Jané-Valbuena](#)¹,
- [Michael Leney-Greene](#)²,
- [Hui Ma](#)^{1,8},
- [Cristin McCabe](#)¹,
- [Daniel E. McLoughlin](#)³⁸,
- [Eric M. Miller](#) ORCID: orcid.org/0000-0002-3243-4968³⁴,
- [Christoph Muus](#)^{2,41},
- [Mari Niemi](#)²³,
- [Robert Padera](#)^{40,42,43},
- [Liiliu Pan](#)³⁴,
- [Deepti Pant](#)^{26,30,31},
- [Carmel Pe'er](#)¹,
- [Jenna Pfiffner-Borges](#)¹,
- [Christopher J. Pinto](#)^{16,38},
- [Jacob Plaisted](#)⁴⁰,

- [Jason Reeves](#)³⁴,
- [Marty Ross](#)³⁴,
- [Melissa Rudy](#)²,
- [Erroll H. Rueckert](#)³⁴,
- [Michelle Siciliano](#)⁴⁰,
- [Alexander Sturm](#)²²,
- [Ellen Todres](#)¹,
- [Avinash Waghray](#)^{44,45},
- [Sarah Warren](#)³⁴,
- [Shuting Zhang](#)²²,
- [Daniel R. Zollinger](#)³⁴,
- [Lisa Cosimi](#)⁴⁶,
- [Rajat M. Gupta](#)^{2,33},
- [Nir Hacohen](#) ORCID: orcid.org/0000-0002-2349-2656^{2,9,47},
- [Hanina Hibshoosh](#)²⁵,
- [Winston Hide](#)^{10,17,18,19},
- [Alkes L. Price](#) ORCID: orcid.org/0000-0002-2971-7975¹⁴,
- [Jayaraj Rajagopal](#)³⁸,
- [Purushothama Rao Tata](#) ORCID: orcid.org/0000-0003-4837-0337⁴⁸,
- [Stefan Riedel](#) ORCID: orcid.org/0000-0002-0573-4957^{10,17},
- [Gyongyi Szabo](#)^{2,10,26},
- [Timothy L. Tickle](#)^{1,12},
- [Patrick T. Ellinor](#)^{49 na2},
- [Deborah Hung](#)^{22,50,51 na2},
- [Pardis C. Sabeti](#)^{2,32,52,53,54 na2},
- [Richard Novak](#) ORCID: orcid.org/0000-0003-0485-4284^{55 na2},
- [Robert Rogers](#)^{26,56 na2},
- [Donald E. Ingber](#) ORCID: orcid.org/0000-0002-4319-6520^{41,55,57 na2},
- [Z. Gordon Jiang](#)^{10,26,27 na2},
- [Dejan Juric](#) ORCID: orcid.org/0000-0003-2983-7704^{16,38 na2},
- [Mehrtash Babadi](#)^{12,13 na2},
- [Samouil L. Farhi](#) ORCID: orcid.org/0000-0003-1359-4568^{1 na2},
- [Benjamin Izar](#) ORCID: orcid.org/0000-0003-2379-6702^{20,21,58,59 na2},
- [James R. Stone](#)^{36 na2},
- [Ioannis S. Vlachos](#) ORCID: orcid.org/0000-0002-8849-808X^{2,10,17,18,19 na2},
- [Isaac H. Solomon](#) ORCID: orcid.org/0000-0003-3432-0902^{40 na2},
- [Orr Ashenberg](#)^{1 na2},
- [Caroline B. M. Porter](#)^{1 na2},
- [Bo Li](#) ORCID: orcid.org/0000-0003-0668-1620^{1,8,16 na2},

- [Alex K. Shalek](#) ORCID: [orcid.org/0000-0001-5670-8778](#)^{2,3,4,5,6,7,10,44,60,61,62} na²,
- [Alexandra-Chloé Villani](#) ORCID: [orcid.org/0000-0001-7461-0408](#)^{2,8,9,16} na²,
- [Orit Rozenblatt-Rosen](#) ORCID: [orcid.org/0000-0001-6313-3570](#)¹ na² nAff63 &
- [Aviv Regev](#) ORCID: [orcid.org/0000-0003-3293-3158](#)^{1,5,53} na² nAff63

[Nature](#) volume **595**, pages 107–113 (2021) [Cite this article](#)

- 35k Accesses
- 3 Citations
- 631 Altmetric
- [Metrics details](#)

Subjects

- [Genetics](#)
- [SARS-CoV-2](#)
- [Viral infection](#)

Abstract

COVID-19, which is caused by SARS-CoV-2, can result in acute respiratory distress syndrome and multiple organ failure^{1,2,3,4}, but little is known about its pathophysiology. Here we generated single-cell atlases of 24 lung, 16 kidney, 16 liver and 19 heart autopsy tissue samples and spatial atlases of 14 lung samples from donors who died of COVID-19. Integrated computational analysis uncovered substantial remodelling in the lung epithelial, immune and stromal compartments, with evidence of multiple paths of failed tissue regeneration, including defective alveolar type 2 differentiation and expansion of fibroblasts and putative *TP63*⁺ intrapulmonary basal-like progenitor cells. Viral RNAs were enriched in mononuclear phagocytic and endothelial lung cells, which induced specific host programs. Spatial analysis in lung distinguished inflammatory host responses in lung regions with and without viral RNA. Analysis of the other tissue atlases showed transcriptional alterations in multiple cell types in heart tissue from donors with COVID-19, and mapped cell types and genes implicated with disease severity based on COVID-19 genome-wide association studies. Our foundational dataset elucidates the biological effect of severe SARS-CoV-2 infection across the body, a key step towards new treatments.

[Download PDF](#)

Main

The host response to severe acute respiratory syndrome coronavirus 2 (SARS-CoV-2) infection ranges from asymptomatic infection to severe coronavirus disease 2019 (COVID-19) and death. The leading cause of mortality is acute lung injury and acute respiratory distress syndrome, or direct complications with multiple organ failure^{1,2,3,4}. Clinical deterioration in acute illness leads to ineffective viral clearance and collateral tissue damage^{1,2,3,4,5}. Severe COVID-19 is also accompanied by an inappropriate pro-inflammatory host immune response and a diminished antiviral interferon response^{6,7,8}.

Many molecular and cellular questions related to COVID-19 pathophysiology remain unanswered, including how cell composition and gene programs shift, which cells are infected, and how associated genetic loci drive disease. Autopsies are crucial to understanding severe COVID-19 pathophysiology^{9,10,11,12}, but comprehensive genomic studies are challenged by long post-mortem intervals (PMIs).

Here, we developed a large cross-body COVID-19 autopsy biobank of 420 autopsy specimens, spanning 11 organs, and used it to generate a single-cell atlas of lung, kidney, liver and heart associated with COVID-19 and a lung spatial atlas, in a subset of 14–18 donors per organ. Our atlases provide crucial insights into the pathogenesis of severe COVID-19.

A COVID-19 autopsy cohort and biobank

We assembled an autopsy cohort of 20 male and 12 female donors, of various ages (>30–>89 years), racial/ethnic backgrounds, intermittent mandatory ventilation (IMV) periods (0–30 days) and days from symptom start to death (Fig. 1a, Supplementary Table 1). A biobank was created with a subset of 17 donors. From most donors, we collected at least lung, heart and liver tissue (Fig. 1a, Extended Data Fig. 1a, [Supplementary Methods](#)), preserving specimens for single-cell and spatial analysis. We optimized single-cell and single-nucleus RNA sequencing (sc/snRNA-Seq) protocols for Biosafety Level 3 and NanoString GeoMx workflows to spatially profile RNA from different tissue compartments by cell composition or viral RNA ([Supplementary Methods](#)).

Fig. 1: Experimental and computational pipeline for a COVID-19 autopsy atlas.



a, Sample processing pipeline. Up to 11 tissue types were collected from 32 donors. **b**, sc/snRNA-Seq analysis pipeline. QC, quality control.

[Full size image](#)

COVID-19 cell atlases

We generated sc/snRNA-Seq atlases of lung ($n = 16$ donors, $k = 106,792$ cells/nuclei, $m = 24$ specimens; donors D1–8, 10–17), heart ($n = 18$, $k = 40,880$, $m = 19$; D1–8, 10–11, 14–17, 27–28, 31–32), liver ($n = 15$, $k = 47,001$, $m = 16$; D1–7, 10–17) and kidney ($n = 16$, $k = 33,872$, $m = 16$; D4–8, 10–12, 14–15, 17, 25–26, 28–30). Although initial tests showed some differences in proportions of cell types between snRNA-Seq and scRNA-Seq, snRNA-Seq performed better overall¹³ (Extended Data Fig. [1b–d](#) and data not shown) and was used for the remaining samples.

We developed a computational pipeline (Fig. 1b) to tackle unique technical challenges. We used CellBender remove-background¹⁴ to remove ambient RNA, which enhanced cell distinction and marker specificity (Extended Data Fig. 1e–h; [Supplementary Methods](#)), we rapidly quality-controlled, pre-processed and batch-corrected the data with cloud-based Cumulus¹⁵ (Extended Data Fig. 2a–g, [Supplementary Methods](#)) and we automatically annotated cells and nuclei by transferring labels from previous atlases (Fig. 2a, Extended Data Fig. 2h, [Supplementary Methods](#)). We refined these labels with manual annotation of subclusters in each main lineage (Fig. 2b, Extended Data Fig. 2i–n, [Supplementary Methods](#)). The automated annotation approach allowed us to compare against other data resources (without clustering or batch correction), while the manual approach enabled us to refine cell identity assignments with detailed domain knowledge.

Fig. 2: A single-cell and single-nucleus atlas of COVID-19 lung.

 [figure2](#)

a, Automatic prediction identifies 28 cell subsets across compartments. UMAP embedding of 106,792 harmonized sc/snRNA-Seq profiles (dots) from 24 tissue samples of 16 lung donors with COVID-19, coloured by automatic annotations (legend). **b**, Epithelial cell subsets. UMAP embedding of 21,661 epithelial cell or nucleus profiles, coloured by manual annotations, with highly expressed marker genes (boxes). **c, d**, Cell composition and expression differences between COVID-19 and healthy lung. **c**, Cell proportions (*x* axis: mean, bar; 95% confidence intervals, line) in each automatically annotated subset (*y* axis) in COVID-19 snRNA-Seq (red, *n* = 16), healthy snRNA-Seq (grey, *n* = 3) and healthy scRNA-Seq (*n* = 8, blue). Cell types shown have a COVID-19 versus healthy snRNA-Seq false discovery rate (FDR) of <0.05 (Dirichlet multinomial regression). **d**, Significance ($-\log_{10}(P)$, *y* axis) versus

magnitude (\log_2 (fold change), *x* axis) of differential expression of each gene (dots; horizontal dashed line, FDR < 0.05) between COVID-19 and healthy lung from a total of 2,000 AT2 cells and 14 studies (two-sided test; [Supplementary Methods](#)). **e, f**, An increased pre-alveolar type 1 transitional cell state (PATS)^{20,21,22} program in pneumocytes in COVID-19 versus healthy lung. **e**, Distribution of PATS signature scores (*y* axis) for 17,655 cells from COVID-19 and 24,000 cells from healthy lung pneumocytes (*x* axis). $P < 2.2 \times 10^{-16}$ (one-sided Mann–Whitney *U* test). **f**, UMAP embedding of 21,661 epithelial cell profiles (dots) coloured by signature level (colour legend, lower right) for the PATS (top) or intrapulmonary basal-like progenitor (IPBLP) cell (bottom) programs. **g**, Model of epithelial cell regeneration in healthy and COVID-19 lung. In healthy alveoli (top), AT2 cells self-renew (1) and differentiate into AT1 cells (2). In COVID-19 alveoli (bottom), AT2 cell self-renewal (1) and AT1 differentiation (2) are inhibited, resulting in PATS accumulation (3) and recruitment of airway-derived IPBLP cells to alveoli (4).

[Full size image](#)

A cell census of the COVID-19 lung

Automatic annotation defined 28 subsets of parenchymal, endothelial and immune cells (Fig. 2a, Supplementary Table 2, [Supplementary Methods](#)), with further manual annotation within subgroupings (Fig. 2b, Extended Data Figs. 2, 4, [Supplementary Methods](#)). Deconvolution of bulk RNA-Seq from the same samples largely agreed (Extended Data Fig. 3a, b, [Supplementary Methods](#)), and our two annotation strategies had 94% agreement (Extended Data Fig. 3c–e).

Among immune cells we distinguished six cell myeloid subsets: $CD14^{high}CD16^{high}$ inflammatory monocytes with antimicrobial properties and five macrophage subsets (Extended Data Figs. 2j, 4b) that were enriched for scavenger receptors, toll-like receptor ligands, inflammatory transcriptional regulators or metabolism genes; four B cell and plasma cell subsets: $BLIMPI^{high}$ plasma cells^{16,17}, $BLIMPI^{intermediate}$ plasma cells, B cells and *JCHAIN*-expressing plasmablasts (Extended Data Figs. 2k, 4b); five T and natural killer (NK) cell subsets: two $CD4^+$ subsets: regulatory T cells (T_{reg} cells) and a metabolically active subset; one $CD8^+$ subset; and two T or NK cell subsets (Extended Data Figs. 2l, 4b), including one with cytotoxic effector genes. The dearth of neutrophils (Fig. 2a, 419 cells) is likely due to freezing or limitations of droplet-based sc/snRNA-Seq¹³.

We identified seven endothelial cell (EC) subsets^{18,19} (Extended Data Figs. 2m, 4b): arterial, venous and lymphatic, capillary aerocytes, capillary EC-1 and capillary EC-2 and a mixed subset ([Supplementary Methods](#)), and three stromal subsets: fibroblasts,

proliferative fibroblasts and myofibroblasts¹⁹ (Extended Data Fig. 2n, Supplementary Table 3).

There were eight epithelial subsets, including club/secretory cells, AT1 cells, AT2 cells, and proliferative AT2 cells (Fig. 2b). One subset corresponded to a previously described AT2 to AT1 transitional cell state (*KRT8*⁺ pre-alveolar type 1 transitional cell state (PATS); PATS/ADI/DATP)^{20,21,22} (Fig. 2b).

Changes in lung cell composition

In comparison with normal lung from a matching region (Fig. 2c, [Supplementary Methods](#)), numbers of AT2 cells were significantly decreased (false discovery rate (FDR) = 2.8×10^{-15} , Dirichlet multinomial regression; [Supplementary Methods](#)), possibly reflecting virally induced cell death^{23,24,25}. Numbers of dendritic cells (FDR = 0.004), macrophages (FDR = 3.6×10^{-10}), NK cells (FDR = 0.018), fibroblasts (FDR = 0.013), lymphatic endothelial cells (FDR = 0.00058) and vascular endothelial cells (FDR = 0.00011) all increased.

Cell proportions varied between donors (Extended Data Fig. 5a,b). Whereas variation was not significantly correlated with PMI, age or sex, IMV was positively correlated with epithelial cell fraction (FDR = 0.007; Spearman $\rho = 0.765$) and negatively correlated with T and NK cell fraction (FDR = 0.041; $\rho = -0.62$). Fewer days on a ventilator may indicate a rapidly deteriorating condition. This is corroborated by the nominally significant positive correlation between epithelial cell fraction and days from symptom start to death ($\rho = 0.671$, $P = 0.004$, but FDR = 0.053).

Induced programs in epithelial cells

There were widespread, cell-type-specific transcriptional changes in lung cell types associated with COVID-19 (Extended Data Fig. 5c, [Supplementary Methods](#)), most notably in *CD16*⁺ monocytes (1,580 upregulated genes), lymphatic endothelial (578), vascular endothelial (317), AT2 (309) and AT1 (307) cells. Within AT2 cells, there was higher expression ($P < 0.0004$) of genes associated with host viral response (Fig. 2d), including those for programmed cell death (*STAT1*), inflammation and adaptive immune response (Supplementary Table 4). Lung surfactant genes were downregulated, consistent with reports from in vitro studies²¹.

Failed paths for AT1 cell regeneration

The PATS program signature was increased in COVID-19 pneumocytes ($P < 2.2 \times 10^{-16}$, one-sided Mann–Whitney U test) (Fig. 2e, Extended Data Fig. 5d). This progenitor program is induced during lung injury^{20,21,22} (for example, idiopathic pulmonary fibrosis), consistent with fibrosis in severe COVID-19^{26,27}. These studies also highlight fibroblast expansion, which we also observed (Fig. 2c).

A subset of PATS program cells, distinct from $KRT5^+ TP63^+$ airway basal cells, expressed canonical ($KRT8/CLDN4/CDKN1A$) and non-canonical ($KRT5/TP63/KRT17$) PATS markers (Fig. 2f, Extended Data Fig. 5d, Supplementary Table 3). These may be $TP63^+$ intrapulmonary basal-like progenitor (IPBLLP) cells, which were identified in H1N1 influenza mouse models²⁸ and act as an emergency cellular reserve for severely damaged alveoli²⁹. The putative IPBLLP cells express interferon virus defence and progenitor cell differentiation genes (Supplementary Table 3). Thus, multiple emergency pathways for alveolar cell regeneration are activated in lung (Fig. 2g, Discussion).

Changed cell composition with viral load

To determine viral load and associated host responses, we analysed donor- and cell-type-specific distribution of SARS-CoV-2 reads (Fig. 3a,b, Extended Data Fig. 6a–d, [Supplementary Methods](#)). Reads spanned the entire SARS-CoV-2 genome, with bias towards positive-sense alignments. A few cells had reads aligning to all viral segments, including the negative strand (Extended Data Fig. 6e), potentially indicating productive infection. Virus detection was not technically driven (Extended Data Fig. 6f–i), and inter-donor variation was consistent with SARS-CoV-2 qRT–PCR on bulk RNA (Extended Data Fig. 6j–l, [Supplementary Methods](#)). Viral load was negatively correlated with days from symptom start to death (Fig. 3c), as previously reported^{30,31}. Bulk RNA-Seq yielded nine unique complete viral genomes from nine donors with high viral loads (Extended Data Fig. 6m, [Supplementary Methods](#)); all genomes carried the D614G allele. We identified no other common respiratory viral co-infections (Extended Data Fig. 6n). Total viral burden per sample (including ambient RNA; [Supplementary Methods](#)) positively correlated with proportions of mast cells, specific macrophage subsets, venular endothelial cells and capillary aerocyte endothelial cells (Extended Data Fig. 6o–u).

Fig. 3: SARS-CoV-2 RNA⁺ single cells are enriched for phagocytic and endothelial cells.

 **figure3**

a, b, Many SARS-CoV-2 RNA⁺ single cells do not express known SARS-CoV-2 entry factors. UMAP embedding of all 106,792 lung cells or nuclei (as in Fig. 2a), showing either **a**, only the 40,581 cells from seven donors containing any SARS-CoV-2 RNA⁺ cell, coloured by viral enrichment score ([Supplementary Methods](#), red: stronger enrichment) and by SARS-CoV-2 RNA⁺ cells (black points), and marked by annotation and FDR of enrichment (legend) or **b**, all 106,792 cells/nuclei, coloured by expression of SARS-CoV-2 entry factors (co-expression combinations with at least 10 cells are shown). Dashed lines, major cell types. **c**, Reduction in SARS-CoV-2 RNA with prolonged symptom onset to death interval (Spearman $\rho = -0.68$, $P < 0.005$, two-sided test). Symptom onset to death (x axis, days) and lung SARS-CoV-2 copies per nanogram input RNA (y axis) for each donor ($n = 16$). **d**, Expression changes in SARS-CoV-2 RNA⁺ myeloid cells. Significantly differentially expressed (DE) host genes (log-normalized and scaled digital gene expression, rows; cutoff: FDR < 0.05 and $\log_2(\text{fold change}) > 0.5$) across SARS-CoV-2 RNA⁺ ($n = 158$) and SARS-CoV-2 RNA⁻ myeloid cells ($n = 790$) (columns).

[Full size image](#)

Genes upregulated in biopsy samples with high versus low or no viral load ([Supplementary Methods](#)) included viral response and innate immune processes ($\log_2(\text{fold change}) > 1.4$, Wald test, FDR-corrected $P < 0.05$; Extended Data Fig. 6v,

Supplementary Table 4) and significantly overlapped with those in bulk RNA-Seq of post-mortem COVID-19 lungs in another study³² (FDR = 3.12×10^{-6} , Kolmogorov–Smirnov test). Downregulated genes ($\log_2(\text{fold change}) < 1.4$, Wald test, FDR-corrected $P < 0.05$) were involved in surfactant metabolism dysfunction and lamellar bodies (secretory vesicles in AT2 cells³³).

Lung cells enriched for SARS-CoV-2 RNA

Myeloid cells were the cell category most enriched for SARS-CoV-2 RNA (158 cells after correction for ambient RNA, FDR < 0.013; Fig. 3a, Extended Data Fig. 6w–y, [Supplementary Methods](#)), with particular enrichment in $CD14^{\text{high}}CD16^{\text{high}}$ inflammatory monocytes (FDR < 0.005) and $LDB2^{\text{high}}OSMR^{\text{high}}YAP1^{\text{high}}$ macrophages (FDR < 0.02; Extended Data Figs. 6x, 7a, b), although enrichment scores in individual donors varied. There was elevated, but non-significantly enriched, viral RNA in endothelial cells, with the capillary EC-2 (cluster 3, FDR < 0.017) and lymphatic endothelial cells (cluster 7, FDR < 0.006) enriched compared with other endothelial subsets (Fig. 3a, Extended Data Figs. 6w, y, 7c, d). There were also SARS-CoV-2 RNA⁺ cells among mast cells, and B and plasma cells, and viral RNA reads in multiple other cell types (Fig. 3a, Extended Data Fig. 6w). Notably, SARS-CoV-2 RNA⁺ cells did not co-express the entry factors ACE2 and TMPRSS2, or other hypothesized entry cofactors (Fig. 3b, Extended Data Fig. 7e–h).

Immune programs in SARS-CoV-2 RNA⁺ cells

SARS-CoV-2 RNA⁺ cells had distinct transcriptional programs compared with SARS-CoV-2 RNA⁻ counterparts, with differentially expressed genes (FDR < 0.05; [Supplementary Methods](#)) in epithelial and myeloid cells, including $PPARG^{\text{high}}CD15L^{\text{high}}$ macrophages and $CD14^{\text{high}}CD16^{\text{high}}$ inflammatory monocytes (Supplementary Table 5). Genes upregulated in epithelial SARS-CoV-2 RNA⁺ cells were enriched for TNF, AP1 and chemokine and cytokine signalling, SARS-CoV-2-driven cell responses in vitro³², and keratinization pathways, which may reflect an injury response (Extended Data Fig. 7j). Genes upregulated in myeloid SARS-CoV-2 RNA⁺ cells were those associated with chemokine and cytokine signalling, and responses to interferon, TNF, intracellular pathogens and viruses (Fig. 3d, Extended Data Fig. 7j–m, Supplementary Table 5), as previously described^{34,35}. Cytokines and viral host response genes were upregulated in both $CD14^{\text{high}}CD16^{\text{high}}$ inflammatory monocytes and $PPARG^{\text{high}}CD15L^{\text{high}}$ macrophages (Extended Data Fig. 7m, Supplementary Table 5), including $CXCL10$ and $CXCL11$, which were upregulated in nasopharyngeal swabs³⁵ and bronchoalveolar lavages³⁴.

A spatial atlas of COVID-19 lung

To provide tissue context, we used Nanostring GeoMx Digital Spatial Profiling (DSP) for transcriptomic profiling from regions of interest ([Supplementary Methods](#)) in 14 donors, including three deceased healthy donors ('healthy') (Extended Data Fig. [1a](#)). Regions of interest spanned a range of anatomical structures and viral abundance on the basis of SARS-CoV-2 RNA hybridization signals; when possible, we segmented them to PanCK⁺ and PanCK⁻, and inflamed and normal-appearing alveoli areas of illumination (AOIs) to capture RNA (Fig. [4a](#), Extended Data Figs. [8a](#), [9a](#), [Supplementary Methods](#)). We acquired high-quality profiles (Extended Data Fig. [8b](#)) from matched AOIs on the basis of distance to morphological landmarks ([Supplementary Methods](#)). SARS-CoV-2 RNA expression varied by donor, with elevated levels in four donors (Extended Data Fig. [8c, d](#), [Supplementary Methods](#)), consistent with viral qRT–PCR and sc/snRNA-Seq. Given the good agreement between a targeted 1,811-gene panel and a whole transcriptome (WTA) panel (18,335 genes) (Extended Data Fig. [8e–g](#), Supplementary Table [6](#)), we focused our analyses on WTA data. For D8–12, 18–24, we contrasted donors with COVID-19 and healthy donors and COVID-19 epithelial and non-epithelial AOIs; for D13–17, we focused on distinct anatomical regions and inflamed versus normal-appearing regions within donors.

Fig. 4: Composition and expression differences between COVID-19 and healthy lungs and between infected and uninfected regions within COVID-19 lungs.

 **figure4**

a, Example of analysed regions. Top: RNAscope (left) and immunofluorescent staining (right) of donor D20 with collection regions of interest (ROIs) and matched areas in white rectangles. Bottom: one ROI (yellow rectangle) from each scan (left and middle) and the segmented collection areas of illumination (AOIs) (right). **b**, Cell composition differences between PanCK⁺ and PanCK⁻ alveolar AOIs and between AOIs from COVID-19 ($n = 9$, 190 AOIs) and healthy (D22–24, 38 AOIs) lungs. Expression scores (colour bar) of cell type signatures (rows) in PanCK⁺ (left) and PanCK⁻ (right) alveolar AOIs (columns) in whole transcriptome (WTA) data from different donors (top colour bar). **c**, Differential gene expression in COVID-19 versus healthy lung. Left: significance ($-\log_{10}(P)$, y axis) and magnitude ($\log_2(\text{fold change})$, x axis) of differential expression of each gene (dots) in WTA data between PanCK⁺ alveoli AOIs from COVID-19 ($n = 78$) and healthy ($n = 18$) lung. Right: significance ($-\log_{10}(q)$) of enrichment (permutation test) of different pathways (rows). **d, e**, Changes in gene expression in SARS-CoV-2 high versus low AOIs within COVID-19 lungs in WTA data. **d**, SARS-CoV-2 high and low alveolar AOIs. PanCK⁺ alveolar

AOIs (dots) rank ordered by their SARS-CoV-2 signature score (*y* axis) in WTA data, and partitioned to high (red), medium (grey) and low (blue) SARS-CoV-2 AOIs. **e**, Significance ($-\log_{10}(P)$, *y* axis) and magnitude ($\log_2(\text{fold change})$, *x* axis) of differential expression of each gene (dots) in WTA data between SARS-CoV-2 high and low AOIs for PanCK⁺ alveoli (AOIs: 17 high, 3 medium, 58 low). Horizontal dashed line, FDR = 0.05; vertical dashed lines, $|\log_2(\text{fold change})| = 2$. FC, fold change. The top 10 differentially expressed genes by fold change are marked.

[Full size image](#)

Inflammatory activation in alveoli

Deconvolution of major cell type composition (Fig. 4b, Extended Data Fig. 8h, Supplementary Table 7, 8, [Supplementary Methods](#)) showed inferred AT1 and AT2 cells dominating the PanCK⁺ compartments and greater cellular diversity in the PanCK⁻ compartment. COVID-19 PanCK⁻ AOIs had increased fibroblast and myofibroblast scores compared with controls, in line with parallel spatial studies^{36,37}.

Comparing COVID-19 alveolar AOIs with control lungs from deceased healthy donors, there was upregulation of IFN α and IFN γ response genes and oxidative phosphorylation pathways (Fig. 4c, Extended Data Fig. 8i–k, Supplementary Table 6), similar to bulk RNA-Seq of highly infected tissue (*IFIT1*, *IFIT3*, *IDO1*, *GZMB*, *LAG3*, *NKG7* and *PRF1*) and to SARS-CoV-2⁺ myeloid cells (*TNFAIP6*, *CXCL11*, *CCL8*, *ISG1* and *GBP5*) and consistent with PANoptosis in a COVID-19 model³⁸. Conversely, TNF, IL2–STAT5 and TGF β signalling as well as apical junction and hypoxia were downregulated. Decreased TNF signalling expression in PanCK⁺ alveoli contrasts with its increase in SARS-CoV-2⁺ epithelial cells in snRNA-Seq and with reported³⁸ synergy between TNF and IFN γ in mouse models of COVID-19.

Comparison of inflamed and normal-appearing AOIs within the same alveolar biopsy samples of COVID-19 lungs (Extended Data Fig. 9, Supplementary Table 9, D13–D17), showed that upregulated genes were enriched for innate immune and inflammatory pathways^{39,40}, including neutrophil degranulation (FDR = 5.2×10^{-17}) and IFN γ (FDR = 3.4×10^{-15}) and interleukin (FDR = 1.4×10^{-13}) signalling. TNF pathway expression was elevated in inflamed tissue, albeit not significantly (FDR = 0.097). Claudins and tight junction pathways were downregulated, corroborating a disrupted alveolar barrier, as in influenza^{41,42}. Cilium assembly genes were enriched when comparing bronchial epithelial AOIs and matched normal-appearing alveoli (Extended Data Fig. 9d, Supplementary Table 9).

Comparison of SARS-CoV-2 high and low AOIs (Fig. 4d, e, Extended Data Fig. 8l, m, [Supplementary Methods](#)) revealed induction of the viral *ORF1ab* and *S* genes and upregulation of chemokine genes (*CXCL2* and *CXCL3*) and immediate early genes in the PanCK⁺ compartment, consistent with snRNA-Seq (Supplementary Table 9, Extended Data Fig. 7i). *NT5C*, which encodes a nucleotidase with a preference for 5'-dNTPs, is consistently upregulated in SARS-CoV-2-high AOIs (Fig. 4e, Extended Data Fig. 8m, Supplementary Table 9). This gene is not known to have a role in lung injury and should be further studied.

COVID-19 effect on heart, kidney and liver

We next profiled liver, heart and kidney by snRNA-Seq with automated and manual annotation of parenchymal, endothelial and immune cells ([Supplementary Methods](#), Extended Data Figs. 10, 11). Although other studies have reported viral reads in COVID-19 non-lung tissues⁴³, we detected very few viral RNA reads in all three tissues, most of which could not be assigned to nuclei (Extended Data Fig. 11l); this absence was confirmed by NanoString DSP and RNAscope (data not shown).

Focusing on heart, both cell composition and gene programs changed between COVID-19 and healthy heart. There was a significant reduction in the proportion of cardiomyocytes and pericytes, and an increase in vascular endothelial cells (Extended Data Fig. 11e). Genes upregulated (FDR < 0.01) in cardiomyocytes, pericytes or fibroblasts (Extended Data Fig. 11g–i, Supplementary Table 10) included *PLCG2*, the cardiac role of which is unknown but which was induced in all major heart cell subtypes (Extended Data Fig. 11j), and *AFDN*, which is upregulated in endothelial cells (Extended Data Fig. 11k), and which encodes a junction adherens complex component⁴⁴ that is necessary for endothelial barrier function. Upregulated pathways include oxidative-stress-induced apoptosis in pericytes, cell adhesion and immune pathways in cardiomyocytes, and cell differentiation processes in fibroblasts (Supplementary Table 10).

COVID-19 cell types related through GWAS

Finally, we aimed to identify genes and cell types associated with COVID-19 risk by integrating our atlas data with genome-wide association studies (GWAS)⁴⁵ for common⁴⁶ variants associated with COVID-19 ([Supplementary Methods](#)). Among 26 genes proximal to six COVID-19 GWAS regions (Supplementary Table 11, [Supplementary Methods](#)), 14 genes had higher average expression in the lung ($P < 0.05$, *t*-test; Extended Data Fig. 12a–d), 21 had significant (FDR < 0.05) expression specificity in at least one lung cell type, including *FOXP4* (chromosome (chr.) 6, AT1 and AT2 cells), and *CCR1* and *CCRL2* (chr. 3, macrophages) (Extended Data Fig. 12e,

Supplementary Table 11), and 18 were differentially expressed (FDR < 0.05) in COVID-19 compared with healthy lung (for example, *SLC6A20* in goblet cells, *CCR5* in CD8⁺ T cells and T_{reg} cells, and *CCR1* in macrophage and CD16⁺ monocytes (Extended Data Fig. 12f, Supplementary Table 11).

We related heritability from GWAS of COVID-19 severity traits to either cell type programs (genes enriched in a cell type in each tissue) or disease progression programs (genes differentially expressed between COVID-19 and controls in a cell type) in each tissue using sc-linker⁴⁷ (Supplementary Methods). AT2 (4.8 \times heritability enrichment, $P = 0.04$), CD8⁺ T cells (4.4 \times , $P = 0.009$) and ciliated cell programs in the lung, proximal convoluted tubule and connecting tubule programs in kidney, and cholangiocyte programs in liver attained nominal (but not Bonferroni-corrected) significance (Extended Data Fig. 12g, h, Supplementary Table 11). Of all disease progression programs, only the club cell program (single-cell level model) had nominally significant heritability enrichment (10.5 \times , $P = 0.04$ for severe COVID-19) (Extended Fig. 12g, Supplementary Table 11).

The highest number of driving genes was observed for lung AT2 cells and spanned several loci, hinting at a polygenic architecture linking AT2 cells with severe COVID-19 (Supplementary Methods, Supplementary Table 11). Implicated GWAS proximity genes include *OAS3* in lung AT2 and club cells, and *SLC4A7* in lung CD8⁺ T cells (Supplementary Table 11), as well as genes at unresolved significantly associated GWAS loci (Extended Data Fig. 12i), such as *FYCO1* (AT2, ciliated, club; chr. 3p), *NFKBIZ* (AT2; chr. 3q) and *DPP9* (AT2; chr. 19) (Supplementary Table 11).

Discussion

We built a biobank of severe COVID-19 autopsy tissue and atlases of COVID-19 lung, heart, liver and kidney (Extended Data Fig. 12j), complementing a sister lung atlas⁴⁸.

Among the changes in lung cell composition in COVID-19, is a reduction in AT2 cells and the presence of PATS and IPBLP-like cells, indicating that multiple regenerative strategies are invoked to re-establish alveolar epithelial cells lost to infection. A serial failure of epithelial progenitors to regenerate at a sufficient rate, first by secretory progenitor cells in the nasal passages and large and small airways, followed by alveolar AT2 cells, PATS and IPBLP cells, may eventually lead to lung failure.

Viral RNA in the lung varied, was negatively correlated with time from symptom start to death, and was primarily detected in myeloid and endothelial cells (as in nonhuman primates⁴⁹); spatial analysis supports high virus levels at the earlier stages of infection^{36,37,50}. Epithelial cells were not enriched in high viral RNA samples or in

SARS-CoV-2⁺ cells, consistent with their excessive death. Cell-associated SARS-CoV-2 unique molecular identifiers may represent a mixture of replicating virus, immune cell engulfment and virions or virally infected cells attached to the cell surface. We did not detect viral RNA in the heart, liver or kidney, but observed other changes, including broad upregulation of *PLCG2*, a target of Bruton's tyrosine kinase (BTK), in the heart⁵¹.

Combining our profiles with GWAS of COVID-19, we related specific cell types to heritable risk, especially AT2, ciliated and CD8⁺ T cells and macrophages, as well as genes in multi-gene regions underlying the association. This analysis can improve as GWAS grows and atlases expand.

Our study was limited by a modest number of donors without pre-selection of features, the terminal time point, limited distinction between viral RNA and true infection, and technical confounders such as PMIs. Nevertheless, our methods would enable studies in diverse diseased or damaged tissues. Future meta-analyses will further enhance its power and provide crucial resources for the community studying host–SARS-CoV-2 biology.

Reporting summary

Further information on research design is available in the [Nature Research Reporting Summary](#) linked to this paper.

Code availability

All samples were initially processed using Cumulus (<https://github.com/klarman-cell-observatory/cumulus>), which we ran on the Terra Cloud platform (<https://app.terra.bio/>). Code for all other analyses is available on GitHub (<https://github.com/klarman-cell-observatory/covid19-autopsy>).

Data availability

Processed sequencing data (sc/snRNA-Seq and bulk) are available in the Gene Expression Omnibus (GEO, <https://www.ncbi.nlm.nih.gov/geo/>) under accession number [GSE171668](#) and raw human sequencing data are available in the controlled access repository DUOS (<https://duos.broadinstitute.org/>), under dataset IDs DUOS-000126, DUOS-000127, DUOS-000128 and DUOS-000129. Viral genome assemblies and short-read sequencing data are publicly available in NCBI's [GenBank](#) and [SRA](#) databases, respectively, under BioProject [PRJNA720544](#). [GenBank](#) accessions for SARS-CoV-2 genomes are [MW885875–MW885883](#). Data for other tissues in the biobank will be released as they are acquired. Further queries can be addressed to: covid19-autopsy-northeast@broadinstitute.org .

The processed data are available on the Single Cell Portal: Lung, https://singlecell.broadinstitute.org/single_cell/study/SCP1052/.

Heart, https://singlecell.broadinstitute.org/single_cell/study/SCP1216/.

Kidney, https://singlecell.broadinstitute.org/single_cell/study/SCP1214/.

Liver, https://singlecell.broadinstitute.org/single_cell/study/SCP1213/.

Nanostring GeoMx raw and normalized count matrices are available in GEO under accession number [GSE163530](#). Raw images will be available upon request. [Source data](#) are provided with this paper.

References

1. 1.

Guan, W.-J. et al. Clinical characteristics of coronavirus disease 2019 in China. *N. Engl. J. Med.* **382**, 1708–1720 (2020).

[CAS](#) [Google Scholar](#)

2. 2.

Puelles, V. G. et al. Multiorgan and renal tropism of SARS-CoV-2. *N. Engl. J. Med.* **383**, 590–592 (2020).

[PubMed](#) [Google Scholar](#)

3. 3.

Huang, C. et al. Clinical features of patients infected with 2019 novel coronavirus in Wuhan, China. *Lancet* **395**, 497–506 (2020).

[CAS](#) [PubMed](#) [PubMed Central](#) [Google Scholar](#)

4. 4.

Xu, Z. et al. Pathological findings of COVID-19 associated with acute respiratory distress syndrome. *Lancet Respir. Med.* **8**, 420–422 (2020).

[CAS](#) [PubMed](#) [PubMed Central](#) [Google Scholar](#)

5. 5.

Varga, Z. et al. Endothelial cell infection and endotheliitis in COVID-19. *Lancet* **395**, 1417–1418 (2020).

[CAS](#) [PubMed](#) [PubMed Central](#) [Google Scholar](#)

6. 6.

Chen, G. et al. Clinical and immunological features of severe and moderate coronavirus disease 2019. *J. Clin. Invest.* **130**, 2620–2629 (2020).

[CAS](#) [PubMed](#) [PubMed Central](#) [Google Scholar](#)

7. 7.

Qin, C. et al. Dysregulation of immune response in patients with coronavirus 2019 (COVID-19) in Wuhan, China. *Clin. Infect. Dis.* **71**, 762–768 (2020).

[CAS](#) [PubMed](#) [Google Scholar](#)

8. 8.

Hadjadj, J. et al. Impaired type I interferon activity and exacerbated inflammatory responses in severe COVID-19 patients. *Science* **369**, 718–724 (2020).

9. 9.

Bian, X.-W. et al. Autopsy of COVID-19 patients in China. *Natl. Sci. Rev.* **7**, 1414–1418 (2020).

[CAS](#) [PubMed Central](#) [Google Scholar](#)

10. 10.

Menter, T. et al. Postmortem examination of COVID-19 patients reveals diffuse alveolar damage with severe capillary congestion and variegated findings in lungs and other organs suggesting vascular dysfunction. *Histopathology* **77**, 198–209 (2020).

[PubMed](#) [PubMed Central](#) [Google Scholar](#)

11. 11.

Wichmann, D. et al. Autopsy findings and venous thromboembolism in patients with COVID-19: a prospective cohort study. *Ann. Intern. Med.* **173**, 268–277 (2020).

[Google Scholar](#)

12. 12.

Bösmüller, H. et al. The evolution of pulmonary pathology in fatal COVID-19 disease: an autopsy study with clinical correlation. *Virchows Arch.* **477**, 349–357 (2020).

[PubMed](#) [PubMed Central](#) [Google Scholar](#)

13. 13.

Slyper, M. et al. A single-cell and single-nucleus RNA-Seq toolbox for fresh and frozen human tumors. *Nat. Med.* **26**, 792 –802 (2020).

[CAS](#) [PubMed](#) [PubMed Central](#) [Google Scholar](#)

14. 14.

Fleming, S. J., Marioni, J. C. & Babadi, M. CellBender remove-background: a deep generative model for unsupervised removal of background noise from scRNA-seq datasets. Preprint at <https://doi.org/10.1101/791699> (2019).

15. 15.

Li, B. et al. Cumulus provides cloud-based data analysis for large-scale single-cell and single-nucleus RNA-seq. *Nat. Methods* **17**, 793–798 (2020).

[CAS](#) [PubMed](#) [PubMed Central](#) [Google Scholar](#)

16. 16.

Shaffer, A. L. et al. Blimp-1 orchestrates plasma cell differentiation by extinguishing the mature B cell gene expression program. *Immunity* **17**, 51–62 (2002).

[CAS](#) [PubMed](#) [Google Scholar](#)

17. 17.

Martins, G. & Calame, K. Regulation and functions of Blimp-1 in T and B lymphocytes. *Annu. Rev. Immunol.* **26**, 133–169 (2008).

[CAS](#) [PubMed](#) [Google Scholar](#)

18. 18.

Schupp, J. C. et al. Integrated single cell atlas of endothelial cells of the human lung. Preprint at <https://doi.org/10.1101/2020.10.21.347914> (2020).

19. 19.

Travaglini, K. J. et al. A molecular cell atlas of the human lung from single-cell RNA sequencing. *Nature* **587**, 619–625 (2020).

[CAS](#) [PubMed](#) [PubMed Central](#) [ADS](#) [Google Scholar](#)

20. 20.

Strunz, M. et al. Alveolar regeneration through a Krt8+ transitional stem cell state that persists in human lung fibrosis. *Nat. Commun.* **11**, 3559 (2020).

[CAS](#) [PubMed](#) [PubMed Central](#) [ADS](#) [Google Scholar](#)

21. 21.

Kobayashi, Y. et al. Persistence of a regeneration-associated, transitional alveolar epithelial cell state in pulmonary fibrosis. *Nat. Cell Biol.* **22**, 934–946 (2020).

[CAS](#) [PubMed](#) [PubMed Central](#) [Google Scholar](#)

22. 22.

Choi, J. et al. Inflammatory signals induce AT2 cell-derived damage-associated transient progenitors that mediate alveolar regeneration. *Cell Stem Cell* **27**, 366–382.e7 (2020).

[CAS](#) [PubMed](#) [PubMed Central](#) [Google Scholar](#)

23. 23.

Ziegler, C. G. K. et al. SARS-CoV-2 receptor ACE2 is an interferon-stimulated gene in human airway epithelial cells and is detected in specific cell subsets across tissues. *Cell* **181**, 1016–1035.e19 (2020).

[CAS](#) [PubMed](#) [PubMed Central](#) [Google Scholar](#)

24. 24.

Sungnak, W. et al. SARS-CoV-2 entry factors are highly expressed in nasal epithelial cells together with innate immune genes. *Nat. Med.* **26**, 681–687 (2020).

[CAS](#) [PubMed](#) [PubMed Central](#) [Google Scholar](#)

25. 25.

Muus, C. et al. Single-cell meta-analysis of SARS-CoV-2 entry genes across tissues and demographics. *Nat. Med.* **27**, 546–559 (2021).

[CAS](#) [PubMed](#) [Google Scholar](#)

26. 26.

Xu, J. et al. SARS-CoV-2 induces transcriptional signatures in human lung epithelial cells that promote lung fibrosis. *Respir. Res.* **21**, 182 (2020).

[CAS](#) [PubMed](#) [PubMed Central](#) [Google Scholar](#)

27. 27.

Grillo, F., Barisione, E., Ball, L., Mastracci, L. & Fiocca, R. Lung fibrosis: an undervalued finding in COVID-19 pathological series. *Lancet Infect. Dis.* **21**, e72 (2021).

[CAS](#) [PubMed](#) [Google Scholar](#)

28. 28.

Vaughan, A. E. et al. Lineage-negative progenitors mobilize to regenerate lung epithelium after major injury. *Nature* **517**, 621–625 (2015).

[CAS](#) [PubMed](#) [ADS](#) [Google Scholar](#)

29. 29.

Fernanda de Mello Costa, M., Weiner, A. I. & Vaughan, A. E. Basal-like progenitor cells: a review of dysplastic alveolar regeneration and remodeling in lung repair. *Stem Cell Reports* **15**, 1015–1025 (2020).

[CAS](#) [PubMed](#) [PubMed Central](#) [Google Scholar](#)

30. 30.

Wölfel, R. et al. Virological assessment of hospitalized patients with COVID-2019. *Nature* **581**, 465–469 (2020).

[ADS](#) [Google Scholar](#)

31. 31.

Walsh, K. A. et al. SARS-CoV-2 detection, viral load and infectivity over the course of an infection. *J. Infect.* **81**, 357–371 (2020).

[CAS](#) [PubMed](#) [PubMed Central](#) [Google Scholar](#)

32. 32.

Blanco-Melo, D. et al. Imbalanced host response to SARS-CoV-2 drives development of COVID-19. *Cell* **181**, 1036–1045.e9 (2020).

[CAS](#) [PubMed](#) [PubMed Central](#) [Google Scholar](#)

33. 33.

Johnson, N. F. Release of lamellar bodies from alveolar type 2 cells. *Thorax* **35**, 192–197 (1980).

[CAS](#) [PubMed](#) [PubMed Central](#) [Google Scholar](#)

34. 34.

Grant, R. A. et al. Circuits between infected macrophages and T cells in SARS-CoV-2 pneumonia. *Nature* **590**, 635–641 (2021).

[CAS](#) [PubMed](#) [ADS](#) [Google Scholar](#)

35. 35.

Butler, D. et al. Shotgun transcriptome, spatial omics, and isothermal profiling of SARS-CoV-2 infection reveals unique host responses, viral diversification, and drug interactions. *Nat. Commun.* **12**, 1660 (2021).

[CAS](#) [PubMed](#) [PubMed Central](#) [ADS](#) [Google Scholar](#)

36. 36.

Park, J. et al. Systemic tissue and cellular disruption from SARS-CoV-2 infection revealed in COVID-19 autopsies and spatial omics tissue maps. Preprint at <https://doi.org/10.1101/2021.03.08.434433> (2021).

37. 37.

Rendeiro, A. F. et al. The spatio-temporal landscape of lung pathology in SARS-CoV-2 infection. Preprint at <https://doi.org/10.1101/2020.10.26.20219584> (2020).

38. 38.

Karki, R. et al. Synergism of TNF- α and IFN- γ triggers inflammatory cell death, tissue damage, and mortality in SARS-CoV-2 infection and

cytokine shock syndromes. *Cell* **184**, 149–168.e17 (2021).

[CAS](#) [PubMed](#) [PubMed Central](#) [Google Scholar](#)

39. 39.

Subramanian, A. et al. Gene set enrichment analysis: a knowledge-based approach for interpreting genome-wide expression profiles. *Proc. Natl Acad. Sci. USA* **102**, 15545–15550 (2005).

[CAS](#) [PubMed](#) [PubMed Central](#) [ADS](#) [Google Scholar](#)

40. 40.

Mootha, V. K. et al. PGC-1 α -responsive genes involved in oxidative phosphorylation are coordinately downregulated in human diabetes. *Nat. Genet.* **34**, 267–273 (2003).

[CAS](#) [PubMed](#) [Google Scholar](#)

41. 41.

van de Sandt, C. E. et al. Human CD8 $^{+}$ T cells damage noninfected epithelial cells during influenza virus infection in vitro. *Am. J. Respir. Cell Mol. Biol.* **57**, 536–546 (2017).

[PubMed](#) [Google Scholar](#)

42. 42.

Short, K. R. et al. Influenza virus damages the alveolar barrier by disrupting epithelial cell tight junctions. *Eur. Respir. J.* **47**, 954–966 (2016).

[CAS](#) [PubMed](#) [Google Scholar](#)

43. 43.

Lemieux, J. E. et al. Phylogenetic analysis of SARS-CoV-2 in Boston highlights the impact of superspreading events. *Science* **371**, eabe3261 (2021).

[CAS](#) [PubMed](#) [Google Scholar](#)

44. 44.

Yu, H. H. & Zallen, J. A. Abl and Canoe/Afadin mediate mechanotransduction at tricellular junctions. *Science* **370**, eaba5528 (2020).

[PubMed](#) [Google Scholar](#)

45. 45.

COVID-19 Host Genetics Initiative. The COVID-19 Host Genetics Initiative, a global initiative to elucidate the role of host genetic factors in susceptibility and severity of the SARS-CoV-2 virus pandemic. *Eur. J. Hum. Genet.* **28**, 715–718 (2020).

[Google Scholar](#)

46. 46.

Severe Covid-19 GWAS Group. Genomewide association study of severe Covid-19 with respiratory failure. *N. Engl. J. Med.* **383**, 1522–1534 (2020).

[Google Scholar](#)

47. 47.

Jagadeesh, K. A. et al. Identifying disease-critical cell types and cellular processes across the human body by integration of single-cell profiles and human genetics. Preprint at <https://doi.org/10.1101/2021.03.19.436212> (2021).

48. 48.

Melms, J. C. et al. A molecular single-cell lung atlas of lethal COVID-19. *Nature* <https://doi.org/10.1038/s41586-021-03569-1> (2021).

49. 49.

Speranza, E. et al. SARS-CoV-2 infection dynamics in lungs of African green monkeys. Preprint at <https://doi.org/10.1101/2020.08.20.258087> (2020).

50. 50.

Desai, N. et al. Temporal and spatial heterogeneity of host response to SARS-CoV-2 pulmonary infection. Preprint at <https://doi.org/10.1101/2020.07.30.20165241> (2020).

51. 51.

Liu, T.-M. et al. Hypermorphic mutation of phospholipase C, γ 2 acquired in ibrutinib-resistant CLL confers BTK independency upon B-cell receptor activation. *Blood* **126**, 61–68 (2015).

[CAS](#) [PubMed](#) [PubMed Central](#) [Google Scholar](#)

52. 52.

Wolf, F. A., Angerer, P. & Theis, F. J. SCANPY: large-scale single-cell gene expression data analysis. *Genome Biol.* **19**, 15 (2018).

[PubMed](#) [PubMed Central](#) [Google Scholar](#)

53. 53.

Korsunsky, I. et al. Fast, sensitive and accurate integration of single-cell data with Harmony. *Nat. Methods* **16**, 1289–1296 (2019).

[CAS](#) [PubMed](#) [PubMed Central](#) [Google Scholar](#)

54. 54.

Schiller, H. B. et al. The Human Lung Cell Atlas: a high-resolution reference map of the human lung in health and disease. *Am. J. Respir. Cell Mol. Biol.* **61**, 31–41 (2019).

[CAS](#) [PubMed](#) [PubMed Central](#) [Google Scholar](#)

55. 55.

Brill, B., Amir, A. & Heller, R. Testing for differential abundance in compositional counts data, with application to microbiome studies. Preprint at <https://arxiv.org/abs/1904.08937> (2019).

56. 56.

Ravindra, N. G. et al. Single-cell longitudinal analysis of SARS-CoV-2 infection in human airway epithelium. Preprint at <https://doi.org/10.1101/2020.05.06.081695> (2020).

[Download references](#)

Acknowledgements

We are deeply grateful to all donors and their families. This paper is part of the Human Cell Atlas (<https://www.humancellatlas.org/publications/>). We acknowledge the contribution of C. Kania, E. Kounaves, N. Lemelin, J. Susterich, J. Teixeira, C. Bernal, M. Berstein, A. Morris, J. N. Ray, A. Awley, A. Araujo and E. Figueroa who all assisted in performing the autopsies at the Massachusetts General Hospital. We thank A. Hupalowska and L. Gaffney for help with figure preparation. We thank M. Veregge, Z. Kramer and C. Jacobs for their contributions in the execution of experimental procedures, and D. Pouli who supported the creation of tissue annotation resources; 10x Genomics, Illumina, BD Biosciences, and NanoString for help and support with instruments and/or lab reagents and technical advice. Portions of this research were conducted on the Ithaca High Performance Computing system, Department of Pathology, BIDMC, and the O2 High Performance Compute Cluster at Harvard Medical School. This project has been funded in part with funds from the Manton

Foundation, Klarman Family Foundation, HHMI, the Chan Zuckerberg Initiative and the Human Tumor Atlas Network trans-network projects SARDANA (Shared Repositories, Data, Analysis and Access). A.R. was an Investigator of the Howard Hughes Medical Institute. This project was also funded by DARPA grant HR0011-20-2-0040 (to D.E.I.) and the US Food and Drug Administration grant HHSF223201810172C (to P.C.S. and A.K.S.). A.-C.V. acknowledges funding support from the National Institute of Health Director's New Innovator Award (DP2CA247831), the Massachusetts General Hospital (MGH) Transformative Scholar in Medicine Award, a COVID-19 Clinical Trials Pilot grant from the Executive Committee on Research at MGH, and the Damon Runyon-Rachleff Innovation Award. G.S. acknowledges support from the NIH R01AA0207440 and U01AA026933 research grants. A.P. acknowledges funding from the following sources U01 HG009379, R01 MH101244, R37 MH107649. We thank all members of the Department of Pathology and Cell Biology at Columbia University Irving Medical Center who led the procurement of autopsy tissues used in this work. This work was supported by National Institute of Health (NIH) grants K08CA222663 (B.I.), R37CA258829 (B.I.), U54CA225088 (B.I.), FastGrants (B.I.) and the Burroughs Wellcome Fund Career Award for Medical Scientists (B.I.). This research was funded in part through the NIH/NCI Cancer Center Support Grant P30CA013696 at Columbia University and used the Molecular Pathology Shared Resource and its Tissue Bank.

Author information

Author notes

1. Orit Rozenblatt-Rosen & Aviv Regev

Present address: Genentech, South San Francisco, CA, USA

2. These authors contributed equally: Toni M. Delorey, Carly G. K. Ziegler, Graham Heimberg, Rachelly Normand, Yiming Yang, Åsa Segerstolpe, Domenic Abbondanza, Stephen J. Fleming, Ayshwarya Subramanian, Daniel T. Montoro, Karthik A. Jagadeesh, Kushal K.

Dey, Pritha Sen, Michal Slyper, Yered H. Pita-Juárez, Devan Phillips, Jana Biermann

3. These authors jointly supervised this work: Patrick T. Ellinor, Deborah Hung, Pardis C. Sabeti, Richard Novak, Robert Rogers, Donald E. Ingber, Z. Gordon Jiang, Dejan Juric, Mehrtash Babadi, Samouil L. Farhi, Benjamin Izar, James R. Stone, Ioannis S. Vlachos, Isaac H. Solomon, Orr Ashenberg, Caroline B. M. Porter, Bo Li, Alex K. Shalek, Alexandra-Chloé Villani, Orit Rozenblatt-Rosen, Aviv Regev

Affiliations

1. Klarman Cell Observatory, Broad Institute of MIT and Harvard, Cambridge, MA, USA

Toni M. Delorey, Graham Heimberg, Yiming Yang, Åsa Segerstolpe, Domenic Abbondanza, Ayshwarya Subramanian, Karthik A. Jagadeesh, Michal Slyper, Devan Phillips, Malika Sud, Liat Amir-Zilberman, Phylicia Dorceus, Joshua Gould, Tyler Harvey, Judit Jané-Valbuena, Hui Ma, Cristin McCabe, Carmel Pe'er, Jenna Pfiffner-Borges, Ellen Todres, Timothy L. Tickle, Samouil L. Farhi, Orr Ashenberg, Caroline B. M. Porter, Bo Li, Orit Rozenblatt-Rosen & Aviv Regev

2. Broad Institute of MIT and Harvard, Cambridge, MA, USA

Carly G. K. Ziegler, Rachelly Normand, Daniel T. Montoro, Pritha Sen, Yered H. Pita-Juárez, Erica Normandin, Siddharth S. Raju, Linus T.-Y. Tsai, Katherine J. Siddle, Shamsudheen K. Vellarikkal, Deepak S. Atri, Jonathan Chen, Jesse M. Engreitz, Michael Leney-Greene, Christoph Muus, Melissa Rudy, Rajat M. Gupta, Nir Hacohen, Gyongyi Szabo, Pardis C. Sabeti, Ioannis S. Vlachos, Alex K. Shalek & Alexandra-Chloé Villani

3. Program in Health Sciences & Technology, Harvard Medical School and Massachusetts Institute of Technology, Boston, MA, USA

Carly G. K. Ziegler & Alex K. Shalek

4. Institute for Medical Engineering & Science, Massachusetts Institute of Technology, Cambridge, MA, USA

Carly G. K. Ziegler & Alex K. Shalek

5. Koch Institute for Integrative Cancer Research, Massachusetts Institute of Technology, Cambridge, MA, USA

Carly G. K. Ziegler, Alex K. Shalek & Aviv Regev

6. Ragon Institute of MGH, MIT, and Harvard, Cambridge, MA, USA

Carly G. K. Ziegler & Alex K. Shalek

7. Harvard Graduate Program in Biophysics, Harvard University, Cambridge, MA, USA

Carly G. K. Ziegler & Alex K. Shalek

8. Center for Immunology and Inflammatory Diseases, Department of Medicine, Massachusetts General Hospital, Boston, MA, USA

Rachelly Normand, Yiming Yang, Pritha Sen, Hui Ma, Bo Li & Alexandra-Chloé Villani

9. Center for Cancer Research, Massachusetts General Hospital, Harvard Medical School, Boston, MA, USA

Rachelly Normand, Nir Hacohen & Alexandra-Chloé Villani

10. Harvard Medical School, Boston, MA, USA

Rachelly Normand, Yered H. Pita-Juárez, Erica Normandin, Pourya Naderi, Yury V. Popov, Sebastian Niezen, Linus T.-Y. Tsai, Jonathan Hecht, Winston Hide, Stefan Riedel, Gyongyi Szabo, Z. Gordon Jiang, Ioannis S. Vlachos & Alex K. Shalek

11. Massachusetts Institute of Technology, Cambridge, MA, USA

Rachelly Normand

12. Data Sciences Platform, Broad Institute of MIT and Harvard,
Cambridge, MA, USA

Stephen J. Fleming, Nikolaos Barkas, Joshua Gould, Timothy L.
Tickle & Mehrtash Babadi

13. Precision Cardiology Laboratory, Broad Institute of MIT and Harvard,
Cambridge, MA, USA

Stephen J. Fleming & Mehrtash Babadi

14. Department of Epidemiology, Harvard T. H. Chan School of Public
Health, Harvard University, Boston, MA, USA

Kushal K. Dey & Alkes L. Price

15. Division of Infectious Diseases, Department of Medicine,
Massachusetts General Hospital, Boston, MA, USA

Pritha Sen

16. Department of Medicine, Harvard Medical School, Boston, MA, USA

Pritha Sen, Christopher J. Pinto, Dejan Juric, Bo Li & Alexandra-
Chloé Villani

17. Department of Pathology, Beth Israel Deaconess Medical Center,
Boston, MA, USA

Yered H. Pita-Juárez, Pourya Naderi, Jonathan Hecht, Winston
Hide, Stefan Riedel & Ioannis S. Vlachos

18. Harvard Medical School Initiative for RNA Medicine, Boston, MA,
USA

Yered H. Pita-Juárez, Pourya Naderi, Winston Hide & Ioannis S.
Vlachos

19. Cancer Research Institute, Beth Israel Deaconess Medical Center,
Boston, MA, USA

Yered H. Pita-Juárez, Winston Hide & Ioannis S. Vlachos

20. Department of Medicine, Division of Hematology/Oncology,
Columbia University Irving Medical Center, New York, NY, USA

Jana Biermann, Johannes C. Melms, Yiping Wang & Benjamin Izar

21. Columbia Center for Translational Immunology, New York, NY, USA

Jana Biermann, Johannes C. Melms, Yiping Wang & Benjamin Izar

22. Infectious Disease and Microbiome Program, Broad Institute of MIT
and Harvard, Cambridge, MA, USA

Zohar Bloom-Ackermann, James Gomez, Victoria M. Tran, Alexander
Sturm, Shuting Zhang & Deborah Hung

23. Institute for Molecular Medicine Finland, Helsinki, Finland

Andrea Ganna & Mari Niemi

24. Analytical & Translational Genetics Unit, Massachusetts General
Hospital, Harvard Medical School, Boston, MA, USA

Andrea Ganna

25. Department of Pathology and Cell Biology, Columbia University
Irving Medical Center, New York, NY, USA

Igor Katsyy & Hanina Hibshoosh

26. Department of Medicine, Beth Israel Deaconess Medical Center,
Boston, MA, USA

Yury V. Popov, Sebastian Niezen, Linus T.-Y. Tsai, Adam
Essene, Deepti Pant, Gyongyi Szabo, Robert Rogers & Z. Gordon

Jiang

27. Division of Gastroenterology, Hepatology and Nutrition, Department of Medicine, Beth Israel Deaconess Medical Center, Boston, MA, USA

Yury V. Popov, Sebastian Niezen & Z. Gordon Jiang

28. Department of Systems Biology, Harvard Medical School, Boston, MA, USA

Siddharth S. Raju

29. FAS Center for Systems Biology, Department of Organismic and Evolutionary Biology, Harvard University, Cambridge, MA, USA

Siddharth S. Raju

30. Division of Endocrinology, Diabetes, and Metabolism, Beth Israel Deaconess Medical Center, Boston, MA, USA

Linus T.-Y. Tsai, Adam Essene & Deepti Pant

31. Boston Nutrition and Obesity Research Center Functional Genomics and Bioinformatics Core Boston, Boston, MA, USA

Linus T.-Y. Tsai, Adam Essene & Deepti Pant

32. Department of Organismic and Evolutionary Biology, Harvard University, Cambridge, MA, USA

Katherine J. Siddle & Pardis C. Sabeti

33. Divisions of Cardiovascular Medicine and Genetics, Brigham and Women's Hospital, Harvard Medical School, Boston, MA, USA

Shamsudheen K. Vellarikkal, Deepak S. Atri & Rajat M. Gupta

34. NanoString Technologies Inc, Seattle, WA, USA

Joseph Beechem, Prajan Divakar, Robin Fropf, Tyler Hether, Eric M. Miller, Liuliu Pan, Jason Reeves, Marty Ross, Erroll H. Rueckert, Sarah Warren & Daniel R. Zollinger

35. Department of Radiology, Beth Israel Deaconess Medical Center, Boston, MA, USA

Olga R. Brook

36. Department of Pathology, Massachusetts General Hospital, Harvard Medical School, Boston, MA, USA

Jonathan Chen & James R. Stone

37. Department of Genetics and BASE Initiative, Stanford University School of Medicine, Stanford, CA, USA

Jesse M. Engreitz

38. Massachusetts General Hospital Cancer Center, Department of Medicine, Massachusetts General Hospital, Boston, MA, USA

Donna M. Fitzgerald, Daniel E. McLoughlin, Christopher J. Pinto, Jayaraj Rajagopal & Dejan Juric

39. Center for Genetic Epidemiology, Department of Preventive Medicine, Keck School of Medicine, University of Southern California, Los Angeles, CA, USA

Steven Gazal

40. Department of Pathology, Brigham and Women's Hospital, Boston, MA, USA

John Grzyb, Robert Padera, Jacob Plaisted, Michelle Siciliano & Isaac H. Solomon

41. John A. Paulson School of Engineering and Applied Sciences, Harvard University, Cambridge, MA, USA

Christoph Muus & Donald E. Ingber

42. Harvard-MIT Division of Health Sciences and Technology,
Cambridge, MA, USA

Robert Padera

43. Department of Pathology, Harvard Medical School, Boston, MA, USA

Robert Padera

44. Harvard Stem Cell Institute, Cambridge, MA, USA

Avinash Waghray & Alex K. Shalek

45. Center for Regenerative Medicine, Massachusetts General Hospital,
Boston, MA, USA

Avinash Waghray

46. Infectious Diseases Division, Department of Medicine, Brigham and
Women's Hospital, Boston, MA, USA

Lisa Cosimi

47. Department of Medicine, Massachusetts General Hospital, Harvard
Medical School, Boston, MA, USA

Nir Hacohen

48. Department of Cell Biology, Duke University School of Medicine,
Durham, NC, USA

Purushothama Rao Tata

49. Cardiovascular Disease Initiative, Broad Institute of MIT and Harvard,
Cambridge, MA, USA

Patrick T. Ellinor

50. Department of Genetics, Harvard Medical School, Boston, MA, USA

Deborah Hung

51. Department of Molecular Biology and Center for Computational and Integrative Biology, Massachusetts General Hospital, Boston, MA, USA

Deborah Hung

52. Department of Immunology and Infectious Diseases, Harvard T. H. Chan School of Public Health, Harvard University, Boston, MA, USA

Pardis C. Sabeti

53. Howard Hughes Medical Institute, Chevy Chase, MD, USA

Pardis C. Sabeti & Aviv Regev

54. Massachusetts Consortium on Pathogen Readiness, Boston, MA, USA

Pardis C. Sabeti

55. Wyss Institute for Biologically Inspired Engineering, Harvard University, Boston, MA, USA

Richard Novak & Donald E. Ingber

56. Massachusetts General Hospital, Boston, MA, USA

Robert Rogers

57. Vascular Biology Program and Department of Surgery, Boston Children's Hospital, Harvard Medical School, Boston, MA, USA

Donald E. Ingber

58. Herbert Irving Comprehensive Cancer Center, Columbia University Irving Medical Center, New York, NY, USA

Benjamin Izar

59. Program for Mathematical Genomics, Columbia University Irving Medical Center, New York, NY, USA

Benjamin Izar

60. Program in Computational & Systems Biology, Massachusetts Institute of Technology, Cambridge, MA, USA

Alex K. Shalek

61. Program in Immunology, Harvard Medical School, Boston, MA, USA

Alex K. Shalek

62. Department of Chemistry, Massachusetts Institute of Technology, Cambridge, MA, USA

Alex K. Shalek

Authors

1. Toni M. Delorey

[View author publications](#)

You can also search for this author in [PubMed](#) [Google Scholar](#)

2. Carly G. K. Ziegler

[View author publications](#)

You can also search for this author in [PubMed](#) [Google Scholar](#)

3. Graham Heimberg

[View author publications](#)

You can also search for this author in [PubMed](#) [Google Scholar](#)

4. Rachelly Normand

[View author publications](#)

You can also search for this author in [PubMed](#) [Google Scholar](#)

5. Yiming Yang

[View author publications](#)

You can also search for this author in [PubMed](#) [Google Scholar](#)

6. Åsa Segerstolpe

[View author publications](#)

You can also search for this author in [PubMed](#) [Google Scholar](#)

7. Domenic Abbondanza

[View author publications](#)

You can also search for this author in [PubMed](#) [Google Scholar](#)

8. Stephen J. Fleming

[View author publications](#)

You can also search for this author in [PubMed](#) [Google Scholar](#)

9. Ayshwarya Subramanian

[View author publications](#)

You can also search for this author in [PubMed](#) [Google Scholar](#)

10. Daniel T. Montoro

[View author publications](#)

You can also search for this author in [PubMed](#) [Google Scholar](#)

11. Karthik A. Jagadeesh

[View author publications](#)

You can also search for this author in [PubMed](#) [Google Scholar](#)

12. Kushal K. Dey

[View author publications](#)

You can also search for this author in [PubMed](#) [Google Scholar](#)

13. Pritha Sen

[View author publications](#)

You can also search for this author in [PubMed](#) [Google Scholar](#)

14. Michal Slyper

[View author publications](#)

You can also search for this author in [PubMed](#) [Google Scholar](#)

15. Yered H. Pita-Juárez

[View author publications](#)

You can also search for this author in [PubMed](#) [Google Scholar](#)

16. Devan Phillips

[View author publications](#)

You can also search for this author in [PubMed](#) [Google Scholar](#)

17. Jana Biermann

[View author publications](#)

You can also search for this author in [PubMed](#) [Google Scholar](#)

18. Zohar Bloom-Ackermann

[View author publications](#)

You can also search for this author in [PubMed](#) [Google Scholar](#)

19. Nikolaos Barkas

[View author publications](#)

You can also search for this author in [PubMed](#) [Google Scholar](#)

20. Andrea Ganna

[View author publications](#)

You can also search for this author in [PubMed](#) [Google Scholar](#)

21. James Gomez

[View author publications](#)

You can also search for this author in [PubMed](#) [Google Scholar](#)

22. Johannes C. Melms

[View author publications](#)

You can also search for this author in [PubMed](#) [Google Scholar](#)

23. Igor Katsyy

[View author publications](#)

You can also search for this author in [PubMed](#) [Google Scholar](#)

24. Erica Normandin

[View author publications](#)

You can also search for this author in [PubMed](#) [Google Scholar](#)

25. Pourya Naderi

[View author publications](#)

You can also search for this author in [PubMed](#) [Google Scholar](#)

26. Yury V. Popov

[View author publications](#)

You can also search for this author in [PubMed](#) [Google Scholar](#)

27. Siddharth S. Raju

[View author publications](#)

You can also search for this author in [PubMed](#) [Google Scholar](#)

28. Sebastian Niezen

[View author publications](#)

You can also search for this author in [PubMed](#) [Google Scholar](#)

29. Linus T.-Y. Tsai

[View author publications](#)

You can also search for this author in [PubMed](#) [Google Scholar](#)

30. Katherine J. Siddle

[View author publications](#)

You can also search for this author in [PubMed](#) [Google Scholar](#)

31. Malika Sud

[View author publications](#)

You can also search for this author in [PubMed](#) [Google Scholar](#)

32. Victoria M. Tran

[View author publications](#)

You can also search for this author in [PubMed](#) [Google Scholar](#)

33. Shamsudheen K. Vellarikkal

[View author publications](#)

You can also search for this author in [PubMed](#) [Google Scholar](#)

34. Yiping Wang

[View author publications](#)

You can also search for this author in [PubMed](#) [Google Scholar](#)

35. Liat Amir-Zilberstein

[View author publications](#)

You can also search for this author in [PubMed](#) [Google Scholar](#)

36. Deepak S. Atri

[View author publications](#)

You can also search for this author in [PubMed](#) [Google Scholar](#)

37. Joseph Beechem

[View author publications](#)

You can also search for this author in [PubMed](#) [Google Scholar](#)

38. Olga R. Brook

[View author publications](#)

You can also search for this author in [PubMed](#) [Google Scholar](#)

39. Jonathan Chen

[View author publications](#)

You can also search for this author in [PubMed](#) [Google Scholar](#)

40. Prajan Divakar

[View author publications](#)

You can also search for this author in [PubMed](#) [Google Scholar](#)

41. Phylicia Dorceus

[View author publications](#)

You can also search for this author in [PubMed](#) [Google Scholar](#)

42. Jesse M. Engreitz

[View author publications](#)

You can also search for this author in [PubMed](#) [Google Scholar](#)

43. Adam Essene

[View author publications](#)

You can also search for this author in [PubMed](#) [Google Scholar](#)

44. Donna M. Fitzgerald

[View author publications](#)

You can also search for this author in [PubMed](#) [Google Scholar](#)

45. Robin Fropf

[View author publications](#)

You can also search for this author in [PubMed](#) [Google Scholar](#)

46. Steven Gazal

[View author publications](#)

You can also search for this author in [PubMed](#) [Google Scholar](#)

47. Joshua Gould

[View author publications](#)

You can also search for this author in [PubMed](#) [Google Scholar](#)

48. John Grzyb

[View author publications](#)

You can also search for this author in [PubMed](#) [Google Scholar](#)

49. Tyler Harvey

[View author publications](#)

You can also search for this author in [PubMed](#) [Google Scholar](#)

50. Jonathan Hecht

[View author publications](#)

You can also search for this author in [PubMed](#) [Google Scholar](#)

51. Tyler Hether

[View author publications](#)

You can also search for this author in [PubMed](#) [Google Scholar](#)

52. Judit Jané-Valbuena

[View author publications](#)

You can also search for this author in [PubMed](#) [Google Scholar](#)

53. Michael Leney-Greene

[View author publications](#)

You can also search for this author in [PubMed](#) [Google Scholar](#)

54. Hui Ma

[View author publications](#)

You can also search for this author in [PubMed](#) [Google Scholar](#)

55. Cristin McCabe

[View author publications](#)

You can also search for this author in [PubMed](#) [Google Scholar](#)

56. Daniel E. McLoughlin

[View author publications](#)

You can also search for this author in [PubMed](#) [Google Scholar](#)

57. Eric M. Miller

[View author publications](#)

You can also search for this author in [PubMed](#) [Google Scholar](#)

58. Christoph Muus

[View author publications](#)

You can also search for this author in [PubMed](#) [Google Scholar](#)

59. Mari Niemi

[View author publications](#)

You can also search for this author in [PubMed](#) [Google Scholar](#)

60. Robert Padera

[View author publications](#)

You can also search for this author in [PubMed](#) [Google Scholar](#)

61. Liiliu Pan

[View author publications](#)

You can also search for this author in [PubMed](#) [Google Scholar](#)

62. Deepti Pant

[View author publications](#)

You can also search for this author in [PubMed](#) [Google Scholar](#)

63. Carmel Pe'er

[View author publications](#)

You can also search for this author in [PubMed](#) [Google Scholar](#)

64. Jenna Pfiffner-Borges

[View author publications](#)

You can also search for this author in [PubMed](#) [Google Scholar](#)

65. Christopher J. Pinto

[View author publications](#)

You can also search for this author in [PubMed](#) [Google Scholar](#)

66. Jacob Plaisted

[View author publications](#)

You can also search for this author in [PubMed](#) [Google Scholar](#)

67. Jason Reeves

[View author publications](#)

You can also search for this author in [PubMed](#) [Google Scholar](#)

68. Marty Ross

[View author publications](#)

You can also search for this author in [PubMed](#) [Google Scholar](#)

69. Melissa Rudy

[View author publications](#)

You can also search for this author in [PubMed](#) [Google Scholar](#)

70. Erroll H. Rueckert

[View author publications](#)

You can also search for this author in [PubMed](#) [Google Scholar](#)

71. Michelle Siciliano

[View author publications](#)

You can also search for this author in [PubMed](#) [Google Scholar](#)

72. Alexander Sturm

[View author publications](#)

You can also search for this author in [PubMed](#) [Google Scholar](#)

73. Ellen Todres

[View author publications](#)

You can also search for this author in [PubMed](#) [Google Scholar](#)

74. Avinash Waghray

[View author publications](#)

You can also search for this author in [PubMed](#) [Google Scholar](#)

75. Sarah Warren

[View author publications](#)

You can also search for this author in [PubMed](#) [Google Scholar](#)

76. Shuting Zhang

[View author publications](#)

You can also search for this author in [PubMed](#) [Google Scholar](#)

77. Daniel R. Zollinger

[View author publications](#)

You can also search for this author in [PubMed](#) [Google Scholar](#)

78. Lissa Cosimi

[View author publications](#)

You can also search for this author in [PubMed](#) [Google Scholar](#)

79. Rajat M. Gupta

[View author publications](#)

You can also search for this author in [PubMed](#) [Google Scholar](#)

80. Nir Hacohen

[View author publications](#)

You can also search for this author in [PubMed](#) [Google Scholar](#)

81. Hanina Hibshoosh

[View author publications](#)

You can also search for this author in [PubMed](#) [Google Scholar](#)

82. Winston Hide

[View author publications](#)

You can also search for this author in [PubMed](#) [Google Scholar](#)

83. Alkes L. Price

[View author publications](#)

You can also search for this author in [PubMed](#) [Google Scholar](#)

84. Jayaraj Rajagopal

[View author publications](#)

You can also search for this author in [PubMed](#) [Google Scholar](#)

85. Purushothama Rao Tata

[View author publications](#)

You can also search for this author in [PubMed](#) [Google Scholar](#)

86. Stefan Riedel

[View author publications](#)

You can also search for this author in [PubMed](#) [Google Scholar](#)

87. Gyongyi Szabo

[View author publications](#)

You can also search for this author in [PubMed](#) [Google Scholar](#)

88. Timothy L. Tickle

[View author publications](#)

You can also search for this author in [PubMed](#) [Google Scholar](#)

89. Patrick T. Ellinor

[View author publications](#)

You can also search for this author in [PubMed](#) [Google Scholar](#)

90. Deborah Hung

[View author publications](#)

You can also search for this author in [PubMed](#) [Google Scholar](#)

91. Pardis C. Sabeti

[View author publications](#)

You can also search for this author in [PubMed](#) [Google Scholar](#)

92. Richard Novak

[View author publications](#)

You can also search for this author in [PubMed](#) [Google Scholar](#)

93. Robert Rogers

[View author publications](#)

You can also search for this author in [PubMed](#) [Google Scholar](#)

94. Donald E. Ingber

[View author publications](#)

You can also search for this author in [PubMed](#) [Google Scholar](#)

95. Z. Gordon Jiang

[View author publications](#)

You can also search for this author in [PubMed](#) [Google Scholar](#)

96. Dejan Juric

[View author publications](#)

You can also search for this author in [PubMed](#) [Google Scholar](#)

97. Mehrtash Babadi

[View author publications](#)

You can also search for this author in [PubMed](#) [Google Scholar](#)

98. Samouil L. Farhi

[View author publications](#)

You can also search for this author in [PubMed](#) [Google Scholar](#)

99. Benjamin Izar

[View author publications](#)

You can also search for this author in [PubMed](#) [Google Scholar](#)

100. James R. Stone

[View author publications](#)

You can also search for this author in [PubMed](#) [Google Scholar](#)

101. Ioannis S. Vlachos

[View author publications](#)

You can also search for this author in [PubMed](#) [Google Scholar](#)

102. Isaac H. Solomon

[View author publications](#)

You can also search for this author in [PubMed](#) [Google Scholar](#)

103. Orr Ashenberg

[View author publications](#)

You can also search for this author in [PubMed](#) [Google Scholar](#)

104. Caroline B. M. Porter

[View author publications](#)

You can also search for this author in [PubMed](#) [Google Scholar](#)

105. Bo Li

[View author publications](#)

You can also search for this author in [PubMed](#) [Google Scholar](#)

106. Alex K. Shalek

[View author publications](#)

You can also search for this author in [PubMed](#) [Google Scholar](#)

107. Alexandra-Chloé Villani

[View author publications](#)

You can also search for this author in [PubMed](#) [Google Scholar](#)

108. Orit Rozenblatt-Rosen
[View author publications](#)

You can also search for this author in [PubMed](#) [Google Scholar](#)

109. Aviv Regev
[View author publications](#)

You can also search for this author in [PubMed](#) [Google Scholar](#)

Contributions

A.K.S., A.-C.V., I.S.V., Z.G.J., O.R.-R. and A.R. conceived and led the study. These authors contributed equally as co-second authors: Z.B.-A., N.B., A.G., J.G., J.C.M., I.K., E.N., P.N., Y.V.P., S.S.R., S.N., L.T.-Y.T., K.J.S., M.Su., V.M.T., S.K.V., Y.W. T.M.D., C.G.K.Z., Å.S., D.A. designed protocols and carried out experiments together with D.P., Z.B.-A., V.M.T., A.S., S.Z., J.G., J.H., E.N., M.Su., C.M., L.T., A.E., D.Pa., L.P., J.C.M., L.A.-Z. C.B.M.P., C.G.K.Z., O.A., R.N., G.H., K.J., K.S., B.L., Y.Y., S.F., A.S., P.N., Y.P.J., P.N., T.He., J.R., W.H., I.S.V., T.M.D. and J.B. designed and performed computational analysis. M.B., N.B., J.G., Y.W., R.G., S.S.R., H.M., P.S., A.W., C.M., M.L.-G., T.H., D.T.M., S.W., D.R.Z., E.R., M.R., E.M., R.F., P.Di., A.G., C.Pe. and M.N. provided input to and assisted with computational analysis. K.J., K.D., A.G., J.E., S.G., A.R. and A.P. contributed methods and performed integrated analysis for GWAS. P.R.T., D.T.M., Z.G.J., Y.P., G.S., S.N., S.R. and J.R. provided clinical and biological expertise. D.F., D.J., D.E.M., C.P., S.K.V., E.K. and J.S. provided clinical expertise, performed sample acquisition and/or administrative coordination at MGH. J.H., R.R., R.N., O.R.B., Z.G.J., Y.P. and D.I. provided clinical expertise, performed sample acquisition and/or administrative coordination at BIDMC. I.H.S., D.A., L.C., J.G., R.P., M.Si., provided clinical expertise, performed sample acquisition and/or administrative coordination at BWH. I.G., H.H. and B.I. provided clinical expertise, performed sample acquisition and/or administrative coordination at CUIMC/NYP. P.D., D.P., J.J-V. and J.B. helped with sample coordination and sample receipt at the Broad Institute. N.B and S.R. performed bulk RNA-Seq deconvolution analysis. E.N., M.R. and K.S. performed viral

qPCR, whole-genome sequencing and phylogenetic analyses. M.S. provided input for sc/snRNA-Seq experiments and protocols. J.J.-V., E.T., O.R.R. and A.-C.V. managed the study and tissue acquisition. T.L.T. contributed computational expertise and advice. T.M.D., C.B.M.P., C.G.K.Z., G.H., R.N., K.J., O.A., B.L., Z.G.J., I.S.V., Y.Y., S.F., A.S., D.T.M., A.K.S., A.-C.V., O.R.-R. and A.R. wrote the manuscript, with input from all authors. D.H., P.C.S., N.H. and P.T.E. supervised research.

Corresponding authors

Correspondence to [Ioannis S. Vlachos](#) or [Alex K. Shalek](#) or [Alexandra-Chloé Villani](#) or [Orit Rozenblatt-Rosen](#) or [Aviv Regev](#).

Ethics declarations

Competing interests

A.R. is a co-founder and equity holder of Celsius Therapeutics, an equity holder in Immunitas, and was an SAB member of ThermoFisher Scientific, Syros Pharmaceuticals, Neogene Therapeutics and Asimov until 31 July 2020. Since 1 August 2020, A.R. has been an employee of Genentech. O.R.-R. is an employee of Genentech as of 19 October 2020. P.Di., R.F., E.M.M., M.Ro., E.H.R., L.P., T.He., J.R., J.B. and S.W. are employees and stockholders at Nanostring Technologies Inc. D.R.Z. is a former employee and stockholder at NanoString Technologies. N.H. holds equity in BioNTech and Related Sciences. T.H. is an employee and stockholder of Prime Medicine as of 13 October 2020. G.H. is an employee of Genentech as of 16 November 2020. R.N. is a founder, shareholder, and member of the board at Rhinostics Inc. P.C.S. is a co-founder and shareholder of Sherlock Biosciences, and a Board member and shareholder of Danaher Corporation. A.K.S. reports compensation for consulting and/or SAB membership from Honeycomb Biotechnologies, Cellarity, Repertoire Immune Medicines, Ochre Bio, Third Rock Ventures and Dahlia Biosciences. Z.G.J. reports grant support from Gilead Science, Pfizer and compensation for consulting from Olix Pharmaceuticals. Y.V.P. reports grant support from Enanta Pharmaceuticals, CymaBay Therapeutics, Morphic Therapeutic; consulting

and/or SAB in Ambys Medicines, Morphic Therapeutics, Enveda Therapeutics, BridgeBio Pharma, as well as being an Editor of *American Journal of Physiology-Gastrointestinal and Liver Physiology*. G.S. reports consultant service in Alnylam Pharmaceuticals, Merck, Generon, Glympse Bio, Inc., Mayday Foundation, Novartis Pharmaceuticals, Quest Diagnostics, Surrozen, Terra Firma, Zomagen Bioscience, Pandion Therapeutics, Inc., Durect Corporation; royalty from UpToDate Inc. and Editor service for *Hepatology Communications*. P.R.T. receives consulting fees from Cellarity Inc. and Surrozen Inc. for work not related to this manuscript. P.T.E. is supported by a grant from Bayer AG to the Broad Institute focused on the genetics and therapeutics of cardiovascular diseases. P.T.E. has also served on advisory boards or consulted for Bayer AG, Quest Diagnostics, MyoKardia and Novartis. B.I. is a consultant for Merck and Volastra Therapeutics. All other authors declare no competing interests.

Additional information

Peer review information *Nature* thanks Christopher Mason, Michael Matthay and the other, anonymous, reviewer(s) for their contribution to the peer review of this work.

Publisher's note Springer Nature remains neutral with regard to jurisdictional claims in published maps and institutional affiliations.

Extended data figures and tables

Extended Data Fig. 1 A COVID-19 autopsy cohort, data quality and ambient RNA removal for a single-cell/nucleus lung atlas.

a, COVID-19 cohort overview. IMV, intermittent mandatory ventilation days; PMI, post-mortem interval; S/s, time from symptom start to death in days. **b–d**, Comparison of cell composition by scRNA-Seq and snRNA-Seq in matched samples. Proportion of cells (*x* axis) of each type (colour code) in sc/snRNA-Seq samples from the same three donors (D3, D8, D12). **e–h**, Cellbender remove-background on a single sample (D1). **e**, CellBender improves cell clustering and expression specificity by removing ambient RNA and empty (non-cell) droplets. UMAP plot of snRNA-Seq profiles (dots) either before (left) or after (right) CellBender processing, coloured by clusters, with CellBender-determined empty droplets in black ($k = 2,508$ droplets removed, $k = 10,687$ cells remaining). **f, g**, CellBender improves specificity of individual genes and cell type signatures. UMAP embedding of single nucleus profiles before CellBender (left) and after CellBender (right) processing, coloured by expression of the surfactant protein gene *SFTPA1* (**f**) or signature score (SCANPY⁵² score_genes function, colour bar) for gene sets specific to lung AT2 (**g**) cells. Colour bar saturation chosen to emphasize low expression. **h**, Improved specificity of surfactant gene expression with CellBender (same sample). Expression level (log (average unique molecular identifier (UMI) count per cell), colour) and percentage of cells with non-zero expression (dot size) of surfactant genes (columns) across cell clusters (rows) before (left) and after (right) CellBender processing. Also shown, for comparison, are the results of an alternative method, DecontX (middle).

[Source data](#)

Extended Data Fig. 2 Quality control and annotation in the COVID-19 lung cell atlas.

a–d, Quality-control metrics for 24 lung samples ($n = 16$ donors). Number of cells or nuclei (**a**, *y* axis) and distributions (median and first and third quartiles) of number of UMIs per cell or nucleus (**b**, *y* axis), number of genes per cell/nucleus (**c**, *y* axis) and fraction of mitochondrial genes per

cell/nucleus (**d**, *y* axis) across the samples (*x* axis) in the lung atlas. scRNA-Seq samples are labelled by a grey circle. **e–g**, Cross-sample integration corrects batch effects. **e**, UMAP (as in Fig. 2a) of 106,792 sc/snRNA-Seq profiles after Harmony⁵³ correction ([Supplementary Methods](#)) coloured by sample ID. **f, g**, Donors and processing protocols across clusters. Number of cells (*y* axis) from different donors (**f**) or processing protocols (**g**) in each Leiden cluster (*x* axis). **h**, Cross validation of automatic annotation.

Percentage of cells (colour bar) annotated in a class by Schiller et al.⁵⁴ that we predict for each class (columns). **i**, Identification of main lineage annotations by manual annotation. UMAP of 106,792 sc/snRNA-Seq profiles after Harmony⁵³ correction (as in Fig. 2a) coloured by manual annotation done in subclustering of each lineage. Dashed lines: chosen compartments for subclustering. **j–n**, Refined annotation of cell subsets within lineages. UMAP embeddings of each selected cell lineage with cells coloured by manually annotated subclusters. Colour legends highlight highly expressed marker genes for select subsets. **j**, myeloid cells ($k = 24,417$ cells/nuclei); **k**, B and plasma cells ($k = 1,693$); **l**, T and NK cells ($k = 9,950$); **m**, endothelial cells ($k = 20,366$); and **n**, fibroblast ($k = 20,925$).

[Source data](#)

[Extended Data Fig. 3 Bulk RNA-Seq deconvolution and comparison of automatic and manual annotations in the COVID-19 lung cell atlas.](#)

a, b, Deconvolution of bulk RNA-Seq libraries from adjacent lung tissue. **a**, Mean proportion (*y* axis, error bars = s.d. estimates from bulk RNA-Seq deconvolution (hatched bars; from MuSiC⁵⁵) and from sc/snRNA-Seq (filled bars) for each of 11 cell subsets (*x* axis) in each of 16 bulk RNA-Seq lung samples (panels) from 10 random samples of 10,000 cells each. **b**, Robustness of cell proportion estimates to the number of single cells sampled for the reference data. Mean proportion (*y* axis, from MuSiC) estimates for each of 11 cell subsets (colour dots) in each of 16 bulk RNA-Seq lung samples (panels) when using three independent samples of 1,000–10,000 cells from the single-cell reference (*x* axis). **c–e**, Agreement between

automated and manual annotations. **c**, High consistency between automatic and manual annotations. The proportion (colour intensity) and number (dot size) of cells with a given predicted annotation (rows) in each manual annotation category (columns). **d, e**, UMAP embedding of myeloid ($k = 24,417$ cells or nuclei) (**d**) and T and NK ($k = 9,950$ cells); (**e**) cell profiles coloured by manually annotated subclusters (left) or automated predictions (right).

[Source data](#)

Extended Data Fig. 4 Manual annotation in the COVID-19 lung cell atlas.

a, b, Identification of main immune lineage annotations. **a**, UMAP of 106,792 sc/snRNA-Seq profiles after Harmony correction (as in Fig. [2a](#)) coloured by expression of genes (colour bar, genes listed below) used to separate immune cell sub-lineages ([Supplementary Methods](#)). **b**, Differentially expressed (DE) genes between subclusters within each lineage. Expression (colour bar) of genes (rows) that are differentially expressed ([Supplementary Methods](#)) across the subclusters (columns) within each compartment. DE genes shown are a union of the following: (i) top 10 DE genes between clusters, (ii) DE genes above an AUC of 0.8 and 0.75 for B/Plasma cells, (iii) pseudo-bulk DE genes above a log(fold change) threshold (thresholds: endothelial = 4.2, T/NK = 3, myeloid = 4, B/plasma = 2) (label on top). **c**, Batch correction within lineage. Fraction of cells/nuclei (y axis) from different processing protocols (left) or different donors (right, $n = 17$) in each subcluster (x axis) after batch correction with Harmony^{[53](#)} within each lineage.

[Source data](#)

Extended Data Fig. 5 Cell-intrinsic programs and epithelial regenerative cell states in the COVID-19 lung cell atlas.

a, b, Differences in cell composition across donors. Percentage of cells (y axis) from each myeloid subset (legend) in each donor (x axis). **b**, Percentage of cells (y axis) from each main lineage (legend) in each donor

(*x* axis), rank ordered by proportion of epithelial cells (blue). **c**, Myeloid, endothelial and pneumocyte cells show substantial changes in cell intrinsic expression profiles in COVID-19 lung. \log_2 (fold change) (*y* axis) between COVID-19 and healthy lung for each elevated gene (dot) in each cell subset (*x* axis, by automatic annotation). Black bars, number of genes with significantly increased expression (adjusted $P < 7.5 \times 10^{-6}$). Computed using a single cell-based differential expression model applied to a meta-differential expression analysis between COVID-19 and healthy samples across 14 studies (see [Supplementary Methods](#)). **d**, PATS and IBPLP cells in COVID-19 lung. UMAP embeddings of 1,550 *KRT8*⁺ PATS-expressing cells (top) or of 1,394 airway epithelial cells (bottom) coloured by IPBLP cells or basal cells (orange, leftmost panels) or characteristic markers (purple, remaining panels).

[Source data](#)

[**Extended Data Fig. 6 SARS-CoV-2-RNA⁺ cells distinguished by sc/snRNA-Seq.**](#)

a, Detection of SARS-CoV-2 UMIs from sc/snRNA-Seq data. SARS-CoV-2 UMIs from all cell barcodes (top) and after ambient correction (second from top). Number (second from bottom) and percentage (bottom) of SARS-CoV-2 RNA⁺ cells after ambient correction ($m = 24$ specimens). **b**, **c**, Effect of ambient RNA on SARS-CoV-2 RNA⁺ detection. Number of SARS-CoV-2 aligning UMI per cell barcode (CB) (*y* axis) in healthy lung (**b**, black), in vitro SARS-CoV-2 infected human bronchial epithelial cells (HBEC)⁵⁶ (**b**, blue) or lung samples from COVID-19 donors at autopsy either with CB with high-quality capture of human mRNA (**b**, red) or after removal of cells whose viral alignments were attributed to ambient contamination (**c**, [Supplementary Methods](#)). **d**, Variation in SARS-CoV-RNA⁺ cells across donors. Percentage of cells (*y* axis) assigned as SARS-CoV-2 RNA⁻ (white), SARS-CoV-2 RNA⁺ (red) or SARS-CoV-2 ambient (grey, [Supplementary Methods](#)) across the donors (*x* axis), sorted by proportion of SARS-CoV-RNA⁺ cells. **e–i**, Viral RNA detection does not correlate with cell quality metrics. **e–h**, Number of SARS-CoV-2 UMIs (before ambient viral correction) for each cell (*y* axis) versus either number

of SARS-CoV-2 genes for that cell (**e**, *x* axis), number of human (GRCh38) genes per cell (**f**, *x* axis), number of human (GRCh38) UMI per cell (**g**, *x* axis) or percentage of human (GRCh38) mitochondrial UMIs per cell (**h**, *x* axis). **i**, Number of retained high-quality cells (*x* axis) and number of SARS-CoV-2 RNA⁺ cells (*y* axis) in each sample (dots) after correction for ambient viral reads. Pearson's *r* = 0.07, two-sided *P* = 0.73. **j–l**, Agreement in viral RNA detection between qPCR and sn/scRNA-Seq. Number of SARS-CoV-2 copies measured by CDC N1 qPCR on bulk RNA extracted from matched tissue samples (*x* axis) and the number of SARS-CoV-2 aligning UMI (*y* axis) for each sample (dot) from all reads (**j**, *P* < 0.0001, two-sided), all reads from high-quality cell barcodes (**k**, *P* < 0.0001), and after viral ambient RNA correction (**l**, *P* = 0.0042). Spearman's ρ reported, two-sided test. **m**, Genetic diversity of SARS-CoV-2. Maximum likelihood phylogenetic tree of 772 SARS-CoV-2 genomes from cases in Massachusetts between January and May 2020. Orange points, donors in this cohort. **n**, Specificity of SARS-CoV-2 infection. $\log_{10}(1 + \text{reads})$ in each donor (columns) assigned to different viruses (rows) by metagenomic classification using Kraken2 from bulk RNA-Seq. Asterisks denote targeted capture. **o–u**, Relation between SARS-CoV-2 RNA and different cell types. Number of SARS-CoV-2 aligning UMIs in each (including all CB) and the proportion of epithelial (**o**), mast (**p**), macrophage *VCAN*^{high}*FCN1*^{high} (**q**), macrophages *CD163*^{high}*MERTK*^{high} (**r**), macrophages *LDB2*^{high}*OSMR*^{high}*YAP1*^{high} (**s**), venular endothelial (**t**) or capillary aerocytes (**u**) cells in these samples (*x* axes). Pearson's *r* denoted in the upper left corner with significance after Bonferroni correction (*P*). **v**, Effect of viral load on bulk RNA profiles. Significance ($-\log_{10}(P)$, *y* axis) and magnitude ($\log_2(\text{fold change})$, *x* axis) of differential expression of each gene (dots) between three donors with highest viral load and six donors with lowest or undetectable viral load profiled by bulk RNA-Seq. Red points, FDR < 0.05. **w–y**, Distribution of SARS-CoV-2 RNA⁺ cells across cell types and subsets. Number of SARS-CoV-2 RNA⁺ cells (*y* axis) from each donor (colour) across major categories (**w**, *x* axis), myeloid subsets (**x**, inflammatory monocytes: 40 cells, five donors; *LDB2*^{high}*OSMR*^{high}*YAP1*^{high} macrophages: 27 cells, five donors; *x* axis), or endothelial subsets (**y**, capillary endothelial cells: 16 cells, four donors; lymphatic endothelial cells: nine cells, three donors; *x* axis).

Source data

Extended Data Fig. 7 Donor-specific enrichment of SARS-CoV-2 RNA⁺ cells and host responses to viral RNA.

a–d, SARS-CoV-2 RNA⁺ cells are enriched in specific lineages and subtypes. **a, c**, UMAP embeddings of either myeloid cells (**a**), or endothelial cells (**c**) from seven donors containing any SARS-CoV-2 RNA⁺ cell, and coloured by viral enrichment score (colour bar; red, stronger enrichment) and by SARS-CoV-2 RNA⁺ cells (black points). **b, d**, Number of SARS-CoV-2 RNA⁺ cells (*y* axis) per cell type/subset (*x* axis) in myeloid (**b**) or endothelial (**d**) subsets. Bar colour, FDR (dark blue, higher significance, [Supplementary Methods](#); *FDR < 0.05). **e–h**, Variation across donors. **e–g**, UMAP embeddings of sc/snRNA-Seq profiles from each of seven donors containing any SARS-CoV-2 RNA⁺ cell (columns), coloured by major cell categories (**e**), expression of SARS-CoV-2 entry factors (**f**) or SARS-CoV-2 RNA enrichment per cluster (**g**, red/blue colour bar; red, high enrichment; black points, SARS-CoV-2 RNA⁺ cells). **h**, Number of SARS-CoV-2 RNA⁺ cells (*y* axis) across major cell types (*x* axis) from each of seven donors containing any SARS-CoV-2 RNA⁺ cell (columns). Bar colour, FDR (dark blue, higher significance). *FDR < 0.05. **i, j**, Normalized enrichment score (bars, right *y* axis) and significance (points, FDR, left *y* axis) (by GSEA^{39,40}, [Supplementary Methods](#)) of different functional gene sets (*x* axis) in genes upregulated in SARS-CoV-2 RNA⁺ epithelial (**i**) or myeloid (**j**) cells. **k**, Expression of SARS-CoV-2 genomic features (log-normalized UMI counts; rows) across SARS-CoV-2 RNA⁺ (*k* = 158 cells) and SARS-CoV-2 RNA⁻ (*k* = 790) myeloid cells (columns). **l, m**, Distribution of normalized expression levels (*y* axis) for select significantly differentially expressed genes between SARS-CoV-2 RNA⁻ and SARS-CoV-2 RNA⁺ cells from all myeloid cells or *CD14*^{high}*CD16*^{high} inflammatory monocytes. DGE, differential gene expression.

Source data

Extended Data Fig. 8 NanoString GeoMx experiment design and analysis.

a, Overview of spatial profiling experiments. **b**, Distribution of sequencing saturation (*y* axis, %) for WTA and CTA AOIs (*x* axis). **c**, **d**, SARS-CoV-2 signature score (*y* axis) for each WTA (**c**) and CTA (**d**) AOI (dots) from each donor (*x* axis). **e**, Overlap of WTA and CTA genes. **f**, **g**, Agreement between WTA and CTA. **f**, Distribution (box, interquartile range; white point, median; violin range, min–max) of Pearson correlation coefficients (*y* axis) between WTA and CTA profiles (for common genes across 296 AOIs). **g**, Pearson correlation coefficient (*y* axis) of WTA and CTA common genes for each AOI pair (dot) from each donor (*x* axis), sorted by distance between WTA and CTA sections (blue, 10 mm; orange, 20 mm; green, 40 mm). **h**, Cell composition differences between PanCK⁺ and PanCK⁻ alveolar AOIs and between AOIs from COVID-19 ($n = 9, 161$ AOIs) and healthy (D22–24, 40 AOIs) lungs. Expression scores (colour bar) of cell type signatures (rows) in PanCK⁺ (left) and PanCK⁻ (right) alveolar AOIs (columns) in CTA data from different donors (top colour bar). **i–k**, Differential gene expression in COVID-19 versus healthy lung. Left: significance ($-\log_{10}(P)$, *y* axis) and magnitude ($\log_2(\text{fold change})$, *x* axis) of differential expression of each gene (dots) in WTA for PanCK⁻ (**i**, 112 COVID-19 versus 20 healthy), and in CTA for PanCK⁺ (**j**, 69 COVID-19 versus 18 healthy) and PanCK⁻ (**k**, 92 COVID-19 versus 22 healthy) alveoli. Horizontal dashed line, FDR = 0.05; vertical dashed lines, $|\log_2(\text{fold change})| = 2$. Right: significance ($-\log_{10}(q)$) of enrichment (permutation test) of different pathways (rows). **l**, **m**, Changes in gene expression in SARS-CoV-2 high versus low AOIs within COVID-19 lungs in WTA data. **l**, PanCK⁻ alveolar AOIs (dots) rank ordered by their SARS-CoV-2 signature score (*y* axis) in WTA data, and partitioned to high (red), medium (grey) and low (blue) SARS-CoV-2 AOIs. **m**, Significance ($-\log_{10}(P)$, *y* axis) and magnitude ($\log_2(\text{fold change})$, *x* axis) of differential expression of each gene (dots) in WTA data between SARS-CoV-2 high and low AOIs for PanCK⁻ alveoli (AOIs: 11 high, six medium, 95 low). Horizontal dashed line, FDR = 0.05.

[Source data](#)

Extended Data Fig. 9 GeoMx WTA DSP analysis of lung biopsy samples reveals region- and inflammation-specific expression programs.

a, Region selection. Serial sections of lung biopsy samples (five donors, D13–17; image depicts serial sections of D14) processed with GeoMx WTA DSP with four-colour staining (DNA, CD45, CD68, PanCK), RNAscope with probes against (SARS-CoV-2 *S* gene (used to derive semiquantitative viral load scores), *ACE2*, *TMPRSS2*), H&E staining and immunohistochemistry (IHC) with anti-SARS-CoV-2 S-protein. Scale bar, 100 µm. **b–d**, Region- and inflammation-specific expression programs. **b**, The first two principal components (PCs, *x* and *y* axes) from lung ROI gene expression profiles from donors D13–17, spanning normal-appearing alveoli (green; D14 = 6 AOIs, D15 = 2 AOIs, D16 = 5 AOIs, D17 = 4 AOIs); inflamed alveoli (magenta; D13 = 14 AOIs, D14 = 18 AOIs, D15 = 7 AOIs, D16 = 3 AOIs, D17 = 8 AOIs); bronchial epithelium (blue; D14 = 2 AOIs, D15 = 1 AOI, D16 = 2 AOIs, D17 = 3 AOIs) and arterial blood vessels (black; D13 = 2 AOIs, D15 = 3 AOIs). **c**, GSEA score (circle size, legend) of the enrichment of the IFN γ pathway in each normal-appearing (green; 6 AOIs) and inflamed (magenta; 18 AOIs) alveolar AOIs (dot) from the section of donor D14 (in **a**), placed in their respective physical coordinates on the tissue section (as in **a**). **d**, Expression (colour bar, log₂(counts per million)) of IFN γ pathway genes (rows) from normal-appearing (green, n = 6) and inflamed (magenta, n = 18) alveoli AOIs (columns) from D14 lung biopsy.

[Source data](#)

Extended Data Fig. 10 A single-nucleus atlas of heart, kidney and liver COVID-19 tissues.

a–c, COVID-19 heart cell atlas. UMAP embedding of 40,880 heart nuclei (dots) (n = 18 donors, m = 19 specimens) coloured by Leiden resolution 1.5 clustering with manual post hoc annotations (**a**) or donors (**c**). **b**.

Proportions of cell types (*y* axis) in each sample. **d–f**, COVID-19 kidney cell atlas. UMAP embedding of 33,872 kidney nuclei (dots) ($n = 16$, $m = 16$) coloured by clustering with manual post hoc annotations (**d**) or donors (**f**). **e**, Proportion of cells (*y* axis) in each sample. **g–i**, COVID-19 liver cell atlas. **g**, **i**, UMAP embedding of 47,001 liver nuclei (dots) ($n = 15$, $m = 16$), coloured by clustering with manual post hoc annotations (**g**) or donors (**i**). **h**, Proportions of cell types (*y* axis) in each sample. **j–l**, Automatic annotations. UMAP embeddings, coloured by predicted cell type labels by automatic annotation for heart (**j**), kidney (**k**) and liver (**l**).

[Source data](#)

Extended Data Fig. 11 Entry factors in heart, kidney and liver COVID-19 tissues and differential gene expression in heart cell atlas.

a–c, SARS-CoV-2 entry factors are expressed in kidney, liver and heart cells. Average expression (dot colour) and fraction of expressing cells (colour, size) of SARS-CoV-2 entry factors (rows) across cell subsets (columns) in the kidney (**a**), liver (**b**) and heart (**c**). **d–k**, Genes and pathways differentially expressed between COVID-19 and healthy heart cells. **d**, log mean expression per cell (dot colour) and fraction of expressing cells (dot size) across cell types from healthy or COVID-19 heart (rows) for select genes (columns) that are differentially expressed between COVID-19 and healthy cells. **e**, Proportions of each cell type for COVID-19 ($n = 15$) and healthy ($n = 28$, two studies) samples (boxplots: middle line, mean; box bounds, first and third quartiles; whiskers, $1.5 \times$ the interquartile range; minima, smallest observed proportion; maxima, highest observed proportion). **f**, UMAP embedding of integrated COVID-19 and healthy snRNA-Seq profiles (dots) coloured by major cell types. Plot limited to a subset of 151,373 high-quality cells for visualization purposes. **g–i**, Cell-type-specific differentially expressed genes in COVID-19 versus healthy nuclei. Differential expression ($\log_2(\text{fold change})$, x axis), and associated significance ($-\log_{10}(P)$, y axis; [Supplementary Methods](#)) for each gene (dot) between COVID-19 and healthy nuclei of cardiomyocytes (**g**), pericytes (**h**) and fibroblasts (**i**). Dashed line, FDR = 0.01. **j, k**, UMAP embedding of the meta-analysis atlas (as in **f**) but showing only COVID-19 (top) or healthy (bottom) nuclei profiles (dots) coloured by expression of *PLCG2* (**j**) or *AFDN* (**k**). **l**, Low levels of viral UMIs in heart, liver and kidney, compared with lung. Cumulative viral read counts as a function of droplet UMI count. In lung (red) most virus-positive droplets are empty droplets (total UMI count approximately 100) with some virus-positive droplets that contain nuclei (UMI count > approximately 1,000), but in heart (green), liver (blue) and kidney (orange), most of the ‘virus-positive’ droplets have fewer than ten total UMI counts, indicating that these reads are not trustworthy.

Source data

Extended Data Fig. 12 Expression of GWAS curated genes across lung, heart, liver and kidney atlases.

a–d, Mean expression (dot colour, $\log(\text{TP10K} + 1)$) and proportion of expressing cells (dot size) for each of 26 curated GWAS implicated genes (columns) in each cell subset (rows) for lung (**a**), heart (**b**), liver (**c**) and kidney (**d**) COVID-19 autopsy atlases. Results only reported for genes with expression in at least one cell subset in the underlying tissue. Some GWAS genes have higher expression in the lung compared with the other three tissues. **e, f**, Mean expression (**e**, z -score relative to all other cell types, colour bar) or differential expression (**f**, z -score of DE analysis of expression in COVID-19 versus healthy cells of the same type) of 25 out of 26 GWAS implicated genes (rows) from six genomic loci associated with COVID-19 (based on summary statistics data from COVID-19 HGI meta analysis⁴⁵ across lung cell types (columns). *ABO* was not considered as it was not reliably recovered in scRNA-Seq data. **g, h**, Cell type and disease progression gene programs in the lung (**g**), liver and kidney (**h**) that contribute to heritability of COVID-19 severity. Magnitude (circle size, E score) and significance (colour, $-\log_{10}(P)$) of the enrichment of cell type programs and cell-type-specific disease programs (columns) that were significantly enriched for COVID-19 or severe COVID-19 phenotypes (rows). All results are conditional on 86 baseline-LDv2.1 model annotations. **i**, Nomination of single best candidate genes at unresolved GWAS significant loci by aggregating gene level information across program classes and cell types. Significance ($-\log_{10}(P)$, *y* axis) of GWAS association signal at locus (*x* axis). Blue boxes, significantly associated loci⁴⁵ at a genome-wide significance level (purple horizontal bar). **j**, Schematic summarizing the key findings and contributions of this study.

Source data

Supplementary information

Supplementary Information

This file contains the Supplementary Methods and full descriptions for Supplementary Tables 1-14.

Reporting Summary

Supplementary Table 1

Clinical meta-data for all donors and extended sample information – see Supplementary Information document for full legend.

Supplementary Table 2

Studies included for building tissue meta-atlases and lung classifier coefficients – see Supplementary Information document for full legend.

Supplementary Table 3

Differentially expressed genes within KRT8+/PATS cell subsets and between the IPBLP and basal cell subsets – see Supplementary Information document for full legend.

Supplementary Table 4

Differentially expressed genes between healthy vs. COVID-19 lung (sc/snRNA-Seq) and between lung biopsies high vs. low/no viral load (bulkRNA-Seq) – see Supplementary Information document for full legend.

Supplementary Table 5

Analyses of SARS-CoV-2 RNA+ cells by cell type and viral sequencing – see Supplementary Information document for full legend.

Supplementary Table 6

Spatial assay probe list and DE genes between COVID-19 and healthy donors – see Supplementary Information document for full legend.

Supplementary Table 7

Differential expression results of snRNA-Seq based on the reconciled annotation – see Supplementary Information document for full legend.

Supplementary Table 8

Cell type markers used for cell type deconvolution of WTA and CTA data in lung spatial data – see Supplementary Information document for full legend.

Supplementary Table 9

Spatial differentially expressed genes in SARS-CoV-2 high *vs.* low and inflamed *vs.* non-inflamed – see Supplementary Information document for full legend.

Supplementary Table 10

COVID-19 heart differential expression analysis and GSEA results – see Supplementary Information document for full legend.

Supplementary Table 11

COVID-19 GWAS gene list, differential expression analysis and Sc-linker heritability results – see Supplementary Information document for full legend.

Supplementary Table 12

Gene signatures used for high-level manual annotation of COVID-19 lung cells.

Supplementary Table 13

List of differential gene expression between sub-clusters of myeloid cells, T and NK cells, B and plasma cells, and endothelial cells in COVID-19 lung, as computed by Pegasus – see Supplementary Information document for full legend.

Supplementary Table 14

List of top genes for LIGER factors of epithelial and fibroblast cells in COVID-19 lung – see Supplementary Information document for full legend.

Source data

Source Data Extended Data Fig. 1

Source Data Extended Data Fig. 2

Source Data Extended Data Fig. 3

Source Data Extended Data Fig. 4

Source Data Extended Data Fig. 5

Source Data Extended Data Fig. 6

Source Data Extended Data Fig. 7

Source Data Extended Data Fig. 8

Source Data Extended Data Fig. 9

Source Data Extended Data Fig. 10

Source Data Extended Data Fig. 11

Source Data Extended Data Fig. 12

Rights and permissions

[Reprints and Permissions](#)

About this article



Check for
updates

Cite this article

Delorey, T.M., Ziegler, C.G.K., Heimberg, G. *et al.* COVID-19 tissue atlases reveal SARS-CoV-2 pathology and cellular targets. *Nature* **595**, 107–113 (2021). <https://doi.org/10.1038/s41586-021-03570-8>

[Download citation](#)

- Received: 16 November 2020
- Accepted: 19 April 2021
- Published: 29 April 2021
- Issue Date: 01 July 2021
- DOI: <https://doi.org/10.1038/s41586-021-03570-8>

Further reading

- [Telemedicine platform COVIDREHAB for remote rehabilitation of patients after COVID-19](#)

- Ilmira R. Gilmutdinova
- , Vasiliy A. Kolyshenkov
- , Kristina A. Lapickaya
- , Anastasiya S. Trepova
- , Valeriia A. Vasileva
- , Andrei N. Prosvirnin
- , Larisa A. Marchenkova
- , Kirill V. Terentev
- , Maxim Y. Yakovlev
- , Andrey P. Rachin
- , Anatoliy D. Fesyun
- & Igor V. Reverchuk

European Journal of Translational Myology (2021)

- **Single-cell atlases dissect tissue destruction by SARS-CoV-2**

- Alexandra Flemming

Nature Reviews Immunology (2021)

- **A molecular single-cell lung atlas of lethal COVID-19**

- Johannes C. Melms
- , Jana Biermann
- , Huachao Huang
- , Yiping Wang
- , Ajay Nair
- , Somnath Tagore
- , Igor Katsyv
- , André F. Rendeiro
- , Amit Dipak Amin
- , Denis Schapiro
- , Chris J. Frangieh
- , Adrienne M. Luoma
- , Aveline Filliol

- , Yinshan Fang
- , Hiranmayi Ravichandran
- , Mariano G. Clausi
- , George A. Alba
- , Meri Rogava
- , Sean W. Chen
- , Patricia Ho
- , Daniel T. Montoro
- , Adam E. Kornberg
- , Arnold S. Han
- , Mathieu F. Bakhoum
- , Niroshana Anandasabapathy
- , Mayte Suárez-Fariñas
- , Samuel F. Bakhoum
- , Yaron Bram
- , Alain Borczuk
- , Xinzhen V. Guo
- , Jay H. Lefkowitch
- , Charles Marboe
- , Stephen M. Lagana
- , Armando Del Portillo
- , Emmanuel Zorn
- , Glen S. Markowitz
- , Robert F. Schwabe
- , Robert E. Schwartz
- , Olivier Elemento
- , Anjali Saqi
- , Hanina Hibshoosh
- , Jianwen Que
- & Benjamin Izar

Nature (2021)

[Download PDF](#)

Associated Content

Single-cell atlases dissect tissue destruction by SARS-CoV-2

- Alexandra Flemming

Advertisement

This article was downloaded by **calibre** from <https://www.nature.com/articles/s41586-021-03570-8>

| [Section menu](#) | [Main menu](#) |

A molecular single-cell lung atlas of lethal COVID-19

[Download PDF](#)

- Article
- [Published: 29 April 2021](#)

A molecular single-cell lung atlas of lethal COVID-19

- [Johannes C. Melms](#) [ORCID: orcid.org/0000-0002-5410-6586](#)^{1,2 na1},
- [Jana Biermann](#) [ORCID: orcid.org/0000-0002-8907-4633](#)^{1,2 na1},
- [Huachao Huang](#)^{3,4,5 na1},
- [Yiping Wang](#)^{1,2 na1},
- [Ajay Nair](#) [ORCID: orcid.org/0000-0003-4521-5614](#)^{5 na1},
- [Somnath Tagore](#)^{6 na1},
- [Igor Katsyv](#)^{7 na1},
- [André F. Rendeiro](#)^{8,9 na1},
- [Amit Dipak Amin](#)^{1,2 na1},
- [Denis Schapiro](#)^{10,11},
- [Chris J. Frangieh](#)^{11,12},
- [Adrienne M. Luoma](#)¹³,
- [Aveline Filliol](#)⁵,
- [Yinshan Fang](#)^{3,4,5},
- [Hiranmayi Ravichandran](#)^{9,14,15},
- [Mariano G. Clausi](#)¹⁶,
- [George A. Alba](#)¹⁷,
- [Meri Rogava](#)^{1,2},
- [Sean W. Chen](#)^{1,2},
- [Patricia Ho](#) [ORCID: orcid.org/0000-0002-4622-8188](#)^{1,2},
- [Daniel T. Montoro](#)^{18,19},
- [Adam E. Kornberg](#)²,
- [Arnold S. Han](#)²,
- [Mathieu F. Bakhoum](#) [ORCID: orcid.org/0000-0001-8989-8205](#)²⁰,
- [Niroshana Anandasabapathy](#)^{9,21,22},
- [Mayte Suárez-Fariñas](#) [ORCID: orcid.org/0000-0001-8712-3553](#)^{23,24},
- [Samuel F. Bakhoum](#)^{25,26},

- [Yaron Bram](#)²⁷,
- [Alain Borczuk](#)^{28,29},
- [Xinzheng V. Guo](#)¹⁶,
- [Jay H. Lefkowitch](#)⁷,
- [Charles Marboe](#)⁷,
- [Stephen M. Lagana](#)⁷,
- [Armando Del Portillo](#)⁷,
- [Emmanuel Zorn](#) ORCID: orcid.org/0000-0001-9985-8389²,
- [Glen S. Markowitz](#)⁷,
- [Robert F. Schwabe](#)^{5,30},
- [Robert E. Schwartz](#) ORCID: orcid.org/0000-0002-5417-5995^{27 na2},
- [Olivier Elemento](#)^{8,9,15 na2},
- [Anjali Saqi](#)^{7 na2},
- [Hanina Hibshoosh](#)^{7 na2},
- [Jianwen Que](#) ORCID: orcid.org/0000-0002-6540-6701^{3,4,5,31 na2} &
- [Benjamin Izar](#) ORCID: orcid.org/0000-0003-2379-6702^{1,2,31,32 na2}

[Nature](#) volume 595, pages 114–119 (2021) [Cite this article](#)

- 30k Accesses
- 2 Citations
- 562 Altmetric
- [Metrics details](#)

Subjects

- [Cellular signalling networks](#)
- [Infection](#)
- [SARS-CoV-2](#)

Abstract

Respiratory failure is the leading cause of death in patients with severe SARS-CoV-2 infection^{1,2}, but the host response at the lung tissue level is poorly understood. Here we performed single-nucleus RNA sequencing of about 116,000 nuclei from the lungs of nineteen individuals who died of COVID-19 and underwent rapid autopsy and seven control individuals. Integrated analyses identified substantial alterations in cellular composition, transcriptional cell states, and cell-to-cell interactions, thereby

providing insight into the biology of lethal COVID-19. The lungs from individuals with COVID-19 were highly inflamed, with dense infiltration of aberrantly activated monocyte-derived macrophages and alveolar macrophages, but had impaired T cell responses. Monocyte/macrophage-derived interleukin-1 β and epithelial cell-derived interleukin-6 were unique features of SARS-CoV-2 infection compared to other viral and bacterial causes of pneumonia. Alveolar type 2 cells adopted an inflammation-associated transient progenitor cell state and failed to undergo full transition into alveolar type 1 cells, resulting in impaired lung regeneration. Furthermore, we identified expansion of recently described *CTHRC1*⁺ pathological fibroblasts³ contributing to rapidly ensuing pulmonary fibrosis in COVID-19. Inference of protein activity and ligand–receptor interactions identified putative drug targets to disrupt deleterious circuits. This atlas enables the dissection of lethal COVID-19, may inform our understanding of long-term complications of COVID-19 survivors, and provides an important resource for therapeutic development.

[Download PDF](#)

Main

Globally, the pandemic of COVID-19, which results from infection with SARS-CoV-2, has led to more than 145 million cases (32 million in the USA) and 3.1 million deaths (570,000 in the USA; figures as of 26 April 2021)¹. Approximately 15% of infected individuals develop severe disease, which can manifest as acute respiratory distress syndrome (ARDS) and is associated with substantial morbidity and mortality^{2,4}.

Previously, single-cell RNA sequencing (scRNA-seq) analyses of healthy individuals have revealed the tissue distribution of host receptors that are required for SARS-CoV-2 entry^{5,6,7}, and examination of bronchoalveolar lavage fluid and blood from patients with COVID-19 of varying severity has identified the effects of SARS-CoV-2 infection on immune responses and cytokine dysregulation^{8,9,10,11,12}. However, owing to the practical limitations of accessing patient tissues, the effects of SARS-CoV-2 at the level of the lung tissue remain unclear. A series of autopsy studies that examined formalin-fixed, paraffin-embedded (FFPE) tissue sections from individuals who died of COVID-19 extended our understanding of virus organotropism, but these studies were limited in their discovery potential by low-plex assays (for example, immunohistochemistry) and/or prolonged post-mortem intervals (PMIs), which adversely affect RNA quality^{13,14,15}.

We established a rapid autopsy program and, under Institutional Review Board approved protocols, collected snap-frozen organ specimens from individuals with COVID-19 within hours of death. We performed single-nucleus RNA-seq (snRNA-

seq) on lung samples from individuals who died from COVID-19 and control individuals to build an atlas that provides insight into the pathophysiology of COVID-19 and provides a key resource for further investigation.

The lung cellular landscape in COVID-19

The COVID-19 cohort consisted of 19 patients (12 males and 7 females) who died at a median age of 72 years (range, 58 to more than 89) (Supplementary Table 1, Extended Data Fig. 1a) and underwent rapid autopsy with a median post-mortem interval (PMI) of 4 h (range, 2–9 h). All had underlying co-morbidities that are associated with increased risk of severe COVID-19¹⁶ (Supplementary Table 1). The control cohort comprised 7 individuals (4 males and 3 females) with a median age of 70 years (range, 67 to 79 years) who underwent lung resection or biopsy in the pre-COVID-19 era (Supplementary Table 1).

Using snRNA-seq¹⁷ and an integrated quality control pipeline (see [Methods](#)), we generated a lung atlas that profiled 116,314 nuclei, including 79,636 from COVID-19-infected lungs and 36,678 from control lungs (Fig. 1a). We used a three-pronged approach for cell-type identification: unbiased identification of cluster markers, discovery of cell types using signatures from reported atlases, and manual curation to sub-stratify cell populations and cell states using expert knowledge (see [Methods](#)). We report cell-type assignment with three levels of granularity: major cell types, intermediate granularity, and fine granularity (Supplementary Table 2). We visualized data with dimensionality reduction using uniform manifold approximation and projection (UMAP) (Fig. 1b, c, Extended Data Fig. 1b–d). We identified nine major cell types: epithelial cells ($n = 30,070$ cells), myeloid cells ($n = 29,632$), fibroblasts ($n = 22,909$), endothelial cells ($n = 5,386$), T and natural killer (NK) lymphocytes ($n = 16,751$), B lymphocytes and plasma cells ($n = 7,236$), neuronal cells ($n = 2,017$), mast cells ($n = 1,464$), and antigen-presenting cells (APCs; primarily dendritic cells) ($n = 849$). At the most granular level, we identified 41 different cell types (Supplementary Table 2).

Fig. 1: Study design and cellular landscape.

 **figure1**

a, Overview of study design. **b**, Major clusters and respective cell-type assignments in UMAP. **c**, Origins of cells with same embedding as in **b**. **d**, Fraction of major cell types in control ($n = 7$) and COVID-19 lungs ($n = 19$). Middle line, median; box edges, 25th and 75th percentiles; whiskers, most extreme points that do not exceed $\pm 1.5 \times$ the interquartile range (IQR). Wilcoxon rank-sum test.

[Full size image](#)

We found significant differences in cell fractions between COVID-19 and control lungs both globally (Fig. [1d](#)) and within the immune and non-immune compartments (Extended Data Fig. [2a-c](#)). There was a reduction in the epithelial cell compartment, due to loss of both alveolar type II (AT2) and type I (AT1) cells, and an increase in monocytes/macrophages, fibroblasts, and neuronal cells; these observations were independent of donor sex (Extended Data Fig. [3a, b](#)).

We found no major differences in the expression of *ACE2*, *CD147* (also known as *BSG*), *NPR1*, *TMPRSS2*, *FURIN* or *CTSL* between COVID-19 and control lungs (Extended Data Fig. [3c-f](#)). This indicates that changes in cell-type proportions were unrelated to the expression of receptors or putative proteases that are important for viral entry, although we cannot exclude the possibility that virus-mediated cell death selectively depletes cells with high expression of these genes. We detected SARS-CoV-2 reads in two patients (Supplementary Table [3](#)), one of whom had HIV/AIDS ($CD4^+$ T cell count 29 per mm³ on hospital admission; 662 unique molecular

identifiers detected in 28 cells), which suggests that viral reads can, in principle, be captured.

Aberrant activation of myeloid cells

Myeloid cells represented a major cellular constituent in COVID-19 lungs and were more prevalent there than in control lungs (Fig. 1d, Extended Data Figs. 2a, c, 4a). We identified monocytes ($n = 3,176$), monocyte-derived macrophages (MDMs; $n = 9,534$), transitioning MDMs ($n = 4,203$), and resident alveolar macrophages (AMs; $n = 12,511$), which were recovered as distinct trajectories in diffusion component (DC) analysis and were more frequent in COVID-19 lungs (Fig. 2a–c, Extended Data Fig. 4b–i, Supplementary Tables 2, 4, 5). Myeloid cells from individuals with COVID-19 were highly and aberrantly activated. For example, MDMs in COVID-19 lungs differentially expressed genes of activation (for example, *CTSB*, *CTSD*, *CTSZ*, *PSAP*) and two long non-coding RNAs, *NEAT1* and *MALAT1*, that are associated with aberrant macrophage activation and impaired T cell immunity¹⁸ (Extended Data Fig. 5a, Supplementary Table 5). AMs, which arise from fetal monocytes and can self-renew¹⁹, were enriched and highly activated in COVID-19 lungs (Fig. 2c, Extended Data Fig. 5a). Notably, COVID-19 AMs showed strongly decreased mRNA and protein expression of the tumour-associated macrophage receptor AXL (Fig. 2d, Extended Data Fig. 5b,c), a receptor tyrosine kinase that is important for coordinated clearance of apoptotic cells (efferocytosis) and subsequent anti-inflammatory regulation during tissue regeneration²⁰. These data suggest that myeloid cells are a major source of dysregulated inflammation in COVID-19.

Fig. 2: Immune responses in COVID-19.



a, UMAP projection highlighting immune cell clusters. **b**, Visualization of myeloid cells using the first three DCs. Inset indicates group assignment. **c**, Fraction of myeloid cells in control ($n = 7$) and COVID-19 lungs ($n = 19$). Middle line, median; box edges, 25th and 75th percentiles; whiskers: most extreme points that do not exceed $\pm 1.5 \times$ IQR. Wilcoxon rank-sum test. **d**, Representative immunofluorescence staining for CD169, AXL and DAPI (large image) in control and COVID-19 lung tissue; top, selected area with overlay; bottom, individual channels. Scale bar, 20 μm . **e, f**, Top 20 recurrently detected *IGHV*-*IGLV* combinations in COVID-19 (e) and corresponding group annotation (f). *Combination for previously described anti-RBD antibody²¹. **g**, UMAP of T/NK cells; inset, group assignments. **h, i**, RNA expression (log-normalized) of *GZMB* (h) and *MKI67* (i) in the same embedding as g.

[Full size image](#)

Plasma and T cell responses

To gain insights into humoral immunity against SARS-CoV-2 infection in the lung, we identified plasma cells (Extended Data Fig. [6a–c](#)) and reconstructed immunoglobulins by determining mRNA co-expression of the variable heavy (*IGHV*) and light (*IGLV*) chains and isotypes on a per cell basis (see [Methods](#); Extended Data Fig. [6d–k](#), Supplementary Table [6](#)). *IGHV1-18-IGLV3-20*, which gives rise to a neutralizing antibody (S309)²¹ against the receptor binding domain (RBD) of the SARS-CoV-2 spike protein, was among the commonly identified *IGHV*-*IGLV* combinations, which suggests that a coordinated antibody response occurred (Fig. [2e, f](#), Extended Data Fig.

[6l](#), [m](#)). In the T/NK cell compartment (Fig. [2g](#)), we distinguished CD8⁺ T cells ($n = 3,561$), T regulatory (T_{reg}) cells ($n = 649$), other CD4⁺ T cells ($n = 7,586$), and NK cells ($n = 2,141$). We found no significant increase in T cell abundances in COVID-19 lungs, and only modest upregulation of cytokines and programs associated with activation and tissue residency of T cells (Fig. [2g–i](#), Extended Data Fig. [7a–i](#)). Although immune response patterns were highly variable (Extended Data Fig. [7j,k](#)), these data suggest that an impaired T cell response might contribute to lethal outcomes in COVID-19 in the context of a principally preserved humoral immune response.

Impaired alveolar epithelial regeneration

Within the epithelial compartment, we identified alveolar epithelial cells (AT1 and AT2 cells; $n = 20,949$), airway epithelial cells (basal, ciliated, club, goblet, and mucous cells; $n = 7,223$), a cluster characterized by the expression of inflammatory and cell cycle genes, including *IRF8*, *B2M*, *MKI67* and *TOP2A* ('cycling epithelium'; $n = 609$), and a cluster showing high expression of the extracellular matrix (ECM) components *COL6A3*, *COL1A2*, and *COL3A1* ('ECM^{high} epithelium'; $n = 1,179$) (Fig. [3a,b](#), Extended Data Fig. [8a–c](#), Supplementary Tables [2](#), [1](#)).

Fig. 3: Impaired lung regeneration and sources of inflammation.



a, b, UMAP of investigated alveolar and airway epithelial cells (**a**) and corresponding group assignments (**b**). **c**, Differential gene expression (log-normalized, scaled; see [Methods](#)) of AT1 and AT2 cells from COVID-19 and control lungs. Columns, single cells; rows, expression of top-regulated genes. Left bar, lineage markers for AT1 (purple) and AT2 (pink) cells. Colour-coded top lanes indicate expression strength of signatures (log-normalized; see [Methods](#)) and group assignment as indicated on the right. exp., expression. **d, e**, Violin plots of *ETV5* and *CAVI* mRNA expression (log-normalized) in AT2 and AT1 cells, respectively; Wilcoxon rank-sum test with Bonferroni correction. **f**, UMAP embedding of AT1 and AT2 cells and identified DATPs; inset indicates group assignments. **g**, Violin plots of DATP signature expression (log-normalized) in AT1 and AT2 cells. Wilcoxon rank-sum test. **h**, First three DCs showing main trajectories of AT2 and AT1 cells and DATPs, expression of DATP signature and group assignment (inset). **i**, Fractions of DATP and AT cells in control ($n = 7$) and COVID-19 lungs ($n = 19$). Middle line, median; box edges, 25th and 75th percentiles; whiskers, most extreme points that do not exceed $\pm 1.5 \times$ IQR. Wilcoxon rank-sum test. **j**, Representative immunofluorescence staining for pro-SPC, KRT8 and DAPI in control and COVID-19 lung tissue; top, representative area with overlay; bottom, small images with individual channels of selected area. Scale bar, 50 μ m. **k, l**, Tissue mass cytometric quantification of IL-1 β (**k**) and IL-6 (**l**) in healthy lung tissue and samples from donors with different infectious aetiologies. Each dot represents quantification of IL-1 β and IL-6 in a region of interest (ROI); two-sided Mann–Whitney *U*-test with Benjamini–Hochberg false discovery rate (FDR) adjustment.

[Full size image](#)

AT2 cells serve as progenitors for AT1 cells during lung regeneration²². AT2 and T1 cells in control lungs formed distinct clusters (Fig. [3a,b](#)) and demonstrated the expected changes in differential gene expression (DGE) analysis, including expression of the lineage markers *SFTPC* and *SFTPB* in AT2 cells, and *CLIC5* and *AGER* in AT1 cells (Fig. [3c](#), Supplementary Table [7](#)). By contrast, clustering of AT2 and AT1 cells in COVID-19 lungs was less discrete, with a substantial portion of cells not overlapping with their control counterparts (Fig. [3b](#)). Both AT2 and AT1 cells from COVID-19 lungs showed decreased overall expression of defining markers (Fig. [3c](#)). COVID-19 AT2 cells displayed decreased expression of *ETV5* (Fig. [3d](#)), a transcription factor that is required for maintaining AT2 cell identity. Decreased *ETV5* expression is associated with differentiation towards AT1 cells²³, indicating that AT2 cells had initiated a regeneration program (Fig. [3d](#), Extended Data Fig. [8d](#)). *CAVI*, a marker of late AT1 maturation²⁴, was expressed at significantly lower levels in AT1 cells from COVID-19 lungs (Fig. [3e](#)). Overall, these data suggest incomplete transition of AT2 to AT1 cells in COVID-19 lungs.

Recent studies have shown that inflammation can induce a cell state that is characterized by failure to fully transition to AT1 cells; this has been termed ‘damage-associated transient progenitors’ (DATPs), ‘alveolar differentiation intermediate’ (ADI), or ‘pre-AT1 transitional cell state’ (PATS)^{25,26,27} (hereafter referred to as DATPs). We used expression of the DATP marker genes (*KRT8*, *CLDN4* and *CDKN1A*)²⁵ to develop a DATP signature (see [Methods](#); Extended Data Fig. [8e–h](#), Supplementary Table [8](#)) and found that alveolar epithelial cells from COVID-19 lungs scored significantly higher for expression of this signature than those from control lungs (Fig. [3f,g](#), Extended Data Fig. [8i](#)). DC analysis separated a main trajectory from AT2 to AT1 cells, while DATPs were primarily localized between AT2 and AT1 cells (Fig. [3h](#), Extended Data Fig. [8j–n](#)). Gene set enrichment analysis (GSEA) of DATPs compared to differentiated AT2 or AT1 cells showed enrichment for TNF α and p53 signalling, and for the hypoxia response via HIF-1 α (Extended Data Fig. [8o](#)), consistent with pathways that have been implicated in DATP in mouse models²⁷. Consistent with overrepresentation of p53 signalling, the majority of DATPs did not undergo cell division (Extended Data Fig. [8p](#)), suggesting that they arrest in the DATP cell state.

DATPs were more frequent in COVID-19 than control lungs (Fig. [3i](#)). Immunofluorescence staining of corresponding tissues showed that the frequency of KRT8 $^+$ and CLDN4 $^+$ DATPs was higher in COVID-19 lungs (Fig. [3j](#), Extended Data Fig. [8r,s](#)), and we observed progressive loss of AT1 cell abundance with increasing time from symptom onset to death (Extended Data Fig. [8t](#)). Overall, these data suggest that, in addition to direct destruction of the alveolar epithelium by viral infection, lung-regenerative processes are impaired in individuals with COVID-19.

We next determined the sources of inflammation that contribute to the DATP cell state, and more generally, to the hyperinflammatory environment in COVID-19 lungs. Capture of the inflammatory cytokine interleukin (IL)-1 β (and others) at an mRNA level may be limited, as the bioactive form of IL-1 β , which has a major role in triggering DATPs²⁵, is generated by cleavage from pro-IL-1 β upon inflammasome activation; thus, protein-level assessment provides complementary information. For this purpose, we leveraged a recently released high-plex imaging mass-cytometry dataset that profiled 237 tissue regions from 23 individuals, including healthy controls; patients with influenza pneumonia, bacterial pneumonia, or ARDS; and ten patients who died from COVID-19²⁸. IL-1 β was more strongly expressed in monocytes and macrophages from individuals with COVID-19 than from healthy individuals or patients in the other disease groups (Fig. [3k](#), Extended Data Fig. [9a–c](#)). IL-6, another key inflammatory cytokine invoked in the pathophysiology of COVID-19, was more abundant in epithelial cells from patients with COVID-19, but was not differentially expressed in macrophages from these patients compared to patients in other disease groups (Fig. [3l](#), Extended Data Fig. [9d–f](#)). Finally, we found that the expression of

type I interferons and interferon response genes in various cell types, including AT2 cells, monocytes, and macrophages, was stronger in patients with COVID-19 than in control donors (Extended Data Fig. 9g, h). Together, these data suggest that myeloid-derived IL-1 β might be a distinguishing feature of COVID-19 compared to other viral or bacterial pneumonias and may contribute to the induction and maintenance of the DATP cell state.

Ectopic tuft-like cells in COVID-19

Among captured airway epithelial cells, we recovered four distinct trajectories: *KRT5* $^+$ *TP63* $^+$ basal ($n = 534$), club ($n = 1,232$), and goblet cells ($n = 1,757$), and one trajectory with fewer cells ($n = 110$) that was primarily found in COVID-19 lungs, which we identify as putative tuft-like cells (Extended Data Fig. 10a–e). Tuft cells are involved in airway inflammation and intestinal tissue regeneration²⁹, but their role in viral pneumonia remains unclear. The numbers of tuft cells (CHAT $^+$ or POU2F3 $^+$) were increased threefold in the upper airways of individuals with COVID-19, and they were ectopically present in the lung parenchyma of COVID-19 but not control lungs (Extended Data Fig. 10f–k). To begin to elucidate a putative role of tuft cells in viral pneumonia, we infected both wild-type and *Pou2f3* $^{-/-}$ mice, which lack tuft cells, with PR8, a laboratory-adapted strain of H1N1 influenza virus (see [Methods](#)). Compared to controls, the lungs of *Pou2f3* $^{-/-}$ mice showed decreased infiltration of macrophages and decreased expression of chemotaxis genes (including *Ccl3* and *Ccl8*) that are also involved in the recruitment of myeloid cells to the lungs of individuals who died of COVID-19 (Extended Data Figs. 9g, h, 11a–l). Although their role needs to be further examined, these ectopic tuft-like cells may contribute to the pathophysiology of COVID-19 (Supplementary Discussion).

Pathological fibroblasts and lung fibrosis

There were significantly more fibroblasts in COVID-19 lungs than in control lungs (Fig. 1d); immunohistochemistry staining for α -smooth muscle actin (α -SMA) validated this finding (Extended Data Fig. 12a–d). The degree of fibrosis (determined by a Sirius red fibrosis score, see [Methods](#)) was correlated with disease duration (Fig. 4a), indicating that lung fibrosis increases over time in COVID-19. We identified five fibroblast subtypes: alveolar ($n = 4,670$), adventitial ($n = 3,773$), pathological ($n = 2,322$), intermediate pathological ($n = 8,779$), and other ($n = 1,099$) (Fig. 4b, Extended Data Fig. 12e). The main driver of differences in the fibroblast cluster was the increased frequency of pathological or intermediate pathological fibroblasts (henceforth collectively referred to as pFBs) in COVID-19 lungs compared to control lungs (Fig. 4c, Extended Data Fig. 12f). pFBs strongly expressed *CTHRC1*, a recently described hallmark gene that defines these cells, and genes of pathological ECM³,

including *COL1A1* and *COL3A1* (Extended Data Fig. 12e, Supplementary Table 9). pFBs are key drivers of lung fibrosis in mouse models and in patients with idiopathic pulmonary fibrosis (IPF) or scleroderma³. Their increased frequency suggests that pFBs promote rapidly evolving lung fibrosis in individuals with COVID-19.

Fig. 4: Pathological fibroblasts and ensuing fibrosis in COVID-19.



a, Coefficient of determination (R^2) of days from symptom onset to death and fibrosis score in COVID-19 samples ($n = 16$, see [Methods](#)). Error bands, 95% s.e. interval on the Pearson correlation. **b**, UMAP of fibroblast (FB) sub-populations; inset indicates group assignments. path., pathological. **c**, Fractions of pathological fibroblasts among all fibroblasts in control ($n = 7$) and COVID-19 lungs ($n = 19$). Middle line, median; box edges, 25th and 75th percentiles; whiskers, most extreme points that do not exceed $\pm 1.5 \times$ IQR. Wilcoxon rank-sum test.

[Full size image](#)

Given the importance of fibroblasts in remodelling of the lung ecosystem, we next investigated ligand–receptor interactions across all major cell types, including fibroblasts (see [Methods](#)). Among the enriched inferred ligand–receptor interactions across all cells were TGF β 1–TGF β receptor 2 and BMP6–ACVR1 (Extended Data Fig. 12g–i, [Supplementary Table 10](#)), which belong to the TGF β family and superfamily, respectively. TGF β signalling has an important role in promoting lung fibrosis and has been implicated in fibroblast-mediated maintenance of the ADI²⁷, which is closely related to the DATP cell state. To investigate potential therapeutic strategies directed against pFBs, we inferred protein activity from single-nucleus transcriptomes followed by comparison of pFBs with other fibroblasts. This analysis predicted that pFBs would show increased activity of JunB and JunD (Extended Data Fig. 12j, [Supplementary Table 11](#)), which induce lung fibrosis in mouse models via enhanced TGF β and STAT3 signalling and are associated with increased production of

IL-1 β ³⁰. Finally, we inferred druggable targets in pFBs (see [Methods](#)) and identified MMP14 and STAT3 as potential targets to abrogate detrimental programs in pFBs (Extended Data Fig. [12j](#), [Supplementary Table 11](#)).

Discussion

We generated a single-cell transcriptome lung atlas of COVID-19 using short-PMI autopsy specimens and control lung samples. Our analysis provides a broad census of the cellular landscape, cell programs, and cell circuits of lethal COVID-19. The additional inference of protein activity and cell-to-cell interactions, and analysis of inflammatory cytokines across various cell types using imaging mass cytometry data, provide a granular perspective of the detrimental consequences of SARS-CoV-2 infection in the lung.

Our analyses suggest interactions among aberrantly activated monocytes/macrophages that produce IL-1 β , inflammation-induced impairment of alveolar epithelial regeneration, and expansion of pathological fibroblasts that promote fibrosis and may impair regeneration (Extended Data Fig. [12f, k](#), [Supplementary Discussion](#)). In addition to these deleterious events, our data suggest that despite a potentially sufficient humoral immune response ([Supplementary Discussion](#)), there was an inadequate T cell response in the lungs of individuals who died of COVID-19. A recent study showed that impaired B cell function in patients with cancer who contracted COVID-19 was not associated with increased mortality³¹, but that lack of an adequate CD8 $^{+}$ T cell response (even in the presence of adequate humoral immunity) was associated with worse viral control and increased mortality³¹. Although our COVID-19 cohort did not include patients with cancer, these data suggest that whereas humoral immunity may be dispensable in the context of adequate T cell immunity against SARS-CoV-2, a lack of appropriate T cell responses in our patients is likely to have contributed to fatal outcomes.

Although our study provides insight into host responses to lethal SARS-CoV-2 infection, it is limited by a small sample size. However, through coordinated efforts, our work will contribute to a collection of studies, including the companion paper by T. M. Delorey et al.³², with streamlined protocols and harmonized metadata to enable integration and combined analyses, and will help to account for important co-variables. Furthermore, because our analysis is focused on lung tissue from patients who died of COVID-19, we have examined only a subset of potential disease phenotypes. Nonetheless, several observations, such as the rapid development of pulmonary fibrosis ([Supplementary Discussion](#)), are likely to be relevant for patients who survive severe COVID-19, and may inform our understanding of the long-term complications seen in these individuals³³.

In conclusion, we have generated a molecular single-cell lung atlas from short-PMI tissue specimens and identified pathological circuits of lethal COVID-19. This atlas establishes an important resource for investigating host responses to SARS-CoV-2 and understanding potential long-term pulmonary sequelae resulting from COVID-19, and provides a basis for therapeutic development for severe disease.

Methods

Tissue collection

All tissue specimens from individuals with lethal COVID-19 (with SARS-CoV-2 infection confirmed by reverse transcription polymerase chain reaction (RT-PCR)) and control individuals were collected at New York Presbyterian Hospital or Columbia University Medical Center under IRB approved protocols (AAAB2667, AAAT0785, AAAS7370). Appropriate consent was obtained from patients or their next of kin. All procedures performed on patient samples were in accordance with the ethical standards of the IRB and the Helsinki Declaration and its later amendments. Samples were selected on the basis of pathological review of corresponding haematoxylin and eosin (H&E)-stained FFPE tissue slides showing pathological involvement of the selected biopsy region from donors with a post-mortem incision time of less than 10 h. The donor age was 59 to more than 89 years. Tissue samples of ~1 cm³ were snap-frozen embedded in Tissue-Tek optimal cutting temperature (OCT) compound (Sakura Finetek USA Inc., Torrance, CA) and stored at -80 °C until processing. For all decedents included in this study, affected lung tissues were removed, and additionally, for a subset of individuals, matching tissues from kidney and heart were collected³². Seven control lung samples were collected from patients without COVID-19. The dataset analysed and presented here focuses on lung specimens from 19 individuals who died of COVID-19 (profiled in 20 experiments) and 7 control (non-COVID-19) individuals.

Sample processing and preparation of single-nucleus suspensions

All samples were processed in a biosafety cabinet equipped to comply with Columbia University safety measures established for working with COVID-19 specimens. Samples were processed as described previously¹⁷ with the following specifications and modifications. For tissue dissociation we used Tween with salts and Tris (TST) buffer. For all wash steps we used salt and Tris (ST) buffer, and all buffers were supplemented with 40 U/ml RNase inhibitor (Thermo Fisher Scientific, Waltham, MA). All buffers were pre-chilled on ice and samples were kept on ice throughout the process to further prevent RNA degradation. In brief, a fraction of the OCT-embedded snap-frozen tissue was broken off and put into a pre-cooled 50-ml tube (Corning, NY)

in a large volume of ice-cold phosphate buffered saline (PBS) and inverted until the OCT was fully dissolve. Tissue was then collected by centrifuging at 300g for 2 min at 4 °C. PBS was decanted, and the tissue was resuspended in 2 ml cold TST buffer, mechanically dissociated using fine scissors and pipettes with decreasing orifice size, and incubated on ice for 5–10 min. The TST was quenched with 8 ml ST buffer, and the suspension was filtered through a 70-µm cell strainer. The tissue/nucleus suspension was pelleted by centrifuging at 500g for 5 min at 4 °C. The supernatant was decanted, and the nuclei were resuspended in 200–1,000 µl ST buffer, filtered through a 40-µm cell strainer attached to a fluorescence-activated cell sorting (FACS) tube (Corning, NY), counted, and immediately processed for single-nucleus RNA sequencing.

Single-nucleus RNA library preparation and sequencing

Single-nucleus suspensions were counted using disposable counting chambers (Bulldog Bio, Portsmouth, NH) on a Leica DMI 1 microscope by a second investigator not involved in tissue processing. A total of 15,000–20,000 nuclei were loaded per channel on a Chromium controller using Chromium Next GEM Single Cell 3' v3.1 reagents (10X Genomics, Pleasanton, CA) placed inside the bio-safety cabinet, and single-nucleus RNA-seq libraries were prepared per the manufacturer's instructions (increasing the recommended initial cDNA amplification cycles by one to account for lower amounts of RNA from nuclei compared to whole cells). Single-nucleus RNA libraries were analysed and quantified using TapeStation D1000 screening tapes (Agilent, Santa Clara, CA) and Qubit HS DNA quantification kit (Thermo Fisher Scientific). Libraries were pooled equimolarly and quantified using quantitative PCR. Libraries were sequenced on a NovaSeq 6000 with S4 flow cell (Illumina, San Diego, CA) using paired-end, single-index sequencing with 28 cycles for read 1, 8 cycles for i7 index, and 91 cycles for read 2.

Generating single-nucleus gene expression matrices

Raw 3' snRNA-seq data were demultiplexed using Cell Ranger (v5.0) 'mkfastq' followed by 'count' to align the sequencing reads and generate a counts matrix. Transcripts were aligned to the human GRCh38 reference genome, which was appended with the entire SARS-CoV-2 genome (severe acute respiratory syndrome coronavirus 2 isolate Wuhan-Hu-1, complete genome, GenBank MN908947.3) as an additional chromosome to the human reference genome. Subsequently, the customized 'GRCh38_SARSCoV2' reference genome was indexed using 'cellranger_mkref' .

Removal of background noise in gene expression matrices

We used the ‘remove-background’ function of CellBender (v.0.2.0) to remove technical ambient RNA counts and empty droplets from the gene expression matrices³⁴. Cell Ranger-generated ‘raw_feature_bc_matrix.h5’ files served as input for CellBender. The parameter ‘expected-cells’ was obtained from the Cell Ranger metric ‘Estimated Number of Cells’, while the parameter ‘total-droplets-included’ was set to a value between 18,000 and 24,000 to represent a point within the plateau of the barcode rank plot in all samples.

Quality control and filtering

The resulting expression matrices were processed individually in R (v.4.0.2) using Seurat (v.3.2.3)³⁵. Filters were applied to keep nuclei with 200–7,500 genes, 400–40,000 unique molecular identifiers (UMIs), and less than 10% mitochondrial reads. In addition, Scrublet was applied to identify and remove doublets with an expected doublet rate ranging from 4 to 9.6% based on the loading rate³⁶. Samples containing fewer than 1,000 nuclei after filtering were excluded from further analyses. Filtered gene–barcode matrices were normalized with the ‘NormalizeData’ function using ‘LogNormalize’ and the top 2,000 variable genes were identified using the ‘vst’ method in ‘FindVariableFeatures’. Gene expression matrices were scaled and centred using the ‘ScaleData’ function. Next, we performed principal component analysis (PCA) as well as UMAP using the first 30 principal components. UMAPs of individual samples were inspected before integration.

Integration of individual samples

Individual samples were integrated in Seurat using the reciprocal PCA (RPCA) pipeline to remove batch effects in large datasets. The ‘SelectIntegrationFeatures’ function was applied to choose the features ranked by the number of datasets they were detected in. Next, the ‘FindIntegrationAnchors’ function selected a set of anchors between different samples using the top 50 dimensions from the RPCA to specify the neighbour search space. Six samples were specified as a reference, including three controls (C51ctr, C52ctr, C53ctr) and three COVID-19 (L01cov, L12cov, L16cov) samples. ‘IntegrateData’ was then applied to integrate the datasets using the pre-computed anchors and the integrated dataset was scaled using ‘ScaleData’. PCA and UMAP dimension reduction based on the top 30 principal components were performed. Nearest-neighbour graphs using the top 30 dimensions of the PCA reduction were calculated and clustering was applied with a resolution of 0.8. Harmony³⁷ was run on the PCA matrix above using default parameters with patient ID as the batch key and 10 iterations.

Cell-type identification

The main cell types were identified by manual annotation of differential gene expression (DGE) between clusters. The ‘FindAllMarkers’ function identified positive markers for each cluster with a minimal fraction of 25% and a log-transformed fold change threshold of 0.25. This initial labelling resulted in the identification of epithelial, endothelial, fibroblast, neuronal, myeloid, APC, mast, T/NK and B/plasma cell populations as well as one low-quality cluster, which we removed. Next, we split the Seurat object into subsets of the main labels and reran scaling, PCA, UMAP dimension reduction, clustering and DGE analysis on each subset. The resulting clusters were annotated manually or by using cell-type-specific single-cell signatures from respective cell atlases, and labels were added to the main object. In addition, cell cycle phases were scored in the subsets using the ‘CellCycleScoring’ function, adjusted for individual cut-offs and added to the main object. Within the myeloid subpopulation, two low-quality clusters (characterized by higher expression of mitochondrial reads) were observed and removed, leaving a total of 116,314 cells for downstream analyses (of 119,535 initial cells after QC). Signatures and canonical markers (Supplementary Table 4) to identify airway basal, club, ciliated, goblet, mucous, AT1, and AT2 cells were obtained from Travaglini et al.³⁸. Alveolar macrophages were scored using a signature based on DGE obtained from Travaglini et al.³⁸ and identified as AMs³⁹ with a module score >0.15. A tuft-cell signature was obtained from Deprez et al.⁴⁰. To further characterize the fibroblast population, fibroblast cells were selected using Seurat’s ‘subset’ function and reanalysed to identify the different fibroblast subtypes. The reanalysis included the standard Seurat workflow with ‘RunPCA,’ ‘FindNeighbours,’ ‘FindClusters,’ and ‘RunUMAP’ performed on the ‘integrated’ assay. The number of PCA dimensions used was 15, with a resolution parameter of 0.5. After the fibroblast cell clusters had been obtained, the DGE in each cluster was computed with ‘FindAllMarkers’ on ‘RNA’ assay (Supplementary Table 9). The fibroblast subtypes were identified by manually curating the cluster DGE with the reported literature, such as the single-cell lung atlas³⁸, lung fibroblast atlas³, single-cell database PanglaoDB⁴¹, and Human Protein Atlas^{42,43,44}. However, these resources were based on scRNA-seq or bulk studies. Therefore, the few reported fibroblast subtype markers were usually not specific or had low expression in snRNA-seq data. Therefore, we compared our subcluster DGE with the literature reported subtype DGE with shared high expression in snRNA-seq or scRNA-seq data. These manually curated lists of fibroblast-subtype-specific marker genes were used to identify fibroblast subtypes in our dataset (Supplementary Table 4). This procedure was used to identify alveolar fibroblasts, adventitial fibroblasts, pericytes, airway smooth muscle, vascular smooth muscle, and mesothelial fibroblasts. Cell clusters with high expression of *COL1A1* and *CTHRC1* were annotated as ‘pathological fibroblasts’ because they have been reported to contribute to the leading edge of fibrosis³. Clusters with lower expression of *COL1A1* and *CTHRC1* compared to pathological fibroblasts, but without any markers for other fibroblast subtypes in their DGE, were annotated as ‘intermediate pathological fibroblasts’. One cell cluster

without distinct DGE was annotated as ‘other fibroblasts’. For visualization purposes, expression scores were plotted in UMAP embeddings or violin plots as log-normalized values (natural logarithm $\ln(1 + x)$), and in dot plots as log-normalized values (natural logarithm $\ln(1 + x)$) that were furthermore centred on 0 with a variance of 1 (scaled).

Cell-type frequency comparison

Unless otherwise noted, we calculated frequencies of cell types in each sample from COVID-19 and control lungs, and compared the medians of the two groups to identify differences in frequency. Significance was assessed using a Wilcoxon rank-sum test.

Module scores for feature expression

The ‘AddModuleScore’ function was applied to calculate the average expression levels of gene signatures on a single-cell level. Mouse-based signatures to identify DATPs and primed and cycling AT2 cells were obtained from Choi et al.²⁵ and converted to human homologue genes. Three genes (*CLDN4*, *KRT8*, *CDKN1A*) comprised the initial DATP signature thus derived. AT1 and AT2 cells were subset from the main Seurat object and reintegrated using the Seurat standard integration with 30 dimensions and a k -neighbours filter of 60 in the ‘FindIntegrationAnchors’ function. First, all AT1 and AT2 cells were scored for the three-gene signature and cells with a module score >0.7 were preliminarily labelled as DATPs. Next, we used DGE to identify additional markers that define the DATP program. We then scored our resulting DATP signature, including 163 genes, to the AT1 and AT2 cells and labelled all cells with a module score of >0.4 as DATPs. T cell scores were obtained by using the Seurat implementation of gene set scoring with 50 bins and a control size equal to the number of genes in the set. Upregulation and downregulation programs (TRM, Tact, Tmem Texh), defined by K. S. P. Devi et al. (unpublished), were used to infer T cell phenotypes. The upregulation and downregulation signatures were scored separately, and the downregulation score was subtracted cell-wise from the upregulation score to obtain the composite score. Effect size was calculated using Cohen’s D (that is, the difference of means divided by the pooled standard deviation).

Diffusion component analysis

We applied diffusion maps as a nonlinear dimensionality reduction technique to examine the major components of variation across subsets of cells. We computed DCs using the ‘DiffusionMap’ function of the Destiny R-package (v3.3.0) with the top 30 principal components used in the k -nearest neighbours algorithm (k -NN)⁴⁵. The epithelial subset consisting of airway basal, club, and goblet cells was reintegrated for the DC analysis using the Seurat standard integration with 30 dimensions and a k -neighbours filter of 50 in the ‘FindIntegrationAnchors’ function. Samples with <50

cells were excluded from reintegration, which removed a total of 10 samples (one control sample and nine COVID-19 samples). Tuft-like cells were identified as cells with DC1 values >0.015 based on an overlap with the tuft-cell signature in the diffusion trajectory that dominated the first DC.

Differential gene expression

DGE was identified by using the Seurat function ‘FindAllMarkers’ on normalized count data to identify positive (overexpressed) markers in each population. The Wilcoxon rank-sum test (two-sided) was used to identify differentially expressed genes between two groups of cells and the log-transformed fold change was set to 0.25. The parameter ‘min.pct’ was set to 0.25 to assure that genes were detected at a minimum fraction of 25% of cells in either of the populations. *P* values were adjusted using Bonferroni correction unless otherwise stated. Differentially expressed genes were plotted in violin plots using log-normalized expression values (natural logarithm $\ln(1 + x)$). For heatmaps and dot plots, expression values were log-normalized (natural logarithm $\ln(1 + x)$) and furthermore centred on 0 with a variance of 1 (scaled).

Differential expression of signature scores

To test differential expression of three immune pathway signatures (type I interferon abbreviated, inflammasome receptors, and chemotaxis, [Supplementary Table 4](#)), we obtained log-normalized expression values ($\ln(1 + x)$) for each gene in the signatures, and summed them for each signature. We then used a two-sided Wilcoxon rank-sum test to test for differential expression of signatures in each cell type, and calculated $\log_2(\text{fold change})$.

Geneset enrichment

Geneset enrichment analyses were performed using the hypeR R-package⁴⁶. The background population of genes was set to all detected genes. Geneset over-representation was determined by hypergeometric test.

B cell chain analysis

To analyse the distribution of heavy and light chains in B cells, the dataset was subset to include only B cells. For the identification of variable chain

regions, we selected the highest expressed heavy and light chain gene of each cell that expressed both heavy (starting with *IGHV*) and light (starting with *IGLV* or *IGKV*) chain-encoding genes. Next, we identified the highest expressed constant chain region among expressed genes following the pattern ‘*IGH[G, M, A, or E][number]*’. The resulting pairs of heavy and light chains were visualized as a heatmap using average linkage for hierarchical clustering analysis and cross-referenced with previously described recurrently observed combinations⁴⁷.

Master regulator analysis and drug target identification

The fibroblast regulatory network in this study was reverse-engineered from snRNA-seq data using the ARACNe-AP^{48,49} algorithm. We generated networks for each sub-cluster and integrated the networks by taking a union of the predictions of all networks. *P* values of Master regulator (MR)–target interactions predicted by the networks were integrated using Fisher’s method. The final fibroblast network contained predictions for 1,341 transcription factors regulating 9,770 target genes through 295,546 interactions. The relative activity of each transcription factor represented in the fibroblast network was inferred using the VIPER^{50,51} algorithm, available as a package through Bioconductor. Conceptually, the VIPER algorithm is similar to the master regulator inference algorithm (MARINA)^{49,52}, which uses the MR targets inferred by the ARACNe^{48,49} algorithm to predict drivers of changes in cellular phenotypes. In addition to calculating the enrichment of ARACNe-predicted targets in the signature of interest, VIPER also considers the regulator mode of action, regulator–target gene interaction confidence, and the pleiotropic nature of each target gene’s regulation. Statistical significance, including *P* value and normalized enrichment score (NES), was estimated by comparison to a null model generated by permuting the samples uniformly at random 1,000 times. Druggable proteins with VIPER-predicted^{50,51,53} aberrant increases in activity were ranked by their $-\log_{10}$ (Bonferroni adjusted *P* value).

Ligand–receptor interaction inference in individual samples

CellPhoneDB⁵⁴ is a curated repository of ligand–receptor interactions along with their subunit architectures, integrated in a statistical framework to infer cell-type-enriched ligand–receptor interactions between cell types in single-cell or single-nucleus transcriptomics data. We used CellPhoneDB to identify ligand–receptor interactions between cell types in each individual control ($n = 7$) and COVID-19 ($n = 19$) snRNA-seq dataset. The ligand–receptor interactions were inferred in each patient separately, as by definition cell-to-cell interactions are biologically meaningful only within an individual. Moreover, separate inference also prevents spurious interactions from being inferred between patients with heterogeneous disease or health statuses. After identifying and annotating different cell types in our snRNA-seq datasets, we followed the recommended procedures for the preparation of input files for local implementation of CellPhoneDB v.2.0.0⁵⁴. In brief, for each individual sample, QC-filtered raw counts matrices were normalized to counts per 10,000 and metadata files were obtained from the respective cell-type annotations. CellPhoneDB analysis was performed with the ‘cellphonedb method statistical_analysis’ command with default parameters.

Cell–cell interaction differences between COVID-19 and control samples

CellPhoneDB analysis of each sample identified the number of ligand–receptor interactions between all nine major cell-types in that sample. We analysed these cell–cell interaction counts between control donors ($n = 7$) and individuals with COVID-19 (19 individuals, 20 samples) to identify the differences in cellular cross-talk between COVID-19 and control lungs. The median cell–cell interaction values from all the control samples formed the overall control lung cell–cell interaction counts. Similarly, the overall COVID-19 lung cell–cell interaction counts were the median from all the COVID-19 samples. The overall control and COVID-19 lung interaction counts were visualized as an interactome using the ‘igraph’ R package with circle layout, where the edge width between two cell types was proportional to the number of interactions between them and the size of a cell-type circle was proportional to its frequency in the snRNA-seq.

Differential enrichment of ligand–receptor interactions between COVID-19 and control samples

CellPhoneDB analysis of each sample identified the significantly enriched ligand–receptor interactions in that sample by computing a mean of the ligand and receptor gene expression for each ligand–receptor interaction together with a corresponding *P* value. To find ligand–receptor interactions that were differentially regulated between COVID and control conditions, we first identified the common interactions across all samples. In brief, we consolidated ligand–receptor expression for controls and COVID-19 separately by taking the median of ligand–receptor mean expressions from 7 control samples or 20 COVID-19 samples (from 19 donors). The minimum value of consolidated ligand–receptor expression in COVID-19 and control samples was set to 0.001 to prevent noise in low expression values from affecting the log(fold change) calculations. $\log_2(\text{control median expression})$ was subtracted from $\log_2(\text{COVID-19 median expression})$ to obtain the $\log_2(\text{fold change})$ of ligand–receptor expression in COVID-19. To compute the *P* value of the $\log_2(\text{fold change})$ for each interaction, we used an unpaired two-sided Wilcoxon rank-sum test for each interaction between COVID-19 and control samples. Adjusted *P* values were obtained using the Benjamini–Hochberg procedure. Interactions with $\log_2(\text{fold change}) \geq |2|$ and FDR $P < 0.1$ were reported as the top differentially enriched interactions in COVID-19.

Tissue preparation and processing for imaging

Lung tissues (human and mouse) were fixed with 4% paraformaldehyde (PFA) at 4 °C overnight with rotation. For paraffin sections, tissues were dehydrated through a 70–100% ethanol gradient and then embedded in paraffin. For cryosections, tissues were sequentially incubated with 20% and 30% sucrose and subsequently embedded in OCT compound. We obtained 8–10- μm -thick cryosections using a cryostat.

Microscopic imaging and quantification

Paraffin sections were dewaxed and rehydrated. Antigen retrieval was performed by high-pressure heating with a commercial antigen unmasking retrieval solution followed by blocking with 5% normal donkey serum. For immunofluorescence staining, the sections were then incubated with the primary antibodies listed in Supplementary Table 12 at 4 °C overnight. Cryosections were washed twice with PBS, and blocked with 5% normal donkey serum, followed by incubation with primary antibodies shown in [Supplementary Table 12](#) at 4 °C overnight. Conjugated secondary antibodies (1:500) were added to the sections and incubated for 2 h at room temperature. Nucleus were stained with DAPI, and images were captured with a Zeiss LSM T-PMT confocal laser-scanning microscope (Carl Zeiss) and Zen 2012 SP1 (black edition) software (Zeiss). Immunohistochemistry for C4d was performed on a Leica Bond 3 automated staining platform. In brief, paraffin sections including both healthy control lung and COVID-19 lung tissues were treated with BOND Epitope Retrieval Solution 2 (Leica) for 20 min and they were incubated with a C4d antibody for 30 min. Immunohistochemistry signals were developed with the Bone Polymer Refine Detection kit (Leica) with treatment with post primary polymer for 20 min and DAB chromogen for 10 min. For quantification, cells were counted by a blinded investigator using tiled stitched 20× images from more than five sections per mouse and included at least three individual lobes or were from representative areas of at least three human control lungs and COVID-19 lungs. Images were processed and analysed using ZEN blue 2.3 (Zeiss) and Adobe Photoshop Creative Suite 6 (Adobe) software in a blinded fashion. DATPs were detected with co-immunostaining for pro-SPC and KRT8 or HTII-280 and CLDN4. DATP percentages were determined by counting KTR8^{hi} pro-SPC⁺ cells over pro-SPC⁺ cells or CLDN4⁺ cells over HTII-280⁺ cells. Macrophages were quantified by counting the total number of CD45⁺CD64⁺ cells over CD45⁺ cells. CHAT⁺ tuft cells were quantified by counting the total number of CHAT⁺ cells over DAPI⁺ airway nuclei (for airway tuft cells) or per mm² of lung parenchyma.

Multiplexed immunofluorescence

Multiplexed immunofluorescence staining of lung tissue from patients who died of COVID-19 and control individuals was performed using CD4, CD8, CD19, CD103, CD163 and granzyme B (GZMB) antibodies

([Supplementary Table 12](#)) with the Opal 7-colour IHC kit (Akoya Bioscience) on a Leica Bond RX automated stainer (Leica Biosystems). FFPE tissue sections (5 µm) were baked for 2 h at 60 °C, followed by automatic deparaffinization, rehydration, and antigen retrieval in BOND Epitope Retrieval Solution 2, pH 9 (Leica Biosystems) for 30 min at 95 °C. Immunofluorescence staining with Opal and tyramide signal amplification (TSA) were performed in six cycles. In each cycle, the tissue was incubated sequentially with a primary antibody for 30 min at room temperature, the secondary antibody conjugated to polymeric horseradish peroxidase (HRP), an Opal fluorophore in TSA buffer, and BOND Epitope Retrieval Solution 1, pH 6 (Leica Biosystems) for 20 min at 95 °C to strip the tissue-bound primary–secondary antibody complexes before the next staining cycle. After nuclear counterstaining with DAPI, slides were coverslipped with Vectrashield HardSet Antifade mounting medium (Vector Laboratories) and 12–15 areas per slide were imaged using the Vectra 3 automated multispectral microscope (Akoya/PerkinElmer) with Vectra 3.0.5 software. Regions of interest were chosen by the pathologist for multispectral imaging (MSI) at 20× magnification and spectral unmixing using the InForm v2.4.6 software (Akoya). Demultiplexed images were exported as 32-bit TIFF files for further analysis.

Multiplexed image analysis

All images were analysed and visualized using QuPath⁵⁵. We used the highest resolution for all described steps. The QuPath project files and additional scripts are available at https://github.com/IzarLab/CUIMC-NYP_COVID_autopsy_lung/tree/main/code/Vectra_image_analysis. First, images were loaded, renamed and segmented using ‘WatershedCellDetection’ based on DAPI intensity with a cell expansion of 4 µm. Further parameter settings for these steps can be found in the ‘Load_and_segmentation.groovy’ script. Next, we created classes and the corresponding classifiers for each of the six markers of interest: CD4, CD19, GZMB, CD103, CD8 and CD163. The thresholds for the individual classifiers (‘ClassifyByMeasurementFunction’) were automatically calculated and adjusted for each patient on the basis of visual inspection of the mean marker expression. If no patient-specific classifier was created, the classifier with the ending ‘_04_A6.json’ was used. All classifiers can be

found in the object classifiers folder as json files. Once performed for all images, the individual assignments for each single cell were exported to a CSV file for downstream analysis and boxplot visualization.

Imaging mass cytometry

Imaging mass cytometry data from post-mortem lung tissue of patients with lung infections and otherwise healthy donors was used²⁸. The dataset comprised 237 images from 23 donors, containing 664,006 single cells for which cell-type identities were derived from the intensity of 36 markers. All analyses were conducted in Python v3.8.2 with the following programs: numpy v1.18.5, scipy v1.4.1, Tifffile 2020.6.3, Networkx v2.5, Scikit-image v0.17.2, Pingouin v0.3.7, and Scanpy v1.6.0. Single cells were labelled as positive for IL-6 or IL-1 β based on their z-score of intensity using Gaussian mixture models (scikit-learn⁵⁶, version 0.23.0) using model selection based on the Davies–Bouldin index⁵⁷. The number of cells positive for a marker in each ablated region of interest (ROI) was normalized by its area, and mean values per disease group and cell type across all ROIs were visualized as bar charts. To assess the significance of changes across both disease groups and cell types, we used a two-sided Mann–Whitney U -test and adjusted P values with the Benjamini–Hochberg FDR adjustment using the pingouin package (version 0.3.9)⁵⁸. Representative regions within the ROIs were displayed as false-colour images by normalizing the signal intensity to the unit scale after clipping the signal below and above the 3rd and 98th percentiles, respectively. Finally, a Gaussian filter with sigma of one pixel (one micrometre) was applied to the images.

Sirius red staining and fibrosis scoring

Paraffin-embedded lung sections were dewaxed, rehydrated and stained for 1.5 h with a picrosirius red solution (1.3% picric acid, 1% fast red and 1% fast green). Four or five fields at 4 \times magnification were taken using a polarized light filter on an Olympus IX71S1F-3 microscope with QCapture Suite Plus (v3.1.3.10) software. Images were quantified (percentage of Sirius red area/total area) using Adobe Photoshop (v 11.0). Pearson

correlations between fibrosis score and days from symptom onset to death were calculated for 16 of 19 patients with COVID-19 for whom samples were available and time from symptom onset to death was reported.

αSMA immunohistochemistry

Antigen retrieval of dewaxed and rehydrated paraffin-embedded lung sections was performed with citrate pH 6, blocked with 3% BSA and incubated with anti-αSMA-FITC (Sigma, F3777) overnight at 4 °C. After incubation with a biotin-anti-FITC antibody (Abcam, ab6655), detection was performed using the Vectastatin Elite ABC-HRP kit (Vector Laboratories, SP-2001) with the DAB Peroxidase Substrate kit (Vector Laboratories, SK-4100), followed by counterstaining with haematoxylin. All reagents and dilutions are listed in [Supplementary Table 12](#). All 7 control slides and 17 available slides from COVID-19 lungs were included in the analysis. Slides were scanned using a Leica SCN400 slide scanner with Leica Scanner Console software (v102.0.7.5) and quantified using the Leica Aperio ImageScope software (v12.4.3.5008) on at least five fields at 10× magnification.

Mice

Mouse studies were approved by the Columbia University Medical Center (CUMC) Institutional Animal Care and Use Committees (IACUC). The *Pou2f3*^{-/-} mouse strain was described previously^{[59](#)}. All mice were maintained on a C57BL/6 and 129SvEv mixed background and housed in the mouse facility at Columbia University according to institutional guidelines. The facility provides a 12-h light–dark cycle, 18–23 °C room temperature and 40–60% humidity. All animal studies used a minimum of three mice per group and sample size was based on pilot experiments and previous experience. Mice were randomized to experiments and 8–12-week-old animals of both sexes were used in equal proportions. The investigators were not blinded to allocation during experiments.

Influenza infection mouse model

A total of 260 plaque forming units (pfu) of influenza A/Puerto Rico/8/1934 H1N1 (PR8) virus (a gift from Dr. Jie Sun at Mayo Clinics, Cleveland) dissolved in 40 µl RPMI medium was pipetted onto the nostrils of anaesthetized mice, whereupon mice aspirated the fluid directly into their lungs. For all procedures, administration of the same volumes of vehicle (RPMI medium) was used as control.

Flow cytometry analysis

Fourteen days after infection, mice were euthanized and transcardially perfused with 10 ml cold PBS. The lungs were then perfused with 1 ml PBS with 2 mg/ml Dispase I and 0.5 mg/ml DNase I and incubated in 5 ml of the above buffer for digestion with gentle shaking for 60 min at room temperature. Lung lobes were removed and physically dissociated, followed by filtering through a 40-µm cell strainer. Cells were pelleted and resuspended in 1 ml lyse RBC buffer followed by incubation on ice for 5 min to remove red blood cells. After washing with FACS buffer (5% FBS, 0.2 mM EDTA in PBS), single cells were collected and immunostained with Fc blocking antibody (5 µg/ml) and a live/dead cell stain kit at room temperature for 10 min. Cells were then washed and incubated with the following antibodies for one hour: PE/cyanine7 anti-mouse CD45 (1:100), FITC anti-mouse CD64 (1:100), and APC anti-mouse F4/80 (1:100). Samples were analysed on LSR II (BD, Biosciences) with four lasers (405 nm, 488 nm, 561 nm, and 635 nm). Data were analysed using FlowJo software (Treestar).

Quantitative RT–PCR (qRT–PCR)

To quantitatively measure the indicated cytokines, human lung tissue samples (three donors for both healthy and COVID-19 samples) or mouse lungs (a minimum of three mice per genotype) were individually homogenized in Trizol and total RNA was extracted using an RNeasy Plus Mini Kit (Qiagen) following the manufacturer's instructions. cDNA was synthesized using the Superscript-IV First-Strand Synthesis System (Invitrogen) and the gene-specific primers were mixed with cDNA templates and iTaq Universal SYBRR Green supermix (Bio-Rad). qPCR was carried out on a CFX Connect real-time PCR detection system (Bio-Rad) in a total volume of 20

μ l. Three technical and biological replicates were performed. Relative fold change was determined by normalizing to *Actb* mRNA for mouse or to *GAPDH* mRNA for human. The primers for qPCR are listed in [Supplementary Table 13](#).

Statistical analysis of imaging and qRT–PCR data

Imaging and qPCR data are presented as means with s.d. of measurements unless stated otherwise. Individual values are plotted and represent independent biological samples unless stated otherwise. Statistical differences between samples were assessed with unpaired Student's *t*-test using GraphPad Prism 9.0 (GraphPad Software Inc., San Diego, CA). *P* values below 0.05 are considered significant.

For multiplexed immunofluorescent images, cell fractions (percentage of total or percentage of parental population) were computed for each field of view individually using Excel 16.45 (Microsoft). After calculating the mean on a per sample basis, we plotted values using GraphPad Prism 9.0 (GraphPad Inc. San Diego, CA) and presented them as means with s.d. of measurements. Statistical differences between samples were assessed with unpaired Student's *t*-test using GraphPad Prism 9.0 (GraphPad Software Inc., San Diego, CA). *P* values below 0.05 are considered significant.

Reporting summary

Further information on research design is available in the [Nature Research Reporting Summary](#) linked to this paper.

Data availability

Processed data are available via the single-cell portal: https://singlecell.broadinstitute.org/single_cell/study/SCP1219. Processed data are also deposited in GEO with accession number [GSE171524](#). Raw data are available on the Broad Data Use and Oversight System: <https://duos.broadinstitute.org> (study ID DUOS-000130). [Source data](#) are provided with this paper.

Code availability

Code is publicly available at https://github.com/IzarLab/CUIMC-NYP_COVID_autopsy_lung.

References

1. 1.

Dong, Y. et al. Epidemiology of COVID-19 among children in china. *Pediatrics* **145**, e20200702 (2020).

[PubMed](#) [Google Scholar](#)

2. 2.

Zhou, F. et al. Clinical course and risk factors for mortality of adult inpatients with COVID-19 in Wuhan, China: a retrospective cohort study. *Lancet* **395**, 1054–1062 (2020).

[CAS](#) [PubMed](#) [PubMed Central](#) [Google Scholar](#)

3. 3.

Tsukui, T. et al. Collagen-producing lung cell atlas identifies multiple subsets with distinct localization and relevance to fibrosis. *Nat. Commun.* **11**, 1920 (2020).

[ADS](#) [CAS](#) [PubMed](#) [PubMed Central](#) [Google Scholar](#)

4. 4.

Bellani, G. et al. Epidemiology, patterns of care, and mortality for patients with acute respiratory distress syndrome in intensive care units in 50 countries. *J. Am. Med. Assoc.* **315**, 788–800 (2016).

[CAS](#) [Google Scholar](#)

5. 5.

Muus, C. et al. Single-cell meta-analysis of SARS-CoV-2 entry genes across tissues and demographics. *Nat. Med.* **27**, 546–559 (2021).

[CAS](#) [PubMed](#) [Google Scholar](#)

6. 6.

Sungnak, W. et al. SARS-CoV-2 entry factors are highly expressed in nasal epithelial cells together with innate immune genes. *Nat. Med.* **26**, 681–687 (2020).

[CAS](#) [PubMed](#) [PubMed Central](#) [Google Scholar](#)

7. 7.

Ziegler, C. G. K. et al. SARS-CoV-2 receptor ACE2 is an interferon-stimulated gene in human airway epithelial cells and is detected in specific cell subsets across tissues. *Cell* **181**, 1016–1035.e19 (2020).

[CAS](#) [PubMed](#) [PubMed Central](#) [Google Scholar](#)

8. 8.

Schulte-Schrepping, J. et al. Severe COVID-19 is marked by a dysregulated myeloid cell compartment. *Cell* **182**, 1419–1440.e23 (2020).

[CAS](#) [PubMed](#) [PubMed Central](#) [Google Scholar](#)

9. 9.

Wilk, A. J. et al. A single-cell atlas of the peripheral immune response in patients with severe COVID-19. *Nat. Med.* **26**, 1070–1076 (2020).

[CAS](#) [PubMed](#) [PubMed Central](#) [Google Scholar](#)

10. 10.

Xu, G. et al. The differential immune responses to COVID-19 in peripheral and lung revealed by single-cell RNA sequencing. *Cell Discov.* **6**, 73 (2020).

[CAS](#) [PubMed](#) [PubMed Central](#) [Google Scholar](#)

11. 11.

Hadjadj, J. et al. Impaired type I interferon activity and inflammatory responses in severe COVID-19 patients. *Science* **369**, 718–724 (2020).

[ADS](#) [CAS](#) [PubMed](#) [PubMed Central](#) [Google Scholar](#)

12. 12.

Blanco-Melo, D. et al. Imbalanced host response to SARS-CoV-2 drives development of COVID-19. *Cell* **181**, 1036–1045.e9 (2020).

[CAS](#) [PubMed](#) [PubMed Central](#) [Google Scholar](#)

13. 13.

Ackermann, M. et al. Pulmonary vascular endothelialitis, thrombosis, and angiogenesis in Covid-19. *N. Engl. J. Med.* **383**, 120–128 (2020).

[CAS](#) [PubMed](#) [PubMed Central](#) [Google Scholar](#)

14. 14.

Puelles, V. G. et al. Multiorgan and renal tropism of SARS-CoV-2. *N. Engl. J. Med.* **383**, 590–592 (2020).

[PubMed](#) [Google Scholar](#)

15. 15.

De Michele, S. et al. Forty postmortem examinations in COVID-19 patients. *Am. J. Clin. Pathol.* **154**, 748–760 (2020).

[CAS](#) [Article](#) [PubMed](#) [Google Scholar](#)

16. 16.

Goyal, P. et al. Clinical characteristics of Covid-19 in New York City. *N. Engl. J. Med.* **382**, 2372–2374 (2020).

[PubMed](#) [Google Scholar](#)

17. 17.

Slyper, M. et al. A single-cell and single-nucleus RNA-seq toolbox for fresh and frozen human tumors. *Nat. Med.* **26**, 792–802 (2020).

[CAS](#) [PubMed](#) [PubMed Central](#) [Google Scholar](#)

18. 18.

Hewitson, J. P. et al. *Malat1* suppresses immunity to infection through promoting expression of Maf and IL-10 in Th cells. *J. Immunol.* **204**, 2949–2960 (2020).

[CAS](#) [PubMed](#) [PubMed Central](#) [Google Scholar](#)

19. 19.

Hoeffel, G. et al. C-Myb⁺ erythro-myeloid progenitor-derived fetal monocytes give rise to adult tissue-resident macrophages. *Immunity* **42**, 665–678 (2015).

[CAS](#) [PubMed](#) [PubMed Central](#) [Google Scholar](#)

20. 20.

Doran, A. C., Yurdagul, A. Jr & Tabas, I. Efferocytosis in health and disease. *Nat. Rev. Immunol.* **20**, 254–267 (2020).

[CAS](#) [PubMed](#) [PubMed Central](#) [Google Scholar](#)

21. 21.

Pinto, D. et al. Cross-neutralization of SARS-CoV-2 by a human monoclonal SARS-CoV antibody. *Nature* **583**, 290–295 (2020).

[ADS](#) [CAS](#) [PubMed](#) [Google Scholar](#)

22. 22.

Barkauskas, C. E. et al. Type 2 alveolar cells are stem cells in adult lung. *J. Clin. Invest.* **123**, 3025–3036 (2013).

[CAS](#) [PubMed](#) [PubMed Central](#) [Google Scholar](#)

23. 23.

Zhang, Z. et al. Transcription factor Etv5 is essential for the maintenance of alveolar type II cells. *Proc. Natl Acad. Sci. USA* **114**, 3903–3908 (2017).

[CAS](#) [PubMed](#) [PubMed Central](#) [Google Scholar](#)

24. 24.

Little, D. R. et al. Transcriptional control of lung alveolar type 1 cell development and maintenance by NK homeobox 2-1. *Proc. Natl Acad. Sci. USA* **116**, 20545–20555 (2019).

[CAS](#) [PubMed](#) [PubMed Central](#) [Google Scholar](#)

25. 25.

Choi, J. et al. Inflammatory signals induce AT2 cell-derived damage-associated transient progenitors that mediate alveolar regeneration. *Cell Stem Cell* **27**, 366–382.e7 (2020).

[CAS](#) [PubMed](#) [PubMed Central](#) [Google Scholar](#)

26. 26.

Kobayashi, Y. et al. Persistence of a regeneration-associated, transitional alveolar epithelial cell state in pulmonary fibrosis. *Nat. Cell Biol.* **22**, 934–946 (2020).

[CAS](#) [PubMed](#) [PubMed Central](#) [Google Scholar](#)

27. 27.

Strunz, M. et al. Alveolar regeneration through a Krt8⁺ transitional stem cell state that persists in human lung fibrosis. *Nat. Commun.* **11**, 3559 (2020).

[ADS](#) [CAS](#) [PubMed](#) [PubMed Central](#) [Google Scholar](#)

28. 28.

Rendeiro, A. F. et al. The spatial landscape of lung pathology during COVID-19 progression. *Nature* <https://doi.org/10.1038/s41586-021-03475-6> (2021).

29. 29.

Westphalen, C. B. et al. Long-lived intestinal tuft cells serve as colon cancer-initiating cells. *J. Clin. Invest.* **124**, 1283–1295 (2014).

[CAS](#) [PubMed](#) [PubMed Central](#) [Google Scholar](#)

30. 30.

Cui, L. et al. Activation of JUN in fibroblasts promotes pro-fibrotic programme and modulates protective immunity. *Nat. Commun.* **11**, 2795 (2020).

[ADS](#) [CAS](#) [PubMed](#) [PubMed Central](#) [Google Scholar](#)

31. 31.

Bange, E. M. et al. CD8 T cells compensate for impaired humoral immunity in COVID-19 patients with hematologic cancer. Preprint at

<https://doi.org/10.21203/rs.3.rs-162289/v1> (2021).

32. 32.

Delorey, T. M. et al. COVID-19 tissue atlases reveal SARS-CoV-2 pathology and cellular targets. *Nature* <https://doi.org/10.1038/s41586-021-03570-8> (2021).

33. 33.

Nalbandian, A. et al. Post-acute COVID-19 syndrome. *Nat. Med.* **27**, 601–615 (2021).

[CAS](#) [PubMed](#) [Google Scholar](#)

34. 34.

Fleming, S. J., Marioni, J. C. & Babadi, M. CellBender remove-background: a deep generative model for unsupervised removal of background noise from scRNA-seq datasets. Preprint at <https://doi.org/10.1101/791699> (2019).

35. 35.

Stuart, T. et al. Comprehensive integration of single-cell data. *Cell* **177**, 1888–1902.e21 (2019).

[CAS](#) [PubMed](#) [PubMed Central](#) [Google Scholar](#)

36. 36.

Wolock, S. L., Lopez, R. & Klein, A. M. Scrublet: computational identification of cell doublets in single-cell transcriptomic data. *Cell Syst.* **8**, 281–291.e9 (2019).

[CAS](#) [PubMed](#) [PubMed Central](#) [Google Scholar](#)

37. 37.

Korsunsky, I. et al. Fast, sensitive and accurate integration of single-cell data with Harmony. *Nat. Methods* **16**, 1289–1296 (2019).

[CAS](#) [PubMed](#) [PubMed Central](#) [Google Scholar](#)

38. 38.

Travaglini, K. J. et al. A molecular cell atlas of the human lung from single-cell RNA sequencing. *Nature* **587**, 619–625 (2020).

[ADS](#) [CAS](#) [PubMed](#) [PubMed Central](#) [Google Scholar](#)

39. 39.

Mould, K. J., Jackson, N. D., Henson, P. M., Seibold, M. & Janssen, W. J. Single cell RNA sequencing identifies unique inflammatory airspace macrophage subsets. *JCI Insight* **4**, 126556 (2019).

[PubMed](#) [Google Scholar](#)

40. 40.

Deprez, M. et al. A single-cell atlas of the human healthy airways. *Am. J. Respir. Crit. Care Med.* **202**, 1636–1645 (2020).

[CAS](#) [PubMed](#) [Google Scholar](#)

41. 41.

Franzén, O., Gan, L. M. & Björkegren, J. L. M. PanglaoDB: a web server for exploration of mouse and human single-cell RNA sequencing data. *Database* **2019**, baz046 (2019).

[PubMed](#) [PubMed Central](#) [Google Scholar](#)

42. 42.

Uhlén, M. et al. Tissue-based map of the human proteome. *Science* **347**, 1260419 (2015).

[Google Scholar](#)

43. 43.

Thul, P. J. et al. A subcellular map of the human proteome. *Science* **356**, eaal3321 (2017).

[Google Scholar](#)

44. 44.

Uhlen, M. et al. A pathology atlas of the human cancer transcriptome. *Science* **357**, eaan2507 (2017).

[Google Scholar](#)

45. 45.

Angerer, P. et al. *destiny*: diffusion maps for large-scale single-cell data in R. *Bioinformatics* **32**, 1241–1243 (2016).

[CAS](#) [PubMed](#) [Google Scholar](#)

46. 46.

Federico, A. & Monti, S. hypeR: an R package for geneset enrichment workflows. *Bioinformatics* **36**, 1307–1308 (2020).

[CAS](#) [PubMed](#) [Google Scholar](#)

47. 47.

Yuan, M. et al. Structural basis of a shared antibody response to SARS-CoV-2. *Science* **369**, 1119–1123 (2020).

[ADS](#) [CAS](#) [PubMed](#) [PubMed Central](#) [Google Scholar](#)

48. 48.

Basso, K. et al. Reverse engineering of regulatory networks in human B cells. *Nat. Genet.* **37**, 382–390 (2005).

[CAS](#) [PubMed](#) [Google Scholar](#)

49. 49.

Lachmann, A., Giorgi, F. M., Lopez, G. & Califano, A. ARACNe-AP: gene network reverse engineering through adaptive partitioning inference of mutual information. *Bioinformatics* **32**, 2233–2235 (2016).

[CAS](#) [PubMed](#) [PubMed Central](#) [Google Scholar](#)

50. 50.

Alvarez, M. J. et al. Functional characterization of somatic mutations in cancer using network-based inference of protein activity. *Nat. Genet.* **48**, 838–847 (2016).

[CAS](#) [PubMed](#) [PubMed Central](#) [Google Scholar](#)

51. 51.

Ding, H. et al. Quantitative assessment of protein activity in orphan tissues and single cells using the metaVIPER algorithm. *Nat. Commun.* **9**, 1471 (2018).

[ADS](#) [PubMed](#) [PubMed Central](#) [Google Scholar](#)

52. 52.

Lefebvre, C. et al. A human B-cell interactome identifies MYB and FOXM1 as master regulators of proliferation in germinal centers. *Mol. Syst. Biol.* **6**, 377 (2010).

[PubMed](#) [PubMed Central](#) [Google Scholar](#)

53. 53.

Alvarez, M. J. et al. A precision oncology approach to the pharmacological targeting of mechanistic dependencies in neuroendocrine tumors. *Nat. Genet.* **50**, 979–989 (2018).

[CAS](#) [PubMed](#) [PubMed Central](#) [Google Scholar](#)

54. 54.

Efremova, M., Vento-Tormo, M., Teichmann, S. A. & Vento-Tormo, R. CellPhoneDB: inferring cell–cell communication from combined expression of multi-subunit ligand–receptor complexes. *Nat. Protocols* **15**, 1484–1506 (2020).

[CAS](#) [PubMed](#) [Google Scholar](#)

55. 55.

Bankhead, P. et al. QuPath: open source software for digital pathology image analysis. *Sci. Rep.* **7**, 16878 (2017).

[ADS](#) [PubMed](#) [PubMed Central](#) [Google Scholar](#)

56. 56.

Pedregosa, F. et al. Scikit-learn: machine learning in Python. *J. Mach. Learn. Res.* **12**, 2825–2830 (2011).

[MathSciNet](#) [MATH](#) [Google Scholar](#)

57. 57.

Davies, D. L. & Bouldin, D. W. A cluster separation measure. *IEEE Trans. Pattern Anal. Mach. Intell.* **1**, 224–227 (1979).

[CAS](#) [PubMed](#) [Google Scholar](#)

58. 58.

Vallat, R. Pingouin: statistics in Python. *J. Open Source Softw.* **3**, 1026 (2018).

[ADS](#) [Google Scholar](#)

59. 59.

Gerbe, F. et al. Intestinal epithelial tuft cells initiate type 2 mucosal immunity to helminth parasites. *Nature* **529**, 226–230 (2016).

[ADS](#) [CAS](#) [PubMed](#) [Google Scholar](#)

[Download references](#)

Acknowledgements

We are grateful to all donors and their families. This work is part of the Human Cell Atlas (www.humancellatlas.org/publications). We thank J. Bhattacharya, I. Tabas, A. Tall and S. Roth for discussions. B.I. is supported by National Institute of Health (NIH) National Cancer Institute (NCI) grants K08CA222663, R37CA258829 and U54CA225088, a FastGrant, the Burroughs Wellcome Fund Career Award for Medical Scientists and the Louis V. Gerstner, Jr. Scholars Program. J.Q. is supported by R01HL152293 and R01HL132996. H. Huang is supported by the Department of Defense (DoD) Discovery Award W81XWH-21-1-0196. A.R. is supported by an NCI T32CA203702 grant. O.E. is supported by Volastra, Janssen and Eli Lilly research grants, NIH grants UL1TR002384, R01CA194547, and Leukemia and Lymphoma Society SCOR 7012-16, SCOR 7021-20 and SCOR 180078-02 grants. R.E.S. is supported by NIH grants NCI R01CA234614, NIAID R01AI107301, NIDDK R01DK121072 and RO3DK117252, and is an Irma Hirschl Trust Research Award Scholar. D.S. is a Damon Runyon Fellow supported by the Damon Runyon Cancer Research Foundation (DRQ-03-20). This research was funded in part through the NIH Support Grant S10RR027050 for flow cytometry analysis and the NIH/NCI Cancer Center Support Grant P30CA013696 at Columbia University Genetically Modified Mouse Model Shared Resource, Molecular Pathology Shared Resource and its Tissue Bank.

Author information

Author notes

1. These authors contributed equally: Johannes C. Melms, Jana Biermann, Huachao Huang, Yiping Wang, Ajay Nair, Somnath Tagore, Igor Katsyy, André F. Rendeiro, Amit Dipak Amin
2. These authors jointly supervised this work: Robert E. Schwartz, Olivier Elemento, Anjali Saqi, Hanina Hibshoosh, Jianwen Que, Benjamin Izar

Affiliations

1. Department of Medicine, Division of Hematology/Oncology,
Columbia University Irving Medical Center, New York, NY, USA

Johannes C. Melms, Jana Biermann, Yiping Wang, Amit Dipak
Amin, Meri Rogava, Sean W. Chen, Patricia Ho & Benjamin Izar
2. Columbia Center for Translational Immunology, Columbia University
Irving Medical Center, New York, NY, USA

Johannes C. Melms, Jana Biermann, Yiping Wang, Amit Dipak
Amin, Meri Rogava, Sean W. Chen, Patricia Ho, Adam E.
Kornberg, Arnold S. Han, Emmanuel Zorn & Benjamin Izar
3. Columbia Center for Human Development, Columbia University
Irving Medical Center, New York, NY, USA

Huachao Huang, Yinshan Fang & Jianwen Que
4. Division of Digestive and Liver Diseases, Columbia University Irving
Medical Center, New York, NY, USA

Huachao Huang, Yinshan Fang & Jianwen Que
5. Department of Medicine, Columbia University Irving Medical Center,
New York, NY, USA

Huachao Huang, Ajay Nair, Aveline Filliol, Yinshan Fang, Robert F.
Schwabe & Jianwen Que
6. Department of Systems Biology, Columbia University Irving Medical
Center, New York, NY, USA

Somnath Tagore
7. Department of Pathology and Cell Biology, Columbia University
Irving Medical Center, New York, NY, USA

Igor Katsyy, Jay H. Lefkowitch, Charles Marboe, Stephen M. Lagana, Armando Del Portillo, Glen S. Markowitz, Anjali Saqi & Hanina Hibshoosh

8. Institute for Computational Biomedicine, Weill Cornell Medicine, New York, NY, USA

André F. Rendeiro & Olivier Elemento

9. Caryl and Israel Englander Institute for Precision Medicine, Weill Cornell Medicine, New York, NY, USA

André F. Rendeiro, Hiranmayi Ravichandran, Niroshana Anandasabapathy & Olivier Elemento

10. Laboratory of Systems Pharmacology, Harvard Medical School, Boston, MA, USA

Denis Schapiro

11. Klarman Cell Observatory, Broad Institute of MIT and Harvard, Cambridge, MA, USA

Denis Schapiro & Chris J. Frangieh

12. Department of Electrical Engineering and Computer Science, Massachusetts Institute of Technology, Cambridge, MA, USA

Chris J. Frangieh

13. Department of Cancer Immunology and Virology, Dana-Farber Cancer Center, Boston, MA, USA

Adrienne M. Luoma

14. Department of Physiology and Biophysics, Weill Cornell Medical College, New York, NY, USA

Hiranmayi Ravichandran

15. WorldQuant Initiative for Quantitative Prediction, Weill Cornell Medicine, New York, NY, USA

Hiranmayi Ravichandran & Olivier Elemento

16. Human Immune Monitoring Core, Columbia University Irving Medical Center, New York, NY, USA

Mariano G. Clausi & Xinzheng V. Guo

17. Department of Medicine, Division of Pulmonary and Critical Care, Massachusetts General Hospital, Boston, MA, USA

George A. Alba

18. Cell Circuits, Broad Institute of MIT and Harvard, Cambridge, MA, USA

Daniel T. Montoro

19. Systems Biology, Harvard Medical School, Boston, MA, USA

Daniel T. Montoro

20. Department of Ophthalmology, University of California San Diego, La Jolla, CA, USA

Mathieu F. Bakhoum

21. Department of Dermatology, Weill Cornell Medical College, New York, NY, USA

Niroshana Anandasabapathy

22. Meyer Cancer Center, Weill Cornell Medical College, New York, NY, USA

Niroshana Anandasabapathy

23. Department of Genetics and Genomic Science, Icahn School of Medicine at Mount Sinai, New York, NY, USA

Mayte Suárez-Fariñas

24. Department of Population Health Science and Policy, Icahn School of Medicine at Mount Sinai, New York, NY, USA

Mayte Suárez-Fariñas

25. Human Oncology and Pathogenesis Program, Memorial Sloan Kettering Cancer Center, New York, NY, USA

Samuel F. Bakhoum

26. Department of Radiation Oncology, Memorial Sloan Kettering Cancer Center, New York, NY, USA

Samuel F. Bakhoum

27. Division of Gastroenterology and Hepatology, Department of Medicine, Weill Cornell Medicine, New York, NY, USA

Yaron Bram & Robert E. Schwartz

28. Department of Pathology and Laboratory Medicine, Weill Cornell Medicine, New York, NY, USA

Alain Borczuk

29. Department of Medicine, Weill Cornell Medicine, New York, NY, USA

Alain Borczuk

30. Institute of Human Nutrition, Columbia University, New York, NY, USA

Robert F. Schwabe

31. Herbert Irving Comprehensive Cancer Center, Columbia University
Irving Medical Center, New York, NY, USA

Jianwen Que & Benjamin Izar

32. Program for Mathematical Genomics, Columbia University, New
York, NY, USA

Benjamin Izar

Authors

1. Johannes C. Melms

[View author publications](#)

You can also search for this author in [PubMed](#) [Google Scholar](#)

2. Jana Biermann

[View author publications](#)

You can also search for this author in [PubMed](#) [Google Scholar](#)

3. Huachao Huang

[View author publications](#)

You can also search for this author in [PubMed](#) [Google Scholar](#)

4. Yiping Wang

[View author publications](#)

You can also search for this author in [PubMed](#) [Google Scholar](#)

5. Ajay Nair

[View author publications](#)

You can also search for this author in [PubMed](#) [Google Scholar](#)

6. Somnath Tagore

[View author publications](#)

You can also search for this author in [PubMed](#) [Google Scholar](#)

7. Igor Katsyy

[View author publications](#)

You can also search for this author in [PubMed](#) [Google Scholar](#)

8. André F. Rendeiro

[View author publications](#)

You can also search for this author in [PubMed](#) [Google Scholar](#)

9. Amit Dipak Amin

[View author publications](#)

You can also search for this author in [PubMed](#) [Google Scholar](#)

10. Denis Schapiro

[View author publications](#)

You can also search for this author in [PubMed](#) [Google Scholar](#)

11. Chris J. Frangieh

[View author publications](#)

You can also search for this author in [PubMed](#) [Google Scholar](#)

12. Adrienne M. Luoma

[View author publications](#)

You can also search for this author in [PubMed](#) [Google Scholar](#)

13. Aveline Filliol

[View author publications](#)

You can also search for this author in [PubMed](#) [Google Scholar](#)

14. Yinshan Fang

[View author publications](#)

You can also search for this author in [PubMed](#) [Google Scholar](#)

15. Hiranmayi Ravichandran
[View author publications](#)

You can also search for this author in [PubMed](#) [Google Scholar](#)

16. Mariano G. Clausi
[View author publications](#)

You can also search for this author in [PubMed](#) [Google Scholar](#)

17. George A. Alba
[View author publications](#)

You can also search for this author in [PubMed](#) [Google Scholar](#)

18. Meri Rogava
[View author publications](#)

You can also search for this author in [PubMed](#) [Google Scholar](#)

19. Sean W. Chen
[View author publications](#)

You can also search for this author in [PubMed](#) [Google Scholar](#)

20. Patricia Ho
[View author publications](#)

You can also search for this author in [PubMed](#) [Google Scholar](#)

21. Daniel T. Montoro
[View author publications](#)

You can also search for this author in [PubMed](#) [Google Scholar](#)

22. Adam E. Kornberg
[View author publications](#)

You can also search for this author in [PubMed](#) [Google Scholar](#)

23. Arnold S. Han

[View author publications](#)

You can also search for this author in [PubMed](#) [Google Scholar](#)

24. Mathieu F. Bakhoun

[View author publications](#)

You can also search for this author in [PubMed](#) [Google Scholar](#)

25. Niroshana Anandasabapathy

[View author publications](#)

You can also search for this author in [PubMed](#) [Google Scholar](#)

26. Mayte Suárez-Fariñas

[View author publications](#)

You can also search for this author in [PubMed](#) [Google Scholar](#)

27. Samuel F. Bakhoun

[View author publications](#)

You can also search for this author in [PubMed](#) [Google Scholar](#)

28. Yaron Bram

[View author publications](#)

You can also search for this author in [PubMed](#) [Google Scholar](#)

29. Alain Borczuk

[View author publications](#)

You can also search for this author in [PubMed](#) [Google Scholar](#)

30. Xinzhen V. Guo

[View author publications](#)

You can also search for this author in [PubMed](#) [Google Scholar](#)

31. Jay H. Lefkowitch

[View author publications](#)

You can also search for this author in [PubMed](#) [Google Scholar](#)

32. Charles Marboe

[View author publications](#)

You can also search for this author in [PubMed](#) [Google Scholar](#)

33. Stephen M. Lagana

[View author publications](#)

You can also search for this author in [PubMed](#) [Google Scholar](#)

34. Armando Del Portillo

[View author publications](#)

You can also search for this author in [PubMed](#) [Google Scholar](#)

35. Emmanuel Zorn

[View author publications](#)

You can also search for this author in [PubMed](#) [Google Scholar](#)

36. Glen S. Markowitz

[View author publications](#)

You can also search for this author in [PubMed](#) [Google Scholar](#)

37. Robert F. Schwabe

[View author publications](#)

You can also search for this author in [PubMed](#) [Google Scholar](#)

38. Robert E. Schwartz

[View author publications](#)

You can also search for this author in [PubMed](#) [Google Scholar](#)

39. Olivier Elemento

[View author publications](#)

You can also search for this author in [PubMed](#) [Google Scholar](#)

40. Anjali Saqi

[View author publications](#)

You can also search for this author in [PubMed](#) [Google Scholar](#)

41. Hanina Hibshoosh

[View author publications](#)

You can also search for this author in [PubMed](#) [Google Scholar](#)

42. Jianwen Que

[View author publications](#)

You can also search for this author in [PubMed](#) [Google Scholar](#)

43. Benjamin Izar

[View author publications](#)

You can also search for this author in [PubMed](#) [Google Scholar](#)

Contributions

B.I. provided overall supervision. J.C.M., H. Huang, J.Q. and B.I. conceived this project. J.C.M., H. Huang, A.D.A., A.F., Y.F., H.R., M.G.C., Y.B., X.V.G., M.R., S.W.C., P.H., A.E.K. and A.S.H performed experiments. J.C.M., J.B., H. Huang, Y.W., A.N., S.T., A.F.R., D.S., C.J.F., A.D.A., A.M.L. and G.A.A. performed analyses. I.K., A.B., J.H.L., C.M., S.M.L., A.D.P., E.Z., G.S.M., A.S. and H. Hibshoosh oversaw and performed tissue collection, and performed pathological review of tissues. D.T.M., M.F.B., N.A., M.S.-F., S.F.B., R.E.S. and O.E. provided signatures, materials and data. R.F.S., R.E.S., O.E. and J.Q. performed coordination of

specific analyses and experiments. R.F.S. oversaw fibroblast experiments and analyses. R.E.S. and O.E. oversaw tissue mass cytometry analysis. J.Q. oversaw in vivo studies. D.S., C.J.F. and A.M.L. contributed equally. J.C.M., H. Huang, A.D.A., J.Q. and B.I. wrote the manuscript. All authors reviewed and approved the final manuscript.

Corresponding authors

Correspondence to [Jianwen Que](#) or [Benjamin Izar](#).

Ethics declarations

Competing interests

B.I. is a consultant for Merck and Volastra Therapeutics. O.E. is a scientific advisor and equity holder in Freenome, Owkin, Volastra Therapeutics and OneThree Biotech. R.E.S. is a member of the scientific advisory board of Miromatrix Inc. and is a speaker and consultant for Alnylam Inc. D.T.M. is a consultant for LASE Innovation, Inc. S.F.B. owns equity in, receives compensation from, and serves as a consultant for and on the Scientific Advisory Board and Board of Directors of Volastra Therapeutics Inc. The other authors declare no competing interests.

Additional information

Peer review information *Nature* thanks Christopher Mason, Michael Matthay and the other, anonymous, reviewer(s) for their contribution to the peer review of this work.

Publisher's note Springer Nature remains neutral with regard to jurisdictional claims in published maps and institutional affiliations.

Extended data figures and tables

Extended Data Fig. 1 Patient information and alternative batch correction.

a, Basic demographics of patients with COVID-19 and control donors.

*Decedents with concurrently profiled heart and/or kidney tissue in

companion study³². †Decedent with two independent lung specimens

profiled. **b**, Effect of PMI on clustering. **c**, Cell-type labels overlaid on UMAP embedding resulting from the batch-corrected PCA matrix using Harmony (see [Methods](#)). **d**, Same embedding as in **c** with annotation of COVID-19 and control groups.

Extended Data Fig. 2 Changes in cellular composition.

a, Fraction of cell types in COVID-19 and control lungs across all cells

(intermediate granularity). **b**, Fraction of cell types in COVID-19 and

control lungs among non-immune cells only. **c**, Fraction of cell types in

COVID-19 and control lungs among immune cells only. Control, $n = 7$

donors; COVID-19, $n = 19$ donors examined over 20 experiments. Middle line, median; box edges, 25th and 75th percentiles; whiskers, most extreme points that do not exceed $\pm 1.5 \times$ IQR. Wilcoxon rank-sum test.

Extended Data Fig. 3 Effect of sex on cellular composition and host receptor expression.

a, b, Cell fractions in female and male individuals for control (**a**; $n = 7$ donors) and COVID-19 lungs (**b**; $n = 19$ donors examined over 20

experiments). Middle line, median; box edges, 25th and 75th percentiles;

whiskers, most extreme points that do not exceed $\pm 1.5 \times$ IQR. Wilcoxon rank-sum test. **c, d**, log-normalized and scaled expression (see [Methods](#)) of selected receptors or putative receptors and proteases or putative proteases involved in SARS-CoV-2 entry in different cell types in control samples from female and male donors. Dot size indicates fraction of cells and colour indicates expression level. **e, f**, As in **c, d** for from COVID-19 lungs.

Extended Data Fig. 4 Global changes in myeloid cells.

a, Quantification of cells with CD163⁺ staining as percentage of all cells in a subset of control and COVID-19 samples ($n = 4$ donors per group). Mean \pm s.d., *t*-test. **b, c**, UMAP embedding with myeloid cell-type assignment (**b**) and group assignment (**c**). **d–f**, Expression scores (log-normalized) for monocyte, macrophage and alveolar macrophage signatures in same UMAP embedding as **b, c**. **g**, First three DCs with annotation of control and COVID-19 lung samples. **h**, First three DCs with expression of the alveolar macrophage signature. **i**, Heatmap of top differentially regulated genes among indicated myeloid sub-populations. Left bar indicates genes that were differentially regulated in the respective cell types. Top lanes indicate cell type and group. Rows indicate log-normalized and scaled expression of genes (see [Methods](#)).

[Extended Data Fig. 5 Differential gene expression in alveolar macrophages.](#)

a, Heatmap of top differentially regulated genes (log-normalized and centred, see [Methods](#)) among indicated alveolar macrophages in COVID-19 and control samples. Top lane indicates cell type and group. Rows indicate expression of genes. **b**, Violin plot of *AXL* expression (log-normalized) in alveolar macrophages from controls and COVID-19 tissues. Wilcoxon rank-sum test with Bonferroni adjusted *P* value indicated on top. **c**, Expression of *AXL* (log-normalized) among major cell types. Expression of this gene was nearly exclusive to fibroblasts and myeloid and epithelial cells.

[Extended Data Fig. 6 Inferred immunoglobulins in plasma cells.](#)

a, b, UMAP embedding of cells within the B/plasma cell cluster (**a**) and corresponding group assignment (**b**). **c**, Selected genes that define cells within the B/plasma cell cluster. Dot size indicates fraction of cells and colour indicates log-normalized and scaled expression level (see [Methods](#)). **d**, Heatmap illustrating the number of cells with combinations of variable heavy (*x*-axis) and light (*y*-axis) chains recovered in plasma cells across all patients. Average linkage was used for hierarchical clustering analysis. The colour of each square indicates the number of cells detected for each

specific pair (colour key). **e**, As in **d**, but indicating the number of control samples with each combination detected (Supplementary Table 6). **f**, As in **e**, but indicating isotype usage in control donors alone (Supplementary Table 6). **g**, As in **e**, but demonstrating isotype usage in patients with COVID-19 (corresponding to Fig. 3e,f; shown are the top 20 combinations; complete list in Supplementary Table 6). **h**, Frequency (y-axis) of variable heavy chains (x-axis) in COVID-19 and control samples. **i**, As in **h**, but for variable light chain usage. **j**, Frequency (y-axis) of variable heavy chains (x-axis) on a per-donor basis. **k**, As in **j**, but for variable light chain usage. **l**, Exemplary H&E-stained image ($n = 19$ donors evaluated) with coloured outlines indicating different immune cell types. Scale bar, 100 μ m. **m**, C4d immunohistochemistry in representative control (left) and COVID-19 (right) samples ($n = 6$ donors per group). Scale bar, 100 μ m.

Extended Data Fig. 7 Activation, residency and dysfunction cell states in T cells.

a, Expression of selected genes in cells of the T/NK cell compartment. Dot size indicates fraction of cells and colour indicates expression level. **b**, Quantification of cells with CD4 $^{+}$ staining as percentage of all cells (y-axis) in control and COVID-19 lungs ($n = 4$ donors per group). **c**, As in **b**, but for CD8 $^{+}$ T cells. Mean \pm s.d., *t*-test. **d–g**, Expression of different program scores (tissue residency memory program, activation score, memory score and exhaustion score, all from K. S. P. Devi et al. (unpublished); see [Methods](#)) in CD4 $^{+}$ T cells (left) and CD8 $^{+}$ T cells (right) among control donors and individuals with COVID-19. Middle line, median; box edges, 25th and 75th percentiles; whiskers, most extreme points that do not exceed $\pm 1.5 \times$ IQR. Wilcoxon rank-sum test. Cohen's *D* is indicated between the whiskers for each comparison (COVID-19 versus control). **h**, Quantification of CD4 $^{+}$ GZMB $^{+}$ T cells as percentage of CD4 $^{+}$ T cells (y-axis) in control and COVID-19 lungs ($n = 4$ donors per group). **i**, As in **h**, but for CD8 $^{+}$ T cells. Mean \pm s.d., *t*-test. **j**, **k**, Representative multiplexed immunofluorescence of lung tissue from a patient with COVID-19 with a pure myeloid infiltrate (**j**) or with a mixed myeloid and lymphoid infiltrate (**k**; $n = 4$ donors per group). Scale bars, 200 μ m.

Extended Data Fig. 8 DATPs and lung regeneration.

a, Expression of selected, previously established cell-type-specific signatures (y-axis) in cell types defined in this study (x-axis). Dot size indicates fraction of cells and colour indicates expression level. **b, c**, Expression of selected genes (y-axis) in different cell types (x-axis), highlighting high expression of B2M in cycling epithelial cells (**b**) and collagen genes in ECM^{high} epithelial cells (**c**). **d**, Fraction of KI67⁺ cells among pro-SPC⁺ cells in structurally preserved versus damaged areas ($n = 3$ distinct areas each) from a COVID-19 lung. Mean \pm s.d., *t*-test. **e–g**, UMAP embedding of alveolar epithelium and expression of selected genes that define the DATP signature. **h**, Composite expression of the three-gene DATP signature. **i**, Expression of the refined DATP signature (see [Methods](#)). **j–n**, First three DCs showing group assignment (**j**), cell or cell-state assignment (**k**), expression of AT2 signature (**l**), AT1 signature (**m**; log-normalized, see [Methods](#)), and effect of PMI (**n**). **o**, Gene set enrichment analysis in DATPs (compared to AT1 and AT2 cells). Rows indicate pathways in descending order of enrichment or significance (see key); *x*-axis indicates FDR. **p**, Inference of G2/M and S phase of individual DATPs (dots) (see [Methods](#)). **q**, Representative immunofluorescence staining (DATP marker CLDN4 and AT2 cell marker HTII-280) in control and COVID-19 lung tissue sections. Dashed boxes indicate areas highlighted to the right of each image. Scale bar, 50 μ m. **r, s**, Quantification of KRT8⁺ (**r**) and CLDN4⁺ (**s**) cells in a subset of tissue sections from control and COVID-19 lungs. Mean \pm s.d., *t*-test. **q–s**, Control, $n = 3$ donors; COVID-19, $n = 4$ donors. **t**, Coefficient of determination (R^2) of days from symptom onset to death and AT2/AT1 ratio. Error bands, 95% standard error interval on the Pearson correlation ($n = 18$ donors).

Extended Data Fig. 9 Cellular sources of inflammatory cytokines.

a, Average frequency of cell types expressing IL-1 β across healthy and disease conditions. **b**, Quantification of IL-1 β across cell types in healthy and disease conditions. Each dot represents a single region of interest (ROI). **c**, Quantification of IL-1 β across healthy and disease conditions and

cell types, including separation of patients with early death (within 14 days of onset of COVID-19 symptoms) and late death (within 30 days of onset of COVID-19 symptoms). **d**, Average frequency of cell types expressing IL-6 across healthy and disease conditions. **e**, Quantification of IL-6 across cell types in healthy and disease conditions. Each dot represents a single region of interest (ROI). **f**, Quantification of IL-6 across across healthy and disease conditions and cell types, including separation of patients with early death (within 14 days of onset of COVID-19 symptoms) and late death (within 30 days of onset of COVID-19 symptoms). **g**, Expression of selected manually curated gene sets of chemotaxis, inflammasome receptors and type I interferon (response) genes across different cell types (y-axis). Dot size indicates significance and colour indicates expression level ($\log_2(\text{fold change})$). **h**, qRT–PCR comparing *IFNA1*, *IFNA2*, *IFNB1*, and *IL-6* mRNA levels in COVID-19 and control lungs ($n = 3$ donors for each group). Mean \pm s.d., *t*-test.

Extended Data Fig. 10 Identification of ectopic tuft-like cells.

a–c, First three DCs of airway epithelial cells with group annotation with cell-type assignment (**a**), group assignment (**b**) and indicating expression of tuft cell signature (**c**) in the same projections. **d**, Expression of previously established signatures identifying cell types in cell types assigned in this study. Dot size indicates fraction of cells and colour indicates expression level (log-normalized and scaled, see [Methods](#)). **e**, Expression of selected cell-type-specific signatures of airway and alveolar epithelium from previous studies in cells identified as tuft-like cells in this study. Signatures in descending order of enrichment or significance. Colour indicates significance. **f**, **g**, Representative immunofluorescence staining of control lungs (**f**; two areas) and COVID-19 (**g**; airway and parenchyma) for KRT5 and CHAT. Arrows indicate CHAT⁺ cells. Scale bar, 50 μm . **h**, Quantification of CHAT⁺ cells in the upper airway epithelium of control and COVID-19 lungs. Mean \pm s.d., *t*-test. **i**, Quantification of CHAT⁺ cells in the alveolar epithelium of control and COVID-19 lungs. Mean \pm s.d., *t*-test. **j**, **k**, Immunofluorescence staining for KRT5 and POU2F3 of control lungs (**j**) and COVID-19 lungs (**k**), including upper airway (left) and

parenchyma (right). White arrows indicate POU2F3⁺ cells. Scale bars, 50 μm. **f–k**, $n = 3$ donors per group.

Extended Data Fig. 11 Role of tuft cells in macrophage infiltration in mouse viral pneumonia model.

a, Immunofluorescence staining for SCGB1A1 and DCLK1 of proximal (left) and distal (right) airway from wild-type (WT) mice at baseline. $n = 3$ mice per group. Arrow, DCLK1⁺ cell. Scale bar, 50 μm. **b**, As in **a**, but in wild-type (left) and *Pou2f3*^{−/−} mice 14 days after infection with H1N1 (PR8). **c**, Quantification of tuft cells as percentage of DCLK1⁺ cells in *Pou2f3*^{−/−} compared to wild-type mice. Mean ± s.d., *t*-test. **d**, **e**, $n = 4$ mice per group. **d**, Immunofluorescence staining for CD45 and CD64 of lung parenchyma from wild-type (left) and *Pou2f3*^{−/−} (right) mice 14 days after infection with H1N1 (PR8). Arrows indicate CD45⁺CD64⁺ macrophages. Scale bar, 50 μm. **e**, Quantification (CD45⁺CD64⁺ cells among CD45⁺ cells) as percentage in *Pou2f3*^{−/−} mice compared to wild-type mice 14 days after infection with H1N1. Mean ± s.d., *t*-test. **f**, **g**, Gating strategy to identify CD45⁺CD64⁺F4/80⁺ cells. **g**, Identification of CD64⁺F4/80⁺ cells (based on gating strategy in **f**) in wild-type (left) and *Pou2f3*^{−/−} mice (right) 14 days after infection with H1N1. **h**, Quantification of flow-cytometric determination of CD45⁺CD64⁺F4/80⁺ cells as percentage of CD45⁺ cells in *Pou2f3*^{−/−} relative to wild-type mice ($n = 3$ per group). Mean ± s.d., *t*-test. **i**, qRT–PCR comparing relative mRNA expression of indicated chemokines and cytokines in *Pou2f3*^{−/−} and wild-type mice 14 days after infection with H1N1 ($n = 3$ per group). Mean ± s.d., *t*-test. **j**, As in **i**, but 44 days after infection with H1N1 ($n = 3$ per group). **k**, Exemplary immunofluorescence staining ($n = 3$ mice per group) for KRT5 and DCLK1 in wild-type mouse 90 days after infection. Arrows indicate DCLK1⁺ cells. Scale bar, 50 μm. **l**, As in **i**, **j**, but comparing expression of indicated chemokines and cytokines in control donors and patients with COVID-19 ($n = 3$ donors per group). Mean ± s.d., *t*-test.

[Source data](#)

Extended Data Fig. 12 Role of fibroblasts, potential drug targets and model of lethal COVID-19.

a, b, Exemplary α SMA immunohistochemical staining of tissue from control (**a**; sample C56; $n = 7$ donors) and COVID-19 samples (**b**; samples L05cov and L06cov; $n = 17$ donors). Scale bars, 500 μm . **c**, Percentage of α -SMA $^{+}$ cells per total area (n as in **a, b**). Mean \pm s.d., *t*-test. **d**, Exemplary Sirius red staining of control (left, n as in **a**) and COVID-19 (right, n as in **b**) samples. Scale bar, 600 μm . **e**, Detailed annotation of fibroblasts in this study and selected marker genes. Dot size indicates fraction of cells and colour indicates expression level (log-normalized and scaled). **f**, Fractions of cell types among all cells in COVID-19 ($n = 19$ donors examined over 20 experiments) and control lungs ($n = 7$ donors). Middle line, median; box edges, 25th and 75th percentiles; whiskers, most extreme points that do not exceed $\pm 1.5 \times$ IQR. Wilcoxon rank-sum test. **g, h**, Inferred cell-to-cell interactions among major cell types (indicated as circles connected by lines) in control (**g**) and COVID-19 (**h**) lung samples. The size of the circle corresponds to the frequency of the respective cell type and the thickness of the lines connecting circles indicates the absolute number of interactions. **i**, Differential enrichment (COVID-19 versus control samples) of specific ligand–receptor interactions (rows) between two different cell types (columns). Dot colour indicates \log_2 (fold change) of inferred ligand–receptor expression in COVID-19 compared to control lungs (unpaired two-sided Wilcoxon rank-sum test); dot size is inversely correlated with Benjamini–Hochberg adjusted *P* (see [Methods](#)). **j**, Inferred protein activity (rows) among cells corresponding to pathological fibroblasts, intermediate pathological fibroblasts, and non-pathological fibroblasts (columns). Proteins with high activity in pathological fibroblasts are highlighted. **k**, Model summarizing potential mechanisms that contribute to morbidity and mortality in patients with COVID-19, focusing on impaired cellular regeneration and rapidly ensuing fibrosis.

Supplementary information

Supplementary Information

This file contains full legends for Supplementary Tables 1-13, a Supplementary Discussion and Supplementary References.

Reporting Summary

Supplementary Information

This file contains an overview of Supplementary Tables 1-13.

Supplementary Table 1

Clinical information of COVID-19 and control donors – see Supplementary Information document for full description.

Supplementary Table 2

Cell type assignment – see Supplementary Information document for full description.

Supplementary Table 3

SARS-CoV-2 reads in L19cov – see Supplementary Information document for full description.

Supplementary Table 4

Gene signatures – see Supplementary Information document for full description.

Supplementary Table 5

Macrophages differential gene expression – see Supplementary Information document for full description.

Supplementary Table 6

Immunoglobulin (IGHV/IGLV usage) – see Supplementary Information document for full description.

Supplementary Table 7

AT cells differential gene expression – see Supplementary Information document for full description.

Supplementary Table 8

Differential gene expression and signature DATP – see Supplementary Information document for full description.

Supplementary Table 9

Fibroblast cluster marker annotation and differential gene expression – see Supplementary Information document for full description.

Supplementary Table 10

Top ligand-receptor interactions – see Supplementary Information document for full description.

Supplementary Table 11

Inferred protein activity and oncotarget – see Supplementary Information document for full description.

Supplementary Table 12

List of antibodies, dilutions, and associated reagents used for immunofluorescent, immunohistochemistry, FACS, and multiplexed immunofluorescence experiments.

Supplementary Table 13

A list of qRT-PCR Primers for human and mouse tagets assessed by qRT-PCR.

Source data

[Source Data Extended Data Fig. 11](#)

Rights and permissions

[Reprints and Permissions](#)

About this article



Check for
updates

Cite this article

Melms, J.C., Biermann, J., Huang, H. *et al.* A molecular single-cell lung atlas of lethal COVID-19. *Nature* **595**, 114–119 (2021).
<https://doi.org/10.1038/s41586-021-03569-1>

[Download citation](#)

- Received: 16 November 2020
- Accepted: 19 April 2021
- Published: 29 April 2021
- Issue Date: 01 July 2021
- DOI: <https://doi.org/10.1038/s41586-021-03569-1>

Further reading

- [**Single-cell atlases dissect tissue destruction by SARS-CoV-2**](#)
 - Alexandra Flemming

Nature Reviews Immunology (2021)
- [**COVID-19 tissue atlases reveal SARS-CoV-2 pathology and cellular targets**](#)
 - Toni M. Delorey
 - , Carly G. K. Ziegler
 - , Graham Heimberg
 - , Rachelly Normand
 - , Yiming Yang
 - , Åsa Segerstolpe
 - , Domenic Abbondanza
 - , Stephen J. Fleming
 - , Ayshwarya Subramanian
 - , Daniel T. Montoro
 - , Karthik A. Jagadeesh
 - , Kushal K. Dey
 - , Pritha Sen
 - , Michal Slyper
 - , Yered H. Pita-Juárez
 - , Devan Phillips
 - , Jana Biermann
 - , Zohar Bloom-Ackermann
 - , Nikolaos Barkas
 - , Andrea Ganna
 - , James Gomez
 - , Johannes C. Melms
 - , Igor Katsyy
 - , Erica Normandin

- , Pourya Naderi
- , Yury V. Popov
- , Siddharth S. Raju
- , Sebastian Niezen
- , Linus T.-Y. Tsai
- , Katherine J. Siddle
- , Malika Sud
- , Victoria M. Tran
- , Shamsudheen K. Vellarikkal
- , Yiping Wang
- , Liat Amir-Zilberstein
- , Deepak S. Atri
- , Joseph Beechem
- , Olga R. Brook
- , Jonathan Chen
- , Prajan Divakar
- , Phylicia Dorceus
- , Jesse M. Engreitz
- , Adam Essene
- , Donna M. Fitzgerald
- , Robin Fropf
- , Steven Gazal
- , Joshua Gould
- , John Grzyb
- , Tyler Harvey
- , Jonathan Hecht
- , Tyler Hether
- , Judit Jané-Valbuena
- , Michael Leney-Greene
- , Hui Ma
- , Cristin McCabe
- , Daniel E. McLoughlin
- , Eric M. Miller
- , Christoph Muus
- , Mari Niemi
- , Robert Padera
- , Liiliu Pan

- , Deepti Pant
- , Carmel Pe'er
- , Jenna Pfiffner-Borges
- , Christopher J. Pinto
- , Jacob Plaisted
- , Jason Reeves
- , Marty Ross
- , Melissa Rudy
- , Erroll H. Rueckert
- , Michelle Siciliano
- , Alexander Sturm
- , Ellen Todres
- , Avinash Waghray
- , Sarah Warren
- , Shuting Zhang
- , Daniel R. Zollinger
- , Lisa Cosimi
- , Rajat M. Gupta
- , Nir Hacohen
- , Hanina Hibshoosh
- , Winston Hide
- , Alkes L. Price
- , Jayaraj Rajagopal
- , Purushothama Rao Tata
- , Stefan Riedel
- , Gyongyi Szabo
- , Timothy L. Tickle
- , Patrick T. Ellinor
- , Deborah Hung
- , Pardis C. Sabeti
- , Richard Novak
- , Robert Rogers
- , Donald E. Ingber
- , Z. Gordon Jiang
- , Dejan Juric
- , Mehrtash Babadi
- , Samouil L. Farhi

- , Benjamin Izar
- , James R. Stone
- , Ioannis S. Vlachos
- , Isaac H. Solomon
- , Orr Ashenberg
- , Caroline B. M. Porter
- , Bo Li
- , Alex K. Shalek
- , Alexandra-Chloé Villani
- , Orit Rozenblatt-Rosen
- & Aviv Regev

Nature (2021)

[Download PDF](#)

Associated Content

[Single-cell atlases dissect tissue destruction by SARS-CoV-2](#)

- Alexandra Flemming

Advertisement

This article was downloaded by **calibre** from <https://www.nature.com/articles/s41586-021-03569-1>

- Article
- [Published: 02 June 2021](#)

A proximity-dependent biotinylation map of a human cell

- [Christopher D. Go](#)^{1,2} na1,
- [James D. R. Knight](#)¹ na1,
- [Archita Rajasekharan](#)³,
- [Bhavisha Rathod](#)¹,
- [Geoffrey G. Hesketh](#) [ORCID: orcid.org/0000-0002-5570-7615](#)¹,
- [Kento T. Abe](#)^{1,2},
- [Ji-Young Youn](#)^{1,2} nAff7,
- [Payman Samavarchi-Tehrani](#)¹,
- [Hui Zhang](#)⁴,
- [Lucie Y. Zhu](#) [ORCID: orcid.org/0000-0002-1048-5377](#)⁴,
- [Evelyn Popiel](#)²,
- [Jean-Philippe Lambert](#) [ORCID: orcid.org/0000-0002-0833-1221](#)¹ nAff8 nAff9,
- [Étienne Coyaud](#)⁵ nAff10,
- [Sally W. T. Cheung](#) [ORCID: orcid.org/0000-0003-0974-8720](#)¹,
- [Dushyandi Rajendran](#)¹,
- [Cassandra J. Wong](#)¹,
- [Hana Antonicka](#) [ORCID: orcid.org/0000-0002-2525-2867](#)³,
- [Laurence Pelletier](#) [ORCID: orcid.org/0000-0003-1171-4618](#)^{1,2},
- [Alexander F. Palazzo](#) [ORCID: orcid.org/0000-0002-9700-1995](#)⁴,
- [Eric A. Shoubridge](#)³,
- [Brian Raught](#)^{5,6} &
- [Anne-Claude Gingras](#) [ORCID: orcid.org/0000-0002-6090-4437](#)^{1,2}

- 16k Accesses
- 368 Altmetric
- [Metrics details](#)

Subjects

- [Computational biology and bioinformatics](#)
- [Proteomics](#)
- [Systems biology](#)

Abstract

Compartmentalization is a defining characteristic of eukaryotic cells, and partitions distinct biochemical processes into discrete subcellular locations. Microscopy¹ and biochemical fractionation coupled with mass spectrometry^{2,3,4} have defined the proteomes of a variety of different organelles, but many intracellular compartments have remained refractory to such approaches. Proximity-dependent biotinylation techniques such as BioID provide an alternative approach to define the composition of cellular compartments in living cells^{5,6,7}. Here we present a BioID-based map of a human cell on the basis of 192 subcellular markers, and define the intracellular locations of 4,145 unique proteins in HEK293 cells. Our localization predictions exceed the specificity of previous approaches, and enabled the discovery of proteins at the interface between the mitochondrial outer membrane and the endoplasmic reticulum that are crucial for mitochondrial homeostasis. On the basis of this dataset, we created [humancellmap.org](#) as a community resource that provides online tools for localization analysis of user BioID data, and demonstrate how this resource can be used to understand BioID results better.

Access options

[Subscribe to Journal](#)

Get full journal access for 1 year

\$199.00

only \$3.90 per issue

[Subscribe](#)

All prices are NET prices.

VAT will be added later in the checkout.

Tax calculation will be finalised during checkout.

Rent or Buy article

Get time limited or full article access on ReadCube.

from \$8.99

[Rent or Buy](#)

All prices are NET prices.

Additional access options:

- [Log in](#)
- [Access through your institution](#)
- [Learn about institutional subscriptions](#)

Fig. 1: Generation and analysis of BioID dataset, and validation strategy.

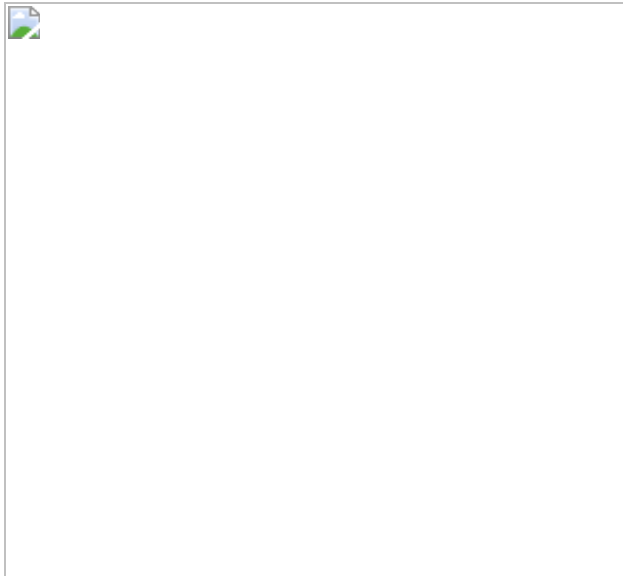


Fig. 2: Localization of proteins using prey-centric analysis.

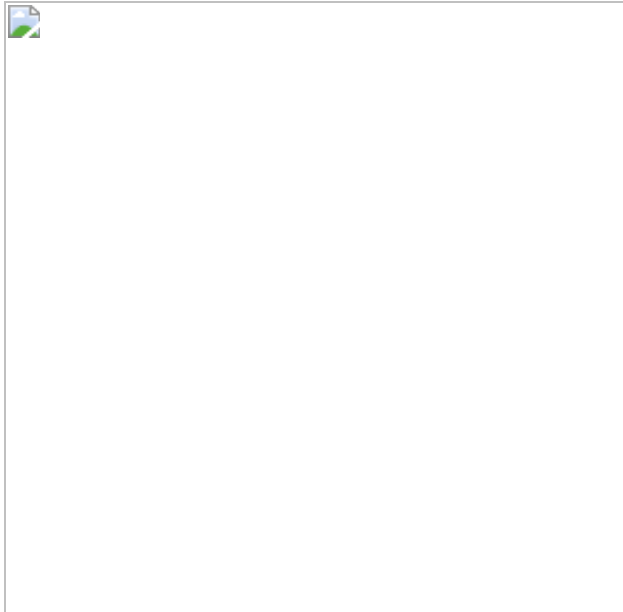
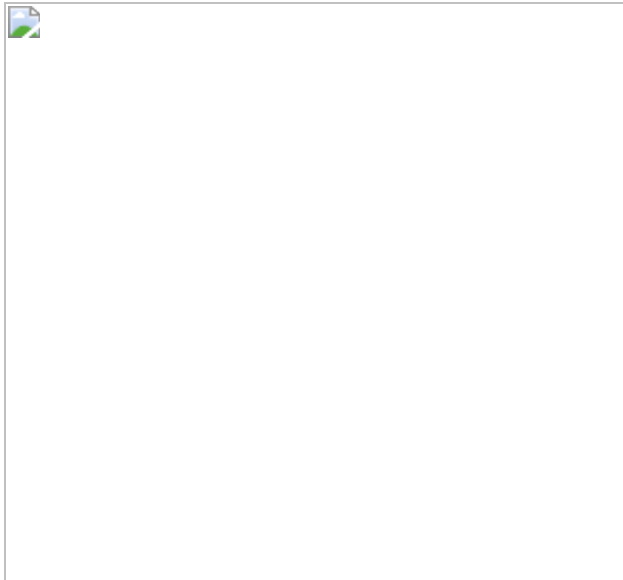


Fig. 3: Discovery of new connections using the humancellmap.



Data availability

Mass spectrometry datasets consisting of raw files and associated peak lists and results files have been deposited in ProteomeXchange through partner Mass spectrometry Interactive Virtual Environment MassIVE (<http://proteomics.ucsd.edu/ProteoSAFe/datasets.jsp>) as complete submissions. Other files include the sample description, the peptide/protein evidence and the complete SAINTexpress output for each dataset, as well as a ‘README’ file that describes the dataset composition and the experimental procedures associated with each submission. The different datasets generated here were submitted as independent entries.

Dataset 1 (Supplementary Table 2):

Go_BioID_humancellmap_HEK293_lowSDS_core_data set_2019 MassIVE ID MSV000084359 and PXD015530. Dataset 2 (Supplementary Table 2): Go_BioID_humancellmap_HEK293_highSDS_core_data set_2019 MassIVE ID MSV000084360 and PXD015531. Dataset 3

(Supplementary Table 18):

Go_BioID_humancellmap_HEK293_prediction_2019 MassIVE ID MSV000084369 and PXD015554. Dataset 4 (Supplementary Table 17): Go_BioID_humancellmap_HEK293_ER-mito_candidates_2019 MassIVE ID MSV000084357 and PXD015528.

Negative-control samples were deposited in the Contaminant Repository for Affinity Purification⁴⁶ (CRApome.org) and assigned samples numbers CC1100 to CC1185 (Supplementary Table 2); this will be part of the next release of the database.

The BioGRID⁴⁷ human database v3.5.169 was downloaded on 13 February 2019 (<https://downloads.thebiogrid.org/BioGRID/Release-Archive/BIOGRID-3.5.169/>). Human gene annotations were downloaded from the GO on 15 February 2019 (GO version date 1 February 2019, http://release.geneontology.org/2019-02-01/annotations/goa_human.gaf.gz). The GO hierarchy (release date 1 February 2019) was downloaded from GO^{48,49} on 15 February 2019 (<http://release.geneontology.org/2019-02-01/ontology/go-basic.obo>). The UniProt database⁵⁰ release 2019_2 was downloaded on 21 February 2019 (ftp.uniprot.org/pub/databases/uniprot/previous_releases/release-2019_02/knowledgebase/uniprot_sprot-only2019_02.tar.gz). The IntAct⁵¹ human database release 2018_11_30 was downloaded on 13 February 2019 (ftp.ebi.ac.uk/pub/databases/intact/2018-11-30/psimitab/intact.txt). Human protein domain annotations and motifs were retrieved from Pfam⁵² (version 32) on 21 February 2019 (ftp.ebi.ac.uk/pub/databases/Pfam/releases/Pfam32.0/proteomes/9606.tsv.gz). ProteomicsDB⁵³ was queried for protein expression information on 14 January 2020 using their API. Text mining data was downloaded from the Compartments database⁵⁴ on 21 January 2020 (<https://compartments.jensenlab.org/Downloads>). [Source data](#) are provided with this paper.

Code availability

Source code used for analysis can be accessed from <https://github.com/knightjdr/cellmap-scripts>.

References

1. 1.

Thul, P. J. et al. A subcellular map of the human proteome. *Science* **356**, eaal3321 (2017).

[Google Scholar](#)

2. 2.

Christoforou, A. et al. A draft map of the mouse pluripotent stem cell spatial proteome. *Nat. Commun.* **7**, 8992 (2016).

[PubMed](#) [PubMed Central](#) [Google Scholar](#)

3. 3.

Itzhak, D. N., Tyanova, S., Cox, J. & Borner, G. H. Global, quantitative and dynamic mapping of protein subcellular localization. *eLife* **5**, e16950 (2016).

[PubMed](#) [PubMed Central](#) [Google Scholar](#)

4. 4.

Orre, L. M. et al. SubCellBarCode: Proteome-wide mapping of protein localization and relocalization. *Mol. Cell* **73**, 166–182 (2019).

[CAS](#) [PubMed](#) [PubMed Central](#) [Google Scholar](#)

5. 5.

Roux, K. J., Kim, D. I., Raida, M. & Burke, B. A promiscuous biotin ligase fusion protein identifies proximal and interacting proteins in mammalian cells. *J. Cell Biol.* **196**, 801–810 (2012).

[CAS](#) [PubMed](#) [PubMed Central](#) [Google Scholar](#)

6. 6.

Gupta, G. D. et al. A dynamic protein interaction landscape of the human centrosome-cilium interface. *Cell* **163**, 1484–1499 (2015).

[CAS](#) [PubMed](#) [PubMed Central](#) [Google Scholar](#)

7. 7.

Youn, J. Y. et al. High-density proximity mapping reveals the subcellular organization of mRNA-associated granules and bodies. *Mol. Cell* **69**, 517–532 (2018).

[CAS](#) [Google Scholar](#)

8. 8.

Rhee, H. W. et al. Proteomic mapping of mitochondria in living cells via spatially restricted enzymatic tagging. *Science* **339**, 1328–1331 (2013).

[ADS](#) [CAS](#) [PubMed](#) [PubMed Central](#) [Google Scholar](#)

9. 9.

Gingras, A. C., Abe, K. T. & Raught, B. Getting to know the neighborhood: using proximity-dependent biotinylation to characterize protein complexes and map organelles. *Curr. Opin. Chem. Biol.* **48**, 44–54 (2019).

[CAS](#) [Google Scholar](#)

10. 10.

Kim, D. I. et al. Probing nuclear pore complex architecture with proximity-dependent biotinylation. *Proc. Natl Acad. Sci. USA* **111**, E2453–E2461 (2014).

[CAS](#) [PubMed](#) [PubMed Central](#) [Google Scholar](#)

11. 11.

Antonicka, H. et al. A high-density human mitochondrial proximity interaction network. *Cell Metab.* **32**, 479–497 (2020).

[CAS](#) [Google Scholar](#)

12. 12.

Botham, A. et al. Global interactome mapping of mitochondrial intermembrane space proteases identifies a novel function for HTRA2. *Proteomics* **19**, e1900139 (2019).

[Google Scholar](#)

13. 13.

Chapple, C. E. et al. Extreme multifunctional proteins identified from a human protein interaction network. *Nat. Commun.* **6**, 7412 (2015).

[ADS](#) [Google Scholar](#)

14. 14.

Eisenberg-Bord, M., Shai, N., Schuldiner, M. & Bohnert, M. A tether is a tether is a tether: tethering at membrane contact sites. *Dev. Cell* **39**, 395–409 (2016).

[CAS](#) [Google Scholar](#)

15. 15.

Branon, T. C. et al. Efficient proximity labeling in living cells and organisms with TurboID. *Nat. Biotechnol.* **36**, 880–887 (2018).

[CAS](#) [PubMed](#) [PubMed Central](#) [Google Scholar](#)

16. 16.

Lee, S. & Min, K. T. The interface between ER and mitochondria: molecular compositions and functions. *Mol. Cells* **41**, 1000–1007 (2018).

[CAS](#) [PubMed](#) [PubMed Central](#) [Google Scholar](#)

17. 17.

Prudent, J. & McBride, H. M. The mitochondria-endoplasmic reticulum contact sites: a signalling platform for cell death. *Curr. Opin. Cell Biol.* **47**, 52–63 (2017).

[CAS](#) [Google Scholar](#)

18. 18.

Rowland, A. A. & Voeltz, G. K. Endoplasmic reticulum-mitochondria contacts: function of the junction. *Nat. Rev. Mol. Cell Biol.* **13**, 607–625 (2012).

[CAS](#) [PubMed](#) [PubMed Central](#) [Google Scholar](#)

19. 19.

Ackema, K. B. et al. Sar1, a novel regulator of ER-mitochondrial contact sites. *PLoS ONE* **11**, e0154280 (2016).

[PubMed](#) [PubMed Central](#) [Google Scholar](#)

20. 20.

Kalia, R. et al. Structural basis of mitochondrial receptor binding and constriction by DRP1. *Nature* **558**, 401–405 (2018).

[ADS](#) [CAS](#) [PubMed](#) [PubMed Central](#) [Google Scholar](#)

21. 21.

Korobova, F., Ramabhadran, V. & Higgs, H. N. An actin-dependent step in mitochondrial fission mediated by the ER-associated formin INF2. *Science* **339**, 464–467 (2013).

[ADS](#) [CAS](#) [Google Scholar](#)

22. 22.

Bersuker, K. et al. A proximity labeling strategy provides insights into the composition and dynamics of lipid droplet proteomes. *Dev. Cell* **44**, 97–112 (2018).

[CAS](#) [Google Scholar](#)

23. 23.

Xu, S. et al. Mitochondrial E3 ubiquitin ligase MARCH5 controls mitochondrial fission and cell sensitivity to stress-induced apoptosis through regulation of MiD49 protein. *Mol. Biol. Cell* **27**, 349–359 (2016).

[CAS](#) [PubMed](#) [PubMed Central](#) [Google Scholar](#)

24. 24.

Chatr-Aryamontri, A. et al. The BioGRID interaction database: 2017 update. *Nucleic Acids Res.* **45** (D1), D369–D379 (2017).

[CAS](#) [Google Scholar](#)

25. 25.

Lambert, J. P. et al. Interactome rewiring following pharmacological targeting of BET bromodomains. *Mol. Cell* **73**, 621–638 (2019).

[CAS](#) [PubMed](#) [PubMed Central](#) [Google Scholar](#)

26. 26.

Kastritis, P. L. et al. Capturing protein communities by structural proteomics in a thermophilic eukaryote. *Mol. Syst. Biol.* **13**, 936 (2017).

[PubMed](#) [PubMed Central](#) [Google Scholar](#)

27. 27.

Omasits, U., Ahrens, C. H., Müller, S. & Wollscheid, B. Protter: interactive protein feature visualization and integration with experimental proteomic data. *Bioinformatics* **30**, 884–886 (2014).

[CAS](#) [Google Scholar](#)

28. 28.

Couzens, A. L. et al. Protein interaction network of the mammalian Hippo pathway reveals mechanisms of kinase-phosphatase interactions. *Sci. Signal.* **6**, rs15 (2013).

[Google Scholar](#)

29. 29.

Banks, C. A., Boanca, G., Lee, Z. T., Florens, L. & Washburn, M. P. Proteins interacting with cloning scars: a source of false positive protein-protein interactions. *Sci. Rep.* **5**, 8530 (2015).

[ADS](#) [CAS](#) [PubMed](#) [PubMed Central](#) [Google Scholar](#)

30. 30.

Allen, M. D. & Zhang, J. Subcellular dynamics of protein kinase A activity visualized by FRET-based reporters. *Biochem. Biophys. Res. Commun.* **348**, 716–721 (2006).

[CAS](#) [Google Scholar](#)

31. 31.

Kessner, D., Chambers, M., Burke, R., Agus, D. & Mallick, P. ProteoWizard: open source software for rapid proteomics tools development. *Bioinformatics* **24**, 2534–2536 (2008).

[CAS](#) [PubMed](#) [PubMed Central](#) [Google Scholar](#)

32. 32.

Shteynberg, D. et al. iProphet: multi-level integrative analysis of shotgun proteomic data improves peptide and protein identification rates and error estimates. *Mol. Cell Proteomics* **10**, M111.007690 (2011).

[PubMed](#) [PubMed Central](#) [Google Scholar](#)

33. 33.

Liu, G. et al. ProHits: integrated software for mass spectrometry-based interaction proteomics. *Nat. Biotechnol.* **28**, 1015–1017 (2010).

[CAS](#) [PubMed](#) [PubMed Central](#) [Google Scholar](#)

34. 34.

Eng, J. K., Jahan, T. A. & Hoopmann, M. R. Comet: an open-source MS/MS sequence database search tool. *Proteomics* **13**, 22–24 (2013).

[CAS](#) [PubMed](#) [PubMed Central](#) [Google Scholar](#)

35. 35.

Keller, A., Nesvizhskii, A. I., Kolker, E. & Aebersold, R. Empirical statistical model to estimate the accuracy of peptide identifications made by MS/MS and database search. *Anal. Chem.* **74**, 5383–5392 (2002).

[CAS](#) [PubMed](#) [PubMed Central](#) [Google Scholar](#)

36. 36.

Nesvizhskii, A. I., Keller, A., Kolker, E. & Aebersold, R. A statistical model for identifying proteins by tandem mass spectrometry. *Anal. Chem.* **75**, 4646–4658 (2003).

[CAS](#) [PubMed](#) [PubMed Central](#) [Google Scholar](#)

37. 37.

Teo, G. et al. SAINTexpress: improvements and additional features in Significance Analysis of INTeractome software. *J. Proteomics* **100**, 37–43 (2014).

[CAS](#) [PubMed](#) [PubMed Central](#) [Google Scholar](#)

38. 38.

Raudvere, U. et al. gProfiler: a web server for functional enrichment analysis and conversions of gene lists (2019 update). *Nucleic Acids Res.* **47** (W1), W191–W198 (2019).

[CAS](#) [PubMed](#) [PubMed Central](#) [Google Scholar](#)

39. 39.

Knight, J. D. R. et al. ProHits-viz: a suite of web tools for visualizing interaction proteomics data. *Nat. Methods* **14**, 645–646 (2017).

[CAS](#) [PubMed](#) [PubMed Central](#) [Google Scholar](#)

40. 40.

Baryshnikova, A. Spatial Analysis of Functional Enrichment (SAFE) in large biological networks. *Methods Mol. Biol.* **1819**, 249–268 (2018).

[CAS](#) [Google Scholar](#)

41. 41.

Shannon, P. et al. Cytoscape: a software environment for integrated models of biomolecular interaction networks. *Genome Res.* **13**, 2498–2504 (2003).

[CAS](#) [PubMed](#) [PubMed Central](#) [Google Scholar](#)

42. 42.

Lee, D. D. & Seung, H. S. Learning the parts of objects by non-negative matrix factorization. *Nature* **401**, 788–791 (1999).

[ADS](#) [CAS](#) [MATH](#) [Google Scholar](#)

43. 43.

Pedregosa, F. et al. Scikit-learn: machine learning in Python. *J. Mach. Learn. Res.* **12**, 2825–2830 (2011).

[MathSciNet](#) [MATH](#) [Google Scholar](#)

44. 44.

van der Maaten, L. J. P. & Hinton, G. E. Visualizing high-dimensional data using t-SNE. *J. Mach. Learn. Res.* **9**, 2579–2605 (2008).

[MATH](#) [Google Scholar](#)

45. 45.

Uhlén, M. et al. Proteomics. Tissue-based map of the human proteome. *Science* **347**, 1260419 (2015).

[Google Scholar](#)

46. 46.

Mellacheruvu, D. et al. The CRAPome: a contaminant repository for affinity purification-mass spectrometry data. *Nat. Methods* **10**, 730–736 (2013).

[CAS](#) [PubMed](#) [PubMed Central](#) [Google Scholar](#)

47. 47.

Stark, C. et al. BioGRID: a general repository for interaction datasets. *Nucleic Acids Res.* **34**, D535–D539 (2006).

[CAS](#) [PubMed](#) [PubMed Central](#) [Google Scholar](#)

48. 48.

The Gene Ontology Consortium. Gene Ontology: tool for the unification of biology. *Nat. Genet.* **25**, 25–29 (2000).

[PubMed](#) [PubMed Central](#) [Google Scholar](#)

49. 49.

The Gene Ontology Consortium. Expansion of the Gene Ontology knowledgebase and resources. *Nucleic Acids Res.* **45** (D1), D331–D338 (2017).

[Google Scholar](#)

50. 50.

UniProt Consortium. UniProt: a worldwide hub of protein knowledge. *Nucleic Acids Res.* **47** (D1), D506–D515 (2019).

[Google Scholar](#)

51. 51.

Orchard, S. et al. The MIntAct project—IntAct as a common curation platform for 11 molecular interaction databases. *Nucleic Acids Res.* **42**, D358–D363 (2014).

[CAS](#) [Google Scholar](#)

52. 52.

Finn, R. D. et al. The Pfam protein families database: towards a more sustainable future. *Nucleic Acids Res.* **44** (D1), D279–D285 (2016).

[CAS](#) [Google Scholar](#)

53. 53.

Samaras, P. et al. ProteomicsDB: a multi-omics and multi-organism resource for life science research. *Nucleic Acids Res.* **48** (D1), D1153–D1163 (2020).

[CAS](#) [Google Scholar](#)

54. 54.

Binder, J. X. et al. COMPARTMENTS: unification and visualization of protein subcellular localization evidence. *Database (Oxford)* **2014**, bau012 (2014).

[Google Scholar](#)

55. 55.

Zecha, J. et al. Peptide level turnover measurements enable the study of proteoform dynamics. *Mol. Cell. Proteomics* **17**, 974–992 (2018).

[CAS](#) [PubMed](#) [PubMed Central](#) [Google Scholar](#)

56. 56.

Burkhardt, J. K. In search of membrane receptors for microtubule-based motors - is kinectin a kinesin receptor? *Trends Cell Biol.* **6**, 127–131 (1996).

[CAS](#) [Google Scholar](#)

57. 57.

St-Denis, N. et al. Phenotypic and interaction profiling of the human phosphatases identifies diverse mitotic regulators. *Cell Rep.* **17**, 2488–2501 (2016).

[CAS](#) [Google Scholar](#)

58. 58.

Li, X. et al. Defining the protein-protein interaction network of the human protein tyrosine phosphatase family. *Mol. Cell. Proteomics* **15**, 3030–3044 (2016).

[CAS](#) [PubMed](#) [PubMed Central](#) [Google Scholar](#)

59. 59.

Rasila, T. et al. Astroprincin (FAM171A1, C10orf38): a regulator of human cell shape and invasive growth. *Am. J. Pathol.* **189**, 177–189 (2019).

[CAS](#) [Google Scholar](#)

60. 60.

Monticone, M. et al. The nuclear genes *Mtfr1* and *Dufd1* regulate mitochondrial dynamic and cellular respiration. *J. Cell. Physiol.* **225**, 767–776 (2010).

[CAS](#) [Google Scholar](#)

[Download references](#)

Acknowledgements

We thank Z.-Y. Lin for profiling PIK3R1 and members of the Gingras laboratory for discussion and advice throughout the project, Q. Morris and S. W. M. Eng for help with NMF, and J. Zhang and many cell biologists for suggestions about bait selection. Work in the Gingras laboratory was supported by a Canadian Institutes of Health Research (CIHR) Foundation Grant (FDN 143301). E.A.S. is supported by a grant from the CIHR (MOP-133530). Proteomics work was performed at the Network Biology Collaborative Centre at the Lunenfeld-Tanenbaum Research Institute, a facility supported by Canada Foundation for Innovation funding, by the Ontario Government, and by Genome Canada and Ontario Genomics (OGI-

139). This research was enabled in part by support provided by Compute Canada (www.computecanada.ca). C.D.G. was supported by a CIHR Banting studentship. A.-C.G. is the Canada Research Chair in Functional Proteomics and the Lea Reichmann Chair in Cancer Proteomics.

Author information

Author notes

1. Ji-Young Youn

Present address: Peter Gilgan Centre for Research and Learning,
Hospital for Sick Children, Toronto, Ontario, Canada

2. Jean-Philippe Lambert

Present address: Department of Molecular Medicine, Cancer Research Centre, Big Data Research Centre, Université Laval, Quebec City, Quebec, Canada

3. Jean-Philippe Lambert

Present address: CHU de Québec-Université Laval Research Center (CHUL), Quebec City, Quebec, Canada

4. Étienne Coyaud

Present address: PRISM INSERM U1192, Université de Lille, Villeneuve d' Ascq, France

5. These authors contributed equally: Christopher D. Go, James D. R. Knight

Affiliations

1. Lunenfeld-Tanenbaum Research Institute, Mount Sinai Hospital, Sinai Health System, Toronto, Ontario, Canada

Christopher D. Go, James D. R. Knight, Bhavisha Rathod, Geoffrey G. Hesketh, Kento T. Abe, Ji-Young Youn, Payman Samavarchi-Tehrani, Jean-Philippe Lambert, Sally W. T. Cheung, Dushyandi Rajendran, Cassandra J. Wong, Laurence Pelletier & Anne-Claude Gingras

2. Department of Molecular Genetics, University of Toronto, Toronto, Ontario, Canada

Christopher D. Go, Kento T. Abe, Ji-Young Youn, Evelyn Popiel, Laurence Pelletier & Anne-Claude Gingras

3. Montreal Neurological Institute and Department of Human Genetics, McGill University, Montreal, Quebec, Canada

Archita Rajasekharan, Hana Antonicka & Eric A. Shoubridge

4. Department of Biochemistry, University of Toronto, Toronto, Ontario, Canada

Hui Zhang, Lucie Y. Zhu & Alexander F. Palazzo

5. Princess Margaret Cancer Centre, University Health Network, Toronto, Ontario, Canada

Étienne Coyaud & Brian Raught

6. Department of Medical Biophysics, University of Toronto, Toronto, Ontario, Canada

Brian Raught

Authors

1. Christopher D. Go

[View author publications](#)

You can also search for this author in [PubMed](#) [Google Scholar](#)

2. James D. R. Knight

[View author publications](#)

You can also search for this author in [PubMed](#) [Google Scholar](#)

3. Archita Rajasekharan

[View author publications](#)

You can also search for this author in [PubMed](#) [Google Scholar](#)

4. Bhavisha Rathod

[View author publications](#)

You can also search for this author in [PubMed](#) [Google Scholar](#)

5. Geoffrey G. Hesketh

[View author publications](#)

You can also search for this author in [PubMed](#) [Google Scholar](#)

6. Kento T. Abe

[View author publications](#)

You can also search for this author in [PubMed](#) [Google Scholar](#)

7. Ji-Young Youn

[View author publications](#)

You can also search for this author in [PubMed](#) [Google Scholar](#)

8. Payman Samavarchi-Tehrani

[View author publications](#)

You can also search for this author in [PubMed](#) [Google Scholar](#)

9. Hui Zhang

[View author publications](#)

You can also search for this author in [PubMed](#) [Google Scholar](#)

10. Lucie Y. Zhu

[View author publications](#)

You can also search for this author in [PubMed](#) [Google Scholar](#)

11. Evelyn Popiel

[View author publications](#)

You can also search for this author in [PubMed](#) [Google Scholar](#)

12. Jean-Philippe Lambert

[View author publications](#)

You can also search for this author in [PubMed](#) [Google Scholar](#)

13. Étienne Coyaud

[View author publications](#)

You can also search for this author in [PubMed](#) [Google Scholar](#)

14. Sally W. T. Cheung

[View author publications](#)

You can also search for this author in [PubMed](#) [Google Scholar](#)

15. Dushyandi Rajendran

[View author publications](#)

You can also search for this author in [PubMed](#) [Google Scholar](#)

16. Cassandra J. Wong

[View author publications](#)

You can also search for this author in [PubMed](#) [Google Scholar](#)

17. Hana Antonicka

[View author publications](#)

You can also search for this author in [PubMed](#) [Google Scholar](#)

18. Laurence Pelletier

[View author publications](#)

You can also search for this author in [PubMed](#) [Google Scholar](#)

19. Alexander F. Palazzo

[View author publications](#)

You can also search for this author in [PubMed](#) [Google Scholar](#)

20. Eric A. Shoubridge

[View author publications](#)

You can also search for this author in [PubMed](#) [Google Scholar](#)

21. Brian Raught

[View author publications](#)

You can also search for this author in [PubMed](#) [Google Scholar](#)

22. Anne-Claude Gingras

[View author publications](#)

You can also search for this author in [PubMed](#) [Google Scholar](#)

Contributions

A.-C.G., C.D.G. and J.D.R.K. conceived the project. A.-C.G., C.D.G., J.D.R.K. and B.R. wrote the paper with input from G.G.H., P.S.-T., J.-Y.Y., J.-P.L. and E.C. C.D.G. generated most of the BioID constructs and cell lines and performed BioID experiments and immunofluorescence studies. J.D.R.K., C.D.G., G.G.H. and A.-C.G. performed data analysis. J.D.R.K. created the humancellmap.org website. K.T.A. contributed the cell model and illustrations. C.J.W. helped with mass spectrometry data acquisition. A.R., H.A. and E.A.S. performed mitochondrial morphology experiments and analysed results. B.R. generated constructs and cell lines for BioID and testing predictions. G.G.H., K.T.A., J.-Y.Y., P.S.-T., H.Z., L.Y.Z., E.P., J.-

P.L., D.R., E.C., S.W.T.C., L.P., B.R. and A.F.P. contributed constructs and cell lines. A.-C.G. supervised the project.

Corresponding author

Correspondence to [Anne-Claude Gingras](#).

Ethics declarations

Competing interests

The authors declare no competing interests.

Additional information

Peer review information *Nature* thanks Luca Scorrano and the other, anonymous, reviewer(s) for their contribution to the peer review of this work.

Publisher's note Springer Nature remains neutral with regard to jurisdictional claims in published maps and institutional affiliations.

Extended data figures and tables

[Extended Data Fig. 1 Overview of the dataset.](#)

a, Cellular compartments targeted for profiling by BioID. Bold numbers on the schematic correspond to the indices in the legend. Italicized numbers in brackets next to the compartment name indicate the number of baits used to profile that compartment after quality control. **b**, Bait similarity and localization. The Jaccard index was calculated between each pair of baits in the core dataset using the list of high confidence (1% FDR) interactors. Baits were clustered using the Euclidean distance and complete linkage method, and clusters optimized using the CBA package in R. The colour gradient next to the bait labels indicates whether a bait shares an expected

localization with both adjacent baits (red), one adjacent bait (light red) or neither adjacent bait (white). Major clusters were manually annotated on the basis of the expected localization of the components.

Extended Data Fig. 2 Factors affecting prey labelling and rationale for prey-wise analysis.

a, After sorting preys by proximity order and grouping by order across baits, the proportion of previously reported preys was calculated for the n th proximity order for $n = 1, 2, \dots, 200$. **b–f**, For each bait, the relative proximity of every prey (proximity order) was calculated from the control-subtracted length-adjusted spectral counts (CLSC) (Methods), such that the prey with the highest CLSC value was considered to be the ‘interactor’ most proximal to the bait and the lowest CLSC value the most distal. **b**, Number of baits with a minimum of n preys at a 1% FDR, for $n = 1, 2, \dots, 200$. **c**, Proximity order versus protein turnover rate (hours) in HeLa cells (turnover data are from ref. ⁵⁵). **d**, Proximity order versus protein expression as represented by the \log_{10} -normalized MS1 iBAQ intensity from ProteomicsDB⁵³. **e**, Proximity order versus the number of lysine residues per protein. **f**, The \log_{10} -normalized MS1 iBAQ intensity of proteins expressed in HEK293 versus HeLa cells from ProteomicsDB⁵³. The similarity in proteomes supports the usage of HeLa data in **c** as suitable HEK293 data was not available. Values along the x axis could reflect zero expression or missing data in HeLa cells. These were ignored when calculating the R^2 value. **g**, Bait comparisons for a pair of mitochondrial matrix proteins. Control-subtracted spectral counts are plotted for all high confidence preys (1% FDR) detected with either bait pair under comparison. AARS2 preferentially enriches components of the mitochondrial ribosome and proteins involved in translation, such as GFM1, MRPS9 and TRMT10C, whereas PDHA1 preferentially interacts with the pyruvate dehydrogenase complex component DLAT and the mitochondrial membrane ATP synthase ATP5F1B. **h**, Pipelines for localizing prey proteins using SAFE⁴⁰ and NMF⁴². In our SAFE pipeline, preys with a correlation across baits ≥ 0.65 are considered interactors and these pairs are used to generate a network that is annotated for GO:CC terms (Methods). In NMF, the bait-prey spectral counts matrix is reduced to

a compartment-prey matrix and compartments are then defined using GO:CC for the compartment's most abundant preys. A 2D network is generated in parallel from the compartment-prey matrix using *t*-SNE⁴⁴.

[Source data](#)

Extended Data Fig. 3 SAFE-based map of the cell and motif enrichment.

a, SAFE-based map of the cell generated from preys with a Pearson correlation score of 0.65 or higher and plotted using Cytoscape with a spring-embedded layout. Each prey is coloured to indicate its primary localization (domain in SAFE terminology) as indicated in the legend. An interactive version of the map can be viewed at humancellmap.org/explore/maps and toggling from NMF to SAFE on the bottom menu. **b**, Pfam regions or motifs enriched in the indicated SAFE domains. The heat map value represents the log₂-transformed fold change between the genes localized to the rank and all preys in the dataset. Only compartments or domains with a significant fold change for at least one motif are displayed on the heat map.

Extended Data Fig. 4 NMF-based correlation map of the cell and motif enrichment.

a, NMF-based map of the cell generated from preys with a Pearson correlation score across NMF ranks of 0.9 or higher and plotted using Cytoscape with a spring-embedded layout. Each prey is coloured to indicate its primary localization (rank in NMF terminology) as indicated in the legend. An interactive version of the map can be viewed at humancellmap.org/explore/maps and toggling from *t*-SNE to correlation on the bottom menu. **b**, Pfam regions or motifs enriched in the indicated NMF ranks. The heat map value represents the log₂-transformed fold change between the genes localized to the rank and all preys in the dataset. Only compartments/ranks with a significant fold change for at least one motif are displayed on the heat map.

Extended Data Fig. 5 Localization benchmarking and experimental validation.

a, Percentage of genes localized to a previously known compartment for each specificity tier using our NMF and SAFE pipelines, compared with the HPA¹ (www.proteinatlas.org) and the fractionation studies of Christoforou² and Itzhak³. Specificity tiers were defined by binning GO:CC terms on the basis of their information content (Methods). Tier 1 terms are the most specific, and tier 5 the least specific. **b**, Percentage of preys localized to a previously known compartment relative to the number of baits they were detected with for NMF and SAFE, respectively. **c**, Percentage of preys localized to a previously known compartment relative to the average number of spectral counts they were seen with for NMF and SAFE. Preys were binned by spectral counts. The left tick mark for each data point indicates the lower bound for the bin (inclusive) and the right tick mark the upper bound (exclusive). **d**, Localization prediction validation strategy and examples. Confidence rankings are as defined in Fig. 2d. Representative immunofluorescence images are shown. NMF scores across the defined ranks, categories and compartments are displayed as seen on humancellmap.org with the highest NMF category corresponding to the localization prediction.

Source data

Extended Data Fig. 6 Topology and moonlighting analysis.

a–c, Predicted versus annotated proportion of protein exposed to the cytosol or lumen for ER transmembrane proteins. **a**, Hypothetical examples of proteins with varying proportions of their sequence exposed to the cytosol or lumen. The extent of labelling by cytosolic or luminal baits should be directly related to proportion of the sequence, and hence lysine residues available for biotinylation, exposed to the respective faces of the membrane that the protein spans. **b**, All transmembrane domain containing prey proteins localized to the cytosolic face of the ER (NMF compartments 3 and 15) and the luminal face (NMF compartment 6), were assigned a CLR score on the basis of their NMF profile (313 proteins). The CLR score of a prey is calculated by taking the score in the cytosolic facing

compartment/maximum score in that compartment and subtracting the corresponding score in the luminal compartment. A score closer to 1 would indicate a protein with a signature at the cytosolic face of the ER membrane but little or no signature in the lumen and a score of -1 would indicate the opposite. A similar sequence-based score was calculated as the fraction of the sequence annotated as cytosolic minus the fraction that is luminal according to UniProt. KTN1 is mis-annotated in UniProt⁵⁶ and should have a sequence score of +0.9742. **c**, Three example of proteins and their topology, CLR and sequence scores. Green examples have predictions matching annotated topology. **d, e**, Moonlighting and connections between compartments. **d**, Primary and secondary localizations of moonlighting preys. Preys with a score of at least 0.15 in each of two non-contiguous NMF compartments were considered to moonlight (a list of non-contiguous compartments is in Supplementary Table 15). The number of preys with a primary localization defined on the vertical axis and a secondary localization defined on the horizontal axis is shown (maximum 18). **e**, Inter-compartment edges were counted for each NMF rank/compartment. An interaction edge was defined between prey pairs having a correlation score across all NMF compartments of at least 0.9. Edges were then defined as ‘intra-compartment’ (if the primary localization for the two preys was the same compartment) or ‘inter-compartment’ (if the primary localization for the two preys was in different compartments) (Supplementary Table 15). Most organelles displayed a much greater proportion of intra-compartment interactions, with the extreme case of the mitochondrial matrix having only 15 inter-compartmental edges out of a total of 37,387 edges. The proportion of inter-compartment edges from the source to each target compartment is shown here. Inter-compartmental edges generally conformed with expectations, for example with edges from the chromatin compartment connecting to other nuclear substructures with which they may exchange components. The NMF rank number is shown in brackets next to the source compartment name.

Source data

Extended Data Fig. 7 Comparison of prey profiles for LMNA tagged with BioID, miniTurbo and TurboID.

a, Spectral counts for significant preys (FDR ≤ 0.01) were plotted for LMNA-BioID versus LMNA-miniTurbo. The average spectral counts value found in controls was subtracted from the detected spectral counts for each prey and the resulting value plotted. Zero values were set to 0.05 to create values suitable for log-transformation of the axes. **b**, LMNA-BioID versus LMNA-TurboID. **c**, LMNA-miniTurbo vs LMNA-TurboID.

[Source data](#)

Extended Data Fig. 8 Analysis of mitochondria–ER contact site candidates.

a, Heat map of genes with a primary localization at the mitochondrial outer membrane and ER membrane/nuclear outer membrane and a secondary localization to the other compartment as computed by NMF. To be included on the heat map, genes required an NMF score of at least 0.15 in the compartments of interest, a score ratio of at least 0.4 between the primary and secondary localization, and a score ratio of at least 2 between the compartments of interest and all other compartments. Bold genes indicate those selected for mitochondrial morphology assays in the following panels. A grey dot on the right side of the plot indicates proteins involved in lipid and cholesterol homeostasis, and a pink dot indicates calcium signalling. **b**, Dot plot view of BioID data for mito–ER contact site candidates highlighting recovery of mitochondrial fission machinery, mito–ER tethers and outer mitochondrial membrane proteins. Asterisks on the heat map indicate spectral counts for prey genes corresponding to the bait that were ignored by SAINT as peptides from the bait confound accurately evaluating the abundance of itself as an interactor. **c**, Mitochondrial morphology is altered by transient expression of GFP-tagged CHMP7 and C18orf32, as monitored by confocal immunofluorescence microscopy in HeLa cells. Cells were fixed and probed with antibodies directed against GFP and COXIV (Methods). The white box indicates the zoomed area displayed in the rightmost panels. Scale bars, 10 μm .

Extended Data Fig. 9 Analysis module at humancellmap.org.

a, Screenshot of the analysis report for the bait PIK3R1. Red circles indicate the following (1) Baits from the humancellmap are sorted from most similar to least similar as calculated by the Jaccard distance. (2) The ten most similar baits to the query in the humancellmap. (3) The average spectral counts for each prey averaged across all baits in the humancellmap database. (4) Expected localizations of the ten most similar baits. (5) Overlap or similarity metrics between the query bait and the top ten most similar baits in the humancellmap. The distance is the Jaccard distance, with a score of 0 for complete prey overlap and 1 for no overlap. The intersection refers to the number of shared preys, and the union refers to the combined number of preys between the query and the indicated bait. (6) The most specific preys for the query. The specificity score is calculated as the fold enrichment of a prey in the query relative to the average across the humancellmap baits used for the comparison. (7) The specificity score calculated against the top ten most similar baits to the query. (8) The specificity score calculated against all baits in the humancellmap. (9) Links to open the heat map or specificity plots at the interactive viewer at ProHits-viz³⁹. (10) Links for data downloads. **b**, Specificity plot for RNGTT showing the control-subtracted spectral counts versus the specificity score (calculation of the specificity score is described in the Methods). RNGTT is a nuclear protein involved in mRNA capping previously profiled by BioID⁷. Humancellmap analysis reported a nuclear localization, with bait-specific interactions including several RNA polymerase II subunits and components of the catalytic subunit of the PP4 phosphatase, as previously reported^{57,58}. **c**, Exploratory analysis of FAM171A1 reveals links to the cytoskeleton. FAM171A1 was predicted by our NMF and SAFE analyses to localize to the cell junction and plasma membrane. Consistent with this prediction, its BioID profile when screened as a bait was most similar to junctional and plasma membrane baits, whereas bait-specific preys included several cytoskeletal proteins, in line with a previous study⁵⁹ that reported a reduction of actin stress fibres after knockdown of FAM171A1. **d**, Specificity plot of MTFR2 showing the high specificity of proteins involved in mitochondrial dynamics. MTFR2 was associated with the mitochondrial outer membrane and peroxisome as a prey protein, with a weak signature at the mitochondrial inner membrane or mitochondrial intermembrane space. When profiled as a bait, the analysis module reports that it is most similar to peroxisomal baits, followed by mitochondrial outer

and inner membrane baits, supporting its predicted localization. Interactions with MTFR1, SLC25A46 and VPS13D were found to be highly specific to MTFR2, consistent with the mitochondrial fragmentation previously observed after overexpression of GFP–MTFR2⁶⁰. e, BRD3 relocalization after JQ1 treatment. BirA-tagged BRD3 was treated with vehicle or JQ1 for 24 h (data from ref. ²⁵) and analysed using the analysis module at humancellmap.org. The Jaccard indices (1 – Jaccard distance) for the top 20 most similar baits were used to create networks in Cytoscape⁴¹ using an edge-weighted spring-embedded layout. Humancellmap baits are coloured on the basis of their expected localization to chromatin or the nucleolus.

[Source data](#)

[Extended Data Fig. 10 BirA*-Flag and GFP–BirA*-Flag control stable cell line, and LMNA-BirA*-Flag and AIFM1-BirA*-Flag bait stable cell line immunofluorescence.](#)

Cell lines were probed by confocal immunofluorescence microscopy in HEK293 Flp-In T-Rex stable cells to assay for localization of the fusion construct and general biotinylation. Cells were fixed and then probed with an antibody to the Flag epitope and streptavidin for biotinylated proteins (Methods). The green channel represents nuclear or mitochondrial staining, the red channel denotes Flag and the blue channel represents streptavidin (biotinylated proteins). Scale bars, 10 μm.

Supplementary information

[Reporting Summary](#)

[Supplementary Tables 1–21](#)

This folder contains 21 .xlsx files (Supplementary Table 1–21) and an SI guide containing table legends.

Source data

[**Source Data Fig. 2**](#)

[**Source Data Fig. 3**](#)

[**Source Data Extended Data Fig. 2**](#)

[**Source Data Extended Data Fig. 5**](#)

[**Source Data Extended Data Fig. 6**](#)

[**Source Data Extended Data Fig. 7**](#)

[**Source Data Extended Data Fig. 9**](#)

Rights and permissions

[Reprints and Permissions](#)

About this article



Cite this article

Go, C.D., Knight, J.D.R., Rajasekharan, A. *et al.* A proximity-dependent biotinylation map of a human cell. *Nature* **595**, 120–124 (2021).
<https://doi.org/10.1038/s41586-021-03592-2>

[Download citation](#)

- Received: 25 September 2019
- Accepted: 29 April 2021

- Published: 02 June 2021
- Issue Date: 01 July 2021
- DOI: <https://doi.org/10.1038/s41586-021-03592-2>

[Access through your institution](#)

[Change institution](#)

[Buy or subscribe](#)

Advertisement

This article was downloaded by **calibre** from <https://www.nature.com/articles/s41586-021-03592-2>

| [Section menu](#) | [Main menu](#) |

- Article
- [Published: 09 June 2021](#)

Defining genome architecture at base-pair resolution

- [Peng Hua](#) ORCID: orcid.org/0000-0003-3774-5033¹,
- [Mohsin Badat](#) ORCID: orcid.org/0000-0003-0744-5427¹ na1,
- [Lars L. P. Hanssen](#) ORCID: orcid.org/0000-0002-2551-2278¹ na1,
- [Lance D. Hentges](#) ORCID: orcid.org/0000-0001-6327-6774^{1,2},
- [Nicholas Crump](#) ORCID: orcid.org/0000-0001-9610-6763¹,
- [Damien J. Downes](#) ORCID: orcid.org/0000-0002-5034-0869¹,
- [Danuta M. Jeziorska](#)¹,
- [A. Marieke Oudelaar](#) ORCID: orcid.org/0000-0002-4016-6158³,
- [Ron Schwessinger](#) ORCID: orcid.org/0000-0001-7829-8503^{1,2},
- [Stephen Taylor](#) ORCID: orcid.org/0000-0002-3559-4334²,
- [Thomas A. Milne](#) ORCID: orcid.org/0000-0002-0413-4271¹,
- [Jim R. Hughes](#) ORCID: orcid.org/0000-0002-8955-7256^{1,2},
- [Doug R. Higgs](#) ORCID: orcid.org/0000-0003-3579-8705⁴ &
- [James O. J. Davies](#) ORCID: orcid.org/0000-0002-4108-4357¹

[Nature](#) volume **595**, pages 125–129 (2021) [Cite this article](#)

- 14k Accesses
- 271 Altmetric
- [Metrics details](#)

Subjects

- [Chromatin structure](#)

- [Gene regulation](#)

Abstract

In higher eukaryotes, many genes are regulated by enhancers that are 10^4 – 10^6 base pairs (bp) away from the promoter. Enhancers contain transcription-factor-binding sites (which are typically around 7–22 bp), and physical contact between the promoters and enhancers is thought to be required to modulate gene expression. Although chromatin architecture has been mapped extensively at resolutions of 1 kilobase and above; it has not been possible to define physical contacts at the scale of the proteins that determine gene expression. Here we define these interactions in detail using a chromosome conformation capture method (Micro-Capture-C) that enables the physical contacts between different classes of regulatory elements to be determined at base-pair resolution. We find that highly punctate contacts occur between enhancers, promoters and CCCTC-binding factor (CTCF) sites and we show that transcription factors have an important role in the maintenance of the contacts between enhancers and promoters. Our data show that interactions between CTCF sites are increased when active promoters and enhancers are located within the intervening chromatin. This supports a model in which chromatin loop extrusion¹ is dependent on cohesin loading at active promoters and enhancers, which explains the formation of tissue-specific chromatin domains without changes in CTCF binding.

Access options

Subscribe to Journal

Get full journal access for 1 year

\$199.00

only \$3.90 per issue

[Subscribe](#)

All prices are NET prices.
VAT will be added later in the checkout.
Tax calculation will be finalised during checkout.

Rent or Buy article

Get time limited or full article access on ReadCube.

from \$8.99

[Rent or Buy](#)

All prices are NET prices.

Additional access options:

- [Log in](#)
- [Access through your institution](#)
- [Learn about institutional subscriptions](#)

Fig. 1: The comparison of MCC with other 3C techniques in erythroid cells at the promoters of the α -globin genes (*Hba-a1* and *Hba-a2*) shows the considerably increased resolution afforded by MCC.

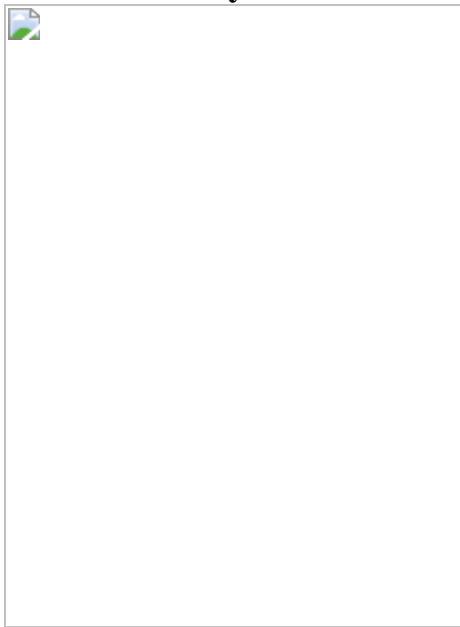


Fig. 2: MCC defines highly specific contacts between promoters and enhancers at many well-characterized loci.

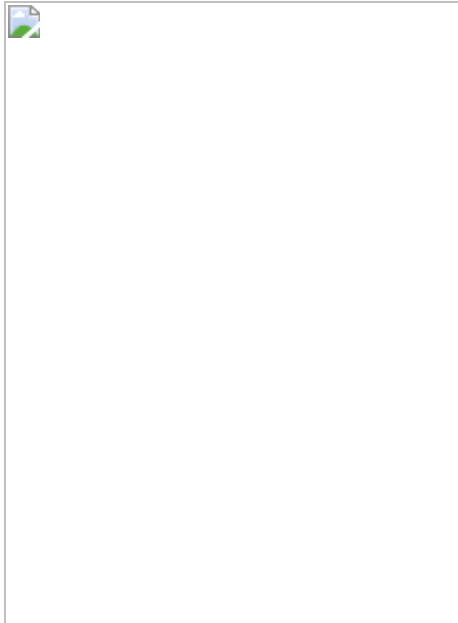


Fig. 3: Contact profiles of the main CTCF boundary element (HS-38) at the α -globin locus are altered with changes in gene expression.

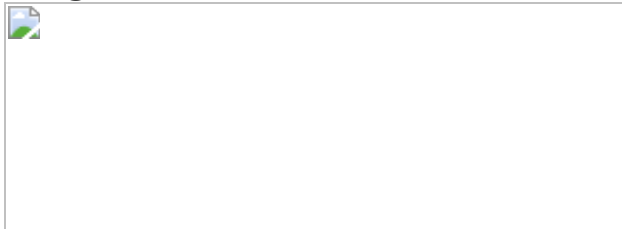
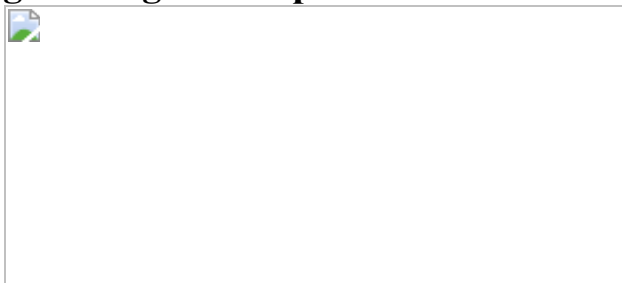


Fig. 4: Single-base-pair resolution analysis of MCC ligation junctions.



Data availability

Sequencing data have been submitted to the NCBI Gene Expression Omnibus ([GSE144336](#) and [GSE153256](#)). Previously published data are available under the following accession codes: GSE67959⁸, GSE97871¹⁴, GSE44286¹⁸, GSE27921³⁷, GSE30203³⁸, GSE51334³⁹. DNase I

hypersensitivity data are available for erythroid cells from ref. ⁴⁰ and for ES cells from UW ENCODE⁴¹. [Source data](#) are provided with this paper.

Code availability

The codes required for analysis of MCC data are available for academic use through the Oxford University Innovation software store (<https://process.innovation.ox.ac.uk/software/p/16529a/micro-capture-c-academic/1>).

References

1. 1.

Sanborn, A. L. et al. Chromatin extrusion explains key features of loop and domain formation in wild-type and engineered genomes. *Proc. Natl Acad. Sci. USA* **112**, E6456–E6465 (2015).

[CAS Article](#) [Google Scholar](#)

2. 2.

Lieberman-Aiden, E. et al. Comprehensive mapping of long-range interactions reveals folding principles of the human genome. *Science* **326**, 289–293 (2009).

[ADS](#) [CAS Article](#) [Google Scholar](#)

3. 3.

Hsieh, T. S., Fudenberg, G., Goloborodko, A. & Rando, O. J. Micro-C XL: assaying chromosome conformation from the nucleosome to the entire genome. *Nat. Methods* **13**, 1009–1011 (2016).

[CAS Article](#) [Google Scholar](#)

4. 4.

Krietenstein, N. et al. Ultrastructural details of mammalian chromosome architecture. *Mol. Cell* **78**, 554–565.e7 (2020).

[CAS](#) [Article](#) [Google Scholar](#)

5. 5.

Hsieh, T. S. et al. Resolving the 3D landscape of transcription-linked mammalian chromatin folding. *Mol. Cell* **78**, 539–553.e8 (2020).

[CAS](#) [Article](#) [Google Scholar](#)

6. 6.

Schoenfelder, S. et al. The pluripotent regulatory circuitry connecting promoters to their long-range interacting elements. *Genome Res.* **25**, 582–597 (2015).

[CAS](#) [Article](#) [Google Scholar](#)

7. 7.

van de Werken, H. J. et al. Robust 4C-seq data analysis to screen for regulatory DNA interactions. *Nat. Methods* **9**, 969–972 (2012).

[Article](#) [Google Scholar](#)

8. 8.

Davies, J. O. et al. Multiplexed analysis of chromosome conformation at vastly improved sensitivity. *Nat. Methods* **13**, 74–80 (2016).

[CAS](#) [Article](#) [Google Scholar](#)

9. 9.

Davies, J. O., Oudelaar, A. M., Higgs, D. R. & Hughes, J. R. How best to identify chromosomal interactions: a comparison of approaches. *Nat. Methods* **14**, 125–134 (2017).

[CAS](#) [Article](#) [Google Scholar](#)

10. 10.

Kornberg, R. D. Chromatin structure: a repeating unit of histones and DNA. *Science* **184**, 868–871 (1974).

[ADS](#) [CAS](#) [Article](#) [Google Scholar](#)

11. 11.

Neph, S. et al. An expansive human regulatory lexicon encoded in transcription factor footprints. *Nature* **489**, 83–90 (2012).

[ADS](#) [CAS](#) [Article](#) [Google Scholar](#)

12. 12.

Hughes, J. R. et al. Analysis of hundreds of *cis*-regulatory landscapes at high resolution in a single, high-throughput experiment. *Nat. Genet.* **46**, 205–212 (2014).

[CAS](#) [Article](#) [Google Scholar](#)

13. 13.

Tan-Wong, S. M. et al. Gene loops enhance transcriptional directionality. *Science* **338**, 671–675 (2012).

[ADS](#) [CAS](#) [Article](#) [Google Scholar](#)

14. 14.

Hanssen, L. L. P. et al. Tissue-specific CTCF–cohesin-mediated chromatin architecture delimits enhancer interactions and function in vivo. *Nat. Cell Biol.* **19**, 952–961 (2017).

[CAS](#) [Article](#) [Google Scholar](#)

15. 15.

.Hentges, L. D., Sergeant, M. J., Downes, D. J., Hughes, J. R. & Taylor, S. LanceOtron: a deep learning peak caller for ATAC-seq, ChIP-seq, and DNase-seq. Preprint at <https://doi.org/10.1101/2021.01.25.428108> (2021).

16. 16.

He, Q., Johnston, J. & Zeitlinger, J. ChIP-nexus enables improved detection of *in vivo* transcription factor binding footprints. *Nat. Biotechnol.* **33**, 395–401 (2015).

[CAS](#) [Article](#) [Google Scholar](#)

17. 17.

Oudelaar, A. M. et al. Single-allele chromatin interactions identify regulatory hubs in dynamic compartmentalized domains. *Nat. Genet.* **50**, 1744–1751 (2018).

[CAS](#) [Article](#) [Google Scholar](#)

18. 18.

Whyte, W. A. et al. Master transcription factors and mediator establish super-enhancers at key cell identity genes. *Cell* **153**, 307–319 (2013).

[CAS](#) [Article](#) [Google Scholar](#)

19. 19.

Hay, D. et al. Genetic dissection of the α -globin super-enhancer *in vivo*. *Nat. Genet.* **48**, 895–903 (2016).

[CAS](#) [Article](#) [Google Scholar](#)

20. 20.

Canver, M. C. et al. *BCL11A* enhancer dissection by Cas9-mediated in situ saturating mutagenesis. *Nature* **527**, 192–197 (2015).

[ADS](#) [CAS](#) [Article](#) [Google Scholar](#)

21. 21.

Ran, F. A. et al. Genome engineering using the CRISPR–Cas9 system. *Nat. Protocols* **8**, 2281–2308 (2013).

[CAS](#) [Article](#) [Google Scholar](#)

22. 22.

Trakarnsanga, K. et al. An immortalized adult human erythroid line facilitates sustainable and scalable generation of functional red cells. *Nat. Commun.* **8**, 14750 (2017).

[ADS](#) [CAS](#) [Article](#) [Google Scholar](#)

23. 23.

Mettananda, S. et al. Editing an α -globin enhancer in primary human hematopoietic stem cells as a treatment for β -thalassemia. *Nat. Commun.* **8**, 424 (2017).

[ADS](#) [Article](#) [Google Scholar](#)

24. 24.

Bak, R. O., Dever, D. P. & Porteus, M. H. CRISPR/Cas9 genome editing in human hematopoietic stem cells. *Nat. Protocols* **13**, 358–376 (2018).

[CAS](#) [Article](#) [Google Scholar](#)

25. 25.

Scott, C. et al. Recapitulation of erythropoiesis in congenital dyserythropoietic anaemia type I (CDA-I) identifies defects in differentiation and nucleolar abnormalities. *Haematologica* <https://doi.org/10.3324/haematol.2020.260158> (2020).

26. 26.

Magoč, T. & Salzberg, S. L. FLASH: fast length adjustment of short reads to improve genome assemblies. *Bioinformatics* **27**, 2957–2963 (2011).

[Article](#) [Google Scholar](#)

27. 27.

Kent, W. J. BLAT—the BLAST-like alignment tool. *Genome Res.* **12**, 656–664 (2002).

[CAS](#) [Article](#) [Google Scholar](#)

28. 28.

Langmead, B. & Salzberg, S. L. Fast gapped-read alignment with Bowtie 2. *Nat. Methods* **9**, 357–359 (2012).

[CAS](#) [Article](#) [Google Scholar](#)

29. 29.

Fornes, O. et al. JASPAR 2020: update of the open-access database of transcription factor binding profiles. *Nucleic Acids Res.* **48**, D87–D92 (2020).

[CAS](#) [Article](#) [Google Scholar](#)

30. 30.

Khan, A. et al. JASPAR 2018: update of the open-access database of transcription factor binding profiles and its web framework. *Nucleic*

Acids Res. **46**, D260–D266 (2018).

[CAS](#) [Article](#) [Google Scholar](#)

31. 31.

Telenius, J. & Hughes, J. R. NGseqBasic - a single-command UNIX tool for ATAC-seq, DNaseI-seq, Cut-and-Run, and ChIP-seq data mapping, high-resolution visualisation, and quality control. Preprint at <https://doi.org/10.1101/393413> (2018).

32. 32.

Feng, J., Liu, T., Qin, B., Zhang, Y. & Liu, X. S. Identifying ChIP-seq enrichment using MACS. *Nat. Protocols* **7**, 1728–1740 (2012).

[CAS](#) [Article](#) [Google Scholar](#)

33. 33.

Zacher, B. et al. Accurate promoter and enhancer identification in 127 ENCODE and Roadmap Epigenomics cell types and tissues by GenoSTAN. *PLoS ONE* **12**, e0169249 (2017).

[Article](#) [Google Scholar](#)

34. 34.

Fisher, R. A. *Statistical Methods for Research Workers* 5th edn (Oliver and Boyd, 1932).

35. 35.

Kent, W. J. et al. The human genome browser at UCSC. *Genome Res.* **12**, 996–1006 (2002).

[CAS](#) [Article](#) [Google Scholar](#)

36. 36.

Quinlan, A. R. & Hall, I. M. BEDTools: a flexible suite of utilities for comparing genomic features. *Bioinformatics* **26**, 841–842 (2010).

[CAS](#) [Article](#) [Google Scholar](#)

37. 37.

Kowalczyk, M. S. et al. Intragenic enhancers act as alternative promoters. *Mol. Cell* **45**, 447–458 (2012).

[CAS](#) [Article](#) [Google Scholar](#)

38. 38.

Stadler, M. B. et al. DNA-binding factors shape the mouse methylome at distal regulatory regions. *Nature* **480**, 490–495 (2011).

[ADS](#) [CAS](#) [Article](#) [Google Scholar](#)

39. 39.

Pope, B. D. et al. Topologically associating domains are stable units of replication-timing regulation. *Nature* **515**, 402–405 (2014).

[ADS](#) [CAS](#) [Article](#) [Google Scholar](#)

40. 40.

Hosseini, M. et al. Causes and consequences of chromatin variation between inbred mice. *PLoS Genet.* **9**, e1003570 (2013).

[CAS](#) [Article](#) [Google Scholar](#)

41. 41.

The ENCODE Project Consortium. An integrated encyclopedia of DNA elements in the human genome. *Nature* **489**, 57–74 (2012).

[ADS](#) [Article](#) [Google Scholar](#)

[Download references](#)

Acknowledgements

J.O.J.D. and P.H. are funded by an MRC Clinician Scientist Award (MRC Clinician Scientist Fellowship MR/R008108) to J.O.J.D. This work was also supported by a Medical Research Council Discovery Award led by D.R.H. (MC_PC_15069). L.D.H., J.R.H. and S.T. developed LanceOtron with support from the National Institutes of Health (USA) grant number R24DK106766. J.R.H. is supported by the MRC Molecular Haematology Unit (MC_UU_00016/14). M.B. is supported by an MRC Clinical Research Training Fellowship (MR/P019633/1). R. Kurita and Y. Nakamura from the RIKEN Tsukuba Branch provided HUDEP-2 cells. We thank V. Iotchkova for advice on the statistical analysis.

Author information

Author notes

1. These authors contributed equally: Mohsin Badat, Lars L. P. Hanssen

Affiliations

1. MRC Molecular Haematology Unit, MRC Weatherall Institute of Molecular Medicine, Radcliffe Department of Medicine, University of Oxford, Oxford, UK

Peng Hua, Mohsin Badat, Lars L. P. Hanssen, Lance D. Hentges, Nicholas Crump, Damien J. Downes, Danuta M. Jeziorska, Ron Schwessinger, Thomas A. Milne, Jim R. Hughes & James O. J. Davies

2. MRC WIMM Centre for Computational Biology, MRC Weatherall Institute of Molecular Medicine, Radcliffe Department of Medicine, University of Oxford, Oxford, UK

Lance D. Hentges, Ron Schwessinger, Stephen Taylor & Jim R. Hughes

3. Max Planck Institute for Biophysical Chemistry, Göttingen, Germany

A. Marieke Oudelaar

4. Laboratory of Gene Regulation, MRC Weatherall Institute of Molecular Medicine, Radcliffe Department of Medicine, University of Oxford, Oxford, UK

Doug R. Higgs

Authors

1. Peng Hua

[View author publications](#)

You can also search for this author in [PubMed](#) [Google Scholar](#)

2. Mohsin Badat

[View author publications](#)

You can also search for this author in [PubMed](#) [Google Scholar](#)

3. Lars L. P. Hanssen

[View author publications](#)

You can also search for this author in [PubMed](#) [Google Scholar](#)

4. Lance D. Hentges

[View author publications](#)

You can also search for this author in [PubMed](#) [Google Scholar](#)

5. Nicholas Crump

[View author publications](#)

You can also search for this author in [PubMed](#) [Google Scholar](#)

6. Damien J. Downes

[View author publications](#)

You can also search for this author in [PubMed](#) [Google Scholar](#)

7. Danuta M. Jeziorska

[View author publications](#)

You can also search for this author in [PubMed](#) [Google Scholar](#)

8. A. Marieke Oudelaar

[View author publications](#)

You can also search for this author in [PubMed](#) [Google Scholar](#)

9. Ron Schwessinger

[View author publications](#)

You can also search for this author in [PubMed](#) [Google Scholar](#)

10. Stephen Taylor

[View author publications](#)

You can also search for this author in [PubMed](#) [Google Scholar](#)

11. Thomas A. Milne

[View author publications](#)

You can also search for this author in [PubMed](#) [Google Scholar](#)

12. Jim R. Hughes

[View author publications](#)

You can also search for this author in [PubMed](#) [Google Scholar](#)

13. Doug R. Higgs

[View author publications](#)

You can also search for this author in [PubMed](#) [Google Scholar](#)

14. James O. J. Davies

[View author publications](#)

You can also search for this author in [PubMed](#) [Google Scholar](#)

Contributions

J.O.J.D. conceived the project, designed, performed and analysed experiments, performed the majority of bioinformatic analyses and wrote the first draft of the manuscript. P.H. analysed data and performed experiments. L.L.P.H. assisted with the design of experiments, performed experiments and assisted with data analysis. M.B. and D.J.D. performed experiments and analysis. L.D.H., A.M.O., R.S. and S.T. contributed to analysis. D.M.J. and N.C. assisted with experiments. T.A.M. and J.R.H. assisted with experimental design and data analysis. D.R.H. provided funding and assisted with experimental design. All authors contributed to writing the manuscript.

Corresponding author

Correspondence to [James O. J. Davies](#).

Ethics declarations

Competing interests

J.O.J.D., D.M.J. and J.R.H. are co-founders of Nucleome Therapeutics. J.O.J.D., J.R.H., D.J.D. and R.S. provide consultancy to the company and D.M.J. is an employee. J.O.J.D. and J.R.H. have filed a provisional patent application on this work (PCT/GB2020/050253).

Additional information

Peer review information *Nature* thanks Ralph Stadhouders and the other, anonymous, reviewer(s) for their contribution to the peer review of this work.

Publisher's note Springer Nature remains neutral with regard to jurisdictional claims in published maps and institutional affiliations.

Extended data figures and tables

Extended Data Fig. 1 Overview of experimental and computational workflow.

a, Cells are initially fixed with formaldehyde and then permeabilized with digitonin. They are subsequently treated with MNase at different concentrations. End repair and ligation are then performed. This results in the ligation of sequences that are in close proximity in the nucleus. DNA is then extracted to generate an MNase 3C library. This library is sonicated to a fragment size of around 200 bp. Illumina sequencing adaptors are added to the library. This library manufacture process is scaled up to maximize the amount of DNA available and the complexity of the libraries. Multiple samples with different sequencing indices are then mixed. The DNA is then denatured and mixed with a pool of biotinylated oligonucleotides. These 120-mer oligonucleotides were designed to capture the central portion of the hypersensitive site at the promoter or the central sequence of CTCF sites guided by a combination of motif analysis and DNase I footprinting. Following a hybridization reaction, a streptavidin bead pull down is performed and the uncaptured material is washed away. The material is PCR amplified and the oligonucleotide capture is repeated to improve the purity. The reads are then sequenced with 300-bp paired-end reads, which allows the entire sequence of each read to be determined as the DNA is fragmented to 200 bp by sonication. **b**, The overview of the data analysis. The raw FASTQ file is processed to reconstruct a single read from paired-end sequencing data. The single reads are then mapped to the 800-bp sequence surrounding the capture oligonucleotide using the non-stringent aligner BLAT. This enables the reads to be cut into 'slices' depending on whether they align to the sequence around the capture site. This strategy allows ligation junctions in the read to be determined with base-pair accuracy. The resulting FASTQ file is aligned to the genome using Bowtie 2 (ref. [28](#)). This file is processed to remove PCR duplicates and the junctions of the 'slices' within the reads are identified. **c**, The different

methods used for data visualization. Simple read pile-ups are generally used. However, the resolution can be further increased by reporting the precise base-pair position of the ligation junctions. As protein binding protects against DNA digestion by MNase, the regions of protein binding can be inferred from footprints in the junction plots that are similar to DNase I footprinting. More detailed localization of the protein-binding site that results in the interaction can be achieved by separating the junction profiles based on whether the read and therefore protein-binding site is upstream or downstream of the junction. Finally, single-base-pair resolution maps of junctions between the capture site and the peaks at regulatory elements can be generated. In the example above the central binding site of the two interacting CTCF sites is protected and the ligation junctions surround this. The direction of the reads at the capture and reporter sites can be used to identify the site of the proteins giving rise to the ligation junctions. This can be plotted with arrow plots. Here this shows that the central CTCF motif at both the capture and reporter site are the origin of the contacts between the two sites. This is more easily visualized using 3D surface plots. These were constructed by converting each data point into a rectangle 20 bp long and 4 bp wide in the direction of the reads giving rise to the interactions. This shows the central binding site of the two CTCF sites giving rise to the interactions and contacts between these central CTCF motif and the neighbouring nucleosomes.

Extended Data Fig. 2 Technical details of library preparation, reproducibility and biases.

a, Optimal MNase 3C library digestion keeps the nucleosome tails intact whereas over digestion leads to the loss of nucleosome linkers. This results in a failure of fragments to re-ligate. Note that the digestion controls show that MNase cuts chromatin into mononucleosomes and that there are very few fragments over 1,000 bp. The fragment size is considerably smaller than DpnII-digested chromatin. **b**, MCC profiles of the *Hba-a1* and *Hba-a2* promoters in erythroid cells showing the interaction profiles derived from MNase-based 3C library preparation using a conventional NP-40-based nuclear extract, compared with data generated from intact cells permeabilized with digitonin. Data from three mice with two aliquots of cells from each mouse treated with two different concentrations of MNase

are shown. Counts are normalized to the total number of reads across the genome. The assay is highly reproducible between replicates. To look for biases caused by MNase digestion, we sequenced the digestion controls. In addition, we sequenced the MNase 3C library without oligonucleotide capture to look for biases resulting from the ligation reaction. The global distribution of reads from the MNase digestion and the ligation junctions from the uncaptured library shows a very similar distribution to background (bottom two panels), without obvious biases towards the hypersensitive sites. **c**, Violin plots of the genome-wide analysis at different classes of element show the number of reads in a 1-kb window around different classes of element compared to control regions 10 kb downstream of the element generated by sequencing of the MNase digestion controls and ligation junctions in the unenriched MNase 3C library. Sequencing of the digestion controls shows no evidence of biases in MNase digestion at enhancers or CTCF sites. There is a small reduction in the number of reads at promoters, possibly due to the loss of smaller fragments from histone-depleted regions in the DNA extraction and sequencing library preparation. Conversely, sequencing of the ligation junctions reveals a slightly higher numbers of junctions at promoters and regulatory elements including CTCF sites, which is probably due to the ligation process. **d**, Analysis of the DNA sequence at ligation junctions detected no biases towards ligation junctions in AT-rich sequences (which MNase is reported to cut preferentially). **e**, Metaplots of the junction count from the uncaptured MNase 3C library at DNase I hypersensitive sites show a small bias to the central 200 bp where there are more junctions, but this is partially offset because the fragment size is reduced in the hypersensitive sites. There was no correlation between the strength of the hypersensitive site and the number of junctions per kb within the site. A model of the background distribution of reads was generated to correct for this effect using a 20-bp moving window across the metaplot of the hypersensitive sites. **f**, Plots of single-normalized MCC data (to the total number of reads across the genome from the viewpoint) compared to double normalization, which corrects for the small bias at hypersensitive sites. This analysis shows that double normalization for the hypersensitive site effect does not significantly change the interaction profile compared withs single normalization. Peak calling with the machine-learning-based peak caller LanceOtron of both single- and double-

normalized data showed that 94% of the significant peaks remains unchanged by this correction ([Supplementary Table 2](#)).

[Source data](#)

Extended Data Fig. 3 Comparison of MCC data generated using different capture sites at active active genes in erythroid cells.

a–d, MCC profiles of the promoters of *Hba-a1* and *Hba-a2* (**a**), *Hbb-b1* and *Hbb-bs* (**b**), *Slc25a37* (**c**) and *Cd47* (**d**) in erythroid and ES cells (anchor points are denoted by red arrows). The interaction profile was markedly different depending on whether the viewpoint was directly over the hypersensitive site at the promoter (central; blue) or shifted 1 kb upstream (red) or 1 kb downstream (green). Data are reported as read pile-ups without windowing and the number of reads is normalized to the total number of reads across the genome. Profiles of NG Capture-C data from the same viewpoint, DNase-seq and ChIP-seq data of H3K4me1, H3K4me3 and CTCF. Bottom, the MCC profile from the central viewpoint in ES cells as a control. At all genes, there are significantly stronger interactions between the central promoter and the known enhancers of the genes (denoted by green arrows) and CTCF-binding sites (denoted by pink or purple arrows depending on motif orientation). **e**, Heat maps showing the punctate nature of promoter–promoter and enhancer–enhancer contacts (compared to randomly chosen sites) using data from the unenriched Hi-C library. The data presented show a 3-kb region around the centre of the hypersensitive site with a 50-bp bin size.

[Source data](#)

Extended Data Fig. 4 Comparison of MCC data generated using capture sites at the promoters of active genes in erythroid and ES cells.

a, MCC profiles from the promoter of *Myc* showing long-range interactions with enhancers of the gene that are more than 1 Mb from the promoter. **b**,

Analysis of the *Sox2* locus showing long-range interactions that are 750 kb from the promoter of the gene, which precisely localize with CTCF-binding sites, DNase-seq (green, ENCODE UW) and ChIP-seq data of H3K4me1, H3K4me3 (ENCODE/LICR), NANOG (GSM1082342), SOX2 (GSM1082341), OCT4 (GSM1082340)¹⁸ and CTCF. **c, d**, MCC profiles of the promoter of *Klf4* (**c**) and *Nanog* (**d**) in ES cells. **e**, MCC profiles of *Hbb* (*Hbb-bs*), the inactive *Hbb-y* gene and the main HS-2 enhancer. Note that the profile from the inactive gene does not show contacts with the hypersensitive enhancers but that it has contacts with the surrounding chromatin compartment. **f**, MCC data using the promoter or enhancer of *Sox2* as the viewpoint in ES cells and data of the enhancer in erythroid cells. **g**, The contacts of the promoter with the gene body for four genes that are transcribed in erythroid cells (*Hemgn*, *Fhdcl*, *Epb4.9* and *Btg2*). These data show no evidence of gene looping between the promoter and the 3' end of the gene. **h**, Metaplot of the number of junctions detected between the promoter and the 4-kb region surrounding the 3' UTR. To account for distance effects, short genes (<10 kb) (left) and long genes (>10 kb) (right) are plotted separately. The comparison between erythroid cells, in which the genes are active, and ES cells, in which the genes are not transcribed, controls for distance and mapping effects. The dot plots show that there are no significant differences between the number of ligation junctions in 500-bp bins surrounding the 3' UTR when genes are in active or inactive states. Short genes, $n = 12$; long genes, $n = 18$. Data are mean \pm s.d., two-way ANOVA, no adjustments were made for multiple comparisons. This shows that there is no change in the number of contacts when the genes change from an active to an inactive state.

[Source data](#)

[Extended Data Fig. 5 Promoters in gene-dense regions make contacts with multiple promoters.](#)

a, Top, MCC profiles from the promoter of *Klf1* showing long-range interactions with multiple promoters in the 400-kb surrounding the gene. However, it is likely that this gene is at least in part controlled locally as the region surrounding the promoter is monomethylated and bound by the erythroid transcription factor GATA1 (data not shown). Bottom, MCC data

for *Cldn13* showing contacts with 25 promoters and enhancers in the surrounding 1.5 Mb. Again, this gene is likely to be controlled at least in part by local regulatory elements. **b**, MCC profiles using the promoters of *Atf5*, *Jund*, *Chd4*, *Gata2a*, *Ddit3*, *Dedd2*, *Mafg* and *Gfer* as viewpoints, show interactions in gene-dense regions. **c**, The number of interacting elements within the 2-Mb region of each viewpoint. Notably, promotor–promotor interactions dominate in these gene-dense regions.

[Source data](#)

Extended Data Fig. 6 MCC of CTCF sites at loci that are active in erythroid or ES cells shows that highly_punctate interactions occur between CTCF sites and that these correlate with the activity of the intervening chromatin.

Note that contacts from CTCF sites do not correlate strongly with DNase I hypersensitivity. **a**, Capture from the CTCF site downstream of the enhancers at the β-globin locus. This site interacts strongly and precisely with the CTCF site upstream of the genes. These sites are in a convergent orientation. These interactions are not present in ES cells when the gene is inactive despite there being similar levels of CTCF occupancy at these sites in both tissues. **b**, Capture at an intergenic CTCF site at the *Cd47* locus in erythroid cells shows strong tissue-specific interactions between convergent sites upstream that are not present in ES cells when the gene is inactive. **c**, At the *Slc25a37* locus (which encodes mitoferrin), the CTCF site downstream of the enhancers interacts strongly with the convergent CTCF site at the promoter of the gene in a tissue-specific manner. **d**, Strong and highly punctate contacts are seen between multiple CTCF sites at the gene-dense *Klf1* locus. **e**, At the *Myc* locus, highly specific, punctate contacts occur between the CTCF sites on either side of the gene and its regulatory elements. These contacts correlate with transcription (the gene is transcribed more in ES cells than erythroid cells). **f**, Similarly, at the *Sox2* locus, highly specific long-range contacts occur between CTCF sites and these are highly tissue-specific (they are absent in erythroid cells in which the gene is inactive). DNase-seq (green) and ChIP-seq of CTCF and RAD21 are shown for both erythroid cells and ES cells. The RAD21 and CTCF ChIP-seq are normalized using a spike-in of human cells.

Extended Data Fig. 7 MCC of CTCF sites in ES cells shows that highly punctate interactions occur between CTCF sites over very long ranges.

a, At *Pou5f1*, tissue-specific contacts occur with a tissue-specific CTCF-binding site that is found in ES cells but not erythroid cells. **b**, At *Klf4*, we captured from a tissue-specific CTCF site, which contacts several CTCF sites in the same orientation in the vicinity. In erythroid cells, this sequence forms no specific contacts with the surrounding chromatin. DNase-seq and ChIP-seq of CTCF and RAD21 are shown for both erythroid and ES cells. **c**, Analysis of sequencing of the unenriched Hi-C-like MNase 3C library confirms highly punctate contacts between CTCF sites from genome-wide data (heatmap with 50-bp bins $\pm 1,500$ bp from the centre of the interacting CTCF sites). **d**, The number of contacts between viewpoint CTCF sites ($n = 95$) and other CTCF sites was calculated in two separate 300-kb windows, one upstream (red) and one downstream (blue) of the viewpoint CTCF site. H3K27ac was analysed separately for both the upstream and downstream 300-kb windows to provide a global estimate of the activity of the enhancers and promoters. The linked data points represent individual loci. Higher levels of H3K27ac on one side of a CTCF site correlated highly significantly with greater numbers of inter-CTCF site contacts (Wilcoxon signed-rank test). **e**, Metaplot of ligation junctions between CTCF sites. These are separated by the relative orientation and position of the viewpoint and interacting CTCF sites. This clearly shows that the orientation and relative position of the CTCF sites strongly determines contact frequency. **f**, Effect of CTCF orientation on ligation junction counts. The x axis displays the distance relative to the viewpoint corrected for orientation of the CTCF at the viewpoint; the y axis displays the junction count corrected for the orientation of the interacting CTCF site. Data are 6 replicates, 82 viewpoints, $n = 14,010$. **g**, Proposed model for the way in which cohesin loading at active enhancer and promoter elements alters CTCF–CTCF contacts using the α -globin locus as a model. In erythroid cells, activity of the α -globin genes and enhancers leads to increased cohesin loading at these sites. This results in loop extrusion and subsequently increased contacts between the CTCF sites upstream of the enhancers and distal to the *Hba-a1* and *Hba-a2* promoters. These contacts

do not occur in ES cells, despite very similar levels of CTCF binding, because the enhancers and promoters are inactive and do not load cohesin.

[Source data](#)

Extended Data Fig. 8 Contacts from CTCF sites are highly correlated with cohesin.

a, MCC profiles of four CTCF sites with low co-occupancy of cohesin as measured by RAD21 ChIP-seq. These sites form no peaks with surrounding CTCF sites. **b**, When high levels of RAD21 coincide with CTCF, the sites form multiple contacts with surrounding CTCF sites. Profiles are included for DNase-seq and ChIP-seq of CTCF and RAD21 in erythroid cells.

Extended Data Fig. 9 Genome-wide analysis of inter-CTCF contacts and peak-calling analysis of MCC.

a, b, MCC profiles of the promoters at the α - and β -globin loci (*Hba-a1* and *Hba-a2*, and *Hbb-b1* and *Hbb-bs*, respectively), DNase-seq and ChIP-seq data of CTCF, RAD21, H3K27ac, NIPBL, GATA1, NF-E2 and KLF1. **c**. Metaplots of RAD21 and CTCF-binding density (RPKM) at the two nearest CTCF-binding sites flanking erythroid- and ES-cell-specific superenhancers in erythroid (red, $n = 190$) and ES (green, $n = 462$) cells. A significant difference in enrichment of RAD21 was found at CTCF sites flanking superenhancers in the different cell types. Higher levels of RAD21 were found at active ES superenhancers in ES cells compared with the same sequence when the enhancers are inactive in erythroid cells. Conversely higher levels of RAD21 were found at active erythroid superenhancers in erythroid cells compared with the same sequence in ES cells. CTCF-binding density of RAD21 and CTCF at random sites ($n = 500$) was quantified as a control and was similar in both cell types. Box plots of RAD21 binding (RPKM) at the two flanking CTCF-binding sites (1-kb region around the centre of the CTCF site) flanking erythroid- and ES-cell-specific superenhancers in erythroid (red) and ES (green) cells. Two-tailed Student's *t*-test; box plots show the median, interquartile range, maximum points within 1.5 \times the interquartile range of quartile 1 or 3. **d**, Heat maps of

10-kb genomic regions surrounding promoters, enhancers or CTCF-binding sites showing DNase I hypersensitivity and ChIP-seq data for H3K27ac, H3K4me3, mediator (MED1), NIPBL, RAD21 and CTCF. The chromatin loader NIPBL is highly enriched at enhancers and promoters compared with CTCF sites. **e**, Manhattan plot showing highly significant peaks of interaction irrespective of the method of peak calling ($-\log_{10}$ transformations of the P values are plotted on the y axis). The data have been peak-called with three different orthogonal methods. MACS2, a custom Poisson-based model and a machine-learning-based model. All of these methods calculate the enrichment over the background data, which has undergone targeted capture. **f**, Histogram of the percentage of peaks falling within the topologically associating domain (TAD) in erythroid cells from promoters and CTCF sites. **g**, Percentage of ligation junctions falling within the TAD in *cis* from erythroid promoters. $n = 576$, data are mean \pm s.d. **h**, Analysis of the strength of contacts at promoters with different classes of element as categorized by GenoSTAN. This analysis shows that promoters broadly contact all classes of element but have a slight predilection to contact promoters and enhancers compared with CTCF sites. By contrast, CTCF sites preferentially contact other CTCF sites compared with other categories. Normalized total numbers of junctions in the 1-kb region surrounding different classes of elements within 400 kb of the viewpoint. $n = 6$, data are mean \pm s.d., two-way ANOVA, Tukey's multiple comparisons test.

[Source data](#)

Extended Data Fig. 10 Base-pair resolution analysis of MCC ligation junctions shows that enhancer–promoter contacts generate complex patterns compared with CTCF sites.

a, Single-base-pair resolution plots of ligation junctions between two CTCF sites, showing that ligation junctions surround the central binding motifs, which are protected from MNase digestion. **b**, Superimposition of the directionality of the reads at the viewpoint and reporter site allows the precise location of the central CTCF-binding motif to be determined. **c**, Directional footprinting of the main enhancer element at the α -globin locus. **d**, Reconstructions of the contacts between the transcription factors and the

promoter using directional footprinting of the viewpoint and enhancer. **e, f**, MCC footprinting shows more complex patterns of ligation junctions at enhancers than at CTCF sites at the *Slc25a37* and *Cd47* loci. **g, h**, Reconstruction metaplots of data from the strongest 150 CTCF–CTCF interactions and 65 enhancer–promoter interactions, showing the complexity of the enhancer–promoter contacts compared with contacts between CTCF sites.

[Source data](#)

Extended Data Fig. 11 Base-pair resolution analysis of MCC ligation junctions at pleotropic enhancers in ES and erythroid cells.

a, To show that MCC could detect subtle changes in chromatin architecture, we captured from gene promoters, such as *Rad51c*, that have active promoters in both erythroid and ES cells and have adjacent hypersensitive enhancers at the same sequence in erythroid and ES cells. **b, c**, MCC data at one of the shared enhancers delineates different patterns of footprinting in erythroid and ES cells. This shows that fine-scale alterations occur in the contacts at the same sequence in the two cell types, which is probably due to differences in the transcription factor repertoire. **d–f**, The gene *Atp5a1* is also active in both erythroid (red) and ES cells (blue) (**d**) and there are contacts in both tissues with the promoter of *Haus1* (**e**) and a local enhancer (**f**). At both of these sites the footprinting is clearly different in the two tissues at sites with the same DNA sequence. This shows fine-scale changes in the contact pattern that result from differences in the DNA-binding proteins in the two cell types.

[Source data](#)

Extended Data Fig. 12 MCC profiles at the main α-globin enhancer show the specific loss of contacts when an NF-E2 site is deleted.

a, Genome editing was used to make a small 2–4-bp deletion, determined by Illumina sequencing, in an NF-E2 consensus motif in the main enhancer at the α -globin locus (termed the R2 enhancer). **b**, ChIP–qPCR showing loss of NF-E2 binding at the R2 enhancer compared with enrichment at the adjacent R1 enhancer. Wild type, $n = 6$; NF-E2 edited, $n = 8$; data mean \pm s.d., two-tailed Mann–Whitney U -test. Note that complete abrogation of NF-E2 binding would not be expected because there are two NF-E2-binding sites in the enhancer, which are separated by 26 bp. **c**, Deletion of the NF-E2-binding site at the R2 enhancer results in a significant reduction in expression of the α -globin genes in erythroid cells from normal donors that have undergone genome editing at the R2 NF-E2 site (editing efficiencies in excess of 90% with Cas9 ribonuclear protein, data not shown). $n = 7$, data are mean \pm s.d., two-tailed Mann–Whitney U -test. **d**, **e**, MCC profiles of the promoters of *HBA1* and *HBA2* in human HUDEP-2 cells (**d**), showing that the interactions with the main enhancer (R2) reduce very specifically (**e**) at the site of an engineered 2–4-bp deletion at the binding site of NF-E2. **f**, In addition, the MCC footprint is specifically altered at the NF-E2-binding site. **g**, Quantification of read depth at all other hypersensitive sites at the α -globin locus showing that the only statistically significant change is at the site of the deletion. Data from the edited clone aligned to a modified hg19 genome with the deletion; $n = 6$, data are mean \pm s.d., two-tailed Mann–Whitney U -test.

[Source data](#)

Supplementary information

[Supplementary Information](#)

This file contains explanatory notes for the columns in Supplementary Table 2.

[Reporting Summary](#)

[Supplementary Table 1](#)

This file contains a summary sheet of the metrics of the sequencing data from the different experiments carried out. In addition, there are individual sheets for each experiment provide the sequencing data metrics for each sample / viewpoint. There is also an included the analysis of the data with respect to topologically associated domains.

Supplementary Table 2

This contains a summary of all of the peak calls in the data performed by the three different methods of peak calling. See Supplementary Information PDF for an explanation of the data columns in this table.

Source data

Source Data Fig. 3

Source Data Fig.4

Source Data Extended Data Fig. 2

Source Data Extended Data Fig. 3

Source Data Extended Data Fig. 4

Source Data Extended Data Fig. 5

Source Data Extended Data Fig. 7

Source Data Extended Data Fig. 9

Source Data Extended Data Fig. 10

Source Data Extended Data Fig. 11

Source Data Extended Data Fig. 12

Rights and permissions

[Reprints and Permissions](#)

About this article



Check for
updates

Cite this article

Hua, P., Badat, M., Hanssen, L.L.P. *et al.* Defining genome architecture at base-pair resolution. *Nature* **595**, 125–129 (2021).
<https://doi.org/10.1038/s41586-021-03639-4>

[Download citation](#)

- Received: 25 February 2020
- Accepted: 13 May 2021
- Published: 09 June 2021
- Issue Date: 01 July 2021
- DOI: <https://doi.org/10.1038/s41586-021-03639-4>

[Access through your institution](#)

[Change institution](#)

[Buy or subscribe](#)

Associated Content

A base-pair view of interactions between genes and their enhancers

- Anne van Schoonhoven
- Ralph Stadhouders

Advertisement

This article was downloaded by **calibre** from <https://www.nature.com/articles/s41586-021-03639-4>

| [Section menu](#) | [Main menu](#) |

- Article
- [Published: 26 May 2021](#)

Structural basis of antifolate recognition and transport by PCFT

- [Joanne L. Parker](#) [ORCID: orcid.org/0000-0003-2964-2720](#)¹ nal,
- [Justin C. Deme](#) [ORCID: orcid.org/0000-0001-8811-9871](#)^{2,3,4} nal,
- [Gabriel Kuteyi](#)¹,
- [Zhiyi Wu](#) [ORCID: orcid.org/0000-0002-7615-7851](#)¹,
- [Jiandong Huo](#)^{5,6,7},
- [I. David Goldman](#)⁸,
- [Raymond J. Owens](#) [ORCID: orcid.org/0000-0002-3705-2993](#)^{5,6,7},
- [Philip C. Biggin](#) [ORCID: orcid.org/0000-0001-5100-8836](#)¹,
- [Susan M. Lea](#) [ORCID: orcid.org/0000-0001-9287-8053](#)^{2,3,4} &
- [Simon Newstead](#) [ORCID: orcid.org/0000-0001-7432-2270](#)^{1,9}

[Nature](#) volume 595, pages 130–134 (2021) [Cite this article](#)

- 5427 Accesses
- 40 Altmetric
- [Metrics details](#)

Subjects

- [Cryoelectron microscopy](#)
- [Drug development](#)
- [Permeation and transport](#)

Abstract

Folates (also known as vitamin B9) have a critical role in cellular metabolism as the starting point in the synthesis of nucleic acids, amino acids and the universal methylating agent *S*-adenylylmethionine^{1,2}. Folate deficiency is associated with a number of developmental, immune and neurological disorders^{3,4,5}. Mammals cannot synthesize folates de novo; several systems have therefore evolved to take up folates from the diet and distribute them within the body^{3,6}. The proton-coupled folate transporter (PCFT) (also known as SLC46A1) mediates folate uptake across the intestinal brush border membrane and the choroid plexus^{4,7}, and is an important route for the delivery of antifolate drugs in cancer chemotherapy^{8,9,10}. How PCFT recognizes folates or antifolate agents is currently unclear. Here we present cryo-electron microscopy structures of PCFT in a substrate-free state and in complex with a new-generation antifolate drug (pemetrexed). Our results provide a structural basis for understanding antifolate recognition and provide insights into the pH-regulated mechanism of folate transport mediated by PCFT.

Access options

Subscribe to Journal

Get full journal access for 1 year

\$199.00

only \$3.90 per issue

[Subscribe](#)

All prices are NET prices.

VAT will be added later in the checkout.

Tax calculation will be finalised during checkout.

Rent or Buy article

Get time limited or full article access on ReadCube.

from \$8.99

[Rent or Buy](#)

All prices are NET prices.

Additional access options:

- [Log in](#)
- [Access through your institution](#)
- [Learn about institutional subscriptions](#)

Fig. 1: Cryo-EM structure of apo and pemetrexed-bound PCFT.

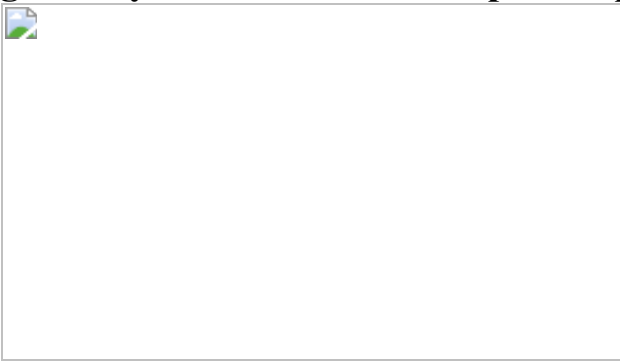


Fig. 2: Mechanism of proton coupling.

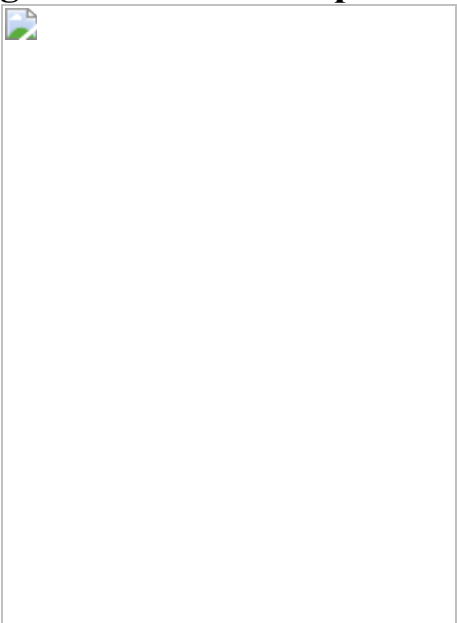
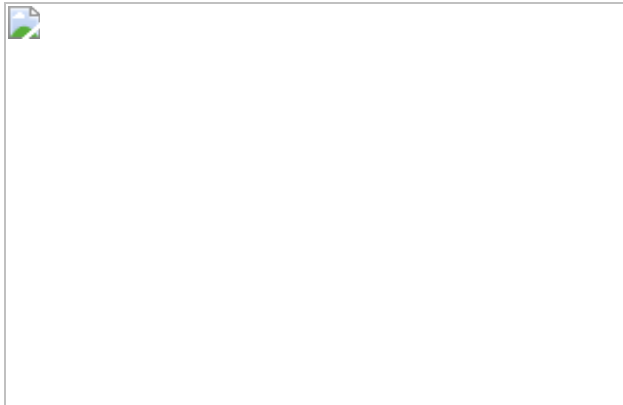


Fig. 3: Alternating-access transport mechanism and antifolate-binding model.



Data availability

The plasmid encoding the chicken PCFT transporter cloned into the pDDGFP-LEU2d expression vector is available from Addgene (165414). The plasmid encoding the nanobody used in this study is available from Addgene (165415). Coordinates for the structures have been deposited in the Protein Data Bank under accession codes PDB [7BC6](#) (PCFT–nanobody) and [7BC7](#) (PCFT–nanobody + pemetrexed). The electron microscopy volumes have been deposited in the Electron Microscopy Data Bank under accession codes [EMD-12140](#) (PCFT–nanobody) and [EMD-12141](#) (PCFT–nanobody + pemetrexed). Any other relevant data are available from the corresponding authors upon reasonable request.

References

1. 1.

Zheng, Y. & Cantley, L. C. Toward a better understanding of folate metabolism in health and disease. *J. Exp. Med.* **216**, 253–266 (2019).

[CAS](#) [PubMed](#) [PubMed Central](#) [Google Scholar](#)

2. 2.

Ducker, G. S. & Rabinowitz, J. D. One-carbon metabolism in health and disease. *Cell Metab.* **25**, 27–42 (2017).

[CAS](#) [PubMed](#) [Google Scholar](#)

3. 3.

Zhao, R., Matherly, L. H. & Goldman, I. D. Membrane transporters and folate homeostasis: intestinal absorption and transport into systemic compartments and tissues. *Expert Rev. Mol. Med.* **11**, e4 (2009).

[PubMed](#) [PubMed Central](#) [Google Scholar](#)

4. 4.

Zhao, R., Aluri, S. & Goldman, I. D. The proton-coupled folate transporter (PCFT-SLC46A1) and the syndrome of systemic and cerebral folate deficiency of infancy: Hereditary folate malabsorption. *Mol. Aspects Med.* **53**, 57–72 (2017).

[CAS](#) [PubMed](#) [Google Scholar](#)

5. 5.

Lucock, M. Folic acid: nutritional biochemistry, molecular biology, and role in disease processes. *Mol. Genet. Metab.* **71**, 121–138 (2000).

[CAS](#) [PubMed](#) [Google Scholar](#)

6. 6.

Zhao, R. & Goldman, I. D. Folate and thiamine transporters mediated by facilitative carriers (SLC19A1-3 and SLC46A1) and folate receptors. *Mol. Aspects Med.* **34**, 373–385 (2013).

[PubMed](#) [Google Scholar](#)

7. 7.

Qiu, A. et al. Identification of an intestinal folate transporter and the molecular basis for hereditary folate malabsorption. *Cell* **127**, 917–928

(2006).

[CAS](#) [PubMed](#) [Google Scholar](#)

8. 8.

Goldman, I. D., Chattopadhyay, S., Zhao, R. & Moran, R. The antifolates: evolution, new agents in the clinic, and how targeting delivery via specific membrane transporters is driving the development of a next generation of folate analogs. *Curr. Opin. Investig. Drugs* **11**, 1409–1423 (2010).

[CAS](#) [PubMed](#) [Google Scholar](#)

9. 9.

Matherly, L. H., Hou, Z. & Gangjee, A. The promise and challenges of exploiting the proton-coupled folate transporter for selective therapeutic targeting of cancer. *Cancer Chemother. Pharmacol.* **81**, 1–15 (2018).

[PubMed](#) [Google Scholar](#)

10. 10.

Zhao, R. et al. The proton-coupled folate transporter: impact on pemetrexed transport and on antifolates activities compared with the reduced folate carrier. *Mol. Pharmacol.* **74**, 854–862 (2008).

[CAS](#) [PubMed](#) [Google Scholar](#)

11. 11.

Bailey, L. B. *Folate in Health and Disease*, 2nd edn (Taylor & Francis, 2010).

12. 12.

Crider, K. S., Bailey, L. B. & Berry, R. J. Folic acid food fortification—its history, effect, concerns, and future directions. *Nutrients* **3**, 370–384 (2011).

[PubMed](#) [PubMed Central](#) [Google Scholar](#)

13. 13.

Visentin, M., Diop-Bove, N., Zhao, R. & Goldman, I. D. The intestinal absorption of folates. *Annu. Rev. Physiol.* **76**, 251–274 (2014).

[CAS](#) [PubMed](#) [PubMed Central](#) [Google Scholar](#)

14. 14.

Kamen, B. A. & Smith, A. K. A review of folate receptor alpha cycling and 5-methyltetrahydrofolate accumulation with an emphasis on cell models in vitro. *Adv. Drug Deliv. Rev.* **56**, 1085–1097 (2004).

[CAS](#) [PubMed](#) [Google Scholar](#)

15. 15.

Zhao, R. et al. A role for the proton-coupled folate transporter (PCFT-SLC46A1) in folate receptor-mediated endocytosis. *J. Biol. Chem.* **284**, 4267–4274 (2009).

[CAS](#) [PubMed](#) [PubMed Central](#) [Google Scholar](#)

16. 16.

Matherly, L. H., Wilson, M. R. & Hou, Z. The major facilitative folate transporters solute carrier 19A1 and solute carrier 46A1: biology and role in antifolate chemotherapy of cancer. *Drug Metab. Dispos.* **42**, 632–649 (2014).

[PubMed](#) [PubMed Central](#) [Google Scholar](#)

17. 17.

Qiu, A. et al. Rodent intestinal folate transporters (SLC46A1): secondary structure, functional properties, and response to dietary folate restriction. *Am. J. Physiol. Cell Physiol.* **293**, C1669–C1678 (2007).

[CAS](#) [PubMed](#) [Google Scholar](#)

18. 18.

Kronn, D. & Goldman, I. D. in *GeneReviews* (eds Adam, M. P. et al.) <https://www.ncbi.nlm.nih.gov/books/NBK1673/> (1993).

19. 19.

Furst, D. E. The rational use of methotrexate in rheumatoid arthritis and other rheumatic diseases. *Br. J. Rheumatol.* **36**, 1196–1204 (1997).

[CAS](#) [PubMed](#) [Google Scholar](#)

20. 20.

Giovannetti, E. et al. Role of proton-coupled folate transporter in pemetrexed resistance of mesothelioma: clinical evidence and new pharmacological tools. *Ann. Oncol.* **28**, 2725–2732 (2017).

[CAS](#) [PubMed](#) [PubMed Central](#) [Google Scholar](#)

21. 21.

Chattopadhyay, S., Moran, R. G. & Goldman, I. D. Pemetrexed: biochemical and cellular pharmacology, mechanisms, and clinical applications. *Mol. Cancer Ther.* **6**, 404–417 (2007).

[CAS](#) [PubMed](#) [Google Scholar](#)

22. 22.

Pascale, R. M., Calvisi, D. F., Simile, M. M., Feo, C. F. & Feo, F. The Warburg effect 97 years after its discovery. *Cancers* **12**, E2819 (2020).

[PubMed](#) [Google Scholar](#)

23. 23.

Desmoulin, S. K., Hou, Z., Gangjee, A. & Matherly, L. H. The human proton-coupled folate transporter: biology and therapeutic applications to cancer. *Cancer Biol. Ther.* **13**, 1355–1373 (2012).

[CAS](#) [PubMed](#) [PubMed Central](#) [Google Scholar](#)

24. 24.

Drew, D. & Boudker, O. Shared molecular mechanisms of membrane transporters. *Annu. Rev. Biochem.* **85**, 543–572 (2016).

[CAS](#) [PubMed](#) [Google Scholar](#)

25. 25.

Huang, Y., Lemieux, M. J., Song, J., Auer, M. & Wang, D.-N. Structure and mechanism of the glycerol-3-phosphate transporter from *Escherichia coli*. *Science* **301**, 616–620 (2003).

[ADS](#) [CAS](#) [PubMed](#) [Google Scholar](#)

26. 26.

Shin, D. S., Zhao, R., Fiser, A. & Goldman, I. D. Role of the fourth transmembrane domain in proton-coupled folate transporter function as assessed by the substituted cysteine accessibility method. *Am. J. Physiol. Cell Physiol.* **304**, C1159–C1167 (2013).

[CAS](#) [PubMed](#) [PubMed Central](#) [Google Scholar](#)

27. 27.

Chen, L. Q. & Pagel, M. D. Evaluating pH in the extracellular tumor microenvironment using CEST MRI and other imaging methods. *Adv. Radiol.* **2015**, 206405 (2015).

[PubMed](#) [PubMed Central](#) [Google Scholar](#)

28. 28.

Mahadeo, K. et al. Properties of the Arg376 residue of the proton-coupled folate transporter (PCFT–SLC46A1) and a glutamine mutant causing hereditary folate malabsorption. *Am. J. Physiol. Cell Physiol.* **299**, C1153–C1161 (2010).

[CAS](#) [Google Scholar](#)

29. 29.

Shin, D. S. et al. Functional roles of aspartate residues of the proton-coupled folate transporter (PCFT-SLC46A1); a D156Y mutation causing hereditary folate malabsorption. *Blood* **116**, 5162–5169 (2010).

[CAS](#) [PubMed](#) [PubMed Central](#) [Google Scholar](#)

30. 30.

Unal, E. S., Zhao, R. & Goldman, I. D. Role of the glutamate 185 residue in proton translocation mediated by the proton-coupled folate transporter SLC46A1. *Am. J. Physiol. Cell Physiol.* **297**, C66–C74 (2009).

[CAS](#) [PubMed](#) [PubMed Central](#) [Google Scholar](#)

31. 31.

Unal, E. S. et al. The functional roles of the His247 and His281 residues in folate and proton translocation mediated by the human proton-coupled folate transporter SLC46A1. *J. Biol. Chem.* **284**, 17846–17857 (2009).

[CAS](#) [PubMed](#) [PubMed Central](#) [Google Scholar](#)

32. 32.

Desmoulin, S. K. et al. Targeting the proton-coupled folate transporter for selective delivery of 6-substituted pyrrolo[2,3-*d*]pyrimidine antifolate inhibitors of de novo purine biosynthesis in the chemotherapy of solid tumors. *Mol. Pharmacol.* **78**, 577–587 (2010).

[CAS](#) [PubMed](#) [PubMed Central](#) [Google Scholar](#)

33. 33.

Wang, L. et al. Synthesis and antitumor activity of a novel series of 6-substituted pyrrolo[2,3-*d*]pyrimidine thienoyl antifolate inhibitors of purine biosynthesis with selectivity for high affinity folate receptors and the proton-coupled folate transporter over the reduced folate carrier for cellular entry. *J. Med. Chem.* **53**, 1306–1318 (2010).

[CAS](#) [PubMed](#) [PubMed Central](#) [Google Scholar](#)

34. 34.

Parker, J. L. & Newstead, S. Method to increase the yield of eukaryotic membrane protein expression in *Saccharomyces cerevisiae* for structural and functional studies. *Protein Sci.* **23**, 1309–1314 (2014).

[CAS](#) [PubMed](#) [PubMed Central](#) [Google Scholar](#)

35. 35.

Diop-Bove, N. K., Wu, J., Zhao, R., Locker, J. & Goldman, I. D. Hypermethylation of the human proton-coupled folate transporter (SLC46A1) minimal transcriptional regulatory region in an antifolate-resistant HeLa cell line. *Mol. Cancer Ther.* **8**, 2424–2431 (2009).

[CAS](#) [PubMed](#) [PubMed Central](#) [Google Scholar](#)

36. 36.

Zhao, R., Gao, F., Hanscom, M. & Goldman, I. D. A prominent low-pH methotrexate transport activity in human solid tumors: contribution to the preservation of methotrexate pharmacologic activity in HeLa

cells lacking the reduced folate carrier. *Clin. Cancer Res.* **10**, 718–727 (2004).

[CAS](#) [PubMed](#) [Google Scholar](#)

37. 37.

Huo, J. et al. Neutralizing nanobodies bind SARS-CoV-2 spike RBD and block interaction with ACE2. *Nat. Struct. Mol. Biol.* **27**, 846–854 (2020).

[CAS](#) [PubMed](#) [Google Scholar](#)

38. 38.

Pardon, E. et al. A general protocol for the generation of nanobodies for structural biology. *Nat. Protocols* **9**, 674–693 (2014).

[CAS](#) [PubMed](#) [Google Scholar](#)

39. 39.

Caesar, J. et al. SIMPLE 3.0. Stream single-particle cryo-EM analysis in real time. *J. Struct. Biol.* **X4**, 100040 (2020).

[CAS](#) [PubMed](#) [PubMed Central](#) [Google Scholar](#)

40. 40.

Punjani, A., Rubinstein, J. L., Fleet, D. J. & Brubaker, M. A. cryoSPARC: algorithms for rapid unsupervised cryo-EM structure determination. *Nat. Methods* **14**, 290–296 (2017).

[CAS](#) [PubMed](#) [Google Scholar](#)

41. 41.

Zivanov, J. et al. New tools for automated high-resolution cryo-EM structure determination in RELION-3. *eLife* **7**, e42166 (2018).

[PubMed](#) [PubMed Central](#) [Google Scholar](#)

42. 42.

Asarnow, D., Palovcak, E. & Cheng, Y. UCSF pyem v.0.5.,
<https://doi.org/10.5281/zenodo.3576630> (2019).

43. 43.

Tan, Y. Z. et al. Addressing preferred specimen orientation in single-particle cryo-EM through tilting. *Nat. Methods* **14**, 793–796 (2017).

[CAS](#) [PubMed](#) [PubMed Central](#) [Google Scholar](#)

44. 44.

Brown, A. et al. Tools for macromolecular model building and refinement into electron cryo-microscopy reconstructions. *Acta Crystallogr. D* **71**, 136–153 (2015).

[CAS](#) [PubMed](#) [PubMed Central](#) [Google Scholar](#)

45. 45.

Afonine, P. V. et al. Real-space refinement in PHENIX for cryo-EM and crystallography. *Acta Crystallogr. D* **74**, 531–544 (2018).

[CAS](#) [Google Scholar](#)

46. 46.

Emsley, P. Tools for ligand validation in Coot. *Acta Crystallogr. D* **73**, 203–210 (2017).

[CAS](#) [Google Scholar](#)

47. 47.

Moriarty, N. W., Grosse-Kunstleve, R. W. & Adams, P. D. Electronic Ligand Builder and Optimization Workbench (eLBOW): a tool for ligand coordinate and restraint generation. *Acta Crystallogr. D* **65**, 1074–1080 (2009).

[CAS](#) [PubMed](#) [PubMed Central](#) [Google Scholar](#)

48. 48.

Prisant, M. G., Williams, C. J., Chen, V. B., Richardson, J. S. & Richardson, D. C. New tools in MolProbity validation: CaBLAM for cryoEM backbone, UnDowser to rethink “waters,” and NGL viewer to recapture online 3D graphics. *Protein Sci.* **29**, 315–329 (2020).

[CAS](#) [PubMed](#) [Google Scholar](#)

49. 49.

Pettersen, E. F. et al. UCSF ChimeraX: structure visualization for researchers, educators, and developers. *Protein Sci.* **30**, 70–82 (2021).

[CAS](#) [PubMed](#) [Google Scholar](#)

50. 50.

Marrink, S. J., Risselada, H. J., Yefimov, S., Tieleman, D. P. & de Vries, A. H. The MARTINI force field: coarse grained model for biomolecular simulations. *J. Phys. Chem. B* **111**, 7812–7824 (2007).

[CAS](#) [PubMed](#) [Google Scholar](#)

51. 51.

Wu, Z., Alibay, I., Newstead, S. & Biggin, P. C. Proton control of transitions in an amino acid transporter. *Biophys. J.* **117**, 1342–1351 (2019).

[ADS](#) [CAS](#) [PubMed](#) [PubMed Central](#) [Google Scholar](#)

52. 52.

Vickery, O. & Corey, R. owenvickery/cg2at: CG2AT2 a fragment based conversion version 0.2, <https://doi.org/10.5281/zenodo.3994618> (2020).

53. 53.

Maier, J. A. et al. ff14SB: improving the accuracy of protein side chain and backbone parameters from ff99SB. *J. Chem. Theory Comput.* **11**, 3696–3713 (2015).

[CAS](#) [PubMed](#) [PubMed Central](#) [Google Scholar](#)

54. 54.

Jämbeck, J. P. M. & Lyubartsev, A. P. An extension and further validation of an all-atomistic force field for biological membranes. *J. Chem. Theory Comput.* **8**, 2938–2948 (2012).

[PubMed](#) [Google Scholar](#)

55. 55.

Petrova, J. et al. Molecular simulation of the structure of folate and antifolates at physiological conditions. *J. Mol. Graph. Model.* **87**, 172–184 (2019).

[CAS](#) [PubMed](#) [Google Scholar](#)

56. 56.

Wang, J., Wolf, R. M., Caldwell, J. W., Kollman, P. A. & Case, D. A. Development and testing of a general amber force field. *J. Comput. Chem.* **25**, 1157–1174 (2004).

[CAS](#) [PubMed](#) [Google Scholar](#)

57. 57.

Bayly, C. I., Cieplak, P., Cornell, W. & Kollman, P. A. A well-behaved electrostatic potential based method using charge restraints for deriving atomic charges: the RESP model. *J. Phys. Chem.* **97**, 10269–10280 (1993).

[CAS](#) [Google Scholar](#)

58. 58.

Jorgensen, W. L., Chandrasekhar, J., Madura, J. D., Impey, R. W. & Klein, M. L. Comparison of simple potential functions for simulating liquid water. *J. Chem. Phys.* **79**, 926–935 (1983).

[ADS](#) [CAS](#) [Google Scholar](#)

59. 59.

Abraham, M. J. et al. GROMACS: high performance molecular simulations through multi-level parallelism from laptops to supercomputers. *SoftwareX* **1-2**, 19–25 (2015).

[ADS](#) [Google Scholar](#)

60. 60.

Bussi, G., Donadio, D. & Parrinello, M. Canonical sampling through velocity rescaling. *J. Chem. Phys.* **126**, 014101 (2007).

[ADS](#) [Google Scholar](#)

61. 61.

Berendsen, H. J., Postma, J. P. M., van Gunsteren, W. F., DiNola, A. & Haak, J. R. Molecular dynamics with coupling to an external bath. *J. Chem. Phys.* **81**, 3684–3690 (1984).

[ADS](#) [CAS](#) [Google Scholar](#)

62. 62.

Parrinello, M. & Rahman, A. Polymorphic transitions in single crystals: a new molecular dynamics method. *J. Appl. Phys.* **52**, 7182–7190 (1981).

[ADS](#) [CAS](#) [Google Scholar](#)

63. 63.

Michaud-Agrawal, N., Denning, E. J., Woolf, T. B. & Beckstein, O. MDAnalysis: a toolkit for the analysis of molecular dynamics simulations. *J. Comput. Chem.* **32**, 2319–2327 (2011).

[CAS](#) [PubMed](#) [PubMed Central](#) [Google Scholar](#)

64. 64.

Gapsys, V., Michielssens, S., Seeliger, D. & de Groot, B. L. pmx: automated protein structure and topology generation for alchemical perturbations. *J. Comput. Chem.* **36**, 348–354 (2015).

[CAS](#) [PubMed](#) [Google Scholar](#)

65. 65.

Goga, N., Rzepiela, A. J., de Vries, A. H., Marrink, S. J. & Berendsen, H. J. Efficient algorithms for Langevin and DPD dynamics. *J. Chem. Theory Comput.* **8**, 3637–3649 (2012).

[CAS](#) [PubMed](#) [Google Scholar](#)

66. 66.

Klimovich, P. V., Shirts, M. R. & Mobley, D. L. Guidelines for the analysis of free energy calculations. *J. Comput. Aided Mol. Des.* **29**, 397–411 (2015).

[ADS](#) [CAS](#) [PubMed](#) [PubMed Central](#) [Google Scholar](#)

67. 67.

Wu, Z. Alchemicalitp: a Gromacs parser for alchemical transformation version 0.1, <https://github.com/xiki-tempula/alchemicalitp> (2020).

68. 68.

The PLUMED consortium. Promoting transparency and reproducibility in enhanced molecular simulations. *Nat. Methods* **16**, 670–673 (2019).

[Google Scholar](#)

69. 69.

Grossfield, A. WHAM: the weighted histogram analysis method version 2.0.10.2., http://membrane.urmc.rochester.edu/wordpress/?page_id=126 (accessed 2020).

[Download references](#)

Acknowledgements

The Central Oxford Structural Microscopy and Imaging Centre is supported by the Wellcome Trust (201536), the EPA Cephalosporin Trust and a Royal Society/Wolfson Foundation Laboratory Refurbishment Grant (WL160052). Computing was supported via the Advanced Research Computing facility (Oxford), the ARCHER UK National Supercomputing Service and JADE (EP/P020275/1) granted via the High-End Computing Consortium for Biomolecular Simulation, (HECBioSim (<http://www.hecbiosim.ac.uk>)), supported by EPSRC (EP/L000253/1). This research was supported by Wellcome awards to S.M.L. (209194;100298), P.C.B. (219531) and S.N. (215519;219531) and through MRC grants to S.M.L. (MR/M011984/1) and J.L.P. (MR/S021043/1). Z.W. is a Wellcome Trust PhD student (203741). Figures were created using BioRender.com, PyMol and ChimeraX.

Author information

Author notes

1. These authors contributed equally: Joanne L. Parker, Justin C. Deme

Affiliations

1. Department of Biochemistry, University of Oxford, Oxford, UK

Joanne L. Parker, Gabriel Kuteyi, Zhiyi Wu, Philip C. Biggin & Simon Newstead

2. Dunn School of Pathology, University of Oxford, Oxford, UK

Justin C. Deme & Susan M. Lea

3. Central Oxford Structural Molecular Imaging Centre, University of Oxford, Oxford, UK

Justin C. Deme & Susan M. Lea

4. Center for Structural Biology, Center for Cancer Research, National Cancer Institute, Frederick, MD, USA

Justin C. Deme & Susan M. Lea

5. Structural Biology, The Rosalind Franklin Institute, Didcot, UK

Jiandong Huo & Raymond J. Owens

6. Division of Structural Biology, The Wellcome Centre for Human Genetics, University of Oxford, Oxford, UK

Jiandong Huo & Raymond J. Owens

7. Protein Production UK, The Research Complex at Harwell, Didcot, UK

Jiandong Huo & Raymond J. Owens

8. Departments of Molecular Pharmacology and Medicine, Albert Einstein College of Medicine, New York, NY, USA
I. David Goldman
9. The Kavli Institute for Nanoscience Discovery, University of Oxford, Oxford, UK
Simon Newstead

Authors

1. Joanne L. Parker
[View author publications](#)
You can also search for this author in [PubMed](#) [Google Scholar](#)
2. Justin C. Deme
[View author publications](#)
You can also search for this author in [PubMed](#) [Google Scholar](#)
3. Gabriel Kuteyi
[View author publications](#)
You can also search for this author in [PubMed](#) [Google Scholar](#)
4. Zhiyi Wu
[View author publications](#)
You can also search for this author in [PubMed](#) [Google Scholar](#)
5. Jiandong Huo
[View author publications](#)
You can also search for this author in [PubMed](#) [Google Scholar](#)
6. I. David Goldman
[View author publications](#)

You can also search for this author in [PubMed](#) [Google Scholar](#)

7. Raymond J. Owens

[View author publications](#)

You can also search for this author in [PubMed](#) [Google Scholar](#)

8. Philip C. Biggin

[View author publications](#)

You can also search for this author in [PubMed](#) [Google Scholar](#)

9. Susan M. Lea

[View author publications](#)

You can also search for this author in [PubMed](#) [Google Scholar](#)

10. Simon Newstead

[View author publications](#)

You can also search for this author in [PubMed](#) [Google Scholar](#)

Contributions

J.L.P. and S.N. conceived the project. G.K. maintained cell stocks, and undertook large-scale expression and tissue culture. J.L.P. and S.N. performed all protein preparation. J.H. and R.J.O. screened the Abcore library. J.C.D. and S.M.L. performed all cryo-EM sample processing, data collection and image analysis. J.C.D., S.M.L. and S.N. constructed the atomic models. I.D.G. contributed the HeLa-derived cell line HeLa R1-11, and provided insights into human mutations and physiology. J.L.P. conducted all transport and biochemical assays. Z.W. and P.C.B. performed all molecular dynamics analysis. J.L.P. and S.N. wrote the manuscript and prepared figures, with contributions and discussions from Z.W., I.D.G., P.C.B., J.C.D. and S.M.L. G.K. and Z.W. contributed equally to this work.

Corresponding authors

Correspondence to [Joanne L. Parker](#) or [Susan M. Lea](#) or [Simon Newstead](#).

Ethics declarations

Competing interests

The authors declare no competing interests.

Additional information

Peer review information *Nature* thanks Larry H. Matherley, D. J. Slotboom and the other, anonymous, reviewer(s) for their contribution to the peer review of this work. Peer reviewer reports are available.

Publisher's note Springer Nature remains neutral with regard to jurisdictional claims in published maps and institutional affiliations.

Extended data figures and tables

[Extended Data Fig. 1 Comparison of human and chicken PCFT homologues.](#)

a, Sequence alignment of PCFT from human (Hs) (Uniprot Q96NT5) and chicken (Gg) (E6Y8U5) coloured via amino acid chemistry. Human and chicken PCFT homologues share an overall 58% identity and 87% similarity. Functionally relevant residues are highlighted with yellow stars, and mutations found to cause hereditary folate malabsorption disorder are in red. **b**, Cell-based uptake assay comparing the transport of ^3H folic acid via human and chicken PCFT at both pH 5.5 and 7.5. The human and chicken homologues transport similar amounts of folic acid to each other and do so only at acidic pH (5.5). $n = 4$ independent experiments, mean and s.d. are shown. **c**, Pemetrexed competition of ^3H folic acid uptake into cells, overexpressing either human or chicken PCFT. The calculated mean (from 4 independent experiments) half-maximal inhibitory concentration values are indicated \pm s.d. **d**, Calculated K_M for folic acid uptake at pH 5.5 by

chicken PCFT in a liposome-based uptake assay. $n = 3$ independent experiments, calculated mean and s.d. values are shown **e**, Effect of pH on PCFT uptake in a liposome-based assay. $n = 3$ independent experiments, with the mean and s.d. shown. **f**, Membrane potential induced through potassium diffusion gradient (plus valinomycin) does not affect transport, an observation that has also been seen for human PCFT in cells³⁴, suggesting that transport is thermodynamically coupled to two protons (assuming a -2 charge on folic acid). $n = 4$ independent experiments, data are mean and s.d.

Extended Data Fig. 2 Characterization of high-affinity nanobody to PCFT.

a, The nanobody identified from a naive llama library has a K_D of about 8 nM for PCFT binding. $n = 3$ independent experiments, calculated mean \pm s.d. shown. **b**, The nanobody blocks uptake of folic acid into liposomes containing PCFT, whereas a non-specific nanobody has no effect. $n = 3$ independent experiments, mean and s.d. shown. **c**, SDS-PAGE analysis of the PCFT–nanobody complex after size exclusion. Experiment was performed four times with similar results. **d**, Representative gel filtration trace of chicken PCFT in DDM:CHS detergent at pH 6.5. The protein elutes as a monomer of about 50 kDa. Insets show Coomassie-stained SDS-PAGE gel of the purified PCFT protein and circular dichroism analysis. Experiment was repeated eight times with similar results. **e**, Analysis of the thermostability of PCFT under different pH conditions (7.5 and 5.5) indicates that acidic pH stabilizes the protein. The presence of both folic acid (FA) or pemetrexed (PMX) further stabilize the protein, but only at acidic pH. Experiments were repeated three times with similar results.

Extended Data Fig. 3 Cryo-EM processing workflow, showing local and global map quality for the PCFT–nanobody complex.

a, Image processing workflow for PCFT–nanobody. **b**, Local-resolution estimation of reconstructed map as determined within RELION. Detergent density omitted for clarity. **c**, Gold-standard FSC curves used for global-resolution estimates within (i) cryoSPARC, (ii) RELION, or (iii) 3DFSC. **d**,

Close-up view of map and side-chain density for transmembrane helices and lateral helix. Volume contoured at threshold level of 0.805.

Extended Data Fig. 4 Analysis of PCFT–pemetrexed complex.

a, Cryo-EM density of PCFT in complex with pemetrexed and nanobody. **b**, In molecular dynamics simulations of the apo structure (grey), the TM1–TM2 loop is positioned such that the entrance to the binding pocket is accessible. In simulations with pemetrexed bound (orange), the loop closes quickly (within 250 ns) as measured by the relative position of Ser68 on the TM1–TM2 loop and Ala308 on the TM7–TM8 loop. **c**, Time course of the distance between the C α atoms of Ser68 and Ala308 for both apo (grey) and pemetrexed-bound (orange) simulations. The closure event observed with pemetrexed bound occurs around 250 ns, and this closed conformation remains stable for the remainder of the simulation. On removal of pemetrexed from the end of the simulation shown in this panel (orange), the TM1–TM2 moves away from the TM7–TM8 loop (blue). The movement is shown in **b** (cyan). **d**, The presence of 2 mM DTT does not alter the uptake of folic acid into liposomes by PCFT, consistent with previous studies on the human transporter³⁵. **e**, The presence of 2 mM DTT does lead to a destabilization of the protein as determined by differential scanning fluorimetry. **f**, View of pemetrexed within the binding cavity, with surface charge highlighted. **g**, Schematic of the binding pose observed for pemetrexed. Hydrogen-bond donors and acceptors are highlighted by directional arrows, the sole charge–charge interaction by a solid line and the π – π interaction in orange. Values indicate distance in Å.

Extended Data Fig. 5 Structural relationship between the observed water pocket and the gating helices in PCFT.

a, Cartoon of PCFT, showing the open and closed states of the extracellular and intracellular gates, respectively. **b**, Molecular dynamic simulations demonstrate the water pocket is both stable and accessible to bulk solvent via the substrate-binding cavity. The space occupied by the polar pocket results in fewer interactions between TM7 and TM10, which is likely to facilitate the movement of the helices against one another during transport.

Extended Data Fig. 6 Cryo-EM processing workflow, showing local and global map quality for the PCFT–nanobody complex bound to pemetrexed.

a, Image processing workflow for pemetrexed-bound PCFT–nanobody. **b**, Local-resolution estimation of reconstructed map as determined within RELION. Detergent density omitted for clarity. Top, full map; bottom, central slab through map. **c**, Gold-standard FSC curves used for global resolution estimates within (i) cryoSPARC, (ii) RELION or (iii) 3DFSC. **d**, Close-up of side-chain density for all transmembrane helices. Volume contoured at threshold level of 0.3. **e**, Density for pemetrexed (PMX) and side chains surrounding PCFT. Volume contoured at threshold level of 0.4.

Extended Data Fig. 7 The effect of Glu407Asn on apo and pemetrexed-bound PCFT and hereditary folate malabsorption mutations in the context of the chicken PCFT structure.

a–e, Alchemical transformations show that a Glu407Asn mutation would stabilize the protein by forming hydrogen bonds with Asn166, while remaining capable of preserving the interaction with the pyrrole amine of pemetrexed. **a**, In the wild-type apo state Glu407 does not interact with Asn166. The Glu407Asn variant, however, can readily hydrogen-bond with Asn166 (**b**), resulting in the Glu407Asn variant being 1.5 kcal mol⁻¹ more stable (**e**) (blue). In the pemetrexed-bound state, Glu407 makes a hydrogen bond with the pyrrole amine group of pemetrexed (PMX) (**c**), which is also preserved in the Glu407Asn variant (**d**). The coordinated hydrogen-bond network among Asn166, Glu407Asn and pemetrexed further stabilizes the protein-bound state by 2 kcal mol⁻¹ compared to the apo state (**e**) (orange). $n = 3$ independent repeats with mean and s.d. plotted. **f**, Cartoon of chicken PCFT structure with residues involved in hereditary folate malabsorption shown as spheres. Asp164 (Asp156) and Arg384 (Arg376) are highlighted as these residues have an important role in the transport mechanism. The table shows the corresponding human residue number and the associated phenotype. PubMed identifiers for the respective studies that describe mutations associated with hereditary folate malabsorption are included.

Extended Data Fig. 8 Analysis of residues involved in proton binding in PCFT.

a, Analysis of wild type and variants of chicken PCFT studied in liposome assays. SDS-PAGE gel showing pre- and post-solubilization of proteoliposomes with 1% DDM:CHS. A proportion of purified PCFT is not folded correctly in the liposome and runs as aggregates on the pre-solubilized samples in the SDS-PAGE gel. Experiments were repeated three times with similar results. **b**, Protonation of D164 results in easier breakage of the salt bridge interaction to R156. There is a free energy barrier of 2 kcal mol⁻¹ associated with the breakage of the R156–D164 salt bridge in the apo state (i and ii). The protonation of the D164 (D^H164) would lower this free energy barrier to a level lower than 0.5 kcal mol⁻¹ (iii and iv) and thus bring it under the level of thermal fluctuation. The presence of pemetrexed does not affect this process. Rather, it controls the likelihood that D164 is protonated in the first place and thus effects the salt bridge stability indirectly. **c**, Convergence of the PMF profile shown in **b**. The PMF profile is computed for the first 20% (blue), 40% (orange), 60% (green), 80% (red) and 100% (purple) of the data. The columns are three repeats of the calculations. **d**, Convergence plots of the protonation free energy. The forward plot (orange lines) is the protonation free energy computed from the first 10% up to 100% of data, in 10% increments. The backward plot (blue lines) is the protonation free energy computed from the final 10% up to 100% of the data, in 10% increments. The columns are three repeats of the calculations. The green line is the final estimate of the free energy for each simulation and the width shows the uncertainty in the multistate Bennet acceptance ratio calculation. **e**, Table showing calculated pK_a and free energy values (mean \pm s.d.). **f**, Western blot analysis of the cell-based assay using an anti-Flag antibody for the PCFT variants and a loading control of anti-β-actin. Experiments were repeated twice with similar results.

Extended Data Fig. 9 Model for ligand-induced closure of the extracellular gate.

a, Structure of PCFT highlighting the extracellular gate helices, TM7 and TM8 (red) and their relationship to the bound pemetrexed molecule (yellow). The arrow indicates the movement required to seal the binding site from the extracellular side of the membrane. The interaction of Phe290 with the benzyl group of pemetrexed is likely to have an important role in triggering gate closure. **b**, Structural comparison between the apo and pemetrexed-bound states reveals repositioning of His289, resulting in the breakage of its interaction with Asn350 and facilitating the movement of TM7. The water pocket substantially enlarges in the pemetrexed-bound state, consistent with greater flexibility in the C-terminal bundle under acidic conditions.

Extended Data Table 1 Cryo-EM data collection, refinement and validation statistics

[Full size table](#)

Supplementary information

[Supplementary Figure](#)

Original SDS PAGE gels used to generate Extended Data Figures 2c, 2d and 8a.

[Reporting Summary](#)

[Peer Review File](#)

Rights and permissions

[Reprints and Permissions](#)

About this article



Check for
updates

Cite this article

Parker, J.L., Deme, J.C., Kuteyi, G. *et al.* Structural basis of antifolate recognition and transport by PCFT. *Nature* **595**, 130–134 (2021).
<https://doi.org/10.1038/s41586-021-03579-z>

[Download citation](#)

- Received: 19 December 2020
- Accepted: 23 April 2021
- Published: 26 May 2021
- Issue Date: 01 July 2021
- DOI: <https://doi.org/10.1038/s41586-021-03579-z>

[Access through your institution](#)

[Change institution](#)

[Buy or subscribe](#)

Advertisement

This article was downloaded by **calibre** from <https://www.nature.com/articles/s41586-021-03579-z>

Amendments & Corrections

- [**Author Correction: Spike mutation D614G alters SARS-CoV-2 fitness**](#) [15 June 2021]
Author Correction •
- [**Author Correction: REV-ERB in GABAergic neurons controls diurnal hepatic insulin sensitivity**](#) [15 June 2021]
Author Correction •
- [**Author Correction: A pooled testing strategy for identifying SARS-CoV-2 at low prevalence**](#) [16 June 2021]
Author Correction •

Author Correction: Spike mutation D614G alters SARS-CoV-2 fitness
[Download PDF](#)

- Author Correction
- [Published: 15 June 2021](#)

Author Correction: Spike mutation D614G alters SARS-CoV-2 fitness

- [Jessica A. Plante](#) ORCID: [orcid.org/0000-0002-4768-7458^{1,2,3}](https://orcid.org/0000-0002-4768-7458) na1,
- [Yang Liu⁴](#) na1,
- [Jianying Liu^{2,3}](#) na1,
- [Hongjie Xia](#) ORCID: [orcid.org/0000-0002-2520-7038⁴](https://orcid.org/0000-0002-2520-7038),
- [Bryan A. Johnson²](#),
- [Kumari G. Lokugamage³](#),
- [Xianwen Zhang⁴](#),
- [Antonio E. Muruato^{2,3}](#),
- [Jing Zou⁴](#),
- [Camila R. Fontes-Garfias⁴](#),
- [Divya Mirchandani^{1,2,3}](#),
- [Dionna Scharton^{1,2,3}](#),
- [John P. Bilello](#) ORCID: [orcid.org/0000-0003-4327-1727⁵](https://orcid.org/0000-0003-4327-1727),
- [Zhiqiang Ku⁶](#),
- [Zhiqiang An⁶](#),
- [Birte Kalveram⁷](#),
- [Alexander N. Freiberg^{2,7,8,9}](#),
- [Vineet D. Menachery^{2,3}](#),
- [Xuping Xie](#) ORCID: [orcid.org/0000-0003-0918-016X⁴](https://orcid.org/0000-0003-0918-016X),
- [Kenneth S. Plante](#) ORCID: [orcid.org/0000-0002-7485-3167^{1,2,3}](https://orcid.org/0000-0002-7485-3167),
- [Scott C. Weaver](#) ORCID: [orcid.org/0000-0001-8016-8556^{1,2,3,8,9,10,11}](https://orcid.org/0000-0001-8016-8556) &

- [Pei-Yong Shi](#) [ORCID: orcid.org/0000-0001-5553-1616^{2,4,8,9,10,11}](#)

[*Nature*](#) volume **595**, page E1 (2021)[Cite this article](#)

- 370 Accesses
- 1 Altmetric
- [Metrics details](#)

Subjects

- [SARS-CoV-2](#)
- [Viral transmission](#)

The [Original Article](#) was published on 26 October 2020

[Download PDF](#)

Correction to: *Nature* <https://doi.org/10.1038/s41586-020-2895-3> Published online 26 October 2020

In the Acknowledgements section of this Article, the NIH grant ‘AI142759’ was incorrectly cited. The correct NIH grants that supported the research should be ‘AI134907, AI145617 and UL1TR001439’. The original Article has been corrected online.

Author information

Author notes

1. These Authors contributed equally: Jessica A. Plante, Yang Liu, Jianying Liu

Affiliations

1. World Reference Center for Emerging Viruses and Arboviruses,
University of Texas Medical Branch, Galveston, TX, USA

Jessica A. Plante, Divya Mirchandani, Dionna Scharton, Kenneth S. Plante & Scott C. Weaver

2. Institute for Human Infections and Immunity, University of Texas
Medical Branch, Galveston, TX, USA

Jessica A. Plante, Jianying Liu, Bryan A. Johnson, Antonio E. Muruato, Divya Mirchandani, Dionna Scharton, Alexander N. Freiberg, Vineet D. Menachery, Kenneth S. Plante, Scott C. Weaver & Pei-Yong Shi

3. Department of Microbiology and Immunology, University of Texas
Medical Branch, Galveston, TX, USA

Jessica A. Plante, Jianying Liu, Kumari G. Lokugamage, Antonio E. Muruato, Divya Mirchandani, Dionna Scharton, Vineet D. Menachery, Kenneth S. Plante & Scott C. Weaver

4. Department of Biochemistry and Molecular Biology, University of
Texas Medical Branch, Galveston, TX, USA

Yang Liu, Hongjie Xia, Xianwen Zhang, Jing Zou, Camila R. Fontes-Garfias, Xuping Xie & Pei-Yong Shi

5. Gilead Sciences, Foster City, CA, USA

John P. Bilello

6. Texas Therapeutics Institute, Brown Foundation Institute of Molecular Medicine, University of Texas Health Science Center at Houston, Houston, TX, USA

Zhiqiang Ku & Zhiqiang An

7. Department of Pathology, University of Texas Medical Branch, Galveston, TX, USA

Birte Kalveram & Alexander N. Freiberg

8. Center for Biodefense and Emerging Infectious Diseases, University of Texas Medical Branch, Galveston, TX, USA

Alexander N. Freiberg, Scott C. Weaver & Pei-Yong Shi

9. Sealy Institute for Vaccine Sciences, University of Texas Medical Branch, Galveston, TX, USA

Alexander N. Freiberg, Scott C. Weaver & Pei-Yong Shi

10. Institute for Translational Sciences, University of Texas Medical Branch, Galveston, TX, USA

Scott C. Weaver & Pei-Yong Shi

11. Sealy Center for Structural Biology and Molecular Biophysics, University of Texas Medical Branch, Galveston, TX, USA

Scott C. Weaver & Pei-Yong Shi

Authors

1. Jessica A. Plante

[View author publications](#)

You can also search for this author in [PubMed](#) [Google Scholar](#)

2. Yang Liu

[View author publications](#)

You can also search for this author in [PubMed](#) [Google Scholar](#)

3. Jianying Liu

[View author publications](#)

You can also search for this author in [PubMed](#) [Google Scholar](#)

4. Hongjie Xia

[View author publications](#)

You can also search for this author in [PubMed](#) [Google Scholar](#)

5. Bryan A. Johnson

[View author publications](#)

You can also search for this author in [PubMed](#) [Google Scholar](#)

6. Kumari G. Lokugamage

[View author publications](#)

You can also search for this author in [PubMed](#) [Google Scholar](#)

7. Xianwen Zhang

[View author publications](#)

You can also search for this author in [PubMed](#) [Google Scholar](#)

8. Antonio E. Muruato

[View author publications](#)

You can also search for this author in [PubMed](#) [Google Scholar](#)

9. Jing Zou

[View author publications](#)

You can also search for this author in [PubMed](#) [Google Scholar](#)

10. Camila R. Fontes-Garfias

[View author publications](#)

You can also search for this author in [PubMed](#) [Google Scholar](#)

11. Divya Mirchandani

[View author publications](#)

You can also search for this author in [PubMed](#) [Google Scholar](#)

12. Dionna Scharton

[View author publications](#)

You can also search for this author in [PubMed](#) [Google Scholar](#)

13. John P. Bilello

[View author publications](#)

You can also search for this author in [PubMed](#) [Google Scholar](#)

14. Zhiqiang Ku

[View author publications](#)

You can also search for this author in [PubMed](#) [Google Scholar](#)

15. Zhiqiang An

[View author publications](#)

You can also search for this author in [PubMed](#) [Google Scholar](#)

16. Birte Kalveram

[View author publications](#)

You can also search for this author in [PubMed](#) [Google Scholar](#)

17. Alexander N. Freiberg

[View author publications](#)

You can also search for this author in [PubMed](#) [Google Scholar](#)

18. Vineet D. Menachery

[View author publications](#)

You can also search for this author in [PubMed](#) [Google Scholar](#)

19. Xuping Xie

[View author publications](#)

You can also search for this author in [PubMed](#) [Google Scholar](#)

20. Kenneth S. Plante

[View author publications](#)

You can also search for this author in [PubMed](#) [Google Scholar](#)

21. Scott C. Weaver

[View author publications](#)

You can also search for this author in [PubMed](#) [Google Scholar](#)

22. Pei-Yong Shi

[View author publications](#)

You can also search for this author in [PubMed](#) [Google Scholar](#)

Corresponding authors

Correspondence to [Xuping Xie](#) or [Kenneth S. Plante](#) or [Scott C. Weaver](#) or [Pei-Yong Shi](#).

Rights and permissions

[Reprints and Permissions](#)

About this article



Check for
updates

Cite this article

Plante, J.A., Liu, Y., Liu, J. *et al.* Author Correction: Spike mutation D614G alters SARS-CoV-2 fitness. *Nature* **595**, E1 (2021).

<https://doi.org/10.1038/s41586-021-03657-2>

Download citation

- Published: 15 June 2021
- Issue Date: 01 July 2021
- DOI: <https://doi.org/10.1038/s41586-021-03657-2>

Download PDF

Advertisement

This article was downloaded by **calibre** from <https://www.nature.com/articles/s41586-021-03657-2>

| [Section menu](#) | [Main menu](#) |

Author Correction: REV-ERB in GABAergic neurons controls diurnal hepatic insulin sensitivity

[Download PDF](#)

- Author Correction
- [Published: 15 June 2021](#)

Author Correction: REV-ERB in GABAergic neurons controls diurnal hepatic insulin sensitivity

- [Guolian Ding](#)^{1,2,3 na1},
- [Xin Li](#)^{3 na1},
- [Xinguo Hou](#) [ORCID: orcid.org/0000-0003-2045-1290](#)^{4 na1},
- [Wenjun Zhou](#)^{3 na1},
- [Yingyun Gong](#) [ORCID: orcid.org/0000-0002-8570-6904](#)^{3,5},
- [Fuqiang Liu](#)⁴,
- [Yanlin He](#) [ORCID: orcid.org/0000-0002-5471-9016](#)^{6,7},
- [Jia Song](#)⁴,
- [Jing Wang](#)⁴,
- [Paul Basil](#)³,
- [Wenbo Li](#) [ORCID: orcid.org/0000-0002-9126-2529](#)³,
- [Sichong Qian](#)³,
- [Pradip Saha](#)^{3,8},
- [Jinbang Wang](#)⁴,
- [Chen Cui](#)⁴,
- [Tingting Yang](#)^{3,6},
- [Kexin Zou](#)^{1,2},
- [Younghun Han](#)⁹,
- [Christopher I. Amos](#)⁹,
- [Yong Xu](#) [ORCID: orcid.org/0000-0002-4908-1572](#)^{6,8},

- [Li Chen](#) ORCID: [orcid.org/0000-0001-7670-8062⁴](https://orcid.org/0000-0001-7670-8062) &
- [Zheng Sun](#) ORCID: [orcid.org/0000-0002-6858-0633^{3,8}](https://orcid.org/0000-0002-6858-0633)

Nature volume **595**, page E2 (2021)[Cite this article](#)

- 367 Accesses
- 3 Altmetric
- [Metrics details](#)

Subjects

- [Hypothalamus](#)
- [Type 2 diabetes](#)

The [Original Article](#) was published on 24 March 2021

[Download PDF](#)

Correction to: *Nature* <https://doi.org/10.1038/s41586-021-03358-w>
Published online 24 March 2021

We would like to add more information to this Article about the knockout mice used, to increase clarity and transparency. The sentence ‘The REV-ERB- α allele generates a truncated protein without a DNA-binding domain⁸ upon Cre recombination and, therefore, could lead to a functionally hypomorphic knockout and/or have effects on transcription that are independent of DNA binding.’ has thererfore been added after the sentence ‘To assess the function of REV-ERB- α and REV-ERB- β in GABAergic neurons, we generated mice with a GABAergic-neuron-specific knockout of REV-ERB- α and REV-ERB- β (hereafter, knockout mice) by crossbreeding *Nr1d1*^{loxP}*Nr1d2*^{loxP} double-floxed mice^{7,8} with *Vgat-ires-cre* (*vbat-cre*) mice.’. The original Article has been corrected online.

Author information

Author notes

1. These authors contributed equally: Guolian Ding, Xin Li, Xinguo Hou, Wenjun Zhou

Affiliations

1. Obstetrics and Gynecology Hospital, Institute of Reproduction and Development, Fudan University, Shanghai, China

Guolian Ding & Kexin Zou

2. Shanghai Key Laboratory of Embryo Original Diseases, Shanghai, China

Guolian Ding & Kexin Zou

3. Department of Medicine, Division of Diabetes, Endocrinology and Metabolism, Baylor College of Medicine, Houston, TX, USA

Guolian Ding, Xin Li, Wenjun Zhou, Yingyun Gong, Paul Basil, Wenbo Li, Sichong Qian, Pradip Saha, Tingting Yang & Zheng Sun

4. Department of Endocrinology, Qilu Hospital of Shandong University, Jinan, China

Xinguo Hou, Fuqiang Liu, Jia Song, Jing Wang, Jinbang Wang, Chen Cui & Li Chen

5. Department of Endocrinology and Metabolism, The First Affiliated Hospital of Nanjing Medical University, Nanjing, China

Yingyun Gong

6. USDA/ARS Children's Nutrition Research Center, Department of Pediatrics, Baylor College of Medicine, Houston, TX, USA

Yanlin He, Tingting Yang & Yong Xu

7. Laboratory of Brain Glycemia and Metabolism Control, Pennington Biomedical Research Center, Baton Rouge, LA, USA

Yanlin He

8. Department of Molecular and Cellular Biology, Baylor College of Medicine, Houston, TX, USA

Pradip Saha, Yong Xu & Zheng Sun

9. Department of Medicine, Section of Epidemiology and Population Sciences, Baylor College of Medicine, Houston, TX, USA

Younghun Han & Christopher I. Amos

Authors

1. Guolian Ding

[View author publications](#)

You can also search for this author in [PubMed](#) [Google Scholar](#)

2. Xin Li

[View author publications](#)

You can also search for this author in [PubMed](#) [Google Scholar](#)

3. Xinguo Hou

[View author publications](#)

You can also search for this author in [PubMed](#) [Google Scholar](#)

4. Wenjun Zhou

[View author publications](#)

You can also search for this author in [PubMed](#) [Google Scholar](#)

5. Yingyun Gong

[View author publications](#)

You can also search for this author in [PubMed](#) [Google Scholar](#)

6. Fuqiang Liu

[View author publications](#)

You can also search for this author in [PubMed](#) [Google Scholar](#)

7. Yanlin He

[View author publications](#)

You can also search for this author in [PubMed](#) [Google Scholar](#)

8. Jia Song

[View author publications](#)

You can also search for this author in [PubMed](#) [Google Scholar](#)

9. Jing Wang

[View author publications](#)

You can also search for this author in [PubMed](#) [Google Scholar](#)

10. Paul Basil

[View author publications](#)

You can also search for this author in [PubMed](#) [Google Scholar](#)

11. Wenbo Li

[View author publications](#)

You can also search for this author in [PubMed](#) [Google Scholar](#)

12. Sichong Qian

[View author publications](#)

You can also search for this author in [PubMed](#) [Google Scholar](#)

13. Pradip Saha

[View author publications](#)

You can also search for this author in [PubMed](#) [Google Scholar](#)

14. Jinbang Wang

[View author publications](#)

You can also search for this author in [PubMed](#) [Google Scholar](#)

15. Chen Cui

[View author publications](#)

You can also search for this author in [PubMed](#) [Google Scholar](#)

16. Tingting Yang

[View author publications](#)

You can also search for this author in [PubMed](#) [Google Scholar](#)

17. Kexin Zou

[View author publications](#)

You can also search for this author in [PubMed](#) [Google Scholar](#)

18. Younghun Han

[View author publications](#)

You can also search for this author in [PubMed](#) [Google Scholar](#)

19. Christopher I. Amos

[View author publications](#)

You can also search for this author in [PubMed](#) [Google Scholar](#)

20. Yong Xu

[View author publications](#)

You can also search for this author in [PubMed](#) [Google Scholar](#)

21. Li Chen

[View author publications](#)

You can also search for this author in [PubMed](#) [Google Scholar](#)

22. Zheng Sun

[View author publications](#)

You can also search for this author in [PubMed](#) [Google Scholar](#)

Corresponding authors

Correspondence to [Li Chen](#) or [Zheng Sun](#).

Rights and permissions

[Reprints and Permissions](#)

About this article



Check for
updates

Cite this article

Ding, G., Li, X., Hou, X. *et al.* Author Correction: REV-ERB in GABAergic neurons controls diurnal hepatic insulin sensitivity. *Nature* **595**, E2 (2021). <https://doi.org/10.1038/s41586-021-03654-5>

[Download citation](#)

- Published: 15 June 2021
- Issue Date: 01 July 2021
- DOI: <https://doi.org/10.1038/s41586-021-03654-5>

[Download PDF](#)

Advertisement

This article was downloaded by **calibre** from <https://www.nature.com/articles/s41586-021-03654-5>

| [Section menu](#) | [Main menu](#) |

Author Correction: A pooled testing strategy for identifying SARS-CoV-2 at low prevalence

[Download PDF](#)

- Author Correction
- [Published: 16 June 2021](#)

Author Correction: A pooled testing strategy for identifying SARS-CoV-2 at low prevalence

- [Leon Mutesa](#) ORCID: [orcid.org/0000-0002-5308-3706](#)^{1,2},
- [Pacificque Ndishimye](#)^{2,3},
- [Yvan Butera](#) ORCID: [orcid.org/0000-0002-0648-2384](#)^{1,2},
- [Jacob Souopgui](#) ORCID: [orcid.org/0000-0003-1526-4431](#)^{1,2,4},
- [Annette Uwineza](#)^{1,2},
- [Robert Rutayisire](#)^{1,2},
- [Ella Larissa Ndoricimpaye](#)²,
- [Emile Musoni](#)²,
- [Nadine Rujeni](#)²,
- [Thierry Nyatanyi](#)²,
- [Edouard Ntagwabira](#)²,
- [Muhammed Semakula](#)²,
- [Clarisse Musanabaganwa](#)²,
- [Daniel Nyamwasa](#)²,
- [Maurice Ndashimye](#)^{2,3},
- [Eva Ujeneza](#) ORCID: [orcid.org/0000-0002-5760-4847](#)³,
- [Ivan Emile Mwikarago](#)²,
- [Claude Mambo Muvunyi](#)²,
- [Jean Baptiste Mazarati](#)²,
- [Sabin Nsanzimana](#)²,
- [Neil Turok](#) ORCID: [orcid.org/0000-0002-1891-8691](#)^{3,5,6} &
- [Wilfred Ndifon](#) ORCID: [orcid.org/0000-0001-6022-432X](#)³

- 333 Accesses
- 2 Altmetric
- [Metrics details](#)

Subjects

- [Population screening](#)
- [SARS-CoV-2](#)
- [Viral infection](#)

The [Original Article](#) was published on 21 October 2020

[Download PDF](#)

Correction to: *Nature* <https://doi.org/10.1038/s41586-020-2885-5> Published online 21 October 2020

In Fig. 2 of this Article, the C_t values for the *orf1ab* gene (shown in Fig. 2b) in samples B16121 and B16122 at 20 \times , 50 \times and 100 \times dilution were accidental duplications of those of the *N* gene (shown in Fig. 2a). The C_t values for *orf1ab* have been corrected in Fig. 2 of the original Article, and Fig. 1 of this Amendment shows the original and corrected Fig. 2b, for transparency. As B16121 and B16122 are both low- C_t samples, this change has no effect on our conclusion that typical samples are easily detected after 100-fold dilution.

Fig. 1: This figure shows the incorrect, as-published version and the corrected version of Fig. 2b of the original Article



[Full size image](#)

In Extended Data Table 2 of this Article, which presents the source data for Fig. 2, the *orf1ab* C_t values for sample B16121 were incorrectly given as 29, 29.74 and 30.54 for 20 \times , 50 \times and 100 \times dilution, respectively, instead of 31, 30.51 and 30.95, respectively. In addition, the *orf1ab* C_t values for sample B16122 were incorrectly given as 26.81, 27.75 and 29.07 for 20 \times , 50 \times and 100 \times dilution, respectively, instead of 28.5, 29.4 and 30.2, respectively. Extended Data Table 2 of the original Article has been corrected online. We thank T. Carey for drawing this error to our attention. The original Article has been corrected online.

Author information

Affiliations

1. Centre for Human Genetics, College of Medicine and Health Sciences, University of Rwanda, Kigali, Rwanda

Leon Mutesa, Yvan Butera, Jacob Souopgui, Annette Uwineza & Robert Rutayisire

2. Rwanda Joint Task Force COVID-19, Rwanda Biomedical Centre, Ministry of Health, Kigali, Rwanda

Leon Mutesa, Pacifique Ndishimye, Yvan Butera, Jacob Souopgui, Annette Uwineza, Robert Rutayisire, Ella Larissa Ndoricimpaye, Emile Musoni, Nadine Rujeni, Thierry Nyatanyi, Edouard Ntagwabira, Muhammed Semakula, Clarisse Musanabaganwa, Daniel Nyamwasa, Maurice Ndashimye, Ivan Emile Mwikarago, Claude Mambo Muvunyi, Jean Baptiste Mazarati & Sabin Nsanzimana

3. African Institute for Mathematical Sciences, Kigali, Rwanda

Pacifique Ndishimye, Maurice Ndashimye, Eva Ujeneza, Neil Turok & Wilfred Ndifon

4. Department of Molecular Biology, Institute of Biology and Molecular Medicine, IBMM, Université Libre de Bruxelles, Gosselies, Belgium

Jacob Souopgui

5. School of Physics and Astronomy, University of Edinburgh, Edinburgh, UK

Neil Turok

6. Perimeter Institute for Theoretical Physics, Waterloo, Ontario, Canada

Neil Turok

Authors

1. Leon Mutesa

[View author publications](#)

You can also search for this author in [PubMed](#) [Google Scholar](#)

2. Pacifique Ndishimye

[View author publications](#)

You can also search for this author in [PubMed](#) [Google Scholar](#)

3. Yvan Butera

[View author publications](#)

You can also search for this author in [PubMed](#) [Google Scholar](#)

4. Jacob Souopgui

[View author publications](#)

You can also search for this author in [PubMed](#) [Google Scholar](#)

5. Annette Uwineza

[View author publications](#)

You can also search for this author in [PubMed](#) [Google Scholar](#)

6. Robert Rutayisire

[View author publications](#)

You can also search for this author in [PubMed](#) [Google Scholar](#)

7. Ella Larissa Ndoricimpaye

[View author publications](#)

You can also search for this author in [PubMed](#) [Google Scholar](#)

8. Emile Musoni

[View author publications](#)

You can also search for this author in [PubMed](#) [Google Scholar](#)

9. Nadine Rujeni

[View author publications](#)

You can also search for this author in [PubMed](#) [Google Scholar](#)

10. Thierry Nyatanyi

[View author publications](#)

You can also search for this author in [PubMed](#) [Google Scholar](#)

11. Edouard Ntagwabira

[View author publications](#)

You can also search for this author in [PubMed](#) [Google Scholar](#)

12. Muhammed Semakula

[View author publications](#)

You can also search for this author in [PubMed](#) [Google Scholar](#)

13. Clarisse Musanabaganwa

[View author publications](#)

You can also search for this author in [PubMed](#) [Google Scholar](#)

14. Daniel Nyamwasa

[View author publications](#)

You can also search for this author in [PubMed](#) [Google Scholar](#)

15. Maurice Ndashimye

[View author publications](#)

You can also search for this author in [PubMed](#) [Google Scholar](#)

16. Eva Ujeneza

[View author publications](#)

You can also search for this author in [PubMed](#) [Google Scholar](#)

17. Ivan Emile Mwikarago

[View author publications](#)

You can also search for this author in [PubMed](#) [Google Scholar](#)

18. Claude Mambo Muvunyi

[View author publications](#)

You can also search for this author in [PubMed](#) [Google Scholar](#)

19. Jean Baptiste Mazarati

[View author publications](#)

You can also search for this author in [PubMed](#) [Google Scholar](#)

20. Sabin Nsanzimana

[View author publications](#)

You can also search for this author in [PubMed](#) [Google Scholar](#)

21. Neil Turok

[View author publications](#)

You can also search for this author in [PubMed](#) [Google Scholar](#)

22. Wilfred Ndifon

[View author publications](#)

You can also search for this author in [PubMed](#) [Google Scholar](#)

Corresponding authors

Correspondence to [Neil Turok](#) or [Wilfred Ndifon](#).

Rights and permissions

[Reprints and Permissions](#)

About this article



Check for
updates

Cite this article

Mutesa, L., Ndishimye, P., Butera, Y. *et al.* Author Correction: A pooled testing strategy for identifying SARS-CoV-2 at low prevalence. *Nature* **595**, E3 (2021).
<https://doi.org/10.1038/s41586-021-03630-z>

[Download citation](#)

- Published: 16 June 2021
- Issue Date: 01 July 2021
- DOI: <https://doi.org/10.1038/s41586-021-03630-z>

[Download PDF](#)

Advertisement

This article was downloaded by **calibre** from <https://www.nature.com/articles/s41586-021-03630-z>

| [Section menu](#) | [Main menu](#) |

Nature Index